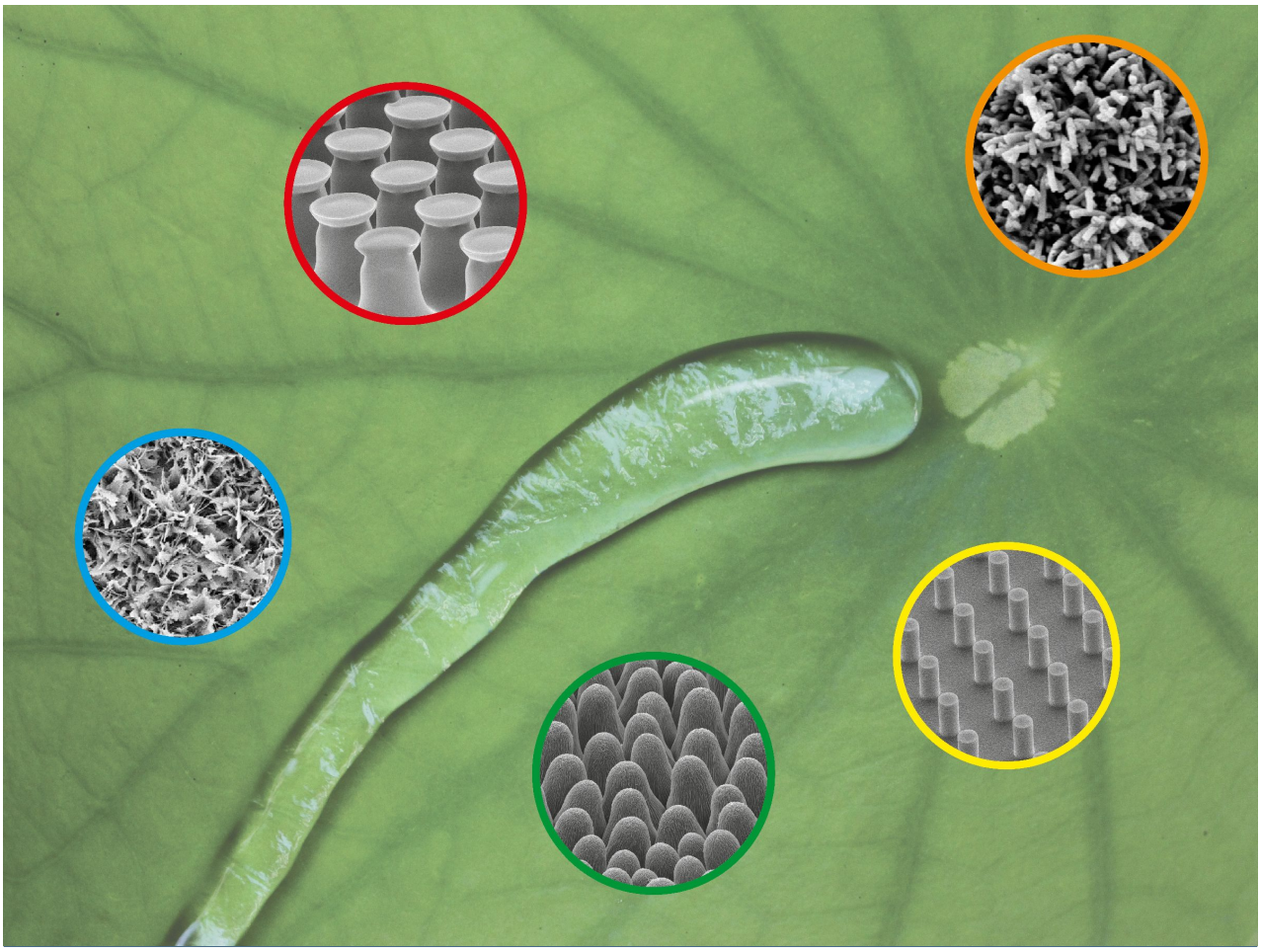
BEILSTEIN JOURNAL OF NANOTECHNOLOGY

Biomimetics on the micro- and nanoscale – The 25th anniversary of the lotus effect

Edited by Matthias Mail, Kerstin Koch, Thomas Speck, William Megill, Stanislav Gorb



Generated on 07 February 2026, 08:43

Imprint

Beilstein Journal of Nanotechnology
www.bjnano.org
ISSN 2190-4286
Email: journals-support@beilstein-institut.de

The *Beilstein Journal of Nanotechnology* is published by the Beilstein-Institut zur Förderung der Chemischen Wissenschaften.

Beilstein-Institut zur Förderung der Chemischen Wissenschaften
Trakehner Straße 7–9
60487 Frankfurt am Main
Germany
www.beilstein-institut.de

The copyright to this document as a whole, which is published in the *Beilstein Journal of Nanotechnology*, is held by the Beilstein-Institut zur Förderung der Chemischen Wissenschaften. The copyright to the individual articles in this document is held by the respective authors, subject to a Creative Commons Attribution license.

The cover image, copyright 2023 Matthias Mail is licensed under the Creative Commons Attribution 4.0 license (https://creativecommons.org/licenses/by/4.0). The reuse, redistribution or reproduction requires that the author, source and license are credited.

BEILSTEIN JOURNAL OF NANOTECHNOLOGY

Biomimetics on the micro- and nanoscale – The 25th anniversary of the lotus effect

Matthias Mail*[1], Kerstin Koch[2], Thomas Speck[3,4,5], William M. Megill[6] and Stanislav N. Gorb[7]

Editorial

Open Access

Address:
[1]Institute of Nanotechnology (INT), Karlsruhe Institute of Technology (KIT), Hermann-von-Helmholtz-Platz 1, D-76344 Eggenstein-Leopoldshafen, Germany, [2]Faculty of Life Sciences, Rhine-Waal University of Applied Sciences, D-47533 Kleve, Germany, [3]Plant Biomechanics Group, Botanic Garden, Faculty of Biology, University of Freiburg, Schänzlestrasse 1, D-79104 Freiburg, Germany, [4]FIT, Freiburg Center for Interactive Materials and Bioinspired Technologies, Georges-Köhler-Allee 105, D-79110 Freiburg, Germany, [5]FMF, Freiburg Materials Research Center, Stefan-Meier-Strasse 21, D-79104 Freiburg, Germany, [6]Centre for Biomimetic and Natural Technologies, Faculty of Technology and Bionics, Rhine-Waal University of Applied Sciences, Marie-Curie-Str. 1, D-47533 Kleve, Germany and [7]Department of Functional Morphology and Biomechanics, Institute of Zoology, Christian-Albrechts-University of Kiel, Am Botanischen Garten 1–9, D-24118 Kiel, Germany

Email:
Matthias Mail* - matthias.mail@kit.edu

* Corresponding author

Keywords:
biomimetic surfaces; hydrophobicity; lotus effect; Salvinia effect; superhydrophobicity; wettability

Beilstein J. Nanotechnol. **2023,** *14,* 850–856.
https://doi.org/10.3762/bjnano.14.69

Received: 06 July 2023
Accepted: 17 July 2023
Published: 03 August 2023

This article is part of the thematic issue "Biomimetics on the micro- and nanoscale – The 25th anniversary of the lotus effect".

Editor-in-Chief: G. Wilde

© 2023 Mail et al.; licensee Beilstein-Institut.
License and terms: see end of document.

In 1997, Wilhelm Barthlott and Christoph Neinhuis published the paper “Purity of the sacred lotus” [1] in which they described the superhydrophobic surfaces and the self-cleaning ability of some plants (the so-called “lotus effect”, see Figure 1). This paper led to a paradigm shift in surface sciences. It generated a lot of interest at the time and continues today to inspire numerous publications and technical developments [2]. Although the phenomenon of the outstanding water repellence of some plant surfaces had been known for over 2000 years, the functional principle behind it and the detailed physicochemistry of superhydrophobic biological surfaces had remained unexplored [3]. Uncovering this water repellence mechanism led to a revolution in the development of such surfaces, which promise huge potential for inspiration for technical innovations and applications.

In 2022, we celebrated the 25th anniversary of this significant botanical publication, which was an important milestone for the field of biomimetics. We, the guest editors of this thematic issue, could imagine no better way to celebrate that achievement than to gather a new set of publications in the fields of biology and materials science. In fact, these publications iden-

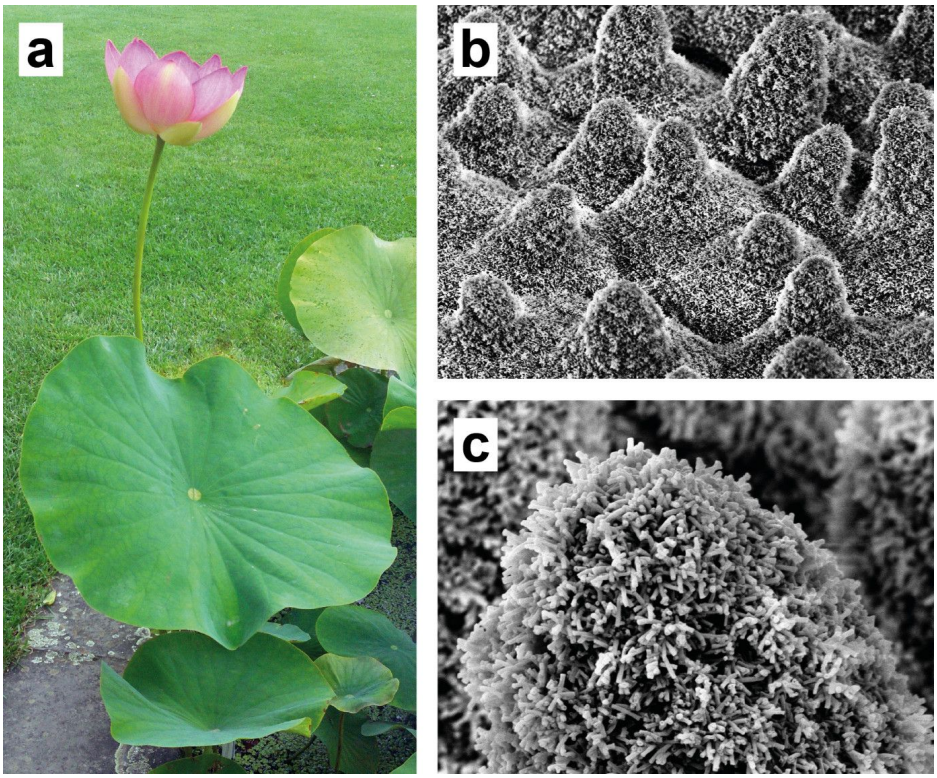


Figure 1: Biological archetype and eponym of the lotus effect: The sacred lotus (*Nelumbo nucifera*). a) Photo of a lotus plant. b) Scanning electron microscopy (SEM) image of the hierarchically structured surface of a lotus leaf. The first level of the surface structure consists of papillae formed by epidermal cells with a height and diameter of several microns. c) This structure is covered by wax crystals, leading to the extreme superhydrophobicity of the surface.

tify current topics in surface biomimetics and provide an overview of the development of superhydrophobic and self-cleaning biological and bioinspired surfaces over the past 25 years.

The field that today is called "biomimetics" is almost as old as human history. Many examples in the literature show that in the early days of humankind the concept of "copying" nature or learning from it arose (e.g., the story of Daedalus and Icarus [4]). This and other examples show that often physical phenomena in animals and plants can be described; however, it is not possible to immediately understand the mechanisms behind them and to transfer those to actual applications. This was also the case with the lotus effect.

Biomimetics was finally given a name in the second half of the last century, interestingly just as humankind was finally achieving Icarus's dream of flying closer to the sun. The big push in the field came with the rapid development of new research techniques and methodologies that enabled detailed investigation of biological archetypes. High-detail microscopy, analysis systems, and novel simulation tools helped to decode the secrets of nature, while new fabrication techniques helped to transfer these findings into technical applications. In the last decades, production methods have enabled the transfer of many outstanding properties of the biological archetypes into innovative biomimetic products at reasonable cost.

These developments helped to bring the field of biomimetics forward, initially by fostering interest in biomimetic approaches, and finally by establishing biomimetics as its own field of science. In this thematic issue, we have gathered 15 publications from several fields of interest, showing the huge diversity of biomimetic approaches.

Surapaneni et al. [5] present in the paper "Polarity in cuticular ridge development and insect attachment on leaf surfaces of *Schismatoglottis calyptrata* (Araceae)" a study of the development of cuticular ridges on the adaxial leaf surfaces during leaf ontogeny of the tropical Araceae *S. calyptrata*. The structure of these microscopic ridges helps plants to defend themselves against pest insects by reducing the frictional forces experienced when they walk on the leaves. This structure might also provide mechanical stability to the growing plant organs and has an impact on the wettability of the leaves. Using polymer replicas of adaxial leaf surfaces at various scales, the surface

structure was quantitatively described with confocal laser scanning microscopy and a surface analysis software. The data show a polar development of cuticular ridges and a basipetal ridge progression during leaf ontogeny. Traction experiments with Colorado potato beetles as model species showed low walking frictional forces on both, freshly unrolled leaves as well as adult leaves. These results extend the understanding of the mechanisms used by plants to defend themselves against herbivorous insects by changes in the leaf morphology on the macro- and microscale.

Li et al. [6], in the paper “Effect of sample treatment on the elastic modulus of locust cuticle obtained by nanoindentation”, investigate the mechanical properties of the cuticle that builds the surface of insects and related groups of animals. The cuticle is one of the most abundant, but least studied biological composites. In their study, the authors use a nanoindentation technique to investigate the effect of freezing, desiccation, and rehydration on the elastic modulus of the hind tibial cuticle of locusts. All of the treatments significantly influenced the mechanical properties of the latter.

Gorb et al. [7], in the paper “Hierachical epicuticular wax coverage on leaves of *Deschampsia antarctica* as a possible adaptation to severe environmental conditions”, used cryo-scanning electron microscopy to study surfaces of *D. antarctica*, one of the only two flowering plants native to Antarctica. The results show that the two-layered wax, which densely covers both leaf surfaces, contributes to the plant's adaptation to severe environmental conditions in Antarctica by increasing its resistance to cold temperatures, icing, harmful UV radiation, and dehydration.

In the paper “Micro-structures, nanomechanical properties and flight performance of three beetles with different folding ratios”, Sun et al. [8] use modern, high-precision instruments to uncover the relationship between wing morphology and flight performance of three species of beetles. They use a high-speed camera to track flapping frequency, quantify the surface geometry of the wings with a super depth-of-field microscope, measure cross-sections of veins of wings via SEM, and characterize the nanomechanical structural and elastic behaviour of the structures using a nanoindenter. The authors use the detailed observations obtained to explore the relative aerodynamical performance of the three species of beetles flying tethered in a wind tunnel. The results show that at low wind speeds, typical during insect flight, the species with the highest folding ratio and highest flapping frequencies produced the highest lift-to-drag ratio. The results are in agreement with other studies of flapping insects with high aspect-ratio wings. The authors then relate the aerodynamic performance of the three species studied to the behavioural ecology requirements of their niches to generate exciting avenues of bioinspiration for flapping micro-air-vehicles.

Bargel et al. [9] discuss in their review paper “Bioselectivity of silk protein-based materials and their bio-inspired applications” the importance of tailoring bioselective, biologically active, and multifunctional materials for biomedical applications in biomaterial research. The review was focused on two major topics, the first one being biological processes and surface interactions involved in the bioselective adhesion of mammalian cells. The second topic of the review was on repellence of microbes on protein-based material surfaces, highlighting the importance of materials made of recombinant spider silk proteins. Biomaterials that stimulate and interact with cell receptors to support binding and subsequent physiological responses of multicellular systems have attracted much interest in the last years. This holds especially true for materials that exhibit microbial repellence or antimicrobial behaviour to reduce inflammation, while at the same time selectively enhance regeneration in host tissues. The authors point out that in this context, protein-based materials and especially silk materials are interesting candidates due to their natural origin, biological activity, and structural properties. These exciting recombinant production technologies allow for application-specific modification to develop adjustable, bioactive materials as shown in this review article.

In the paper "Design of a biomimetic, small-scale artificial leaf surface for the study of environmental interactions" by Huth et al. [10], the authors developed wax-coated artificial leaf surfaces with chemical composition and wettability of wheat (*Triticum aestivum*) leaves. Such artificial leaves are of interest for in vitro studies of interactions of plant surfaces with living organisms and the non-living environment, as demonstrated by Huth et al. [11], where the artificial leaves were used to investigate the influence of wax chemistry and surface wettability on the development of *Blumeria graminis*, the pathogenic wheat powdery mildew.

In “Interaction between honeybee mandibles and propolis”, Saccardi et al. [12] report on the honeybee propolis, a substance used by bees to seal their hive and protect the colony against pathogens. Since propolis is quite a sticky substance, the authors analysed whether the mandibles of the bees show specific anti-adhesive properties, enabling them to manipulate the propolis. Adhesion experiments with propolis and bee mandibles were performed and the mandibles were analysed using (cryo-) scanning electron microscopy, indicating that a fluid substance covers the medial surface of the mandibles reducing propolis adhesion.

Weiser et al. [13] take biomimetics into industrial production with their paper "Roll-to-roll fabrication of superhydrophobic pads covered with nanofur for the efficient clean-up of oil spills". Nanofurs are densely packed hairy surfaces which demonstrate superhydrophobicity, functioning similarly to the lotus leaf whose science we are celebrating with this thematic issue. As with many biomimetic inventions, the complexity of their structure which gives them their properties also makes them difficult to manufacture. Nanofurs are created relatively easily in a lab environment; however, a durable, environmentally friendly, cost-effective, and large-scale industrial production has been elusive so far. The authors present a new technique that has the potential to achieve the breakthrough the researchers in the field have been searching for. This technique uses a typical industrial process in which a continuous film is run over and between rollers. The so-called roll-to-roll process takes the material through a few steps. In the first step, a molten polypropylene layer is laminated onto a carrier film and run over rollers to cool down. Then the combined laminate is forced through a gap between a hot sandblasted roller and a cold smooth one. The surface roughness and temperature difference create the hairy structured surface on the polypropylene side. In the final step, the structured film is separated from the carrier. The authors were able to set the hair length and density with the usual industrial control variables of speed, temperature, and gap width. The obtained result was a very satisfactory nearly superhydrophobic material which the authors used to create an effective oil–water separation product they called nanopads. What this paper demonstrates, in addition to the not insignificant contribution it makes to the science of structured surfaces, is that with a bit of creativity and a solid understanding of industrial processes, complex structured biomimetic inventions can indeed be effectively brought to the market.

Lifka et al. [14] stick to the nanofibre and production topics in their paper "Laser-processed antiadhesive bionic combs for handling nanofibers inspired by nanostructures on the legs of cribellate spiders". Here the challenge is to handle nanofibres which naturally stick to surfaces due to the van der Waals energy of surface interaction. Spiders which regularly process nanofibres into silk have evolved a structure on the surface of their hind legs to which the nanofibres do not stick. The authors use the geometry of the spider system to develop an elegant mathematical model of the interaction between the fibres and the surface. They then test their predictions using a structured metal mimic of the spider legs. They find that for some metals, in which they were able to generate surface geometries that corresponded to the boundary conditions of their model, the peel-off force is lower over the structured surface than over a polished one. Their understanding of the relationship between the surface structure and the peel-off force will now make it possible to tune and then scale up the fabrication of tools to handle nanofibres in industrial processes.

Fibre–surface interactions are also the main theme in "Growing up in a rough world: scaling of frictional adhesion and morphology of the Tokay gecko (*Gekko gecko*)" by Cobos and Higham [15]. In the excitement of the biomimetic abstraction and development process, in particular when it looks like it is leading to a product, one can sometimes miss some of the important secondary features of the biological archetypes. This paper reminds us of this as it explores the relationship of gecko foot pad adhesion and the geometry of the setae with age and size of the animals. The authors find that the diameter of the fibres and their density in the toepad do not change with size in this species. The toepads scale isometrically with body size, and the setae get relatively shorter with body size. The scaling is also reflected in the adhesive forces the animals are able to produce on surfaces of varying roughness. These observations make specific predictions about the behavioural ecology of this species in the wild. They also remind us to keep looking at the archetypes and closely related species for further inspiration as we develop our biomimetic abstractions into actual products.

This theme is picked up again by Konrad et al [16] who describe their nonlinear journey through bioinspiration in "Straight roads into nowhere – obvious and not-so-obvious biological models for ferrophobic surfaces". The challenge to be solved was to protect copper air delivery tubes from molten iron during the smelting process. The initial concept was to maintain a layer of air between the vulnerable copper surface and the molten iron. The obvious archetypes, *Salvinia* and *Collemba*, which do something similar in their natural environments, were selected as likely sources of bioinspiration. It quickly became obvious that the intricate physics of both archetypes was not appropriate for the industrial conditions of the steel oven. The project would have stopped there had it not been for the combined knowledge of other biological processes by the authors. They looked to a seemingly unrelated archetype, the xylem system of trees, which uses pits instead of extrusions to create its surface properties. This led the team to a new approach and eventually to a successful product. The authors present the case study as a reminder that the breadth of biological knowledge is still the foundation on which biomimetics is built.

The paper by Mail et al. [17] "Dry under water: air retaining properties of large-scale elastomer foils covered with mushroom-shaped surface microstructures" focuses on superhydrophobic surfaces, not only on water repellency, but also on the capability of some surfaces to keep stable air layers under water – the so-called Salvinia Effect. Such air layers are of great

importance for drag reduction (passive air lubrication), antifouling, sensor applications, or oil–water separation. Up to now, based on the investigations of some biological role models (e.g., the floating fern *Salvinia* or the backswimmer *Notonecta*), several prototypes of such surfaces have been developed. In this publication, the authors analyse a novel biomimetic surface, which was initially developed for a different purpose, for its air retaining properties: an adhesive elastomeric film with mushroom-shaped surface microstructures that mimic the adhesion system of animals. They show that this elastomer foil provides good air retention capabilities and is a promising material for the development of an economically and efficient biomimetic air retaining surface, which could be produced on large scales. Furthermore, this publication shows some nice examples of the multi-functionality of some biological surfaces as well as of some biomimetic developments.

Rounding out the thematic issue and looking into the future, Leivas and Barbosa [18] present their model for "Atmospheric water harvesting using functionalized carbon nanocones". The challenge of harvesting water directly from air of varying humidity is a tantalizing one. There are several biological examples in both the animal and plant kingdoms which could serve as archetypes for dehumidifiers or water purifiers. The authors here present a model based on a carbon nanotube structure that might finally provide a route to the breakthrough in this field. Their archetype, the Namibian desert beetle, uses a geometric separation of hydrophilic and hydrophobic regions to harvest and drive water along its body. The authors built on this inspiration to develop carbon nanotube cones which similarly separate the regions. Their model predicts the specific geometry and surface properties that will be required to create a low-pressure system for harvesting water vapour.

Rebora et al. [19], in the paper "The origin of black and white coloration of the Asian tiger mosquito *Aedes albopictus* (Diptera, Culicidae)" analysed the reflectance spectra of the white scales as well as the micro- and nanostructure of the black and white scales on the tarsi of *A. albopictus*. The results show that the white colour is produced by the hierarchical micro- and nanostructure of the surface. The reflection of light depends on the angle of incidence. In addition to superhydrophobicity, these results suggest that the scales have another function – their hierarchical structures produce the brilliant white colour, and therefore the surface is multifunctional.

In the paper "Suspension feeding in Copepoda (Crustacea) – a numerical model of setae acting in concert", Filippov et al. [20] present a numerical modelling approach to understand the influence of different parameters on the feeding efficiency of suspension feeding in common Crustacea. The results show that a system combining long and short setae with different mechanical properties has the best performance. The numerical simulation can in future be easily adapted to other systems and therefore be used for biomimetic developments (e.g., in the field of filtration technologies).

These examples on the one hand handle with biomimetic ideas that are more popular and on the other hand show some extreme cases, where nature provides highly specialized, sophisticated solutions (see Figure 2 for examples). In many cases, nature provides the first solution for a technical problem that has not

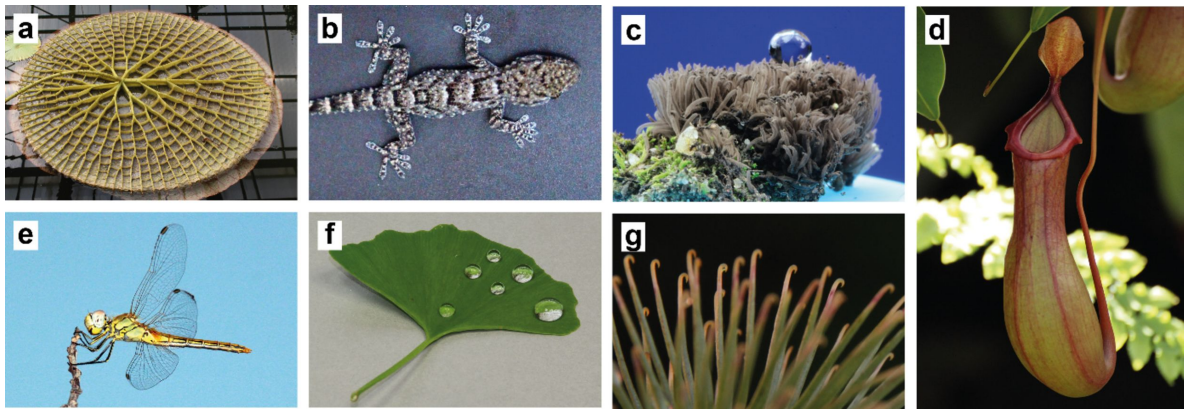


Figure 2: Biological archetypes – The photographs show just a few examples of the incredible diversity of "biological prototypes" nature provides, which enable the development of biomimetic solutions on a brought spectra of different fields of application. a) A floating leaf of a giant water lily (*Victoria*), a nice example of a light-weight structure. b) A gecko – one of the best-known archetypes for biomimetic adhesion. c) An example of the curiosities that nature holds – a slime mould whose spores exhibit superhydrohobic properties. d) A pitcher plant, which has on the edges a special and very slippery surface to prevent insects from climbing out. This surface structure is the opposite of adhesive surfaces. e) A dragonfly. Archetype for robotic applications but also known for their superhydrophobic and transparent wings. f) An example of the early evolution of superhydrophobic surfaces: the leaf of a ginkgo tree. g) Probably one of the best-known examples of biomimetic developments: the greater burdock (*Arctium lappa*) – the archetype for the Velcro tape.

been solved for a long time. In other cases, the biological systems, and therefore their related biomimetic solutions, often show a much higher efficiency than the majority of all previous non-biomimetic engineering solutions.

The diversity of biomimetic approaches is incredible and the sheer number of topics, projects, and publications gives only a brief idea of how many solutions living nature still can provide – as long as we look carefully and with the right mindset. Considering that current publications roughly estimate a total number of 10.000.000 different species living on our planet and that only about 20% of them are known, one can easily understand the incredible number of new possible findings in the field of biomimetics. This also shows how important it is to protect the environment and biodiversity, as all those organisms in addition to their ecological role in the biosphere are potential biological "prototypes" for technical developments, which might significantly contribute for a "greener future".

Taking into account the fast development of biomimetics as a research field in recent years, we took the 25th anniversary of the lotus effect publication as the perfect occasion for this thematic issue. The issue continues the reputable tradition of this journal, building on four previous thematic issues with biomimetic topics [21-24]. The publications gathered in the present thematic issue give an idea of the great variety of areas in this exciting field of biomimetics, and many different cases where nature could help us to find solutions for technical problems. By seeing this exciting diversity of ideas, functionalities, and solutions, we are very much looking forward to the developments of this field in the next 25 years.

Matthias Mail, Kerstin Koch, Thomas Speck, William M. Megill and Stanislav N. Gorb

Eggenstein-Leopoldshafen, Kleve, Freiburg, and Kiel, July 2023

ORCID® iDs

Matthias Mail - https://orcid.org/0000-0002-9732-8453
Kerstin Koch - https://orcid.org/0000-0003-4311-4481
Thomas Speck - https://orcid.org/0000-0002-2245-2636
William M. Megill - https://orcid.org/0000-0002-9682-5730
Stanislav N. Gorb - https://orcid.org/0000-0001-9712-7953

References

1. Barthlott, W.; Neinhuis, C. *Planta* **1997,** *202,* 1–8. doi:10.1007/s004250050096
2. Barthlott, W.; Mail, M.; Neinhuis, C. *Philos. Trans. R. Soc., A* **2016,** *374,* 20160191. doi:10.1098/rsta.2016.0191
3. Barthlott, W. Self-Cleaning Surfaces in Plants: The Discovery of the Lotus Effect as a Key Innovation for Biomimetic Technologies. In *Handbook of Self-Cleaning Surfaces and Materials: From Fundamentals to Applications;* Zhang, X.; Tryk, D.; Irie, H.; Fujishima, A., Eds.; Wiley-VCH: Weinheim, Germany, 2023; Vol. 1, pp 359–369. doi:10.1002/9783527690688.ch15
4. Speck, T.; Neinhuis, C. *Naturwiss. Rundsch.* **2004,** *57,* 177–191.
5. Surapaneni, V. A.; Aust, T.; Speck, T.; Thielen, M. *Beilstein J. Nanotechnol.* **2021,** *12,* 1326–1338. doi:10.3762/bjnano.12.98
6. Li, C.; Gorb, S. N.; Rajabi, H. *Beilstein J. Nanotechnol.* **2022,** *13,* 404–410. doi:10.3762/bjnano.13.33
7. Gorb, E. V.; Kozeretska, I. A.; Gorb, S. N. *Beilstein J. Nanotechnol.* **2022,** *13,* 807–816. doi:10.3762/bjnano.13.71
8. Sun, J.; Li, P.; Yan, Y.; Song, F.; Xu, N.; Zhang, Z. *Beilstein J. Nanotechnol.* **2022,** *13,* 845–856. doi:10.3762/bjnano.13.75
9. Bargel, H.; Trossmann, V. T.; Sommer, C.; Scheibel, T. *Beilstein J. Nanotechnol.* **2022,** *13,* 902–921. doi:10.3762/bjnano.13.81
10. Huth, M. A.; Huth, A.; Schreiber, L.; Koch, K. *Beilstein J. Nanotechnol.* **2022,** *13,* 944–957. doi:10.3762/bjnano.13.83
11. Huth, M. A.; Huth, A.; Schreiber, L.; Koch, K. *Small Sci.* **2023,** *3,* 2200092. doi:10.1002/smsc.202200092
12. Saccardi, L.; Brümmer, F.; Schiebl, J.; Schwarz, O.; Kovalev, A.; Gorb, S. *Beilstein J. Nanotechnol.* **2022,** *13,* 958–974. doi:10.3762/bjnano.13.84
13. Weiser, P.; Kietz, R.; Schneider, M.; Worgull, M.; Hölscher, H. *Beilstein J. Nanotechnol.* **2022,** *13,* 1228–1239. doi:10.3762/bjnano.13.102
14. Lifka, S.; Harsányi, K.; Baumgartner, E.; Pichler, L.; Baiko, D.; Wasmuth, K.; Heitz, J.; Meyer, M.; Joel, A.-C.; Bonse, J.; Baumgartner, W. *Beilstein J. Nanotechnol.* **2022,** *13,* 1268–1283. doi:10.3762/bjnano.13.105
15. Cobos, A. J.; Higham, T. E. *Beilstein J. Nanotechnol.* **2022,** *13,* 1292–1302. doi:10.3762/bjnano.13.107
16. Konrad, W.; Neinhuis, C.; Roth-Nebelsick, A. *Beilstein J. Nanotechnol.* **2022,** *13,* 1345–1360. doi:10.3762/bjnano.13.111
17. Mail, M.; Walheim, S.; Schimmel, T.; Barthlott, W.; Gorb, S. N.; Heepe, L. *Beilstein J. Nanotechnol.* **2022,** *13,* 1370–1379. doi:10.3762/bjnano.13.113
18. Leivas, F. R.; Barbosa, M. C. *Beilstein J. Nanotechnol.* **2023,** *14,* 1–10. doi:10.3762/bjnano.14.1
19. Rebora, M.; Salerno, G.; Piersanti, S.; Kovalev, A.; Gorb, S. N. *Beilstein J. Nanotechnol.* **2023,** *14,* 496–508. doi:10.3762/bjnano.14.41
20. Filippov, A. E.; Krings, W.; Gorb, S. N. *Beilstein J. Nanotechnol.* **2023,** *14,* 603–615. doi:10.3762/bjnano.14.50
21. Barthlott, W.; Koch, K. *Beilstein J. Nanotechnol.* **2011,** *2,* 135–136. doi:10.3762/bjnano.2.16
22. Gorb, S. N.; Koch, K. *Beilstein J. Nanotechnol.* **2014,** *5,* 1450–1451. doi:10.3762/bjnano.5.157
23. Gorb, S.; Speck, T. *Beilstein J. Nanotechnol.* **2017,** *8,* 403–407. doi:10.3762/bjnano.8.42
24. Gorb, S. N.; Koch, K.; Heepe, L. *Beilstein J. Nanotechnol.* **2019,** *10,* 481–482. doi:10.3762/bjnano.10.48

License and Terms

This is an open access article licensed under the terms of the Beilstein-Institut Open Access License Agreement (https://www.beilstein-journals.org/bjnano/terms), which is identical to the Creative Commons Attribution 4.0 International License (https://creativecommons.org/licenses/by/4.0). The reuse of material under this license requires that the author(s), source and license are credited. Third-party material in this article could be subject to other licenses (typically indicated in the credit line), and in this case, users are required to obtain permission from the license holder to reuse the material.

The definitive version of this article is the electronic one which can be found at:
https://doi.org/10.3762/bjnano.14.69

BEILSTEIN JOURNAL OF NANOTECHNOLOGY

Polarity in cuticular ridge development and insect attachment on leaf surfaces of *Schismatoglottis calyptrata* (Araceae)

Venkata A. Surapaneni*[1,2,3], Tobias Aust[1], Thomas Speck[1,2,3,4] and Marc Thielen[1,2,3]

Full Research Paper

Open Access

Address:
[1]Plant Biomechanics Group, Botanic Garden, Faculty of Biology, University of Freiburg, Schänzlestrasse 1, 79104 Freiburg, Germany, [2]FIT, Freiburg Center for Interactive Materials and Bioinspired Technologies, Georges-Köhler-Allee 105, 79110 Freiburg, Germany, [3]FMF, Freiburg Materials Research Center, Stefan-Meier-Strasse 21, 79104 Freiburg, Germany and [4]Cluster of Excellence livMatS@ FIT-Freiburg Center for Interactive Materials and Bioinspired Technologies, University of Freiburg, Georges-Köhler-Allee 105, 79110 Freiburg, Germany

Email:
Venkata A. Surapaneni* - svamarnadh@gmail.com

* Corresponding author

Keywords:
cuticular ridges; insect adhesion; leaf surfaces; ontogeny; polarity; surface replication

Beilstein J. Nanotechnol. **2021,** *12,* 1326–1338.
https://doi.org/10.3762/bjnano.12.98

Received: 22 June 2021
Accepted: 10 November 2021
Published: 01 December 2021

This article is part of the thematic issue "Biomimetics on the micro- and nanoscale – The 25th anniversary of the lotus effect".

Associate Editor: K. Koch

© 2021 Surapaneni et al.; licensee Beilstein-Institut.
License and terms: see end of document.

Abstract

The plant cuticle is a multifunctional barrier that separates the organs of the plant from the surrounding environment. Cuticular ridges are microscale wrinkle-like cuticular protrusions that occur on many flower and leaf surfaces. These microscopic ridges can help against pest insects by reducing the frictional forces experienced when they walk on the leaves and might also provide mechanical stability to the growing plant organs. Here, we have studied the development of cuticular ridges on adaxial leaf surfaces of the tropical Araceae *Schismatoglottis calyptrata*. We used polymer replicas of adaxial leaf surfaces at various ontogenetic stages to study the morphological changes occurring on the leaf surfaces. We characterized the replica surfaces by using confocal laser scanning microscopy and commercial surface analysis software. The development of cuticular ridges is polar and the ridge progression occurs basipetally with a specific inclination to the midrib on *Schismatoglottis calyptrata* leaves. Using Colorado potato beetles as model species, we performed traction experiments on freshly unrolled and adult leaves and found low walking frictional forces of insects on both of these surfaces. The changes in the micro- and macroscale morphology of the leaves should improve our understanding of the way that plants defend themselves against insect herbivores.

Introduction

The plant cuticle is a thin non-cellular membrane that covers most of the above-ground organs of land plants. It is a composite matrix consisting of cutin and cutan as its main components, contains intracuticular waxes, and typically is covered by an outer layer of epicuticular waxes. The cuticle and the underlying epidermal cell wall are linked by a transition region that is

rich in cellulose, hemicellulose, and pectin [1-5]. The outer peripheral layer of the cuticle may show various microscopic morphological structures such as cuticular ridges, epicuticular wax crystals, trichomes, and hairy structures [4,6]. The cuticular structures together with the epidermal cell shape and the cuticle chemistry provide the leaf surface with multiple functions [7]. In particular, cuticular ridges on some leaf surfaces have been found to reduce the frictional forces of insects during walking and may increase the hydrophobicity of the leaf surfaces [8,9]. On petals, they might act additionally as diffraction gratings producing structural colors to attract pollinators [10-12]. Ridges are relatively robust compared with other cuticular morphologies [8] such as epicuticular wax crystals. They may also provide mechanical stability to the growing organs by possibly avoiding cuticle cracking and maintaining structural integrity during rapid leaf area expansion [13,14].

Recently, a study of 75 different eudicot species has shown that their leaf growth is polar (or direction-dependent) and diverse and has identified four characteristic growth patterns: (1) basipetal, (2) acropetal, (3) diffused, and (4) bidirectional [15]. Such polarity in leaf growth is a result of direction-dependent cell differentiation, maturation, and proliferation processes along or perpendicular to the direction of the midrib [15-21]. One aspect that would be interesting to know is whether cuticular structures such as ridges also display such polarity during growth in the proximodistal or mediolateral axes. This is the focus of the present study. Such knowledge will help in understanding the mechanical basis of morphological changes and structural integrity of plant surfaces. Whereas the architecture of the cuticular structures and the associated functionalities have been well studied, detailed analyses concerning growth-induced changes in the morphology of cuticular structures are largely absent. Hong et al. [22] have reported that the cuticular ridges on *Arabidopsis thaliana* sepals develop basipetally, and that the ridge progression coincides with the growth and maturation of epidermal cells. Recently, Surapaneni et al. [23] have reported that, on the leaves of *Hevea brasiliensis* trees, the cuticular ridges also have a polarity during development but are characterized by an acropetally directed progression. They have also found that the ridge development coincided with the directional color changes occurring on the leaf surfaces.

Our preliminary microscopic examination and visual observations have shown that such directional color changes also occur on the cuticular ridge containing adaxial leaf surfaces of *Schismatoglottis calyptrata* (Roxb.) Zoll. & Moritzi, *Ailanthus altissima* (Mill.) Swingle and *Aesculus parviflora* Walter. In *S. calyptrata,* the leaves are rolled in leaf sheaths during bud formation and unroll during maturation, and thus, it is a worthwhile plant model to understand the development of cuticular ridges on the leaf surfaces with such varying macromorphology. Therefore, we have chosen *S. calyptrata* as a model plant in this study and tested the presence of polarity in the ridge development on the adaxial leaf surfaces. In addition, we have also tested the walking frictional forces of insects on freshly unrolled and adult adaxial leaf surfaces. *S. calyptrata* (Araceae) is a monocotyledonous species that has variegated leaves and that is distributed from Southwest China to Vanuatu [24,25]. It grows typically in tropical forest understories, forms stoloniferous (horizontal stems close to the soil surface) colonies, and can grow up to 60 cm tall. They are usually 15–50 cm long, variegated with grey-green or yellowish green spots, and form up to six leaves per crown [25,26]. In this study, we have used polymer replicas of the *S. calyptrata* leaf surfaces at various ontogenetic stages for morphometric analyses. Polymer replication of the leaf surfaces helps to avoid artifacts arising from leaf dehydration during time-consuming microscopical analyses, especially with regard to the imaging of young leaf surfaces [7,23]. By means of confocal microscopy experiments, we demonstrate that polarity in ridge development also occurs on leaves of *S. calyptrata* and that the surface roughness of the leaves increases as the leaves mature. Previous studies have found reduced insect adhesive forces on rough plant surfaces [8,9,23,27-31]. By performing traction experiments using Colorado potato beetles (*Leptinotarsa decemlineata*) as model insect species, we show that the walking frictional forces of insects are reduced as well on freshly unrolled as on adult leaf surfaces.

Results

Leaf ontogeny and replication

Leaves were in the rolled state at stage 1 (5 days from bud formation) and stage 2 (10 days from bud formation). After exponential leaf growth (Supporting Information File 1, Figure S1), the leaves unrolled at stage 3, after 12–26 days from bud appearance. Stage 4 occurred at a leaf age of 22–35 days, when the growth of the leaves as measured from the length of the midrib ceased. The leaf sizes (the leaf sheath to tip length in stages 1 and 2; midrib lengths in stages 3 and 4) varied from 0.5–5 cm at stage 1, 7–10 cm at stage 2, 11–21 cm at stage 3, to 15–24 cm at stage 4.

The polydimethylsiloxane (PDMS, positive mold) replicas of the leaf surfaces aided the study of the ontogenetic variation in the morphology of the ridges. Some leaf material, but only at stages 2A and 3, remained attached to the epoxy (negative mold) replicas during the replication process. However, in contrast to the results from Surapaneni et al. [23] on *H. brasiliensis* leaves, potassium hydroxide (KOH) treatment removed all the plant material from the epoxy surfaces, and

thus, clean PDMS replicas from all leaf stages could be obtained.

Structure of the cuticle – temporal and spatial changes

Figure 1 shows *S. calyptrata* leaves at their different ontogenetic stages (Figure 1a) and the corresponding confocal laser scanning microscopy (CLSM) observations (Figure 1b–f) on leaf microstructures. A schematic representation of the leaves and the corresponding locations of smooth and ridged morphologies is provided in Figure 2. The ontogenetic variations in roughness on the *S. calyptrata* leaf surfaces are given as the arithmetic average roughness (*Ra*) versus leaf stage in Figure 3a and as the ridge aspect ratio (*AR*) versus leaf stage in Figure 3b.

The roughness values of the leaf replicas revealed significant differences within leaf stages (Kruskall–Wallis, χ^2 for Ra = 103.24, χ^2 for AR = 109.24, df = 4, $p < 0.001$, n, S1 = 20, n, S2–S4 = 30). Figure 1b and Figure 1d demonstrate leaf surfaces with smooth epidermal cells without any cuticular structuring at stages 1 and 2B, respectively. The presence of a ridge-like structure along some anticlinal fields on the surfaces of the leaves at stage 2B (arrow in Figure 1d) was found. However, the *Ra* and *AR* of the ridges did not change significantly from

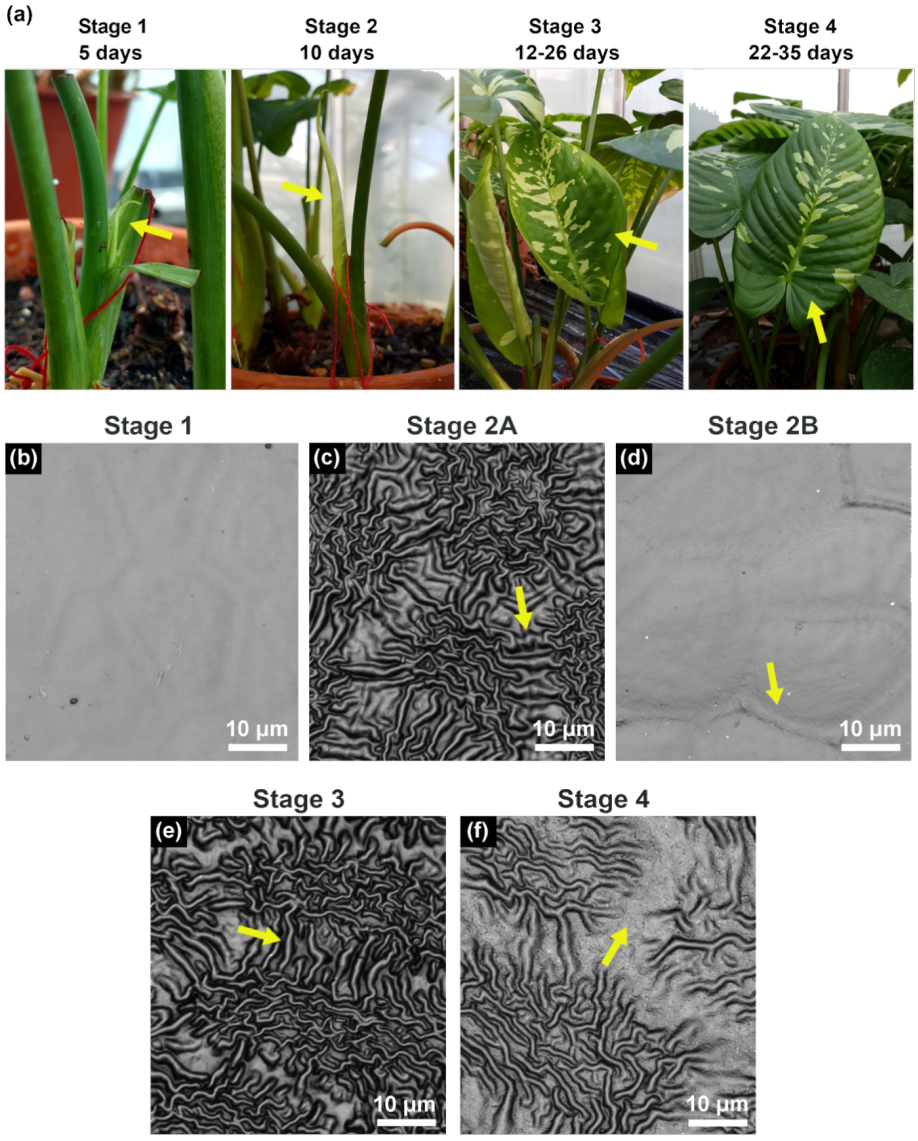


Figure 1: Leaf ontogeny and cuticular ridge development. (a) Leaf development from bud appearance during the various ontogenetic stages in *Schismatoglottis calyptrata*. (b–f) CLSM images of leaf replica surfaces during the different ontogenetic stages. Leaf surfaces contained smooth cells at stage 1 and stage 2B, high aspect ratio zig-zag shaped ridges at stages 2A and 3, and less dense and low aspect ratio ridges at stage 4. Arrows indicate: (a) leaves at the respective stages; (c) and (e) thick and long ridges connecting the peripheries of the adjacent cells; (d) a ridged structure along the anticlinal field; (f) the anticlinal field free of ridges.

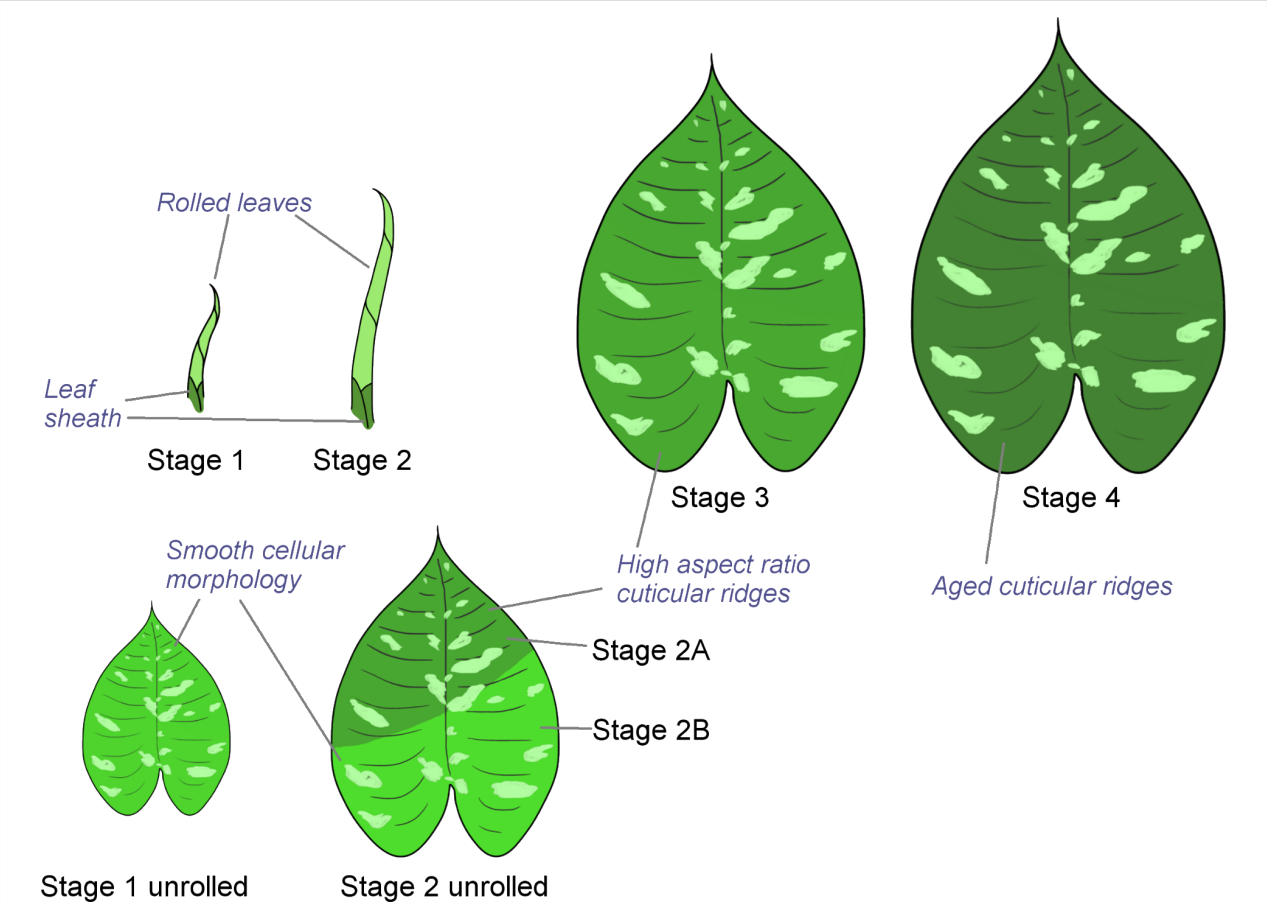


Figure 2: Schematic representation of leaf growth stages of *Schismatoglottis calyptrata* and their respective surface microstructures. At stages 1 and 2, leaves are normally in the rolled position. The schematics show the leaf colors when the leaves were unrolled manually.

stage 1 to stage 2B (*Ra*: $p = 1$, *AR*: $p = 1$, n, S1 = 20, n, S2B = 30). A basipetal progression (apex to base) of the cuticular ridges occurred with the growth of the leaves during stage 2. The morphometric analysis revealed the rapid formation of high aspect ratio cuticular ridges in the region close to the apex (stage 2A, Figure 1c). Accordingly, the *Ra* and *AR* values increased significantly at stage 2A when compared with stage 1 and stage 2B (*Ra* and *AR*: $P < 0.001$, $n = 30$). At stage 3, the entire surface of the leaves was covered with cuticular ridges as shown in Figure 1e, and no significant difference was observed in *Ra* and *AR* when compared with those of stage 2A (*Ra*: $P = 1$, *AR*: $P = 1$, $n = 30$). At stages 2A and 3, additionally, the anticlinal fields were characterized by thick and long ridges that connected the ridge islands on the adjacent cells (arrows in Figure 1c,e). As leaf growth progresses, the cuticular ridges have been reported to disappear on leaf or sepal surfaces [22,32]. However, cuticular ridges were still present on *S. calyptrata* leaf surfaces even at stage 4. Nevertheless, they were characterized by reduced height and increased spacing between the ridges (see Table 1), probably caused by cell growth (Figure 1f). The AR value decreased, but the *Ra* value did not vary significantly when compared with the values at stage 3 (*Ra*: $p = 0.26$, *AR* = 0.04, $n = 30$). A comparison of the CLSM recordings of leaf surfaces at all stages (Figure 1b–f) showed that the cells grew unevenly when they reached adult stages. Therefore, with the uneven growth of the cells, the ridges elongated (reduced zig-zag pattern), and the anticlinal fields between the cells became mostly free of cuticular ridges (arrows in Figure 1f). We observed no notable differences in the ridge dimensions between the dark green regions and the yellowish green regions on the variegated leaf surfaces (average of three spots in the dark green region: *Rc* = 0.76 µm, *Rsm* = 3.0 µm, *AR* = 0.25; in the yellowish green region: *Rc* = 0.88 µm, *Rsm* = 3.03 µm, *AR* = 0.29).

The mean values of the roughness parameters are shown in Table 1. These values of mean height (*Rc*) and spacing (*Rsm*) of the ridges at the intermediate stages 2A and stage 3 are more than twice the values in the corresponding stages 2B and 3 (stage 2B: *Rc* = 0.36 µm, *Rsm* = 1.10 µm; stage 3: *Rc* = 0.42 µm, *Rsm* = 1.13 µm) on the leaves of the *H. brasiliensis* tree [23]. Surapaneni et al. [23] reported that

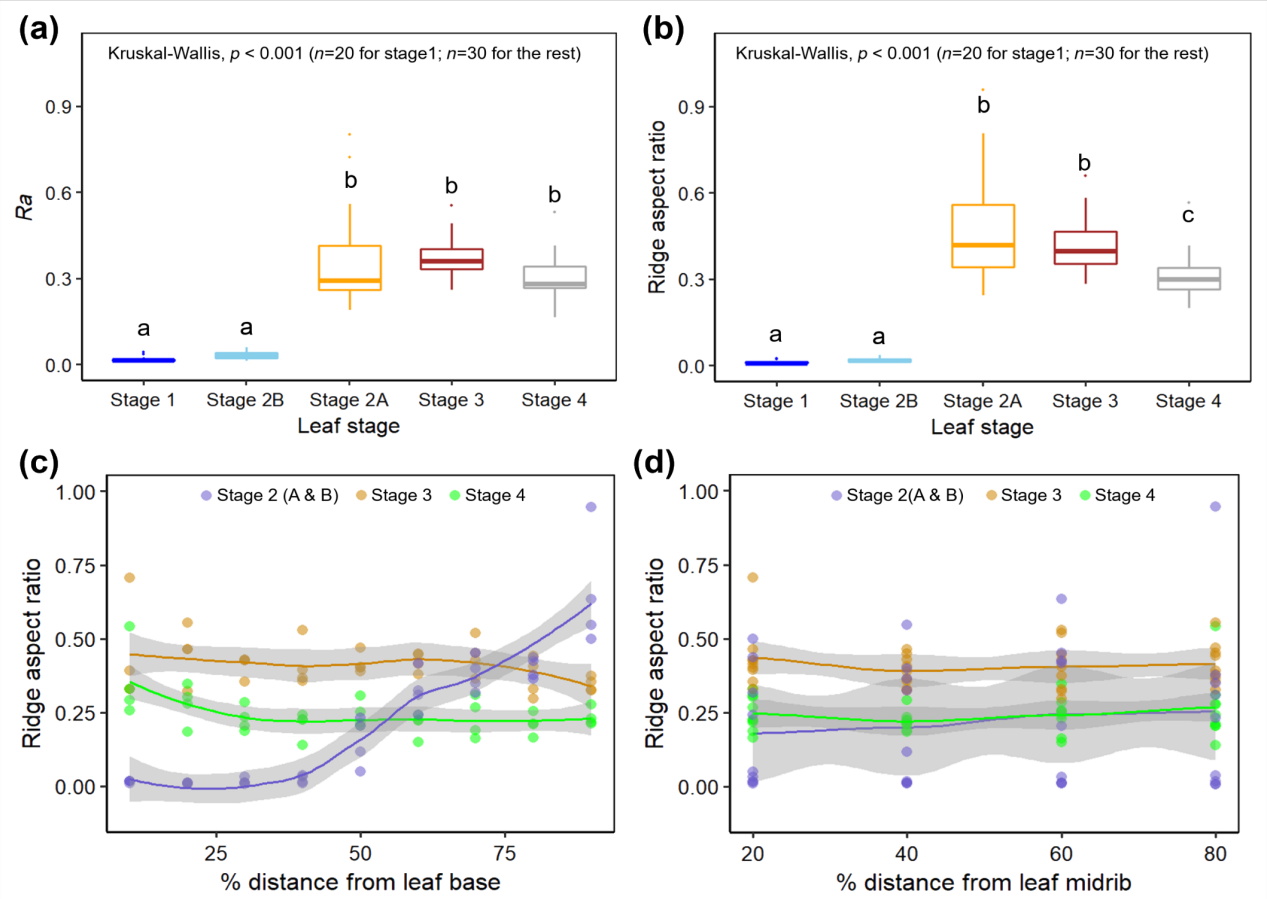


Figure 3: The plots show (a) the variation in the arithmetic average roughness (*Ra*) of the leaf surfaces with different growth stages, (b) the variation in the ridge aspect ratio with different leaf growth stages, (c) the spatial variation of the ridge aspect ratio along the direction of the midrib as percentage distance from the base of the leaf, and (d) the variation of ridge aspect ratio perpendicular to the direction of the midrib as percentage distance from the midrib. The gray shading around the lines represents the 95% confidence interval.

Table 1: Mean values of roughness parameters of cuticular ridges on leaf surfaces of *Schismatoglottis calyptrata* at stages 2A, 3, and 4.

Stage	*Ra* in µm	*Rc* in µm	*Rsm* in µm	*AR* = *Rc*/*Rsm*
stage 2A	0.36	1.03	2.16	0.48
stage 3	0.37	1.06	2.61	0.41
stage 4	0.30	0.88	2.90	0.31

KOH treatment was unsuccessful in removing plant material from the negative epoxy replicas. In the present study, the higher roughness (particularly, mean spacing) values on *S. calyptrata* leaf surfaces might have resulted in the easy of removal of plant material from the epoxy negatives.

Figure 3c and Figure 3d show the variation in the aspect ratio values in the proximodistal axis and the variation in the aspect ratio values along the mediolateral axis, respectively. The data were smoothened within stages by using the loess (local linear smoothing) method. We found an almost linear increase in the ridge aspect ratio beyond 40% from the base of leaves at stage 2. The area above 40% essentially represents stage 2A when the ridges start developing rapidly. At stage 3, the overall ridge aspect ratio reduced and showed further reduction beyond 70% from the leaf base. During stage 4, the aspect ratio continued to decrease slightly, until approximately 30% from the leaf base and remained constant thereafter. The aspect ratio was mostly constant in the direction perpendicular to the midrib for stages 2, 3, and 4 (Figure 3d).

The ridge progression on *S. calyptrata* leaves did not occur parallel to the proximodistal axis but at a specific inclination to the midrib (Figure 2). This could also be clearly observed from the difference in light reflection from the epoxy replicas. Figure 4 shows a typical epoxy replica of a leaf at stage 2 displaying the inclined ridge progression line. CLSM analysis showed that the surface of the transparent region of the epoxy replica corresponded to that of smooth unstructured cells, whereas the surface of the opaque region was covered with dense cuticular ridges.

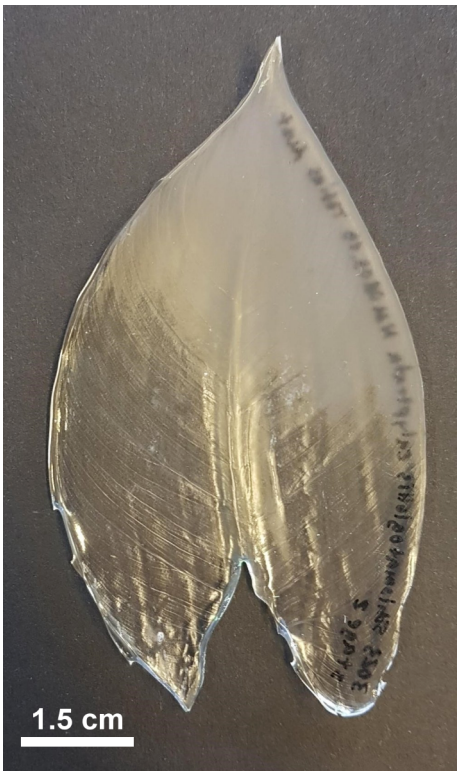


Figure 4: A typical epoxy replica of the surface of a leaf at growth stage 2 having a ridge progression inclined with the midrib. The transparent region represents stage 2B and contains smooth cells. The opaque region represents stage 2A and contains densely arranged high aspect ratio cuticular ridges. The inclined ridge progression might be the result of uneven exposure of the leaves to the outside environment.

Analysis of individual epidermal cells demonstrated the change of size and orientation of the cells and the ridge islands during the ontogeny (Figure 5). Figure 5a demonstrates the demarcation of ridge islands and the periphery. The variation in the area of ridge islands and the epidermal cells during ontogeny are plotted as boxplots in Figure 5b. There are significant differences in the cell size (Kruskall–Wallis, $\chi^2 = 51.35$, df = 4, $p < 0.001$, $n = 12$) and ridge island size (Kruskall–Wallis, $\chi^2 = 25.18$, df = 2, $p < 0.001$, $n = 12$) during ontogeny. Pairwise analysis of cell area showed no significant differences between adjacent stages (Figure 5b). The cell size is, however, significantly different between stages 1 and 3 ($p < 0.001$, $n = 12$), stages 1 and 4 ($p < 0.001$, $n = 12$), stages 2A and 4 ($p < 0.01$, $n = 12$), stages 2B and 3 ($p < 0.01$, $n = 12$) and stages 2B and 4 ($p < 0.001$, $n = 12$). Note that the cell size data are normally distributed and the variances are homogenous. Since the data were collected from the same leaf replica, it was assumed that the data were not independent. If the data were assumed to be independent, ANOVA analysis showed significant differences ($p < 0.001$, $n = 12$) in cell size between all the stages except between stages 1 and 2B ($p < 0.80$, $n = 12$). The size of ridge islands differes significantly between adjacent leaf stages ($p < 0.01$ between stages 2A and 3 and stages 3 and 4, and $p < 0.001$ between stages 2A and 4; $n = 12$). Figure 5b also shows that the difference between the median values of cell and ridge island areas increases with leaf growth, demonstrating the increase in the area of the periphery or the anticlinal region with cell growth. The variation in the density of cells and ridge islands (as number of cells per square millimeter and ridge islands per square millimeter, respectively) with leaf growth is shown in Table 2. The density of the ridge islands is almost twice as that of the cells in all stages of ridge progression and growth. Figure 5c shows the frequency distribution of the orientation of the long axes of cells and ridge islands with respect to the midrib of the leaf at all growth stages. Typical examples of data on the orientation of ridges in the ridge islands and the periphery regions for the different growth stages are shown in Supporting Information File 2. The analysis showed that, in the periphery region the ridges were radially oriented relative to the centre of the ridge island during all stages of ridge progression and growth. In the ridge islands, however, the ridges had a complex zig-zag-like orientation during stage 2A. Similarly, during stage 3, the ridges were mostly oriented in a zig-zag manner, although on some cells longitudinal alignment of the ridges along the long axes of the cells was observed. During stage 4, the ridge orientation was mostly longitudinally oriented along the long axes of the cells.

Insect traction forces

The maximum insect traction forces on freshly unrolled (stage 3) and adult (stage 4) *S. calyptrata* leaves differed significantly from those on glass (Kruskal–Wallis, $p < 0.01$, $n = 7$). Figure 6 shows the variation in the traction forces of insects on glass and leaf surfaces. When compared with the forces on glass ($F_{median} = 11.79$ mN), the traction forces of insects are reduced significantly on stage 3 ($F_{median} = 2.02$ mN, $p < 0.05$, $n = 7$) and stage 4 ($F_{median} = 1.56$ mN, $p < 0.01$, $n = 7$) leaves. However, the forces did not differ significantly between stage 3 and stage 4 leaves ($p = 1.00$, $n = 7$).

Discussion

In this study, we have demonstrated that the morphology of the cuticular ridges on the adaxial side of *S. calyptrata* leaves changes significantly during leaf ontogeny. Similar to *H. brasiliensis* [23], the ontogenetic changes on *S. calyptrata* leaf surfaces revealed three distinct levels of cuticular morphology that coincided with the color changes on the leaf surfaces, albeit with few differences. Supporting Information File 1, Figure S2 shows the comparison of these distinct morphological levels on *H. brasiliensis* and *S. calyptrata* leaf surfaces. The first level is characterized by smooth epidermal cells with no

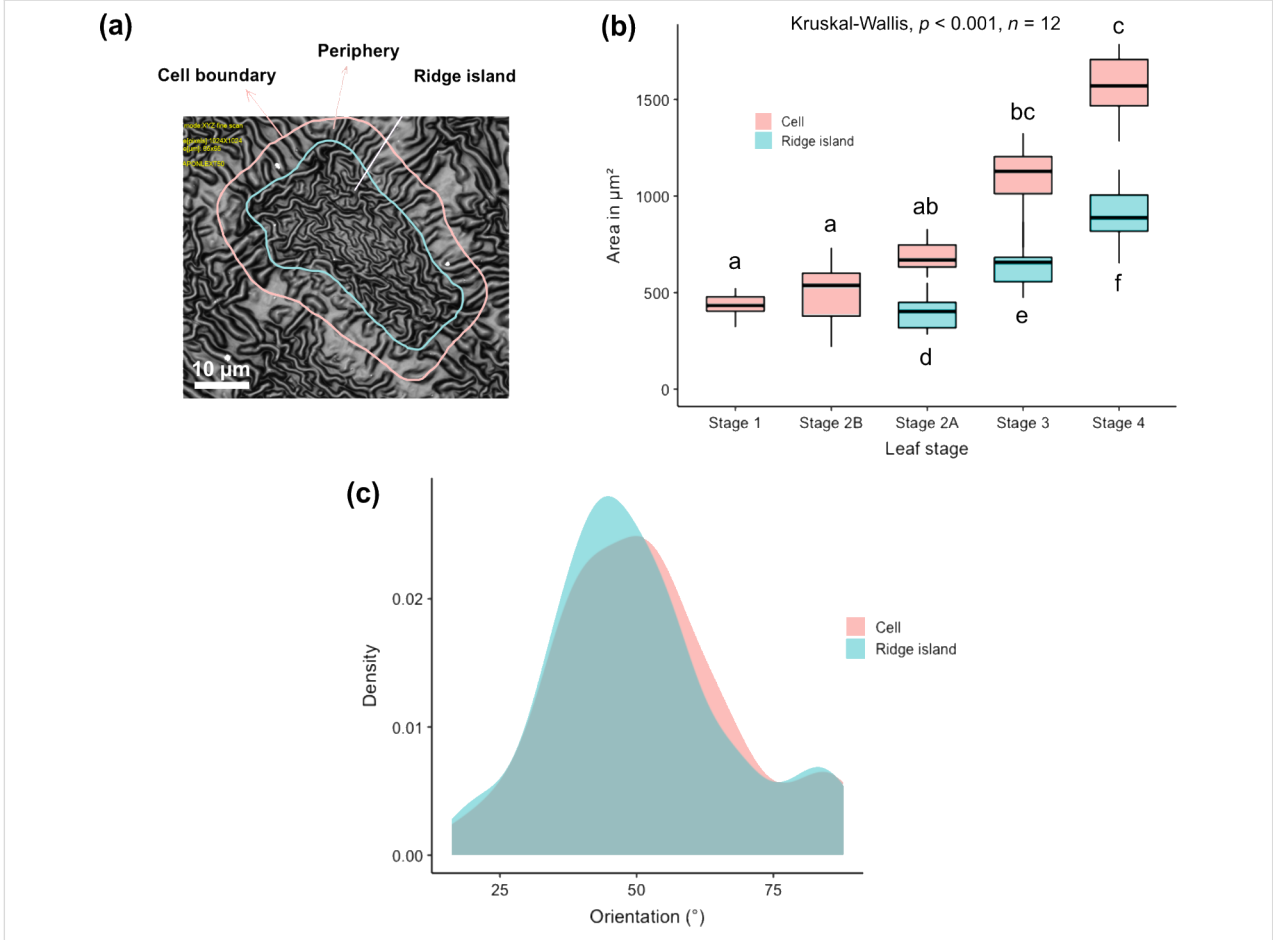


Figure 5: Cell size and orientation. (a) The outlines show the area of the epidermal cell as the sum of areas of ridge island, where the ridges are arranged in a nearly zig-zag pattern, and periphery, where the ridges are arranged nearly radially with respect to the center of the ridge island, (b) the boxplots show the increase in the area of cells (in pink) and ridge islands (in blue) with leaf growth, and (c) shows frequency density plots of orientations of the long axes of cells (in pink) and ridge islands (in blue) with respect to the midrib of the leaf.

Table 2: The variation in the density of cells and ridge islands (as number of cells per square millimeter) with leaf growth.

Stage	Density of ridge islands per square millimeter (*r*)	Density of cells per square millimeter (*c*)	*r*/*c*
stage 1		2322.41	
stage 2A	2482.52	1423.08	1.74
stage 2B		2000.21	
stage 3	1609.37	892.44	1.80
stage 4	1115.81	626.60	1.78

superimposed cuticular structures, which occurred from the bud appearance until stage 1 in both species, and further in stage 2A (region towards apex) in *H. brasiliensis* (Supporting Information File 1, Figure S2a) and stage 2B (region towards base) in *S. calyptrata* (Supporting Information File 1, Figure S2d). The second level pertains to densely arranged high aspect ratio ridges oriented in a zig-zag manner, which developed acropetally from stages 2B and 3 in *H. brasiliensis* (Supporting Information File 1, Figure S2b) and basipetally from stages 2A and 3 in *S. calyptrata* (Supporting Information File 1, Figure S2e). In this level, the ridges on *S. calyptrata* leaf surfaces were thicker and more loosely packed (also see Results section) with larger mean spacing between the ridges when compared with those on *H. brasiliensis* leaves. These morphological dissimilarities of the cuticular ridges might have contributed to the differences in plant material separability from the negative molds in both species. In addition to possible chemical interactions between leaf material and epoxy during replication, the mean

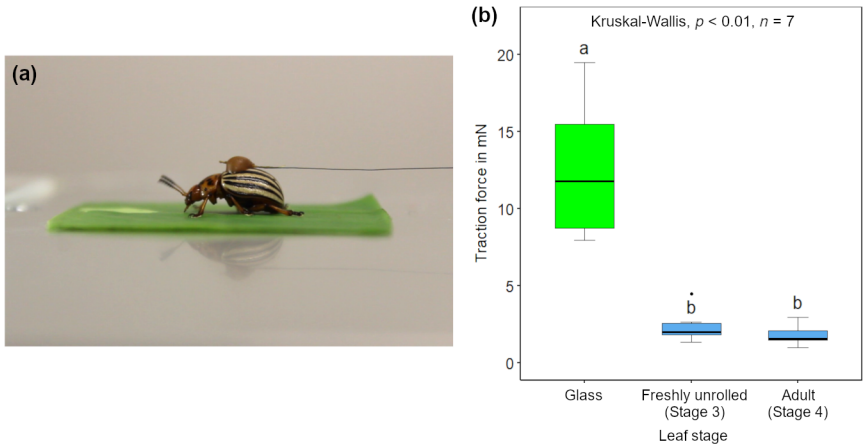


Figure 6: Insect traction forces: (a) A female Colorado potato beetle walking on a *Schismatoglottis calyptrata* leaf sample and (b) traction forces (in mN) of female Colorado potato beetles on glass, freshly unrolled (stage 3) and adult (stage 4) leaf samples (n = 7).

spacing between the ridges might be a factor enabling the efficient separation of plant material from the epoxy negative molds during polymer replication. The third level is characterized by aged and uniformly aligned low aspect ratio ridges in a labyrinth-type arrangement (at stages 4 and 5) in *H. brasiliensis* (Supporting Information File 1, Figure S2c), and low aspect ratio, thick, elongated and spaced ridges with smooth anticlinal fields (at stage 4) in *S. calyptrata* (Supporting Information File 1, Figure S2f). In this level, in *S. calyptrata* leaf surfaces, the ridges also have predominantly longitudinal orientation representing stretching of the ridges during cell expansion. From the second level to the third level, the ridge islands and the anticlinal fields undergo growth-induced expansion resulting in the observed morphological changes and alignment of ridges. Hong et al. [22] also reported that the densely arranged cuticular ridges on wild-type *Arabidopsis* sepals form at an intermediate stage with a basipetal progression and that the density of the ridges reduces as the cells mature. They have also shown that, on *Arabidopsis* sepals, the cells beneath the ridges mature at the same time as ridges form over the cells. Assuming that this is also the case in *S. calyptrata* leaves, the levels of ridge formation, development, and morphology appear to follow a general pattern based on the underlying cellular processes in both leaves and sepals.

In contrast to *H. brasiliensis* leaves and *Arabidopsis* sepals, the ridge progression on S. *calyptrata* leaves occurs with a specific inclination to the midrib. Notably, *S. calyptrata* leaves remain rolled-up from bud formation until stage 3. Moreover, when the ridges start to develop (stage 2A, in the region close to the leaf apex), the region close to the base of the leaves still lies within the leaf sheath, and the leaf margin over the rolled leaf covers the leaf in an inclined fashion (intuitive from a simple rolled paper experiment). The rolling of the leaves during the initial developmental stages might be an evolutionary trait because of various abiotic factors such as water stress, temperature, and excess radiation and/or might represent a defense mechanism against, for example, insects or viruses [33-35]. When the leaves are rolled, the intensity of light reaching each underlying layer of the rolled-up leaf and the transpiration properties within each layer will be different. Such unevenness in the exposure of the leaf to the external environment might result in the inclined ridge progression on the *S. calyptrata* leaves. Also, the presence of ridges on the leaf surfaces might reduce friction, thereby, avoiding damage between the delicate rolled leaf layers during unrolling and growth.

Previous studies on cuticular ridge development [22,23] and our observations of *S. calyptrata* leaves as presented in this study also establish that the formation and the development of cuticular ridges on plant leaf and sepal surfaces display polarity in various plant species, probably correlated with the polarity in leaf and sepal growth. Whereas cuticular ridge development is known to have polarity, we need to understand the mechanical effects required for such development. During young leaf stages, the thickness of the cuticle is usually low, and the growth of the leaves is, in general, accompanied by the thickening of the cuticle, because of the addition of cuticular material [3]. Martens [36] predicted that the overproduction of cuticle material induces the formation of cuticular ridges, a predication supported by a recent model [37]. In environments with high temperatures, low humidity, and high light intensity, plants are known to develop thicker and (more) waxy cuticles [38-40]. Therefore, as described in the previous section, the ridge development on the leaves (Figure 2 and Figure 4) might depend upon the way that leaves are covered and protected (by being rolled) during growth and their interaction with the external environment.

Mechanically, when the strain in the cuticle (induced by the simultaneous isotropic production of the cuticle and anisotropic expansion of the underlying cells) increases beyond a critical strain value, ridges start to develop [37,41,42]. Moreover, the amount of polysaccharide and cutin components present in the cuticle probably influences the stiffness and elastic behavior of the cuticle–cell wall interface [43] and certainly affects ridge formation. The thickened cuticle provides structural support to the growing epidermal cells [14], and the ridges might help in maintaining the structural integrity of the cuticle by avoiding cracking during rapid leaf expansion. The way that the amount and arrangement of the cuticular components vary during the cellular growth processes throughout ontogeny might determine the differences in cuticular morphology among the various plant species or the means by which polarity is established in cuticular (ridge) development in a given species. Vice versa, the variation in the morphology of the ridges and the underlying mechanics should enable inferences to be made regarding the underlying structure of the cuticle–cell wall interface. A better understanding of these processes might also provide insights for bioinspired growth or swelling-induced microstructures for technical applications [44].

The morphological changes in the cuticular structure of plant leaves during ontogeny have been demonstrated to influence insect attachment [23]. Our experiments showed reduced traction forces of the model insects (female *L. decemlineata*, Coleoptera) on freshly unrolled and adult *S. calyptrata* adaxial leaf surfaces. The reduction in the traction forces of the beetles was almost 83% on the freshly unrolled leaf and almost 87% on the adult leaf, when compared with those on glass. Earlier studies have found similarly large reduction in the traction forces of Colorado potato beetles on leaves with cuticular ridges and their replicas when compared with those on glass [8,23]. Therefore, from the point of leaf unrolling until adult leaf stages of *S. calyptrata,* the cuticular structure may influence the attachment and, thus, the activity of herbivores or pollinators (associated with the order, Coleoptera [45]). During young stages, however, the *S. calyptrata* leaves remain rolled-up, a type of macroscale morphology that might also reduce herbivory [34].

Conclusion

CLSM measurements of PDMS replicas of *Schismatoglottis calyptrata* leaves have shown that the cuticular ridges display pronounced polarity and morphologically distinct levels during development. We have found smooth cellular surfaces on young leaf surfaces and ridges developing basipetally on leaf surfaces at an intermediate leaf stage. As soon as ridge development starts, the ridge aspect ratio immediately increases almost linearly on the same leaf in the direction parallel to the midrib. The aspect ratio, however, is significantly reduced on adult (aged) leaf surfaces, with the anticlinal fields being almost free of ridges. The variations in the morphology of cuticular ridges shown in the present study and from previous studies suggest a general (three-level) pattern of ridge development in various plant species and organs. We have also found that ridge progression occurs at an inclination to the proximodistal axis on *Schismatoglottis calyptrata* leaves, possibly a result of leaf rolling and nonuniform exposure to the environment during early leaf stages. Our results can be extrapolated to the mechanistic basis of cuticular structure (ridge) development and might, thus, be of interest with regard to bioinspired applications. While the macroscale morphology of the leaves is expected to influence insect attachment during young leaf stages, the cuticular microstructuring on the leaf surfaces influences insect attachment during mature leaf stages.

Experimental

Leaf collection and ontogenetic stages

S. calyptrata plants (potted plant <0.5 m height) were cultivated in the glass houses of the Botanic Garden of the University of Freiburg, Germany. The average temperature and average relative humidity in the glass houses were 22.6 ± 2.6 °C and 73.5 ± 11.0%, respectively. Voucher specimens (FB 15013) of the leaves are deposited in the herbarium of Freiburg, University of Freiburg, Germany. The leaf growth was monitored from bud to adult stages. Initial trial experiments by using a confocal laser scanning microscope helped in the classification of the growth stages, which is based on the microstructural morphology of the adaxial leaf surfaces and leaf age. In total, four ontogenetic stages were defined. Stage 1 leaves had smooth epidermal cells with no cuticular structuring. As the young *S. calyptrata* leaves were still rolled-up at this stage, the ontogenetic stage was defined based on an arbitrarily chosen leaf age, namely five days from bud formation. Stage 2 leaves had cuticular ridges covering half (50 ± 10%) of the leaf surface. This was subdivided into stage 2A representing the area toward the apex of the leaves and stage 2B representing the area toward the base of the leaves. Since stage 2 leaves also remained in a rolled-up state, we conducted initial trial experiments to estimate the age of the leaves (after 10 days from bud formation) and collected the leaves at this age. The length of the leaves at stages 1 and 2 was considered to be the length from the end of the leaf sheath to the tip of the leaf. The leaves unrolled at stage 3. At this stage, the entire surfaces were covered with cuticular ridges. Stage 4 leaves were adult leaves the growth of which (as deduced from the length of the midrib) was completed.

Surface replication and characterization

Replication of the leaf surface was carried out using a two-step molding approach (Epoxy-PDMS) as described in Kumar et al.

[46] and Surapaneni et al. [23], except that the entire adaxial leaf surfaces of *S. calyptrata* (leaf area: 15–293 cm^2) were replicated in our study. The leaves of *S. calyptrata* at stages 1 and 2 were un-rolled gently before replication, and all the leaves were attached to a clean flat plate by using double-sided adhesive tape (Tesa SE, Norderstedt, Germany) with the adaxial side of the leaves facing upward. The replication process was started within 10 min after the leaves were cut. Epoxy (Epoxy Resin L & Hardener S, Toolcraft, Conrad Electronic SE, Hirschau, Germany; resin to hardener mixing ratio of 10:4.8) negative molds were then obtained from the leaf (master) surfaces. After the epoxy molds were cured, polydimethylsiloxane (PDMS, Bluesil ESA 7250 A & B kit, Bluestar Silicones GmbH, Leverkusen, Germany; weight ratio of 10:1) positive molds dyed in red were obtained from the negative molds and allowed to cure. A detailed explanation of the replication process is given in Kumar et al. [46] and Surapaneni et al. [23], and is shown schematically in Figure 7a and Figure 7b. A total of three leaves in stages 2, 3 and 4, respectively, and two leaves in stage 1 were replicated.

The replicas of freshly cut leaves at the different ontogenetic stages were characterized using a confocal laser scanning microscope (CLSM, Olympus LEXT OLS4000, 405 nm laser, Olympus Corporation, Tokyo, Japan). To assess the statistical differences in ridge morphology on the leaf surfaces of *S. calyptrata* during ontogeny, ten different spots/areas (65 × 65 µm) on both sides of the midrib of each leaf replica were recorded. In order to study the spatial variation in ridge morphology, single leaf replicas from stages 2 (2A and 2B together), 3, and 4 were tested, and a total of 36 spots (130 × 130 µm) on the left side of the midrib of the leaves were recorded. These spots lay at the intersections of four equal divisions parallel to the midrib and nine equal divisions perpendicular to the midrib of the leaves. The distances from the midrib at each vertical division were measured to obtain the divisions in the parallel direction (Supporting Information File 1, Figure S3). Commercial

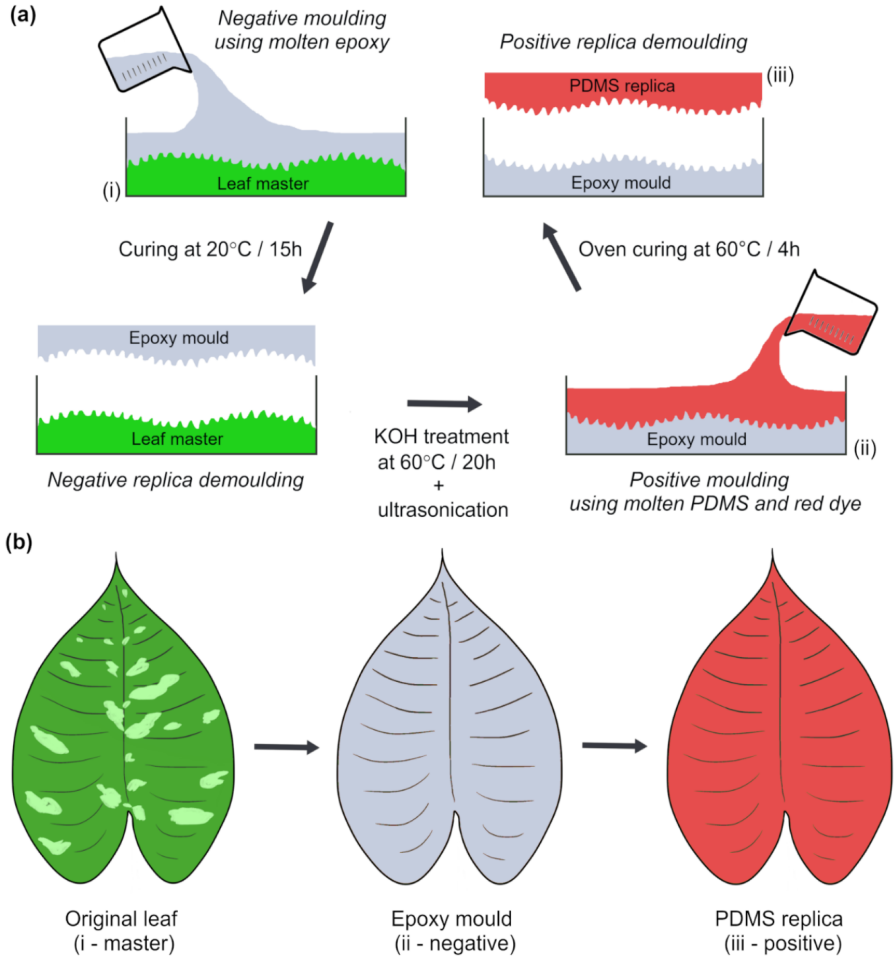


Figure 7: Schematic representation of (a) the replication process of *Schismatoglottis calyptrata* leaf surfaces and (b) original, epoxy negative and PDMS positive replicas. The leaves at stages 1 and 2 were unrolled for replication and the adaxial side of the leaves at all stages were replicated.

surface analysis software (Mountains Map Premium version 7.4, Digital Surf SARL, Besançon, France) was used to analyze the CLSM measurements. After the filtering of median noise, zig-zag profile lines of at least 200 µm in length were taken on the topographic layer of each spot. A standard Gaussian filter (8 µm) was applied to the profiles in order to separate waviness and roughness. In order to compare the variation in the ridge morphology during growth, we calculated standard line roughness parameters, namely *Rc* (mean height), *Rsm* (mean spacing), *Ra* (arithmetic mean height) [47], and the aspect ratio of the ridges defined as $AR = Rc/Rsm$.

In addition, we selected single epidermal cells within the spots, and on each cell, we differentiated between "ridge island" as the central region with zig-zag or longitudinal arrangement of ridges (i.e., ridges not radially arranged) and "periphery" as the transition zone between the ridge island and the anticlinal field, featuring ridges that are radially oriented with respect to the cell center. The center of the anticlinal field was used to demarcate the adjacent cells. A total of twelve epidermal cells were analysed within each ontogenetic stage. We used ImageJ software (FIJI, version 1.53f51) to assess the ontogenetic differences in size and orientation of the ridge islands and the epidermal cells (ridge island + periphery, also see Figure 5a). The directionality plugin (version 2.3.0) in ImageJ software was used to analyse the orientation of ridges in the ridge island and the periphery at different growth stages.

Insect traction experiments

Insect walking frictional forces were measured on a freshly unrolled (stage 3) and an adult (stage 4) *S. calyptrata* leaf and were compared with the forces on a clean glass slide. The glass slide was cleaned with acetone followed by isopropyl alcohol before performing the traction experiments. For these experiments, female Colorado potato beetles (*Leptinotarsa decemlineata*, Coleoptera: Chrysomelidae) with hairy tarsal attachment system were used as model insect species. The beetles were collected from an organically farmed potato field in Kirchzarten area near Freiburg, Germany, kept in a terrarium and were fed with potato leaves. The lighting conditions were fixed at a day–night regime of 16L:8D by using a lamp (Osram Lumilux Daylight 860, 58 W). Insect traction experiments were performed with a total of seven beetles as described in Prüm et al. [8] and Surapaneni and co-workers [23]. A highly sensitive force transducer (FORT 25, force range: 0–0.25 N, World Precision Instruments Inc., Sarasota, USA) was used to measure maximum walking frictional forces of insects on the leaf surfaces. The elytra of each beetle was attached to the force transducer using a human hair by using a small drop of molten beeswax. The insects were allowed to walk actively for at least 2 min on the experimental samples and the forces were recorded on a computer. Only data from walking in a straight line with less than a ±2° variation were analysed. Within each measurement, the median of the 15 highest local maxima with a minimum interval of 3 s between neighbouring force peaks was extracted. Supporting Information File 3 shows a potato beetle walking on the leaf surface. The average mass of the beetles was 0.17 g. The experiments were conducted under an average temperature of 23.8 ± 0.4 °C and humidity of 41.5 ± 2.1% RH.

Statistics

The roughness, traction force and cell size data were analyzed using Kruskal–Wallis test followed by pairwise multiple comparisons using Dunn's test adjusted with the Bonferroni correction. All statistical tests were performed using *R* software environment version 3.6.1 [48]. The experimental data (the raw data and the code) for this study is publicly available on https://freidok.uni-freiburg.de/data/193850 [49].

Supporting Information

Supporting Information File 1

Additional figures.
[https://www.beilstein-journals.org/bjnano/content/supplementary/2190-4286-12-98-S1.pdf]

Supporting Information File 2

Orientation of ridges in ridge islands and periphery.
The orientation data was collected from the ridge islands and the periphery of a cell using the directionality plugin of the ImageJ software. The data shows typical variation in the ridge orientation (angle with horizontal) at different growth stages.
[https://www.beilstein-journals.org/bjnano/content/supplementary/2190-4286-12-98-S2.pdf]

Supporting Information File 3

Colorado potato beetle (*Leptinotarsa decemlineata*) walking on a *Schismatoglottis* leaf sample.
[https://www.beilstein-journals.org/bjnano/content/supplementary/2190-4286-12-98-S3.mp4]

Acknowledgements

We thank the gardeners of the Botanic Garden, University of Freiburg, for cultivating the *S. calyptrata* plants.

Funding

This work was supported by Marie Skłodowska-Curie grant (grant agreement No. 722842, ITN Plant-inspired Materials and Surfaces–PlaMatSu) under the European Union's Horizon 2020

research and innovation program. T.S. and V.A.S. acknowledge additional funding by the Deutsche Forschungsgemeinschaft (DFG, German Research Foundation) under Germany's Excellence Strategy – EXC-2193/1 – 390951807.

Author Contributions

M.T. and T.S. designed and supervised the study. Data collection, data assessment, and statistical analyses were carried out jointly by T.A. and V.A.S. Data evaluation and the discussion of results was a joint effort by all authors (V.A.S., T.A., T.S., and M.T.). V.A.S. contributed to the first draft of the manuscript, and T.S. and M.T. improved further versions. All authors gave final approval for publication.

ORCID® iDs

Venkata A. Surapaneni - https://orcid.org/0000-0002-6241-9048
Thomas Speck - https://orcid.org/0000-0002-2245-2636
Marc Thielen - https://orcid.org/0000-0002-7773-6724

References

1. Holloway, P. J. Structure and histochemistry of plant cuticular membranes: an overview. In *The Plant Cuticle;* Cutler, D. F.; Alvin, K. L.; Price, C. E., Eds.; Academic Press: London, U.K., 1982; pp 1–32.
2. Kerstiens, G. *Plant Cuticles: An Integrated Functional Approach; Environmental plant biology series;* BIOS Scientif. Publ.: Oxford, 1996.
3. Jeffree, C. E. The fine structure of the plant cuticle. In *Biology of the plant cuticle;* Riederer, M.; Müller, C., Eds.; *Annual plant reviews*, Vol. 23; Blackwell Publishing: Oxford, United Kingdom, 2006; pp 11–125. doi:10.1002/9780470988718.ch2
4. Koch, K.; Bhushan, B.; Barthlott, W. *Soft Matter* **2008,** *4,* 1943–1963. doi:10.1039/b804854a
5. Yeats, T. H.; Rose, J. K. C. *Plant Physiol.* **2013,** *163,* 5–20. doi:10.1104/pp.113.222737
6. Barthlott, W.; Ehler, N. *Raster-Elektronenmikroskopie der Epidermis-Oberflächen von Spermatophyten;* Tropische und subtropische Pflanzenwelt 19; Akademie der Wissenschaften und der Literatur Mainz. F. Steiner Verlag [in Komm.]: Wiesbaden, 1977.
7. Kumar, C.; Palacios, A.; Surapaneni, V. A.; Bold, G.; Thielen, M.; Licht, E.; Higham, T. E.; Speck, T.; Le Houérou, V. *Philos. Trans. R. Soc., A* **2019,** *377,* 20180265. doi:10.1098/rsta.2018.0265
8. Prüm, B.; Seidel, R.; Bohn, H. F.; Speck, T. *J. R. Soc., Interface* **2012,** *9,* 127–135. doi:10.1098/rsif.2011.0202
9. Prüm, B.; Bohn, H. F.; Seidel, R.; Rubach, S.; Speck, T. *Acta Biomater.* **2013,** *9,* 6360–6368. doi:10.1016/j.actbio.2013.01.030
10. Li-Beisson, Y.; Pollard, M.; Sauveplane, V.; Pinot, F.; Ohlrogge, J.; Beisson, F. *Proc. Natl. Acad. Sci. U. S. A.* **2009,** *106,* 22008–22013. doi:10.1073/pnas.0909090106
11. Whitney, H. M.; Kolle, M.; Andrew, P.; Chittka, L.; Steiner, U.; Glover, B. J. *Science* **2009,** *323,* 130–133. doi:10.1126/science.1166256
12. Vignolini, S.; Moyroud, E.; Hingant, T.; Banks, H.; Rudall, P. J.; Steiner, U.; Glover, B. J. *New Phytol.* **2015,** *205,* 97–101. doi:10.1111/nph.12958
13. Casado, C. G.; Heredia, A. *Physiol. Plant.* **2001,** *111,* 220–224. doi:10.1034/j.1399-3054.2001.1110213.x
14. Domínguez, E.; Heredia-Guerrero, J. A.; Heredia, A. *New Phytol.* **2011,** *189,* 938–949. doi:10.1111/j.1469-8137.2010.03553.x
15. Das Gupta, M.; Nath, U. *Plant Cell* **2015,** *27,* 2785–2799. doi:10.1105/tpc.15.00196
16. Poethig, R. S.; Sussex, I. M. *Planta* **1985,** *165,* 158–169. doi:10.1007/bf00395038
17. Donnelly, P. M.; Bonetta, D.; Tsukaya, H.; Dengler, R. E.; Dengler, N. G. *Dev. Biol. (Amsterdam, Neth.)* **1999,** *215,* 407–419. doi:10.1006/dbio.1999.9443
18. Nath, U.; Crawford, B. C. W.; Carpenter, R.; Coen, E. *Science* **2003,** *299,* 1404–1407. doi:10.1126/science.1079354
19. Efroni, I.; Eshed, Y.; Lifschitz, E. *Plant Cell* **2010,** *22,* 1019–1032. doi:10.1105/tpc.109.073601
20. Andriankaja, M.; Dhondt, S.; De Bodt, S.; Vanhaeren, H.; Coppens, F.; De Milde, L.; Mühlenbock, P.; Skirycz, A.; Gonzalez, N.; Beemster, G. T. S.; Inzé, D. *Dev. Cell* **2012,** *22,* 64–78. doi:10.1016/j.devcel.2011.11.011
21. Kuchen, E. E.; Fox, S.; Barbier de Reuille, P.; Kennaway, R.; Bensmihen, S.; Avondo, J.; Calder, G. M.; Southam, P.; Robinson, S.; Bangham, A.; Coen, E. *Science* **2012,** *335,* 1092–1096. doi:10.1126/science.1214678
22. Hong, L.; Brown, J.; Segerson, N. A.; Rose, J. K. C.; Roeder, A. H. K. *Mol. Plant* **2017,** *10,* 560–574. doi:10.1016/j.molp.2017.01.002
23. Surapaneni, V. A.; Bold, G.; Speck, T.; Thielen, M. *R. Soc. Open Sci.* **2020,** *7,* 201319. doi:10.1098/rsos.201319
24. Hay, A.; Yuzammi. *Telopea* **2000,** *9,* 1–177. doi:10.7751/telopea20002008
25. Wong, S. Y.; Hoe, Y. C.; Boyce, P. C. *Aroideana* **2016,** *39,* 71–100.
26. Hay, A. *Sandakania* **1996,** *7,* 1–30.
27. Gorb, E. V.; Gorb, S. N. *Entomol. Exp. Appl.* **2002,** *105,* 13–28. doi:10.1046/j.1570-7458.2002.01028.x
28. Gorb, E.; Voigt, D.; Eigenbrode, S. D.; Gorb, S. *Arthropod-Plant Interact.* **2008,** *2,* 247–259. doi:10.1007/s11829-008-9049-0
29. Scholz, I.; Bückins, M.; Dolge, L.; Erlinghagen, T.; Weth, A.; Hischen, F.; Mayer, J.; Hoffmann, S.; Riederer, M.; Riedel, M.; Baumgartner, W. *J. Exp. Biol.* **2010,** *213,* 1115–1125. doi:10.1242/jeb.035618
30. Prüm, B.; Seidel, R.; Bohn, H. F.; Speck, T. *Beilstein J. Nanotechnol.* **2012,** *3,* 57–64. doi:10.3762/bjnano.3.7
31. Voigt, D.; Goodwyn, P. P.; Fujisaki, K. *Arthropod-Plant Interact.* **2018,** *12,* 415–421. doi:10.1007/s11829-017-9591-8
32. Bringe, K.; Schumacher, C. F. A.; Schmitz-Eiberger, M.; Steiner, U.; Oerke, E.-C. *Phytochemistry* **2006,** *67,* 161–170. doi:10.1016/j.phytochem.2005.10.018
33. O'Toole, J. C.; Cruz, R. T. *Plant Physiol.* **1980,** *65,* 428–432. doi:10.1104/pp.65.3.428
34. Grubb, P. J.; Jackson, R. V.; Barberis, I. M.; Bee, J. N.; Coomes, D. A.; Dominy, N. J.; De La Fuente, M. A. S.; Lucas, P. W.; Metcalfe, D. J.; Svenning, J.-C.; Turner, I. M.; Vargas, O. *Ann. Bot. (Oxford, U. K.)* **2008,** *101,* 1379–1389. doi:10.1093/aob/mcn047
35. Kadioglu, A.; Terzi, R. *Bot. Rev.* **2007,** *73,* 290–302. doi:10.1663/0006-8101(2007)73[290:adamlr]2.0.co;2
36. Martens, P. *Protoplasma* **1933,** *20,* 483–515. doi:10.1007/bf02674844
37. Antoniou Kourounioti, R. L.; Band, L. R.; Fozard, J. A.; Hampstead, A.; Lovrics, A.; Moyroud, E.; Vignolini, S.; King, J. R.; Jensen, O. E.; Glover, B. J. *J. R. Soc., Interface* **2013,** *10,* 20120847. doi:10.1098/rsif.2012.0847

38. Bergen, J. Y. *Bot. Gaz. (Chicago)* **1904,** *38,* 285–296. doi:10.1086/328550
39. Lee, B.; Priestley, J. H. *Ann. Bot. (Oxford, U. K.)* **1924,** *os-38,* 525–545. doi:10.1093/oxfordjournals.aob.a089915
40. Juniper, B. E. *J. Linn. Soc. London, Bot.* **1960,** *56,* 413–419. doi:10.1111/j.1095-8339.1960.tb02509.x
41. Cerda, E.; Mahadevan, L. *Phys. Rev. Lett.* **2003,** *90,* 074302. doi:10.1103/physrevlett.90.074302
42. Chung, J. Y.; Nolte, A. J.; Stafford, C. M. *Adv. Mater. (Weinheim, Ger.)* **2011,** *23,* 349–368. doi:10.1002/adma.201001759
43. Lopez-Casado, G.; Matas, A. J.; Dominguez, E.; Cuartero, J.; Heredia, A. *J. Exp. Bot.* **2007,** *58,* 3875–3883. doi:10.1093/jxb/erm233
44. Bergmann, J. B.; Moatsou, D.; Surapaneni, V. A.; Thielen, M.; Speck, T.; Wilts, B. D.; Steiner, U. *Adv. Mater. Interfaces* **2020,** *7,* 2000129. doi:10.1002/admi.202000129
45. Hoe, Y. C.; Gibernau, M.; Wong, S. Y. *Plant Biol.* **2018,** *20,* 563–578. doi:10.1111/plb.12687
46. Kumar, C.; Le Houérou, V.; Speck, T.; Bohn, H. F. *R. Soc. Open Sci.* **2018,** *5,* 172132. doi:10.1098/rsos.172132
47. Leach, R. K. *Fundamental Principles of Engineering Nanometrology,* 1st ed.; Micro & nano technologies series; Elsevier, William Andrew: Amsterdam, 2010. doi:10.1016/c2009-0-20339-4
48. *R Development Core Team; R,* version 3.6.1; R Foundation for Statistical Computing: Vienna, 2010.
49. Surapaneni, V. A.; Aust, T.; Speck, T.; Thielen, M. Polarity in cuticular ridge development and insect attachment on leaf surfaces of Schismatoglottis calyptrata (Araceae), Version 2. FreiDok plus, 2021; https://freidok.uni-freiburg.de/data/193850. doi:10.6094/unifr/193850

License and Terms

This is an open access article licensed under the terms of the Beilstein-Institut Open Access License Agreement (https://www.beilstein-journals.org/bjnano/terms), which is identical to the Creative Commons Attribution 4.0 International License (https://creativecommons.org/licenses/by/4.0). The reuse of material under this license requires that the author(s), source and license are credited. Third-party material in this article could be subject to other licenses (typically indicated in the credit line), and in this case, users are required to obtain permission from the license holder to reuse the material.

The definitive version of this article is the electronic one which can be found at:
https://doi.org/10.3762/bjnano.12.98

BEILSTEIN JOURNAL OF NANOTECHNOLOGY

Effect of sample treatment on the elastic modulus of locust cuticle obtained by nanoindentation

Chuchu Li*[1], Stanislav N. Gorb[1] and Hamed Rajabi[2]

Full Research Paper

Open Access

Address:
[1]Functional Morphology and Biomechanics, Institute of Zoology, Kiel University, Kiel, Germany and [2]Division of Mechanical Engineering and Design, School of Engineering, London South Bank University, London, UK

Email:
Chuchu Li* - cli@zoologie.uni-kiel.de

* Corresponding author

Keywords:
biomimetics; cuticle; locust; material properties; mechanical testing; nanoindentation; water content

Beilstein J. Nanotechnol. **2022,** *13,* 404–410.
https://doi.org/10.3762/bjnano.13.33

Received: 17 January 2022
Accepted: 14 April 2022
Published: 22 April 2022

This article is part of the thematic issue "Biomimetics on the micro- and nanoscale – The 25th anniversary of the lotus effect".

Associate Editor: T. Glatzel

© 2022 Li et al.; licensee Beilstein-Institut.
License and terms: see end of document.

Abstract

Cuticle is one of the most abundant, but least studied, biological composites. As a result, it has contributed very little to the field of biomimetics. An important step to overcome this problem is to study cuticle biomechanics by means of accurate mechanical measurements. However, due to many reasons, mechanical testing on fresh cuticle specimens is not always possible. Hence, researchers often use stored specimens to measure properties of arthropod cuticle. Our knowledge about the influence of different treatment methods on cuticle properties is currently very limited. In this study, we investigated the effect of freezing, desiccation, and rehydration on the elastic modulus of the hind tibial cuticle of locusts obtained by nanoindentation. We found that all the mentioned treatments significantly influence cuticle properties. This is in contrast to previous reports suggesting that freezing did not significantly influence the elastic modulus of native cuticle specimens tested in bending. In the light of our data, we suggest that changes of the elastic modulus of cuticle are not solely due to changes of the water content. Our results provide a platform for more accurate measurements of cuticle properties.

Introduction

Cuticle is a lightweight material that forms the whole exoskeleton of insects, from the flexible intersegmental membrane to the stiff jaws and claws. Cuticle of each insect body part has undergone adaptations that enable it to withstand loads and displacements that are unique to that body part. Such adaptations are achieved through changes in, inter alia, microstructure and sclerotization and have provided cuticle with one of the widest recorded ranges of the elastic modulus ever, that is, 1 kPa to 20 GPa [1].

Owing to developments in mechanical testing [2] and imaging techniques [3] and the use of evolutionary algorithms [4], our

knowledge about the biomechanics of insect cuticle has been widely broadened recently. However, cuticle remains to be one of the least studied biological materials. This is mostly because measuring the mechanical properties of insect cuticle is very challenging in practice. One of these challenges is associated with the rather fast desiccation rate of cuticle, as it loses its water shortly after removal from insect body [5]. Only small changes in the water content can significantly influence cuticle properties and, thereby, the obtained results [6-8].

Mechanical testing of fresh cuticle samples, in contrast, is not always possible. For example, when insects are not locally available, or when they cannot be kept in a laboratory, insect specimens must be stored. Thus, it is necessary to know how sample treatment methods may affect the properties of cuticle. A recent study by Aberle et al. [9] tried to address this question by testing cuticle specimens that were stored using standard procedures, including maintaining samples in water, ethanol, and glutaraldehyde as well as freezing and desiccating them. The authors tested the differently treated samples by three-point-bending tests and found that all the treatments, except for freezing, significantly affect the elastic modulus of fresh locust tibial cuticle [9].

A recent study suggests that, in addition to the treatment procedure, cuticle properties can also be influenced by the testing method [10]. There are significant differences between the elastic moduli of cuticle specimens tested in bending, nanoindentation, tension, and uniaxial compression [10]. This raises the question whether results obtained by Aberle et al. [9] would still be valid if another testing method, such as nanoindentation, is used for measuring cuticle properties. To address this question, here we study the effect of different sample treatments, including freezing, desiccation, and rehydration, on the elastic modulus of the cuticle of desert locust, a well-established model species in studies of insect cuticle. We used nanoindentation as the testing method because it is one of the most widely used experimental approaches for measuring cuticle properties. Furthermore, unlike most macromechanical testing methods, the properties obtained from nanoindentations are not influenced by the geometry of specimens. Hence, nanoindentation is one of the most suitable methods to measure the mechanical properties of cuticle specimens, which usually have complicated shapes. We chose locust hind tibiae as they were used in the former study by Aberle et al. [9], enabling us to compare our results with those from the literature. Our results not only allowed us to systematically analyze the effect of different treatments on the mechanical properties of insect cuticle but also to provide a guideline for more accurate measurements of the mechanical properties of insect cuticle in the future.

Materials and Methods

Ethics

All procedures in this study comply with ethical guidelines at Kiel University.

Sample preparation and treatment

The desert locusts *Schistocerca gregaria* were obtained from pet shops in Kiel, Germany. They were raised under controlled temperature (25–30 °C) and humidity (30%–40%), kept under natural day/night light and fed with fresh vegetables. Prior to any experiment, insects were euthanized with CO_2. We used only adult individuals, 21 days after imaginal molt. Hind leg tibiae were cut off directly below the femur–tibia joint with sharp razors and subdivided into four groups. Specimens in each group were subjected to one of the following treatments. (i) Fresh treatment: The samples in this group were used in their fresh state quickly after being cut from the body (less than 2 min) without any additional treatment. (ii) Freezing treatment: Fresh hind tibiae were stored in 0.5 mL Eppendorf tubes (Carl Roth GmbH & Co. KG, Karlsruhe, Germany) and kept at −20 °C for 48 h without medium. Frozen samples were thawed for 15 min in distilled water to room temperature. (iii) Desiccation treatment: Fresh hind tibiae were air dried for 48 h at room temperature. Air drying is one of the most common methods for drying cuticle samples. In the following, we refer to the air dried tibiae as desiccated specimens. (iv) Rehydration treatment: Desiccated hind tibiae were immerged into distilled water and kept at 4 °C for 48 h without medium.

Mechanical testing

Pieces of about 2.0 × 0.5 × 0.5 mm^3 size were separated from the middle part of the hind tibiae using a razor blade. They were then glued (5925 Ergo, Kisling AG, Wetzikon, Switzerland) on a sample holder within 2 min after separation from the tibiae. To avoid desiccation, except for desiccation treatment, small pieces of wet cotton were used to surround the tibiae (Figure 1b). The wet cotton pieces were covered by a layer of parafilm (BEMIS Packaging Deutschland GmbH, Rheinbach, Germany) [11]. Prior to testing, the cross section of the specimens was polished with sandpaper with a grain diameter of 0.3 µm (ITW Test & Measurement GmbH, Esslingen, Germany). We performed the indentations normal to the cross section of the tibiae. This resulted in the measurement of the elastic moduli of the tibial cuticle in the longitudinal direction (along the axis of tibia) (Figure 1).

The specimens were indented using a SA2 Nanoindenter (MTS Nano Instruments, Oak Ridge, TN, USA) equipped with a Berkovich diamond tip. The elastic modulus of the specimens was measured using the continuous stiffness measurement

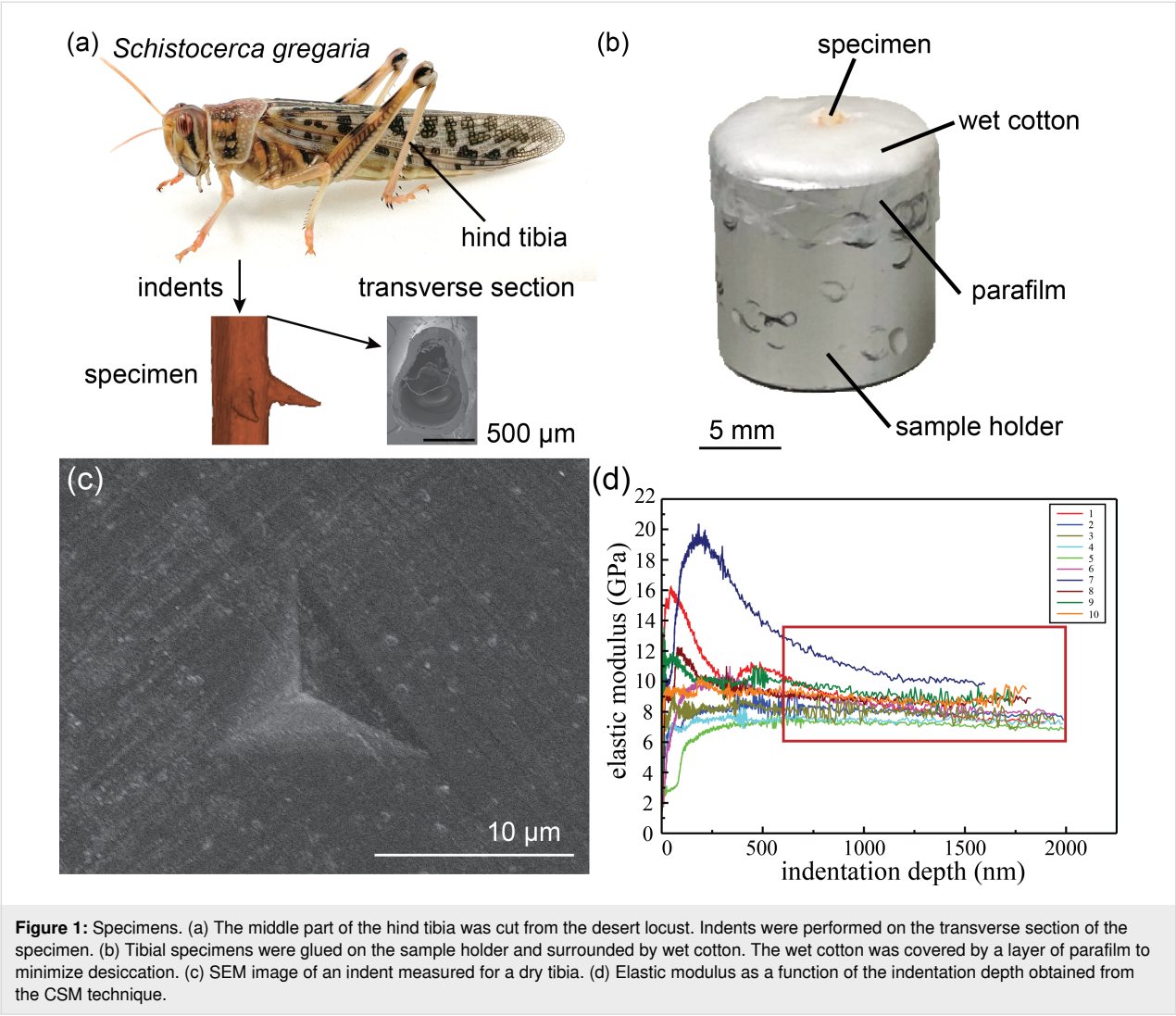


Figure 1: Specimens. (a) The middle part of the hind tibia was cut from the desert locust. Indents were performed on the transverse section of the specimen. (b) Tibial specimens were glued on the sample holder and surrounded by wet cotton. The wet cotton was covered by a layer of parafilm to minimize desiccation. (c) SEM image of an indent measured for a dry tibia. (d) Elastic modulus as a function of the indentation depth obtained from the CSM technique.

(CSM) technique. CSM is a well-established technique for obtaining the elastic modulus continuously as a function of the indentation depth (Figure 1d). The method involves applying a dynamic load on the top of the static load while loading. The dynamic unloading part is then used to measure the stiffness, which is further processed to calculate the elastic modulus of the cuticle [12,13]. Nanoindentations were performed on the cross sections of the tibiae on ten preset indentation sites. The distance between adjacent indentation sites was set to be larger than 30 µm, to avoid the interference between consecutive measurements. In all indentations, maximum indentation depth, strain rate, harmonic displacement, and harmonic frequency were set as 2.0 µm, 0.05 s^{-1}, 1.0 nm, and 75 Hz, respectively. The Poisson's ratio of the tibia specimens was assumed to be 0.3 [14]. The allowable drift rate was set as 0.10 nm/s to minimize the effect of vibration and thermal drift during measurements [11]. We have only used the left hind tibiae of desert locust for mechanical testing. In total, 20 left hind tibiae from 20 locust individuals underwent four treatments, namely fresh (n = 5), freezing (n = 5), desiccation (n = 5), and rehydration (n = 5). The elastic modulus reported for each indentation is the average value of the elastic moduli measured during indentations from 0.6 to 2.0 µm (red box, Figure 1d). The elastic modulus of each tibia is the average elastic modulus obtained from ten indents.

Water content and evaporation rate measurements

To measure the water content of the specimens, paired weight measurements were performed before and after the treatments. The weight of small cut tibiae was measured twice, once at the beginning and again after 4 h (to allow for full desiccation), using an ultramicrobalance UMX2 (Sartorius Lab Instruments GmbH & Co. KG, Göttingen, Germany). In total, 30 specimens from 15 individuals were measured. The weights of 15 right hind tibiae were first measured as fresh, then after desiccation,

and finally after rehydration, while 15 left hind tibiae were measured for freezing treatment. The evaporation rates of three more fresh and three more frozen specimens were measured by continuous recording of the weight of the specimens every minute for 3 h.

Statistics

The elastic moduli and water content were compared between the different treatment groups. Significant differences were tested by one-way ANOVA tests. All statistical analyses were performed with Sigmaplot v.12.5 (Systat Software GmbH, Erkrath, Germany). All values shown in the manuscript are mean ± standard deviation (s.d.).

Results

Influence of sample treatment on the elastic modulus of cuticle

We measured the elastic moduli of hind tibiae in different treatment groups. The results obtained from nanoindentation are presented in Figure 2a. The elastic modulus values of the frozen specimens are reported from our previous study [11]. The elastic moduli of the fresh, frozen, desiccated, and rehydrated hind tibiae are 4.8 ± 0.2, 7.3 ± 0.2, 9.4 ± 0.5, and 6.2 ± 0.2 GPa, respectively. Significant differences were found between each of the two different treatment groups (Holm–Sidak one-way ANOVA, $P < 0.001$).

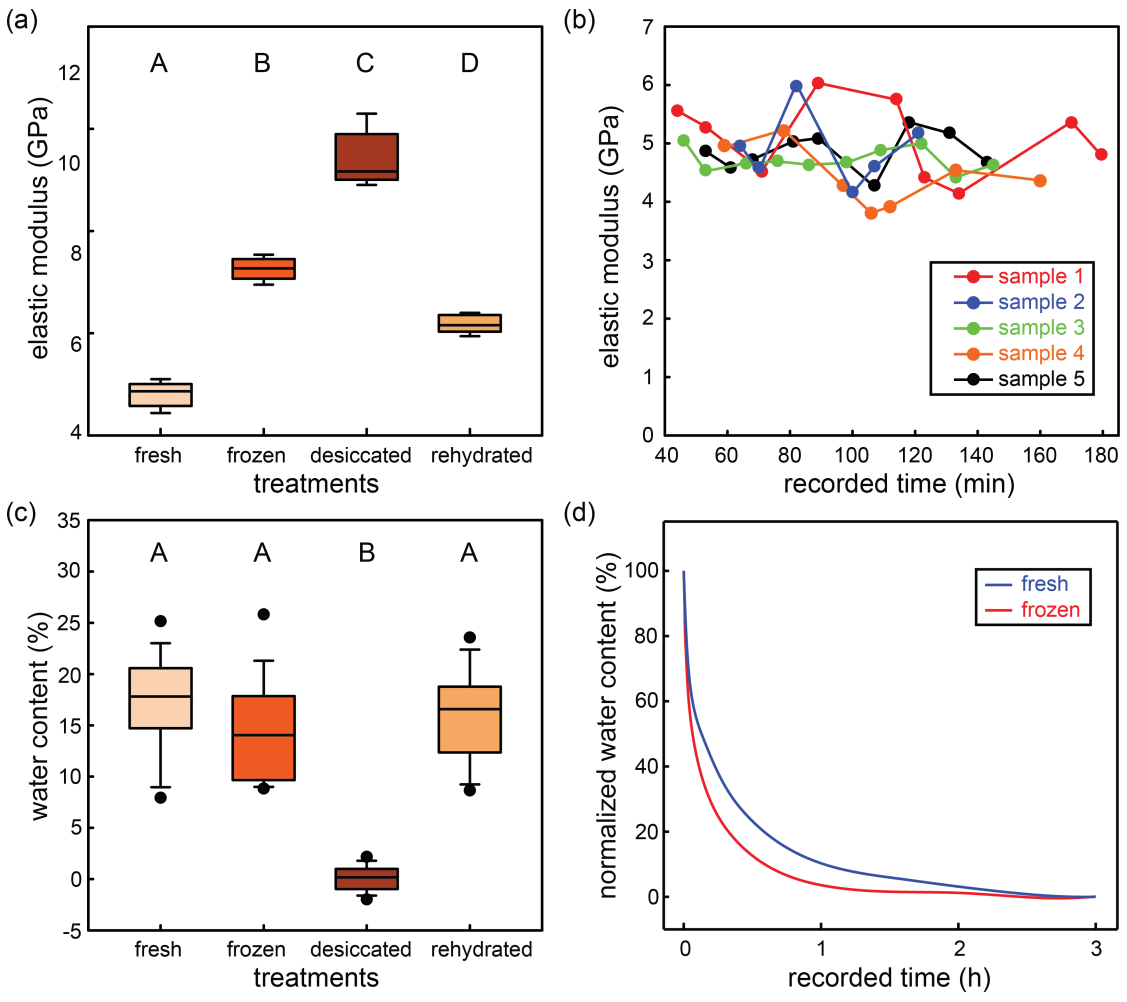


Figure 2: Elastic modulus and water content of specimens in different treatment groups. (a) The elastic moduli of fresh (n = 5), frozen (n = 5), desiccated (n = 5), and rehydrated (n = 5) hind tibiae are 4.8 ± 0.2, 7.3 ± 0.2, 9.4 ± 0.5, and 6.2 ± 0.2 GPa, respectively. Significant differences were determined via Holm–Sidak one-way ANOVA. Different capital letters indicate significant differences ($P < 0.001$). (b) Elastic modulus of fresh tibiae as a function of the recorded time. Different samples are presented in different colors. Each data point represents the elastic modulus obtained from a distinct indentation site. (c) Water contents of fresh (n = 15), frozen (n = 15), desiccated (n = 15), and rehydrated (n = 15) hind tibiae. Significant differences were determined via Kruskal–Wallis one-way ANOVA on ranks. Different capital letters indicate significant differences ($P < 0.05$). (d) Water contents of fresh (n = 3) and frozen tibiae (n = 3) as function of the time.

It is important to note that the results were consistent over time and no specific trend was observed in the values obtained from the measurements during the course of indentations (Figure 2b and Figure 3). In addition, the elastic moduli of the tibiae remained almost constant by increasing the indentation depth (Figure 1d).

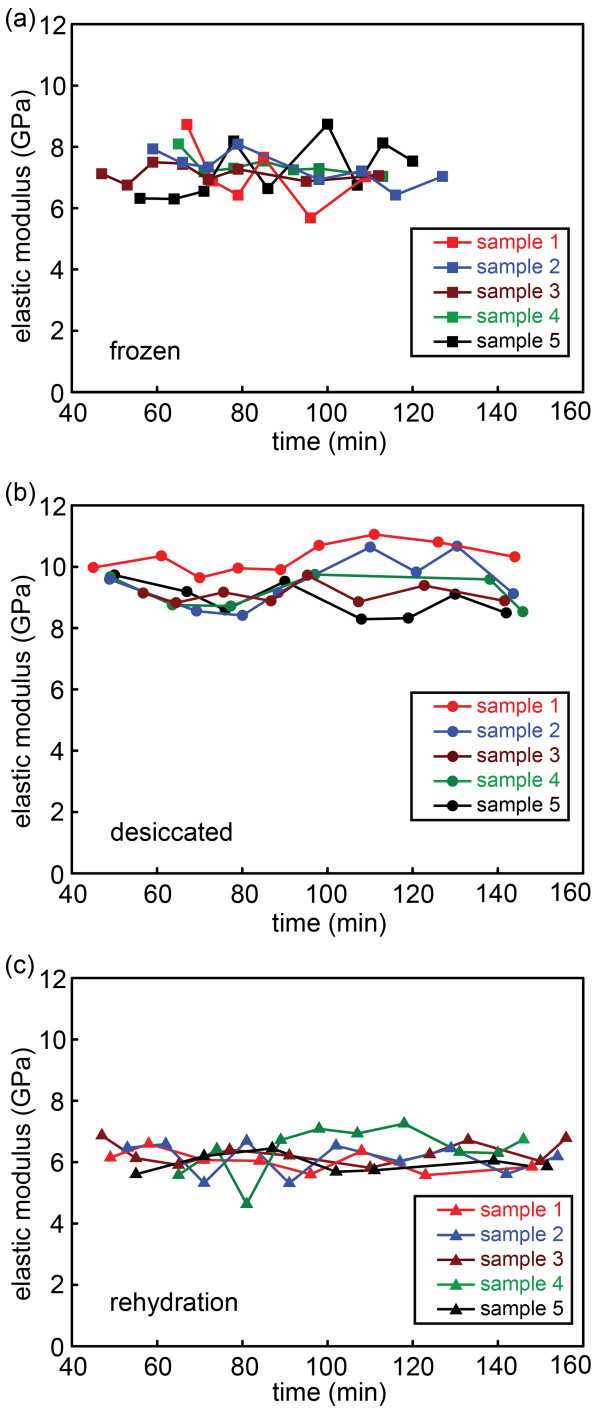


Figure 3: Elastic modulus of (a) frozen, (b) desiccated and (c) rehydrated tibiae against recorded time. Different colors represent different samples.

Water content and evaporation rates during different treatments

We measured the changes in weight of the cuticle samples caused by desiccation in the different treatment groups. This allowed us to measure the water content of the cuticle specimens. The water contents are presented by the ratio between the lost weight of a specimen and its original weight. The water content of fresh, frozen, desiccated, and rehydrated tibiae were (17.11 ± 4.98)%, (14.03 ± 4.69)%, (0.08 ± 1.16)% and (15.81 ± 4.33)%, respectively (Figure 2c). Significant differences were found between fresh/frozen/rehydrated tibiae and desiccated samples (Kruskal–Wallis one-way ANOVA on ranks, $P < 0.05$). The normalized water content of fresh and frozen tibiae as a function of the recorded time is shown in Figure 2d.

Discussion

Mechanical characterization of fresh cuticle

The mechanical properties of insect cuticle are strongly influenced by the level of hydration [6-8]. Hence, to obtain realistic data, performing mechanical tests on fresh cuticle samples is necessary. Giving that it is not always possible to perform mechanical measurements on living insects, two methods are frequently used to characterize the properties of “fresh” cuticle: (i) testing cuticle samples immediately after removal from living insects [5] and (ii) submerging the specimens in water before and during the test [8]. However, both of these two methods have limitations. As shown in the present study, 60% of the water content of our cuticle specimens evaporated within 15 min after removal from the insect body (Figure 2d). This can potentially lead to a significant change in the measured properties even during this short period of time. Storing the specimens in water can also cause overhydration. The increased amount of water can result in swelling of specimens, which can consequently reduce the cuticle stiffness [9,15].

Here, we suggest a new protocol that can be used to measure the elastic modulus of cuticle specimens in their native state. The level of hydration of freshly dissected cuticle specimens is maintained by surrounding them with wet pieces of cotton. In this way, the specimens can absorb water from the wet cotton pieces without being overhydrated. Our results suggest that this is a more suitable method to measure the elastic modulus of dissected cuticle specimens. We found no clear trend in the elastic modulus of our specimens prepared in this way during three hours of testing (Figure 2b and Figure 3), which additionally suggests that this preparation could maintain the water content of our specimens.

Effect of treatments on the elastic modulus of cuticle

Effect of desiccation

It is well known that desiccation can change the mechanical properties, for example, stiffness and hardness, of insect cuticle. The increase in the elastic modulus, in particular, can be rather large, up to more than tenfold of the stiffness of cuticle in the native state [16]. This is because water makes cuticle soft and compliant. A significant increase was also observed in the elastic modulus of our specimens after desiccation. The elastic modulus of the desiccated specimens was about twice that of the fresh specimens. This relatively small increase in the elastic modulus observed here is likely due to a higher level of sclerotization of our cuticle specimens in comparison to the previously tested ones. A highly sclerotized cuticle sample contains less water in comparison to a less sclerotized sample. Thereby, desiccation would have a lesser effect on the properties of sclerotized samples.

Effect of rehydration

In a previous study, Klocke and Schmitz [8] measured the elastic modulus of rehydrated specimens of locust sternal cuticle. They found that the elastic moduli obtained from their experiments were higher than those reported in the literature for similar cuticle parts. They, therefore, suggested that rewetting of a cuticle specimen might not return its hydration level to the native state. Our results also showed that the elastic modulus of rehydrated cuticle sample is significantly higher than that of fresh specimens. However, surprisingly, we found no significant difference between the water content of the fresh and rehydrated cuticle samples (Figure 2c). This raises the question about the source of the observed difference between the elastic moduli of fresh and rehydrated cuticles. It might be due to the changes in the interaction of water molecules with the chitin of the cuticle after rehydration. Insect cuticle is a biological composite with a protein matrix and embedded chitin fibers [17]. It is the only biological composite that has been modelled successfully using the modified Voigt estimate of the composite elastic modulus [15]. According to the Voigt model, the effective elastic modulus parallel to the fibers in a unidirectional fiber composite, such as locust hind tibial cuticle [11], can be estimated by [15]

$$E = E_f V_f + E_m V_m, \quad (1)$$

where E_f and V_f are, respectively, elastic modulus and volume fraction of the fibers, and E_m and V_m are elastic modulus and volume fraction of the matrix, respectively.

Most of the water in the cuticle is associated with the protein matrix, where free water can be added to or taken from [1]. Thus, the elastic modulus of the matrix might not show a difference between the fresh and rehydrated states. The elastic modulus of fibers, however, is affected by the density of effective hydrogen bonds (H-bonds) [18]. Addition or removal of water can presumably disrupt these structural H-bonds and, therefore, affect the elastic modulus of cuticle [15]. This effect, based on the results of our study and those previously reported by Klocke and Schmitz [8], is likely to be irreversible.

Effect of freezing

According to our results, the elastic modulus of frozen tibia is significantly higher than that of fresh and rehydrated cuticle. This is in contradiction to the previously reported data obtained from three-point bending tests [9], which showed no significant difference between the elastic moduli of fresh and frozen tibiae. This contradiction is probably due to one key reason, namely the different desiccation rates of specimens prepared for nanoindentation and bending tests. In fact, desiccation of natively hydrated cuticle samples is an inevitable process if they are not continuously supplied by hemolymph. The desiccation rate is faster near cuticle surfaces. Hence, it is likely that small nanoindentation specimens are more prone to desiccation than larger bending tests specimens, which have smaller surface areas with respect to their total volume. It must be clarified whether the desiccation discussed here happens during the nanoindentation measurement instead of during the freezing process.

Water content of locust tibial cuticle

According to previous reports, the water content of cuticle varies between 12% and 75%, depending on the sclerotization level [1]. Our results indicated a water content of ca. 17%, which is in agreement with literature data. Nevertheless, previous studies on locust hind tibia showed that the water content of this body part can be up to 47% [5,9]. We expect this difference is due to the influence of hydrated soft tissues (e.g., membranes and muscles) that are attached to the interior wall of the tibial cuticle. In our study, we carefully removed the inner tissues, whereas the previous studies have been performed on the whole tibia.

Conclusion

The complex relationship between multiple factors, such as microstructure, material composition, and sclerotization, has provided cuticle with properties that are unique to this biological material. Understanding the mechanisms behind the remarkable properties of cuticle can inspire the design of engineering composites with enhanced properties. Specifically, cuticle can help us to develop ceramics with improved fracture toughness or overcome limitations of existing engineering materials by combining conflicting properties. A first step towards these

aims is to develop guidelines for measuring cuticle properties accurately.

Our results show that none of the examined treatment methods, that is, freezing, desiccation, and rehydration, can represent the elastic modulus of native cuticle specimens when tested by nanoindentation. Considering that no significant difference was found between the water content of the fresh, frozen, and rehydrated specimens, the difference in their elastic moduli cannot be solely attributed to the presence/absence of water. Instead, other additional factors, such as desiccation rate and/or how the water molecules interact with other molecules within the cuticle, are important. Our study can be used as a template for future studies that aim to measure cuticle properties using nanoindentation or other nano- or micromechanical testing methods.

Data Accessibility

All supporting data are made available in the article.

Authors' Contributions

Conceptualization: SNG and HR; formal analysis: CL; funding acquisition: CL and SNG; investigation: CL; methodology: CL, HR, and SNG; resources: SNG; supervision: HR and SNG; validation: CL; visualization: CL; writing – original draft preparation: CL and HR; writing – review and editing: CL, HR and SNG.

Funding

This study was financially supported by the "China Scholarship Council" to CL (Grant no. 201706400069), and the Deutsche Forschungsgemeinschaft (DFG) to SNG (Project no. 410547361).

ORCID® iDs

Chuchu Li - https://orcid.org/0000-0001-5524-828X
Stanislav N. Gorb - https://orcid.org/0000-0001-9712-7953
Hamed Rajabi - https://orcid.org/0000-0002-1792-3325

References

1. Vincent, J. F. V.; Wegst, U. G. K. *Arthropod Struct. Dev.* **2004,** *33,* 187–199. doi:10.1016/j.asd.2004.05.006
2. Lucca, D. A.; Herrmann, K.; Klopfstein, M. J. *CIRP Ann.* **2010,** *59,* 803–819. doi:10.1016/j.cirp.2010.05.009
3. Michels, J.; Gorb, S. N. *J. Microsc. (Oxford, U. K.)* **2012,** *245,* 1–16. doi:10.1111/j.1365-2818.2011.03523.x
4. Eshghi, S. h.; Jafarpour, M.; Darvizeh, A.; Gorb, S. N.; Rajabi, H. *J. R. Soc., Interface* **2018,** *15,* 20180312. doi:10.1098/rsif.2018.0312
5. Dirks, J.-H.; Taylor, D. *J. Exp. Biol.* **2012,** *215,* 1502–1508. doi:10.1242/jeb.068221
6. Enders, S.; Barbakadse, N.; Gorb, S. N.; Arzt, E. *J. Mater. Res.* **2004,** *19,* 880–887. doi:10.1557/jmr.2004.19.3.880
7. Schöberl, T.; Jäger, I. L. *Adv. Eng. Mater.* **2006,** *8,* 1164–1169. doi:10.1002/adem.200600143
8. Klocke, D.; Schmitz, H. *Acta Biomater.* **2011,** *7,* 2935–2942. doi:10.1016/j.actbio.2011.04.004
9. Aberle, B.; Jemmali, R.; Dirks, J.-H. *Arthropod Struct. Dev.* **2017,** *46,* 138–146. doi:10.1016/j.asd.2016.08.001
10. Stamm, K.; Saltin, B. D.; Dirks, J.-H. *Appl. Phys. A: Mater. Sci. Process.* **2021,** *127,* 329. doi:10.1007/s00339-021-04439-3
11. Li, C.; Gorb, S. N.; Rajabi, H. *Acta Biomater.* **2020,** *103,* 189–195. doi:10.1016/j.actbio.2019.12.013
12. Li, X.; Bhushan, B. *Mater. Charact.* **2002,** *48,* 11–36. doi:10.1016/s1044-5803(02)00192-4
13. Kossovich, E. L.; Borodich, F. M.; Epshtein, S. A.; Galanov, B. A.; Minin, M. G.; Prosina, V. A. *Appl. Phys. A: Mater. Sci. Process.* **2019,** *125,* 195. doi:10.1007/s00339-018-2282-1
14. Rajabi, H.; Jafarpour, M.; Darvizeh, A.; Dirks, J.-H.; Gorb, S. N. *J. R. Soc., Interface* **2017,** *14,* 20170310. doi:10.1098/rsif.2017.0310
15. Kitchener, A.; Vincent, J. F. V. *J. Mater. Sci.* **1987,** *22,* 1385–1389. doi:10.1007/bf01233138
16. Vincent, J. F. V. *J. Bionic Eng.* **2004,** *1,* 4–8. doi:10.1007/bf03399449
17. Neville, A. C. *Biology of the arthropod cuticle;* Springer Verlag: Berlin, Germany, 1975. doi:10.1007/978-3-642-80910-1
18. Nissan, A. H. *Macromolecules* **1976,** *9,* 840–850. doi:10.1021/ma60053a026

License and Terms

This is an open access article licensed under the terms of the Beilstein-Institut Open Access License Agreement (https://www.beilstein-journals.org/bjnano/terms), which is identical to the Creative Commons Attribution 4.0 International License (https://creativecommons.org/licenses/by/4.0). The reuse of material under this license requires that the author(s), source and license are credited. Third-party material in this article could be subject to other licenses (typically indicated in the credit line), and in this case, users are required to obtain permission from the license holder to reuse the material.

The definitive version of this article is the electronic one which can be found at:
https://doi.org/10.3762/bjnano.13.33

BEILSTEIN JOURNAL OF NANOTECHNOLOGY

Hierachical epicuticular wax coverage on leaves of *Deschampsia antarctica* as a possible adaptation to severe environmental conditions

Elena V. Gorb*[1], Iryna A. Kozeretska[2] and Stanislav N. Gorb[1]

Full Research Paper

Open Access

Address:
[1]Department of Functional Morphology and Biomechanics, Zoological Institute, Kiel University, Am Botanischen Garten 9, 24118 Kiel, Germany and [2]National Antarctic Scientific Center of Ukraine, Taras Shevchenko Boulevard 16, 01601 Kyiv, Ukraine

Email:
Elena V. Gorb* - egorb@zoologie.uni-kiel.de; Stanislav N. Gorb - sgorb@zoologie.uni-kiel.de

* Corresponding author

Keywords:
cryo-SEM; microstructure; plant; surface; wax projection

Beilstein J. Nanotechnol. **2022,** *13,* 807–816.
https://doi.org/10.3762/bjnano.13.71

Received: 27 May 2022
Accepted: 10 August 2022
Published: 22 August 2022

This article is part of the thematic issue "Biomimetics on the micro- and nanoscale – The 25th anniversary of the lotus effect".

Associate Editor: K. Koch

© 2022 Gorb et al.; licensee Beilstein-Institut.
License and terms: see end of document.

Abstract

Using cryo scanning electron microscopy, the surface micromorphology of vegetative (leaf blade and ligule) and generative (pedicel and outer glume) organs in *Deschampsia antarctica*, one of the only two flowering plants native to Antarctica, was examined. Whereas the pedicel and outer glume were wax-free, both leaf sides had a prominent epicuticular wax coverage consisting of two superimposed layers: polygonal rodlets formed by fused irregular platelets (the lower wax layer) and membraneous platelets (the upper wax layer). Although the adaxial (inner) and abaxial (outer) leaf surfaces showed a similar microstructure of the wax coverage, they differed in the thickness ratio between lower and upper wax layer. The ligule bore a very loose wax coverage composed of separate scale-like projections or clusters of them. We suppose that the two-layered wax densely covering both leaf surfaces might contribute to the plant adaptation to severe environmental conditions in Antarctica due to an increase of its resistance against cold temperatures, icing, harmful UV radiation, and dehydration. The presence of the epicuticular wax on the abaxial leaf side and the ligule as well as the hierarchical structure of the wax coverage on both leaf surfaces is described in *D. antarctica* for the first time.

Introduction

The Antarctic hair grass *Deschampsia antarctica* É. Desv. (Poaceae) is one of the only two flowering plants native to Antarctica, where it inhabits northern and western parts of the Antarctic Peninsula and adjacent islands free of permanent ice and snow in summer [1]. These perennial, 3–20 cm high plants have leaves with narrow folded or V-shaped ribbed leaf blades and true panicle inflorescences. They grow either as a separate clump or form a dense and continuous cover spreading from

one to several hundred square meters and occupy all favourable places for growing, such as rocks, hollows, corniches, and beaches, either poor or overrich with semidecomposed organics soils [2,3].

Compared to the other flowering plant species native to Antarctica, the Antarctic pearlworts *Colobanthus quitensis* Kunth Bartl. (Caryophyllaceae), which is rather rare and mainly relays on an avoidance strategy (i.e., it grows near higher clumps of *D. antarctica* or in hollows between stones avoiding direct influence of unfavorable abiotic factors), the Antarctic hair grass not only uses the avoidance strategy, but also grows in separate agglomerations or forms thick covers on the unprotected ground surface [3]. Especially in the latter case, *D. antarctica* plants are fully exposed to the cold desert climate of Antarctica, including low temperatures, moisture deficit, and strong ultraviolet radiation [2,4].

In view of the remarkable success of this plant species in the colonization of the Maritime Antarctica (i.e., ice- and snow-free lands along the Antarctic Peninsula, its associated islands, and coastal regions around the rest of the Antarctic continent accounting for less than 1% of the Antarctica territory [5]), intensive experimental investigations were recently performed on structural, physiological, genetical, and molecular biological characteristics of *D. antarctica*, in order to find specialized adaptations to severe environmental conditions that ensure this evolutionary success [2-4,6]. Structural studies that have been focused mainly on anatomical and ultrastructural characterization of leaves [4,7-12] did not reveal any qualitative traits allowing for a distinction of this plant from other polar species and explaining its better survival in the Antarctica region. The leaves exhibit xerophytic (i.e., typical for plants growing in arid places) morphological and anatomical attributes, and the general anatomical features of mesophyll cells are similar to those of other plant species growing in cold regions [13] and to those in other grass leaves. However, the surfaces of *D. antarctica* that are exposed to the environment in the first place have not been especially examined in this respect.

In this study, we examined the microstructure of epidermal surfaces in different organs of the *D. antarctica* plant, which are usually exposed to the environment, using cryo scanning electron microscopy (cryo-SEM) allowing for a high-resolution imaging of frozen and fractured samples in native condition, that is, without treatment in strong solvents, such as ethanol or acetone, usually needed in the sample preparation for conventional scanning electron microscopy. This method provided qualitatively new information about the superficial layers on vegetative organs studied in this plant species. Based on the obtained results and literature data, we discuss a possible role of the complex, hierarchical epicuticular wax coverage on the leaf surfaces in the adaptation of *D. antarctica* to the severe Antarctic environment. Additionally, the results obtained from this highly specialized plant species might be potentially interesting for biomimetics of technical surfaces or surface coatings exposed to similar harsh environments (e.g., strong UV irradiation, low temperatures, and icing).

Experimental

Plant material

D. antarctica plants used in this study were collected in the vicinity of Henryk Arctowski Polish Antarctic Station, King George Island, Maritime Antarctica (62°09′50″ S, 58°28′7″ W) during X Ukrainian and XXX Polish Antarctic Expeditions in 2005/2006 (permission AP no. 013-06 to Iryna A. Kozeretska for collection of plant material in the King George Island region, Maritime Antarctica). A separate, small clump of mature plants bearing fully developed flowers was completely dug up including roots, planted into a small plastic flower pot filled with topical soil, and transported to the laboratory.

The surfaces of the following organs were examined (Figure 1): (i) vegetative organs, namely the inner (adaxial) and outer (abaxial) sides of the leaf blade in mature and young leaves as well as the abaxial side of the ligule (a membrane on the adaxial side of the junction of the leaf sheath and leaf blade); and (ii) generative organs, namely the pedicel (a stalk of a single spikelet (collection of flowers (florets) in a grass inflorescence)) and the abaxial surface of the outer, lower glume (a bract below a spikelet). For each organ, we studied three samples belonging to three different plants.

Microscopy

The leaf and inflorescence surfaces were at first studied on fresh, untreated samples in a binocular microscope Leica MZ 12.5 with a built-in videocamera Leica IC A (Leica Microsystems GmbH, Wetzlar, Germany). For cryo-SEM, we used either entire structures (glume and ligule) or small pieces (ca. 1 cm long for pedicle and ca. 1 cm^2 for other samples) cut out with a razor blade from the plant. All surfaces were examined in the native state. Additionally, the leaf blade surfaces were studied after treatment in cold chloroform for 20 s. Plant samples were either glued with Tissue-Tek® O.C.T.™ Compound (Sakura® Finetek Europe B.V., Zoeterwoude, Netherlands) to holders or mechanically gripped in a small vice on holders and then frozen in a cryo-stage preparation chamber at −140 °C (Gatan ALTO 2500 cryo-preparation system, Gatan Inc., Abingdon, UK). Frozen samples, either entire or fractured with a cold metal fracture knife in the cryo-stage preparation chamber, were sputter-coated with gold–palladium (6 nm thickness) and examined in frozen condition (−120 °C) in a cryo-SEM Hitachi

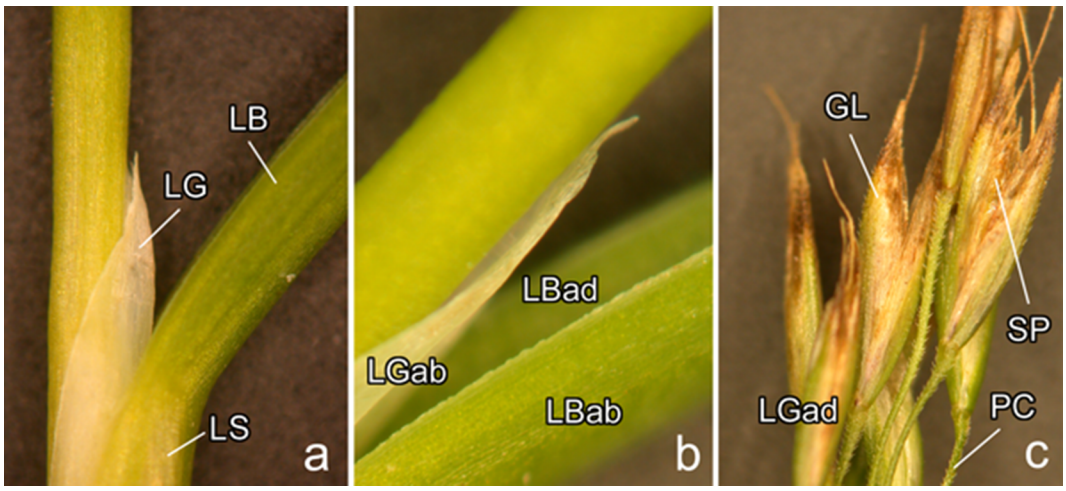


Figure 1: Plant organs and surfaces examined. (a, b) Vegetative organs: the inner, adaxial (LBad) and outer, abaxial (LBab) sides of the leaf blade (LB) and the outer, abaxial (LGab) side of the ligule (LG). (c) Generative organs: the pedicel (PC) and the outer, abaxial side (GLab) of the outer, lower glume (GL). LS, leaf sheath; SP, spikelet.

S-4800 (Hitachi High-Technologies Corporation, Tokyo, Japan) at 3 kV accelerating voltage.

Description of trichomes was performed according to [14]. Types of epicuticular wax structures were identified according to [15]. Morphometric variables of surface features were measured from digital images using the software SigmaScan Pro version 5.0.0 (SPSS Inc., Chicago, USA). The data are given in the text as mean ± SD for n = 10.

Results and Discussion

Micromorphology of plant surfaces

In *D. antarctica*, both leaf lamina sides have characteristic furrowed surfaces, with rather thin and deep grooves, that are caused by shapes of long (>200 µm) and narrow (width: 10.88 ± 1.98 µm) epidermal cells (Figure 2c). In the surface view (i.e., view from above), leaves bear a very dense epicuticular wax coverage composed of numerous membraneous platelets (Figure 2a,d) called here the upper (outer) wax layer. At very high magnifications (probably due to damage by the electron beam), the platelets often looked like being interconnected (Figure 2b). These microscopic, very thin flat projections (length: 0.75 ± 0.08 µm; thickness: 38 ± 6 nm) oriented almost perpendicularly to the epidermal surfaces have no specific arrangement. On the abaxial side, fine thread-like extensions on the margins of the platelets are better seen and the projections seem to be slightly inclined relative to the underlying surface (Figure 2e); these peculiarities are even more expressed in young leaves. On some micrographs, when platelets were removed/damaged, another layer of projections called here the lower (inner) wax layer became exposed (Figure 2f).

The fractured samples clearly show the hierarchical organization of the wax coverage on both leaf lamina sides, which is composed of the two superimposed layers of wax projections (Figure 3a,b,d). Whereas the lower layer is rather compact and consists of densely packed polygonal rodlets (length: 0.42 ± 0.10 µm; width: 0.19 ± 0.03 µm) situated perpendicular to the leaf blade surface and formed by tightly placed and fused thin (thickness: 27 ± 4 nm) irregular platelets, the loose upper layer is represented by separate, but entangled, membraneous platelets having elongated irregular shapes (Figure 3b–e). The connection between layers is provided by outgrowths of some lower platelets, which finally turn into upper platelets (Figure 3c,e). The thickness ratio between the lower wax layer and the upper one on the adaxial leaf side is smaller compared to that on the abaxial side (ca. 0.5 vs ca. 0.8, respectively). After treatment with cold chloroform, the epicuticular wax coverage completely disappeared from both leaf lamina surfaces.

A very similar structure of the epicuticular wax coverage (two-layered, with superimposed wax platelets connected through stalks formed as outgrowths of lower projections) was previously found in trapping organs (pitchers) of several representatives of the carnivorous plants from the genus *Nepenthes* (Nepenthaceae) such as *N. alata* Blanco, *N. fusca* Danser, *N. macrophylla* Jebb and Cheek, *N. mirabilis* (Lour.) Druce, and *N. rafflesiana* Jack [16,17]. The waxy (slippery) zone located inside the pitchers is highly specialized for trapping and retaining of insect prey mainly due to contamination of attachment organs of insects [16], reduction of the real contact area between the plant surface and insect adhesive devices [16,18], and absorption of the insect adhesive fluid [19]. Whereas the upper wax platelets are rather fragile and can be easily broken

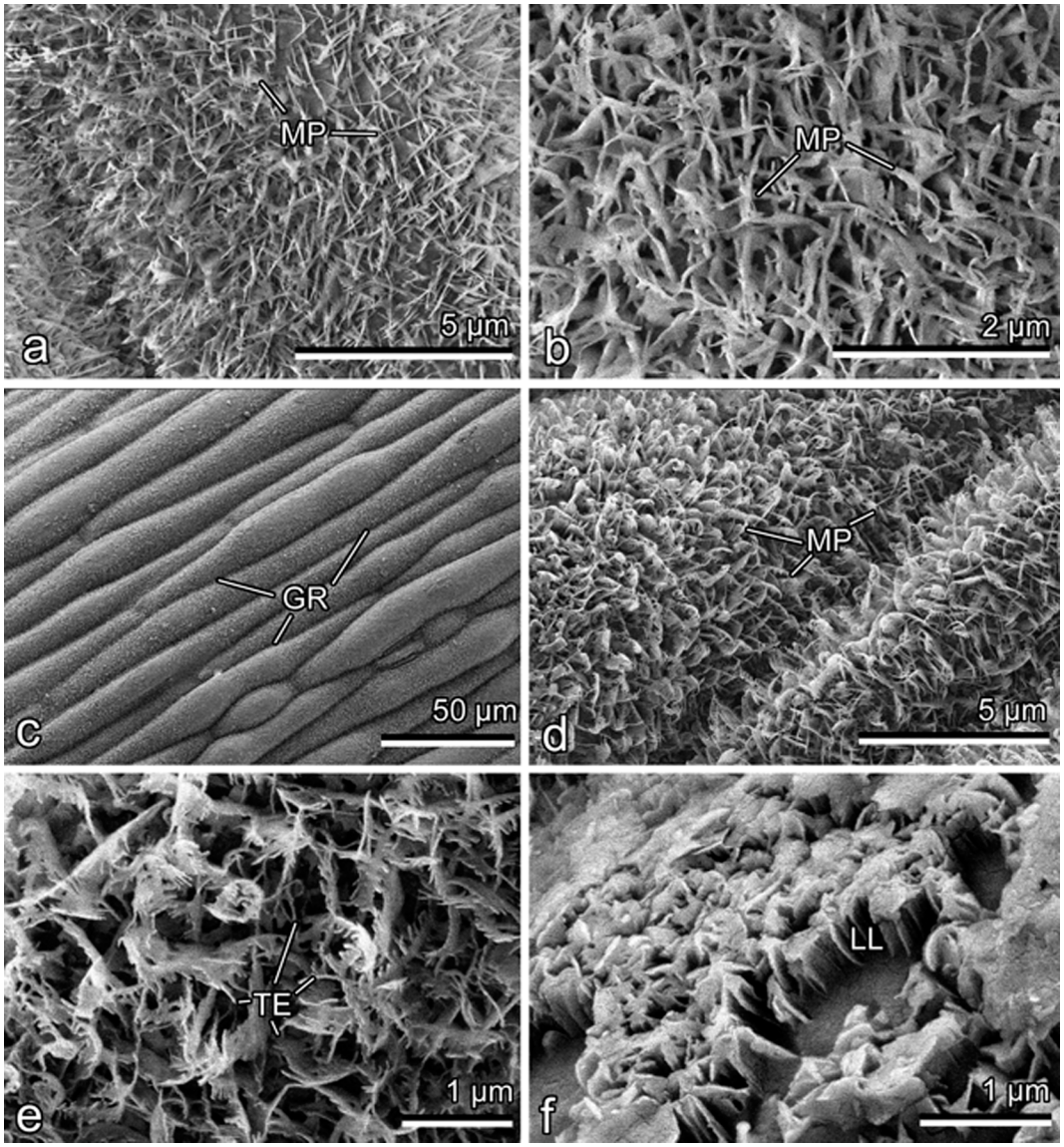


Figure 2: Cryo-SEM micrographs of leaf lamina surfaces. (a, b) Adaxial side. (c–f) Abaxial side. GR, groove; LL, lower wax layer; TE, thread-like extension of the platelet margin; MP, membraneous platelet.

into small pieces and removed from the slippery zone thus contaminating insect attachment organs, the pitchers still remain fully functional in terms of insect trapping owing to the presence of rather stable lower-layer wax projections [16,17]. Taking into account the above consideration about the *Nepenthes* wax, we suggest for leaves of *D. antarctica* that the presence of the two wax layers increases the chance of the wax coverage to fulfill its functions in case when the upper wax layer is for some reasons damaged or removed. Partial damage and/or even removal of the upper layer are very much possible under natural conditions, since the connection of upper projections with the lower layer is realized through very thin and delicate structures (outgrowths of some lower platelets; see Figure 3e), which can readily brake. In this study, we observed such defects in the wax coverage in a few leaf samples, where upper wax platelets were absent and only the lower wax layer remained exposed (see Figure 2f).

The coarsely furrowed abaxial surface of the ligule (Figure 4a) bears a very loose epicuticular wax coverage consisting of either (i) single, separate scale-like projections of irregular shapes (however, often almost semicircular) with regular margins, which vary greatly in size and protrude perpendicularly from the pitcher surface (Figure 4b,c), or (ii) larger projections, gradually changing into platelets and arranged in more or less radial clusters (Figure 4d). In case the clusters become

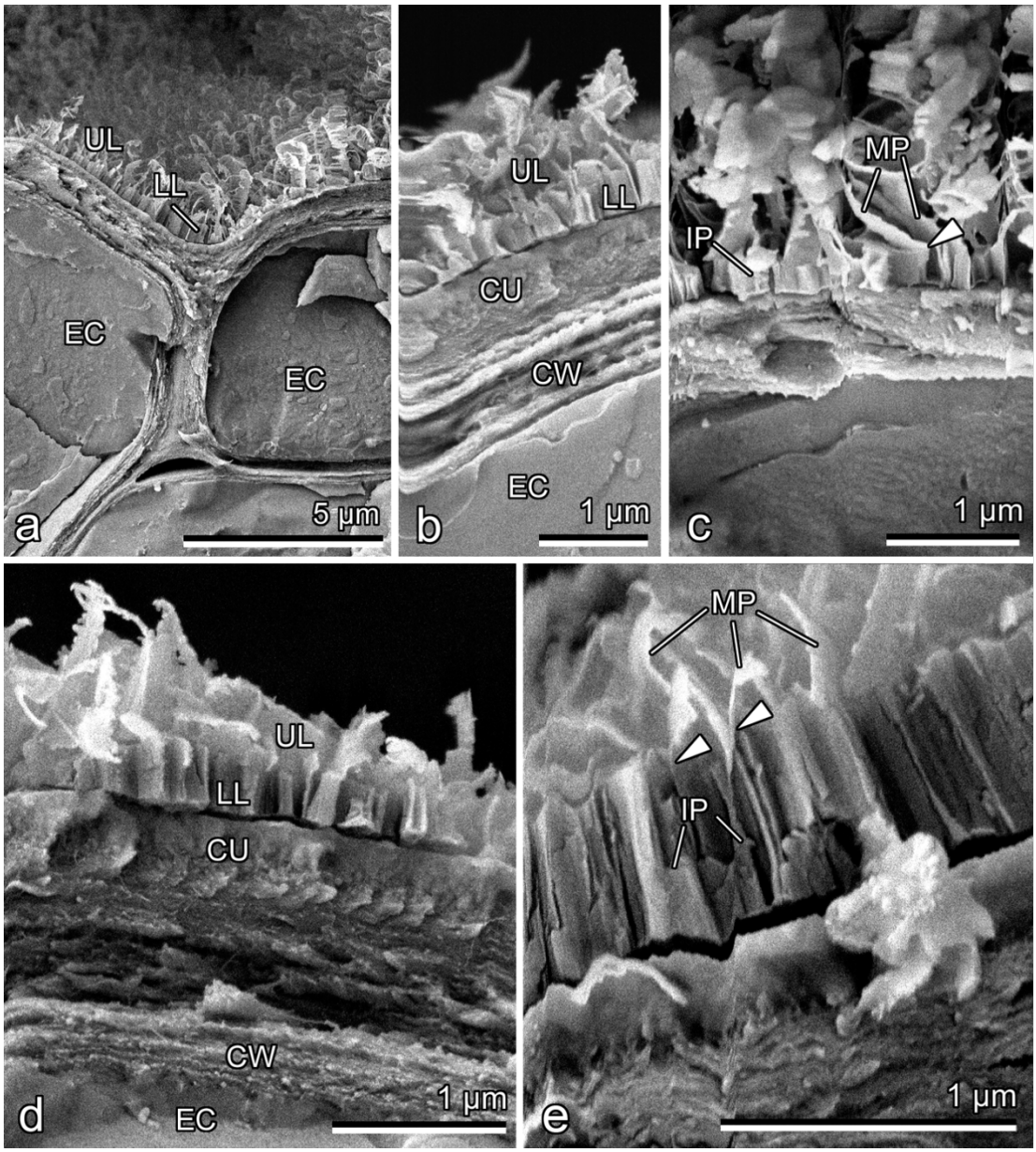


Figure 3: Cryo-SEM micrographs of the fractured epidermis of the leaf lamina. (a–c) Adaxial side. (d, e) Abaxial side. CU, cuticle; CW, outer cell wall of the epidermal cell; EC, epidermal cell; IP, lower irregular platelet; LL, lower wax layer; MP, upper membraneous platelet; UL, upper wax layer. Arrowhead points on the connection between lower and upper platelets.

interconnected, they build a loose foam-like coverage on the surface (Figure 4e), which turns into a continuous smooth wax layer when mechanically smeared (Figure 4f). The above two types of wax projections very much resemble wax structures observed previously in developing pitchers of the carnivorous plant *N. alata* at the initial developmental stages of wax projections (stages 1 and 2, respectively) [20].

Both surfaces of the studied generative organs of *D. antarctica* have a noticeably ridged appearance at rather low magnifications (Figure 5a,d). While in the outer glume, the furrows are relatively similar in width (4.52 ± 1.09 µm) (Figure 5e), the pedicel surface shows a clear pattern of alternating narrow (1.38 ± 0.36 µm) and wide (4.66 ± 0.70 µm) furrows (Figure 5b). Additionally, the pedicel is equipped with regularly distributed, inclined, cone-shaped trichomes (length: 99.91 ± 14.00 µm; diameter at the base: 30.48 ± 4.90 µm) with a tapered tip pointing to the apical direction (Figure 5a,c), whereas the glume has smaller trichomes (length: 62.87 ± 7.38 µm; diameter at the base: 13.36 ± 2.51 µm) of the similar type only on margins (Figure 5d). The pedicel bears also stomata scattered over the ridged surface (Figure 5b). At high

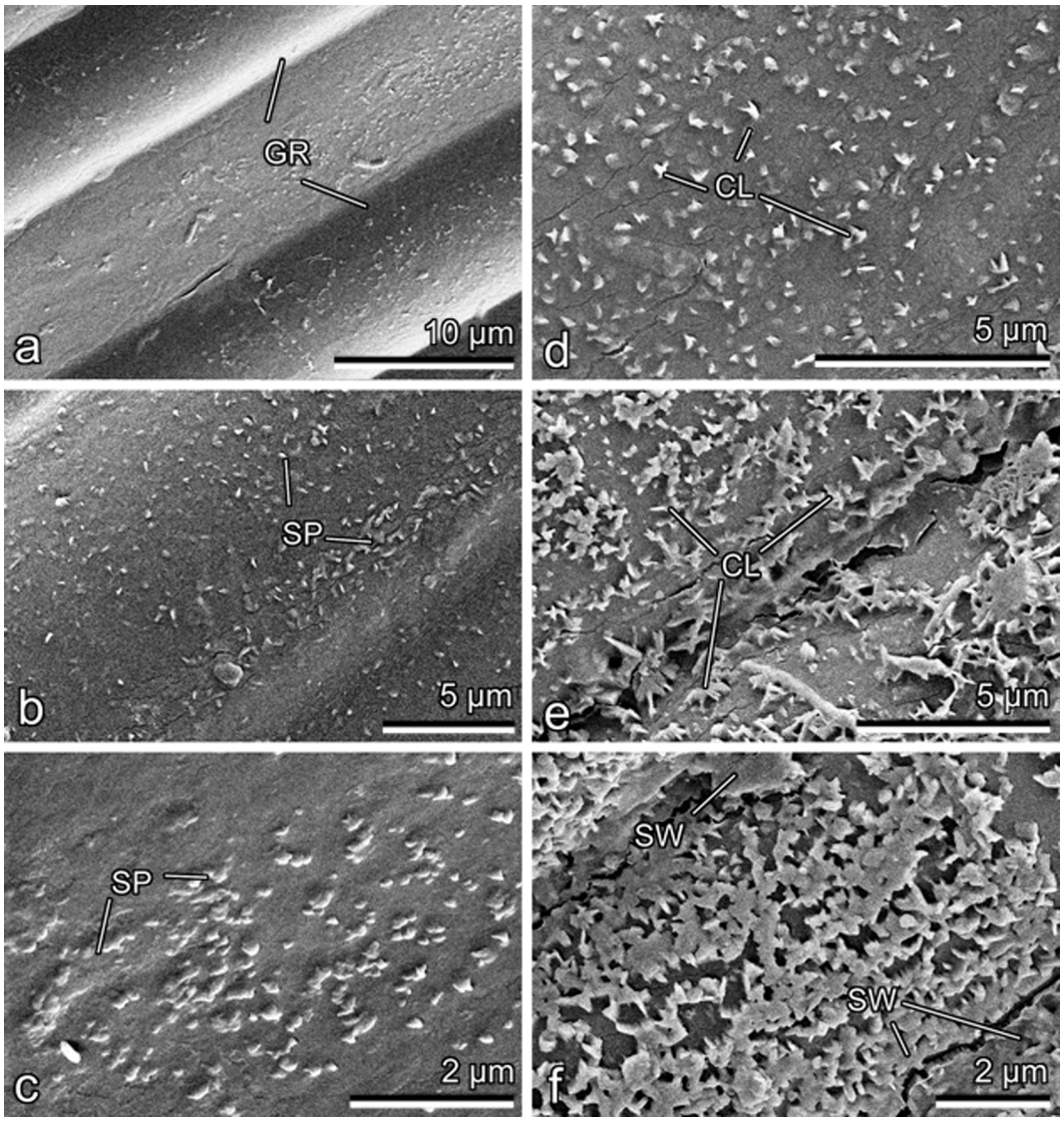


Figure 4: Cryo-SEM micrographs of the abaxial side of the ligule. (a) General view of the surface. (b–e) Wax projections. (f) The surface with smeared wax. GR, groove; CL, cluster of projections; SP, scale-like projection; SW, smeared wax layer.

magnifications, groups of rather flat cuticular folds can be found at some sites on the pedicel surface (Figure 5c, inset), whereas the glume surface shows regularly distributed, rounded/oval, relatively flat, sub-microscopic (length/diameter: 0.54 ± 0.14 µm) protrusions (Figure 5f). Both the pedicel and glume surfaces are lacking prominent epicuticular wax projections.

For the plant species studied, the epicuticular wax coverage has been previously shown (using SEM) and described only on one (adaxial) leaf lamina side [9], where small strands prostrate on each other forming a dense tangle on the entire leaf surface including stomata, whereas the abaxial side lacks the wax coverage. A dense wax coverage on the adaxial leaf surface was later alluded to by Kyryachenko et al. [6] based on the work of Romero and co-workers [10]. However, the latter authors [10] have not referred to the wax, which is nevertheless seen on the SEM images. Also in a more recent review on origin and adaptations of Antarctic flowering plants, Parnikoza et al. [2] mentioned a thick layer of wax covering leaves of *D. antarctica*, however, without any corresponding original literature citation. In another *Deschampsia* species (*D. caespitosa*), the epicuticular wax was reported only on the adaxial leaf side [21]. Using cryo-SEM, we detected and describe here in detail the epicuticular wax coverage on both leaf lamina sides and on the ligule in *D. antarctica* for the first time. Whereas plates [22] and platelets [23-25] as typical wax projections have been previously reported for many Poaceae

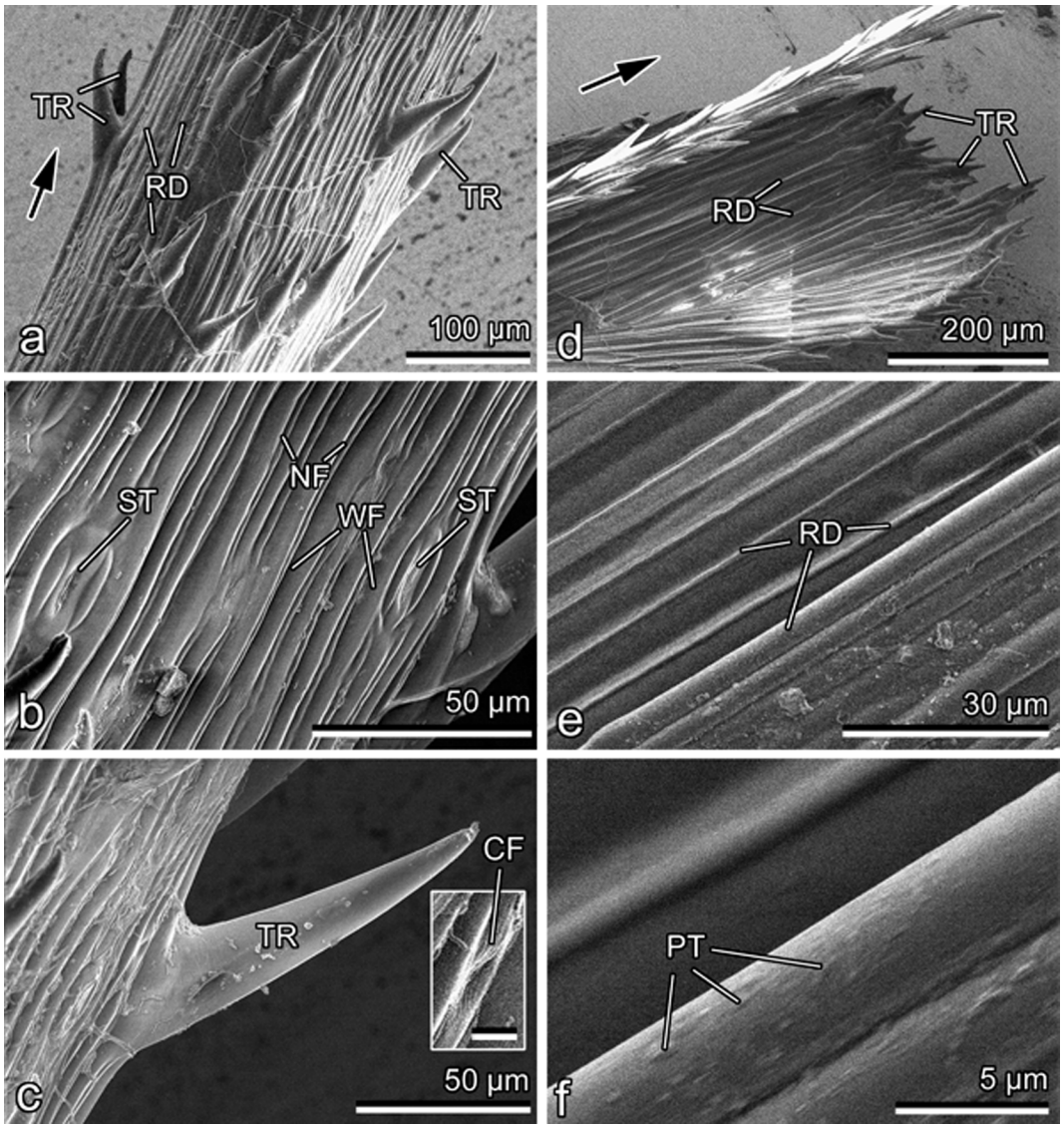


Figure 5: Cryo-SEM micrographs of the surfaces in the generative organs. (a–c) The pedicel. (d–f) The abaxial side of the glume. The inset in (c) shows cuticular folds. CF, cuticular fold; NF, narrow furow; PT, protrusion; RD, ridge; ST, stoma; TR, trichome; WF, wide furrow. The arrows in (a) and (b) show the apical direction for (a–c) and (d–f), respectively. Scale bar in (c): 5 µm.

species, the hierarchical, two-layered epicuticular wax coverage described here in *D. antarctica* is the first to be discovered in grasses.

Epicuticular wax coverage as an adaptation to severe environmental conditions

The Antarctic hair grass *D. antarctica* is a cushion-forming plant growing along the other vegetation of the Antarctic coast, which consists mainly of about 130 cryptogams (mosses, liverworths, and lichens) and only one other flowering plant species, the Antarctic pearlwort *C. quitensis*, below latitudes of 60°S down to approximately 68°S in the Antarctica [26]. These plants can tolerate the extreme conditions of the Antarctica. They are capable of surviving long winter periods of total or almost total darkness, during which photosynthesis cannot take place, and of growing in short summer times lasting from only a few days to a few months, depending on various factors [27,28].

Growing in the cold desert climate of Antarctica, *D. antarctica* experiences above all effects of very cold and dry conditions. In the Maritime Antarctica, maximum daily air temperatures in summer (January) range between 0 and 6 °C, with mean temperatures of 2.8–6 °C [27,29]. The winter temperatures are between −10 and −20 °C [30], although the Antarctic Peninsula has warmed at a rate of 3.8 °C per century [31]. The mean

annual temperature rose by ca. 2.6 °C and the mean summer temperature by ca. 1.5 °C over the past 50 years [32,33]. It is astonishing that this plant is still able to function (both photosynthesis and respiration) at the freezing point, when the rate at which it photosynthesizes drops to ca. 30–40% of that reached during the most favourable conditions estimated in controlled laboratory experiments as 13 °C [27]. Compared to *C. quitensis,* the general cold endurance for *D. antarctica* is very high: The median lethal dose LD_{50} (a measure of the lethal dose of, e.g., a toxin, radiation, or pathogen required to kill half the members of a tested population after a specified test duration) is around −26 °C for *D. antarctica*, compared to −5 °C for *C. quitensis* [3,34]. This remarkable frost resistance of *D. antarctica*, which is achieved through different biochemical adaptations, such as the production of antifreeze proteins that are secreted into the apoplast [35], can be a good explanation why this plant species not only uses the avoidance strategy as *C. quitensis* does, but also grows in separate clumps and can form rather big and thick cushion-like clusters in the Maritime Antarctica. To our opinion, the relatively thick (up to 1.3 µm) two-layered epicuticular wax coverage found in the present study on both leaf lamina sides in *D. antarctica* might also contribute to the plant resistance against low temperatures. The relatively compact lower (inner) wax layer separates well the epidermal cell surface from the cold environment, whereas the upper (outer) wax layer with air-filled spaces between wax projections represents an effective isolation material due to its conspicuous foam-like structure.

Additionally, a recent cryo-SEM experimental study performed with six plant species (*Prunus laurocerasus* L. (Rosaceae) and *Ficaria verna* Huds. (Ranunculaceae) with smooth leaves, *Bellis perennis* L. (Asteraceae) and *Cerastium brachypetalum* Pers. (Caryophyllaceae) with hairy leaves, and *Narcissus pseudonarcissus* L. (Amaryllidaceae) and *Tulipa gesneriana* L. (Liliaceae) with waxy leaves), which in nature may be potentially exposed to freezing temperatures, showed that surface icing and, consequently, the plant cell freezing rate might be significantly reduced due to the presence of three-dimensional epicuticular wax structures [36]. It was found that on waxy leaves, icing started from nucleation sites on the surface of wax projections or in nanoscale depressions between them. This is why the real contact area of ice crystals was limited to a few sites at the nanoscale on or between wax projections. After thawing, water drops flow off the surface and therefore cannot be potentially re-frozen. The study demonstrated the following effects caused by the wax coverage: (i) Air pockets between wax projections prevent direct contact between the plant cuticle and ice crystals, and (ii) after thawing, the fluid water is removed and further re-freezing on the plant surface is averted. Based on the above data, we suppose that the microstructured wax covering both leaf surfaces in *D. antarctica* also could be involved in the anti-icing mechanism of this plant species thus contributing to its frost resistance.

In addition, during the growing season between December and February, the day length is about 20 h in the Antarctic Peninsula [26] and the maximum photosynthetic photon flux density under the full midday sun in January can reach up to 2000 $\mu mol \cdot m^{-2} \cdot s^{-1}$ in the Maritime Antarctica [27,37]. Protection against harmful ultraviolet radiation has been previously reported as one of the principal functions of plant surfaces bearing microstructured epicuticular waxes. It is achieved through the increased reflection and scattering of the incoming radiation by minute wax projections [38,39]. Being covered by the prominent upper (outer) epicuticular wax layer composed of separate/interconnected wax projections of submicrometer size (ca. 0.8 µm long and ca. 40 nm thick), which are almost perpendicularly oriented to the epidermal surface, the distinctly furrowed leaf lamina surfaces of *D. antarctica* seem to be well equipped for the successful scattering of strong radiation. Experimental studies with altered levels of UV-B radiation and *D. antarctica* showed no significant effect of enhanced or reduced radiation on the relative growth rate and leaf photosynthesis of the plants [40].

Moisture, being one of the most important abiotic factors affecting the vegetation in Antarctica, is provided mainly by atmospheric water vapor and local melt supplies from fallen snow, drift snow, and permafrost, whereas stream runoff is extremely rare [28]. Precipitation in the Maritime Antarctica ranges from 100 mm per year (Margarita Bay) to 400 mm per year (South Shetland Islands) [26]. In general, a continuous epicuticular wax layer is known to serve as an transport barrier limiting the uncontrolled water loss in plants [38,41]. The presence of a thick wax coverage has been considered as one of typical xeromorphic features (i.e., structural characteristics that leaves of plants growing under arid conditions have in common in order to drastically lessen the water loss from leaves and are, therefore, classed as adaptational mechanisms to withstand drought [42]). Such leaf characteristics as small epidermal cells, high cell density per area, considerable leaf thickness, thick-walled tissues, thick cuticles, and some other structural features typical of xerophytes were repeatedly revealed in *D. antarctica* by different authors [4,8-12]. As for the epicuticular wax in this plant species, it has been previously reported that the wax on both epidermis and stomata contributes to the resistance of water vapor diffusion from the mesophyll to the outside and to the control of cuticle transpiration, reducing in this way the water loss by the leaf blade [9]. Also, authors associated the epicuticular wax on leaves along with certain anatomical features of the leaf mesophyll cells [4,8] to the protection of

D. antarctica against dehydration. Based on our cryo-SEM results, we assume that, in this plant species, particularly the compact lower wax layer, which resembles the wax crusts characteristic for many succulents (e.g., Asclepiadaceae and Cactaceae) [15], plays a crucial role in the protection from water loss.

Biomimetic potential

Since the discovery of the lotus effect [43], different properties of superhydrophobic surfaces in plants, which are highly relevant for modern technologies, such as self-cleaning, fluid drag reduction, or holding air layers at a surface, have been described and their biomimetic applications have been discussed. Phylogenetic trees indicate that superhydrophobicity evolved as a consequence of the conquest of land about 450 million years ago and may be a key innovation in the evolution of terrestrial life [44]. Recently, interesting anti-icing and controlled-icing properties of plant surfaces bearing wax projections and trichome coverage were experimentally studied [36]. The presence of ice on many technical surfaces can potentially cause failure of materials and structures. Therefore, numerous studies were focused on so-called anti-icing surfaces. The widely accepted engineering approach is physical and chemical de-icing of surfaces (numerous recent developments are reviewed in [45]). The so-called ice-phobicity might be one of the possible strategies to reduce the formation of ice. In other words, the liquid should be removed before it freezes to the surface. The superhydrophobicity of the surface might well contribute to such an effect, which has been previously suggested in the literature on bioinspired passive anti-icing and ice-phobic surfaces [36,45]. The present study on *D. antarctica* provides interesting data about surface adaptations in the plant adapted to low temperatures of Antarctica. Two layers of particulate wax observed here may potentially lead to an increase of the freezing time due to the shift of ice nucleation from the cuticle surface to the tips of wax projections. This, in turn, helps to keep an air layer between the wax particles under conditions of reduced water vapor. Moreover, superhydrophobic surfaces in combination with strong air flow can lead to newly formed ice particles being blown off, since the real contact area and, consequently, the adhesion/friction on the nanoscale rough surface is rather low [46,47].

Conclusion

A cryo-SEM examination of the vegetative (leaf blade and ligule) and generative (pedicel and outer glume) organs in *D. antarctica* revealed a prominent epicuticular wax coverage on surfaces of both vegetative organs studied. Whereas the ligule is loosely covered with separate scale-like projections or clusters of them, both leaf sides bear a hierarchical, two-layered wax coverage composed of polygonal rodlets formed by fused irregular platelets in the lower (inner) wax layer and membraneous platelets in the upper (outer) wax layer. Both leaf surfaces show a rather similar microstructure of the wax coverage and differ mainly in the thickness ratio between lower and upper wax layer. The presence of the prominent epicuticular wax on the abaxial leaf side and ligule has been found for the first time here. Also, the hierarchical structure of the wax coverage on both leaf surfaces resembling that described for the slippery (waxy) zone of several species of carnivorous plants from the genus *Nepenthes* has been discovered in *D. antarctica* in this study. The present study on *D. antarctica* provides not only interesting data about surface adaptations in the plant adapted to low temperatures of Antarctica, but also about possible strategies of anti-icing coatings of technical surfaces. Future detailed experimental studies on *D. antarctica* can provide more reliable information on the functional mechanisms behind the specific wax coverage in this plant.

Acknowledgements

Authors express gratitude to State Institution National Antarctic Scientific Centre, Ministry of Education and Science of Ukraine and Department of Antarctic Biology PAS for comprehensive support during the expedition. We are deeply grateful to Dr. Hans-Ulrich Peter (Friedrich Schiller University Jena, Germany) for his kind help with the transportation of the samples.

ORCID® iDs

Elena V. Gorb - https://orcid.org/0000-0002-9051-6259
Iryna A. Kozeretska - https://orcid.org/0000-0002-6485-1408
Stanislav N. Gorb - https://orcid.org/0000-0001-9712-7953

References

1. Longton, R. E. *Can. J. Bot.* **1979,** *57,* 2264–2278. doi:10.1139/b79-273
2. Parnikoza, I.; Kozeretska, I.; Kunakh, V. *Am. J. Plant Sci.* **2011,** *2,* 381–395. doi:10.4236/ajps.2011.23044
3. Ozheredova, I. P.; Parnikoza, I. Y.; Poronnik, O. O.; Kozeretska, I. A.; Demidov, S. V.; Kunakh, V. A. *Cytol. Genet. (Engl. Transl.)* **2015,** *49,* 139–145. doi:10.3103/s0095452715020085
4. Szczuka, E.; Giełwanowska, I.; Leszczuk, A.; Domaciuk, M.; Pietrusiewicz, J.; Bednara, J. *Ann. Univ. Mariae Curie-Sklodowska, Sect. C* **2013,** *68,* 25–33. doi:10.2478/v10067-012-0031-y
5. Convey, P. Antarctic Ecosystems. In *Encyclopedia of Biodiversity;* Levin, S. A., Ed.; Elsevier: San Diego, CA, USA, 2013; pp 179–188. doi:10.1016/b978-0-12-384719-5.00264-1
6. Kyryachenko, S. S.; Kozeretska, I. A.; Rakusa-Sushchevski, S. *Tsitol. Genet.* **2005,** *39,* 75–80.
7. Giełwanowska, I.; Szczuka, E. *Polar Biol.* **2005,** *28,* 951–955. doi:10.1007/s00300-005-0024-2
8. Giełwanowska, I.; Szczuka, E.; Bernara, J.; Górrecki, R. *Ann. Bot. (Oxford, U. K.)* **2005,** *96,* 1109–1119. doi:10.1093/aob/mci262
9. Vieira, R. C.; Mantovani, A. *Rev. Bras. Bot.* **1995,** *18,* 207–220.

10. Romero, M.; Casanova, A.; Iturra, G.; Reyes, A.; Montenegro, G.; Alberdi, M. *Rev. Chil. Hist. Nat.* **1999,** *72,* 411–425.
11. Nuzhyna, N.; Parnikoza, I.; Poronnik, O.; Kozeretska, I.; Kunakh, V. Anatomical features of different chromosomal forms of *Deschampsia antarctica* E. Desv. In *Proceedings of the 27th International Polar Conference,* Rostock, Germany, March 25–29, 2018; p 137.
12. Nuzhyna, N.; Parnikoza, I.; Poronnik, O.; Kozeretska, I.; Kunakh, V. *Pol. Polar Res.* **2019,** *40,* 361–383. doi:10.24425/ppr.2019.130903
13. Körner, C.; Larcher, W. Plant Life in Cold Climates. In *Plants and Temperature;* Long, S. P.; Woodward, F. Y., Eds.; Cambridge University Press: Cambridge, UK, 1988; pp 25–27.
14. Voigt, D.; Gorb, E.; Gorb, S. *Arthropod-Plant Interact.* **2007,** *1,* 221–243. doi:10.1007/s11829-007-9021-4
15. Barthlott, W.; Neinhuis, C.; Cutler, D.; Ditsch, F.; Meusel, I.; Theisen, I.; Wilhelmi, H. *Bot. J. Linn. Soc.* **1998,** *126,* 237–260. doi:10.1111/j.1095-8339.1998.tb02529.x
16. Gorb, E.; Haas, K.; Henrich, A.; Enders, S.; Barbakadze, N.; Gorb, S. *J. Exp. Biol.* **2005,** *208,* 4651–4662. doi:10.1242/jeb.01939
17. Benz, M. J.; Gorb, E. V.; Gorb, S. N. *Arthropod-Plant Interact.* **2012,** *6,* 147–158. doi:10.1007/s11829-011-9171-2
18. Scholz, I.; Bückins, M.; Dolge, L.; Erlinghagen, T.; Weth, A.; Hischen, F.; Mayer, J.; Hoffmann, S.; Riederer, M.; Riedel, M.; Baumgartner, W. *J. Exp. Biol.* **2010,** *213,* 1115–1125. doi:10.1242/jeb.035618
19. Gorb, E. V.; Hofmann, P.; Filippov, A. E.; Gorb, S. N. *Sci. Rep.* **2017,** *7,* 45483. doi:10.1038/srep45483
20. Gorb, E. V.; Baum, M. J.; Gorb, S. N. *Sci. Rep.* **2013,** *3,* 3078. doi:10.1038/srep03078
21. Palmer, P. G.; Tucker, A. E. *Smithson. Contrib. Bot.* **1983,** 1–72. doi:10.5479/si.0081024x.53
22. Jeffree, C. E. The Fine Structure of the Plant Cuticle. In *Biology of the Plant Cuticle;* Riederer, M.; Müller, C., Eds.; Blackwell Publishing: Oxford, UK, 2006; pp 11–125. doi:10.1002/9780470988718.ch2
23. Jetter, R.; Kunst, L.; Samuels, A. L. Composition of Plant Cuticular Waxes. In *Biology of the Plant Cuticle;* Riederer, M.; Müller, C., Eds.; Blackwell Publishing: Oxford, UK, 2006; pp 145–181. doi:10.1002/9780470988718.ch4
24. Koch, K.; Dommisse, A.; Barthlott, W.; Gorb, S. N. *Acta Biomater.* **2007,** *3,* 905–909. doi:10.1016/j.actbio.2007.05.013
25. Roth-Nebelsick, A.; Ebner, M.; Miranda, T.; Gottschalk, V.; Voigt, D.; Gorb, S.; Stegmaier, T.; Sarsour, J.; Linke, M.; Konrad, W. *J. R. Soc., Interface* **2012,** *9,* 1965–1974. doi:10.1098/rsif.2011.0847
26. Alberdi, M.; Bravo, L. A.; Gutiérrez, A.; Gidekel, M.; Corcuera, L. J. *Physiol. Plant.* **2002,** *115,* 479–486. doi:10.1034/j.1399-3054.2002.1150401.x
27. Edwards, J. A.; Smith, R. I. L. *Br. Antarct. Surv. Bull.* **1988,** *81,* 43–63.
28. Antarctica - Plant life | Britannica. https://www.britannica.com/place/Antarctica/Plant-life (accessed Aug 10, 2021).
29. Zuñiga, G. E.; Alberdi, M.; Corcuera, L. J. *Environ. Exp. Bot.* **1996,** *36,* 393–399. doi:10.1016/s0098-8472(96)01026-x
30. Jackson, A. E.; Seppelt, R. D. *Physiol. Plant.* **1995,** *94,* 25–30. doi:10.1111/j.1399-3054.1995.tb00779.x
31. Vaughan, D. G.; Marshall, G. J.; Connolley, W. M.; Parkinson, C.; Mulvaney, R.; Hodgson, D. A.; King, J. C.; Pudsey, C. J.; Turner, J. *Clim. Change* **2003,** *60,* 243–274. doi:10.1023/a:1026021217991
32. Day, T. A.; Ruhland, C. T.; Grobe, C. W.; Xiong, F. *Oecologia* **1999,** *119,* 24–35. doi:10.1007/s004420050757
33. Xiong, F. S.; Mueller, E. C.; Day, T. A. *Am. J. Bot.* **2000,** *87,* 700–710. doi:10.2307/2656856
34. Casanova, M. A. Eficiencia fotoquímica del PSII en *Deschampsia antarctic*a (Desv.): una gramínea tolerante a la congelación. Magister Thesis, Universidad Austral de Chile, Chile, 1997.
35. Bravo, L. A.; Griffith, M. *J. Exp. Bot.* **2005,** *56,* 1089–1096.
36. Gorb, S. N.; Gorb, E. V. *Sci. Nat.* **2022,** *109,* 24. doi:10.1007/s00114-022-01789-7
37. Schroeter, B.; Olech, M.; Kappen, L.; Heitland, W. *Antarct. Sci.* **1995,** *7,* 251–260. doi:10.1017/s0954102095000356
38. Barthlott, W. Scanning Electron Microscopy of the Epidermal Surface in Plants. In *Scanning Electron Microscopy in Taxonomy and Functional Morphology;* Claugher, D., Ed.; Clarendon Press: Oxford, UK, 1990; pp 69–94.
39. Bargel, H.; Koch, K.; Cerman, Z.; Neinhuis, C. *Funct. Plant Biol.* **2006,** *33,* 893–910. doi:10.1071/fp06139
40. Rozema, J.; Broekman, R.; Lud, D.; Huiskes, A. H. J.; Moerdijk, T.; de Bakker, N.; Meijkamp, B.; van Beem, A. *Plant Ecol.* **2001,** *154,* 101–115. doi:10.1023/a:1012956230160
41. Schönherr, J. Resistance of Plant Surfaces to Water Loss: Transport Properties of Cutin, Suberin and Associated Lipids. In *Encyclopedia of Plant Physiology;* Lange, O. L.; Nobel, P. S.; Osmond, C. B.; Ziegler, H., Eds.; Springer: Berlin, Germany, 1982; Vol. 12B, pp 153–179. doi:10.1007/978-3-642-68150-9_7
42. Allaby, M., Ed. *The Concise Oxford Dictionary of Botany;* Oxford University Press: Oxford, UK, 1994.
43. Barthlott, W.; Neinhuis, C. *Planta* **1997,** *202,* 1–8. doi:10.1007/s004250050096
44. Barthlott, W.; Mail, M.; Neinhuis, C. *Philos. Trans. R. Soc., A* **2016,** *374,* 20160191. doi:10.1098/rsta.2016.0191
45. Li, Q.; Guo, Z. *J. Mater. Chem. A* **2018,** *6,* 13549–13581. doi:10.1039/c8ta03259a
46. Liu, W.; Chen, H.; Shen, Y.; Wu, Z. *J. Bionic Eng.* **2019,** *16,* 794–805. doi:10.1007/s42235-019-0097-1
47. Xu, Y.; Shen, Y.; Tao, J.; Lu, Y.; Chen, H.; Hou, W.; Jiang, B. *Phys. Chem. Chem. Phys.* **2020,** *22,* 1168–1173. doi:10.1039/c9cp05449a

License and Terms

This is an open access article licensed under the terms of the Beilstein-Institut Open Access License Agreement (https://www.beilstein-journals.org/bjnano/terms), which is identical to the Creative Commons Attribution 4.0 International License (https://creativecommons.org/licenses/by/4.0). The reuse of material under this license requires that the author(s), source and license are credited. Third-party material in this article could be subject to other licenses (typically indicated in the credit line), and in this case, users are required to obtain permission from the license holder to reuse the material.

The definitive version of this article is the electronic one which can be found at: https://doi.org/10.3762/bjnano.13.71

BEILSTEIN JOURNAL OF NANOTECHNOLOGY

Micro-structures, nanomechanical properties and flight performance of three beetles with different folding ratios

Jiyu Sun[1], Pengpeng Li[1], Yongwei Yan[1], Fa Song[1], Nuo Xu[1] and Zhijun Zhang[*2]

Full Research Paper

Open Access

Address:
[1]Key Laboratory of Bionic Engineering (Ministry of Education, China), Jilin University, Changchun, 130022, P.R. China and [2]Key Laboratory of CNC Equipment Reliability (Ministry of Education) and School of Mechanical and Aerospace Engineering, Jilin University, Changchun, 130022, P.R. China

Email:
Zhijun Zhang[*] - zhijunzhang@jlu.edu.cn

* Corresponding author

Keywords:
beetle hind wings; flight performance; folding ratio; nanoindentation; wind tunnel

Beilstein J. Nanotechnol. **2022,** *13,* 845–856.
https://doi.org/10.3762/bjnano.13.75

Received: 11 May 2022
Accepted: 10 August 2022
Published: 26 August 2022

This article is part of the thematic issue "Biomimetics on the micro- and nanoscale – The 25th anniversary of the lotus effect".

Guest Editor: M. Mail

© 2022 Sun et al.; licensee Beilstein-Institut.
License and terms: see end of document.

Abstract

When beetles are not in flight, their hind wings are folded and hidden under the elytra to reduce their size. This provided inspiration for the design of flapping-wing micro aerial vehicles (FWMAVs). In this paper, microstructures and nanomechanical properties of three beetle species with different wing folding ratios living in different environments were investigated. Factors affecting their flight performance, that is, wind speed, folding ratio, aspect ratio, and flapping frequency, were examined using a wind tunnel. It was found that the wing folding ratio correlated with the lift force of the beetles. Wind speed, folding ratio, aspect ratio, and flapping frequency had a combined effect on the flight performance of the beetles. The results will be helpful to design new deployable FWMAVs.

Introduction

Regarding the benefits of scientific research, rescue, surveying, mapping, and many other aspects in the development of micro aerial vehicles (MAVs), miniaturization of aircraft has become a popular research topic [1]. Owing to their small size, light weight, flexibility and concealment, MAVs have completed a series of tasks that are difficult or impossible for larger aircraft [2]. Due to unsteady aerodynamic effects, flapping wings may be a more energy-efficient flight mode than modes achieved with traditional fixed and rotor wings [3-6]. The lift-to-power metric of the revolving wing declines rapidly with decreasing Reynolds numbers, resulting in a hovering performance that is at least a factor of two lower than the flapping wing at Reynolds numbers less than about 100 [7]. Flapping-wing micro-aerial vehicles (FWMAVs) are increasingly favored by scientists worldwide for their excellent flight performance due to unsteady aerodynamic mechanisms in the low Reynolds num-

ber range [8-10]. In the application of MAVs, flapping wings are becoming more common [11]. Deployable FWMAVs make MAVs smaller in size, lighter, and harder to detect [12,13].

Insects can hover, fly in any direction, turn quickly in the air, and resist interference caused by the external environment, showing strong agility, maneuverability, and stability. This has raised great interest to study the mechanism of the high lift generated by insects in flight and to imitate the flight of insects [14,15]. Insect wings play a major role here. Hence, examining their flight parameters is crucially important to design biomimetic FMAVs [16,17]. It is increasingly clear that most insects obtain useful force with the help of aerodynamic mechanisms that require torsion, often with transverse bending, and other deformations including alteration of the effective area [18]. The butterfly can increase the aspect ratio by spreading the forewings to generate maximum lift and increase the lift-to-drag ratio during flapping flight. Thus, it significantly enhances the maneuverability through rapidly changing the flight speed by changing its flapping frequency and amplitude [19]. In studies regarding the flapping frequencies and angles of wings and the lift characteristics of *Anax goliathus*, *Trypoxylus dichotomus*, and *Oncotympane maculaticollis*, it was found that their flapping lifts were different because of the different sizes and shapes of the wings [20]. Additionally, the elasticity of insect wings also has an impact on the aerodynamic characteristics. By studying the flexible deformations and aerodynamic characteristics of cicada wings during flapping, it was found that their flexibility can increase their mean lift coefficient [21]. In rhinoceros beetles, the elytra is also involved in aerodynamics during takeoff, producing an interaction force between the elytra and the hind wings [22].

To avoid damage or hinder the movement on the ground, the hind wings of beetles are folded to reduce their size and to hide under the elytra [23,24]. The foldable wings of beetles have attracted the interest of aerospace engineering scientists as well as entomologists [25]. Knowledge about the folding mechanism of beetle hind wings can be used to design deployable FWMAVs [16,26]. Rapidly deployable wings based on the design of origami mechanisms [27] and foldable artificial wings imitating *Allomyrina dichotoma* have opened up new prospects for foldable structures in MAVs [28]. The folding pattern and geometric and kinematic parameters of beetle hind wings have a critical effect on the flight performance and will be useful regarding the design of biomimetic MAVs.

Wind tunnels are an effective tool to investigate flapping-wing flight and aerodynamic characteristics [29]. The wing tip trajectories of the hind wings of a beetle species (*Protaetia brevitarsis*) were captured during wind tunnel tests and, based on the results, bioinspired wings and a linkage-mechanism flapping system were designed [26]. The flow behavior of live rhinoceros beetle flapping hind wings was studied by using a smoke wind tunnel and a high-speed camera [30]. Combining wind tunnels and high-speed cameras, the relationships between wing shapes, flapping flight lift, and aerodynamic efficiency of dragonflies [31] and fruit flies [32] were examined. In addition, the influence of frequency and wind speed on the aerodynamic characteristics (such as the lift, drag, and vortex) of MAV prototypes with different wing types were also tested in wind tunnels [33-36].

Various beetle species have different hind wing folding methods, and their folding ratios (i.e., the ratio between folding length of the hind wings and the length of the hind wings) are different. In this paper, three beetle species from different living environments were selected to explore the influence of different folding ratios on their flight performance through wind tunnel tests. The aspect ratios and flapping frequencies and the influence of the flow velocity on their lift-to-drag ratio are discussed in the following, which will provide some reference for the design of biomimetic deployable FWMAVs.

Materials and Methods

Beetles

Three beetle species with different folding ratios, *Protaetia brevitarsis*, *Anoplophora chinensis*, and *Trypoxylus dichotomus*, were selected for the experiments. The three adult *P. brevitarsis* used in the experiment were captured in Nanchang, Jiangxi Province, China, and the three adult *A. chinensis* and the three adult *T. dichotomus* were captured in Nanyang, Henan Province, China. The parameters of hind wings of the three beetle species are shown in Table 1. The body length of *P. brevitarsis* was 21.41 ± 1.58 mm, the body width was 13.09 ± 0.55 mm, and the body weight was 0.72 ± 0.13 g. The body length of *A. chinensis* was 27.65 ± 2.54 mm, the body width was 10.28 ± 1.07 mm, and the body weight was 1.01 ± 0.35 g. The body length of *T. dichotomus* was 43.96 ± 2.42 mm, the body width was 23.74 ± 1.53 mm, and the body weight was 5.27 ± 0.16 g. All insects were acclimated under standard laboratory conditions (ventilation room, 25 ± 1 °C, 60% ± 5% humidity, 12 h light/dark cycle) and had free access to standard water and food. All procedures were conducted in accordance with the "Guiding Principles in the Care and Use of Animals" (China) and were approved by the ethics committee of experimental animal welfare of Jilin University.

High-speed camera

A high-speed camera (Phantom V711, Vision Research Inc., USA) was used to obtain the postures and flapping

Table 1: Beetle hind wing parameters.

Beetle	*P. brevitarsis*	*A. chinensis*	*T. dichotomus*
body weight (g)	0.72 ± 0.13	1.01 ± 0.35	5.27 ± 0.16
hind wing area (mm^2)	181.341 ± 15.35	238.02 ± 56.63	801.72 ± 111.75
hind wing extented length (mm)	26.47 ± 1.36	29.34 ± 4.32	53.60 ± 4.28
hind wing folded length (mm)	11.58 ± 0.76	9.98 ± 1.46	22.33 ± 2.15
folding ratio	0.44	0.34	0.42
flapping frequency (Hz)	90	45	43
aspect ratio	3.86	3.64	3.59
wing loading (g/dm^2)	19.85	21.22	32.87

frequencies of the three beetles during flight. A camera speed of 2000 frames/s (shutter speed: 0.1 ms, resolution: 1280 × 800 pixels) was used to measure the flapping period of the beetle in flight and to determine its flapping frequency.

Microscopic morphologies of hind wings of beetles

A super depth-of-field microscope (VHX-6000, Keyence, Japan) was used to obtain images of the fully unfolded and folded hind wings of the three beetles. To obtain the macroscopic structures of the hind wings of the three beetles, the hind wings were first removed with a scalpel and rinsed with distilled water and then dried and pasted flat on a slide for observation.

Scanning electron microscopy (SEM) (Model EVO-18, Carl Zeiss Microimaging Inc., Germany) was used to obtain morphological images of cross sections of the hind wings of three beetles at the same locations of different wing veins.

Nanoindentation properties

The nanomechanical characteristics were tested using a nanoindenter (TriboIndenter, Hysitron Inc., USA). The reduced Young's modulus, E_r, is calculated as

$$E_r = \frac{\sqrt{\pi}}{2\beta}\frac{S}{\sqrt{A_c}},$$

where β is a constant related to the shape of the head (for a Berkovich indenter, the value is 1.034). A_c is contact the area and a polynomial function of contact depth. S is the contact stiffness. A Berkovich tip with a tip radius of approximately 100 nm was used for the tests. In order to study the effect of nanomechanical properties of different veins on the lift of the beetle hind wings, the same location of the same vein of three beetles was selected for testing. Six test positions were selected, namely the anterior of the costal (I), the end of the costal (II), media posterior (III), cubitus anterior (IV), anal posterior (V), and wing membrane (VI) (see below Figure 3). A force of 100 μN was applied to the veins and the loading rate and holding time remained constant at 10 μN/s and 10 s, respectively.

Wind tunnel

The wind tunnel test was performed in a low-speed straight-flow wind tunnel at the Key Laboratory of Bionic Engineering, Jilin University, China. The main parameters of the wind tunnel are shown in Table 2. The abdomen of the beetle was attached with AB glue (Epoxy Resin Liquid Adhesive Strong Adhesive, HOU-FC220) to the bracket, which was connected to the force balance (load cell) after adjustment. Flight behavior and body angles of each beetle were ensured to be the same in flight (Figure 1). The selected load cell (LH-SZ-02, Shanghai Liheng, China; 0–20 N ± 0.2 mN) has the advantages of small size, high precision, and fast response, suitable for the flight performance tests of insects and MAVs.

Table 2: Main parameters of the wind tunnel.

Test section parameters	Value
working section shape	Rectangle
working section area (mm^2)	650 × 450
length of working section (mm)	1000
turbulent intensity (%)	<0.3
regulator form of wind speed	Hot-wire sensor
range of wind speed (m/s)	0–10
airflow nonuniformity of working section (%)	<3

Three species of beetles were divided into groups of three. After each beetle was attached to the bracket with AB glue at an angle of attack of 0°, the wind speed was adjusted to 1.0, 1.5, 2.0, 2.5, and 3.0 m/s. Thrust and lift of each beetle at the moment of hover flight at different wind speeds were measured through the force balance. Also, the drag at rest at different wind speeds was measured. After obtaining the lift-to-drag ratio of each

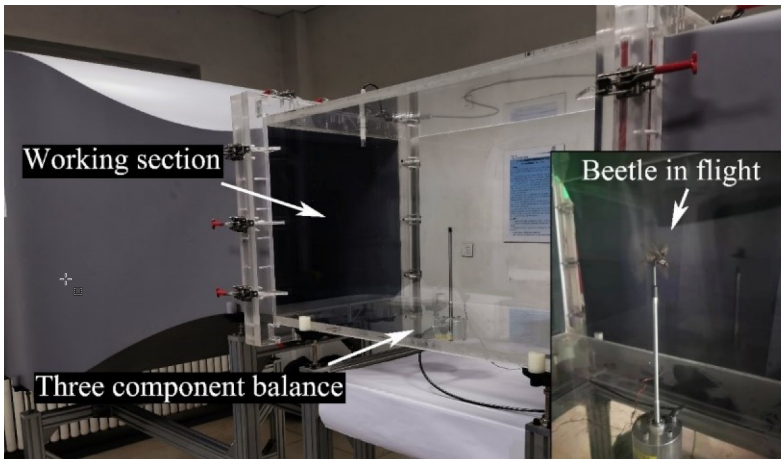


Figure 1: The low-speed straight-flow wind tunnel and the beetle during test.

beetle at different wind speeds, the average lift-to-drag ratio of each group of beetles was taken as the lift-to-drag ratio of this species of beetles.

Results and Discussion

Beetle flying attitude

Figure 2 shows a flapping cycle of the three beetles obtained using a high-speed camera. The flapping frequency of each beetle was calculated by measuring the time required for one flapping cycle. The flapping period of *P. brevitarsis* was 11 ms, and the flapping frequency was 90 Hz. For *A. chinensis*, the values were 22 ms and 45 Hz, respectively, and for *T. dichotomus*, the values were 23 ms and 43 Hz, respectively.

The wingtip path of the upstroke almost overlapped with the wingtip path at the beginning of the downstroke in one flapping cycle. The reason for this is that the beetles needed to rapidly increase the vertical lift at the beginning of the upstroke [37]. The flapping amplitude of the hind wings of *P. brevitarsis* during flight was smaller than that of *A. chinensis* and *T. dichotomus*, which means that the higher flapping frequency was needed [38]. Also, it was found that the flapping amplitude

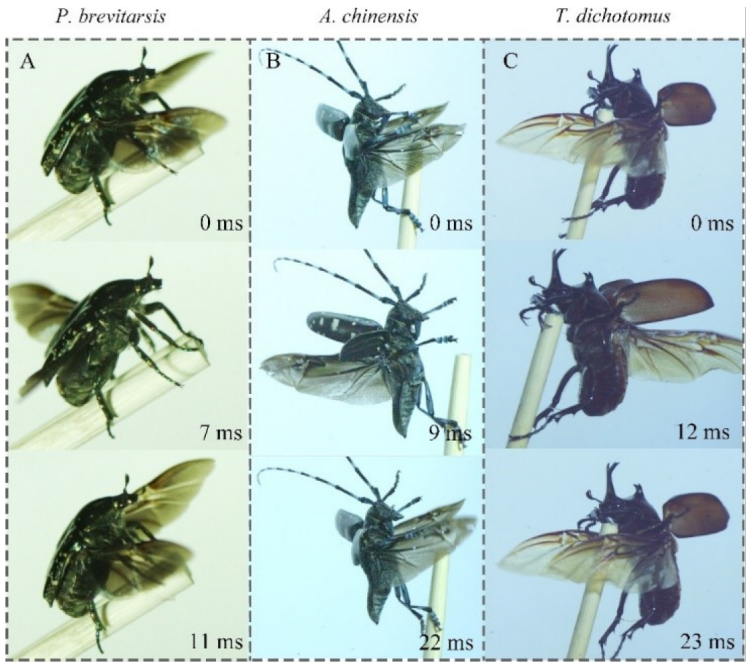


Figure 2: (A), (B), and (C) show one flapping cycle of *P. brevitarsis*, *A. chinensis*, and *T. dichotomus*, respectively.

of the elytra of the three beetles will vary with the flapping angle of the hind wings, and the elytra will flap almost synchronous with the hind wings. A similar phenomenon was found in dung beetles (*Heliocopris hamadryas*), whose elytra contributed to produce lift [39]. In addition, the hind wings of beetles twist to a certain extent during flight. The rotational lift is an important factor affecting the aerodynamics of the beetle [30].

Hind wing unfolding and folding morphology

The hind wings of the three beetles were folded in a V-shape when they were not in flight (Figure 3). For *P. brevitarsis*, *A. chinensis*, and *T. dichotomus*, body weight, body and extented hind wing lengths are increasing and are positively correlated (Table 1). In contrast, the flapping frequency is decreasing. Folding ratio, aspect ratio (i.e., the ratio between square of the wingspan and wing area), and the wing loading (i.e., the weight of the beetle divided by the wing area) of the three beetles were calculated. The folding ratio of *A. chinensis* was the smallest (0.34), and those of *P. brevitarsis* and *T. dichotomus* were similar (0.44 and 0.42, respectively). Aspect ratio and wing loading show an opposite trend.

Folding angle and folded states of the hind wings of three beetles are shown in Figure 3. The folding angle of the hind wings of *P. brevitarsis* is close to 120° (Figure $3A_2$), and the folding angle of the hind wings of *T. dichotomus* is close to 90° (Figure $3C_2$). The hind wings of *A. chinensis* overlapped when folded (Figure $3B_2$), and the folded length of the hind wings was smaller than the folded length of the other two species. Comparing the folding sites of the hind wings of the three beetles, the costal (C) and the media posterior (MP) of the hind wings of *P. brevitarsis* and *T. dichotomus* both were found to be folded, while the C of the hind wings of *A. chinensis* was found to be less folded, and the MP was not folded at the folding sites at all. This could be the reason for the folding ratio of the hind wings of *A. chinensis* being smaller.

Figure $3A_3$–A_7, Figure $3B_3$–B_7, and Figure $3C_3$–C_7 show cross-sectional morphologies of different wing veins of the hind wings of three beetles at the same position obtained using SEM. The images show that the cross-sectional shapes are all nearly elliptical, while all were basically hollow, similar to blood vessels. This structure provides support for the beetles in spreading their hind wings or during flight [40]. Comparing the cross sections of different wing veins of the hind wings of the same beetles, the diameter of the C (Figure $3A_3$) was found to be larger than that of the MP (Figure $3A_4$) and the cubitus anterior (CuA) (Figure $3A_7$). Also, the diameter of the posterior end of the C (Figure $3A_5$) was smaller than that of the anterior end (Figure $3A_3$). Additionally, the wall thickness of the hind wing veins on the dorsal side was thicker than that on the ventral side. This was also found in the Asian ladybeetle (*Harmonia Axyridis*) [41]. Thicker wing veins are good for sustaining greater forces and preventing the hind wings from being damaged [42].

Nanomechanical analysis of the hind wings

Nanomechanical test results are shown in Figure 4. The nanomechanical properties of the hind wings of the three beetles change according to the same trend. The maximum values of the reduced Young's modulus, E_r, were all measured at test point II (the end of the costal) and were 6.530, 7.652, and 6.645 GPa for *P. brevitarsis*, *A. chinensis*, and *T. dichotomus*, respectively. The higher E_r helps the beetle to resist external forces and prevents wing damage [43]. The values of E_r and hardness H of cubitus anterior, anal posterior, and wing membrane were smaller than those of the costal and media posterior. It was also found that the E_r of costal of *P. brevitarsis* was smaller than those of *A. chinensis* and *T. dichotomus*, which possibly affected the deformation ability of the hind wing. Thus, the lift-to-drag ratio of *P. brevitarsis* was relatively large.

Influence of wind speed, folding ratio, aspect ratio, and flapping frequency on the lift-to-drag ratio

The wind tunnel test results of the three beetles at wind speeds of 1.0, 1.5, 2,0, 2.5, and 3.0 m/s are shown in Figure 5. With increasing wind speed, the lift-to-drag ratios of all three beetles show a decreasing trend (Figure 5A). When the wind speed increased, the drags of the beetles also increased, while the lift did not change significantly. At low wind speeds (<2.0 m/s), the drag on the beetle was small and the lift was relatively stable. Thus, the lift-to-drag ratio was higher than that at higher wind speeds (≥2.0 m/s). In addition, the lift-to-drag ratio of *P. brevitarsis* is obviously different from that of *A. chinensis* and *T. dichotomus*. It is significantly higher at low wind speeds and becomes gradually similar to the lift-to-drag ratio of the other two beetles at high wind speeds. For all three beetles, fluctuations of the lift-to-drag ratio were obvious at low wind speeds. At 1 m/s wind speed, the range of fluctuation of the lift-to-drag ratio was 10.5–16.0 for *P. brevitarsis*, 2.2–6.0 for *A. chinensis*, and 3.0–4.8 for *T. dichotomus*. At high wind speeds, the range of the lift-to-drag ratios gradually decreased and stabilized. For *P. brevitarsis*, although the downward trend of lift was not obvious (at low wind speed) (Figure 5B), the lift-to-drag ratio still rapidly descended. The reason for this is that, when the insect size decreased, the wing speed decreased (due to reduced wing length), while the wing drag increased (due to increased air viscosity) [44]. In addition, *P. brevitarsis* with a higher folding ratio was significantly affected by wind. Its peak lift force with increasing wind speeds appeared earlier than that

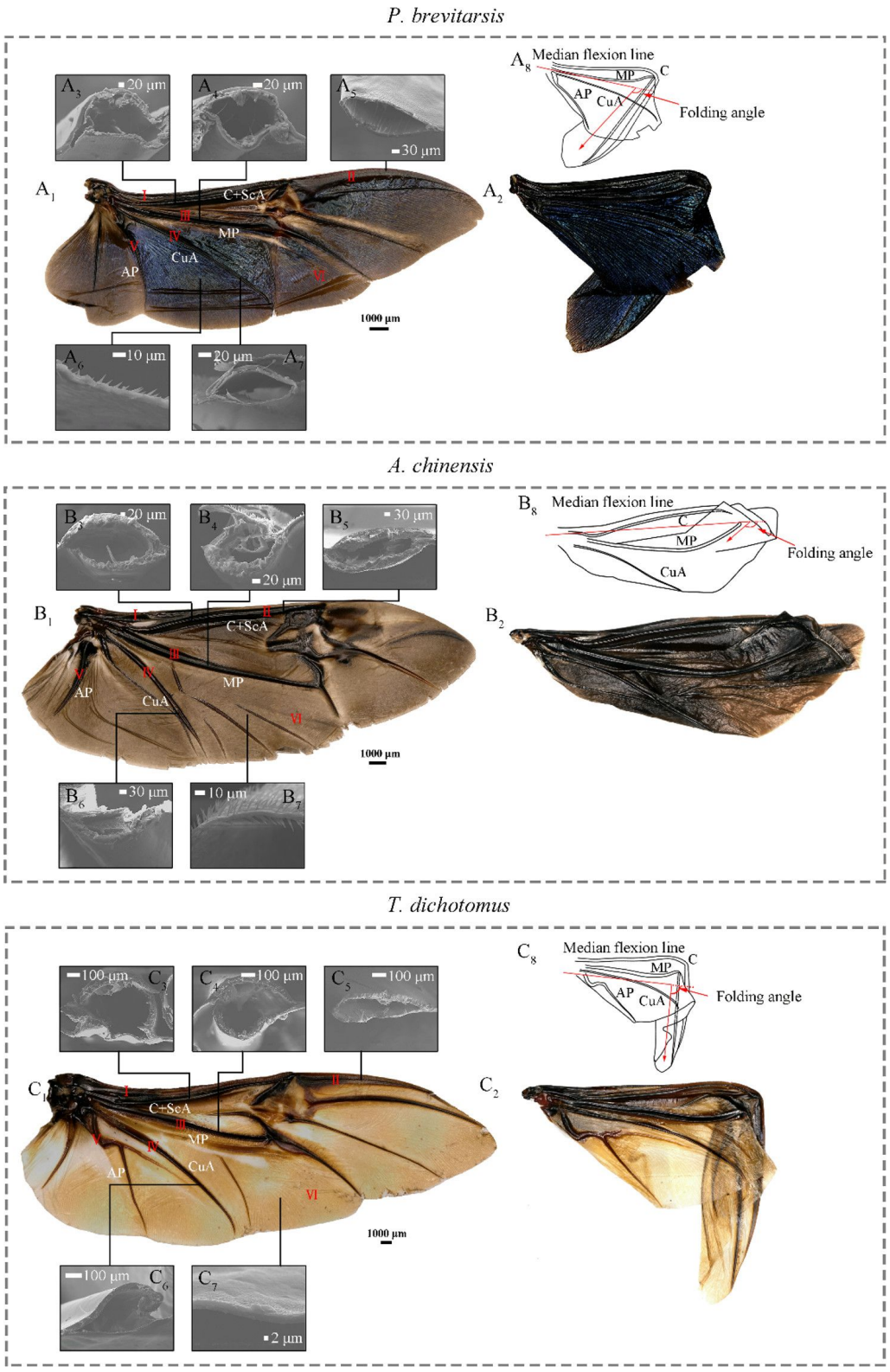


Figure 3: (A), (B), and (C) show hind wings of *P. brevitarsis*, *A. chinensis*, and *T. dichotomus*, respectively. (A_1) and (A_2), (B_1) and (B_2), and (C_1) and C_2 show the extended and folded hind wings of *P. brevitarsis*, *A. chinensis*, and *T. dichotomus*, respectively. (A_3–A_7), (B_3–B_7), and (C_3–C_7) show cross-sectional morphologies of costal "C", media posterior "MP", the posterior end of "C", wing membrane, and anal posterior "AP" of the three beetles, respectively.

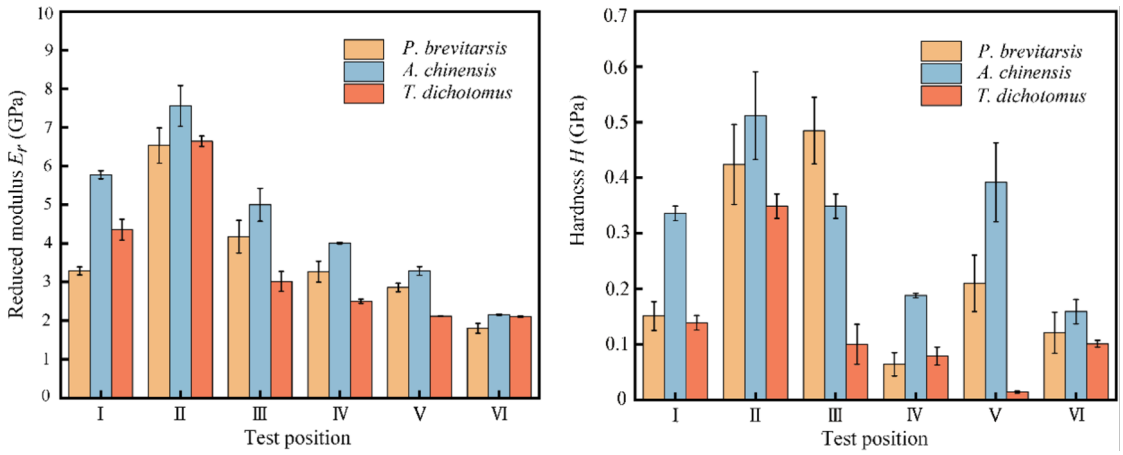


Figure 4: Nanomechanical test results of the anterior of the costal (I), the end of the costal (II), media posterior (III), cubitus anterior (IV), anal posterior (V), and wing membrane (VI).

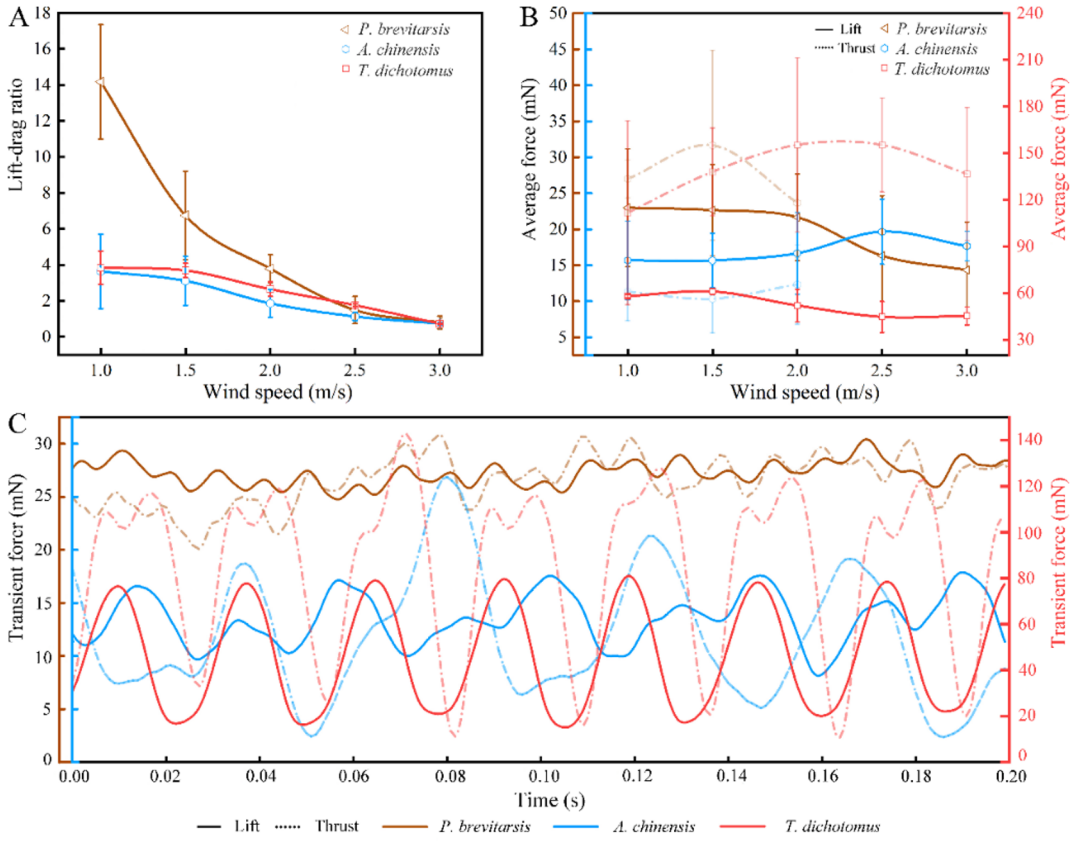


Figure 5: Aerodynamic characteristics of the three beetles. (A), (B), and (C) show the average lift-to-drag ratio, average aerodynamic force at different wind speeds, and the transient force curves of the three beetles (flapping time period of 0.2 s), respectively.

of the other two beetles. This led to a larger decline of its lift-to-drag ratio compared to the other two beetles. So for *P. brevitarsis*, the effect of wind was greater than for the other beetles because of its small size. Considering only aspect ratio, wing area, or flapping frequency, the change trends of the lift-to-drag ratios of three beetles were not consistent. However, it was found that the lift-to-drag ratios of three beetles at low wind speeds varied directly with their folding ratio.

The aerodynamic force at different wind speeds of the three beetles is shown in Figure 5B. It was found that the thrust of the beetles at different wind speeds was greater than their lift (except for *A. chinensis*). The lift of *T. dichotomus* was the biggest because its wing area was much larger than that of the other beetles. When the wind speed increased, the lift of three beetles wing in flapping motion first showed an increasing trend; but when the wind speed reached a certain value, the lift decreased. The drag increased with the wind speed. The order of the lift force peak values with increasing wind speeds was *P. brevitarsis*, *T. dichotomus*, and then *A. chinensis*. It was consistent with their folding ratio. A possible reason is that when the wind speed reaches a certain threshold, the hind wings would undergo passive deformation reducing the wing area, which results in decreased lift. A higher folding ratio of hind wings leads to easier deformation with increasing wind speed (Figure 6).

When the wind speed reached a certain value (Figure 5B) and the wings were flapping, lift and drag increased at the same time. At this time, the beetle could change its flight speed and obtain more lift or thrust to improve the flight efficiency and reduce the energy loss. When the wind speed reached a larger value, the lift decreased and the drag increased, and the aerodynamic performance of beetles was poor. At this time, continuing to maintain the original flight attitude and relying on the ability of the beetles to resist the wind causes insufficient lift to fly. Thus, at wind speeds greater than 2.0 m/s, there was no thrust for *P. brevitarsis* and *A. chinensis*. This means that, although the two beetles were flapping their hind wings, there was no forward movement. In nature, beetles could change lift, drag, and the moment of body rotation by changing the flight speed and the angle of attack to fly stably in different incoming flows and reduce energy consumption.

The transient force curves of the three beetles for a flapping time period of 0.2 s are shown in Figure 5C. The trends of lift and thrust curves of the three beetles show some convergence. As the lift of the beetle increases, the thrust also increases. In addition, the peak of lift and drag produced by *T. dichotomus*

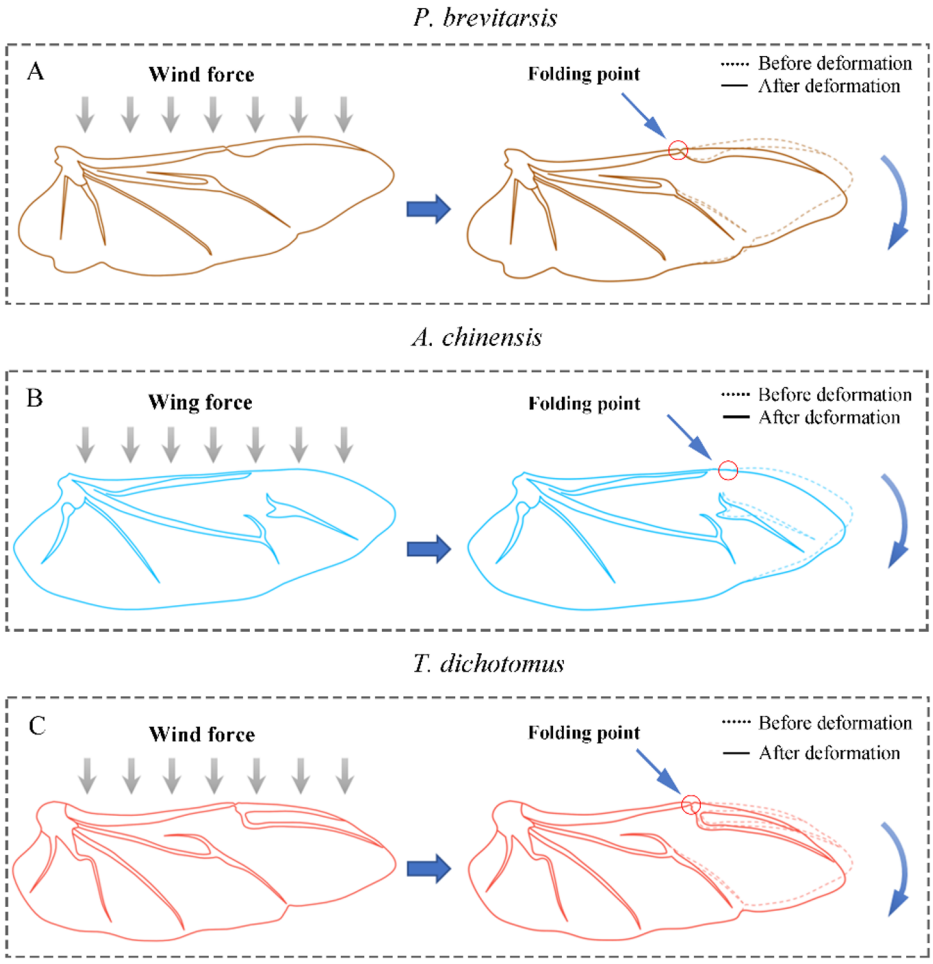


Figure 6: Schematic diagram of passive deformation of the hind wings of the three beetles.

was the largest, up to 80 and 140 mN, respectively. Although *P. brevitarsis* is the smallest beetle, its peak lift and thrust were greater than that of *A. chinensis.* When the beetle is exposed to the wind force during flight, the hind wings undergo backward bending and passive deformation at the folding points, which directly decreases wing area (S_w) and body frontal area (S_b), which is helpful to reduce the profile drag and parasite drag (Figure 6).

The total drag on a beetle is equal to the sum of three aerodynamic components, as $D = D_{ind} + D_{pro} + D_{par}$, where the components are induced drag D_{ind}, profile drag D_{pro}, and parasite drag D_{par}. D_{ind} represents the cost of generating lift, D_{pro} is the drag of the wings and D_{par} is due to skin friction and the drag from the body form [45]. It was found that the wingspan b and S_w of the hind wings decrease simultaneously when passive deformation occurs. This changes the aspect ratio, b^2/S_w, and $D_{ind} = 2L^2/\pi\rho b^2 v^2$). Thus, the drag reduction mainly comes from $D_{pro} = 0.5\rho v^2 S_w C_{Dpro}$ and $D_{par} = 0.5\rho v^2 S_b C_{Dpar}$, in which C_{Dpro} and C_{Dpar} are the dimensionless drag coefficient and the body drag coefficient, respectively. It might also be the reason for the high lift-to-drag ratio of *P. brevitarsis* at wind speeds lower than 2.0 m/s. The largest reduction of S_w and S_b led to the largest reduction in total drag compared to the other two beetles.

A multifactor analysis of variance was performed regarding the influence of folding ratio and wind speed on the lift-to-drag ratio. The results are shown in Table 3 (significance level is 0.05). The significance of the effect of the folding ratio and wind speed on the lift-to-drag ratio was less than 0.05, indicating that both folding ratio and wind speed would affect the lift-to-drag ratio of beetles. In this test, at low wind speeds (<2.0 m/s), the higher folding ratio was found to yield a better lift-to-drag ratio. With the increase of wind speed, the lift-to-drag ratio gradually decreased, and the effect of the folding ratio on the lift-to-drag ratio was no longer obvious.

There is a correlation between aerodynamic forces and aspect ratio. Increasing the aspect ratio increases the average aerodynamic loads, and a smaller aspect ratio prevents the airflow from separating at the top and bottom [46]. Using butterfly wings as a prototype to design bionic wings with different aspect ratios and through wind tunnel tests and numerical simulations, it was found that a higher aspect ratio of bionic wings leads to a higher lift-to-drag ratio [19]. The three-dimensional effect of flow is weakened with increasing aspect ratio, which increases the aerodynamic coefficient [47]. Based on beetle hind wing models with different geometries, the average lift force was found to increase with increasing aspect ratio in a certain range [12]. Compared with the other two beetles, *P. brevitarsis* had a larger range of variation. This might be because the large aspect ratio of the wing yields a greater wing flexibility [48].

The flapping frequency of *P. brevitarsis*, *A. chinensis*, and *T. dichotomus* were 90, 45, and 43 Hz, respectively. It was found that *P. brevitarsis* had a higher flapping frequency and lift-to-drag ratio than the other beetles. The flapping frequencies of *A. chinensis* and *T. dichotomus* were similar. Especially, at low wind speeds, a higher flapping frequency yields a better lift-to-drag ratio. A bionic flexible FWMAV was tested in a wind tunnel to explore the effects of different flapping frequencies and aspect ratios on the aerodynamic performance. The flapping frequency played a crucial role in lift generation. Higher flapping frequencies yielded more lift. Also, a wing with a higher aspect ratio could significantly increase the lift [49]. For low flapping frequencies, the lift change is not obvious, but for high flapping frequencies, the lift increase is obvious [50]. The flapping frequency was found to affect inertial acceleration

Table 3: Tests of between-subjects effects.

Source	Type III sum of squares	df	Mean square	F	Sig.	Partial eta squared
corrected model	481.580[a]	14	34.399	20.324	0.000	0.905
intercept	513.760	1	513.760	303.543	0.000	0.910
folding ratio	94.102	2	47.051	27.799	0.000	0.650
wind speed	234.388	4	58.597	34.621	0.000	0.822
folding ratio × wind speed	153.090	8	19.136	11.306	0.000	0.751
error	50.766	30	1.693	–	–	–
total	1046.116	45	–	–	–	–
corrected total	532.356	44	–	–	–	–

[a]R^2 = 0.905 (adjusted R^2 = 0.860).

and aerodynamic pressure, thus affecting inertial force and aerodynamic force; with the increase of flapping frequency, their increment was relatively consistent [51]. For a four-wings FWMAV, the lift was increasing linearly with the flapping frequency [52]. Also, the increase in flapping frequency improves the thrust of the flapping [53].

Research on the living environments and living habits of the three beetles found that *P. brevitarsis* mostly live in farmland and loose soil, and the environmental conditions are relatively humid. Adults come out at night and have a strong flying ability. *P. brevitarsis* also has a strong migratory ability, moves quickly, and generally flies approximately 50 m [54-56]. *A. chinensis* lives mostly inside trunks of trees or in small closed forests, feeding on young leaves and bark [57]. *T. dichotomus* often lives in areas with well-developed forestry and thick trees und conditions native to a forest, feeding on the sap that flows from the surface of the bark. During the day, they mostly rest in shady and humid environments such as soil and move more in the evening hours [58,59]. Compared with the other two beetles, the living environment of *P. brevitarsis* is more open and offers a better flying environment. Long-term living habits improved its flying ability with better aerodynamic characteristics. Due to the narrow living environment, the flight performance of *A. chinensis* and *T. dichotomus* is not as good as that of *P. brevitarsis*. A study of the wing loading of the three beetles revealed that *P. brevitarsis* had the smallest wing loading of 19.85 g/dm^2 matching its fast-moving nature. The wing loading of *A. chinensis* was 21.22 g/dm^2, and the wing loading of *T. dichotomus* was 32.87 g/dm^2. A lower wing loading leads to a better maneuverability [60]. Additionally, the wing loading affected the overload capacity of the aircraft, that is, the smaller the wing loading, the greater the overload of the aircraft [61]. Both *P. brevitarsis* and *A. chinensis* had smaller wing loadings, but *P. brevitarsis* had a higher lift-to-drag ratio, which might be due to higher folding ratio, aspect ratio, and flapping frequency. Although lift and drag of *P. brevitarsis* were more obviously affected by the wind speed, its excellent flight performance provides input for improving the maneuverability of MAVs.

Conclusion

In this work, the effects of different hind wing parameters on the flight performance of beetles were studied through wind tunnel tests. Three beetle species with different living environments and different folding ratios were selected as the test objects in this study. The unfolded and folded morphology and the nanomechanical properties of the hind wings of the three beetles and the cross-sectional morphology of different wing veins were observed and tested with super depth-of-field microscopy, nanoindentation, and scanning electron microscopy. Thus, the folding ratios, reduced Young's modulus, and hardness were determined. The flapping frequency was calculated by observing one flapping cycle with a high-speed camera. The effects of wind speed, folding ratio, aspect ratio, and flapping frequency on the lift-to-drag ratio of the beetles were examined in a low-speed straight-flow wind tunnel. The results showed that wind speed, folding ratio, aspect ratio, and flapping frequency had a combined effect on the flight performance of the beetles. Beetles with a more open living environment have a larger folding ratio, aspect ratio, flapping frequency, and wing loading, as well as better flight performance. The living environment of *P. brevitarsis* is relatively open, and its wing loading is also the smallest, reaching 19.85 g/dm^2. This basic study will help to understand the effect of different beetle hind wing parameters on the flapping, which will be helpful for the design of biomimetic deployable FWMAVs.

Funding

This work was supported by the National Natural Science Foundation of China (grant number 31970454), the Aviation Science Foundation of China (2020Z0740R4001), the 111 Project (B16020) of China.

Disclosure

All authors have seen and agree with the contents of the article and there is no conflict of interest, including specific financial interest and relationships and affiliations relevant to the subject of article.

ORCID® iDs

Jiyu Sun - https://orcid.org/0000-0002-7056-0981

References

1. Meresman, Y.; Husak, J. F.; Ben-Shlomo, R.; Ribak, G. *R. Soc. Open Sci.* **2020,** *7,* 200277. doi:10.1098/rsos.200277
2. Kitagawa, K.; Sakakibara, M.; Yasuhara, M. *J. Visualization* **2009,** *12,* 393–400. doi:10.1007/bf03181882
3. Nguyen, Q.-V.; Chan, W. L.; Debiasi, M. *Proc. SPIE* **2015,** *9429,* 94290U. doi:10.1117/12.2085714
4. Ho, S.; Nassef, H.; Pornsinsirirak, N.; Tai, Y.-C.; Ho, C.-M. *Prog. Aerosp. Sci.* **2003,** *39,* 635–681. doi:10.1016/j.paerosci.2003.04.001
5. Wu, J.; Sun, M. *Acta Mech. Sin.* **2005,** *21,* 411–418. doi:10.1007/s10409-005-0064-4
6. Nguyen, Q.-V.; Chan, W. L.; Debiasi, M. *J. Bionic Eng.* **2016,** *13,* 235–248. doi:10.1016/s1672-6529(16)60297-4
7. Zheng, L.; Hedrick, T.; Mittal, R. *Bioinspiration Biomimetics* **2013,** *8,* 036001. doi:10.1088/1748-3182/8/3/036001
8. Muhammad, A.; Nguyen, Q. V.; Park, H. C.; Hwang, D. Y.; Byun, D.; Goo, N. S. *J. Bionic Eng.* **2010,** *7,* 134–141. doi:10.1016/s1672-6529(09)60185-2
9. Khan, Z. A.; Agrawal, S. K. *AIAA J.* **2011,** *49,* 1354–1365. doi:10.2514/1.j050447

10. Ha, N. S.; Nguyen, Q. V.; Goo, N. S.; Park, H. C. *Exp. Mech.* **2012,** *52,* 1535–1549. doi:10.1007/s11340-012-9611-7
11. Throneberry, G.; Hassanalian, M.; Abdelkefi, A. *Drones* **2019,** *3,* 49. doi:10.3390/drones3020049
12. Liu, C.; Li, P.; Song, F.; Sun, J. *Comput. Biol. Med.* **2021,** *135,* 104642. doi:10.1016/j.compbiomed.2021.104642
13. Sun, J. *Science* **2020,** *370,* 1165. doi:10.1126/science.abf1925
14. Yang, L. J.; Marimuthu, S. Acoustic comparison of PET and Latex wings for flapping micro-air-vehicles. In *IEEE 10th International Conference on Nano/Micro Engineered and Molecular Systems (NEMS),* 2015; pp 172–174. doi:10.1109/nems.2015.7147403
15. Phan, H. V.; Park, H. C. *J. Bionic Eng.* **2016,** *13,* 449–457. doi:10.1016/s1672-6529(16)60318-9
16. Geisler, T.; Topczewska, S. *Int. J. Appl. Mech. Eng.* **2015,** *20,* 53–64. doi:10.1515/ijame-2015-0004
17. Geisler, T. *Int. J. Appl. Mech. Eng.* **2016,** *21,* 837–847. doi:10.1515/ijame-2016-0049
18. Wootton, R. J. *J. Exp. Biol.* **1999,** *202,* 3333–3345. doi:10.1242/jeb.202.23.3333
19. Rubio, J. E.; Chakravarty, U. K. *Acta Mech.* **2019,** *230,* 4273–4286. doi:10.1007/s00707-019-02503-x
20. Du, G.; Sun, M. *Appl. Math. Mech. (Engl. Ed.)* **2008,** *29,* 731–743. doi:10.1007/s10483-008-0605-9
21. Bin Abas, M. F.; Bin Mohd Rafie, A. S.; Bin Yusoff, H.; Bin Ahmad, K. A. *Chin. J. Aeronaut.* **2016,** *29,* 1159–1177. doi:10.1016/j.cja.2016.08.003
22. Lee, B.; Park, H.; Kim, S.-T. *J. Mech. Sci. Technol.* **2015,** *29,* 5281–5288. doi:10.1007/s12206-015-1130-x
23. Geisler, T. *Acta Mech. Autom.* **2012,** *6,* 37–44.
24. Du, J.; Hao, P. *Nanomaterials* **2018,** *8,* 667. doi:10.3390/nano8090667
25. Saito, K.; Yamamoto, S.; Maruyama, M.; Okabe, Y. *Proc. Natl. Acad. Sci. U. S. A.* **2014,** *111,* 16349–16352. doi:10.1073/pnas.1409468111
26. Liu, C.; Li, P.; Song, F.; Stamhuis, E. J.; Sun, J. *Comput. Biol. Med.* **2022,** *140,* 105085. doi:10.1016/j.compbiomed.2021.105085
27. Dufour, L.; Owen, K.; Mintchev, S.; Floreano, D. A drone with insect-inspired folding wings. In *IEEE/RSJ International Conference on Intelligent Robots and Systems (IROS),* 2016; pp 1576–1581. doi:10.1109/iros.2016.7759255
28. Truong, Q.-T.; Argyoganendro, B. W.; Park, H. C. *J. Bionic Eng.* **2014,** *11,* 449–458. doi:10.1016/s1672-6529(14)60057-3
29. De Wagter, C.; Koopmans, A.; de Croon, G.; Remes, B.; Ruijsink, R. Autonomous Wind Tunnel Free-Flight of a Flapping Wing MAV. *Advances in Aerospace Guidance, Navigation and Control;* Springer: Berlin, Heidelberg, 2013; pp 603–621. doi:10.1007/978-3-642-38253-6_35
30. Lee, B.; Oh, S.; Choi, H.; Park, H. *J. Mech. Sci. Technol.* **2020,** *34,* 209–218. doi:10.1007/s12206-019-1222-0
31. Bomphrey, R. J.; Nakata, T.; Henningsson, P.; Lin, H.-T. *Philos. Trans. R. Soc., B* **2016,** *371,* 20150389. doi:10.1098/rstb.2015.0389
32. Meng, X.; Liu, Y.; Sun, M. *J. Bionic Eng.* **2017,** *14,* 75–87. doi:10.1016/s1672-6529(16)60379-7
33. Zakaria, M. Y.; Bayoumy, A. M.; Elshabka, A. M. Experimental Aerodynamic Characteristics of Flapping Membrane Wings. In *13th International Conference on aerospace science,* 2009; pp 1–18. doi:10.21608/asat.2009.23736
34. Liu, L.; Zhang, X. J.; He, Z. X. J. *Theor. Appl. Inf. Technol.* **2012,** *45,* 542–550.
35. Chen, P.; Joshi, S.; Swartz, S. M.; Breuer, K. S. Bat-Inspired Flapping Flight. In *22nd AIAA/ASME/AHS Adaptive Structures Conference,* 2014; pp 1120 ff. doi:10.2514/6.2014-1120
36. Nian, P.; Song, B.; Xuan, J.; Yang, W.; Dong, Y. *IEEE Access* **2019,** *7,* 47891–47903. doi:10.1109/access.2019.2909916
37. Truong, T. V.; Le, T. Q.; Byun, D.; Park, H. C.; Kim, M. *J. Bionic Eng.* **2012,** *9,* 177–184. doi:10.1016/s1672-6529(11)60113-3
38. Phan, H. V.; Truong, Q. T.; Park, H. C. *Bioinspiration Biomimetics* **2019,** *14,* 066006. doi:10.1088/1748-3190/ab3d55
39. Johansson, L. C.; Engel, S.; Baird, E.; Dacke, M.; Muijres, F. T.; Hedenström, A. *J. R. Soc., Interface* **2012,** *9,* 2745–2748. doi:10.1098/rsif.2012.0053
40. Sun, J.; Liu, C.; Bhushan, B.; Wu, W.; Tong, J. *Beilstein J. Nanotechnol.* **2018,** *9,* 812–823. doi:10.3762/bjnano.9.75
41. Sun, J. Y.; Liu, C.; Du, R. J.; Zhang, Z. J. *Microstructural characteristics and nanomechanical properties of hind wings of the Asian ladybeetle, harmonia axyridis*. In *017 7th International Conference on Manipulation, Manufacturing and Measurement on the Nanoscale (3M-NANO),* 2017; pp 215–218. doi:10.1109/3m-nano.2017.8286285
42. Sun, J.; Wu, W.; Ling, M.; Bhushan, B.; Tong, J. *Beilstein J. Nanotechnol.* **2016,** *7,* 904–913. doi:10.3762/bjnano.7.82
43. Sun, J.; Liu, C.; Bhushan, B. *J. Mech. Behav. Biomed. Mater.* **2019,** *94,* 63–73. doi:10.1016/j.jmbbm.2019.02.031
44. Lyu, Y. Z.; Sun, M. *J. Insect Physiol.* **2021,** *134,* 104293. doi:10.1016/j.jinsphys.2021.104293
45. Hedenstrom, A.; Liechti, F. *J. Exp. Biol.* **2001,** *204,* 1167–1175. doi:10.1242/jeb.204.6.1167
46. Shademan, M.; Naghib-Lahouti, A. *Adv. Aerodyn.* **2020,** *2,* 14. doi:10.1186/s42774-020-00038-7
47. Luo, G.; Sun, M. *Acta Mech. Sin.* **2005,** *21,* 531–541. doi:10.1007/s10409-005-0072-4
48. Ryu, Y.; Chang, J. W.; Chung, J. *Aerosp. Sci. Technol.* **2019,** *86,* 558–571. doi:10.1016/j.ast.2019.01.013
49. Deng, S.; Percin, M.; van Oudheusden, B.; Remes, B.; Bijl, H. *Int. J. Micro Air Veh.* **2014,** *6,* 105–115. doi:10.1260/1756-8293.6.2.105
50. Jongerius, S. R.; Lentink, D. *Exp. Mech.* **2010,** *50,* 1323–1334. doi:10.1007/s11340-010-9411-x
51. Yang, W.; Song, B.; Song, W.; Wang, L. *Chin. Sci. Bull.* **2012,** *57,* 2887–2897. doi:10.1007/s11434-012-5249-1
52. Cheng, C.; Wu, J.; Zhang, Y.; Li, H.; Zhou, C. *Adv. Aerodyn.* **2020,** *2,* 16. doi:10.1186/s42774-020-00040-z
53. Tan, X.; Zhang, W.; Ke, X.; Zou, C.; Liu, W.; Cui, F.; Wu, X. S.; Li, H. Y. *Development of Flapping-wing Micro Aerial vehicle in Asia*. In *Proceedings of the 10th World Congress on Intelligent Control and Automation (WCICA 2012),* 2012; pp 3939–3942. doi:10.1109/wcica.2012.6359130
54. Lowrey, S.; De Silva, L.; Hodgkinson, I.; Leader, J. *J. Opt. Soc. Am. A* **2007,** *24,* 2418–2425. doi:10.1364/josaa.24.002418
55. Miao, J.; Wu, Y.-Q.; Li, K.-B.; Jiang, Y.-L.; Gong, Z.-j.; Duan, Y.; Li, T. *J. Insect Behav.* **2015,** *28,* 175–182. doi:10.1007/s10905-015-9487-3
56. Hegedüs, R.; Szél, G.; Horváth, G. *Vision Res.* **2006,** *46,* 2786–2797. doi:10.1016/j.visres.2006.02.007
57. Hérard, F.; Maspero, M. *J. Pest Sci.* **2019,** *92,* 117–130. doi:10.1007/s10340-018-1014-9
58. Kojima, W.; Ishikawa, Y.; Takanashi, T. *Naturwissenschaften* **2014,** *101,* 687–695. doi:10.1007/s00114-014-1199-6
59. Hongo, Y. *J. Ethol.* **2006,** *24,* 201–204. doi:10.1007/s10164-006-0202-x
60. Terblanche, J. S.; Anderson, B. *Naturwissenschaften* **2010,** *97,* 775–780. doi:10.1007/s00114-010-0693-8

61. Almbro, M.; Kullberg, C. *J. Insect Behav.* **2012,** *25,* 441–452. doi:10.1007/s10905-011-9309-1

License and Terms

This is an open access article licensed under the terms of the Beilstein-Institut Open Access License Agreement (https://www.beilstein-journals.org/bjnano/terms), which is identical to the Creative Commons Attribution 4.0 International License (https://creativecommons.org/licenses/by/4.0). The reuse of material under this license requires that the author(s), source and license are credited. Third-party material in this article could be subject to other licenses (typically indicated in the credit line), and in this case, users are required to obtain permission from the license holder to reuse the material.

The definitive version of this article is the electronic one which can be found at:
https://doi.org/10.3762/bjnano.13.75

BEILSTEIN JOURNAL OF NANOTECHNOLOGY

Bioselectivity of silk protein-based materials and their bio-inspired applications

Hendrik Bargel[‡1], Vanessa T. Trossmann[‡1], Christoph Sommer[1] and Thomas Scheibel[*1,2,3,4,5]

Review

Open Access

Address:
[1]Department of Biomaterials, University of Bayreuth, Prof.-Rüdiger-Bormann-Str. 1, 95447 Bayreuth, Germany, [2]Bayreuth Center of Material Science and Engineering (BayMat), University of Bayreuth, Universitätsstr. 30, 95440 Bayreuth, Germany, [3]Bavarian Polymer Institute (BPI), University of Bayreuth, Universitätsstr. 30, 95440 Bayreuth, Germany, [4]Bayreuth Center of Colloids and Interfaces (BZKG), University of Bayreuth, Universitätsstr. 30, 95440 Bayreuth, Germany and [5]Bayreuth Center for Molecular Biosciences (BZMB), University of Bayreuth, Universitätsstr. 30, 95440 Bayreuth, Germany

Email:
Thomas Scheibel[*] - thomas.scheibel@bm.uni-bayreuth.de

* Corresponding author ‡ Equal contributors

Keywords:
antifouling; bacteriostatic; biofouling; bioselective cell adhesion; spider silk protein

Beilstein J. Nanotechnol. **2022,** *13,* 902–921.
https://doi.org/10.3762/bjnano.13.81

Received: 31 March 2022
Accepted: 23 August 2022
Published: 08 September 2022

This article is part of the thematic issue "Biomimetics on the micro- and nanoscale – The 25th anniversary of the lotus effect".

Guest Editor: M. Mail

© 2022 Bargel et al.; licensee Beilstein-Institut.
License and terms: see end of document.

Abstract

Adhesion to material surfaces is crucial for almost all organisms regarding subsequent biological responses. Mammalian cell attachment to a surrounding biological matrix is essential for maintaining their survival and function concerning tissue formation. Conversely, the adhesion and presence of microbes interferes with important multicellular processes of tissue development. Therefore, tailoring bioselective, biologically active, and multifunctional materials for biomedical applications is a modern focus of biomaterial research. Engineering biomaterials that stimulate and interact with cell receptors to support binding and subsequent physiological responses of multicellular systems attracted much interest in the last years. Further to this, the increasing threat of multidrug resistance of pathogens against antibiotics to human health urgently requires new material concepts for preventing microbial infestation and biofilm formation. Thus, materials exhibiting microbial repellence or antimicrobial behaviour to reduce inflammation, while selectively enhancing regeneration in host tissues are of utmost interest. In this context, protein-based materials are interesting candidates due to their natural origin, biological activity, and structural properties. Silk materials, in particular those made of spider silk proteins and their recombinant counterparts, are characterized by extraordinary properties including excellent biocompatibility, slow biodegradation, low immunogenicity, and non-toxicity, making them ideally suited for tissue engineering and biomedical applications. Furthermore, recombinant production technologies allow for application-specific modification to develop adjustable, bioactive materials. The present review focusses on biological processes and surface interactions involved in the bioselec-

tive adhesion of mammalian cells and repellence of microbes on protein-based material surfaces. In addition, it highlights the importance of materials made of recombinant spider silk proteins, focussing on the progress regarding bioselectivity.

Review

1 Introduction

1.1 Bioadhesive protein surfaces

Biological adhesion is important for all organisms such as plants, animals, bacteria, and fungi, covering a wide range of biological aspects including reproduction, growth and settlement, dynamic attachment during locomotion, self-healing, protection against as well as attachment of microbes, and prey hunting [1-6]. A variety of different adhesion mechanisms exist to manage the different challenges of interfacial adhesion. In turn, natural biological adhesives are complex materials that have evolved to meet the various functional demands. Bioadhesion can be found in the range of the micro- to the macroscale [7]. Adhesion principles include contact mechanical principles such as capillary interactions, viscous forces, non-covalent interactions (e.g., van der Waals forces), and adhesive chemistry of biopolymers (various types of glues) [5]. On the level of tissues, multiple cell types work together to perform complex tasks, based on their hierarchical arrangement governing the exchange of information between different cell types. To achieve proper organization and communication, cells produce a large number of adhesion molecules that mediate cell contact phenomena based on receptor–ligand interactions [8]. The ability of mammalian cells to adhere to other cells, tissues, or the extracellular matrix (ECM) via specific molecular interactions plays a critical role in many biological processes including embryogenesis, development of neuronal tissue, hemostasis, immune response, and inflammation [9]. The adhesive interactions of cells between each other and with ECM proteins (often of specific molecular nature), have important key functions in embryonic and organ development, the maintenance of vascular and epithelial integrity, and host defense [10].

The so-called cellular adhesion molecules (CAMs) can be generally divided into five discrete groups that include cadherins, selectins, members of the immunoglobulin superfamily (IgSF), integrins, and others such as mucins. Moreover, certain enzymes such as the vascular adhesion protein 1 (VAP-1) are known to be involved in cell adhesion [11,12]. The distinction of CAM subcategories reflects both structural differences as well as binding to different ligands. Cadherins, selectins, and members of the IgSF are known to mediate cell–cell adhesion, while integrins typically bind to extracellular matrix proteins [12]. As a special case, immune cell integrins also bind to ligands both soluble and on other cells. Additional classification of the CAMs relates to their ligands and type of adhesion. Selectins bind to carbohydrates based on calcium-dependent regulation, cadherins form mostly homotypic contacts also in a calcium-regulated manner, while the IgSF subfamily of nectins is able to form both homotypic and heterotypic interactions [10]. Comprehensive overviews of molecular structure and adhesion mechanisms of various CAM can be found in dedicated reviews [9,10,12,13].

Cadherins are associated with cell–cell adhesive interactions in solid tissues and are involved in processes such as embryonic development, formation of the epithelial layers of the skin and intestine, and axonal formation in the nervous system [9]. The structural integrity of cadherin molecules is stabilized by calcium ions, and their essential role in proper adhesion contacts is reflected in the abbreviated protein family name "**ca**lcium-**d**ependent ad**her**ent prote**ins**" [14]. The N-terminal domain of cadherin dimers on one cell is responsible for mediating homotypic binding contacts with their homologues on an adjacent cell in an antiparallel manner. This region also defines binding specificity [15]. Some cadherin receptors are also able to bind to different cadherins. Classic cadherin function is involved in key intracellular structures, such as in adherens junctions (zona adherens and adhesion junctions) and protein complexes composed of E-type cadherins tethered to the actin cytoskeleton through the linker protein group of catenins [15]. One example is cardiac muscle, in which β-catenin localizes to adherens junctions, which are critical for electrical and mechanical coupling between adjacent cardiomyocytes [9].

The immunoglobulin superfamily is one of the largest and most diverse protein families. They are characterized by the presence of at least one immunoglobulin or immunoglobulin-like domain. Most members are type-I transmembrane proteins with an extracellular Ig domain, transmembrane domain, and a cytoplasmic tail [16]. IgSF proteins play a critical role in the development of the nervous system, in embryonic development, and in immune and inflammatory responses [9]. Particularly in the immune system, IgSF members play a critical role in cellular adhesion, and well-known examples include major histocompatibility complex (MHC) class I and II molecules, proteins of the T cell receptor (TCR) complex, intercellular adhesion molecules (ICAMs), and vascular cell adhesion molecules (VCAMs) [17]. Mucosal addressing cell adhesion molecule-1 (MAdCAM-1) and activated leukocyte cell adhesion molecules (ALCAMs) also belong to this family of adhesion receptors and are impor-

tant in leukocyte trafficking events [10]. These proteins serve as ligands for integrins on the endothelial cells. IgSF molecules are divided into several subfamilies, including nectins and selectins. Whereas nectins mediate cell–cell adhesion in various tissues including endothelium, epithelium, and neural tissue [12], selectins are single-chain transmembrane glycoproteins that mediate calcium-dependent binding to sugar moieties [10]. Their most prominent function is associated with the initial stage of the rolling cell adhesion cascade in which selectin binding enables rolling and cell arrest [18].

Integrins are large heterodimeric glycoproteins constituting a diverse family of adhesion molecules. They play a critical role in important biological functions, including embryogenesis, maintenance of tissue integrity, immune response, and inflammation. Integrins consist of two subunits, α- and β- chains, spanning the cell membrane and forming the receptor in the plasma membrane, characterized by noncovalent interactions [10]. Integrins bind to a large variety of ligands, and the majority belong to two categories. The first category are cell surface molecules of the immunoglobulin supergene family, for example, ICAMs and vascular cell adhesion molecule 1 (VCAM-1), and the second category includes larger-sized ECM protein components such as fibronectin, fibrinogen, vitronectin, and complement component iC3b [13]. Divalent cations, such as Mg^{2+} and Ca^{2+}, are involved in ligand binding. Individual integrins can bind more than one ligand, and vice versa. However, the cellular environment may influence ligand specificity within a particular cell interaction [9]. Generally, integrin-mediated interactions involve a complex series of events including activation, ligand binding, reorganization of the cytoskeleton, and adhesion [13]. In this context, integrin activation is regulated in response to signal cascades inside the cell known as an "inside-out" process initiated by other cell surface receptors, such as chemokine receptors and selectins. The subsequent interaction with cytoplasmic factors leads to a conformational switch in the extracellular integrin binding region from a non-adhesive (inactive) to an adhesive state [19]. Moreover, adhesive interactions also include activation outside the cell (outside-in process) mediated by the cytosolic domains of the integrin α- and β-subunits. The recruitment of either leukocytes or platelets from the blood circulation are examples that require both signalling pathways [9].

Cells in their native tissue environment are surrounded by a unique, complex ECM consisting of a variety of molecules and proteins showing a diversity of assembled morphologies, structures and folding states, which are essential for their assigned functions. Besides structural and mechanical support, the present proteins are direct interaction partners for the cellular receptors mentioned above and contain binding sites for further biologically active molecules, including growth factors, which stimulate several subsequent cellular responses, such as growth or differentiation [20-23]. Prominent examples of ECM proteins are collagens, laminins, fibronectin, and elastin, which contain several short peptide recognition and binding motifs in their amino acid sequence for interaction with specific cellular surface integrins or other types of receptors [23]. Within the ECM, fibronectin is the best-known attachment site for cells by interacting with members of the integrin family of cell surface proteins. However, fibronectin is a multifunctional adhesion molecule, also binding to other protein constituents of the ECM such as fibrin, collagen, and heparin [24]. Thus, fibronectin is involved in several physiological events such as embryonic differentiation, cell morphology, cell migration, and thrombosis [19]. The function of fibronectin as a cell-binding molecule involves its recognition by integrins through short peptide motifs, among them the prominent Arg–Gly–Asp (RGD) and Leu–Asp–Val–Pro (LDVP) sequences [19].

1.2 Applications of bio-inspired selective surface modifications

The increasing knowledge on natural receptor–ligand binding mechanisms led to various approaches in the last years to increase both cellular adhesion on surfaces of biomaterials and biosensors, as well as for therapeutic drug carrier systems against infections, inflammatory and auto-immune diseases, and for anti-tumor treatments [10,25]. One main goal in developing bioactive, bioadhesive, and functional biomaterial scaffolds for tissue engineering, is the enhanced support and regeneration of injured or non-functional tissues or parts thereof.

Apart from the development of sophisticated synthetic polymer systems [26,27], protein-based and bioinspired materials have nowadays an enormous impact [28,29]. Biomaterials based on native collagen, keratin, elastin, silk, and their recombinant, engineered counterparts become increasingly popular in biomedicine and tissue engineering, since they exhibit promising chemical and physical properties, such as bioactivity, structural integrity, and cell stimulation [29,30]. Biomimetic materials modulating specific cellular responses and tissue regeneration have been developed by adjusting and modifying materials using bioactive and bioadhesive molecules, such as full-length ECM proteins or functional peptide fragments thereof. These ligands interact with cell receptors for guiding cellular responses, such as cell proliferation or specific matrix degradation [31-34]. Compared to full-length proteins, short, bioactive peptide sequences show several advantages due to their size, including similar function, controllable, inexpensive, and synthetic production in high amounts, facile processing, simple modification, accessibility, and no animal origin [31,33].

Many reviews have summarized biologically active peptide sequences regarding their natural origin, their functions, their cellular effects, the targeted tissues, or the engineered and designed scaffolds [31-36]. The most prominent and important adhesive peptide sequence used for functionalization and increasing the bioadhesiveness of a material is the tripeptide RGD, naturally occurring in various ECM proteins including fibronectin, vitronectin, laminin, and collagen [34,35,37-41]. This frequently used peptide has been shown to increase the bioadhesiveness of biomaterials by interacting with cellular integrin receptors and, thus, allows for interaction and attachment of many different cell types [23,33,34,36,39,42-44]. Some integrin types interact with their ligands by recognizing specific ligand motifs. For instance, α4 integrins recognize the Leu–Asp–Val–Pro (LDVP) motif in fibronectin, the Leu–Asp–Thr–Ser (LDTS) sequence in MAdCAM-1, and Ile–Asp–Ser (IDS) in VCAM-1 [19]. Another example of selective adhesion of cells expressing one type of integrin has been achieved by click chemistry to immobilize peptidomimetics of α5β1- or αvβ3-selective RGD peptides [45]. Two other commonly used adhesive peptides to promote cellular interactions with biomaterials are the pentapeptides IKVAV (Ile–Lys–Val–Ala–Val) and YIGSR (Tyr–Ile–Gly–Ser–Arg), which are naturally present in laminin and are used for increasing bioadhesiveness and cellular interactions with biomaterials [23,33-35,41,46-48]. Functionalization of material surfaces is consistently one important step in tissue engineering, especially in the case of implants, where the interaction of cells with the surface is desired [32,44]. However, in the case of 3D structures, bioactive factors must be present in the bulk material and surround the incorporated cells [31,33,34]. For the usage as implant, biocompatible biomaterial implant surfaces should demonstrate different properties adopted to the needed requirements to allow for a successful incorporation in the human body depending on the aimed application (Figure 1). Therefore, the interactions of proteins, microbes, and cells should be guided by material-related surface properties to create bioinert, bioactive, or biomimetic biomaterials.

1.3 Antiadhesive and anti-fouling protein surfaces

Nature has evolved a diverse portfolio of anti-adhesive, antimicrobial and antifouling methods. Biofouling can be defined as the undesired attachment and growth of life on artificial surfaces [49]. One general strategy to inhibit

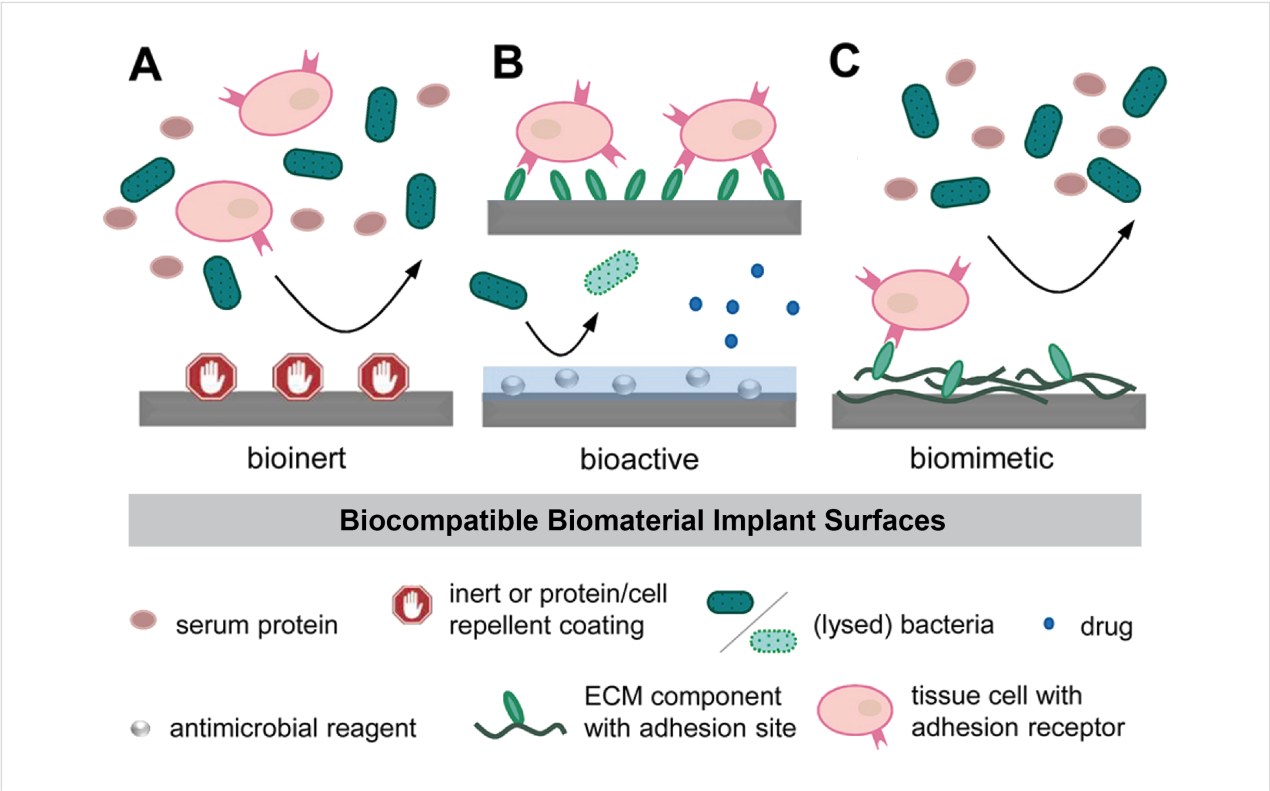


Figure 1: Material-related properties guiding the interactions of proteins, microbes and cells on biomaterial surfaces. (A) Bioinert surfaces hinder the adsorption of proteins, and no interaction and adhesion of cells and microbes is possible. (B) Bioactive surfaces actively stimulate their surrounding by releasing factors or agents to allow for cellular interaction (bioadhesion) or combat against microbes. (C) Biomimetic surfaces are designed to mimic natural ECM composition to guide cellular interactions and tissue regeneration, while repelling proteins and microbes. Figure 1 was adapted from reference [32] (© 2021 S. Spiller et al., published by De Gruyter, distributed under the terms of the Creative Commons Attribution 4.0 International License, https://creativecommons.org/licenses/by/4.0).

biofilm formation and microbial colonialization is microbial repellence since it targets a direct inhibition of bacterial adherence on a surface. Various approaches can be distinguished according to their basic defense mechanism. These are (A) surface topography, which disturbs and inhibits the initial adhesion based on morphological features, (B) material modification, where intrinsic chemical and physical properties result in microbe-repellence, and (C) additives and coatings that inhibit initial attachment or directly kill microbes (see Figure 2) [50].

Natural surfaces provide many examples of anti-adhesive topography, including nanostructured pikes on Cicada wings [51], micro-structured and patterned riblets of the shark skin scales [52], hierarchically micro- and nanostructured ultrahydrophobic surfaces with self-cleaning ability, such as Lotus leaves and insect wing analogues [53-55], and the superhydrophobic air-retaining surfaces of *Salvinia* floating fern leaves and of the water bug *Notonecta glauca* [53,56]. Based on such blueprints, bioinspired anti-adhesion and antifouling surfaces have been successfully generated by soft photolithography, micromolding or nanopatterning techniques [57]. Moreover, the biomimetic application Sharklet® textured similarly to shark skin has not only been reported to be antiadhesive against green algae spores and bacterial cells but to even display antiviral attachment properties [58]. Superhydrophobic surfaces inspired by the Lotus-effect® (>150° contact angle) have been found to diminish bacterial adhesion due to reduced protein surface adsorption [59-61]. Superhydrophobicity relies on the combination of chemical composition, surface structuring on the micro-/nanoscale, and the introduction of low-surface-energy compounds [62]. Various studies demonstrated that the adhesion of *Staphylococcus aureus, Pseudomonas aeruginosa*, and *Escherichia coli* (*E. coli*) bacteria was significantly reduced on superhydrophobic coatings obtained from fluorinated silica colloids, thin film deposition of silicone elastomers or nanoengineered superhydrophobic surfaces of Teflon®-coated aluminium [63-65]. Superhydrophobic surfaces have also been reported to be unfavorable for mammalian cell attachment and growth. This may be due to the fact that the proteins in the ECM (such as fibronectin, vitronectin, collagen, and laminin) are adsorbed in a denatured state, and their orientation becomes unsuitable for cell binding [66]. Cells (e.g., osteoblasts) are more likely to attach to more hydrophilic surfaces and exhibit

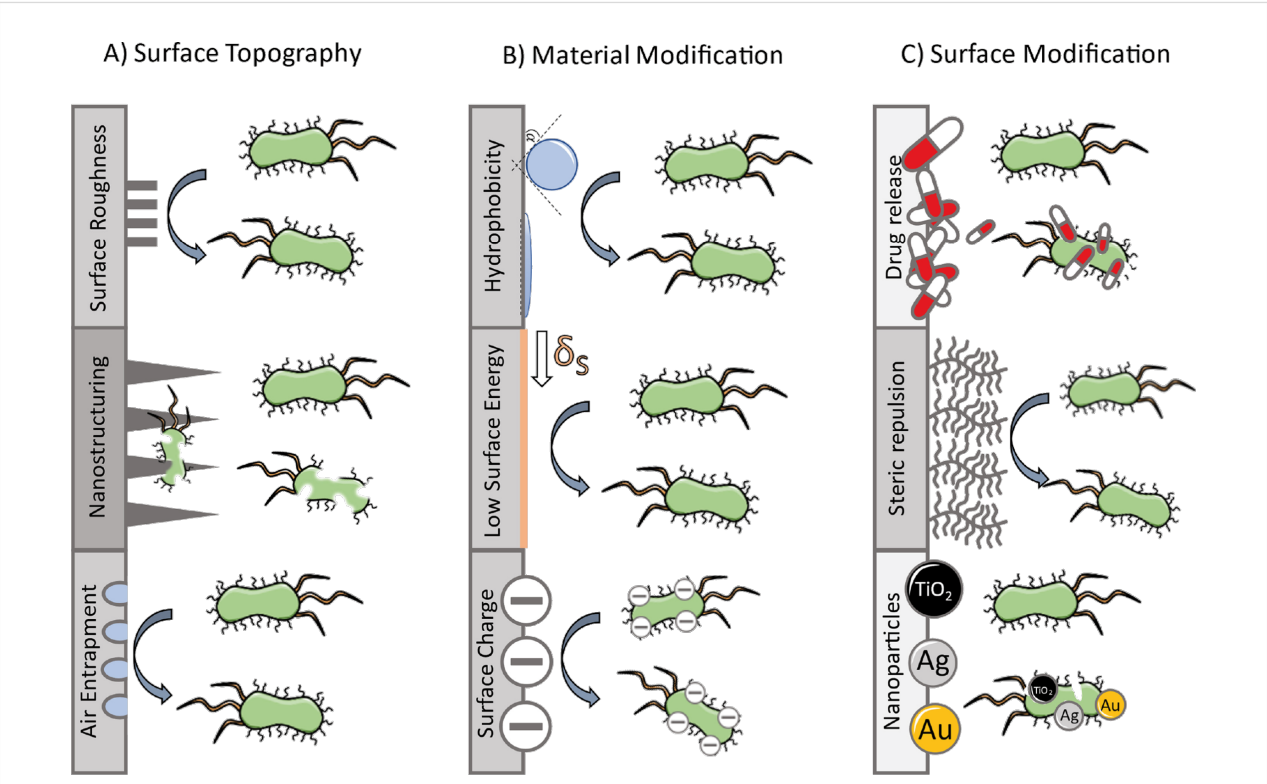


Figure 2: Common antimicrobial approaches regarding the general defense mechanisms (A) surface topography, (B) material modification, and (C) surface modification. Repellent surfaces are displayed in grey, biocide mechanisms in light grey, and contact killing materials in dark grey. Figure 2 was reproduced from reference [50]. (© 2021 D. Sonnleitner et al., published by Elsevier B. V., distributed under the terms of the Creative Commons Attribution-Non-Commercial-NoDerivatives 4.0 International Licence, https://creativecommons.org/licenses/by-nc-nd/4.0/). This content is not subject to CC BY 4.0.

the strongest adhesion at contact angles between 60° and 80° [66].

The contrary material property of highly hydrophilic surfaces also effectively reduces protein and, subsequently, microbial adhesion. A theoretical study analysed the contribution to either adhesion or repellency of steric repulsion, van der Waals attraction, and hydrophobic interaction free energies of surface-bound hydrophilic polyethylene oxide (PEO) polymer [67]. Greater surface density and chain length of terminally attached PEO chains were reported to correlate to a lower van der Waals attractive component. In turn, steric repulsion of the polymer chains against protein molecules increases, while a tightly bound water layer creates a physical and energetic barrier and renders interactions with approaching proteins or bacteria thermodynamically unfavorable [50]. The concept of steric repulsion based on a hydration layer through hydrogen bonding and/or ionic solvation has been reported for various materials such as poly(*N*-isopropylacrylamide) (PNIPAAm) [68,69], dextrans [69], poly(ethyleneimine) (PEI) [70,71], and chitosan [72].

Concerning proteins, several studies have reported different molecules to generate effective antiadhesive, antimicrobial, and antibiofouling properties, including the formation of an oriented monolayer of bacterial flagellin proteins on hydrophobic surfaces [73], a reduction of oral bacteria adhesion on dental brackets by more than 95% due to a reduced surface free energy [74], and the fabrication of antifouling coatings through fluorous media-assisted thermal treatment of stable, hydrophilic protein films [75]. One prominent natural route to prevent the colonization and infection with microbes on cells, tissues, and material surfaces is to block adhesion of bacteria and inhibit attachment to host cells. Microbial cells utilize a variety of extracellular structures such as flagella, pili, fimbriae, and curli fibres, as well as outer membrane proteins to attach to almost every surface [50,76]. During the reversible attachment phase of bacterial biofilm formation, surface pre-conditioning occurs due to soluble organic and inorganic macromolecules that absorb on the underlying materials. The various locomotive appendices, the glycocalyx, and hydrophobic molecules mediating non-specific binding interactions help bacterial attachment even in presence of repulsive forces [77,78]. To address the target protein molecules involved in bacterial adhesion, specific drugs are studied that can disrupt the formation of these molecules. One example are pilicides, derivatives of ring-fused 2-pyridones, which block the correct folding of the pili or fimbriae crucial to bacterial pathogenesis by inhibiting the chaperone–usher polymerization pathway in Gram-negative microorganisms involved in pili protein synthesis [79]. For instance, the inhibitor targets pilus chaperone PapD, thereby reducing the adhesion to cell lines by 90% [80]. These pilicides inhibit curli formation in uropathogenic *E. coli* by preventing the polymerization of protein CsgA and FimC, the chaperone protein of the type-I pili [81]. Once in close contact with mammalian cells, bacteria begin to develop quasi-irreversible attachments by forming stronger bonds with the surface mediated by adhesion proteins or polysaccharides also binding to components of the ECM [50]. The most important adhesion proteins produced by numerous bacteria and virus particles involve surface lectins, known as adhesins and hemagglutinins, that bind to complimentary tissue-specific host cell-surface glycoproteins and glycolipids [82]. Blocking these bacterial lectins by their analogues or suitable carbohydrates has been reported as a possible route for preventing and treating microbial infections [78]. For example, a novel group of adhesins widely found in Gram-negative pathogens has been described, termed multivalent adhesion molecule (MAM7) [83]. The adhesin genes are constitutively expressed, and adhesins are themselves involved in the initial attachment phase of pathogens, by interacting with both the host cell receptor phosphatidic acid and the co-receptor fibronectin. Recombinant production of MAM7 and subsequent coupling on polymer beads has been reported to decrease the surface attachment and infection of pathogens, mimicking the bacterial surface display of the adhesins. Pre-treatment of host cells with MAM7-based inhibitors has shown to inhibit bacterial infection with a range of important clinical pathogens, including *Vibrio parahaemolyticus, Vibrio cholerae, Yersinia pseudotuberculosis*, and enteropathogenic *E. coli* [83,84].

Another protein-based antimicrobial strategy in nature is the use of antimicrobial peptides (AMPs) [85]. These molecules are short-length amphipathic peptide molecules (between 10 and 50 amino acids), usually with cationic charges and hydrophobic residues, and are naturally produced by all multicellular organisms as immune response elements. They are involved in multiple interactions in and outside the cells in response to infections and microbial assault [86]. Mammalian AMPs are generally produced in epithelial tissues of the testis, skin, gastrointestinal tract, and respiratory tract, as well as in leukocyte cells such as monocytes, neutrophils, and others, thus forming a central part of mammalian innate immunity [87]. The multitude of immuno-functional roles of the broad-spectrum antimicrobial peptides includes (1) eliminating bacterial growth through direct antimicrobial activity, (2) inhibiting biofilm-specific signalling pathways, and (3) modulating the innate immune responses resulting in the inhibition of potentially harmful inflammation reactions [85,86,88]. In order to highlight the multifaceted nature of AMPs, the term host defense proteins (HDPs) was coined [89]. HDPs are rich in cationic amino acids (e.g., arginine and lysine), and amino acids with hydrophobic side chains (e.g., tryptophan, phenylalanine, tyro-

sine, leucine, isoleucine, and valine). This composition renders them amphiphilic, which is crucial to their mode of action and promotes their attachment to the bacterial surface/membrane residues [85]. HDPs have properties of cell-penetrating peptides and can translocate across membranes of prokaryotic, but also eukaryotic, cells [90]. The main mode of action of these peptides is promotion of adhesion through the cationic groups to the anionic bacterial membranes and their lipopolysaccharides (a component of the outer membrane of most Gram-negative bacteria), enabling insertion into the membrane driven by clusters of hydrophobic residues [85,91]. As a consequence, the microbial membranes are permeabilized, associated with membrane perturbation and dissipation of the transmembrane potential, which results in bacterial cell lysis and death [92]. In humans, over 120 HDPs have been identified, and typical examples include lysozyme, defensins, histatins, lactoferricin, kinocidins, ribonuclease, dermcidin, and cathelicidins [93]. In the cathelicidin family of HDPs, named by the ability to inhibit the protease cathepsin L, the amphipathic, helical peptide LL-37 is the only cathelicidin-derived HDP found in humans [87,91]. It was reported that this peptide is able to inhibit *Pseudomonas* biofilm formation at 1/16 of its minimum inhibitory concentration (MIC) for planktonic organisms [94], and, subsequently, it was demonstrated that a distinct subset of HDP peptides can be addressed specifically as antibiofilm peptides, with similar overall amino acid compositions but distinct structure–activity relationships compared to those of antimicrobial peptides [95]. As a result of the multiple functionalities of HDPs, several amphiphilic antimicrobial molecules have recently been developed mimicking both structure and functional aspects of the antimicrobial peptides, such as all-D amino acid peptides [96], β-peptides [97], and peptide isomers known as peptoids, (oligo N-substituted glycines) [98]. In addition, the transfer of the general molecular structure of AMPs/HDPs has led to peptide-mimicking polymers and surface-engineered polymeric-brush-tethered AMPs. These approaches are promising for establishing biomaterials and medical devices with antifouling and antibacterial properties, but with reduced susceptibility to enzymatic degradation [85]. General advantages of AMPs/HDPs and mimicking polymer systems over antibiotics as a new generation of antimicrobial agents are their functional diversity, broad spectrum of potential practical applications such as tissue repair, the protection of implanted devices, low potential of bacterial resistance due to their multiple bacterial targets, and host/non-host microbe specificity [85,86,99].

1.4 Importance of (protein-based) bioselective materials

One of the biggest threats to human health worldwide is the rapid emergence of multidrug-resistant pathogens, due to the overuse of broad-spectrum antibiotics [100]. The rising rates of antimicrobial and antiviral resistance of infectious bacteria, viruses, and fungi and their related diseases impact all aspects of modern medicine. Recent outbreaks of severe diseases such as Ebola, influenza, and even more so the severe acute respiratory syndrome (SARS) and the pandemic SARS-CoV-2, have tremendously increased the urgency for new concepts and materials that prevent pathogenic microbial infestation and contact-based spreading due to contaminations of surfaces leading to biofilm formation [101]. In contrast, for biomaterials and their biomedical application (such as implants and wound dressings), cell-friendly and adhesive properties are necessary [66]. Ideally, bioselective materials that promote host cell adhesion while simultaneously preventing microbial infestation and biofouling would exhibit a best-of-both-worlds approach for a number of biomedical applications. For instance, it has been shown that the surface modification of glass substrates with the cell-binding motif RGD of fibronectin and collagen significantly enhanced 3T3 fibroblast cell adhesion. RGD further showed no specific binding affinity towards both clinically relevant bacteria *E. coli* or *S. aureus*, and collagen reduced *E. coli*, but enhanced *Staphylococcus aureus* (*S. aureus*) adhesion [102]. Similar results were obtained for chemically coupled RGD and collagen to an antimicrobial polymeric multilayer composed of dextran sulfate and chitosan [103].

One way to achieve bioselective, biocompatible, and multifunctional materials for biomedical applications is the utilization of natural protein materials shown to accomplish the desired properties and derived bio-inspired materials thereof. Protein-based materials are interesting candidates due to their natural origin, biological activity, and structural properties. Among them are silk materials, in particular one made of spider silk proteins [104]. These are well-studied examples characterized by extraordinary properties including excellent biocompatibility, slow biodegradation, low immunogenicity, and non-toxicity, making them ideally suited for tissue engineering and biomedical applications [105-107]. This review focuses on achievements made with silk-based protein materials and highlights the interaction with mammalian cells and microbes as far as the important aspect of bioselective surfaces is concerned.

2 Natural silk proteins

2.1 Silk protein classification

The term silk generally refers to extracorporeal, proteinaceous structural materials, mostly in the form of threads [108,109]. Silk proteins evolved around 250 million years ago and are present in a variety of recent arthropod families, most prominently in silkworms and spiders, but also in bees, wasps, and ants [110]. Silks fulfill numerous functions, including prey capture, dispersal, reproduction, adhesion, and building cocoons, nests, egg sacs, and stalks [6,110]. Silk proteins are

biochemically diverse but do share common elements. They usually consist of large proteins that contain long motifs of highly repetitive amino acid sequences rich in alanine, serine, and/or glycine [111]. Moreover, the proteins are stored as highly concentrated silk dope solutions in specialized glands and solidify in a spinning process often associated with shear forces accompanied by their folding into a single dominant secondary structure [112]. Due to both convergent evolution (i.e., silks have been "invented" independently several times), and adaptation to specific functions, the amino acid sequence and protein structure varies considerably, resulting in a versatile class of proteins [112]. Silks are known as semicrystalline materials since they consist of ordered, crystalline structures embedded in an amorphous matrix. The regular secondary structure within one type of silk allows for the condensed packing of protein, as well as the formation of hydrogen bonds, leading to tightly connected intra- and inter-protein chains [111]. While the crystalline regions exhibit a high hydrogen bond density accounting for the strength of a silk fibre, the unordered amorphous regions with less hydrogen bond density induce flexibility [109].

Besides considerable variations in arthropods, the silk of silkworms and related moths, and that of orb-weaving spiders share some features. Their silk proteins are often of high molecular weight, and whilst the termini are hydrophilic, the repetitive cores are composed of alternating large hydrophobic amino acid sequence blocks interspersed with short hydrophilic parts. Interestingly, in both insect (fibroin) and spider (spidroin) silk fibres the core is composed of fibrils that are oriented along the fibre axis and contain nanometre-sized β-sheet crystallites [113,114]. Silkworm silk contains mainly three different proteins, namely a heavy chain fibroin, a light chain fibroin linked via disulfide bonds to the former one, and a P25 glycoprotein associated via noncovalent hydrophobic interactions as a putative stabilizer of the fibre complex integrity [115]. Recently, it has been reported that the accessory Filippi's glands of silkworms appear to regulate posttranslational modifications of fibroin heavy chain molecules, necessary for a tight cocoon architecture [116]. Silk fibroins make up to 75–83 wt % of raw silkworm silk, while sericins, hydrophilic proteins forming a connective coating, constitute 17–25% of the weight of the fibre. Fibroins contain very few cysteine residues, whereas glycine, alanine, serine, and tyrosine make up more than 90 mol %. The fibroins largely contain blocks of $(GAGAGS)_n$, which are responsible for the anisotropic β-sheet-rich nanocrystals [108]. Sericins are based on glue-like serine-rich glycoproteins with rubber-elastic properties [110]. In addition, a further small protein group named seroins was discovered in lepidopteran silk and is known to possess AMP-like antimicrobial activities. It is produced in the silk gland, but also to a lesser extent in the midgut and fat body [117]. As a consequence of its immunogenic and allergic properties, the sericin coating of silkworm silk fibres has to be removed before further processing or use in medical applications in a process known as degumming [108,112].

Spider silks display a much higher degree of diversity, with up to seven different silk types found in the more highly derived group of orb web spiders [108]. This enables spiders to produce mechanically stable web constructions as well as dragline fibres and, at the same time, to wrap their eggs and utilize sticky glue silk for prey capture. The different silks are named after the spidroin-producing spinning glands, such as major and minor ampulla, flagelliform, aggregate and piriform glands, which produce the scaffold thread, an auxiliary spiral, the catching spiral and its glue, and the net anchors. Aciniform and cylindriform silk, in contrast, are used for the egg case [118]. Spider silk consists of 99% spidroins plus some additional lipids, glycoproteins, and ions such as phosphate. The core domain of spidroins consists of short motifs with 10–50 amino acids, which are present in larger modular units, often copied up to several hundred times, giving spidroins a high molecular weight of several hundred kilodaltons [109]. The core domains are flanked by two globular terminal domains, both highly conserved and very similar in many spider species [119]. These globular domains fulfill important control functions concerning protein solubility in the gland reservoir and in the assembly of spidroins into silk threads. The various spidroins of spiders differ in their amino acid sequences to yield the specific properties and functions of the silks. However, some conserved motifs like polyalanine (A_n, poly-A), glycine–alanine (GA), glycine–glycine–X (GGX) and glycine–proline–glycine–$(X)_n$ ($GPG(X)_n$, where X is typically tyrosine, leucine, or glutamine) are abundant in the repetitive core regions in various spidroins [120]. Similar to silkworm silk, poly-A and GA sequences in the spider dragline thread form nanocrystalline hydrophobic β-sheets aligned along the fibre axis, which are embedded in a matrix of more hydrophilic GGX and $GPG(X)_n$ regions responsible for helical and spring-like secondary structures with fewer hydrogen bonds and higher elasticity [114]. The best-studied silk type is the major ampullate silk (MA) used by spiders for web radii and their dragline. It consists of several proteins known as major ampullate spidroins (MaSps). The most prominent spidroins are MaSp1 and MaSp2, differing mainly in their proline content [114], while in some spiders also short MaSp1 variants, and MaSp3 and MaSp4 proteins have been identified [121,122].

2.2 Silk-based materials and their properties

Materials based on arthropod silk proteins attracted increasing attention among material scientists in the last decades. The

prominent cocoon silk of several silk moths, produced for the wrapping of cocoons during metamorphosis from larvae to adult moths, has been used by humans for millennia [108]. The application of silkworm silk covers a wide range from traditional textiles to technical fabrics and cosmetic articles including skin care, shampoos, and lotions. Traditional utilization of silk fibres as sutures for wounds are known for centuries due to their strength, biocompatibility, and low immunogenicity [104], and silkworm silk surgical threads are commercially available [108]. Moreover, silk-based polymeric materials have also been reported to be suitable as tissue scaffolds due to their biocompatibility and their highly tunable morphologies and mechanical properties. Exemplary, silkworm silk has been studied as a matrix material for tissue-engineered anterior cruciate ligaments [123], and silk fibroin/nanohydroxyapatite composite hydrogels have been studied regarding bone tissue engineering [124].

Spider silk has also been widely used as a multifunctional material for fishing nets, wound coverings, and sutures for surgery for centuries in Australasia and Greece [108]. Since then, it came in focus of researchers worldwide. Natural spider silk has the potential to be used for tissue engineering and biomedical applications. For instance, NIH 3T3 cells showed increased adhesion and proliferation on fabricated, sterilized wovens made of native, unmodified spider dragline silk fibres from *Nephila clavipes* over five days [125]. Furthermore, Wendt et al. showed that naturally occurring spider dragline silk fibres from *Nephila* species could be processed into wovens for culturing first fibroblasts for two weeks before seeding keratinocytes on top to develop a bilayered skin model consisting of an artificial dermis and epidermis [126].

Strikingly, silk materials from silkworms and spiders share a set of highly interesting properties, including mechanical and chemical stability, biocompatibility for mammalian cells and tissues, persistence against microbial degradation and, moreover, potential microbe-repellent and antimicrobial features [50]. Several studies reported antibacterial properties, reduced biofilm formation, and bacterial repellency of both natural silkworm [127-129] and spider silk threads and cocoons [130-136]. However, the status of the intrinsic properties of silk materials in the context of microbial defense is a matter of debate in the scientific community [137,138]. While some of the inconsistencies seem to be related to methodological aspects of the reports in doubt, a misunderstanding of the distinction between the three mechanisms of biofilm inhibition, namely microbial repellency, microbiocidal activity, and contact killing, may foster the discussion on the anti-fouling properties of silk protein materials [50]. Concerning spider silk materials, it has been reported that they seem to prevent bacterial attachment to the surface and biofilm formation instead of being antimicrobial [136].

3 Engineered silk protein-based materials

3.1 Recombinant spider silk technology

The unique properties of spider silk make it a promising candidate for biomedical and tissue engineering applications [105-107]. However, the amounts that could be harvested from spiders are low, and the farming of most spiders is not possible due to their territorial behaviour. Therefore, different recombinant production systems have been developed over time to generate spider silk proteins in appropriate amounts and quality [139,140]. The Johansson research group used the amino acid sequence of the spider *Euprosthenops australis* as inspiration and developed the recombinant spider silk protein 4RepCT comprising four repetitions of a sequence with a polyalanine-rich and a glycine-rich block, as well as a non-repetitive C-terminal domain [141,142]. Another recombinant system is based on the dragline silk of the European garden spider *Araneus diadematus*: Two native spidroins of this silk, namely *Araneus diadematus* fibroin (ADF) 3 and 4, have been used as blueprints for generating the engineered variants eADF3(AQ12) and eADF4(C16). Both proteins contain polyalanine-rich sequences, but eADF4(AQ12) contains two sequence modules (A and Q), while eADF4(C16) comprises only one module (C), repeated either twelve or 16 times, respectively, to generate artificial spider silk proteins [143]. Due to a glutamic acid residue in the C-module, eADF4(C16) is negatively charged [143]. Replacing this amino acid yielded a positively charged eADF4(κ16) and an uncharged eADF4(Ω16) variant, where the glutamic acid residue is exchanged with a lysine or glutamine residue, respectively [144-146]. The dragline silk of *Nephila clavipes* inspired the recombinant spider silk proteins 6mer and 15mer, in which the consensus sequence is repeated six or 15 times, respectively [147]. These recombinant spider silk proteins have been developed using genetic engineering to generate the appropriate gene sequence of interest. In all these cases, recombinant protein production was achieved using bacteria (*E. coli*) [141-143,147]. The usage of genetic engineering further allows for diverse modifications on the genetic level, including site-specific amino acid changes leading to differently charged proteins [144-146] and the addition of short amino acid sequences [114,148-154] or whole domains [155-157] and even proteins [158-160].

3.2 Cell adhesive silk material surfaces

Since the engineered ADF4 sequences lack cell binding sequences, biological interaction and cell attachment is quite limited to recombinant spider silk materials made thereof [161]. Cell culture studies on film surfaces using Balb 3T3 fibroblasts [148], neonatal rat cardiomyocytes [162], human induced

pluripotent stem cell (hiPSC) derived cardiomyocytes [150], keratinocytes, myoblasts, or neuronal cells [163] revealed that negatively eADF4(C16) and uncharged eADF4(Ω16) surfaces do not allow good and sufficient cell attachment necessary for tissue engineering applications. However, several independent studies showed that the materials made of the positively charged eADF4(κ16) variant enabled partial cell adhesion due to the positive surface charge derived from lysine residues in the primary amino acid sequence [150,162,163]. Since cells expose many negatively charged molecules on their cellular surface, charge modification is often used to guide cellular interaction [164-166]. In the example of the recombinant 4RepCT spider silk, several charged amino acid residues in the primary protein sequence create a material surface that allows for the growth of primary fibroblasts without further modification [167].

As mentioned above, bioselective cell adhesion could be generated by attaching or introducing binding sites, for example, peptide sequences such as RGD, for specific interaction with cellular receptors [41]. In case of recombinant eADF4-based silk, the RGD peptide was genetically (C-terminal) and chemically (N-terminal) coupled to eADF4(C16) to selectively allow for cell attachment on materials made thereof. Fusing the integrin non-binding peptide RGE, showing a residue substitution of aspartate with glutamate thus rendering an identical charge distribution, was applied as a control. Cell culture studies using Balb 3T3 fibroblasts revealed that the RGD peptide enhanced primary cell attachment with increased spread morphology and proliferation on films independently of chemical or genetic modification. The unmodified eADF4(C16) and eADF4(C16)-RGE control surfaces showed less or no cell interaction [148]. In addition, eADF4(C16)-RGD films allowed for adhesion and spreading of neonatal rat cardiomyocytes and hiPSC-derived cardiomyocytes, and further supported their cellular functions, such as beating and contraction [150,168]. The C-terminal genetic modification of the uncharged eADF4(Ω16) and positively charged eADF4(κ16) variant with RGD also enabled the attachment of hiPSC-derived cardiomyocytes and the development of their cell-specific functions on flat films (Figure 3A) [150]. In another study, eADF4(C16) was modified with biomineralization and collagen-binding peptides, yielding an increased osteoblast attachment on these functionalized variants [149].

Genetic modification of 4RepCT led to recombinant spider silk proteins containing linear RGD, RGE, IKVAV, and YIGSR sequences at their N-terminal end. Cell culture analysis using primary cells (fibroblasts, keratinocytes, endothelial, and Schwann cells) revealed that these peptide tags had a clear positive impact on early cell attachment and spreading (Figure 3B). Especially, adhesion and spreading of Schwann cells were influenced in case of the IKVAV modification. Nevertheless, after a longer incubation time (24 h) all modified surfaces supported cell growth [152]. Another study compared the influence of different N-terminally fused RGD-containing peptides on cell behaviour (keratinocytes, endothelial, and human mesenchymal stem cells). It could be shown that all RGD peptides enhanced the adhesiveness of these spider silk surfaces, but the disulfide-bridged, fibronectin-derived integrin-binding RGD peptide showed the highest impact on cell adhesion [151]. RGD-modified FN-4Rep-CT silk could also be used to generate self-assembled membranes, allowing for the adhesion of endothelial cells on the one side and smooth muscle cells on the other side, as well as the diffusion of relevant molecules, making this material promising for vascular tissue engineering [170].

In addition to flat films or coatings, recombinant spider silk proteins based on eADF4 can be processed into 3D scaffolds, such as foams or hydrogels due to their self-assembly properties [169,171-174]. Balb 3T3 fibroblasts adhered to porous foams made of eADF4(C16)-RGD and showed spreading and cell elongation along the foam walls, while cellular aggregates were formed in and on unmodified eADF4(C16) foams, because the cells preferred cell-cell-contacts over cell-material-interactions (Figure 3C) [169]. Additionally, it could be shown that osteoblasts, fibroblasts, keratinocytes, and myoblasts adhere to eADF4(C16)-RGD hydrogels, while they could not attach to unmodified eADF4(C16) hydrogels [174]. A previously published in vivo study of an arteriovenous loop model in rats showed that RGD-functionalized spider silk hydrogels significantly enhanced angiogenesis by forming new blood vessels compared to unmodified eADF4(C16) hydrogels [175].

4RepCT could also be processed in 3D foams for cell culture analysis [154,167,176]. Foams of the genetically modified 4RepCT variants carrying RGD, RGE, IKVAV, and YIGSR sequences were analysed in presence of pancreatic cells for insulin production. While the adhesion and formation of islets was clearly enhanced on RGD-modified foams, a high insulin production was measured for RGD- and YIGSR-modified foams after two days. Although all spider silk scaffolds could be used for culturing pancreatic cells with long-term maintenance of function, the bioactive RGD peptide modification showed the most promising results for in vivo applications (Figure 3D) [154]. One other study analysed the impact of the location of RGD sequences inside the 4RepCT protein on cell behaviour. Therefore, different RGD-containing peptides were genetically introduced at the N-terminus or between repetitive units of the 4RepCT silk protein. The analysis using pancreatic

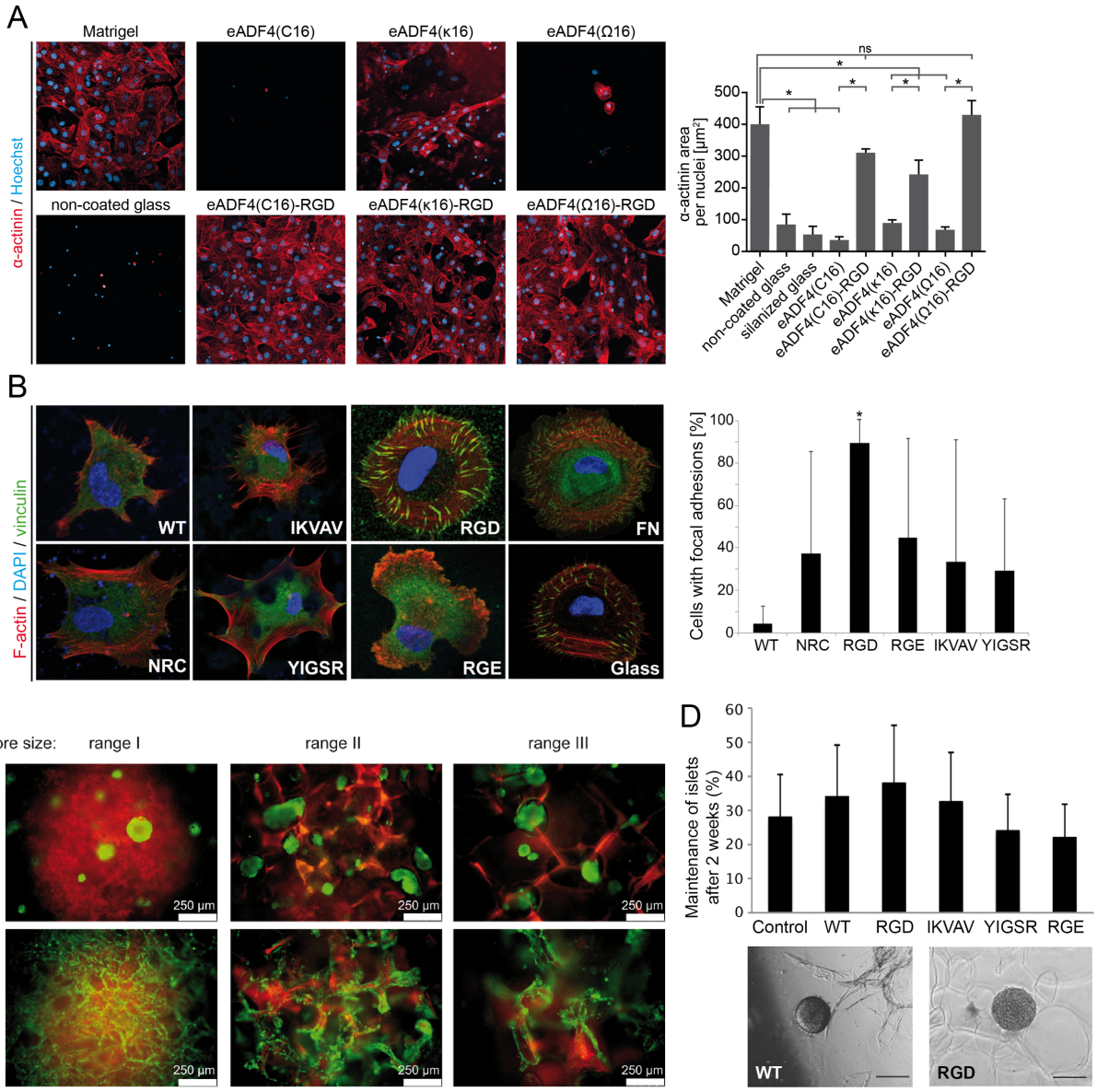


Figure 3: Bioselective, cell adhesive spider silk surfaces. (A) hiPSC-derived cardiomyocytes adhere and spread on spider silk films made of eADF4(C16)-RGD, eADF4(κ16), eADF4(κ16)-RGD, and eADF4(Ω16)-RGD and on control films made of Matrigel. Figure 3A was reprinted from reference [150], Materials Today Bio, vol. 11, by T. U. Esser; V. T. Trossmann; S. Lentz; F. B. Engel; T. Scheibel, "Designing of spider silk proteins for human induced pluripotent stem cell-based cardiac tissue engineering", article no. 100114, Copyright (2021) The Authors, with permission from Elsevier. This content is not subject to CC BY 4.0. (B) Human dermal fibroblasts attachment and spreading behaviour on unmodified (WT) and peptide (NRC, RGD, RGE, IKVAV, and YIGSR)-functionalized 4RepCT spider silk films compared to control surfaces (glass and fibronectin (FN)) after 3 h. Figure 3B was reprinted with slight adaptation from reference [152], Biomaterials, vol. 34, issue 33, by M. Widhe; U. Johansson; C.-O. Hillerdahl; M. Hedhammar, "Recombinant spider silk with cell binding motifs for specific adherence of cells", pages 8223-8234, Copyright (2013), with permission from Elsevier. This content is not subject to CC BY 4.0. (C) Balb 3T3 fibroblasts showed enhanced adhesion, spreading, and elongation on foams made of eADF4(C16)-RGD (lower panel) compared to unmodified eADF4(C16) ones (upper panel) independent of the pore size. Figure 3C was reprinted with permission from [169], Copyright 2016 American Chemical Society. This content is not subject to CC BY 4.0. (D) Human pancreatic islets could adhere, survive, and maintain their function on functionalized foams made of unmodified (WT) and peptide (RGD, RGE, IKVAV, and YIGSR)-functionalized 4RepCT foams. Figure 3D was adapted from reference [154] (© 2015 U. Johansson et al., published by PLOS, distributed under the terms of the Creative Commons Attribution 4.0 International License, https://creativecommons.org/licenses/by/4.0/).

islet cells revealed that peptides inside the protein sequence enhanced cluster formation and total number of these islets, but the viability and functionality of the clusters was enhanced on all RGD-modified substrates [176]. The multitude of studies using functionalized recombinant spider silk in tissue engineering confirmed the high impact and suitability of bioadhe-

sive spider silk protein-based materials for applications in that field.

3.3 Antimicrobial silk-based surfaces

As already pointed out in section 2.2, no uniform hypothesis has been formulated so far for spider silk surfaces concerning their microbial repellence and persistence against microbial degradation. For example, one study reported increased bacterial growth on spider silk webs of *Linothele fallax* and *Linothele megatheloides* and discussed that spider silk proteins may serve as nutrients for various microbes [177], whereas other studies provided clear evidence that spider silks of the species *Tegenaria domestica, Nephila pilipes, Hippasa holmerae*, and *Cyrtophora moluccensis* are microbe-repellent [131,136]. More species have been studied in other reports, and as one result thereof it is clear that microbial repellence is not a general trait in spider silks [178]. One way to characterize this issue is through the analysis of genetically engineered silk proteins, allowing for a precise control of the design and modifications of the underlying amino acid sequence motifs and the structure–property relationships of tailored silk materials. Thus, intrinsic antimicrobial properties of materials based on recombinant silk proteins can also be analysed in greater detail. Modifications with specific functions, for example, AMPs against biofouling, enzymes, and nanoparticles, open further roads towards antimicrobial or repellent protein-based materials. As an example, Harris et al. studied coatings made of recombinant spider silk proteins based on the dragline silk amino acid sequence of *Nephila clavipes* MaSp1 and MaSp2 on a variety of substrates [179]. The authors reported an intrinsic ability of the recombinant spider silk proteins to prevent biofouling due to bacterial manifestation. In addition, functionalization of the silk proteins with antimicrobial biologicals displayed increased inhibition of surface fouling [179]. Fusion proteins combining recombinant MaSp1 spider silk proteins from *Nephila clavipes* with the AMPs human neutrophil defensin 2 and 4 (HNP-2, HNP-4) and hepcidin, showed antimicrobial activity against Gram-negative *E. coli* and Gram-positive *Staphylococcus aureus* [180]. A more recent study reported on the fusion protein 2Rep-HNP1 consisting of two repeats of the *Euprosthenops australis* MaSp1 repetitive core region and the AMP human neutrophil defensin 1 active peptide (HNP-1) to create antimicrobial silk as a promising new suture material [181]. The tagged 2Rep-HNP1 retained a broad-spectrum antimicrobial activity above 90% against the same bacterial pathogens mentioned above [181]. Another approach aimed to take advantage of the combined usage of natural silk fibroin as a bulk scaffold and a coating with recombinant spider silk proteins functionalized with specific modifications [182]. The recombinant spider silk protein 4RepCT was fused with two AMP motifs with antimicrobial activity, namely magainin I (Mag-4RC) and lactoferricin (Lac-4RC), successfully inhibiting biofilm development of the skin-infecting bacteria *Pseudomonas aeruginosa* (*P. aeruginosa*) and *Staphylococcus epidermidis* (Figure 4A) [183].

Introducing antimicrobial properties on surfaces and coatings using antibacterial agents in silks is an advantageous route to reduce or inhibit microbial infestation. The concentration of the antibacterial agent could be locally increased without exceeding toxicity limits as opposed to conventional antibiotic delivery methods in solution. One approach to make materials antimicrobial is to implement metallic nanoparticles in the bulk material. Silver ions in solution have shown antibacterial properties and are widely used in medicine [185]. The release of silver ions from silver nanoparticles (AgNPs) resulted in enhanced chemical, physical, and biological properties [186,187]. In addition to bactericidal properties, physical damage of bacterial membranes by AgNPs was also observed, causing cell leakage and, eventually, cell death [187,188]. A variety of studies focused on the modification of silkworm silk, including plateless silver coating techniques [189] and various coupling mechanisms of silver or gold nanoparticles [190-192]. In addition, the modification of regenerated sericin using crosslinking or surface-linking to titanium dioxide nanoparticles displayed strong activity against different microbes, resulting in loss of cell integrity and subsequent cell death [193-195]. AgNPs produced with sericin as a reducing agent in situ effectively inhibited the growth of *E. coli*, *S. aureus*, and *P. aeruginosa* in radial diffusion assays [194,195].

The genetic introduction of silver binding sites into recombinant spider silk proteins from *Nephila clavipes* MaSp1 dragline silk has been reported, for example, by Currie and co-workers [196]. The study confirmed the effective chimeric coupling of silver ions from a solution, resulting in potent inhibitory effects on both Gram-positive and Gram-negative bacteria [196]. Apart from silver, carbon in the shape of nanodiamonds incorporated into electrospun silk nanofibres showed antibacterial behaviour [197]. As another example, the antibacterial properties of selenium nanoparticles could further be enhanced by coating them with positively charged recombinant eADF4(κ16) silk proteins (Figure 4B) [184]. In addition, cytotoxicity testing showed that the coated selenium particles are safe to use at certain concentrations in biological applications since they showed acceptable cytotoxicity on Balb 3T3 mouse fibroblasts and HaCaT human skin keratinocytes [184]. Composite films and hydrogels made of recombinant eADF4(C16) spider silk and mesoporous silica nanoparticles (MSN) loaded with the aminoglycoside antibiotics gentamycin, neomycin, and kanamycin as well as the antimycotic amphotericin B, exhibited excellent antimicrobial properties [198]. Surface antimicrobial activities against *E. coli*

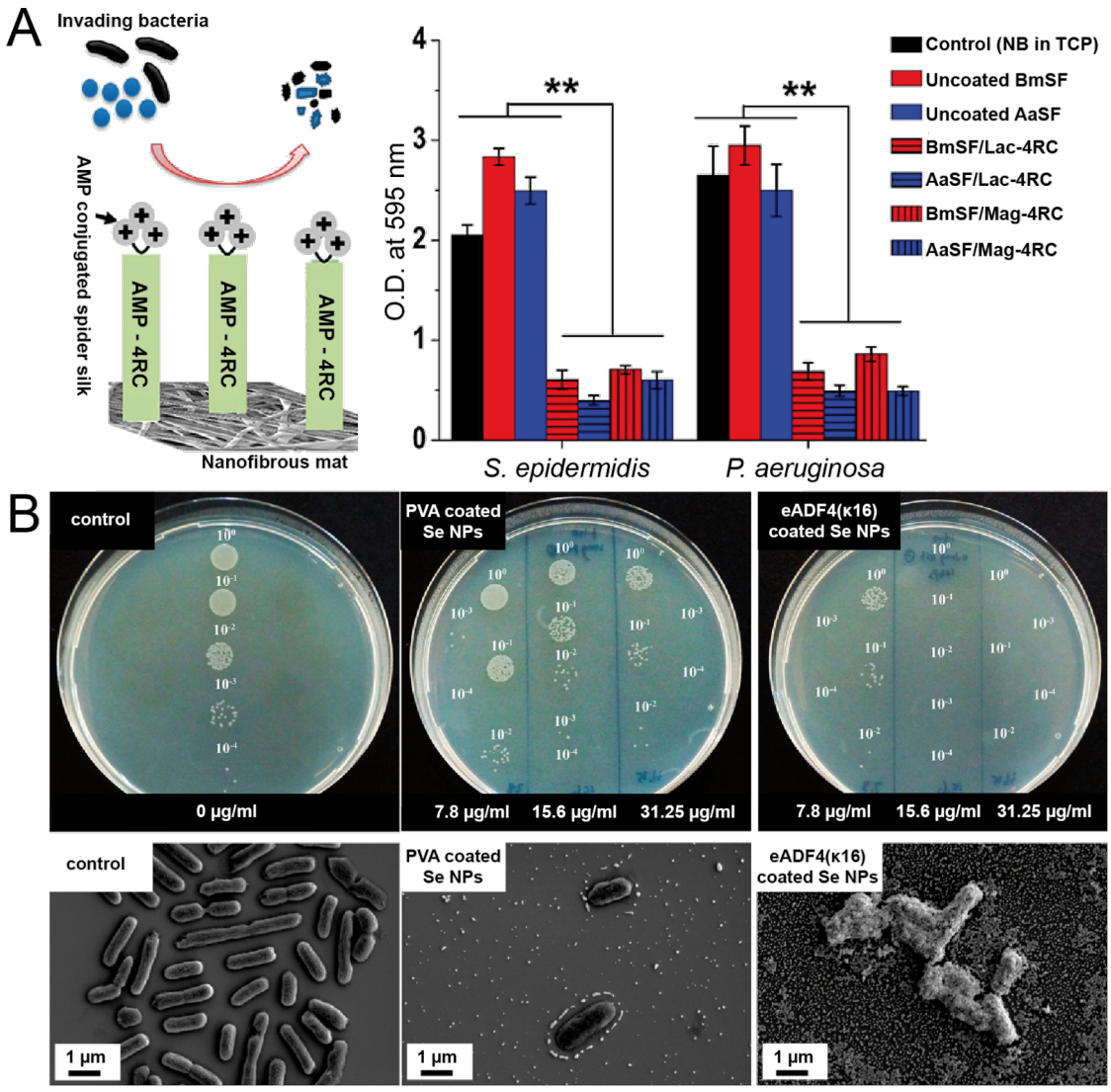


Figure 4: Antimicrobial spider silk materials. (A) Nanofibrous silk fibroin mats (BmSF and AaSF) are coated with recombinant 4RepCT spider silk proteins functionalized with magainin I (Mag-4RC) or lactoferricin (Lac-4RC) cationic antimicrobial peptides. Crystal violet staining (O.D. at 595 nm) of *S. epidermidis* and *P. aeruginosa* bacteria reveals significantly lower biofilm formation on spider silk-coated silk fibroin mats compared to uncoated ones. Figure 4A was adapted with permission from [183], Copyright 2018 American Chemical Society. This content is not subject to CC BY 4.0. (B) Images of agar plates of a colony-forming unit assay and representative scanning electron images of *E. coli* bacteria without and after a treatment using polyvinyl alcohol (PVA) and eADF4(κ16) spider silk-coated selenium (Se) nanoparticles (NPs) in comparison to a particle-free control. Concentrations as indicated. 10^0 represents the original solution of bacteria without or with appropriate particles, while 10^{-1}, 10^{-2}, 10^{-3}, and 10^{-4} indicate, respectively, 10-, 100-, 1000- and 10000-fold dilutions of the original suspension. Figure 4B was adapted from reference [184] ("Enhanced Antibacterial Activity of Se Nanoparticles Upon Coating with Recombinant Spider Silk Protein eADF4(κ16)", © 2020 Huang et al., published and licensed by Dove Medical Press Ltd., distributed under the terms of the Creative Commons Attribution-NonCommercial 3.0 Unported License, http://creativecommons.org/licenses/by-nc/3.0/). This content is not subject to CC BY 4.0.

and *Pichia pastoris* with sustained release of antibiotics could be monitored over the course of 15 days, even at their MIC [198]. Furthermore, the inclusion of antibiotics/antimycotics did not impair the cytocompatibility of the composite materials and promoted fibroblast cell adhesion and proliferation [198].

By incorporating the non-natural methionine analogue L-azidohomoalanine (L-Aha) into the recombinant 4RepCT spider silk protein, site-specific chemical incorporation of two fluorophores and an antibiotic was conducted using copper-catalysed azide–alkyne cycloaddition (a type of click chemistry) [199]. The assembled silk fibres decorated with the broad-spectrum antibiotic levofloxacin showed significant antibiotic activity over at least five days [199]. In another approach, the same recombinant spider silk was successfully functionalized with bacteriolytic or anti-biofouling enzymes for bioactive surface

coatings [200]. The group developed recombinant 4RepCT spider silk proteins functionalized with the peptidoglycan degrading endolysin SAL-1 from the staphylococcal bacteriophage SAP-1 and the biofilm-matrix-degrading enzyme dispersin B from *Aggregatibacter actinomycetemcomitans* [200].

3.4 Antiadhesive properties

Besides antimicrobial strategies with a limited number of microbe-killing agents, antiadhesive, anti-fouling, and/or microbe-repellent surfaces are a long-term antimicrobial approach. To this end, it was exemplarily demonstrated that implants and catheters coated with the recombinant spider silk protein eADF4(C16) show significantly reduced adhesion and proliferation of mammalian cells compared to untreated ones [163,201,202]. When transplanted into rats in vivo, eADF4(C16)-coated medical grade silicone implants showed a significant reduction in periprosthetic fibrous capsule formation. Furthermore, the recombinant spider silk protein coatings acted as a bioshield, improved the biocompatibility and significantly decreased the foreign body response to the implant [201,202]. Additionally, it was shown that coatings made of eADF4(C16) silk protein on silicone surfaces could also enhance microbe-repellent properties against four opportunistic infection-related strains, leading to reduced microbial adherence up to 99.7% in comparison to uncoated silicone surfaces [203]. Zhang et al. reported a different repellent effect, due to triboelectric charging of a film made from recombinant spider silk proteins based on a MaSp1 sequence [204]. A potential difference between the positively charged surface and the bacteria was generated by their self-powered triboelectric nanogenerator, which builds up electrical charges of up to 135 V. An extracellular transmission of electrons impairs the bacterial morphology and leads to death of the bacteria by inducing a burst of reactive oxygen species inside the bacterial cytoplasm [204].

Spider silk proteins have also been analysed as far as thrombosis and blood coagulation is concerned. Weiss et al. analysed the effect of surface net charge of several recombinant spider silk variants on the formation of the biomolecular corona in contact with whole blood [205]. The study could show that negatively charged or almost neutral spider silk material surfaces prevented blood clotting, while the positively charged ones interacted predominantly with fibrinogen-based proteins, correlating with increased blood clotting [205]. In another study, silk proteins were functionalized with heparin to prevent thrombosis, reporting an intrinsic ability of the recombinant spider silk proteins to prevent blood clotting [179]. Recently, a heparin-binding and antimicrobial mimicking peptide based on the consensus heparin binding amino acid motif (HBM) was genetically linked to a recombinant MaSp2-based spider silk protein [206]. The fusion protein displayed heparin binding and anticoagulant properties, as well as an intrinsic property to inhibit bacterial growth due to the antimicrobial properties [206].

Finally, a systematic study of different variants of engineered *Araneus diadematus* spidroins ADF3 and ADF4 aimed to demonstrate that the intrinsic microbe-repellence of eADF4(C16) spider silk can be altered by a single amino acid exchange in the repetitive unit. The change of negatively charged glutamate in eADF4(C16) to uncharged glutamine in eADF4(Ω16) resulted in nano-structural changes in films and hydrogels, which in turn resulted in the attachment of some microbes [145,146]. It was concluded that size and distribution of crystalline patches within the silk surface structure are crucial to create anti-fouling, microbe-repellent surfaces, in line with the argumentation that antifouling effects of spider silk surfaces are due to nanostructural features of silk [145,146,207]. Simultaneously, bioselectivity of the silk protein material was achieved by introducing the cell adhesion motif RGD to eADF4(C16), resulting in selective mammalian cell adhesion [145,146]. Figure 5 shows a summary of this recombinant spider silk protein approach for bioselective, microbe-repellent surface effects in comparison to silk fibroin.

Conclusion

Combining microbial repellence with bioselective cell binding is a crucial step towards multifunctional and specific biomaterial applications. A controllable protein-based platform could provide a long-term sustainable and environmentally friendly (in patients and globally) material for this approach. Thus, there is great interest in developing advanced green materials that inhibit microbial adhesion to surfaces while simultaneously promoting selective mammalian cell growth. Arthropod silk materials, and, in particular, spider silk and their recombinant protein mimics, have been demonstrated to be ideally suited candidates to this end. Established recombinant spidroins provide defined protein composition and structure–function relationships, as well as the possibility to incorporate modifications for tailored functionality. Furthermore, such spidroins could be processed into several material forms and are inherently biocompatible and non-toxic. Thus, engineered spider silks provide a huge potential for future biomaterial applications due to the large variety of possible modifications, for instance, the integration of various cell binding motifs or AMPs. These important properties demonstrate the great ability of spider silk-based materials for the usage as bioselective, microbe-resistant coatings for technical as well as biomedical applications and tissue engineering.

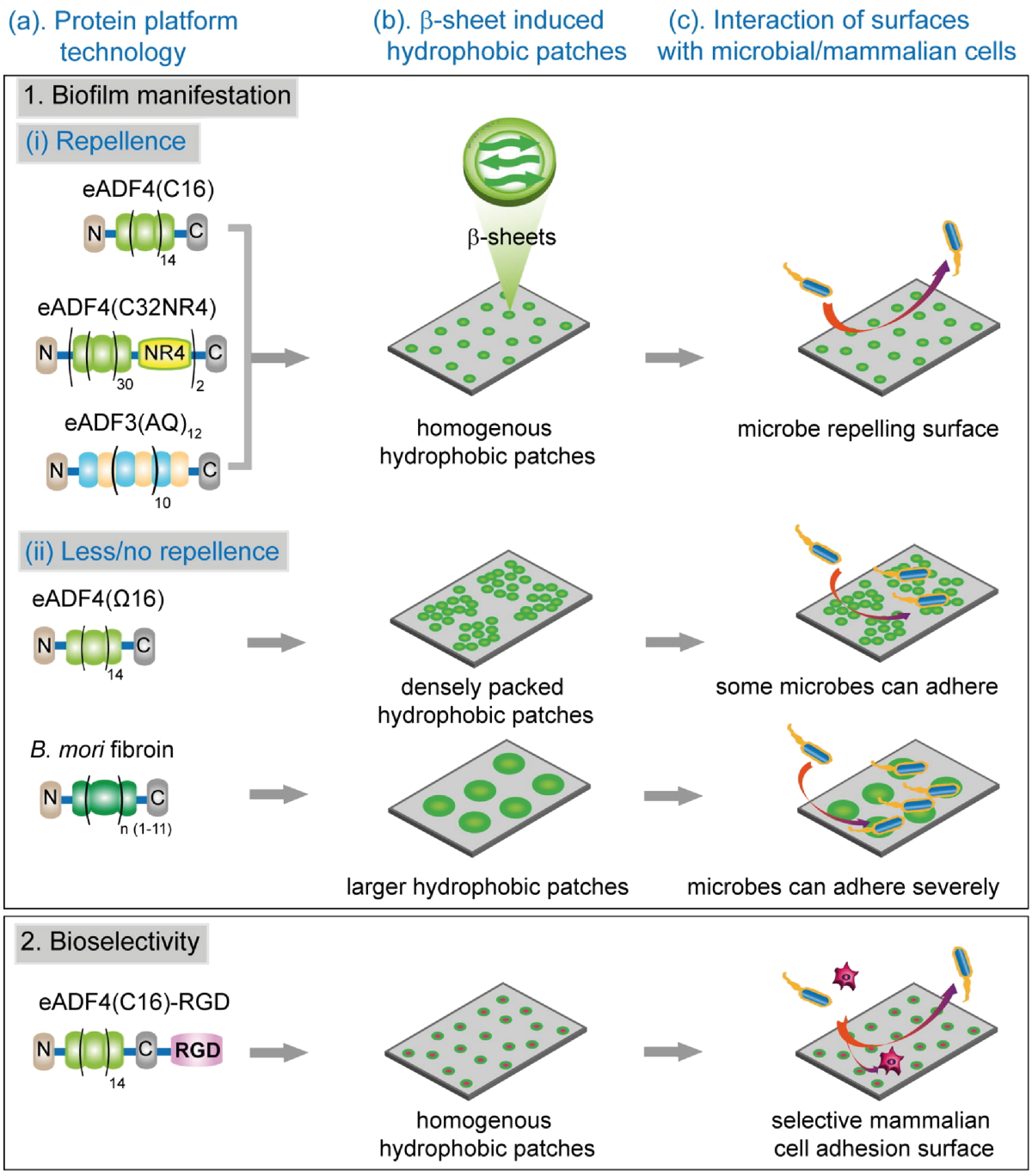


Figure 5: Engineered spider silk proteins for controlled microbial repellence and bioselective cell attachment. Compared to natural silk fibroin from *Bombyx mori*, the recombinant spider silk protein eADF4(C16) shows microbe-repellent behaviour and could be genetically modified (eADF4(C16)-RGD) to selectively allow for the attachment of mammalian cells to generate a multifunctional surface for biomedical applications. Figure 5 was reproduced from reference [146], (© 2020 Kumari et al., published by Elsevier B. V., distributed under the terms of the Creative Commons Attribution-Non-Commercial-NoDerivatives 4.0 International Licence, https://creativecommons.org/licenses/by-nc-nd/4.0/). This content is not subject to CC BY 4.0.

Funding

The authors would like to thank the EU, EFRE-project "Ziel ETZ 2014-2020" grant number 331, and the Federal Ministry of Education and Research (BMBF), project "Silk Repell", grant number 13XP5178A for financial support. Furthermore, the authors thank Nicholas Chan for proofreading the manuscript.

ORCID® iDs

Thomas Scheibel - https://orcid.org/0000-0002-0457-2423

References

1. Fazleabas, A. T.; Kim, J. J. *Science* **2003,** *299,* 355–356. doi:10.1126/science.1081277
2. Keckes, J.; Burgert, I.; Frühmann, K.; Müller, M.; Kölln, K.; Hamilton, M.; Burghammer, M.; Roth, S. V.; Stanzl-Tschegg, S.; Fratzl, P. *Nat. Mater.* **2003,** *2,* 810–813. doi:10.1038/nmat1019
3. Melzer, B.; Steinbrecher, T.; Seidel, R.; Kraft, O.; Schwaiger, R.; Speck, T. *J. R. Soc., Interface* **2010,** *7,* 1383–1389. doi:10.1098/rsif.2010.0140
4. Hofman, A. H.; van Hees, I. A.; Yang, J.; Kamperman, M. *Adv. Mater. (Weinheim, Ger.)* **2018,** *30,* 1704640. doi:10.1002/adma.201704640
5. Gorb, S. N. *Philos. Trans. R. Soc., A* **2008,** *366,* 1557–1574. doi:10.1098/rsta.2007.2172
6. Grunwald, I.; Rischka, K.; Kast, S. M.; Scheibel, T.; Bargel, H. *Philos. Trans. R. Soc., A* **2009,** *367,* 1727–1747. doi:10.1098/rsta.2009.0012
7. Smith, A. M. *Biological Adhesion,* 2nd ed.; Springer: Cham, Switzerland, 2016; p 378.
8. Rozario, T.; DeSimone, D. W. *Dev. Biol. (Amsterdam, Neth.)* **2010,** *341,* 126–140. doi:10.1016/j.ydbio.2009.10.026
9. Petruzzelli, L.; Takami, M.; Humes, H. D. *Am. J. Med.* **1999,** *106,* 467–476. doi:10.1016/s0002-9343(99)00058-3
10. Harjunpää, H.; Llort Asens, M.; Guenther, C.; Fagerholm, S. C. *Front. Immunol.* **2019,** *10,* 1078. doi:10.3389/fimmu.2019.01078
11. Sperandio, M. *FEBS J.* **2006,** *273,* 4377–4389. doi:10.1111/j.1742-4658.2006.05437.x
12. Samanta, D.; Almo, S. C. *Cell. Mol. Life Sci.* **2015,** *72,* 645–658. doi:10.1007/s00018-014-1763-4
13. Aplin, A.; Howe, A.; Alahari, S.; Juliano, R. *Pharmacol. Rev.* **1998,** *50,* 197–263.
14. Patel, S. D.; Chen, C. P.; Bahna, F.; Honig, B.; Shapiro, L. *Curr. Opin. Struct. Biol.* **2003,** *13,* 690–698. doi:10.1016/j.sbi.2003.10.007
15. Yap, A. S.; Brieher, W. M.; Gumbiner, B. M. *Annu. Rev. Cell Dev. Biol.* **1997,** *13,* 119–146. doi:10.1146/annurev.cellbio.13.1.119
16. Wai Wong, C.; Dye, D. E.; Coombe, D. R. *Int. J. Cell Biol.* **2012,** 340296. doi:10.1155/2012/340296
17. Cayrol, R.; Wosik, K.; Berard, J. L.; Dodelet-Devillers, A.; Ifergan, I.; Kebir, H.; Haqqani, A. S.; Kreymborg, K.; Krug, S.; Moumdjian, R.; Bouthillier, A.; Becher, B.; Arbour, N.; David, S.; Stanimirovic, D.; Prat, A. *Nat. Immunol.* **2008,** *9,* 137–145. doi:10.1038/ni1551
18. Kappelmayer, J.; Nagy, B. *BioMed Res. Int.* **2017,** 6138145. doi:10.1155/2017/6138145
19. Zhao, J.; Santino, F.; Giacomini, D.; Gentilucci, L. *Biomedicines* **2020,** *8,* 307. doi:10.3390/biomedicines8090307
20. Hynes, R. O. *Science* **2009,** *326,* 1216–1219. doi:10.1126/science.1176009
21. Berrier, A. L.; Yamada, K. M. *J. Cell. Physiol.* **2007,** *213,* 565–573. doi:10.1002/jcp.21237
22. Legate, K. R.; Wickström, S. A.; Fässler, R. *Genes Dev.* **2009,** *23,* 397–418. doi:10.1101/gad.1758709
23. Han, W. M.; Jang, Y. C.; García, A. J. The Extracellular Matrix and Cell–Biomaterial Interactions. In *Biomaterials Science,* 4th ed.; Wagner, W. R.; Sakiyama-Elbert, S. E.; Zhang, G.; Yaszemski, M. J., Eds.; Academic Press, 2020; pp 701–715. doi:10.1016/b978-0-12-816137-1.00045-3
24. Pankov, R.; Yamada, K. M. *J. Cell Sci.* **2002,** *115,* 3861–3863. doi:10.1242/jcs.00059
25. De Marco, R.; Greco, A.; Calonghi, N.; Dattoli, S. D.; Baiula, M.; Spampinato, S.; Picchetti, P.; De Cola, L.; Anselmi, M.; Cipriani, F.; Gentilucci, L. *Pept. Sci.* **2018,** *110,* e23081. doi:10.1002/bip.23081
26. Zhang, J.; Jiang, X.; Wen, X.; Xu, Q.; Zeng, H.; Zhao, Y.; Liu, M.; Wang, Z.; Hu, X.; Wang, Y. *JPhys Mater.* **2019,** *2,* 032004. doi:10.1088/2515-7639/ab1af5
27. Mano, J. F. *Adv. Eng. Mater.* **2008,** *10,* 515–527. doi:10.1002/adem.200700355
28. Gagner, J. E.; Kim, W.; Chaikof, E. L. *Acta Biomater.* **2014,** *10,* 1542–1557. doi:10.1016/j.actbio.2013.10.001
29. Choi, S. M.; Chaudhry, P.; Zo, S. M.; Han, S. S. Advances in Protein-Based Materials: From Origin to Novel Biomaterials. In *Cutting-Edge Enabling Technologies for Regenerative Medicine;* Chun, H. J.; Park, C. H.; Kwon, I. K.; Khang, G., Eds.; Springer: Singapore, 2018; pp 161–210. doi:10.1007/978-981-13-0950-2_10
30. Annabi, N.; Mithieux, S. M.; Camci-Unal, G.; Dokmeci, M. R.; Weiss, A. S.; Khademhosseini, A. *Biochem. Eng. J.* **2013,** *77,* 110–118. doi:10.1016/j.bej.2013.05.006
31. Shin, H.; Jo, S.; Mikos, A. G. *Biomaterials* **2003,** *24,* 4353–4364. doi:10.1016/s0142-9612(03)00339-9
32. Spiller, S.; Clauder, F.; Bellmann-Sickert, K.; Beck-Sickinger, A. G. *Biol. Chem.* **2021,** *402,* 1271–1288. doi:10.1515/hsz-2021-0144
33. Hosoyama, K.; Lazurko, C.; Muñoz, M.; McTiernan, C. D.; Alarcon, E. I. *Front. Bioeng. Biotechnol.* **2019,** *7,* 205. doi:10.3389/fbioe.2019.00205
34. Huettner, N.; Dargaville, T. R.; Forget, A. *Trends Biotechnol.* **2018,** *36,* 372–383. doi:10.1016/j.tibtech.2018.01.008
35. Yamada, K. M. *J. Biol. Chem.* **1991,** *266,* 12809–12812. doi:10.1016/s0021-9258(18)98761-2
36. Pountos, I.; Panteli, M.; Lampropoulos, A.; Jones, E.; Calori, G. M.; Giannoudis, P. V. *BMC Med.* **2016,** *14,* 103. doi:10.1186/s12916-016-0646-y
37. Ruoslahti, E.; Pierschbacher, M. D. *Cell* **1986,** *44,* 517–518. doi:10.1016/0092-8674(86)90259-x
38. Pierschbacher, M. D.; Hayman, E. G.; Ruoslahti, E. *J. Cell. Biochem.* **1985,** *28,* 115–126. doi:10.1002/jcb.240280205
39. Hersel, U.; Dahmen, C.; Kessler, H. *Biomaterials* **2003,** *24,* 4385–4415. doi:10.1016/s0142-9612(03)00343-0
40. Pierschbacher, M. D.; Ruoslahti, E. *Nature* **1984,** *309,* 30–33. doi:10.1038/309030a0
41. Ruoslahti, E. *Annu. Rev. Cell Dev. Biol.* **1996,** *12,* 697–715. doi:10.1146/annurev.cellbio.12.1.697
42. Bellis, S. L. *Biomaterials* **2011,** *32,* 4205–4210. doi:10.1016/j.biomaterials.2011.02.029
43. Pfaff, M. Recognition Sites of RGD-Dependent Integrins. *Integrin-Ligand Interaction;* Springer: Boston, MA, USA, 1997; pp 101–121. doi:10.1007/978-1-4757-4064-6_4
44. Mertgen, A.-S.; Trossmann, V. T.; Guex, A. G.; Maniura-Weber, K.; Scheibel, T.; Rottmar, M. *ACS Appl. Mater. Interfaces* **2020,** *12,* 21342–21367. doi:10.1021/acsami.0c01893

45. Rechenmacher, F.; Neubauer, S.; Mas-Moruno, C.; Dorfner, P. M.; Polleux, J.; Guasch, J.; Conings, B.; Boyen, H.-G.; Bochen, A.; Sobahi, T. R.; Burgkart, R.; Spatz, J. P.; Fässler, R.; Kessler, H. *Chem. – Eur. J.* **2013,** *19,* 9218–9223. doi:10.1002/chem.201301478
46. Grant, D. S.; Tashiro, K.-I.; Segui-Real, B.; Yamada, Y.; Martin, G. R.; Kleinman, H. K. *Cell* **1989,** *58,* 933–943. doi:10.1016/0092-8674(89)90945-8
47. Graf, J.; Iwamoto, Y.; Sasaki, M.; Martin, G. R.; Kleinman, H. K.; Robey, F. A.; Yamada, Y. *Cell* **1987,** *48,* 989–996. doi:10.1016/0092-8674(87)90707-0
48. Graf, J.; Ogle, R. C.; Robey, F. A.; Sasaki, M.; Martin, G. R.; Yamada, Y.; Kleinman, H. K. *Biochemistry* **1987,** *26,* 6896–6900. doi:10.1021/bi00396a004
49. Sullivan, T.; O'Callaghan, I. *Biomimetics* **2020,** *5,* 58. doi:10.3390/biomimetics5040058
50. Sonnleitner, D.; Sommer, C.; Scheibel, T.; Lang, G. *Mater. Sci. Eng., C* **2021,** *131,* 112458. doi:10.1016/j.msec.2021.112458
51. Ivanova, E. P.; Hasan, J.; Webb, H. K.; Truong, V. K.; Watson, G. S.; Watson, J. A.; Baulin, V. A.; Pogodin, S.; Wang, J. Y.; Tobin, M. J.; Löbbe, C.; Crawford, R. J. *Small* **2012,** *8,* 2489–2494. doi:10.1002/smll.201200528
52. May, R. M.; Magin, C. M.; Mann, E. E.; Drinker, M. C.; Fraser, J. C.; Siedlecki, C. A.; Brennan, A. B.; Reddy, S. T. *Clin. Transl. Med.* **2015,** *4,* 9. doi:10.1186/s40169-015-0050-9
53. Barthlott, W.; Mail, M.; Bhushan, B.; Koch, K. *Nano-Micro Lett.* **2017,** *9,* 23. doi:10.1007/s40820-016-0125-1
54. Watson, G. S.; Green, D. W.; Cribb, B. W.; Brown, C. L.; Meritt, C. R.; Tobin, M. J.; Vongsvivut, J.; Sun, M.; Liang, A.-P.; Watson, J. A. *ACS Appl. Mater. Interfaces* **2017,** *9,* 24381–24392. doi:10.1021/acsami.7b08368
55. Barthlott, W.; Neinhuis, C. *Planta* **1997,** *202,* 1–8. doi:10.1007/s004250050096
56. Barthlott, W.; Schimmel, T.; Wiersch, S.; Koch, K.; Brede, M.; Barczewski, M.; Walheim, S.; Weis, A.; Kaltenmaier, A.; Leder, A.; Bohn, H. F. *Adv. Mater. (Weinheim, Ger.)* **2010,** *22,* 2325–2328. doi:10.1002/adma.200904411
57. Tripathy, A.; Sen, P.; Su, B.; Briscoe, W. H. *Adv. Colloid Interface Sci.* **2017,** *248,* 85–104. doi:10.1016/j.cis.2017.07.030
58. Liu, Q.; Brookbank, L.; Ho, A.; Coffey, J.; Brennan, A. B.; Jones, C. J. *PLoS One* **2020,** *15,* e0244518. doi:10.1371/journal.pone.0244518
59. Koc, Y.; de Mello, A. J.; McHale, G.; Newton, M. I.; Roach, P.; Shirtcliffe, N. J. *Lab Chip* **2008,** *8,* 582–586. doi:10.1039/b716509a
60. Pernites, R. B.; Santos, C. M.; Maldonado, M.; Ponnapati, R. R.; Rodrigues, D. F.; Advincula, R. C. *Chem. Mater.* **2012,** *24,* 870–880. doi:10.1021/cm2007044
61. Stallard, C. P.; McDonnell, K. A.; Onayemi, O. D.; O'Gara, J. P.; Dowling, D. P. *Biointerphases* **2012,** *7,* 31. doi:10.1007/s13758-012-0031-0
62. Zhu, H.; Guo, Z.; Liu, W. *Chem. Commun.* **2014,** *50,* 3900–3913. doi:10.1039/c3cc47818a
63. Privett, B. J.; Youn, J.; Hong, S. A.; Lee, J.; Han, J.; Shin, J. H.; Schoenfisch, M. H. *Langmuir* **2011,** *27,* 9597–9601. doi:10.1021/la201801e
64. Crick, C. R.; Ismail, S.; Pratten, J.; Parkin, I. P. *Thin Solid Films* **2011,** *519,* 3722–3727. doi:10.1016/j.tsf.2011.01.282
65. Hizal, F.; Rungraeng, N.; Lee, J.; Jun, S.; Busscher, H. J.; van der Mei, H. C.; Choi, C.-H. *ACS Appl. Mater. Interfaces* **2017,** *9,* 12118–12129. doi:10.1021/acsami.7b01322
66. Cai, S.; Wu, C.; Yang, W.; Liang, W.; Yu, H.; Liu, L. *Nanotechnol. Rev.* **2020,** *9,* 971–989. doi:10.1515/ntrev-2020-0076
67. Jeon, S. I.; Lee, J. H.; Andrade, J. D.; De Gennes, P. G. *J. Colloid Interface Sci.* **1991,** *142,* 149–158. doi:10.1016/0021-9797(91)90043-8
68. Ista, L. K.; Mendez, S.; Lopez, G. P. *Biofouling* **2010,** *26,* 111–118. doi:10.1080/08927010903383455
69. Bosker, W. T. E.; Patzsch, K.; Stuart, M. A. C.; Norde, W. *Soft Matter* **2007,** *3,* 754–762. doi:10.1039/b618259c
70. Haldar, J.; An, D.; Álvarez de Cienfuegos, L.; Chen, J.; Klibanov, A. M. *Proc. Natl. Acad. Sci. U. S. A.* **2006,** *103,* 17667–17671. doi:10.1073/pnas.0608803103
71. Wong, S. Y.; Li, Q.; Veselinovic, J.; Kim, B.-S.; Klibanov, A. M.; Hammond, P. T. *Biomaterials* **2010,** *31,* 4079–4087. doi:10.1016/j.biomaterials.2010.01.119
72. Buzzacchera, I.; Vorobii, M.; Kostina, N. Y.; de los Santos Pereira, A.; Riedel, T.; Bruns, M.; Ogieglo, W.; Möller, M.; Wilson, C. J.; Rodriguez-Emmenegger, C. *Biomacromolecules* **2017,** *18,* 1983–1992. doi:10.1021/acs.biomac.7b00516
73. Kovacs, B.; Patko, D.; Klein, A.; Kakasi, B.; Saftics, A.; Kurunczi, S.; Vonderviszt, F.; Horvath, R. *Sens. Actuators, B* **2018,** *257,* 839–845. doi:10.1016/j.snb.2017.11.027
74. Liu, X.; Peng, L.; Meng, J.; Zhu, Z.; Han, B.; Wang, S. *Nanoscale* **2018,** *10,* 2711–2714. doi:10.1039/c7nr08844b
75. Wang, L.-S.; Gopalakrishnan, S.; Lee, Y.-W.; Zhu, J.; Nonnenmann, S. S.; Rotello, V. M. *Mater. Horiz.* **2018,** *5,* 268–274. doi:10.1039/c7mh00933j
76. Bullitt, E.; Makowski, L. *Nature* **1995,** *373,* 164–167. doi:10.1038/373164a0
77. Garrett, T. R.; Bhakoo, M.; Zhang, Z. *Prog. Nat. Sci.* **2008,** *18,* 1049–1056. doi:10.1016/j.pnsc.2008.04.001
78. Asadi, A.; Razavi, S.; Talebi, M.; Gholami, M. *Infection (Munich, Ger.)* **2019,** *47,* 13–23. doi:10.1007/s15010-018-1222-5
79. Piatek, R.; Zalewska-Piatek, B.; Dzierzbicka, K.; Makowiec, S.; Pilipczuk, J.; Szemiako, K.; Cyranka-Czaja, A.; Wojciechowski, M. *BMC Microbiol.* **2013,** *13,* 131. doi:10.1186/1471-2180-13-131
80. Pinkner, J. S.; Remaut, H.; Buelens, F.; Miller, E.; Åberg, V.; Pemberton, N.; Hedenström, M.; Larsson, A.; Seed, P.; Waksman, G.; Hultgren, S. J.; Almqvist, F. *Proc. Natl. Acad. Sci. U. S. A.* **2006,** *103,* 17897–17902. doi:10.1073/pnas.0606795103
81. Eidam, O.; Dworkowski, F. S. N.; Glockshuber, R.; Grütter, M. G.; Capitani, G. *FEBS Lett.* **2008,** *582,* 651–655. doi:10.1016/j.febslet.2008.01.030
82. Soto, G. E.; Hultgren, S. J. *J. Bacteriol.* **1999,** *181,* 1059–1071. doi:10.1128/jb.181.4.1059-1071.1999
83. Krachler, A. M.; Ham, H.; Orth, K. *Proc. Natl. Acad. Sci. U. S. A.* **2011,** *108,* 11614–11619. doi:10.1073/pnas.1102360108
84. Krachler, A. M.; Mende, K.; Murray, C.; Orth, K. *Virulence* **2012,** *3,* 389–399. doi:10.4161/viru.20816
85. Etayash, H.; Hancock, R. E. W. *Pharmaceutics* **2021,** *13,* 1820. doi:10.3390/pharmaceutics13111820
86. Zasloff, M. *Nature* **2002,** *415,* 389–395. doi:10.1038/415389a
87. Dürr, U. H. N.; Sudheendra, U. S.; Ramamoorthy, A. *Biochim. Biophys. Acta, Biomembr.* **2006,** *1758,* 1408–1425. doi:10.1016/j.bbamem.2006.03.030
88. Lai, Y.; Gallo, R. L. *Trends Immunol.* **2009,** *30,* 131–141. doi:10.1016/j.it.2008.12.003
89. Hancock, R. E. W.; Sahl, H.-G. *Nat. Biotechnol.* **2006,** *24,* 1551–1557. doi:10.1038/nbt1267

90. Lau, Y. E.; Rozek, A.; Scott, M. G.; Goosney, D. L.; Davidson, D. J.; Hancock, R. E. W. *Infect. Immun.* **2005,** *73,* 583–591. doi:10.1128/iai.73.1.583-591.2005
91. Duplantier, A. J.; van Hoek, M. L. *Front. Immunol.* **2013,** *4,* 143. doi:10.3389/fimmu.2013.00143
92. Wimley, W. C.; Hristova, K. *J. Membr. Biol.* **2011,** *239,* 27–34. doi:10.1007/s00232-011-9343-0
93. Wang, G.; Li, X.; Wang, Z. *Nucleic Acids Res.* **2016,** *44,* D1087–D1093. doi:10.1093/nar/gkv1278
94. Overhage, J.; Campisano, A.; Bains, M.; Torfs, E. C. W.; Rehm, B. H. A.; Hancock, R. E. W. *Infect. Immun.* **2008,** *76,* 4176–4182. doi:10.1128/iai.00318-08
95. de la Fuente-Núñez, C.; Korolik, V.; Bains, M.; Nguyen, U.; Breidenstein, E. B. M.; Horsman, S.; Lewenza, S.; Burrows, L.; Hancock, R. E. W. *Antimicrob. Agents Chemother.* **2012,** *56,* 2696–2704. doi:10.1128/aac.00064-12
96. Lee, J.-K.; Park, Y. *Int. J. Mol. Sci.* **2020,** *21,* 5632. doi:10.3390/ijms21165632
97. Godballe, T.; Nilsson, L. L.; Petersen, P. D.; Jenssen, H. *Chem. Biol. Drug Des.* **2011,** *77,* 107–116. doi:10.1111/j.1747-0285.2010.01067.x
98. Bicker, K. L.; Cobb, S. L. *Chem. Commun.* **2020,** *56,* 11158–11168. doi:10.1039/d0cc04704j
99. Beckloff, N.; Laube, D.; Castro, T.; Furgang, D.; Park, S.; Perlin, D.; Clements, D.; Tang, H.; Scott, R. W.; Tew, G. N.; Diamond, G. *Antimicrob. Agents Chemother.* **2007,** *51,* 4125–4132. doi:10.1128/aac.00208-07
100. Tagliabue, A.; Rappuoli, R. *Front. Immunol.* **2018,** *9,* 1068. doi:10.3389/fimmu.2018.01068
101. Bloom, D. E.; Cadarette, D. *Front. Immunol.* **2019,** *10,* 549. doi:10.3389/fimmu.2019.00549
102. He, T.; Shi, Z. L.; Fang, N.; Neoh, K. G.; Kang, E. T.; Chan, V. *Biomaterials* **2009,** *30,* 317–326. doi:10.1016/j.biomaterials.2008.09.049
103. He, T.; Zhang, Y.; Lai, A. C. K.; Chan, V. *Biomed. Mater.* **2015,** *10,* 015015. doi:10.1088/1748-6041/10/1/015015
104. Altman, G. H.; Diaz, F.; Jakuba, C.; Calabro, T.; Horan, R. L.; Chen, J.; Lu, H.; Richmond, J.; Kaplan, D. L. *Biomaterials* **2003,** *24,* 401–416. doi:10.1016/s0142-9612(02)00353-8
105. Salehi, S.; Koeck, K.; Scheibel, T. *Molecules* **2020,** *25,* 737. doi:10.3390/molecules25030737
106. Aigner, T. B.; DeSimone, E.; Scheibel, T. *Adv. Mater. (Weinheim, Ger.)* **2018,** *30,* 1704636. doi:10.1002/adma.201704636
107. Kiseleva, A. P.; Krivoshapkin, P. V.; Krivoshapkina, E. F. *Front. Chem. (Lausanne, Switz.)* **2020,** *8,* 554. doi:10.3389/fchem.2020.00554
108. Scheibel, T.; Zahn, H.; Krasowski, A. Silk. *Ullmann's Encyclopedia of Industrial Chemistry;* John Wiley & Sons, 2016; pp 1–15. doi:10.1002/14356007.a24_095.pub2
109. Herold, H. M.; Scheibel, T. *Z. Naturforsch., C: J. Biosci.* **2017,** *72,* 365–385. doi:10.1515/znc-2017-0050
110. Sehnal, F.; Sutherland, T. *Prion* **2008,** *2,* 145–153. doi:10.4161/pri.2.4.7489
111. Garb, J. E.; Ayoub, N. A.; Hayashi, C. Y. *BMC Evol. Biol.* **2010,** *10,* 243. doi:10.1186/1471-2148-10-243
112. Sutherland, T. D.; Young, J. H.; Weisman, S.; Hayashi, C. Y.; Merritt, D. J. *Annu. Rev. Entomol.* **2010,** *55,* 171–188. doi:10.1146/annurev-ento-112408-085401
113. Andersson, M.; Johansson, J.; Rising, A. *Int. J. Mol. Sci.* **2016,** *17,* 1290. doi:10.3390/ijms17081290
114. Saric, M.; Scheibel, T. *Curr. Opin. Biotechnol.* **2019,** *60,* 213–220. doi:10.1016/j.copbio.2019.05.005
115. Inoue, S.; Tanaka, K.; Arisaka, F.; Kimura, S.; Ohtomo, K.; Mizuno, S. *J. Biol. Chem.* **2000,** *275,* 40517–40528. doi:10.1074/jbc.m006897200
116. Sehadova, H.; Zavodska, R.; Rouhova, L.; Zurovec, M.; Sauman, I. *Int. J. Mol. Sci.* **2021,** *22,* 13523. doi:10.3390/ijms222413523
117. Kucerova, L.; Zurovec, M.; Kludkiewicz, B.; Hradilova, M.; Strnad, H.; Sehnal, F. *Sci. Rep.* **2019,** *9,* 3797. doi:10.1038/s41598-019-40401-3
118. Eisoldt, L.; Smith, A.; Scheibel, T. *Mater. Today* **2011,** *14,* 80–86. doi:10.1016/s1369-7021(11)70057-8
119. Eisoldt, L.; Thamm, C.; Scheibel, T. *Biopolymers* **2012,** *97,* 355–361. doi:10.1002/bip.22006
120. Bittencourt, D.; Oliveira, P. F.; Prosdocimi, F.; Rech, E. L. *Genet. Mol. Res.* **2012,** *11,* 2360–2380. doi:10.4238/2012.august.13.10
121. Thamm, C.; Scheibel, T. *Biomacromolecules* **2017,** *18,* 1365–1372. doi:10.1021/acs.biomac.7b00090
122. Collin, M. A.; Clarke, T. H., III; Ayoub, N. A.; Hayashi, C. Y. *Int. J. Biol. Macromol.* **2018,** *113,* 829–840. doi:10.1016/j.ijbiomac.2018.02.032
123. Altman, G. H.; Horan, R. L.; Lu, H. H.; Moreau, J.; Martin, I.; Richmond, J. C.; Kaplan, D. L. *Biomaterials* **2002,** *23,* 4131–4141. doi:10.1016/s0142-9612(02)00156-4
124. Ribeiro, M.; de Moraes, M. A.; Beppu, M. M.; Garcia, M. P.; Fernandes, M. H.; Monteiro, F. J.; Ferraz, M. P. *Eur. Polym. J.* **2015,** *67,* 66–77. doi:10.1016/j.eurpolymj.2015.03.056
125. Kuhbier, J. W.; Allmeling, C.; Reimers, K.; Hillmer, A.; Kasper, C.; Menger, B.; Brandes, G.; Guggenheim, M.; Vogt, P. M. *PLoS One* **2010,** *5,* e12032. doi:10.1371/journal.pone.0012032
126. Wendt, H.; Hillmer, A.; Reimers, K.; Kuhbier, J. W.; Schäfer-Nolte, F.; Allmeling, C.; Kasper, C.; Vogt, P. M. *PLoS One* **2011,** *6,* e21833. doi:10.1371/journal.pone.0021833
127. Yang, M.; Shuai, Y.; Zhou, G.; Mandal, N.; Zhu, L.; Mao, C. *ACS Appl. Mater. Interfaces* **2014,** *6,* 13782–13789. doi:10.1021/am503214g
128. Pedregal-Cortés, R.; Toriz, G.; Delgado, E.; Pollack, G. H. *Biofouling* **2019,** *35,* 732–741. doi:10.1080/08927014.2019.1653863
129. Chigama, H.; Yokoi, T.; Furuya, M.; Yokota, K.; Kanetaka, H.; Kawashita, M. *J. Mater. Sci.: Mater. Med.* **2020,** *31,* 49. doi:10.1007/s10856-020-06388-4
130. Amaley, A.; Gawali, A. A.; Akarte, S. R. *Indian J. Arachnol.* **2014,** *3,* 8–11.
131. Wright, S.; Goodacre, S. L. *BMC Res. Notes* **2012,** *5,* 326. doi:10.1186/1756-0500-5-326
132. Tahir, H. M.; Zaheer, A.; Rasheed, A.; Mukhtar, M. K.; Yaqoob, R.; Liaqat, I.; Ahsan, M. M. *Acta Zool. Bulg.* **2018,** *70,* 593–598.
133. Tahir, M.; Sattar, A.; Qamar, S.; Mukhtar, M.; Liaqat, I.; Ali, M.; Zaheer, A.; Arshad, N.; Yaqoob, R.; Naseem, S. *J. Anim. Plant Sci.* **2019,** *29,* 625–628.
134. Carl, N. K.; Alexander, E. D.; Taylor, A. S.; Jessica, A. R.; Jonathan, N. P. *J. Arachnol.* **2015,** *43,* 394–399.
135. Makover, V.; Ronen, Z.; Lubin, Y.; Khalaila, I. *J. R. Soc., Interface* **2019,** *16,* 20180581. doi:10.1098/rsif.2018.0581
136. Zhang, S.; Piorkowski, D.; Lin, W.-R.; Lee, Y.-R.; Liao, C.-P.; Wang, P.-H.; Tso, I.-M. *J. Exp. Biol.* **2019,** *222,* jeb214981. doi:10.1242/jeb.214981
137. Kaur, J.; Rajkhowa, R.; Afrin, T.; Tsuzuki, T.; Wang, X. *Biopolymers* **2014,** *101,* 237–245. doi:10.1002/bip.22323

138. Fruergaard, S.; Lund, M. B.; Schramm, A.; Vosegaard, T.; Bilde, T. *iScience* **2021,** *24,* 103125. doi:10.1016/j.isci.2021.103125
139. Whittall, D. R.; Baker, K. V.; Breitling, R.; Takano, E. *Trends Biotechnol.* **2021,** *39,* 560–573. doi:10.1016/j.tibtech.2020.09.007
140. Heidebrecht, A.; Scheibel, T. *Adv. Appl. Microbiol.* **2013,** *82,* 115–153. doi:10.1016/b978-0-12-407679-2.00004-1
141. Hedhammar, M.; Rising, A.; Grip, S.; Martinez, A. S.; Nordling, K.; Casals, C.; Stark, M.; Johansson, J. *Biochemistry* **2008,** *47,* 3407–3417. doi:10.1021/bi702432y
142. Stark, M.; Grip, S.; Rising, A.; Hedhammar, M.; Engström, W.; Hjälm, G.; Johansson, J. *Biomacromolecules* **2007,** *8,* 1695–1701. doi:10.1021/bm070049y
143. Huemmerich, D.; Helsen, C. W.; Quedzuweit, S.; Oschmann, J.; Rudolph, R.; Scheibel, T. *Biochemistry* **2004,** *43,* 13604–13612. doi:10.1021/bi048983q
144. Doblhofer, E.; Scheibel, T. *J. Pharm. Sci.* **2015,** *104,* 988–994. doi:10.1002/jps.24300
145. Kumari, S.; Lang, G.; DeSimone, E.; Spengler, C.; Trossmann, V. T.; Lücker, S.; Hudel, M.; Jacobs, K.; Krämer, N.; Scheibel, T. *Data Brief* **2020,** *32,* 106305. doi:10.1016/j.dib.2020.106305
146. Kumari, S.; Lang, G.; DeSimone, E.; Spengler, C.; Trossmann, V. T.; Lücker, S.; Hudel, M.; Jacobs, K.; Krämer, N.; Scheibel, T. *Mater. Today* **2020,** *41,* 21–33. doi:10.1016/j.mattod.2020.06.009
147. Rabotyagova, O. S.; Cebe, P.; Kaplan, D. L. *Biomacromolecules* **2009,** *10,* 229–236. doi:10.1021/bm800930x
148. Wohlrab, S.; Müller, S.; Schmidt, A.; Neubauer, S.; Kessler, H.; Leal-Egaña, A.; Scheibel, T. *Biomaterials* **2012,** *33,* 6650–6659. doi:10.1016/j.biomaterials.2012.05.069
149. Neubauer, V. J.; Scheibel, T. *ACS Biomater. Sci. Eng.* **2020,** *6,* 5599–5608. doi:10.1021/acsbiomaterials.0c00818
150. Esser, T. U.; Trossmann, V. T.; Lentz, S.; Engel, F. B.; Scheibel, T. *Mater. Today Bio* **2021,** *11,* 100114. doi:10.1016/j.mtbio.2021.100114
151. Widhe, M.; Shalaly, N. D.; Hedhammar, M. *Biomaterials* **2016,** *74,* 256–266. doi:10.1016/j.biomaterials.2015.10.013
152. Widhe, M.; Johansson, U.; Hillerdahl, C.-O.; Hedhammar, M. *Biomaterials* **2013,** *34,* 8223–8234. doi:10.1016/j.biomaterials.2013.07.058
153. Nilebäck, L.; Hedin, J.; Widhe, M.; Floderus, L. S.; Krona, A.; Bysell, H.; Hedhammar, M. *Biomacromolecules* **2017,** *18,* 846–854. doi:10.1021/acs.biomac.6b01721
154. Johansson, U.; Ria, M.; Åvall, K.; Dekki Shalaly, N.; Zaitsev, S. V.; Berggren, P.-O.; Hedhammar, M. *PLoS One* **2015,** *10,* e0130169. doi:10.1371/journal.pone.0130169
155. Saric, M.; Eisoldt, L.; Döring, V.; Scheibel, T. *Adv. Mater. (Weinheim, Ger.)* **2021,** *33,* 2006499. doi:10.1002/adma.202006499
156. Jansson, R.; Lau, C. H.; Ishida, T.; Ramström, M.; Sandgren, M.; Hedhammar, M. *Biotechnol. J.* **2016,** *11,* 687–699. doi:10.1002/biot.201500412
157. Jansson, R.; Thatikonda, N.; Lindberg, D.; Rising, A.; Johansson, J.; Nygren, P.-Å.; Hedhammar, M. *Biomacromolecules* **2014,** *15,* 1696–1706. doi:10.1021/bm500114e
158. Humenik, M.; Mohrand, M.; Scheibel, T. *Bioconjugate Chem.* **2018,** *29,* 898–904. doi:10.1021/acs.bioconjchem.7b00759
159. Thatikonda, N.; Nilebäck, L.; Kempe, A.; Widhe, M.; Hedhammar, M. *ACS Biomater. Sci. Eng.* **2018,** *4,* 3384–3396. doi:10.1021/acsbiomaterials.8b00844
160. Thatikonda, N.; Delfani, P.; Jansson, R.; Petersson, L.; Lindberg, D.; Wingren, C.; Hedhammar, M. *Biotechnol. J.* **2016,** *11,* 437–448. doi:10.1002/biot.201500297
161. Leal-Egaña, A.; Lang, G.; Mauerer, C.; Wickinghoff, J.; Weber, M.; Geimer, S.; Scheibel, T. *Adv. Eng. Mater.* **2012,** *14,* B67–B75. doi:10.1002/adem.201180072
162. Petzold, J.; Aigner, T. B.; Touska, F.; Zimmermann, K.; Scheibel, T.; Engel, F. B. *Adv. Funct. Mater.* **2017,** *27,* 1701427. doi:10.1002/adfm.201701427
163. Borkner, C. B.; Wohlrab, S.; Möller, E.; Lang, G.; Scheibel, T. *ACS Biomater. Sci. Eng.* **2017,** *3,* 767–775. doi:10.1021/acsbiomaterials.6b00306
164. Leal-Egaña, A.; Díaz-Cuenca, A.; Boccaccini, A. R. *Adv. Mater. (Weinheim, Ger.)* **2013,** *25,* 4049–4057. doi:10.1002/adma.201301227
165. Blau, A. *Curr. Opin. Colloid Interface Sci.* **2013,** *18,* 481–492. doi:10.1016/j.cocis.2013.07.005
166. De Rosa, M.; Carteni', M.; Petillo, O.; Calarco, A.; Margarucci, S.; Rosso, F.; De Rosa, A.; Farina, E.; Grippo, P.; Peluso, G. *J. Cell. Physiol.* **2004,** *198,* 133–143. doi:10.1002/jcp.10397
167. Widhe, M.; Bysell, H.; Nystedt, S.; Schenning, I.; Malmsten, M.; Johansson, J.; Rising, A.; Hedhammar, M. *Biomaterials* **2010,** *31,* 9575–9585. doi:10.1016/j.biomaterials.2010.08.061
168. Kramer, J. P. M.; Aigner, T. B.; Petzold, J.; Roshanbinfar, K.; Scheibel, T.; Engel, F. B. *Sci. Rep.* **2020,** *10,* 8789. doi:10.1038/s41598-020-65786-4
169. Schacht, K.; Vogt, J.; Scheibel, T. *ACS Biomater. Sci. Eng.* **2016,** *2,* 517–525. doi:10.1021/acsbiomaterials.5b00483
170. Tasiopoulos, C. P.; Gustafsson, L.; van der Wijngaart, W.; Hedhammar, M. *ACS Biomater. Sci. Eng.* **2021,** *7,* 3332–3339. doi:10.1021/acsbiomaterials.1c00612
171. Schacht, K.; Scheibel, T. *Biomacromolecules* **2011,** *12,* 2488–2495. doi:10.1021/bm200154k
172. DeSimone, E.; Schacht, K.; Pellert, A.; Scheibel, T. *Biofabrication* **2017,** *9,* 044104. doi:10.1088/1758-5090/aa90db
173. Neubauer, V. J.; Trossmann, V. T.; Jacobi, S.; Döbl, A.; Scheibel, T. *Angew. Chem., Int. Ed.* **2021,** *60,* 11847–11851. doi:10.1002/anie.202103147
174. Schacht, K.; Jüngst, T.; Schweinlin, M.; Ewald, A.; Groll, J.; Scheibel, T. *Angew. Chem., Int. Ed.* **2015,** *54,* 2816–2820. doi:10.1002/anie.201409846
175. Steiner, D.; Winkler, S.; Heltmann-Meyer, S.; Trossmann, V. T.; Fey, T.; Scheibel, T.; Horch, R. E.; Arkudas, A. *Biofabrication* **2021,** *13,* 045003. doi:10.1088/1758-5090/ac0d9b
176. Shalaly, N. D.; Ria, M.; Johansson, U.; Åvall, K.; Berggren, P.-O.; Hedhammar, M. *Biomaterials* **2016,** *90,* 50–61. doi:10.1016/j.biomaterials.2016.03.006
177. Szymkowiak, P.; Tsiareshyna, M.; Koczura, R. *Biologia (Cham, Switz.)* **2020,** *75,* 1679–1683. doi:10.2478/s11756-020-00426-w
178. Alicea-Serrano, A. M.; Bender, K.; Jurestovsky, D. *J. Arachnol.* **2020,** *48,* 84–89. doi:10.1636/0161-8202-48.1.84
179. Harris, T. I.; Gaztambide, D. A.; Day, B. A.; Brock, C. L.; Ruben, A. L.; Jones, J. A.; Lewis, R. V. *Biomacromolecules* **2016,** *17,* 3761–3772. doi:10.1021/acs.biomac.6b01267
180. Gomes, S. C.; Leonor, I. B.; Mano, J. F.; Reis, R. L.; Kaplan, D. L. *Biomaterials* **2011,** *32,* 4255–4266. doi:10.1016/j.biomaterials.2011.02.040
181. Liu, F. Y. C. *bioRxiv* **2021**. doi:10.1101/2021.03.26.437269

182. Nilebäck, L.; Chouhan, D.; Jansson, R.; Widhe, M.; Mandal, B. B.; Hedhammar, M. *ACS Appl. Mater. Interfaces* **2017,** *9,* 31634–31644. doi:10.1021/acsami.7b10874
183. Chouhan, D.; Thatikonda, N.; Nilebäck, L.; Widhe, M.; Hedhammar, M.; Mandal, B. B. *ACS Appl. Mater. Interfaces* **2018,** *10,* 23560–23572. doi:10.1021/acsami.8b05853
184. Huang, T.; Kumari, S.; Herold, H.; Bargel, H.; Aigner, T. B.; Heath, D. E.; O'Brien-Simpson, N. M.; O'Connor, A. J.; Scheibel, T. *Int. J. Nanomed.* **2020,** *15,* 4275–4288. doi:10.2147/ijn.s255833
185. Brennan, S. A.; Ní Fhoghlú, C.; Devitt, B. M.; O'Mahony, F. J.; Brabazon, D.; Walsh, A. *Bone Jt. J.* **2015,** *97-B,* 582–589. doi:10.1302/0301-620x.97b5.33336
186. Li, Y.; Lin, Z.; Zhao, M.; Xu, T.; Wang, C.; Hua, L.; Wang, H.; Xia, H.; Zhu, B. *ACS Appl. Mater. Interfaces* **2016,** *8,* 24385–24393. doi:10.1021/acsami.6b06613
187. Seong, M.; Lee, D. G. *Curr. Microbiol.* **2017,** *74,* 661–670. doi:10.1007/s00284-017-1235-9
188. Khalandi, B.; Asadi, N.; Milani, M.; Davaran, S.; Abadi, A. J. N.; Abasi, E.; Akbarzadeh, A. *Drug Res. (Stuttgart, Ger.)* **2017,** *67,* 70–76. doi:10.1055/s-0042-113383
189. Yu, D.; Kang, G.; Tian, W.; Lin, L.; Wang, W. *Appl. Surf. Sci.* **2015,** *357,* 1157–1162. doi:10.1016/j.apsusc.2015.09.074
190. Tang, B.; Li, J.; Hou, X.; Afrin, T.; Sun, L.; Wang, X. *Ind. Eng. Chem. Res.* **2013,** *52,* 4556–4563. doi:10.1021/ie3033872
191. Tang, B.; Sun, L.; Kaur, J.; Yu, Y.; Wang, X. *Dyes Pigm.* **2014,** *103,* 183–190. doi:10.1016/j.dyepig.2013.12.008
192. Nadiger, V. G.; Shukla, S. R. *J. Text. Inst.* **2016,** *107,* 1543–1553. doi:10.1080/00405000.2015.1129756
193. Doakhan, S.; Montazer, M.; Rashidi, A.; Moniri, R.; Moghadam, M. B. *Carbohydr. Polym.* **2013,** *94,* 737–748. doi:10.1016/j.carbpol.2013.01.023
194. He, H.; Cai, R.; Wang, Y.; Tao, G.; Guo, P.; Zuo, H.; Chen, L.; Liu, X.; Zhao, P.; Xia, Q. *Int. J. Biol. Macromol.* **2017,** *104,* 457–464. doi:10.1016/j.ijbiomac.2017.06.009
195. Tao, G.; Cai, R.; Wang, Y.; Liu, L.; Zuo, H.; Zhao, P.; Umar, A.; Mao, C.; Xia, Q.; He, H. *Mater. Des.* **2019,** *180,* 107940. doi:10.1016/j.matdes.2019.107940
196. Currie, H. A.; Deschaume, O.; Naik, R. R.; Perry, C. C.; Kaplan, D. L. *Adv. Funct. Mater.* **2011,** *21,* 2889–2895. doi:10.1002/adfm.201100249
197. Khalid, A.; Bai, D.; Abraham, A. N.; Jadhav, A.; Linklater, D.; Matusica, A.; Nguyen, D.; Murdoch, B. J.; Zakhartchouk, N.; Dekiwadia, C.; Reineck, P.; Simpson, D.; Vidanapathirana, A. K.; Houshyar, S.; Bursill, C. A.; Ivanova, E. P.; Gibson, B. C. *ACS Appl. Mater. Interfaces* **2020,** *12,* 48408–48419. doi:10.1021/acsami.0c15612
198. Kumari, S.; Bargel, H.; Scheibel, T. *Macromol. Rapid Commun.* **2020,** *41,* 1900426. doi:10.1002/marc.201900426
199. Harvey, D.; Bardelang, P.; Goodacre, S. L.; Cockayne, A.; Thomas, N. R. *Adv. Mater. (Weinheim, Ger.)* **2017,** *29,* 1604245. doi:10.1002/adma.201604245
200. Seijsing, F.; Nilebäck, L.; Öhman, O.; Pasupuleti, R.; Ståhl, C.; Seijsing, J.; Hedhammar, M. *MicrobiologyOpen* **2020,** *9,* e993. doi:10.1002/mbo3.993
201. Zeplin, P. H.; Berninger, A.-K.; Maksimovikj, N. C.; van Gelder, P.; Scheibel, T.; Walles, H. *Handchir., Mikrochir., Plast. Chir.* **2014,** *46,* 336–341. doi:10.1055/s-0034-1395558
202. Zeplin, P. H.; Maksimovikj, N. C.; Jordan, M. C.; Nickel, J.; Lang, G.; Leimer, A. H.; Römer, L.; Scheibel, T. *Adv. Funct. Mater.* **2014,** *24,* 2658–2666. doi:10.1002/adfm.201302813
203. Sommer, C.; Bargel, H.; Raßmann, N.; Scheibel, T. *MRS Commun.* **2021,** *11,* 356–362. doi:10.1557/s43579-021-00034-y
204. Zhang, Y.; Zhou, Z.; Sun, L.; Liu, Z.; Xia, X.; Tao, T. H. *Adv. Mater. (Weinheim, Ger.)* **2018,** *30,* 1805722. doi:10.1002/adma.201805722
205. Weiss, A. C. G.; Herold, H. M.; Lentz, S.; Faria, M.; Besford, Q. A.; Ang, C.-S.; Caruso, F.; Scheibel, T. *ACS Appl. Mater. Interfaces* **2020,** *12,* 24635–24643. doi:10.1021/acsami.0c06344
206. Mulinti, P.; Diekjürgen, D.; Kurtzeborn, K.; Balasubramanian, N.; Stafslien, S. J.; Grainger, D. W.; Brooks, A. E. *Bioengineering* **2022,** *9,* 46. doi:10.3390/bioengineering9020046
207. Zha, R. H.; Delparastan, P.; Fink, T. D.; Bauer, J.; Scheibel, T.; Messersmith, P. B. *Biomater. Sci.* **2019,** *7,* 683–695. doi:10.1039/c8bm01186a

License and Terms

This is an open access article licensed under the terms of the Beilstein-Institut Open Access License Agreement (https://www.beilstein-journals.org/bjnano/terms), which is identical to the Creative Commons Attribution 4.0 International License (https://creativecommons.org/licenses/by/4.0). The reuse of material under this license requires that the author(s), source and license are credited. Third-party material in this article could be subject to other licenses (typically indicated in the credit line), and in this case, users are required to obtain permission from the license holder to reuse the material.

The definitive version of this article is the electronic one which can be found at:
https://doi.org/10.3762/bjnano.13.81

BEILSTEIN JOURNAL OF NANOTECHNOLOGY

Design of a biomimetic, small-scale artificial leaf surface for the study of environmental interactions

Miriam Anna Huth*[1], Axel Huth[1], Lukas Schreiber[2] and Kerstin Koch[1]

Full Research Paper

Open Access

Address:
[1]Faculty of Life Sciences, Rhine-Waal University of Applied Sciences, Marie-Curie-Str. 1, 47533 Kleve, Germany and [2]IZMB, Department of Ecophysiology, University of Bonn, Kirschallee 1, 53115 Bonn, Germany

Email:
Miriam Anna Huth* - miriam-anna.huth@hochschule-rhein-waal.de

* Corresponding author

Keywords:
recrystallization; surface properties; wax composition; wetting; wheat

Beilstein J. Nanotechnol. **2022,** *13,* 944–957.
https://doi.org/10.3762/bjnano.13.83

Received: 19 May 2022
Accepted: 16 August 2022
Published: 13 September 2022

This article is part of the thematic issue "Biomimetics on the micro- and nanoscale – The 25th anniversary of the lotus effect".

Guest Editor: M. Mail

© 2022 Huth et al.; licensee Beilstein-Institut.
License and terms: see end of document.

Abstract

The cuticle with its superimposed epicuticular waxes represents the barrier of all aboveground parts of higher plant primary tissues. Epicuticular waxes have multiple effects on the interaction of plants with their living and non-living environment, whereby their shape, dimension, arrangement, and chemical composition play significant roles. Here, the ability of self-assembly of wax after isolation from the leaves was used to develop a small-scale wax-coated artificial leaf surface with the chemical composition and wettability of wheat (*Triticum aestivum*) leaves. By thermal evaporation of extracted plant waxes and adjustment of the evaporated wax amounts, the wettability and chemical character of the microstructure of the surface of wheat leaves were transferred onto a technical surface. For the use of these artificial leaves as a test system for biotic (e.g., germination of fungal pathogens) and non-biotic (e.g., applied surfactants) interactions on natural leaf surfaces, the chemical composition and the wetting behavior should be the same in both. Therefore, the morphology, chemistry, and wetting properties of natural and artificial surfaces with recrystallized wax structures were analyzed by scanning electron microscopy, gas chromatography–mass spectrometry, and by the determination of water contact angles, contact angle hysteresis, and tilting angles. Wheat leaves of different ages were covered exclusively with wax platelets. The extracted wheat wax was composed of alcohols, aldehydes, esters, and acids. The main component was 1-octacosanol. The waxes recrystallized as three-dimensional structures on the artificial surfaces. The three tested wetting parameters resembled the ones of the natural surface, providing an artificial surface with the chemical information of epicuticular waxes and the wetting properties of a natural leaf surface.

Introduction

Cuticle

One of the largest interfaces on earth is formed by thin layers that are a few nanometers to micrometers thin, namely the wax layers of the plant cuticle [1]. The plant cuticle is a thin extracellular membrane superimposed on the epidermal cells of all higher, non-woody, aboveground plant surfaces. It is basically composed of an insoluble polymeric matrix, cutin, and soluble

hydrophobic waxes. The plant cuticle is known to have a variety of vital functions (Figure 1). Among other things, it protects against herbivores and pathogens, provides mechanical stability, reflects harmful UV radiation [2-6], and mainly protects the plant from desiccation [7,8]. The cuticular waxes contribute significantly to this barrier function.

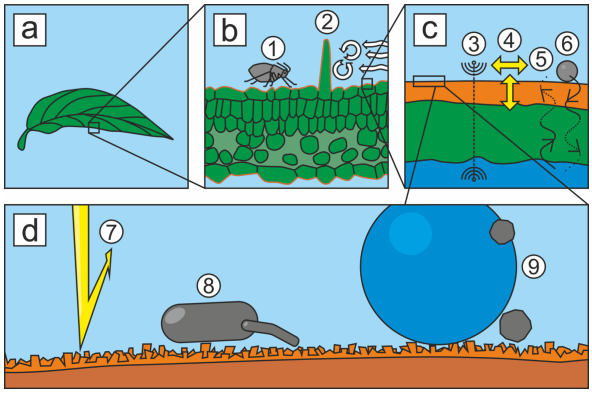


Figure 1: Drawings of a leaf surface at different magnifications and main functions of the cuticle. (a) Leaf, (b–d) leaf cross sections in increasing magnifications; (c) orange: cuticle, green: cell wall, blue: cytoplasm, (d) orange: epicuticular wax crystals, brown: cuticle. (1) Reduction of arthropod pest attachment, (2) complex functions of trichomes, for example, generation of air turbulences, (3) host-pathogen recognition/signaling for cell development, (4) resistance to mechanical stress, (5) control of water loss, (6) control of solute uptake, (7) protection from hazardous radiation, (8) reduction of spore, bacterial, and viral attachment, (9) self-cleaning ability (modified after [9]).

Plant waxes

Plant waxes are complex mixtures of long-chain aliphatic and cyclic hydrocarbon compounds with different functional groups [10]. Typical wax components are fatty acids, alcohols, ketones, aldehydes, and triterpenes, but the exact wax composition is species- and organism-specific [11]. The waxes are differentiated into intracuticular waxes, which are incorporated into the cutin matrix, and epicuticular waxes, which are deposited on the polymer. Intra- and epicuticular waxes differ not only in their localization, but also in their chemical composition [12,13]. Epicuticular waxes form the outermost layer of the plant cuticle and, thus, the first contact site of the plant with its biotic and abiotic environment. They form a thin crystalline wax film (less than 1 µm) and often various three-dimensional emerging wax crystals in the nano- and micrometer range (0.5–100 µm) [14-16]. Recrystallization of extracted plant waxes has shown that the diverse microstructures of epicuticular waxes arise by self-assembly and that the micromorphology of wax structures is largely determined by their chemical composition [15,17-23]. Platelets, which mostly have a high primary alcohol content, are among the most common wax structures. An overview of the morphology of various wax structures has been given by Barthlott and co-workers [24].

Wetting

The wettability of leaves plays an important role in the interaction of plants with the environment, such as the interaction with pathogens and the formation of biofilms [25,26]. A measure of the degree of wetting is the contact angle θ (CA). It describes the angle between the liquid–vapor interface and the liquid–solid interface. According to the CA, surfaces can be classified as superhydrophilic ($0° < \theta < 10°$), hydrophilic ($10° \leq \theta < 90°$), hydrophobic ($90° \leq \theta < 150°$), and superhydrophobic ($150° \leq \theta < 180°$) [27]. Due to its chemical composition, the cuticle is generally a hydrophobic surface. However, plant surfaces show a large variability of cell shapes, surface structures, and hierarchical structures (a combination of micro- and nanostructures) [27]. Due to this structural diversity and different chemical modifications, plant surfaces can have different wetting properties, ranging from superhydrophobic to superhydrophilic [28]. An overview of the diverse microstructures and their influence on the wettability of plant surfaces is given by several reviews [27,29-31].

Wetting states

Young was the first to formulate a description of the wetting state in 1805. According to Young's equation, the CA depends on the three interfacial tensions liquid–solid, liquid–gas, and solid–gas [32]. He describes an ideal static CA on a homogeneous, smooth, non-deformable, and inert surface. Natural and technical surfaces hardly correspond to these ideal conditions. Wenzel [33] and Cassie and Baxter [34] studied CAs on rough surfaces, assuming that the liquid penetrates perfectly into the depressions of the surface (homogeneous wetting). Cassie and Baxter [34] describe heterogeneous wetting in which the liquid does not penetrate the depressions of the surface. Air pockets form under the liquid, which reduce the contact between the solid surface and the liquid. In nature, ideal Wenzel or Cassie–Baxter wetting stages rarely occur. However, often so-called mixed wetting stages exist [35].

Contact angle hysteresis and tilting angle

The wetting stages are closely related to the contact angle hysteresis (CAH) and the tilting angle (TA). Both quantities are therefore used to adequately describe the wettability of rough and heterogeneous surfaces. CAH is a qualitative measure of the mobility of a droplet on a surface [36]. The larger the hysteresis, the harder a droplet rolls off [37]. CAH is defined as the difference between the advancing and the receding CA. It can be determined for a droplet with varying volume or for a droplet on an inclined plane. The angle of inclination at which a droplet starts to roll off is called the TA α. Superhydrophobic surfaces with a low TA ($\alpha < 10°$) and a small CAH have the ability to self-clean [9]. This property is also known as the Lotus effect, named after the best-known example of a self-

cleaning surface, the leaf of the lotus plant (*Nelumbo nucifera* Gaertn., Nelumbonaceae).

Biomimetic surfaces

The wettability properties of plant surfaces have often been a source of inspiration for the development of biomimetic materials. For example, biomimetic surfaces offer the possibility to study interfacial phenomena of plant surfaces such as the splash behavior of liquids or the adhesion of insects under laboratory conditions [38,39]. In the past, long-chain hydrocarbons as well as native wax extract were recrytallized to mimic the native leaf structures and their associated properties [21,39-42]. Different methods of recrystallization have been developed and used in previous studies [17,20,21,43-46]. A fast method, for example, is recrystallization from a solution. However, this process has the disadvantage that it can lead to a heterogeneous distribution of the wax mass and to a variety of structures that often do not correspond to the original wax type [20,42]. Due to the ring-shaped accumulation and the resulting pattern, this effect is called the "coffee drop effect" [47,48]. This undesirable effect can be avoided by the solvent-free process of physical vapor deposition (PVD), so that a homogeneous distribution of the wax masses can be achieved [42].

Aim of this study

In the present study, the wettability and chemical character of a natural leaf surface were transferred to technical surfaces by the process of PVD. Wheat, one of the most important crops worldwide, served as the biological model. The artificial surfaces imitating the leaves should have the same chemical and wetting properties as leaf surfaces. To prove these criteria, the chemical composition of the native and transferred wax extracts, the morphology of native and recrystallized wax crystals and the wetting properties of native and artificial surfaces were analyzed. Such artificial surfaces allow for the study of biotic interactions, for example, pathogen interactions, but also non-biotic interactions such as the behavior of liquids and surfactants used in agricultural spraying applications. An artificial test system is independent of the environmental influences to which plants in a field are exposed. It can be developed in large numbers with little resources towards the detailed understanding of interfacial effects under laboratory conditions.

Experimental

Plant material

Wheat plants (*Triticum aestivum* L., Poaceae, variety Ponticus, Strube D&S GmbH, Söllingen, Germany) were cultivated in the greenhouse (GH plants, temp. day: 18 °C, temp. night: 12 °C) in pots with arable soil, sand, and universal soil (1:1:2). The plants were irrigated and fertilized (2.5% Universol Blue 18-11-18 + 2.5 MgO + TE, Everris International BV, Heerlen, Netherlands) manually once a week. In addition, outdoor plants (OD plants) were cultivated in the experimental garden of the Rhine-Waal University of Applied Sciences, Kleve, Germany, under preferably realistic cultivation conditions in order to be able to compare their wax morphology and chemistry with those of the plants cultivated under laboratory conditions. The plants were sown by hand. The row spacing was approx. 35 cm and the grain spacing approx. 10 cm. Fertilizer was applied once with saltpeter granules (YaraLiva CALCINIT, Yara GmbH & Co. KG, Dülmen, Germany). A total of about 100 plants each were grown in the greenhouse and outdoors.

In all conducted experiments, the second, third, and fourth leaves were harvested when the fifth leaf was fully developed (Supporting Information File 1, Figure S1). The leaves at the second position were the oldest and the leaves at the fourth position were the youngest ones. Chemical composition, wax structures, and wettability were characterized separately for leaves of different ages in order to find or exclude possible variations (see following sections). In the following, the leaves are referred to as leaf 2, 3, and 4 according to their positions on the plant.

Development of artificial leaf surfaces

Wax for recrystallization was extracted from wheat leaves of outdoor plants by immersing the leaves in chloroform (99.9% HPLC grade, Carl Roth GmbH und Co. KG, Karlsruhe, Germany) for 20 s. The extracts were then filtered (ROTI-LABO type 113A, 110 mm diameter, Carl Roth GmbH und Co. KG, Karlsruhe, Germany). The filtrate was finally dried under a fume hood until the solvent was completely evaporated. The recrystallization of wax structures on clean glass (cover glass, 18 × 18 mm) was carried out by PVD, resulting in a wax coating of the complete glass. The device for recrystallization (Figure 2) consisted of a glass chamber (Vakuum- und Industrieservice Meier GmbH, Borken, Germany), a holder for the samples to be coated, a flat heater made of high-performance ceramics (40 Ω, BACH Resistor Ceramics GmbH, Werneuchen, Germany), a laboratory power supply unit, and a vacuum pump (Duo 5M, Pfeiffer Vacuum GmbH, Asslar, Germany). To create a vacuum of 4×10^{-3} mbar, air was pumped out for 30 min. The amount of wax deposited on the samples can be varied by the distance between the evaporation point and the sample or by changing the amount of wax to be evaporated. Here, three different amounts of wax (small amount: 700 µg, medium amount: 1400 µg, and large amount: 2800 µg) were placed on the heating plate heated up to 200 °C and evaporated to obtain different wettabilities of the samples. The distance between the heating plate with the wax source and the samples to be coated was 4 cm. After wax deposition, samples were stored in an oven at 50 °C for 72 h. In the following, the artificial sur-

faces are named according to the amount of wax used for wax coating.

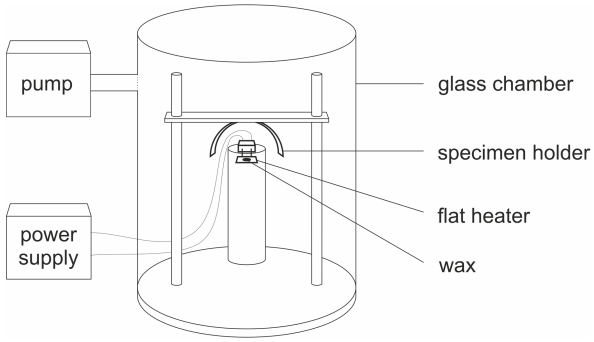


Figure 2: Schematic drawing of the device for wax vaporization by PVD.

Scanning electron microscopy of wax morphology

The morphologies of the wax on the upper (adaxial) and lower (abaxial) leaf sides (leaf 2, 3, and 4, $n = 3$) as well as of recrystallized wax structures on glass ($n = 3$) were analyzed by scanning electron microscopy (SEM, Gemini Supra 40 VP, Zeiss, Oberkochen, Germany). The middle part of fresh wheat leaves was cut into small pieces (approx. 0.3 × 0.5 cm) using a scalpel and attached to aluminium SEM sample holders (diameter 2.4 cm, Plano, Wetzlar, Germany) with conductive double-sided adhesive tape (Leit-Tabs, Plano, Wetzlar, Germany). The samples were coated with a thin gold layer (99.9% purity, approx. 8 nm) using a sputter coater (Cressington 108 auto SE, Elektronen-Optik-Service GmbH, Dortmund, Germany; 60 s, 30 mA, 0.1 mbar). Glasses coated with wax were mounted and sputter-coated in the same way as the wheat leaf pieces. SEM analysis of all samples was carried out at a voltage of 10 kV using the secondary electron detector. The working distance was 4–7 mm.

Atomic force microscopy analysis of recrystallized structures

The thickness of the wax coating on glass (1400 µg) was examined with an atomic force microscope (AFM, NanoWizard II, JPK instruments, Berlin, Germany). For this purpose, the recrystallized wax layer on the glass was partially removed with a razor blade. The sample was then attached to a microscope slide with double-sided adhesive tape. The AFM recordings were performed in tapping mode (amplitude: 0.05 V; frequency: 302.9 kHz, line rate: 0.3 Hz, set point: 940 mV) with tapping cantilevers (Tap300-G, Budget Sensors, Sofia, Bulgaria). The acquired height and amplitude images (50 × 50 µm) were processed and analyzed using JPK´s data analysis software (JPK Data Processing, version 4.2.62). At the edge of the wax layer, the height differences between the wax layer and the uncoated glass were measured using the cross-section tool ($n = 20$).

Analysis of the chemical composition of wax

Fresh leaves were cut from intact plants and immediately processed. To extract the epicuticular waxes of the greenhouse plants, three leaves per leaf age were combined for one replicate and dipped for 20 s in 20 mL chloroform. Five independent biological replicates were analyzed ($n = 5$). For the extraction of epicuticular wax from outdoor plants, leaf 2, 3, and 4 were pooled together for one replicate. Here the analysis of six independent biological replicates was performed ($n = 6$). Leaves were scanned immediately after wax extraction using a scanner (LA2400 with Winrhizo, Regent Instruments Inc., Québec, Canada) to determine the leaf areas. Tetracosane (C_{24} alkane, $c = 0.2$ mg·mL^{-1}, Merck KGaA, Darmstadt, Germany) was added to 50 µL of each extract as an internal standard. An aliquot of each wax extract was taken for chemical analysis. The volumes of the aliquots were reduced to 200 µL at 70 °C under a stream of gaseous nitrogen. To ensure that the wax composition did not change due to the evaporation process, the chemical composition of the wax coating of the artificial surfaces (1400 µg) was analyzed too ($n = 4$). For this purpose, the wax was stripped with collodion (4%, Merck KGaA, Darmstadt, Germany). The collodion strip was then placed in 10 mL chloroform and 100 µL tetracosane was added as an internal standard. All samples were derivatized with 20 µL bis(trimethylsilyl)trifluoroacetamide (BSTFA) for 45 min at 70 °C. 20 µL of pyrimidine (Merck KGaA, Darmstadt, Germany) was used as catalyst. The waxes were analyzed quantitatively with a gas chromatograph coupled with a flame ionization detector (GC–FID, 6890N, Agilent Technologies Sales & Services, column: DB-1; 30 m × 0.32 mm, 0.1 µm; J&W, Agilent Technologies Sales & Services GmbH & Co. KG, Waldbronn, Germany). The qualitative analysis of the wax components was carried out with a gas chromatograph coupled with a mass spectrometer (GC–MS, 5973, Agilent Technologies Sales & Services GmbH & Co. KG, Waldbronn, Germany). The individual wax monomers were identified by their fragments formed by electron impact ionisation using HP-Chemstation software (Hewlett Packard Cooperation, Palo Alto, USA). The injection volume was 1 µL and the carrier gas was hydrogen for GC–FID and helium for GC–MS.

Analysis of the wetting properties

The wetting properties of wheat leaves (OD) and glass with and without wax coating were analyzed by determining the static CA, the TA, and the CAH of a water droplet (aqua dest., droplet volume: 5 µL; $n = 15$). For this purpose, a goniometer (OCA 35, DataPhysics Instruments GmbH, Filderstadt, Germany)

equipped with a digital camera (RM-6740CL, JAI, Copenhagen, Denmark) was used. The CAH was determined on an inclined plane just before the droplet rolled off (tilting plate method). The CAs were measured in the first frame of the videos in which the CAH and the TAs were determined. The leaves were tilted in a way that the drops rolled off longitudinally to the leaf venation. If a drop rolled off immediately after deposition, the CA and the CAH were not measurable. The TA was set to 0.1° in these cases. The wetting properties of leaf 2, 3 and 4 and of their upper and lower sides were analyzed separately (for each leaf $n = 15$).

Utilization of the artificial leaf surface

To comparatively investigate the biotic interactions of the artificial leaf surfaces, wheat leaves and the artificial leaf surfaces (1400 µg) were inoculated with conidia (asexual spores) of powdery mildew (*Blumeria graminis* (DC.) Speer f. sp. *tritici*, Erysiphaceae), a natural pathogen of wheat. Conidia from infested wheat plants (provided by Prof. Ulrich Schaffrath, Lehrstuhl und Institut für Biologie III (Pflanzenphysiologie), RWTH Aachen, Germany) were cultivated on wheat plants (20 °C, 12 h/12 h day/night rhythm, 76% rel. air humidity). Infested plants used for inoculation were always shaken manually one day before inoculation to remove old conidia. This procedure should ensure that only fresh conidia are transferred during inoculation. For inoculation, freshly cut turgescent leaves ($n = 5$) and the artificial leaf surface ($n = 10$) were placed on the bottom of an inoculation tower (height: 80 cm, length: 25 cm, width: 25 cm). Plants whose leaves clearly showed powdery mildew pustules were then shaken out over the surfaces. After 1 h, the inoculated surfaces were removed from the inoculation tower and incubated in the dark at 20 °C on a wet paper towel in a petri dish to achieve 100% relative air humidity. The germination success of 100 conidia on the different surfaces was examined using a digital microscope (VHX-600 DSO, Keyence, Osaka, Japan). Leaf pieces were cut and decolorized with ethanol/acetic acid (3:1, v/v) for 24 h until the leaves were bleached. For this purpose, the leaf pieces were placed on papers soaked with the ethanol/acetic acid mixture. To fix the structures, the leaf pieces were then transferred to papers soaked with lactoglycerol (lactic acid/glycerol/H_2O, 1:1:1.3, v/v/v; lactic acid: ≥95% L-(+)-lactic acid, Carl Roth GmbH und Co. KG, Karlsruhe, Germany; glycerol: ≥99%, Carl Roth GmbH und Co. KG, Karlsruhe, Germany) for about 3 h. The fungal structures were then stained with trypan blue (Sigma-Aldrich, St. Louis, USA, 0.05% in lactoglycerol).

Data analysis

The data were statistically analyzed with the help of the software R Studio (R Core Team (2021). R: A language and environment for statistical computing. R Foundation for Statistical Computing, Vienna, Austria. URL https://www.R-project.org/). To evaluate significant differences ($p < 0.05$) in the wax composition and in the wetting properties between natural and artificial surfaces, a Kruskal–Wallis test followed by a post hoc Dunn test was performed. Differences in the wax composition between leaves 2, 3, and 4 were determined by an ANOVA test followed by a post hoc Tukey test.

Results

SEM analysis of wax morphology

SEM analysis showed that wheat leaves were covered with wax platelets (Figure 3a). The platelets had irregular edges and were very close to each other. Both leaf sides, leaves of different ages, and leaves from greenhouse and outdoor plants showed the same wax structures (Supporting Information File 1, Figure S2). The surface of the plants grown outdoors showed alterations in the wax layer (Supporting Information File 1, Figure S3).

Macroscopically, vapor deposition with the wheat wax resulted in a white opaque homogeneous coating on the glass (Figure 4). SEM images showed three-dimensional, granularly recrystallized structures on all wax-coated artificial surfaces, with a homogenous distribution (Figure 3b–d). With increasing evaporated wax mass, the amount of wax and especially the layer thickness of the recrystallized structures increased. The structures were interconnected and formed a net-like structure with infrequent scales between them.

AFM analysis of recrystallized structures

Like the SEM analysis, the AFM analysis showed granule-shaped structures on the artificial surface (1400 µg). By removing the wax with a razor blade, a distinct edge was created, showing a 1.12 ± 0.23 µm thick wax layer (Figure 5).

Analysis of chemical composition of wax

The wax monomers and the amount of wax per square centimeter leaf area of wheat leaves were chemically analyzed. The amount of wax increased with the decreasing age of the leaf (leaf 2: 11.5 ± 1.2 µg·cm^{-2}, leaf 3: 13.6 ± 0.8 µg·cm^{-2}, and leaf 4: 17.3 ± 1.5 µg·cm^{-2}). The wax compositions of leaves 2, 3, and 4 of the greenhouse plants were analyzed separately to investigate age-specific differences, but only slight differences were detected in the relative wax composition (Supporting Information File 1, Figure S4). Therefore, the wax of leaves 2, 3, and 4 was not further separated for the subsequent recrystallization experiments. The total amounts of wax of green house plants and outdoor plants were the same with 14.2 ± 2.8 and 15.7 ± 0.7 µg·cm^{-2}, respectively (Figure 6). The comparison of the wax composition of greenhouse plants and outdoor plants showed no significant differences in the amounts of the

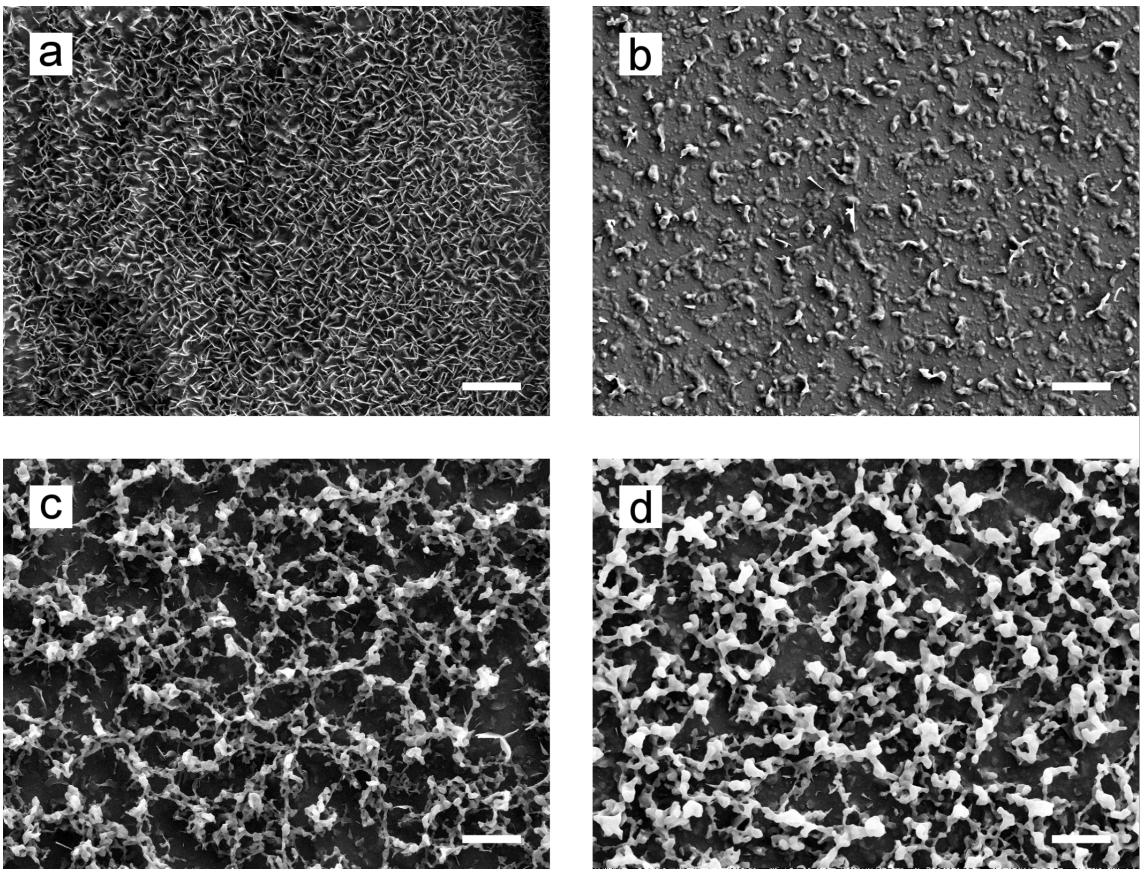


Figure 3: SEM micrographs of wax structures. (a) Natural leaf surface of wheat, (b–d) artificial surfaces coated with different evaporated wax masses: 700 µg (b); 1400 µg (c); 2800 µg (d); scale bars: 4 µm. On the natural surface, wax platelets in a dense arrangement were visible. On all artificial surfaces, granule-shaped structures were observed.

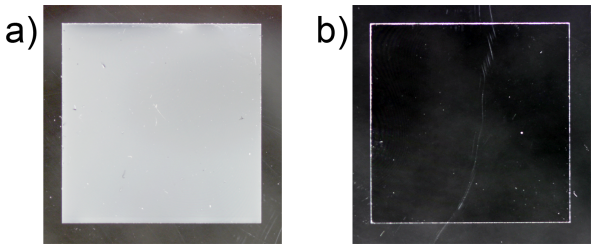


Figure 4: Photographs of glass cover slides before and after coating. (a) Pure non-treated glass (18 × 18 mm), (b) glass coated with wheat wax (1400 µg).

substance classes. Both waxes were mainly composed of alcohols (GH: 11.9 ± 2.4 µg·cm^{-2}, OD: 13.2 ± 0.6 µg·cm^{-2}). The main component was 1-octacosanol (GH: 10.6 ± 2.0 µg·cm^{-2}, OD: 11.7 ± 0.5 µg·cm^{-2}). Besides the alcohols, small amounts of esters (GH: 1.0 ± 0.2 µg·cm^{-2}, OD: 1.2 ± 0.1 µg·cm^{-2}) and aldehydes (GH: 0.9 ± 0.2 µg·cm^{-2}, OD: 1.0 ± 0.14 µg·cm^{-2}) were detected. Acids were detected in traces (GH: 0.2 ± 0.02 µg·cm^{-2}, OD: 0.2 ± 0.04 µg·cm^{-2}).

The chemical composition of the wax coating was checked to determine whether the wax composition had changed during the coating process. The wax coating of an artificial leaf surface was composed of the same substances in comparable amounts as the waxes of the natural leaves. The total amount of wax on the coated artificial surface (1400 µg) was, with a value of 15.6 ± 2.6 µg·cm^{-2}, the same as for the wheat leaves. The amount of alcohols (13.5 ± 2.2 µg·cm^{-2}), esters (1.1 ± 0.2 µg·cm^{-2}), aldehydes (0.8 ± 0.1 µg·cm^{-2}), and acids (0.3 ± 0.07 µg·cm^{-2}) did not differ significantly from the amounts found in wax of wheat leaves. 1-octacosanol was, with a value of 12.1 ± 2.0 µg·cm^{-2}, also the main component. Significant differences in the amounts of single wax components between the waxes of greenhouse plants, of outdoor plants, and wax-coated artificial leaf surfaces were only found for substances with amounts below 0.5 µg·cm^{-2}.

Analysis of wetting properties

All wheat leaves were highly hydrophobic (leaf 2, 3, and 4) on the upper and the lower leaf sides. The deposited water droplets appeared spherical (Figure 7a). The CAs of water ranged be-

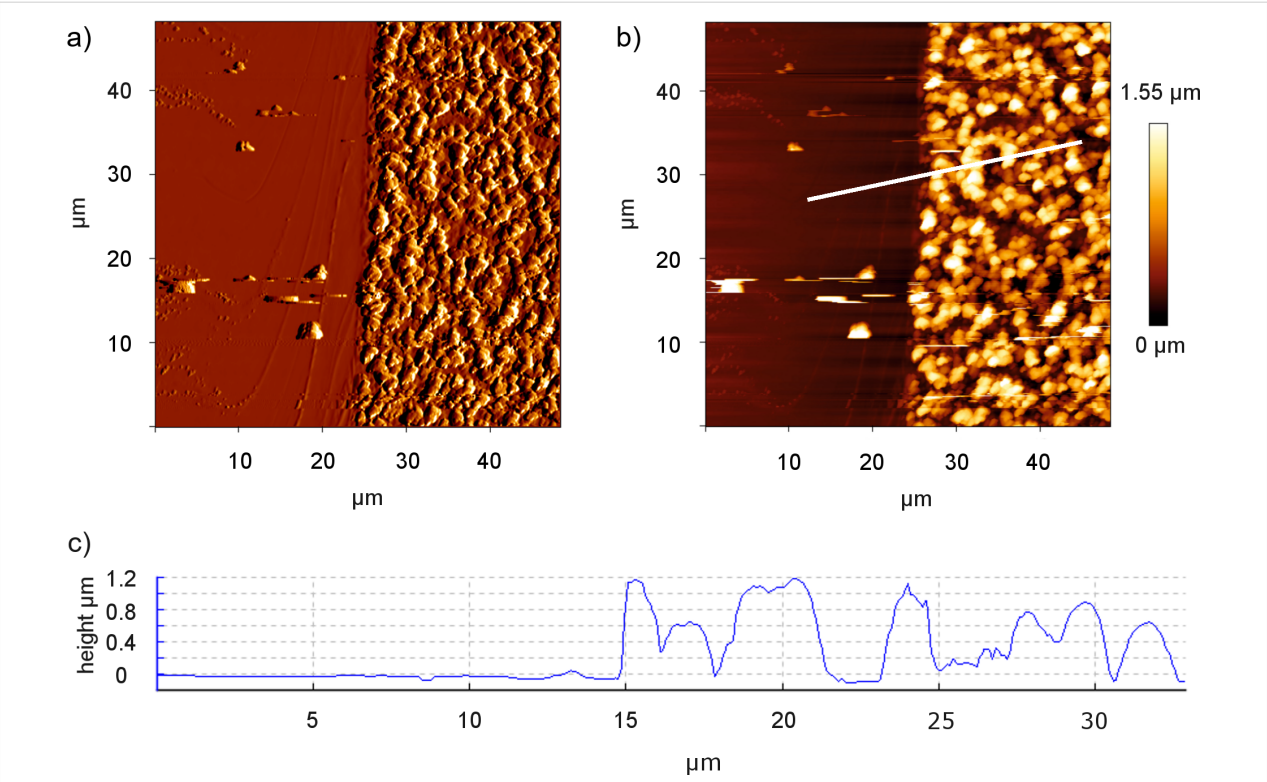


Figure 5: Results of AFM investigation of the wheat wax layer on glass (artificial leaf surface; 1400 µg). (a) Amplitude image, (b) height image. The white line indicates where the cross section in (c) was made. (c) Cross section. On the left side of each image: glass after the removal of the coating, on the right side: structure of the wax coating.

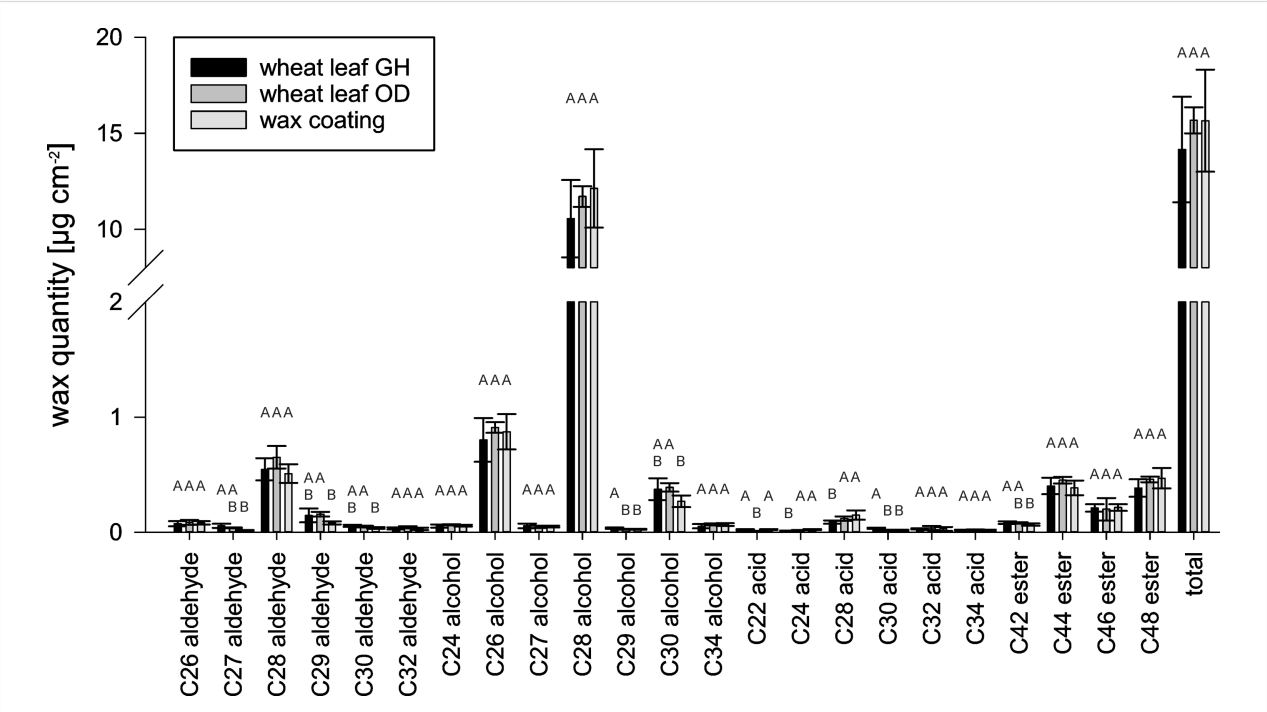


Figure 6: Chemical composition of wheat wax. GH: greenhouse plants (n = 15); OD: outdoor plants (n = 6). Wax coating: wax layer of a wheat wax-coated glass (n = 4). Different letters indicate significant differences in the amounts of the wax components between wheat leaves from GH, OD, and the artificial leaf surface ($p < 0.05$, tested by a Kruskal–Wallis test followed by a post hoc Dunn test).

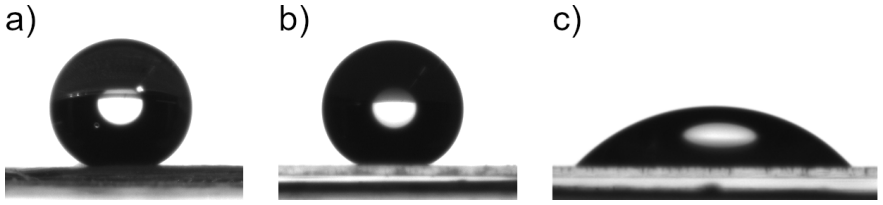


Figure 7: Goniometer photographs of water droplets. (a) On a turgescent wheat leaf (CA = 144°), (b) on a wax-coated artificial surface (1400 µg, CA = 155°), and (c) on clean non-treated glass (CA = 46°); all mentioned CAs are the individual CAs of the water droplets shown in the images.

tween 127.5° ± 13.6° and 147.5° ± 11.7°. The deposited droplets rolled off from all leaves at TAs ranging from 10.8° ± 7.3° up to 29.4° ± 15.6°. The CAH values varied from 8.2° ± 8.3° to 25° ± 10.3° (Table 1). The CA, TA, and CAH values of the upper surface of leaf 3 were compared with the values of the wax-coated artificial surfaces for the following experiments.

Table 1: Wetting properties of wheat leaves (OD, mean ± SD, n = 15).[a]

Sample	CA [°]	TA [°]	CAH [°]
leaf 2 upper side	143.6 ± 9.3	26.2 ± 14.1	22 ± 10.6
leaf 3 upper side	147.5 ± 11.7	15.7 ± 10.8	8.2 ± 8.3
leaf 4 upper side	141.7 ± 11.8	10.8 ± 7.3	9.0 ± 8.3
leaf 2 lower side	139.8 ± 17.5	28.6 ± 14	25.0 ± 10.3
leaf 3 lower side	140.5 ± 15.6	29.4 ± 15.6	23.1 ± 12.5
leaf 4 lower side	127.5 ± 13.6	31.3 ± 21.3	23.2 ± 12.7

[a]CA: contact angle, TA: tilting angle, CAH: contact angle hysteresis.

The artificial surfaces were also hydrophobic (Figure 7b). In contrast to clean, non-treated glass (Figure 7c), the CA of the wax-coated surfaces were all in the hydrophobic range. The smallest CA, 110.1° ± 12.0°, was measured on the artificial surface, on which the small wax amount was evaporated. The CAs of the artificial samples with medium (154.7° ± 8.8°) and with large amounts of evaporated and recrystallized wax (148° ± 4.7°) did not differ from those of the wheat leaves (147.5° ± 11.7°) (Figure 8a).

As on clean, non-treated glass, the droplets did not roll off the artificial surfaces with small amounts of wax. Therefore, neither TA nor CAH could be measured on these surfaces. On the artificial surfaces with the large amount of wax, the droplets only rolled off at higher TA (38.9° ± 14.6°) than on the wheat leaves (15.7° ± 15.1°). The TA of the artificial surfaces covered with the medium wax mass (14.9° ± 13.8°) was the same as on the wheat leaves (Figure 8b). The CAH of artificial surfaces with the medium wax mass (17.6° ± 10.6°) was also the same as that of the wheat leaves (8.2° ± 8.3°). The CAH of the artificial sur-

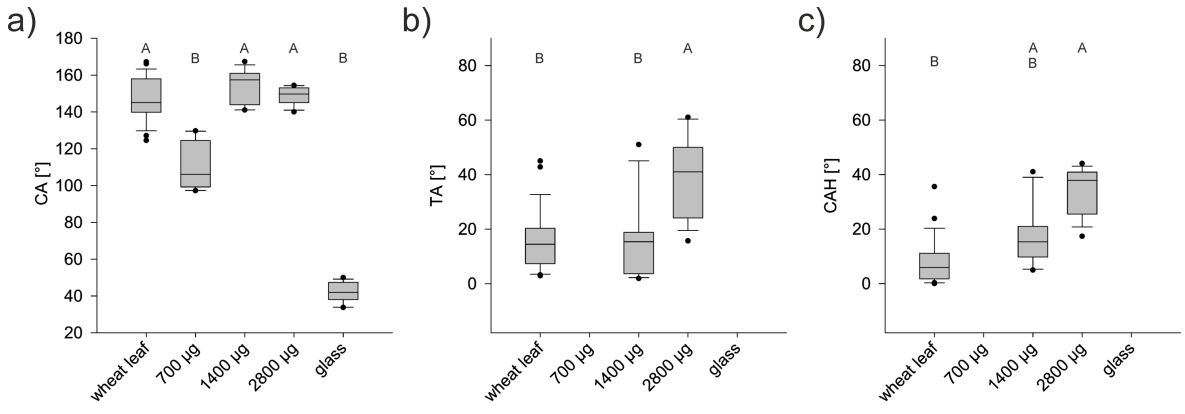


Figure 8: Wetting properties of the natural wheat leaf and the artificial surfaces covered with 700, 1400, or 2800 µg recrystallized epicuticular wheat wax. (a) Contact angle (CA), (b) tilting angle (TA), and (c) contact angle hysteresis (CAH) of water droplets (5 µL). The droplets on glass did not roll off, hence, neither TA nor CAH were measurable. Different letters indicate significant differences between the values of the different surfaces (p < 0.05, tested by a Kruskal–Wallis test followed by a post Hoc Dunn test).

faces covered with the high wax mass was higher (33.5° ± 8.8°) than that of the natural surfaces (Figure 8c).

Utilization of the artificial leaf surface

Since the artificial surface with the medium wax mass had the same wetting properties as the wheat leaves, this artificial surface was selected as "artificial leaf surface" for an inoculation experiment with fungal spores. For this purpose, wheat leaves and the artificial surfaces were inoculated with conidia of wheat powdery mildew. The microscopic images show that the fungal spores germinated and differentiated on both the natural and the artificial surface (Figure 9). The germination rates were 76.8% ± 13.2% on the wheat leaf and 48.6% ± 12.6% on the artificial leaf surface.

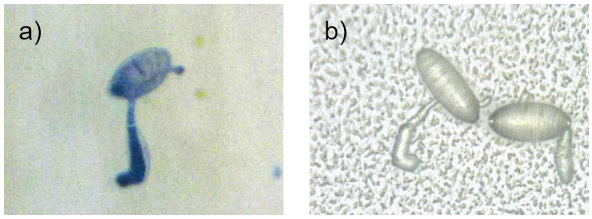


Figure 9: Digital microscopy images of powdery mildew conidia at 1000× magnification. (a) On a wheat leaf, stained with trypan blue, (b) on the artificial leaf surface. Fungal conidia differentiated on both surfaces, clearly indicated by the development of the hooked appressorium.

Discussion

Plant surfaces have specific physicochemical properties due to the cuticle and, in particular, due to the epicuticular waxes deposited on it. In previous studies, bio-inspired technical surfaces were often used with surface properties only partially corresponding to those of the natural surfaces. In the present work, an artificial leaf surface was developed that corresponded to the plant leaf surface in its chemical properties and its wettability.

Wax morphology

Natural surface

First, the surface properties of the natural wheat leaf were characterized. For wheat leaves, platelets as well as tubules have been previously described as wax structures [17,20,49-52]. Further, the wax structures can vary depending on the developmental stage of the plant [49]. SEM investigation showed platelets on all leaves of different ages (Figure 3a, Supporting Information File 1, Figure S2). This result meets the expectations, as tubules were described for other plant organs such as leaf sheets, stems, and glumes [50,51,53,54], or only on the abaxial sides of the glaucous flag leaves of plants at a later stage of development [50,51]. In our study, the structures of both leaf sides were the same (Supporting Information File 1, Figure S2). This is in accordance with other studies. In Koch et al. [20] and Wang et al. [53] plants in a comparable developmental stage were investigated. A network of densely packed wax platelets was also described for both sides of the leaf [53].

Abiotic factors such as temperature, humidity, pollution, and radiant energy might cause changes in the wax morphology [55-57]. To take this into account, wheat plants were also cultivated outdoors under natural growth conditions. No culture-specific differences in the wax morphology were observed. As with the greenhouse plants, the leaves of the plants cultivated outdoors were covered with wax platelets. Hence, the wax morphology of the investigated wheat leaves showed no developmental and ecological variability. The wax platelets could therefore be used as a native model for the development of artificial leaf surfaces.

Artificial surfaces

As a decisive prerequisite for the applicability of the artificial surface as bio-inspired leaf surface, it was defined that the artificial surface needs to have a homogeneous coating and uniform wettability. Previous recrystallization studies have shown that a homogeneous coating can be produced by thermal evaporation [40,46,58-60]. In the present work, a homogeneous coating was also achieved with this method, as can be seen in the photograph (Figure 4) and in the SEM micrograph (Figure 3). The latter showed that the wax recrystallized to granular structures with single plates between the granular network. However, after deposition of the lowest wax mass, almost no plates were formed, indicating that the polar and amorphous substrate prevents the formation of a platelet structure. In contrast, higher wax masses lead to a growth of the platelets on the wax deposited below. It was clearly visible that the individual plates were not formed directly on the substrate, but stood on a granular layer. Koch et al. [20] demonstrated that on non-polar substrates, such as highly ordered pyrolytic graphite, wax composed of primary alcohols recrystallize into platelets, as on the wheat leaves. Even though the recrystallized structures in the present study did not exactly match the native wax structures, the wetting properties of the artificial leaf surfaces were similar to those of the natural leaf. The glass substrate used here offers an easy-to-handle and inexpensive way to develop large numbers of wax-coated samples with wetting properties that are similar to that of the natural leaf.

Wax chemistry

Natural surface

Next to the wax morphology, the wax chemistry of wheat leaves was analyzed, as it plays an important role in the functionality of the leaf surface. The extracted wheat wax was composed of alcohols, aldehydes, esters, and acids. The main component was 1-octacosanol (Figure 6). The results are in

agreement with previous studies on the wax chemistry of other wheat varieties [20,50,61,62]. β-Diketone, which is a component of wax tubules, has so far only been detected in wax of wheat leaves at later developmental stages and other plant organs [50,53,61,63-66]. Alkanes, which were detected in wheat wax in some other studies, were not a component of the wax examined here [20,52,53,62-64].

Developmental changes can have an influence on the wax composition [67,68]. Therefore, the composition of epicuticular waxes of leaves of different ages was analyzed in the greenhouse-cultured plants to examine whether there were any differences. The total wax amount decreased from leaf 2 to leaf 4, that is, from older to younger leaves. The decrease in wax amounts was evenly distributed over all substance classes, so that there were no notable differences in the relative wax composition and the corresponding wax morphology (Supporting Information File 1, Figure S4).

Abiotic factors can have an influence on the amount of epicuticular wax. For example, previous studies have shown that higher temperatures, reduced humidity, increased UV radiation, or drought stress can lead to increased wax accumulation [55,64,69-71]. Therefore, it was also examined whether there were differences in the wax chemistry between the greenhouse plants and the outdoor plants. The results showed hardly any differences between the differently cultivated plants. The total wax amount and the amounts of the single substance classes were the same (Figure 6). Consistent with the results of the wax morphology study, the wax composition of wheat appears to be strongly genetically fixed and little influenced by environmental factors. Thus, the wax extracts of plants growing outdoors or indoors can be used for the development of artificial leaf surfaces.

Artificial surfaces

To make sure that wax composition had not changed during the coating process, the wax layer of a coated artificial leaf surface was analyzed. By comparison of the native wax with the wax recrystallized after thermal evaporation, we could show that the wax still had the same chemical composition as the wax on the native leaves. In the wax precipitate on glass, the same substances were detected in the same amounts as in the wax that was vaporized (Figure 6). Thus, no transformation of substances had taken place and the wax composition was stable. In a previous study, the wax composition of leek wax was also found to be thermally stable [72].

Since the evaporated substances spread uniformly in vacuum from the point source and the samples were placed in an arc above the substance source, in previous studies, the wax coverage was calculated approximately from the quotient of the evaporated masses and the surface area of a hemisphere [42,58,72,73]. The analysis of the wax coating of the evaporated surface performed here, in contrast, allowed for an accurate measurement of the wax coverage. At 15.7 ± 2.6 $\mu g \cdot cm^{-2}$, it was the same as the wax coating of a wheat leaf (Figure 6). The wax coating of the technical surface thus corresponded in its chemical properties both qualitatively and quantitatively to the wax coating of the natural surface.

Wetting properties

Natural surface

The wetting behavior of a plant surface is relevant for the interaction of the plant with its biological and non-biological environment. For instance, surface moisture plays a crucial role in the development of fungal diseases in plants [74]. Also, the wettability has to be considered in the context of the application of agrochemicals [75]. Thus, as a criterion for success it can be postulated that an artificial in vitro test system should reflect the wettability of the native surface. Consequently, in addition to wax morphology and wax chemistry, the wettability of wheat leaves was investigated.

Often, only the CAs are used to describe the wettability. However, specifying CAs alone to describe wettability can be misleading and insufficient [75,76]. For example, a droplet with a high CA may stick to an inclined surface or roll off easily, depending on the wettability state. Therefore, the CAH and the TA of wheat leaves were also determined the present work.

The investigated wheat leaves were all hydrophobic (Table 1), which is in agreement with results of previous studies [29,50,77,78]. The CAH values ranged from 8.2° ± 8.3° to 25.0° ± 10.3° and the TAs ranged from 10.8° ± 7.3° to 31.3° ± 21.3° (Table 1). Wheat leaves are not vertically oriented to the plant axis. TAs provide information on droplet adhesion on such inclined surfaces. For wheat leaves, we could not find any comparative values for TAs in the literature. In the context of active ingredient application and uptake, Peirce et al. [78] investigated the retention of applied water droplets on wheat leaves. In this study, high CAs and very low CAH were also found, which indicates the ability for self-cleaning. However, the investigated plants were cultivated in the greenhouse. Weather-related damage to the leaves of the outdoor plants examined in the present study possibly caused the larger CAH and TAs and the high standard deviations.

Droplets generally rolled off rapidly from the wheat leaves. Microscopic images taken during the wetting measurements indicated that the water droplets did not completely fill the space between the anticlinal cell walls. Both observations suggest

Cassie wetting or intermediate wetting. Cassie wetting was also assumed in a previous wettability study on wheat leaves [78]. In individual specimens, however, the water droplets remained attached to the surface and did not roll off even at a TA of 90°. In such samples, the wax layer was probably damaged or contaminated. Both wax alteration and contamination can lead to a change in wettability [75,79]. No damage or contamination was visible to the naked eye in the leaves used. SEM images of the leaves from the field cultures, however, showed clear damage in the wax layer (removed and flattened crystals) on the leaf surfaces in some cases (Supporting Information File 1, Figure S3). Presumably, a transition to Wenzel wetting takes place at damaged or dirty areas, so that the droplets no longer roll off. In the case of a drop on a rough surface, liquid is pressed between the cavities by the Laplace pressure. If the liquid penetrates into the cavities so far that it touches the substrate, a transition of the wetting states takes place [75]. Whether a transition occurs or not is influenced by the shape and dimensions of the supporting structures and by the droplet size [80]. In the present study, the droplet volume was always the same, but the structures determining the wetting may have been destroyed or masked by particles such that a transition could take place. To evaluate the wetting properties, it is advisable to use plants from greenhouse cultures, as their surfaces are less heterogeneous. The experiments in this work have shown that wax morphology and wax composition were barely influenced by the cultivation conditions (Figure 6). Nevertheless, plants in greenhouse cultures are better protected from phytopathogens and from wind and rain abrasion of wax. In this work, however, the wettability of outdoor grown plants was studied to be close to natural conditions.

Artificial surfaces

In this work, an artificial leaf surface was developed which, in addition to the same wax chemistry, also should have the same wetting properties as a natural leaf. This goal was achieved by vapor deposition with the medium amount of the wax extract. The surface coated in this way resembled the natural surface regarding all three studied wetting parameters (Figure 8).

The chemical analysis had shown that the wax composition of the wax coating on glass corresponds to that of the natural leaf surface. However, not only the wax chemistry but also the wax structure plays a role for the wettability. The different amounts of wax used made it possible to vary the structures and, thus, the wettability of the artificial surfaces. For example, the CA of the artificial surface covered with the small amount of evaporated wax was smaller than that of the wheat leaf. Hence, these artificial surfaces were more wettable than the natural ones (Figure 8a). Water droplets deposited did not roll off even at TAs of up to 90°. Presumably the water drops are not on the structures but sink in between them, resulting in Wenzel wetting [33]. On microstructured Si wafers, it could be shown that, depending on the height and the distance of the supporting columns of the surface, a transition from Cassie wetting to Wenzel wetting takes place. These and other criteria for the transition of a wetting stage were summarized by Bhushan and Jung [73].

The artificial surfaces vapor-deposited with 1400 and 2800 µg wax were as hydrophobic as the wheat leaves. However, the wax coating of the surface coated with 2800 µg appeared to be unstable. It seemed that rolling droplets carried wax particles on their surface and left a slight trace in the coating (data not shown). No loss of wax was observed on the artificial surface that was vapor-deposited with 1400 µg wax.

Utilization of the artificial leaf surface

Here, an artificial leaf surface was developed that mimics the physicochemical properties of a natural leaf surface. The morphology of the recrystallized structures was not a 1:1 copy of the native structures, but the properties were still transferred. This proves that the thermal evaporation process made it possible to transfer the surface properties of the native surface to the technical surface. To the best of the authors' knowledge, no artificial surface exists to date that reflects the wetting properties in addition to the chemistry of the epicuticular waxes. In previous studies, sophisticated systems provided with wax mixtures or with individual wax components were used to investigate the germination behavior of fungal spores [62,81-83]. These had the same wax chemistry, but the wettability was higher than that of the leaf surface. Also in this study, fungal spores were applied to the artificial leaf surface as a first application test. The microscopic analysis showed that the spores germinate and differentiate on the artificial leaf surface. Even though the number of germinated spores was lower than on the natural leaf, the spores were able to germinate on our artificial leaf surface. Hence, the here developed artificial leaf surface offers an opportunity to study interactions of the plant surface ex situ. In contrast to the natural leaf, the artificial leaf surface is less complex and easily adjustable.

Conclusion

In this work, an artificial leaf surface was developed by vapor depositing a wax mixture on glass substrates, which mimics the physicochemical properties of a natural leaf. The thermal evaporation process allowed for a homogeneous coating of the glass with three-dimensional structures. By coating with the medium amount of wax (1400 µg), the wettability and the wax composition of the wheat leaf surface could be successfully transferred to the technical surface. For native and artificial leaf surfaces, a detailed wettability and chemical analysis was performed to

ensure that the artificial system represented the physicochemical characters of the natural leaf surface. With this biomimetic surface, a test system is available for the first time that represents both the chemical signals of the waxes and the wettability of the plant surface. Such an artificial leaf surface offers promising possibilities to investigate interfacial phenomena of the plant surface in detail under controlled conditions. In addition to study the germination of phytopathogenic fungi, other conceivable uses would be, for example, to study the application and retention of various liquids and active ingredients.

Supporting Information

Supporting Information includes a photograph of a harvested wheat plant at the five-leaf stage (Figure S1) to show which leaves were used for the experiments, SEM micrographs of crystalline wax platelets on both sides of wheat leaves of different ages (Figure S2), a micrograph of damage in the wax layer of a wheat leaf of plant cultivated outdoors (Figure S3), and a diagram of the chemical composition of wheat wax of leaves of different ages (Figure S4).

Supporting Information File 1

Additional experimental data.
[https://www.beilstein-journals.org/bjnano/content/supplementary/2190-4286-13-83-S1.pdf]

ORCID® iDs

Miriam Anna Huth - https://orcid.org/0000-0003-4492-4654
Axel Huth - https://orcid.org/0000-0002-3749-4361
Lukas Schreiber - https://orcid.org/0000-0001-7003-9929
Kerstin Koch - https://orcid.org/0000-0003-4311-4481

References

1. Zeisler-Diehl, V. V.; Barthlott, W.; Schreiber, L. Plant Cuticular Waxes: Composition, Function, and Interactions with Microorganisms. In *Hydrocarbons, Oils and Lipids: Diversity, Origin, Chemistry and Fate;* Wilkes, H., Ed.; Springer International Publishing: Cham, Switzerland, 2018; pp 1–16. doi:10.1007/978-3-319-54529-5_7-1
2. Tukey, H. B., Jr. *Annu. Rev. Plant Physiol.* **1970,** *21,* 305–324. doi:10.1146/annurev.pp.21.060170.001513
3. Grant, R. H.; Jenks, M. A.; Rich, P. J.; Peters, P. J.; Ashworth, E. N. *Agric. For. Meteorol.* **1995,** *75,* 263–281. doi:10.1016/0168-1923(94)02210-b
4. Barnes, J. D.; Percy, K. E.; Paul, N. D.; Jones, P.; McLaughlin, C. K.; Mullineaux, P. M.; Creissen, G.; Wellburn, A. R. *J. Exp. Bot.* **1996,** *47,* 99–109. doi:10.1093/jxb/47.1.99
5. Eigenbrode, S. D. *Arthropod Struct. Dev.* **2004,** *33,* 91–102. doi:10.1016/j.asd.2003.11.004
6. Reina-Pinto, J. J.; Yephremov, A. *Plant Physiol. Biochem.* **2009,** *47,* 540–549. doi:10.1016/j.plaphy.2009.01.004
7. Kerstiens, G. *J. Exp. Bot.* **1996,** *47* (Suppl. 1), 50–60. doi:10.1093/oxfordjournals.jxb.a022915
8. Riederer, M.; Schreiber, L. *J. Exp. Bot.* **2001,** *52,* 2023–2032. doi:10.1093/jexbot/52.363.2023
9. Koch, K.; Bhushan, B.; Barthlott, W. *Prog. Mater. Sci.* **2009,** *54,* 137–178. doi:10.1016/j.pmatsci.2008.07.003
10. Jetter, R.; Kunst, L.; Samuels, A. Composition of plant cuticular waxes. In *Biology of the plant cuticle;* Riederer, M.; Müller, C., Eds.; Blackwell Publishing: Oxford, UK, 2006; pp 145–181. doi:10.1002/9780470988718.ch4
11. Nawrath, C. *Curr. Opin. Plant Biol.* **2006,** *9,* 281–287. doi:10.1016/j.pbi.2006.03.001
12. Jetter, R.; Schäffer, S.; Riederer, M. *Plant, Cell Environ.* **2000,** *23,* 619–628. doi:10.1046/j.1365-3040.2000.00581.x
13. Buschhaus, C.; Jetter, R. *J. Exp. Bot.* **2011,** *62,* 841–853. doi:10.1093/jxb/erq366
14. Ensikat, H. J.; Neinhuis, C.; Barthlott, W. *Int. J. Plant Sci. (Chicago, IL, U. S.)* **2000,** *161,* 143–148. doi:10.1086/314234
15. Koch, K.; Neinhuis, C.; Ensikat, H.-J.; Barthlott, W. *J. Exp. Bot.* **2004,** *55,* 711–718. doi:10.1093/jxb/erh077
16. Koch, K.; Ensikat, H.-J. *Micron* **2008,** *39,* 759–772. doi:10.1016/j.micron.2007.11.010
17. Jeffree, C. E.; Baker, E. A.; Holloway, P. J. *New Phytol.* **1975,** *75,* 539–549. doi:10.1111/j.1469-8137.1975.tb01417.x
18. Jetter, R.; Riederer, M. *Bot. Acta* **1995,** *108,* 111–120. doi:10.1111/j.1438-8677.1995.tb00840.x
19. Koch, K.; Bhushan, B.; Barthlott, W. Multifunctional plant surfaces, smart materials. In *Handbook of Nanotechnology;* Bhushan, B., Ed.; Springer: Berlin, Heidelberg, 2010; pp 1399–1436. doi:10.1007/978-3-642-02525-9_41
20. Koch, K.; Barthlott, W.; Koch, S.; Hommes, A.; Wandelt, K.; Mamdouh, W.; De-Feyter, S.; Broekmann, P. *Planta* **2006,** *223,* 258–270. doi:10.1007/s00425-005-0081-3
21. Koch, K.; Dommisse, A.; Barthlott, W. *Cryst. Growth Des.* **2006,** *6,* 2571–2578. doi:10.1021/cg060035w
22. Koch, K.; Dommisse, A.; Niemietz, A.; Barthlott, W.; Wandelt, K. *Surf. Sci.* **2009,** *603,* 1961–1968. doi:10.1016/j.susc.2009.03.019
23. Huth, M. A.; Huth, A.; Koch, K. *Beilstein J. Nanotechnol.* **2021,** *12,* 939–949. doi:10.3762/bjnano.12.70
24. Barthlott, W.; Neinhuis, C.; Cutler, D.; Ditsch, F.; Meusel, I.; Theisen, I.; Wilhelmi, H. *Bot. J. Linn. Soc.* **1998,** *126,* 237–260. doi:10.1111/j.1095-8339.1998.tb02529.x
25. Leveau, J. H. J. *Curr. Opin. Microbiol.* **2019,** *49,* 41–49. doi:10.1016/j.mib.2019.10.002
26. Doan, H. K.; Leveau, J. H. J. *Phytopathology* **2015,** *105,* 1036–1042. doi:10.1094/phyto-02-15-0050-rvw
27. Koch, K.; Bhushan, B.; Barthlott, W. *Soft Matter* **2008,** *4,* 1943–1963. doi:10.1039/b804854a
28. Holder, C. D. Advances and future research directions in the study of leaf water repellency. In *Forest-Water Interactions;* Levia, D. F., Ed.; Springer International Publishing: Cham, Switzerland, 2020; pp 261–278. doi:10.1007/978-3-030-26086-6_11
29. Holloway, P. J. *Pestic. Sci.* **1970,** *1,* 156–163. doi:10.1002/ps.2780010411
30. Koch, K.; Barthlott, W. *Philos. Trans. R. Soc., A* **2009,** *367,* 1487–1509. doi:10.1098/rsta.2009.0022
31. Barthlott, W.; Mail, M.; Neinhuis, C. *Philos. Trans. R. Soc., A* **2016,** *374,* 20160191. doi:10.1098/rsta.2016.0191

32. Young, T. *Philos. Trans. R. Soc. London* **1805,** *95,* 65–87. doi:10.1098/rstl.1805.0005
33. Wenzel, R. N. *Ind. Eng. Chem.* **1936,** *28,* 988–994. doi:10.1021/ie50320a024
34. Cassie, A. B. D.; Baxter, S. *Trans. Faraday Soc.* **1944,** *40,* 546–551. doi:10.1039/tf9444000546
35. Bormashenko, E. Y. *Physics of wetting: Phenomena and applications of fluids on surfaces;* Walter de Gruyter: Berlin, Germany, 2017. doi:10.1515/9783110444810
36. Law, K.-Y.; Zhao, H. *Surface wetting: characterization, contact angle, and fundamentals;* Springer International Publishing: Cham, Switzerland, 2016. doi:10.1007/978-3-319-25214-8
37. Roach, P.; Shirtcliffe, N. J.; Newton, M. I. *Soft Matter* **2008,** *4,* 224–240. doi:10.1039/b712575p
38. Koch, K.; Grichnik, R. *Philos. Trans. R. Soc., A* **2016,** *374,* 20160183. doi:10.1098/rsta.2016.0183
39. Gorb, E.; Böhm, S.; Jacky, N.; Maier, L.-P.; Dening, K.; Pechook, S.; Pokroy, B.; Gorb, S. *Beilstein J. Nanotechnol.* **2014,** *5,* 1031–1041. doi:10.3762/bjnano.5.116
40. Bhushan, B.; Jung, Y. C.; Niemietz, A.; Koch, K. *Langmuir* **2009,** *25,* 1659–1666. doi:10.1021/la802491k
41. Pechook, S.; Pokroy, B. *Adv. Funct. Mater.* **2012,** *22,* 745–750. doi:10.1002/adfm.201101721
42. Niemietz, A.; Wandelt, K.; Barthlott, W.; Koch, K. *Prog. Org. Coat.* **2009,** *66,* 221–227. doi:10.1016/j.porgcoat.2009.07.009
43. Chambers, T. C.; Ritchie, I. M.; Booth, M. A. *New Phytol.* **1976,** *77,* 43–49. doi:10.1111/j.1469-8137.1976.tb01499.x
44. Jetter, R.; Riederer, M. *Planta* **1994,** *195,* 257–270. doi:10.1007/bf00199686
45. Meusel, I.; Neinhuis, C.; Markstädter, C.; Barthlott, W. *Plant Biol.* **2000,** *2,* 462–470. doi:10.1055/s-2000-5961
46. Koch, K.; Bhushan, B.; Jung, Y. C.; Barthlott, W. *Soft Matter* **2009,** *5,* 1386. doi:10.1039/b818940d
47. Deegan, R. D.; Bakajin, O.; Dupont, T. F.; Huber, G.; Nagel, S. R.; Witten, T. A. *Nature* **1997,** *389,* 827–829. doi:10.1038/39827
48. Truskett, V. N.; Stebe, K. J. *Langmuir* **2003,** *19,* 8271–8279. doi:10.1021/la030049t
49. Troughton, J. H.; Hall, D. M. *Aust. J. Biol. Sci.* **1967,** *20,* 509–526. doi:10.1071/bi9670509
50. Netting, A. G.; von Wettstein-Knowles, P. *Planta* **1973,** *114,* 289–309. doi:10.1007/bf00387943
51. von Wettstein-Knowles, P. *J. Ultrastruct. Res.* **1974,** *46,* 483–498. doi:10.1016/s0022-5320(74)90069-0
52. Adamski, N. M.; Bush, M. S.; Simmonds, J.; Turner, A. S.; Mugford, S. G.; Jones, A.; Findlay, K.; Pedentchouk, N.; von Wettstein-Knowles, P.; Uauy, C. *Plant J.* **2013,** *74,* 989–1002. doi:10.1111/tpj.12185
53. Wang, Y.; Wang, J.; Chai, G.; Li, C.; Hu, Y.; Chen, X.; Wang, Z. *PLoS One* **2015,** *10,* e0143671. doi:10.1371/journal.pone.0143671
54. Wang, J.; Jeewani, D. C.; Wang, Z. *Int. J. Agric. Biol.* **2019,** *21,* 1249–1255.
55. BAKER, E. A. *New Phytol.* **1974,** *73,* 955–966. doi:10.1111/j.1469-8137.1974.tb01324.x
56. Jetter, R.; Riederer, M.; Lendzian, K. J. *New Phytol.* **1996,** *133,* 207–216. doi:10.1111/j.1469-8137.1996.tb01887.x
57. Koch, K.; Hartmann, K. D.; Schreiber, L.; Barthlott, W.; Neinhuis, C. *Environ. Exp. Bot.* **2006,** *56,* 1–9. doi:10.1016/j.envexpbot.2004.09.013
58. Bhushan, B.; Koch, K.; Jung, Y. C. *Soft Matter* **2008,** *4,* 1799–1804. doi:10.1039/b808146h
59. Bhushan, B.; Koch, K.; Jung, Y. C. *Ultramicroscopy* **2009,** *109,* 1029–1034. doi:10.1016/j.ultramic.2009.03.030
60. Bhushan, B.; Koch, K.; Jung, Y. C. *Appl. Phys. Lett.* **2008,** *93,* 093101. doi:10.1063/1.2976635
61. Tulloch, A. P. *Phytochemistry* **1973,** *12,* 2225–2232. doi:10.1016/0031-9422(73)85124-6
62. Hansjakob, A.; Bischof, S.; Bringmann, G.; Riederer, M.; Hildebrandt, U. *New Phytol.* **2010,** *188,* 1039–1054. doi:10.1111/j.1469-8137.2010.03419.x
63. Bianchi, G.; Lupotto, E.; Borghi, B.; Corbellini, M. *Planta* **1980,** *148,* 328–331. doi:10.1007/bf00388119
64. Bi, H.; Kovalchuk, N.; Langridge, P.; Tricker, P. J.; Lopato, S.; Borisjuk, N. *BMC Plant Biol.* **2017,** *17,* 85. doi:10.1186/s12870-017-1033-3
65. Racovita, R. C.; Hen-Avivi, S.; Fernandez-Moreno, J.-P.; Granell, A.; Aharoni, A.; Jetter, R. *Phytochemistry* **2016,** *130,* 182–192. doi:10.1016/j.phytochem.2016.05.003
66. Zhang, Z.; Wei, W.; Zhu, H.; Challa, G. S.; Bi, C.; Trick, H. N.; Li, W. *PLoS One* **2015,** *10,* e0140524. doi:10.1371/journal.pone.0140524
67. Jetter, R.; Schäffer, S. *Plant Physiol.* **2001,** *126,* 1725–1737. doi:10.1104/pp.126.4.1725
68. Bringe, K.; Schumacher, C. F. A.; Schmitz-Eiberger, M.; Steiner, U.; Oerke, E.-C. *Phytochemistry* **2006,** *67,* 161–170. doi:10.1016/j.phytochem.2005.10.018
69. Huggins, T. D.; Mohammed, S.; Sengodon, P.; Ibrahim, A. M. H.; Tilley, M.; Hays, D. B. *J. Agron. Crop Sci.* **2018,** *204,* 49–61. doi:10.1111/jac.12227
70. Mohammed, S.; Huggins, T. D.; Beecher, F.; Chick, C.; Sengodon, P.; Mondal, S.; Paudel, A.; Ibrahim, A. M. H.; Tilley, M.; Hays, D. B. *Crop Sci.* **2018,** *58,* 679–689. doi:10.2135/cropsci2017.07.0454
71. Hunsche, M.; Noga, G. *Acta Physiol. Plant.* **2011,** *33,* 1785–1792. doi:10.1007/s11738-011-0717-9
72. Niemietz, A. Molekulare Architektur epikutikularer Wachskristalle und die Generierung biomimetischer Oberflächen zur Analyse von Grenzflächeninteraktionen in mikro- und nanoskaligen Dimensionen. Ph.D. Thesis, Rheinische Friedrich-Wilhelms-Universität Bonn, Bonn, Germany, 2011.
73. Bhushan, B.; Jung, Y. C. *Prog. Mater. Sci.* **2011,** *56,* 1–108. doi:10.1016/j.pmatsci.2010.04.003
74. Huber, L.; Gillespie, T. J. *Annu. Rev. Phytopathol.* **1992,** *30,* 553–577. doi:10.1146/annurev.py.30.090192.003005
75. Taylor, P. *Curr. Opin. Colloid Interface Sci.* **2011,** *16,* 326–334. doi:10.1016/j.cocis.2010.12.003
76. Ras, R. H.; Tian, X.; Bayer, I. S. Superhydrophobic and superoleophobic nanostructured cellulose and cellulose composites. In *Handbook of Nanocellulose and Cellulose Nanocomposites;* Hanieh, K.; Ishak, A.; Sabu, T.; Alain, D., Eds.; Wiley-VCH: Weinheim, Germany, 2017; pp 731–760. doi:10.1002/9783527689972.ch22
77. Dorr, G. J.; Wang, S.; Mayo, L. C.; McCue, S. W.; Forster, W. A.; Hanan, J.; He, X. *Exp. Fluids* **2015,** *56,* 143. doi:10.1007/s00348-015-2012-9
78. Peirce, C. A. E.; Priest, C.; McBeath, T. M.; McLaughlin, M. J. *Soft Matter* **2016,** *12,* 209–218. doi:10.1039/c5sm01380a
79. Koch, K.; Bennemann, M.; Bohn, H. F.; Albach, D. C.; Barthlott, W. *Bioinspiration Biomimetics* **2013,** *8,* 036005. doi:10.1088/1748-3182/8/3/036005
80. Bhushan, B.; Jung, Y. C. *J. Phys.: Condens. Matter* **2008,** *20,* 225010. doi:10.1088/0953-8984/20/22/225010

81. Zabka, V.; Stangl, M.; Bringmann, G.; Vogg, G.; Riederer, M.; Hildebrandt, U. *New Phytol.* **2008,** *177,* 251–263. doi:10.1111/j.1469-8137.2007.02233.x
82. Ringelmann, A.; Riedel, M.; Riederer, M.; Hildebrandt, U. *Planta* **2009,** *230,* 95–105. doi:10.1007/s00425-009-0924-4
83. Hansjakob, A.; Riederer, M.; Hildebrandt, U. *Plant Pathol.* **2011,** *60,* 1151–1161. doi:10.1111/j.1365-3059.2011.02467.x

License and Terms

This is an open access article licensed under the terms of the Beilstein-Institut Open Access License Agreement (https://www.beilstein-journals.org/bjnano/terms), which is identical to the Creative Commons Attribution 4.0 International License (https://creativecommons.org/licenses/by/4.0). The reuse of material under this license requires that the author(s), source and license are credited. Third-party material in this article could be subject to other licenses (typically indicated in the credit line), and in this case, users are required to obtain permission from the license holder to reuse the material.

The definitive version of this article is the electronic one which can be found at:
https://doi.org/10.3762/bjnano.13.83

BEILSTEIN JOURNAL OF NANOTECHNOLOGY

Interaction between honeybee mandibles and propolis

Leonie Saccardi*[1,2], Franz Brümmer[1], Jonas Schiebl[2], Oliver Schwarz[2], Alexander Kovalev[3] and Stanislav Gorb[3]

Full Research Paper

Open Access

Address:
[1]University of Stuttgart, IBBS, Research Unit Biodiversity and Scientific Diving, Stuttgart, Germany, [2]Department Biomechatronic Systems, Fraunhofer Institute for Manufacturing Engineering and Automation IPA, Stuttgart, Germany and [3]Department Functional Morphology and Biomechanics, Zoological Institute, Kiel University, Kiel, Germany

Email:
Leonie Saccardi* - leonie.saccardi@gmx.de

* Corresponding author

Keywords:
adhesion; *Apis mellifera*; bee mandibles; honeybee; propolis

Beilstein J. Nanotechnol. **2022,** *13,* 958–974.
https://doi.org/10.3762/bjnano.13.84

Received: 27 May 2022
Accepted: 17 August 2022
Published: 14 September 2022

This article is part of the thematic issue "Biomimetics on the micro- and nanoscale – The 25th anniversary of the lotus effect".

Associate Editor: K. Koch

© 2022 Saccardi et al.; licensee Beilstein-Institut.
License and terms: see end of document.

Abstract

In a biomimetic top-down process, challenging the problem of resin deposition on woodworking machine tools, an adequate biological model was sought, which hypothetically could have developed evolutionary anti-adhesive strategies. The honeybee (*Apis mellifera*) was identified as an analogue model since it collects and processes propolis, which largely consists of collected tree resin. Propolis is a sticky substance used by bees to seal their hive and protect the colony against pathogens. In spite of its stickiness, honeybees are able to handle and manipulate propolis with their mandibles. We wanted to know if beneficial anti-adhesive properties of bee mandibles reduce propolis adhesion. The anatomy of bee mandibles was studied in a (cryo-)scanning electron microscope. Adhesion experiments were performed with propolis on bee mandibles to find out if bee mandibles have anti-adhesive properties that enable bees to handle the sticky material. A scale-like pattern was found on the inside of the mandible. Fresh mandibles were covered with a seemingly fluid substance that was at least partially removed during the washing process. Propolis adhesion on bee mandibles was measured to be 1 J/m^2 and was indeed significantly lower compared to five technical materials. Propolis adhesion was higher on mandibles that were washed compared to fresh, unwashed mandibles. Results indicate that the medial surface of the mandible is covered with a fluid substance that reduces propolis adhesion. First results suggested that the surface pattern does do not have a direct effect on propolis adhesion.

Introduction

Nature has solutions for many of the problems and challenges humans face, since different creatures have adapted to similar challenges during their evolution. A common problem category in technology is unwanted adhesion; whether it is cake sticking to the cake tray, smeared glasses, or industrial production processes where unwanted build-up occurs. Specifically, this problem also occurs in woodworking processes, where escaping resins contaminate the cutting edge of the tools and, subse-

quently, blunt the carbide cutting edges through abrasion. This was the starting point of a biomimetic top-down development process that led to the anatomical investigation of honeybee mandibles.

The hypothesis is that animal species that regularly have close contact with resinous plants or even actively harvest resins may have developed counter-stickiness strategies. This is because animals that permanently stick to a plant are deprived of further reproduction, which exerts a significant evolutionary selection pressure. The honeybee (*Apis mellifera*) was chosen as a possible model because it collects and processes propolis, a sticky and ductile material, that is created by mixing plant resins, wax, and other substances. Similar to tree resins, which contaminate the surfaces of processing tools, propolis also adheres well to different types of surfaces [1].

Bees use propolis as a building material, for example to seal cracks and smooth out the internal walls of the hive [2,3]. In addition to its mechanical functions, propolis also has chemical properties that protect the colony and contribute to the social immunity [4]. Because of its strongly adhesive nature, propolis is sometimes referred to as bee glue [2,5].

Anatomy of bee body parts handling propolis

The mouthparts of bees are used to collect food, water, and resin [6]. They are therefore adapted to extract liquids as well as to grasp and manipulate objects [5,6]. The mouthparts consist of labrum, mandibles, maxillae, and labium. The labium is used as a tongue to take up liquids while the mandibles are responsible for tasks involving grasping [5,6]. The mandibles of the bee are instrumental in processing propolis, but they are also used for other tasks such as biting through cell caps and modelling wax [7]. The mandibles, sometimes also called jaws, are situated laterally on the lower part of the bee's head (see Figure 3) and operate transversely [7,8]. Mandibles of worker bees are spoon-shaped and differ from those of the queen and drones, which have a more pointed apex and a subapical notch [7,8]. The medial surface of the mandible has not been studied in detail before but has been described as concave and ridged [8]. The cuticle of mandibles is particularly strong due to bonding of long chitin chains and sclerotization (crosslinking of proteins in the cuticle) [6].

Foraging and handling of propolis

Worker bees exhibit a division of labour based on age (polyethism) [9] in which duties such as brood rearing are usually performed by younger bees while middle-aged bees process propolis in the hive and older bees collect resins [10]. Honeybees mainly forage resins from buds, though they also have been reported to collect resin from tree barks and fruit surfaces [4,11,12]. It is also unclear how exactly propolis bees detect suitable resin sources. Some plants might release chemicals that are picked up by bees [4,13]. Some bees have also been observed probing different plants before collecting resin [14]. When they have found a resin source, they start by first biting off a piece of resin and working it with the mandibles [4,15]. The front legs are used to pass the resin from the mandibles to the mid legs and then from there to the corbiculae [15,16]. Once both corbiculae are fully loaded with resin, the propolis bee returns to the hive, where other so-called cementing bees unload it using their mandibles and subsequently mix it with wax [4,15]. The resulting material is now called propolis [4]. Cementing bees then attach propolis to the walls of the hive and smooth it out with their mandibles [10,11]. The mandibles play the most important role in the oral apparatus of bees when processing resin and propolis.

Anti-adhesive strategies in biology

One might expect that highly adhesive substances such as resin and propolis stick to the bee's mouthparts and legs rendering them unusable. But bees are able to process these sticky substances and apparently without being negatively affected by them. It is therefore possible that anti-adhesive properties minimize adhesion of resins and propolis to their body parts. Various anti-adhesive strategies have been found in nature. Different mechanisms can lead to low adhesion. Possible strategies to reduce adhesion on the insect cuticle, as suggested in [16], are specific surface chemistry, surface microstructures, an easy-to-break solid layer preventing strong bonding, or a fluid layer providing cohesion failure.

Resin adhesion on stingless bees

One example for possibly anti-adhesive surfaces that is especially relevant to this work, are Bornean stingless bees (Hymenoptera, Meliponini). Similar to honeybees, stingless bees harvest resin to build their nests and defend it against intruders [17]. Resin can easily be removed from the mandible surface without leaving residue behind [18,19]. It was therefore suggested that stingless bees might temporarily lubricate their mandibles to reduce resin adhesion [19]. In [20], it was observed that stingless bees were not able to handle propolis until they reached a certain age. They suggested that this might be due to gland development and production of glandular substances [20].

Objective

The main objective of this work was to understand the interaction between honeybee mandibles and propolis. The hypothesis is that beneficial anti-adhesive properties have evolved to handle propolis without being hindered by resin contamination. Possibly, these anti-adhesive properties could serve as an inspi-

ration to help solve problems such as resin contaminating woodworking tools.

The anatomy of bee mandibles has previously been described [6-8,19], though not with a detailed focus on the medial surface of the mandible tip (see below in Figure 3B). However, this part is especially interesting in terms of propolis processing, since this surface is in intensive contact with the sticky material during biting and shaping it. Therefore, the anatomy of bee mandibles was studied, focusing on the medial surface of the mandible tip to find possible reasons for reduced adhesion. Once physical and adhesive propolis properties as well as the anatomy of bee mandibles were characterized, it was possible to test whether propolis adhesion is indeed reduced on bee mandibles. Therefore, adhesion experiments with propolis were performed on bee mandibles.

Materials and Methods

Propolis and insects

Propolis

Raw propolis provided by private beekeeper Dr. Oliver Schwarz (Stuttgart, Germany) (Figure 1A) was harvested and homogenised as described in [1]. For homogenisation, propolis chunks were mixed, frozen finely ground and subsequently stored at −20 °C (Figure 1B). The pulverizing procedure was based on a method that is used to produce propolis extract [21]. To prevent contamination, propolis was only handled wearing gloves cleaned with ethanol (Rotipuran®, ≥99.8%, p.a., Carl Roth GmbH & Co. KG, Karlsruhe, Germany).

Insects

Adult worker bees (*Apis mellifera*) were collected in gardens in Kiel (Germany) in July 2019 and immediately used for experiments. They are hereinafter referred to as „nectar collectors“. In October 2018, bees were taken directly from the hive (Stuttgart, Germany). They are further named „hive bees“. They were kept in a cage and provided with water and honey until they were prepared for experiments. The remaining bees were frozen and stored at −20 °C for three months to be used in further experiments.

Honeybees (*Apis mellifera*), returning to the hive with resin attached to their pollen baskets, were caught and subsequently frozen in September and October 2018. These resin-collecting bees will be henceforth referred to as “propolis bees”.

Imaging and structural studies

Bee mandibles were prepared and subsequently examined with binoculars, a scanning electron microscope (SEM), and a confocal 3D laser scanning microscope in order to identify anatomy and surface structure.

Anatomy of the honeybee mandible

Mandibles of all collected bees were prepared under binoculars by carefully separating them from the insect’s head with a scalpel (Figure 2). General morphology, structures, and contamination of every prepared mandible were studied with a binocular microscope (Leica M205 A, Leica Microsystems GmbH, Wetzlar, Germany) equipped with a camera (Leica DFC420) prior to further experiments. For the following anatomical studies, mandibles of nectar collector and hive bees were then washed with acetone and water. They were air-dried, mounted on holders (inside up), sputter-coated with a 10 nm thick layer of gold–palladium and studied using a SEM (Hitachi S-4800, Hitachi High-Technologies Corp., Tokyo, Japan) at 3 kV accelerating voltage. Images of the spoon-shaped mandible tip were

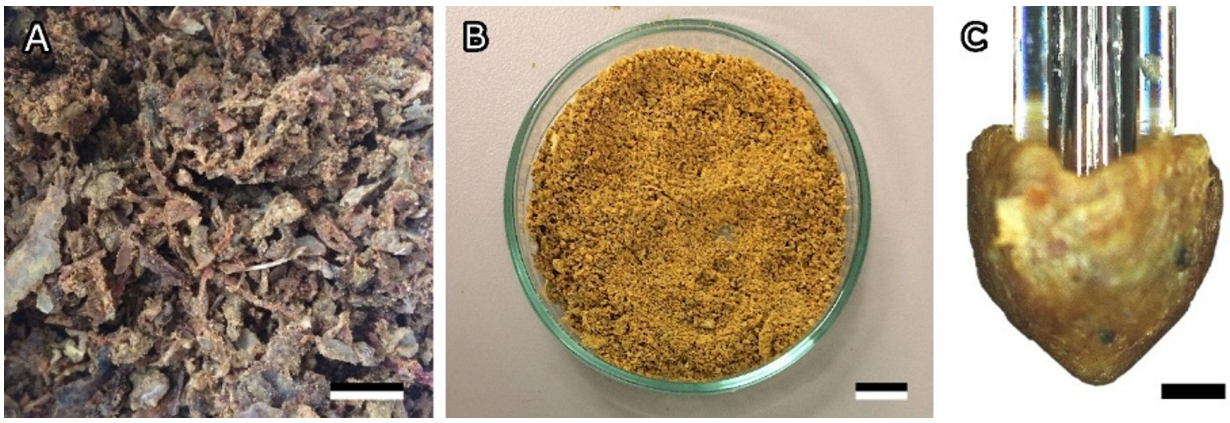


Figure 1: Bee propolis. (A) Raw propolis as collected from the hive. (B) Homogenised propolis powder. (C) Cone-shaped propolis sample used for adhesion tests. Scale bar: 1 cm (A, B), 500 µm (C). Figure 1 was reproduced from [1] (© 2021 Saccardi, Schiebl, Weber, Schwarz, Gorb and Kovalev, published by Frontiers, distributed under the terms of the Creative Commons Attribution 4.0 International License, https://creativecommons.org/licenses/by/4.0).

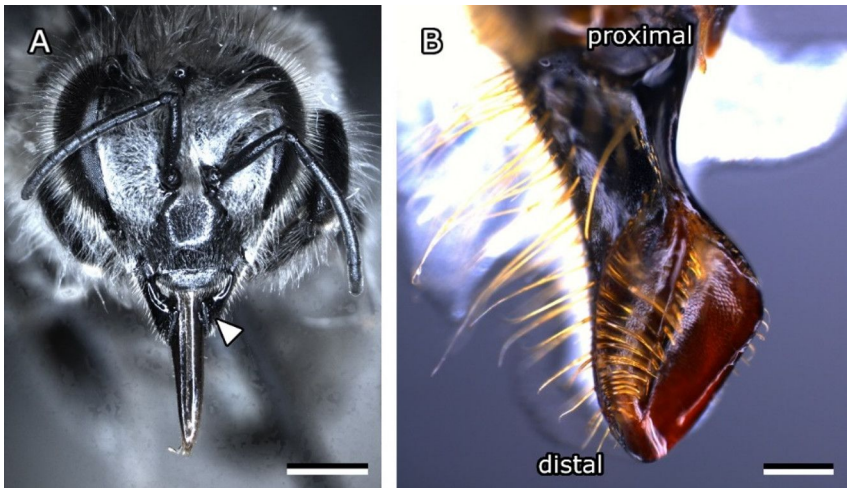


Figure 2: Head and mandible of a worker bee. (A) Frontal view of a honeybee head with an arrow pointing to the outside of the left mandible. Scale bar: 1 mm. (B) Medial surface of the left mandible of a worker bee. Proximal and distal ends are marked. Scale bar: 200 µm.

taken systematically and later assembled into one high resolution image. Higher magnified pictures were taken in characteristic areas of the mandible surface. For one additional experiment, instead of air-drying, four washed mandibles were dried using a critical-point-drier (Leica EM CPD300) and subsequently studied in the SEM.

Surface structures on bee mandibles

Surface structures on mandibles were studied in the SEM as described above. Additionally, the medial surface profile of the mandible was studied on fresh, chloroform-washed specimens fixed to a glass slide using a drop of a melted mixture of 50% paraffin wax and 50% colophony. The mandibles were examined with a confocal 3D laser scanning microscope (Keyence VK-X250; Keyence Corporation, Osaka, Japan). The MultiFile-Analyser software (Version 1.2.6.106, Keyence Corporation, Osaka, Japan) was used to measure profiles and the structural dimensions in different areas of the mandible.

Surface structures on propolis bee mandibles

Freshly defrosted and prepared mandibles of propolis bees were studied in the cryo-SEM in the frozen state so the resin contaminations did not dry out. They were placed on holders (medial surface up), rapidly frozen on the table in the preparation chamber at −140 °C, sputter coated with gold palladium (3 nm), and studied at −120 °C with a cryoSEM (Hitachi S-4800, Hitachi High-Technologies Corp., Tokyo, Japan) equipped with a cryopreparation system (Gatan ALTO 2500, Gatan, Inc., Abingdon, UK) at 3 kV accelerating voltage.

Image processing

SEM images were processed using Gimp, version 2.10.14. All adjustments were applied to the whole image. Color levels, contrast, and brightness were adjusted, and scale bars and other labels were added. Profiles measured with the confocal 3D laser scanning microscope were digitized using WebPlotDigitizer (version 4.2, https://automeris.io/WebPlotDigitizer, Ankit Rohatgi, San Francisco, USA).

Investigation of propolis adhesion on mandibles

Insect preparation for adhesion tests

After insects for experiments were caught, they were placed and stored in the freezer at −20 °C for a minimum of 15 min and up to many months. The mandibles were prepared as described above (Figure 2). Without further treatment a mandible was then glued, inside facing up, to a glass slide using a drop of a melted mixture of 50% paraffin wax and 50% colophony to avoid unwanted movement during adhesion experiments. The spoon-shaped, distal part of the mandible was oriented using a binocular microscope so that the flat area near the sharp edge of the mandible was parallel to the glass surface. Adhesion experiments on mandibles were carried out immediately after fixing the mandible to the slide to avoid material desiccation.

Test method

Adhesion experiments were performed in a manner similar to that in [1]. Just before each adhesion experiment, a small amount of homogenised propolis powder was defrosted and kneaded into a homogeneous mass. Cone-shaped propolis samples with a spherical tip were subsequently formed by hand wearing ethanol-cleaned gloves (Figure 1C). The topography of the sample was analysed using a 3D optical profilometer (Keyence VR 3100; Keyence Corporation, Osaka, Japan). The profile of the sample was measured along five lines arranged in a star shape going through the highest point of the tip. To esti-

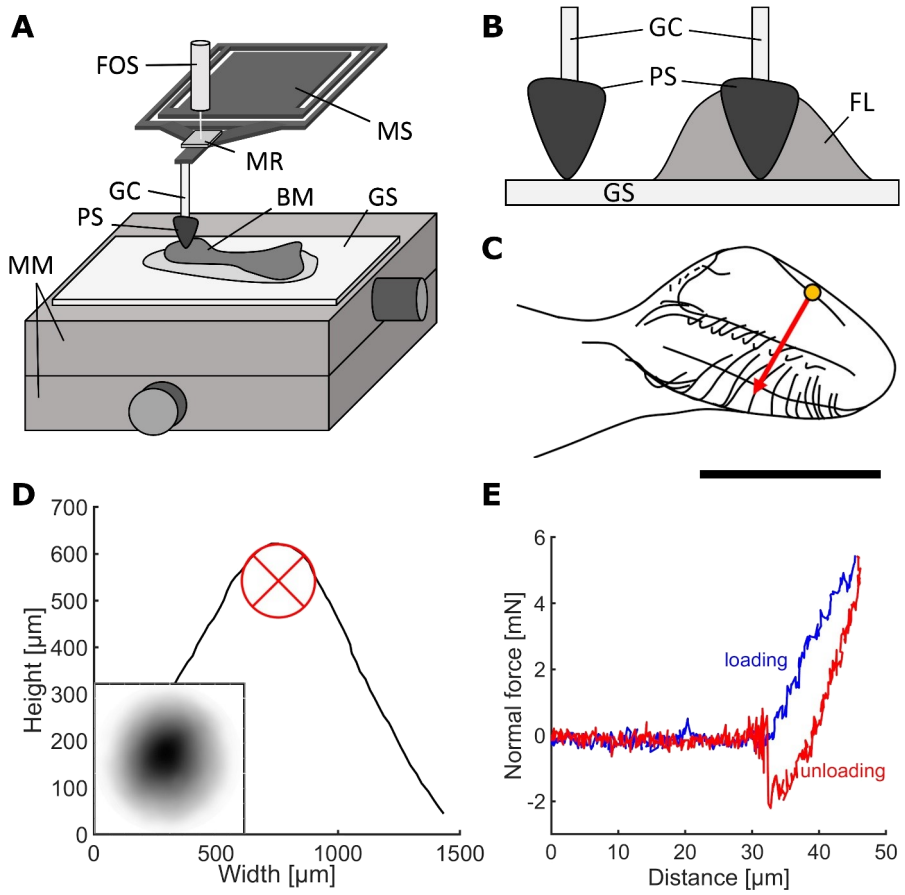


Figure 3: Adhesion experiments. (A) Experimental set-up for adhesion testing with the Basalt-01 mechanical tester (Tetra GmbH). (B) Propolis contact in the presence of fluid (mineral oil) and without fluid. (C) Schematic of a bee mandible. Adhesion measurements were conducted along the arrow, the circle represents the size of the contact area. Scale bar: 500 µm. (D) 3D profile of a propolis sample. The inscribed circle was used to estimate the tip radius. The small subimage depicts the sample topography with darker areas being higher than lighter areas. (E) Typical force–distance curve obtained from adhesion experiments. BM, bee mandible (optional); FL, fluid; FOS, fibre-optic sensor; GC, glass capillary; GS, glass slide or other substrate material; MM, micro-manipulators; MR, mirror; MS, metal spring; PS, propolis sample. Figure 3A was adapted and Figure 3B, D, and E were reproduced from [1] (© 2021 Saccardi, Schiebl, Weber, Schwarz, Gorb and Kovalev, published by Frontiers, distributed under the terms of the Creative Commons Attribution 4.0 International License, https://creativecommons.org/licenses/by/4.0).

mate the radius at the sample tip, a circle was fitted to the sample profiles in the five orientations (Figure 3D). The radii of the circles were measured and then averaged.

The effective elastic modulus and pull-off force of propolis were measured with a microforce measurement device (Basalt-01; Tetra GmbH, Ilmenau, Germany) [22-24]. The device mainly consists of micromanipulators as a platform holding the substrate material, a metal spring (springs with spring constants of 618 N/m and 539 N/m were used) and a fibre-optic sensor (Figure 3A). The piezo drive moves the spring down to load and up to unload the sample. A shortened glass capillary (5 µL micropipet Blaubrand® IntraEND, Brand GmbH & Co. KG, Wertheim, Germany) was attached to the metal spring with cyanoacrylate glue (5925 Ergo® Elastomer–Kisling GmbH, Bad Mergentheim, Germany). The freshly formed, cone-shaped sample of propolis was then mounted on the tip of the capillary without any additional glue. The propolis sample was brought into contact with the substrate and retracted from the surface as soon as the load force reached 5 mN. The load was chosen to resemble the force applied by bees when handling propolis. As no studies exist on mandibular forces and pressures of honeybees, pressures measured at the tip of mandibles of predacious coleoptera [25] where used as a reference point. Tip pressures were calculated as suggested by [25]:

$$P = \frac{F_a}{A}, \quad (1)$$

where F_a is the applied force and A is the contact area obtained from the contact radius.

With each propolis sample, a set of ten single measurements was performed, each on a different spot on the spoon-shaped tip

of the bee mandible, starting at the sharp edge and moving towards the hairy edge (Figure 3C). Another measurement with an extended contact time of 60 s was performed on the flat area of the bee mandible. Afterwards, six reference measurements were carried out on a smooth, clean glass surface (standard microscopy slides (soda lime glass); Carl Roth GmbH & Co. KG, Karlsruhe, Germany) with the same propolis sample.

Experiments were carried out at room temperature (24.00 ± 0.53 °C) and a relative humidity of 36.80% ± 9.0%. For every condition, 50–150 single tests were performed on different spots of the mandible (N = 5–15 propolis samples and mandibles, n = 10 measurements on mandible per sample). After the adhesion experiments, the substrate material was examined under a binocular microscope (Leica M205 A) in order to find possible propolis residues/prints in the contact area. Adhesion tests on fresh mandibles were performed in July and November. As a reference, propolis adhesion on bee mandibles was compared to propolis adhesion measured on glass under dry and fluid conditions [1]. For the reference experiments in fluid conditions, a drop of oil (mineral oil, light, Sigma-Aldrich, St. Louis, USA) was placed on the glass surface as described in [1] and shown in Figure 3B. Oil was chosen because we assumed that the mandibles surface might be oily.

Evaluation of a potential coating of the mandibles

As previously suggested, a fluid layer covering the mandible surface could be a strategy to reduce adhesion [16]. Therefore, fresh, untreated bee mandibles were studied in the frozen state, as cryo-SEM has been reported to be a successful method for visualizing biological fluids such as lipids and water-based solutions [26]. Cryo-SEM was performed as described in section “Surface structures on propolis bee mandibles”.

Additionally, visualization of the mandible cuticle and any additional surface layers was performed using cryo-SEM on fresh fractures of untreated bee mandibles. Mandibles were tightly clamped into a metal holder and frozen in the preparation chamber (−140 °C). The samples were then fractured within the preparation chamber by cutting off a part of the mandible tip using a cold scalpel blade mounted on a user-controlled handle. Fractured samples were then sputter coated and examined in a frozen state as described above.

Where possible, the contact angle of the substance coating the mandible surface was measured on SEM images of fresh fractures of untreated bee mandibles using Gimp, version 2.10.14. For this purpose, two measurement lines were drawn: one along the surface of the cuticle and one along the surface of the substance on top of the cuticle. The angle was then measured between the two lines.

Furthermore, different solvents were used to wash fresh mandibles in order to try removing any potential surface coating. Mandibles were washed in an ultrasonic bath with distilled water for 10 min or with either chloroform (Rotisolv® HPLC stabilised with 1% ethanol, Carl Roth GmbH & Co. KG), or acetone (Rotipuran® ≥99.8%, p. a. ACS ISO, Carl Roth GmbH & Co. KG) for 5 min followed by 5 min washing with distilled water. Distilled water was used as an agent for removing hydrophilic substances from the surface of bee mandibles. Chloroform and acetone are known to remove hydrophobic substances and the wax layer from mandibles [27]. The ultrasonic bath facilitates the dissolving procedure and particle removal from the surface.

To visualise the effect of washing, dry untreated mandibles and mandibles treated with the different solvents were examined using a SEM as described before (section “Anatomy of the honeybee mandible”). Mandibles washed with chloroform and water were studied in the cryo-SEM as described above for untreated mandibles.

Adhesion on washed bee mandibles

To test the effect of potential surface coatings on propolis, adhesion experiments with propolis were performed on mandibles washed with the different methods as described for untreated bee mandibles (section “Investigation of propolis adhesion on mandibles”).

Adhesion on resin replicas of bee mandibles

In order to test how shape and surface structures of the mandibles affect adhesion, replicas of bee mandibles were made using a two-step moulding method [26,28]. The method allows one to replicate the surface structure with nanometre precision. Replication substitutes chemical complex and heterogeneous biological surfaces with a well-studied epoxy surface. In this way the effect of surface chemistry on adhesion was excluded. First, washed mandibles fixed to glass slides, as described above (section “Investigation of propolis adhesion on mandibles”), were covered with a two-component dental wax (Affinis light body, ISO 4823, polyvinylsiloxane, Coltène Whaledent AG, Altstätten, Switzerland). After the wax was cured, the mandibles were removed from the mould, the cavity was filled with Spurr epoxy resin (Spurr’s low viscosity kit; Plano, Wetzlar, Germany, composition: vinyl cyclohexene dioxide 10 g, diglycidyl ether of polypropylene glycol 6 g, nonenyl succinic anhydride 26 g, and S-1 dimethylaminoethanol 0.4 g [29]) and covered with a smooth sheet of dental wax to create a level surface for the mandible replica to stand on. The resin

mandibles were cured at 70 °C for 48 h, demoulded and fixed to a glass slide using double-sided adhesive tape. A binocular microscope (Leica M205 A) was used to visually check whether the features of the real mandibles, especially the surface structures, were successfully replicated in the artificial mandibles.

Adhesion experiments with propolis were carried out as described for real bee mandibles (section "Investigation of propolis adhesion on mandibles"). For mandible replicas, reference measurements were performed on the smooth resin substrate. 50–60 single tests were performed on different spots of the mandible replica (N = 5–6 propolis samples and mandibles, n = 10 measurements on mandible per sample).

Data analysis and statistics

Adhesion experiments were evaluated as described in [1] using Matlab, version R2015b. The unloading part of force–distance curves (Figure 3E) acquired from adhesion experiments was fitted according to the JKR theory [30]:

$$a^3 = \frac{3R}{4E}\left[F_\mathrm{a} + 3\pi R\Delta\gamma + \sqrt{6\pi R F_\mathrm{a}\Delta\gamma + \left(3\pi R\Delta\gamma\right)^2}\right], \quad (2)$$

where a is the contact radius, F_a is the applied load, R is the tip radius, and E and $\Delta\gamma$ are the effective elastic modulus and the work of adhesion, respectively. The work of adhesion $\Delta\gamma$ is the energy per unit of area needed to separate two bodies in contact. It was chosen as a measure of adhesion because it is independent of the contact area. To characterize viscoelastic properties of propolis, a generalized Maxwell model was used [31]. The viscosity of the sample was estimated from experimental force curves using the following equation [32,33]:

$$F_\mathrm{a} = \frac{4\sqrt{R}d^{1.5}}{3\left(1-\nu^2\right)}\left(E_\infty + E_1 e^{-\frac{E_1 t}{\eta_1}} + E_2 e^{-\frac{E_2 t}{\eta_2}}\right), \quad (3)$$

where d is the displacement, t is the time under load, $E_\infty/E_1/E_2$ and η_1/η_2 are the Young's moduli and viscosities of the static and the two dynamic components, and ν is the Poisson ratio assumed to be equal to 0.49 [33].

The data were statistically analysed using the software R, version 3.6.1. Data was tested for normal distribution and variance homogeneity using Kolmogorov–Smirnov and Levene's tests, respectively. The comparison of propolis adhesion under different conditions and on different substrates was performed with a one-way ANOVA and a pairwise multiple comparison procedure (Tukey test). An unpaired two-sample t-test was performed to compare the mean Young's modulus of propolis at 24 and 26 °C. Correlation analysis of Young's modulus and work of adhesion obtained from adhesion experiments was performed by calculating the Pearson correlation coefficient.

Results

Honeybee mandible

When bees handle propolis, the mandibles are the first surfaces that will come into contact with plant resin or propolis. They were thus analysed using various imaging methods.

Anatomy of the bee mandible

The anatomy of the worker bee mandibles (*Apis mellifera*) was studied using a binocular microscope and SEM on acetone-cleaned specimens. Mandibles have a strong stem at the proximal end and a concave, spoon-shaped tip at the distal end (Figure 2B). The medial surface of this tip was examined more extensively because it is used by bees to process and form propolis (Figure 4A). The spoon-shaped tip tapers towards the distal apex. On one side it exhibits an edge densely covered by smooth, long, and flexible hairs (hairy edge), reaching over half of the mandible medial surface (Figure 4A,G), while the edge on the opposite site is sharp and hairless (sharp edge). Though, short, thin hairs grow on the mandible outside close to the sharp edge. A ridge runs along the centre of the medial surface of the mandible tip (central ridge) fading towards the apex. It is spiked with stiff, slightly grooved bristles that are curved towards the sharp edge (Figure 4A,D).

An elevated ledge lies next to the hairy edge. The area between the central ridge and the ledge seems to form a channel that runs from the stem to the apex. A groove runs along the inside of the stem merging into the channel area on the tip (Figure 3A,F). On the other side of the central ridge (Figure 3A,D), there is a flat area reaching up to the sharp edge. A smaller ridge starts at the proximal end of the sharp edge and is angled towards the apex but stopping at about the same height as the bristles and hairs. The outside of the mandible is covered with hairs evenly.

Surface structures on bee mandibles

SEM micrographs also revealed that bee mandibles are covered with anisotropic scale-like micropatterns (Figure 4). Most of the scales on the medial surface of the mandible were pentagonal or hexagonal, though the shape and proportions varied depending on the area they cover. The scales in the flat area measured 18.1 ± 2.4 µm/9.55 ± 1.3 µm at their minimum/maximum width, respectively (Figure 4B). However, closer to the apex and the sharp edge, the structures were less pronounced and eventually seemed to fade completely (Figure 4C,E). In the channel area, the structures were rounder (9.34 ± 0.77 µm/8.21 ± 0.82 µm) and had blunt edges

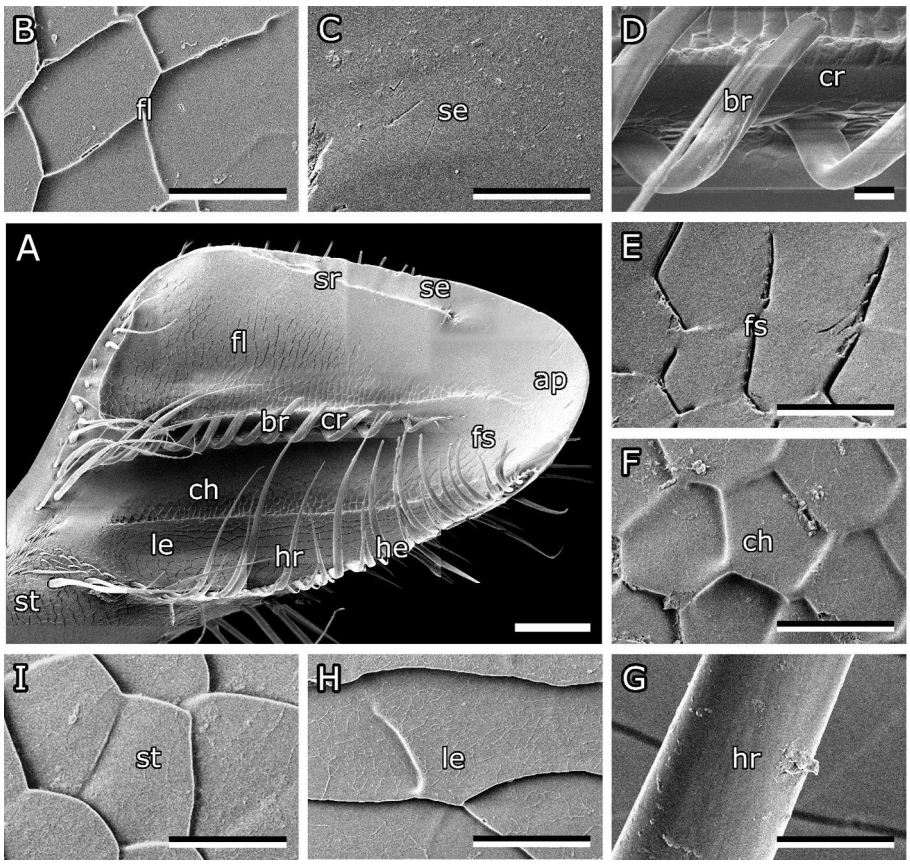


Figure 4: Anatomy of the bee mandible. (A) Medial surface of left bee mandible. Characteristic features are labelled. (B–I) Higher magnified images of areas labelled in (A). (B) Scales in flat area. (C) Smooth surface near the sharp edge. (D) Curved bristles along the central ridge. (E) Fading structures towards the apex. (F) Scales in channel area. (G) Hair growing on the hairy edge. (H) Oblong scales on the ledge. (I) Scales on the stem of the mandible. ap, apex; br, bristles; ch, channel area; cr, central rigde; fl, flat area; fs, faded structures; hr, hair; he, hairy edge; le, ledge; se, sharp edge; sr, small ridge; st, stem. Scale bars 100 µm (A), 10 µm (B–I).

(Figure 4F). Scales on the ledge on the other hand had an oblong shape (31.67 ± 9.34 µm/9.05 ± 2.25 µm) and were oriented parallel to the hairy edge (Figure 4H). The scales on the outside of the mandible are more rounded and form rows of scales that are not clearly separated (12.62 ± 2.71 µm/12.72 ± 1.49 µm) (Figure 4I).

Scale profile

A 3D laser scanning microscope was used to study the topography of these structures on the medial surface of the mandible (Figure 5). The scales are flat or slightly convex and overlap or form steps between them. The step height between the scales was measured to be 0.71 ± 0.26 µm in most areas of the mandible. Though, in areas, were the scale pattern seemed to fade, the step heights were smaller (0.05–0.30 µm). In the flat area the scales descended towards the apex, while scales in the channel area were not oriented in a clear direction and scales on top of the ledge were descending towards the hairy edge.

Propolis bees

For the sake of distinction, we refer to bees that were caught when they returned to the hive with resin attached to their corbiculae as “propolis bees”. Their untreated mandibles were visually examined to compare them to regular worker bees in terms of morphology and contaminations. Mandibles of propolis collecting bees exhibited the same form and features as those of regular worker bees, though they were covered with resin to varying degrees. Some mandibles were completely filled with resin (Figure 6A), while others only had resin remnants stuck in hairs (Figure 6B). However, all types of resin contaminations were easily removed with fine forceps and no resin residues were left behind. Bristles along the central ridge of propolis bees were often more damaged compared to regular worker bees (Figure 4A and Figure 6C). Especially the tips were regularly blunt or broken off. Untreated mandibles of regular worker bees that were not observed collecting propolis were often contaminated with small crumbs and pollen particles but not with resin.

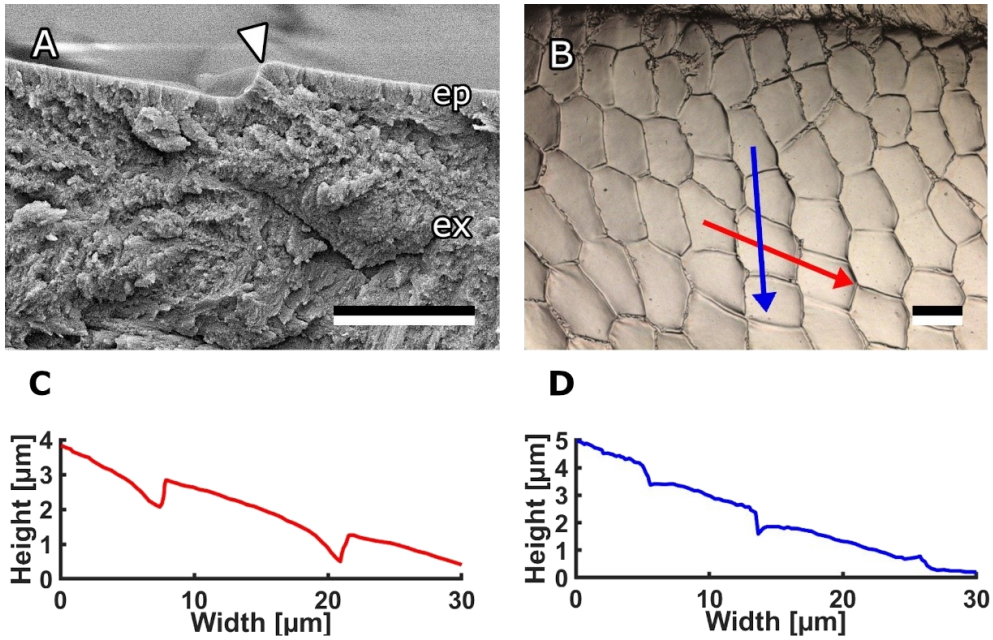


Figure 5: Profile of scales on bee mandibles. (A) Cryo-SEM micrograph of mandible cuticle. The arrowhead indicates the step between two scales. (B) 3D laser scanning microscope image of medial surface of the mandible in the channel area. (C) Profile of scales in along the red arrow in (B). (D) Profile of scales along the blue arrow in (B). Scale bars: 2 µm (A), 10 µm (B).

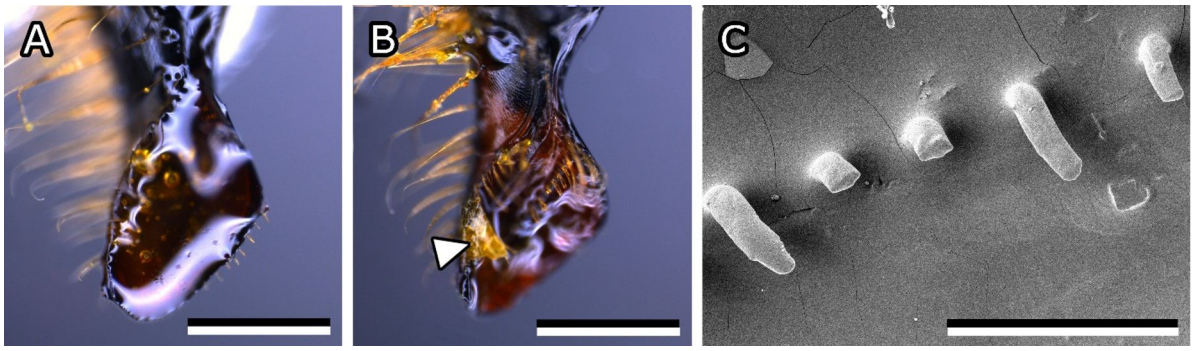


Figure 6: Mandibles of propolis bees. (A) Mandible tip completely covered with resin. (B) Resin residues on mandible. The arrowhead points to resin rests adhering to the hairs on the mandible. (C) SEM micrograph of central ridge and bristles covered by resin. Scale bars: 500 µm (A,B), 100 µm (C).

Propolis adhesion on bee mandibles

The adhesion of propolis samples on several untreated bee mandibles (BM) was measured to determine whether mandibles of bees possess anti-adhesive properties. No statistical differences were found between work of adhesion values of single measurements that were conducted on different positions of the bee mandible (P = 0.995). For some measurements, near the hairy edge of the bee mandible the point of contact was not clearly distinguishable in the loading curve due to hair touching the sample before it contacted the cuticle. However, in the unloading curve the adhesive failure (pull-off) was easy to identify in most cases.

In contrast to the pull-off force, the work of adhesion does not depend on the radius of the sample. Therefore, the work of adhesion value is hereafter used to compare adhesion from different adhesion experiments. Adhesion of propolis on fresh and previously frozen bee mandibles was compared to the data obtained on glass in dry and fluid conditions (in oil) (Figure 7A, Table 1). An analysis of variance (ANOVA) was performed to find out, whether statistical differences exist between adhesion values on these surfaces. The P-value was found to be smaller than the significance level α = 0.001. Therefore, a posthoc Tukey test was conducted to find pairwise differences. P-values smaller than α = 0.05 were found to be significant.

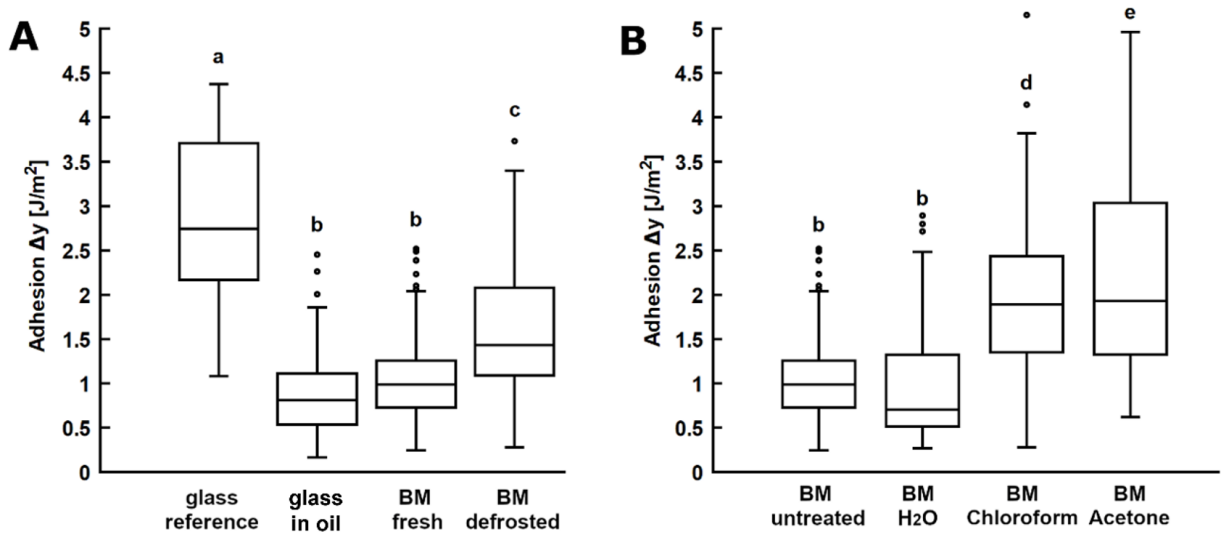


Figure 7: Propolis adhesion on bee mandibles. (A) Adhesion of propolis on bee mandibles compared to glass. Adhesion experiments with propolis samples were carried out on the following substrates: a dry glass surface (glass reference), a glass surface with a drop of oil (glass in oil), freshly prepared, untreated mandibles (BM fresh), defrosted and subsequently prepared mandibles (BM defrosted). (B) Adhesion on bee mandibles washed with different methods. Adhesion experiments with propolis samples were carried out on the following substrates: freshly prepared, untreated mandibles (BM untreated), freshly prepared mandibles washed with water (BM H_2O), prepared mandibles washed with chloroform and water (BM chloroform), prepared mandibles washed with acetone and water (BM acetone). All experiments were conducted using the micro-force tester Basalt-01 at room temperature (24 °C) with a maximum applied force of 5 mN (N = 5–8 propolis samples per condition, n = 10 individual measurements per sample). The ends of the boxes define the 25th and 75th percentiles, with a line at the median and error bars defining the 10th and 90th percentiles. Conditions marked with different letters differ significantly from each other (one-way ANOVA, $P < 0.001$ and Tukey test, $P < 0.05$).

Table 1: Propolis adhesion on mandibles. Work of adhesion and pull-off forces obtained from adhesion experiments conducted using Basalt-01 mechanical tester (Tetra GmbH, Ilmenau, Germany). If not stated differently, tests were carried out at room temperature (24 °C) with a set normal force of 5 mN and a contact time of 0 s or 60 s (N = 5–15 propolis samples and corresponding mandibles per condition, n = 10 individual measurements per sample). Mean values and standard deviations (s.d.) are given. Reference measurements on glass in dry and wet conditions were reported by [1]. BM, bee mandible.

		Work of adhesion [J/m^2]		Pull-off force [mN]	
Substrate	*N*n*	mean	s.d.	mean	s.d.
reference (dry glass)	80	2.96	1.27	2.12	0.77
reference (glass in oil)	60	0.90	0.55	0.74	0.36
BM, fresh	150	1.01	0.21	0.71	0.33
BM, defrosted	50	1.66	0.51	1.23	0.45
BM, water-washed	50	0.99	0.53	0.91	0.51
BM, chloroform-washed	100	1.87	0.49	1.45	0.77
BM, acetone-washed	50	2.14	1.20	1.58	0.55
BM, fresh, 60 s	5	2.66	0.42	2.70	0.81
BM, chloroform-washed, 60 s	10	4.20	1.12	3.37	0.91
BM, acetone-washed, 60 s	5	3.38	1.19	2.58	0.32
BM, replica	60	3.29	1.19	2.84	0.62

The mean work of adhesion on fresh, untreated mandibles was measured to be 1.01 ± 0.21 J/m^2 (pull-off force: 0.71 ± 0.33 mN), which is significantly lower than adhesion on dry glass (2.96 ± 1.27 J/m^2, $P < 0.0001$) (as well as all other analysed dry technical surfaces) [1]. Moreover, work of adhesion on fresh mandibles of bees was comparable to adhesion measured on glass in the presence of fluid (mineral oil) (0.90 ± 0.55 J/m^2, $P = 1.0$) [1].

There were no significant differences between adhesion on fresh mandibles caught and tested in October and July (P = 0.9999). Compared to fresh mandibles, propolis adhered significantly stronger to mandibles that had been stored in the freezer (−20 °C) for three months prior to the experiment (1.66 ± 0.51 J/m^2, P = 0.0613).

Compared to the work of adhesion on fresh bee mandibles where the propolis sample was retracted as soon as the maximum load was reached, the work of adhesion increased significantly to 3.45 ± 1.44 J/m^2 (P < 0.0001) when the contact time of the propolis sample was increased to 60 s.

Surface coating on bee mandibles

To figure out possible reasons for low propolis adhesion on bee mandibles, freeze fractures of freshly prepared mandibles were studied in the cryo-SEM (Figure 8). The different layers of the cuticle (endo-, exo-, and epicuticle) were clearly distinguishable on fractured samples. On fresh mandibles, an additional, possibly fluid, layer was present on top of the epicuticle. The layer thickness varied depending on the area of the mandible. The layer was thickest (8.37 ± 3.32 µm) in the channel between the ledge and central ridge (Figure 8B). In the flat area the layer measured 1.56 ± 1.04 µm in thickness (Figure 8C–F). Close to the unstructured sharp edge the layer

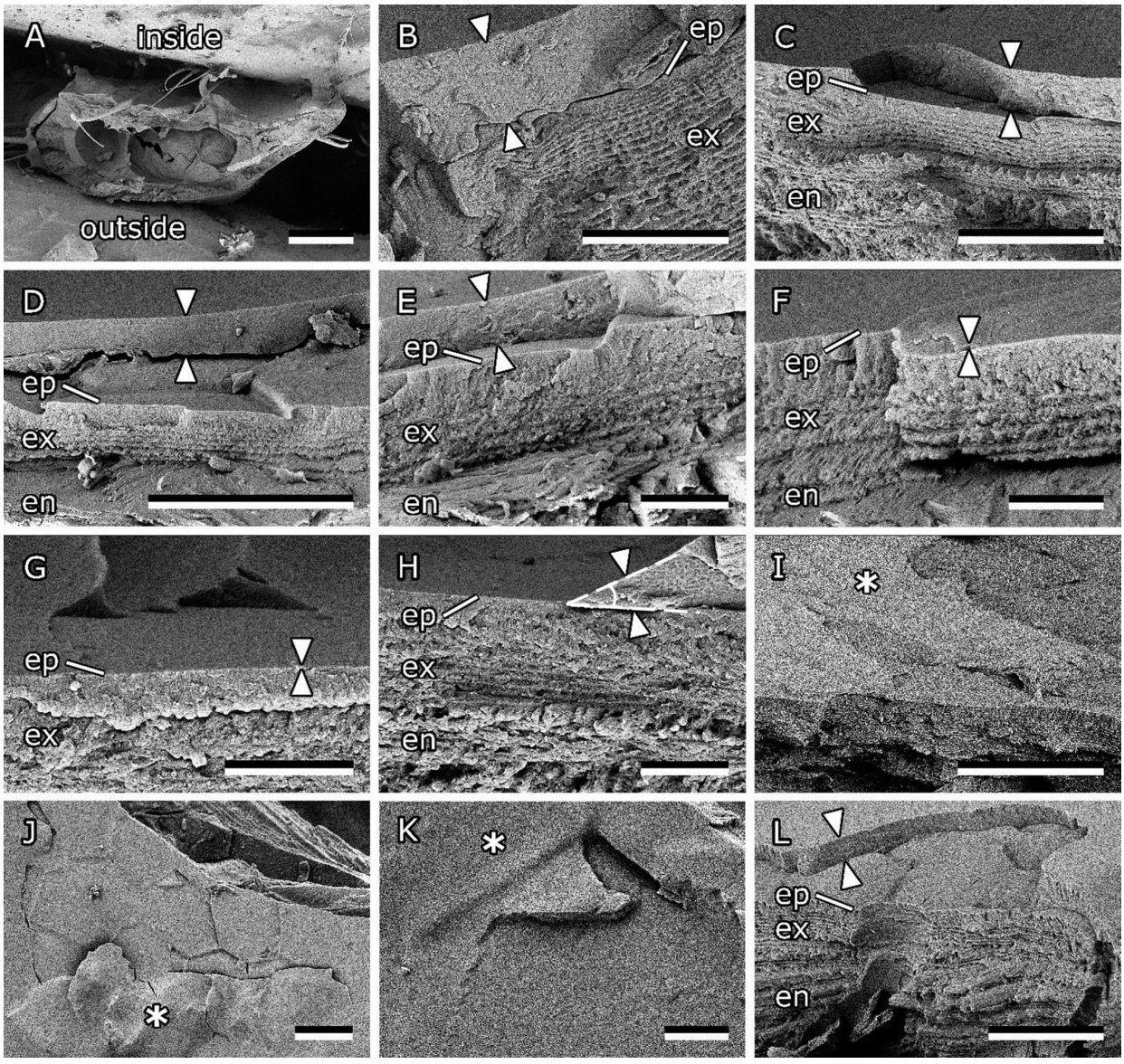


Figure 8: Fractures of freshly prepared, frozen bee mandibles. (A) Overview of mandible fracture. Inside and outside are marked. (B) Cuticle in channel area. (C–F) Cuticle in the flat area. (G,H) Cuticle near the sharp edge. (H) Contact angle of surface coating on cuticle (25°). (I–K) Angled top view of flat area. (L) Cuticle on outside of mandible. ep, epicuticle; ex, exocuticle; en, endocuticle. Arrowheads indicate the surface layer on top of the cuticle. Asterisks mark the top view of the surface layer. Scale bars: 100 µm (A), 10 µm (B–D,I,J,L), 2 µm (E–H,K).

was thin (0.053 ± 0.015 µm) (Figure 8G,H). In some places the contact angle of the surface layer on the cuticle could be measured on SEM images (Figure 8H). Varying angles between 8° and 30° were found. On the medial surface of the frozen mandible the substance overspreading the surface partially hid the scales, especially in the channel area (Figure 9A–C). Residues of this substance were still visible in dried specimens studied in regular SEM.

Different washing treatments were applied in order to remove the surface layer from the mandibles. Examination in the SEM showed that on mandibles washed with water the residues of the substance covering the surface were still present to a similar extent as on untreated mandibles studied with the same method (Figure 9D–F). On mandibles washed with acetone (Figure 9G–I) and chloroform (Figure 9J–L) the majority of the surface coating was removed. Though, cryo-SEM studies of chloroform-washed mandibles showed that minor remnants of the surface coating remained on some areas of the epicuticle even after washing (Figure 10).

Adhesion on washed bee mandibles

Adhesion of propolis was tested on washed bee mandibles and compared to adhesion on untreated specimens (Figure 7B,

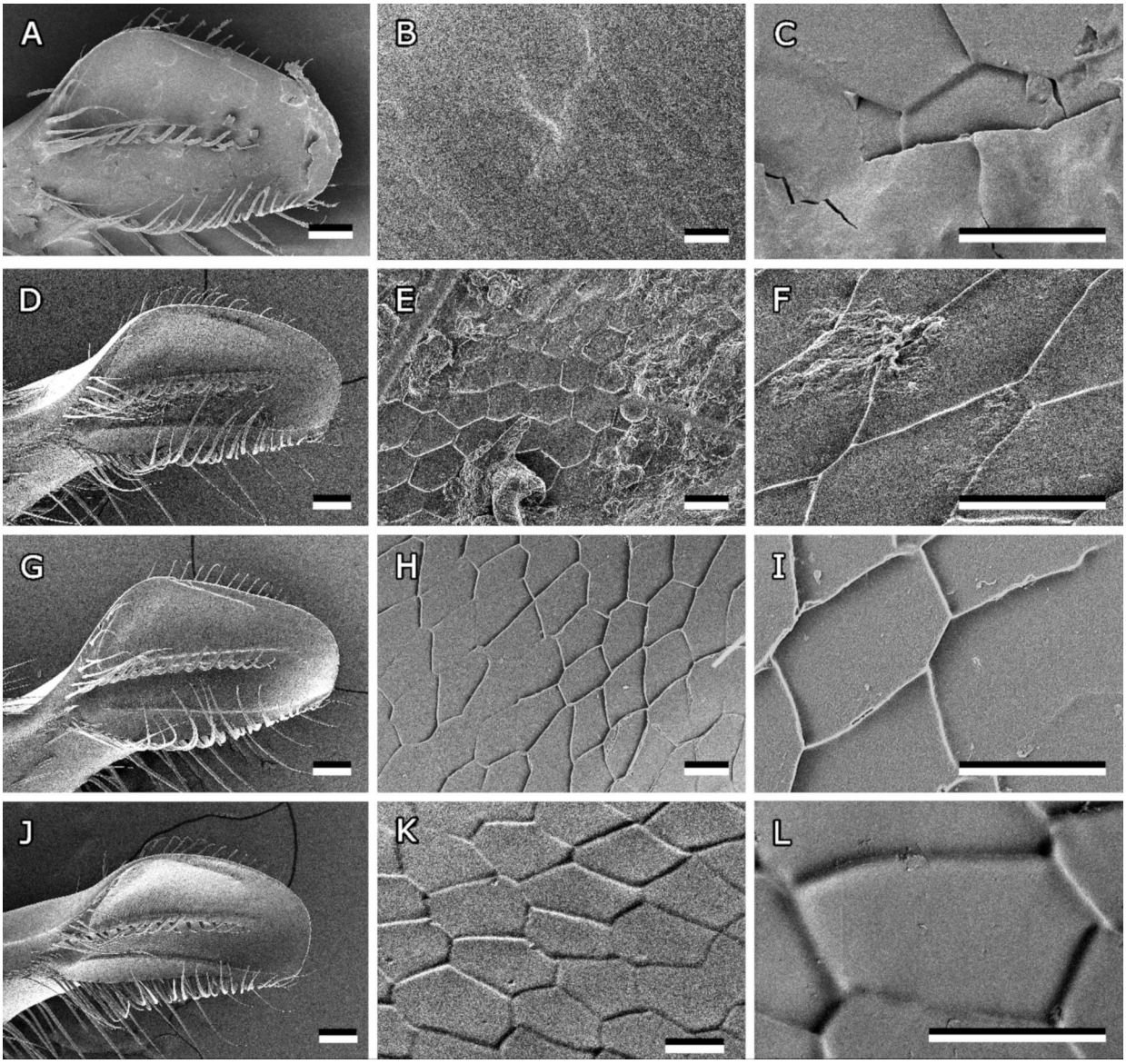


Figure 9: Bee mandibles washed with different methods. (A–C) Cryo-SEM micrographs of untreated bee mandibles (overview and close-up of flat area). (D–F) SEM micrographs of bee mandibles washed with water. (E) channel area, (F) flat area. (G–I) SEM micrographs of bee mandibles washed with acetone and water (mandible overview and close-up of flat area). (J–L) SEM micrographs of bee mandibles washed with chloroform and water (mandible overview and close-up of flat area). Scale bars: 100 µm (A,D,G,J), 10 µm (B,C,E,F,H,I,K,L).

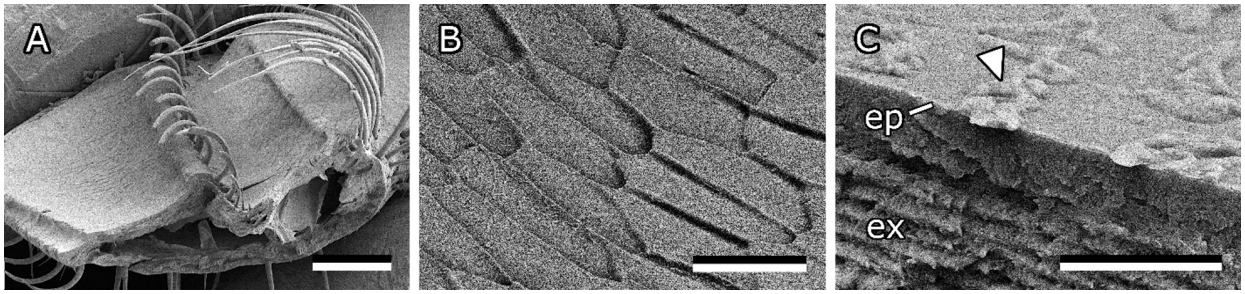


Figure 10: Fractures of bee mandibles washed with chloroform. (A) Cryo-SEM micrograph of fractured bee mandible. (B) Cryo-SEM micrograph of scales on washed mandible. (C) Cryo-SEM micrograph of fractured cuticle. Arrowheads indicate residues on epicuticle. ep, epicuticle; ex, exocuticle. Scale bars: 100 µm (A), 10 µm (B), 2 µm (C).

Table 1). Treatment with water alone had no significant effect on propolis adhesion on mandibles. The work of adhesion on mandibles washed with water was measured to be 0.99 ± 0.53 J/m^2 (P = 1.0). Compared to fresh, untreated mandibles, a significantly higher work of adhesion of 1.87 ± 0.49 J/m^2 (P = 0.0014) was measured on mandibles washed with chloroform and water and an even higher work of adhesion of 2.14 ± 1.20 J/m^2 (P < 0.0001) on mandibles washed with acetone and water. The work of adhesion of propolis on washed bee mandibles was significantly higher, when the contact time was increased to 60 s and compared to values for 0 s (chloroform-washed: P < 0.0001, acetone-washed P = 0.0236). Comparing the work of adhesion obtained from tests with a 60 s contact time performed on untreated and washed mandibles shows a significantly higher propolis adhesion on washed mandibles (P < 0.0001).

Artificial bee mandible

In order to test the effect of the surface structures and topography of the mandible as well as material properties on propolis adhesion, further adhesion experiments were performed. The morphology of real mandibles including the microstructures were successfully replicated in mandible replica made from Spurr's epoxy resin (Figure 11A). Propolis adhesion was subsequently tested on these replicated mandibles and compared to adhesion on the smooth Spurr substrate and fresh bee mandibles (Figure 11B, Table 1). There was no significant difference between propolis work of adhesion on replicated resin mandibles

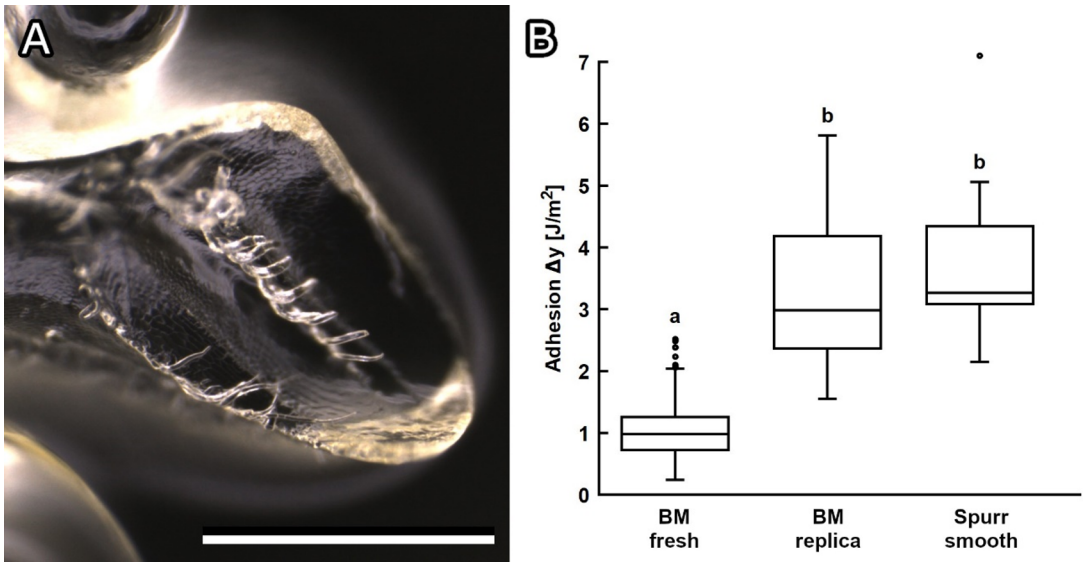


Figure 11: Replica of bee mandible. (A) Bee mandible replica made of Spurr's epoxy resin. (B) Propolis adhesion on real and replicated bee mandibles and smooth resin surface. The adhesion experiments were conducted using the micro-force tester Basalt-01 at room temperature (24 °C) with a maximum applied force of 5 mN (N = 5–8 propolis samples per condition, n = 10 individual measurements per sample). The ends of the boxes define the 25th and 75th percentiles, with a line at the median and error bars defining the 10th and 90th percentiles. Conditions marked with different letters differ significantly from each other (one-way ANOVA, P < 0.001 and Tukey test, P < 0.05). Scale bar: 500 µm (A).

(3.29 ± 1.19 J/m^2) and on a smooth surface of Spurr's resin ($P = 1.0$). Adhesion on fresh bee mandibles was however significantly lower than on both substrates made from Spurr's resin ($P < 0.0001$).

Discussion

Anatomy of honeybee mandibles

A honeybee mandible is a highly specialised organ that is used for multiple purposes such as feeding, defence, and propolis foraging and processing [6,7]. Using their mandibles, honeybees can handle propolis, apparently without being negatively affected by the sticky material. The anatomy of the mandible was therefore studied to understand its interaction with propolis. The stable construction of the mandible, especially the thick stem, is well suited to handle tough material like propolis. The medial surface of the mandible is in particularly close contact with propolis during processing and was therefore examined more closely. The medial surface of the spoon-shaped mandible tip was previously described as ridged and concave [8]. We found that there were several ridges and ledges on the medial surface of the mandible forming a channel between them. A hairless and sharp edge on one side could be used to cut materials as it has been suggested for the mandible of stingless bees [19]. Long flexible hairs grow on one edge and reach over half of the mandible. Stiff bristles spike the centre ridge. These hairs could play a role in cleaning as they could help to brush off contamination.

Surface structures on bee mandibles

Microstructures were found on the medial surface of honeybee mandibles. These anisotropic structures looked like scales and their proportions and orientation differed depending on the location on the mandible. The structures faded and eventually disappeared towards the apex and hairless edge of the mandible. It is possible that the scales in these areas are worn out by intensive use. However, it can be assumed that this is the normal morphology of the mandibles, as all examined mandibles had this characteristic. Anisotropic structures are also present on other animals such as snakes and were proposed to support anisotropic properties, for example, anisotropic friction [34]. The scales on bee mandibles are mostly oriented towards the apex and might help the bee to remove contaminations and maybe even help to handle and form sticky substances. Similar scale patterns are found on many insects [35], for example, in the trochanter of ants [19]. In contrast to honeybee mandibles, no microstructures were found on the medial surface of stingless bee mandibles [19].

Mandibles of propolis bees

Mandibles of propolis bees exhibited the same features as mandibles of regular worker bees. They were however frequently contaminated with varying amounts of resin. This shows that bees do not seem to be able to completely prevent resin adhesion. Nevertheless, resin residues were easy to remove from the mandibles and did not adhere strongly to the mandible surface. Worker bees that were not observed foraging resin did not show similar contaminations. This could indicate that bees are able to clean their mandibles and get rid of resin contaminations. But bees exhibit a division of labour and older bees are believed to be responsible for resin foraging [10]. Therefore, it cannot be assumed that all bees collected for adhesion tests have already been in contact with resin during their lifetime. An observation of propolis bees in the hive would be helpful to find out more about cleaning behaviour and effectiveness. This could prove to be difficult as propolis bees are rarely observed even outside the hive. The bristles on mandibles of propolis bees were often more damaged than those of normal workers. This could be a simple sign of aging or a consequence of increased stress during the processing of resin.

Propolis adhesion on bee mandibles

It has been reported [2] that propolis is a very sticky substance. Previous studies showed that propolis work of adhesion on glass is approximately 3 J/m^2 (Table 2, [1]). We performed adhesion experiments with propolis on the medial surface of bee mandibles to understand how bees are able to interact with this substance. Low propolis adhesion (1 J/m^2) occurred on fresh bee mandibles compared to technical surfaces such as glass, steel, PTFE, or Spurr resin (Table 2, [1]). Propolis work of adhesion on bee mandibles was of a similar magnitude to that measured on glass under fluid conditions (0.9 J/m^2 [1]). It was shown before that the adhesion of propolis does not show a great dependence on the substrate material [1]. It is therefore unlikely that the surface chemistry of the bee cuticle alone is responsible for the low adhesion. Possible mechanisms to reduce adhesion could be surface microstructures, an easy-to-break solid layer preventing strong bonding, or a fluid layer provid-

Table 2: Propolis adhesion on different substrates. Table 2 was reproduced from [1] (© 2021 Saccardi, Schiebl, Weber, Schwarz, Gorb and Kovalev, published by Frontiers, distributed under the terms of the Creative Commons Attribution 4.0 International License, https://creativecommons.org/licenses/by/4.0).

Substrate	*N*·*n*	Work of adhesion [J/m^2]		Pull-off force [mN]	
		mean	s.d.	mean	s.d.
Glass	80	2.96	1.28	2.12	0.77
PTFE	50	2.91	0.71	1.43	0.72
Steel	50	2.29	0.82	1.98	0.51
Spurr	50	3.61	0.95	3.35	0.87

ing cohesion failure [16]. The adhesion on mandibles stored in the freezer for a longer period was higher than on those freshly prepared. This could indicate that an at least partially volatile substance on the mandible reduces adhesion of propolis. Similar adhesion was measured in all areas of the bee mandible. However, the exact contact area was hard to control and see during testing, making it difficult to compare positions.

Surface coating on bee mandibles

Freeze fractures of bee mandibles clearly showed the construction of the bee mandible. Like the cuticles of most insects, it consists of endocuticle, exocuticle, and epicuticle [36]. Fractures also revealed that an additional, possibly fluid, layer is present on top of the mandibular epicuticle. From the cryo-SEM images similar to that in Figure 8H it is even possible to determine the contact angle of the fluid on the epicuticle. This substance has a relatively small contact angle (<30°) on the cuticle and is therefore likely to easily spread across the mandible surface. The layer was found to be thicker in the channel area and thinner towards the apex and hairless edge of the mandible.

Effect of surface coating on propolis adhesion

Our results suggest that above-mentioned layer reduces propolis adhesion, as adhesion is very low on fresh, untreated mandibles but significantly higher on mandibles washed with acetone or chloroform. SEM analysis also showed that the fluid layer was mostly removed after treatment with either acetone or chloroform. The fluid probably prevents direct contact between propolis and the mandible surface as described previously for other insects [16]. When the bee processes propolis, it only comes into contact with the liquid on the mandible surface and as the contact is removed, cohesive failure occurs. Part of the fluid sticks to the propolis sample, while the rest remains on the epicuticle. When longer contact occurs between mandible and propolis, the material has time to relax and adapt to the surface and probably to displace the fluid layer in some areas, leading to higher adhesion. The fact that the surface coating on the mandible can be removed with acetone or chloroform but not water suggests it might be a waxy or oily substance [16,37]. The low contact angle (<30°) of the substance suggests that the mandible surface might be oleophilic. This is consistent with observations that insect cuticles are generally rather wetted by oils than by water [38]. There are different possibilities for the origin of the lubricating layer. It has previously been suggested that the fluid secreted by the mandibular gland might help to reduce adhesion of propolis and waxes on mandibles [7,39]. For stingless bees, lubricating substances were suggested to originate from mandibular, salivary, or cephalic glands [19,40]. It was also suggested that due to gland development, only older stingless bees are able to handle propolis [20].

Mandibular glands of honeybees have been found to have a high potential to produce lipids [41]. Glucose oxidase, produced in the mandibular glands, has been found in propolis [42,43]. Which could be an indicator of bees handling propolis with mandibles covered in mandibular secretion. The opening of the mandibular gland was not visible on our micrographs, but it has been described to open on the inside of the mandible base (proximal end) [7]. The fluid might be guided from the mandibular gland to the mandible tip through the groove on the stem of the mandible and then through the channel on the medial surface of the mandible tip. This groove was previously suggested to channel liquid to the mandible tip [6,19]. Bees possibly help the spreading of fluid across the mandible surface by moving and rubbing their mandibles against each other as they do during grooming [44]. In [19], it was also suggested that regurgitated nectar or honey could be used to lubricate mandibles of stingless bees. Another possible origin of the adhesion-reducing fluid on mandibles might be secretion through pore canals as the cuticle of insects often contains pore canals that transport lipid-containing secretions [45]. Cuticular lipids such as alkanes, alkenes, and fatty acids are present on the head and other body parts of honeybees [46]. Their functions include nestmate recognition and protection against desiccation [46]. More alkanes have been found on the bodies of forager bees compared to nursing bees [47].

Effect of the mandible surface structure on adhesion

In some cases, it has been described that microstructures can reduce adhesion by decreasing the contact area [48,49]. The trochanter of ants (*Camponotus sericeiventris*) is structured with scales that were suggested to lower adhesion [19]. Resin adhesion on these scales was significantly lower than on the unstructured mandibles of stingless bees [19]. As scale-like microstructures were found on honeybee mandibles, their effect on propolis adhesion was tested. For this purpose, the form of the mandibles, including the scale-like microstructures, was replicated in resin in order to be able to have a direct comparison between propolis adhesion on the same material in mandible and smooth form. Propolis adhesion on the mandible replica did not differ significantly from that on a smooth resin control surface. It, therefore, seems like the structures on mandibles do not directly affect propolis adhesion. It is, however, likely that the scales help to spread the fluid over the surface to create an even layer. Structures also prevent the fluid from flowing off easily. In unstructured areas of the mandible, the layer was thinner. It has previously been described that structures facilitate the spreading of fluid [50]. For instance, structures on *Nepenthes alata* and lizard skin have been found to enhance unidirectional liquid transportation [51]. The contact area of propolis in our adhesion experiments was smaller than in reality when a bee handles propolis. On a bigger scale, hair and

overall topography of the mandible could also reduce propolis adhesion, as they might prevent full contact with the mandible surface.

Outlook

Reduced propolis adhesion was observed on the surface of bee mandibles. The anti-adhesive strategy found in bees might also be helpful in solving technological adhesive problems, for instance, unwanted resin contamination of woodworking tools.

The next step in the further course of the top-down development process is the attempt to further understand the principle of the presumed anti-adhesive strategy of the honeybee and to verify it in replicas. The abstraction of the principle or structures found and the transfer to the technosphere with an effectiveness test under technical production processes are the next steps in the top-down procedure.

Conclusion

Studying the interaction between propolis and bee mandibles revealed that propolis adhesion is indeed reduced on bee mandibles. Propolis adhesion is four times reduced in the presence of a natural secretion layer on top of the mandibular epicuticle, while the scale-like micropattern on the mandible might help the spreading of the fluid. The lubricating layer could be removed with organic solvents. In addition, the hair on mandibles is likely to help in the cleaning process.

Acknowledgements

We thank Dr. Helmut Horn for catching and collecting propolis bees for this work.

ORCID® iDs

Leonie Saccardi - https://orcid.org/0000-0002-0485-2716
Franz Brümmer - https://orcid.org/0000-0003-4108-2746
Jonas Schiebl - https://orcid.org/0000-0002-5276-004X
Alexander Kovalev - https://orcid.org/0000-0002-9441-5316
Stanislav Gorb - https://orcid.org/0000-0001-9712-7953

References

1. Saccardi, L.; Schiebl, J.; Weber, K.; Schwarz, O.; Gorb, S.; Kovalev, A. *Front. Mech. Eng.* **2021,** *7,* 660517. doi:10.3389/fmech.2021.660517
2. Bankova, V. S.; de Castro, S. L.; Marcucci, M. C. *Apidologie* **2000,** *31,* 3–15. doi:10.1051/apido:2000102
3. Burdock, G. A. *Food Chem. Toxicol.* **1998,** *36,* 347–363. doi:10.1016/s0278-6915(97)00145-2
4. Simone-Finstrom, M.; Spivak, M. *Apidologie* **2010,** *41,* 295–311. doi:10.1051/apido/2010016
5. Bankova, V. *J. Ethnopharmacol.* **2005,** *100,* 114–117. doi:10.1016/j.jep.2005.05.004
6. Goodman, L. *Form and function in the honey bee;* International Bee Research Association: Monmoth, UK, 2003.
7. Snodgrass, R. E. *The anatomy of the honey bee;* Washington: Government Printing Office: Washington, D.C., USA, 1910. doi:10.5962/bhl.title.87234
8. Carreck, N. L.; Andree, M.; Brent, C. S.; Cox-Foster, D.; Dade, H. A.; Ellis, J. D.; Hatjina, F.; van Englesdorp, D. *J. Apic. Res.* **2013,** *52,* 1–40. doi:10.3896/ibra.1.52.4.03
9. Calderone, N. W. *Apidologie* **1998,** *29,* 127–158. doi:10.1051/apido:19980108
10. Nakamura, J.; Seeley, T. D. *Behav. Ecol. Sociobiol.* **2006,** *60,* 339–349. doi:10.1007/s00265-006-0170-8
11. Alfonsus, E. C. *Glean. Bee Cult.* **1933,** *61,* 92–93.
12. Kumazawa, S.; Nakamura, J.; Murase, M.; Miyagawa, M.; Ahn, M.-R.; Fukumoto, S. *Naturwissenschaften* **2008,** *95,* 781–786. doi:10.1007/s00114-008-0383-y
13. Park, Y. K.; Paredes-Guzman, J. F.; Aguiar, C. L.; Alencar, S. M.; Fujiwara, F. Y. *J. Agric. Food Chem.* **2004,** *52,* 1100–1103. doi:10.1021/jf021060m
14. Teixeira, É. W.; Negri, G.; Meira, R. M. S. A.; Message, D.; Salatino, A. *Evidence-Based Complementary Altern. Med.* **2005,** *2,* 85–92. doi:10.1093/ecam/neh055
15. Meyer, W.; Ulrich, W. *Bee World* **1956,** *37,* 25–36. doi:10.1080/0005772x.1956.11094916
16. Voigt, D.; Gorb, S. *J. Exp. Biol.* **2008,** *211,* 2647–2657. doi:10.1242/jeb.019273
17. Leonhardt, S. D.; Blüthgen, N. *Biotropica* **2009,** *41,* 730–736. doi:10.1111/j.1744-7429.2009.00535.x
18. Gastauer, M.; Campos, L. A. O.; Wittmann, D. *Rev. Bras. Entomol.* **2011,** *55,* 234–240. doi:10.1590/s0085-56262011005000018
19. Gastauer, M.; Campos, L. A. O.; Wittmann, D. *An. Acad. Bras. Cienc.* **2013,** *85,* 1189–1196. doi:10.1590/s0001-37652013000300018
20. dos Santos, C. G.; Blochtein, B.; Megiolaro, F. L.; Imperatriz-Fonseca, V. L. *Neotrop. Entomol.* **2010,** *39,* 691–696. doi:10.1590/s1519-566x2010000500003
21. Bankova, V.; Bertelli, D.; Borba, R.; Conti, B. J.; da Silva Cunha, I. B.; Danert, C.; Eberlin, M. N.; I Falcão, S.; Isla, M. I.; Moreno, M. I. N.; Papotti, G.; Popova, M.; Santiago, K. B.; Salas, A.; Sawaya, A. C. H. F.; Schwab, N. V.; Sforcin, J. M.; Simone-Finstrom, M.; Spivak, M.; Trusheva, B.; Vilas-Boas, M.; Wilson, M.; Zampini, C. *J. Apic. Res.* **2019,** *58,* 1–49. doi:10.1080/00218839.2016.1222661
22. Gorb, E.; Kastner, V.; Peressadko, A.; Arzt, E.; Gaume, L.; Rowe, N.; Gorb, S. *J. Exp. Biol.* **2004,** *207,* 2947–2963. doi:10.1242/jeb.01128
23. Gorb, S.; Scherge, M. *Proc. R. Soc. London, Ser. B* **2000,** *267,* 1239–1244. doi:10.1098/rspb.2000.1133
24. Jiao, Y.; Gorb, S.; Scherge, M. *J. Exp. Biol.* **2000,** *203,* 1887–1895. doi:10.1242/jeb.203.12.1887
25. Wheater, C. P.; Evans, M. E. G. *J. Insect Physiol.* **1989,** *35,* 815–820. doi:10.1016/0022-1910(89)90096-6
26. Gorb, S. N.; Voigt, D.; Gorb, E. V. Visualisation of small fluid droplets on biological and artificial surfaces using the cryo-SEM approach. In *Modern Research and Educational Topics in Microscopy;* Méndez-Vilas, A.; Diaz, J., Eds.; Formatex: Badajoz, Spain, 2007; pp 812–819.
27. Gorb, S. N.; Kesel, A.; Berger, J. *Arthropod Struct. Dev.* **2000,** *29,* 129–135. doi:10.1016/s1467-8039(00)00020-7
28. Koch, K.; Schulte, A. J.; Fischer, A.; Gorb, S. N.; Barthlott, W. *Bioinspiration Biomimetics* **2008,** *3,* 046002. doi:10.1088/1748-3182/3/4/046002
29. Spurr, A. R. *J. Ultrastruct. Res.* **1969,** *26,* 31–43. doi:10.1016/s0022-5320(69)90033-1

30. Johnson, K. L.; Kendall, K.; Roberts, A. D. *Proc. R. Soc. London, Ser. A* **1971,** *324,* 301–313. doi:10.1098/rspa.1971.0141
31. Christensen, R. *Theory of viscoelasticity,* 2nd ed.; Academic Press: London, UK, 1982. doi:10.1016/b978-0-12-174252-2.x5001-7
32. Cheng, L.; Xia, X.; Scriven, L. E.; Gerberich, W. W. *Mech. Mater.* **2005,** *37,* 213–226. doi:10.1016/j.mechmat.2004.03.002
33. Kovalev, A.; Filippov, A.; Gorb, S. N. *J. Comp. Physiol., A* **2018,** *204,* 409–417. doi:10.1007/s00359-018-1248-2
34. Filippov, A.; Gorb, S. N. *Sci. Rep.* **2013,** *3,* 1240. doi:10.1038/srep01240
35. Vincent, J. F. V.; Wegst, U. G. K. *Arthropod Struct. Dev.* **2004,** *33,* 187–199. doi:10.1016/j.asd.2004.05.006
36. Locke, M. *J. Biophys. Biochem. Cytol.* **1961,** *10,* 589–618. doi:10.1083/jcb.10.4.589
37. Cheremisinoff, N. P. *Industrial solvents handbook, revised and expanded;* Taylor & Francis: Boca Raton, FL, USA, 2003. doi:10.1201/9780203911334
38. Pal, R. *Bull. Entomol. Res.* **1950,** *41,* 121–139. doi:10.1017/s0007485300027528
39. Örösi-P´l, Z. *Bee World* **1957,** *38,* 70–73. doi:10.1080/0005772x.1957.11094979
40. Dos Santos, C. G.; Megiolaro, F. L.; Serrão, J. E.; Blochtein, B. *Ann. Entomol. Soc. Am.* **2009,** *102,* 137–143. doi:10.1603/008.102.0115
41. Fujita, T.; Kozuka-Hata, H.; Hori, Y.; Takeuchi, J.; Kubo, T.; Oyama, M. *PLoS One* **2018,** *13,* e0191344. doi:10.1371/journal.pone.0191344
42. Zhang, C.-P.; Zheng, H.-Q.; Hu, F.-L. *J. Food Sci.* **2011,** *76,* C75–C79. doi:10.1111/j.1750-3841.2010.01941.x
43. Ruguo, Z.; Hua, Z.; Hong, Z.; Ying, F.; Kun, L.; Wenwen, Z. *Procedia Eng.* **2011,** *18,* 101–106. doi:10.1016/j.proeng.2011.11.016
44. Jander, R. *Physiol. Entomol.* **1976,** *1,* 179–194. doi:10.1111/j.1365-3032.1976.tb00960.x
45. Scherge, M.; Gorb, S. N. *Phys. Today* **2002,** *55* (6), 53. doi:10.1063/1.1496378
46. Abou-Shaara, H.; Singl, A. R.; Al-Ghamdi, A. A. *Environ. Exp. Biol.* **2013,** *11,* 185–188.
47. Kather, R.; Drijfhout, F. P.; Martin, S. J. *J. Chem. Ecol.* **2011,** *37,* 205–212. doi:10.1007/s10886-011-9909-4
48. Helbig, R.; Nickerl, J.; Neinhuis, C.; Werner, C. *PLoS One* **2011,** *6,* e25105. doi:10.1371/journal.pone.0025105
49. Peisker, H.; Gorb, S. N. *J. Exp. Biol.* **2010,** *213,* 3457–3462. doi:10.1242/jeb.043661
50. Lee, Y.; Matsushima, N.; Yada, S.; Nita, S.; Kodama, T.; Amberg, G.; Shiomi, J. *Sci. Rep.* **2019,** *9,* 7787. doi:10.1038/s41598-019-44243-x
51. Sun, W.; Tang, L.; Hong, W.; Zhan, Y.; Yang, B.; Liu, J. *RSC Adv.* **2019,** *9,* 7842–7848. doi:10.1039/c8ra08768g

License and Terms

This is an open access article licensed under the terms of the Beilstein-Institut Open Access License Agreement (https://www.beilstein-journals.org/bjnano/terms), which is identical to the Creative Commons Attribution 4.0 International License (https://creativecommons.org/licenses/by/4.0). The reuse of material under this license requires that the author(s), source and license are credited. Third-party material in this article could be subject to other licenses (typically indicated in the credit line), and in this case, users are required to obtain permission from the license holder to reuse the material.

The definitive version of this article is the electronic one which can be found at:
https://doi.org/10.3762/bjnano.13.84

BEILSTEIN JOURNAL OF NANOTECHNOLOGY

Roll-to-roll fabrication of superhydrophobic pads covered with nanofur for the efficient clean-up of oil spills

Patrick Weiser[1], Robin Kietz[1], Marc Schneider[1,2], Matthias Worgull[1,2] and Hendrik Hölscher[*1]

Full Research Paper

Open Access

Address:
[1]Institute of Microstructure Technology (IMT), Karlsruhe Institute of Technology (KIT), P.O. box 36 40, 76021 Karlsruhe, Germany and [2]Karlsruhe Nano Micro Facility for information-driven Material Structuring and Characterization (KNMFi), Karlsruhe Institute of Technology (KIT), Hermann-von-Helmholtz-Platz 1, 76344 Eggenstein-Leopoldshafen, Germany

Email:
Hendrik Hölscher[*] - hendrik.hoelscher@kit.edu

* Corresponding author

Keywords:
hot embossing; lotus effect; nanofur; nanopads; oil spill cleanup; oil water separation; roll-to-roll; R2R; superhydrophobicity

Beilstein J. Nanotechnol. **2022,** *13,* 1228–1239.
https://doi.org/10.3762/bjnano.13.102

Received: 16 May 2022
Accepted: 29 September 2022
Published: 31 October 2022

This article is part of the thematic issue "Biomimetics on the micro- and nanoscale – The 25th anniversary of the lotus effect".

Guest Editor: M. Mail

© 2022 Weiser et al.; licensee Beilstein-Institut.
License and terms: see end of document.

Abstract

Superhydrophobic surfaces, which self-clean through rinsing with water, have gained significant importance during the last decades. A method to fabricate such a surface featuring the lotus effect, solely through structuring, is hot pulling of a polymer surface. This technique provides the so-called nanofur, which consists of a polymer surface densely covered with a polymeric fur of extremely thin hair-like structures. Here, we present a continuous roll-to-roll process for the fabrication of a thin polymeric film covered with nanofur from polypropylene. Our process enables structuring of large areas of the order of square meters using industry standard machinery. This opens up many possible applications for nanofur that could previously not be realized because of the limitations of conventional hot embossing regarding structurable area. The structured film is subsequently processed into an exemplary product, that is, so-called nanopads; polymeric sandwiches of polypropylene film covered with nanofur and filled with an oil-absorbing material. These are well-suited for the cleanup of small oil spills.

Introduction

Self-cleaning surfaces utilizing the famous lotus effect have gained significant importance during the last twenty-five years [1]. Prominent examples include wall colors that let dust and soil drop off when it rains [2], hydrophobic coatings for glass surfaces (e.g., cameras at toll stations or windshields for better visibility [3]), anti-graffiti paints [4], as well as textiles that repel unwanted dirt [5,6]. The lotus effect is commonly achieved by hierarchical nano- and micro-structuring of surfaces made from materials with low surface energy leading to very high contact angles (above 150°). This strategy is inspired by the lotus leaf [1] but can be found on many other surfaces in nature, too [7].

Multiple techniques exist to prepare self-cleaning surfaces. Direct laser writing and electron beam lithography have been employed successfully to create superhydrophobic surfaces. However, due to low writing speeds these approaches are not viable for surface areas larger than a few square millimeters [8,9]. Various (soft) lithography techniques have been employed to create superhydrophobic surfaces; however, these generally rely on copying surface information from a master (e.g., a lotus leaf) [9,10] and are therefore often limited in size. Superhydrophobic surfaces could also be prepared using various dry/wet etching techniques including electrochemical HF etching, stain etching, metal-assisted etching, and reactive ion etching [9,11]. So-called "nanograss" or "black silicon" is a surface modification of silicon where the surface is covered with millions of tiny needle-like structures with high aspect ratio. These needles render superhydrophobic properties to the surface. Such surfaces can either be prepared using a RIE process [12] or a laser-assisted etching process described by Mazur et al. [13], which requires expensive silicon wafers as substrate as well as a femtosecond laser source [11,14]. All mentioned processes require potentially hazardous chemicals, chambers creating a suitable process environment, or extensive and costly operations to form superhydrophobic surfaces. Hence, they are not particularly well suited for upscaling.

A rather cost-effective and, therefore, widely used method for obtaining superhydrophobic surfaces is the use of silica-based films, which can be applied by dipping the object in gel or via aerosol spray [15]. While providing excellent superhyrophobicity and an easy application even on very large surfaces, these films are not particularly durable. Other options for chemically treated superhydrophobic surfaces, such as the use of fluorinated silanes, fluoropolymer coatings, and carbon nanotubes, exist, but are either rather costly to apply and/or potentially harmful to the environment.

A much simpler and cheaper option is the fabrication of polymeric nanofur [16]. Its surface is covered with many tiny, hair-like structures and has a high potential for up-scaling because it can be produced with minimal, very simple and cost-effective tools and molds [17]. On the lab scale, the fabrication of nanofur can be easily achieved with sand-blasted steel plates serving as form inserts in a hot embossing machine [18]. However, in this case the fabrication is limited to areas of some square centimeters. These sizes are not sufficient for commercial applications.

To overcome this hurdle and to allow for the cost-effective fabrication of thin polymeric nanofur, we developed a continuous roll-to-roll (R2R) process. For that, we combine classical film extrusion with roll-to-roll structuring [2,19-22]. The overall process relies only on tools frequently used in industry, thereby enabling the cost-effective upscaling of nanofur fabrication for commercial applications.

Furthermore, we demonstrate the subsequent processing of the thin polymeric nanofur into an exemplary product, namely so-called nanopads. These are an aid for the efficient cleaning of oil spills due to the efficient oil–water separation ability of nanofur [23]. The polymeric pads are 48 mm in diameter and filled with an oil-absorbing material. On the outside, they are covered with superhydrophobic and oleophilic nanofur, which repels water and attracts oil at the same time. In order to utilize this feature in an efficient way and to allow for continuous oil absorption, the polymer foils are equipped with tiny holes through which oil is absorbed and finally saved in the embedded oil-absorbing material.

Results and Discussion

This chapter is written in two parts. The first one describes the fabrication process for large area nanofur, and the second one deals with the production of an exemplary product from that nanofur. This split is done for better clarity since these are essentially two separate processes.

Roll-to-roll fabrication of nanofur

Nanofur is a polymeric surface covered with a dense fur of very thin and long hair-like structures [16]. This arrangement causes a significant increase of the contact angle of water droplets. The fractal structure minimizes contact area as well as adhesion forces between surface and water droplet, thereby equipping the surface with self-cleaning properties equivalent to the lotus effect [24]. Additionally, the high increase of surface area increases the spreading of non-polar liquids. Therefore, a nanofur surface separates oil and water efficiently [16,17,23].

In the abovementioned studies, the fabrication of nanofur was based on a hot-pulling process, which is commonly realized in a hot-embossing machine utilizing sandblasted steel-plates as mold inserts. It is an interesting feature of this procedure that a surface with nanostructures is realized without elaborate and costly lithography. Nanofur can be hot-pulled from several types of polymers [16]. Nonetheless, the surface area per process step is limited to some square centimeters since hot embossing is a serial process [18]. In the view of commercial applications, however, a continuous process is highly desirable.

As demonstrated here, the continuous fabrication of superhydrophobic nanofur is possible in a roll-to-roll (R2R) process. Figure 1 outlines the two universal process steps. First, a thin polymer foil is extruded on a sacrificial layer (Figure 1a). In a second step, the nanofur is hot-pulled from this extruded film in

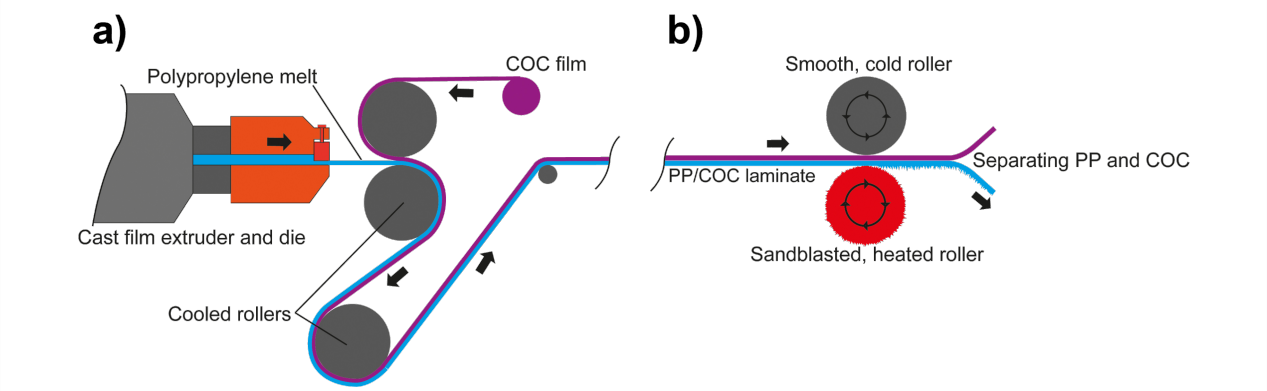


Figure 1: Schematic showing the roll-to-roll fabriction of a thin nanofur film by the example of PP and COC. (a) Coextrusion of PP on the COC support layer. The PP is extruded through a cast film die and laminated onto a previously extruded COC film in the calender. The PP and COC films stick strongly together but do not mix. (b) Hot pulling of nanofur from the PP film with a sandblasted roller. The COC film serves as a support layer keeping the PP from melting completely and thus enables transport through the calender. The gap size is set slightly below the nominal film thickness so that the films experience minimal embossing forces. Temperature of the sandblasted roller is set slightly above the melting temperature of the polymer. Finaly, the structured PP and the sacrificial support layer of COC can easily be separated in a peeling motion.

a R2R machine with a sandblasted roller. Subsequently, the nanofur film can be peeled of the sacrificial layer (Figure 1b). This sacrificial film is needed to provide the suitable process stability during the hot-pulling step. For comparably thick and stable polymer films (thicker than 1 mm) it is also possible to omit this support layer. In the following, however, we focus on thin nanofur films fabricated with a sacrificial layer because these are well-suited for the subsequent processing into nanopads introduced in the introduction and described in more detail in the following section.

We selected polypropylene (PP) as base material for the hot pulling of nanofur for three reasons. First, even its flat surface features a comparable high contact angle (95–100°, depending on the exact type [25-27]), which helps to achieve a high contact angle also for the structured surface. Second, we know from previous studies that it has a comparable wide process window for the hot pulling of nanofur [28]. Third, polypropylene is well-suited to be laminated on films of cyclic olefin copolymer (COC). As shown by Kolew [29], these two polymer types adhere strongly but do not mix during the extrusion process. Hence, the combination of PP and COC is a good match for the fabrication of nanofur with the R2R process sketched in Figure 1.

For that, we extruded a 250 µm thick COC film (TOPAS COC 8007s) in a lab extruder (Collin E20E - E30E) (Figure 2a). Since COC is non-hygroscopic, drying of the granulate is not necessary. The polymer melt was extruded at a temperature of 260 °C at 60 bar. Behind the extruder, there is a calender with smooth, temperature-controlled rollers (Collin CR 72/72/72-200 T) smoothing out and rolling up the film at about 1.3 m/min.

After the preparation of this COC film, which serves as sacrificial support layer, polypropylene is processed into a 150 µm thick film using the same extruder (Figure 2a). During this process, sketched in Figure 1a, the film is laminated onto the COC film resulting in a PP/COC sandwich. In our case this laminate was coiled and subsequently structured in a lab calender (Figure 2b). However, in an upscaled commercial process the structuring might follow the lamination process directly in a combined machinery.

For the structuring of the PP film, schematically shown in Figure 1b, the roller serving as structuring tool was prepared in two steps. First, it was sandblasted with cast iron particles with a diameter of 0.8–1.2 mm and afterwards with white corundum with a particle size of 53–75 µm. This procedure results in a surface topography of craters and edges with finer spikes on top. This sandblasted roller is mounted in a two-roller calender (Figure 2b) and heated (Figure 2c). Best quality nanofur in terms of high contact angles is obtained if the temperature is set slightly above the melting point of the respective PP type (170 °C in our case). For this temperature the viscosity of the polymer melt was sufficient to enable the hot-pulling process. The second roller of the calender was unheated and had a smooth surface. The gap between the rollers was adjusted to be slightly thinner (a few tens of micrometers) than the nominal material thickness. In this way, the laminated films experience only minimal embossing forces during their pass through the calender and the rough sandblasted surface of the heated roller pulls tiny polymer hairs out of the melted surface of the PP film. During this structuring step, the COC layer serves as a support layer enabling the processing of thin nanofur films that would melt entirely and/or stick to the hot roller without the COC support film.

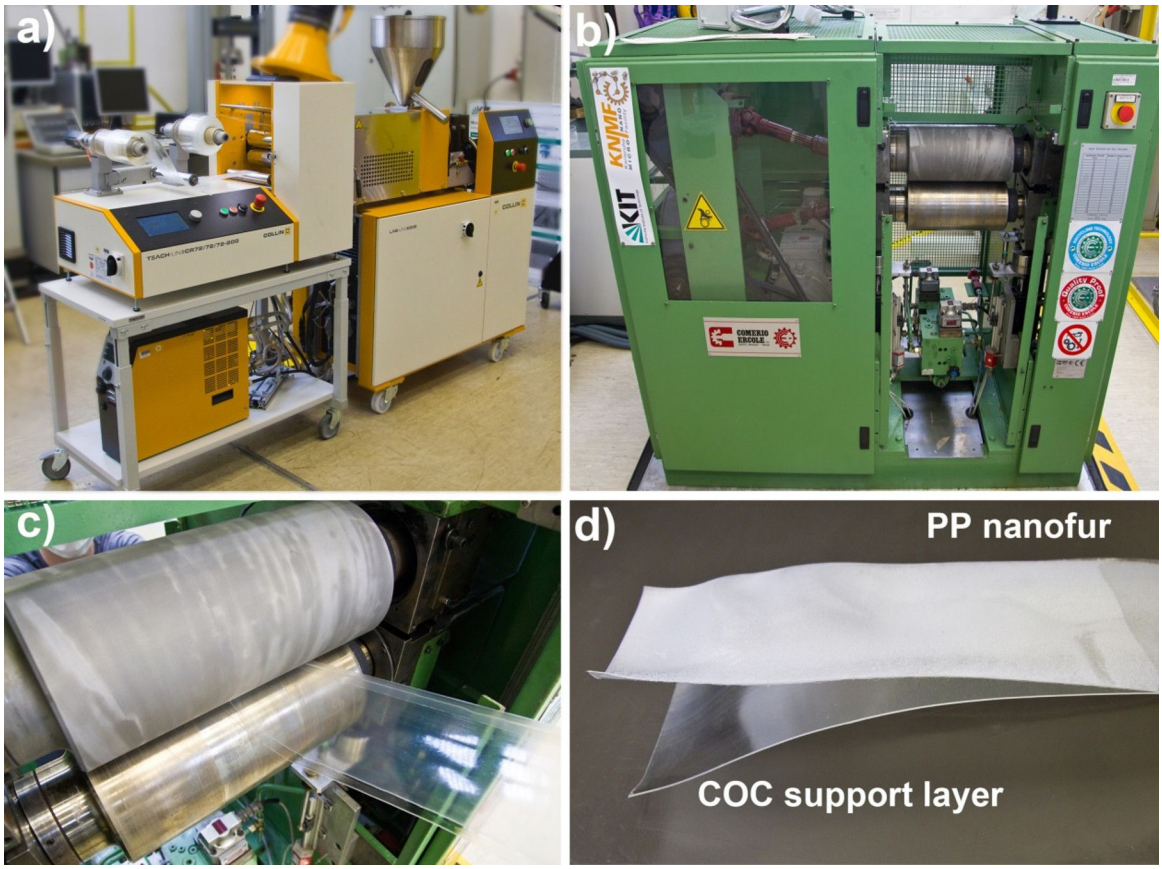


Figure 2: Photos showing the essential fabrication steps of thin nanofur. (a) Extrusion line with rolling unit to co-extrude the thin PP film onto the COC support film. The right roll is the coiled COC film; the left one is the completed PP/COC laminate. (b) Photo of the lab calender utilized to structure the PP film. (c) Close-up of the rollers of the lab calender. In this machine the upper sandblasted roller is heated and gets in contact with the PP side of the laminate. In this way, the nanofur hairs are pulled out of the PP film. The lower roller is smooth and not heated, but presses the film sandwich against the upper sandblasted roller. (d) Finally, PP and COC are separated through peeling.

After structuring, the PP film can be separated from the COC either by hand or, in the case of later envisioned commercial applications, by two winding rollers that separate the two foils with a peeling motion (Figure 2d). The SEM (Zeiss Evo 10) picture in Figure 3a reveals the typical crater-like topography of nanofur with hair on the crater edges [16]. Typical contact

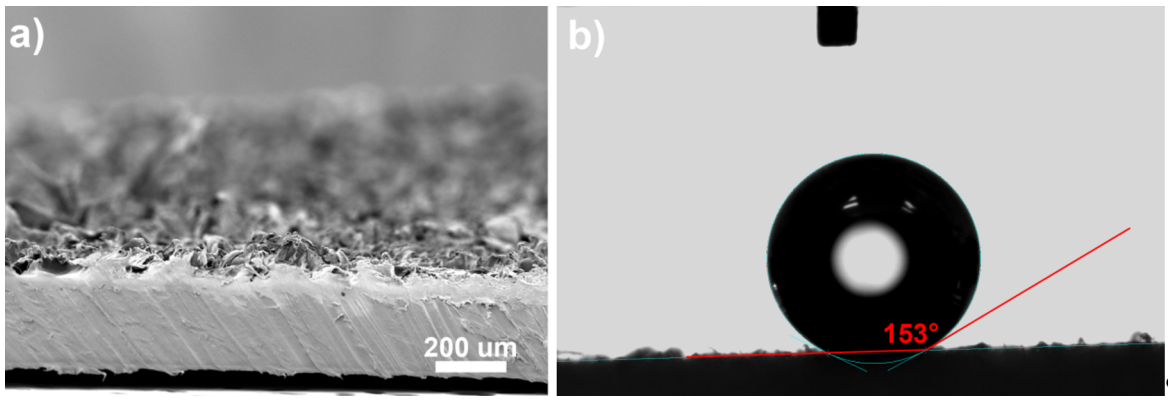


Figure 3: (a) SEM picture of a side cut of a PP nanofur film (view angle 84°). (b) A water droplet of 1 µL on top of the PP nanofur. The contact angle at this spot was 153°.

angles of water on top of the nanofur are around the super hydrophobicity limit of 150° (see Figure 3b). This makes droplets easily roll off a sample even at minimal tilt (see the video in Supporting Information File 1). Contact angles were measured on a Dataphysics OCA 20 contact angle measurement machine using distilled water in the sessile drop method with a droplet volume of 1 µL. Due to the hydrophobic nature of the surface, drops tend to roll to areas with lower contact angles when performing measurements. This leads to slightly lowered average contact angles. The relatively high measurement uncertainty of contact angle measurements, especially on hydrophobic surfaces, can further distort the measured values [30].

The quality of the nanofur in terms of its hydrophobicity and oil absorption quantity depends on several processing factors including length of the hairs, their density, and their overall uniformity over the whole film area. The most important parameter for high-quality nanofur is the gap size between the upper and lower roller. It should be set to a few tens of micrometers below the nominal material thickness; the contact angle is highest if the roller just touches the surface without applying high embossing forces. In this case it was set to 350 µm (the nominal thickness of the PP/COC laminate was 400 µm). Since the polymer laminate has small variations in thickness, a tradeoff must be made between setting the gap at the optimal thickness for maximum contact angle and setting it below the nominal thickness to compensate thickness variations in the processed film and to structure the film more uniformly. If the gap size is set just at or slightly above the nominal thickness, only the thickest parts of the film are structured. If the gap is too small, no hairs are pulled out of the material, and the resulting structures look as if they had been flattened. Figure 4 shows nanofur produced with a correctly set gap size vs “nanofur” produced with a too narrow gap size.

The hair length can be controlled via the conveying speed of the calender. Slower conveying speeds lead to longer hairs. To a certain extent this can be beneficial because, in general, hairs with high aspect ratio led to high contact angles. However, if the hairs become too long and thin, they might bend under the weight of the water droplets. Furthermore, hair apexes might penetrate water drops. These two effects might slow the speed at which water droplets roll off even if the surface is still superhydrophobic. If the conveying speed is set too high, the hairs are too short and water droplets might touch the surface between the hairs. In this so-called Wenzel state, the droplets are pinned [16]. The video in Supporting Information File 2 shows the effects of hair length on roll-off speed and angle.

The hair density of the nanofur is indirectly controlled via the sandblasting of the structured roller. The optimal roughness of the roller depends also on the actual polymer type. For polypropylene (PP), polyethylene (PE), and polycarbonate (PC), we obtained the best results by sandblasting the roller first with 0.8–1.2 mm cast iron particles and subsequently with white corundum with a particle size of 53–75 µm. For polylactide (PLA), smaller corundum particles with a size of 8–10 µm had to be used for the second sandblasting step to obtain a sufficient hair density [28].

In particular, attention must be paid to the polymer residue left on the structuring roller (Figure 2c). If the residue polymer stays on the hot roller for too long, especially with oxygen present under ambient conditions, it might decompose and inhibit the structuring process. We observed that this effect

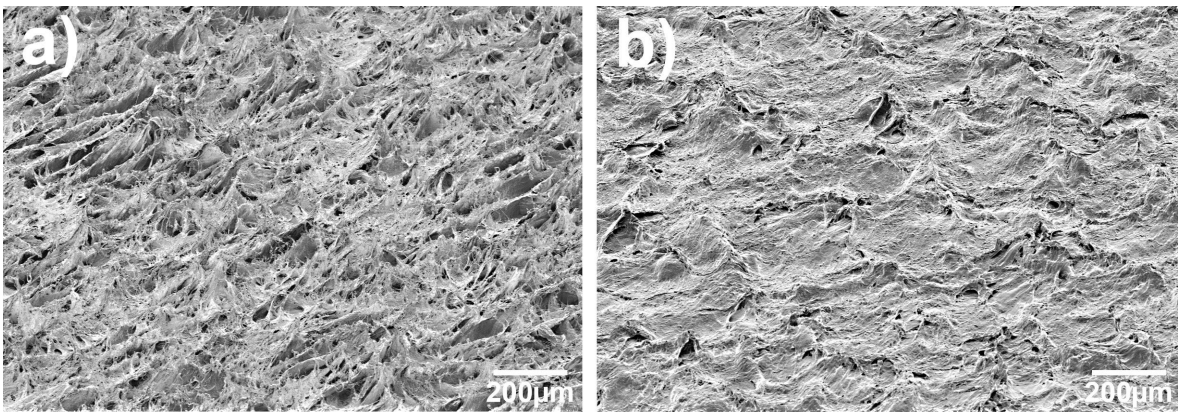


Figure 4: (a) Nanofur produced with a gap size set 50 µm below the nominal material thickness. Many long hairs are pulled out of the material. (b) Nanofur produced with a gap size set 500 µm below nominal material thickness. No hairs are pulled out of the material, the structures look as if they had been flattened. We conclude that a gap size just below the nominal thickness results in good quality nanofur while still structuring the film uniformly, compensating minor thickness variations in the film.

leads to reduced quality of the nanofur, that is, reduced contact angles. It is therefore important to keep the process running in a continuous fashion as old residues are replaced by newer polymer material. Actually, the contact angle is highest when the roller is newly sandblasted and therefore not covered with any polymer residue. Once the heated and sandblasted roller is covered with residues of polymer the quality of the nanofur reduces slightly.

In order to quantify this effect, we measured the contact angles along a 25 m long film of PP nanofur produced in the fashion described above (see Figure 5). The contact angle is about 154° at first but dropped by 4° after the first turns of the rollers before it became nearly constant with values slightly below 150°. While technically slightly below the limit for superhydrophobicity, these contact angles are still sufficient for almost all typical applications, since the droplets easily roll off the surface even at minimal tilt of the sample. Furthermore the rather large measurement uncertainty of contact angle measurements, especially in the hydrophobic regime, has to be taken into account [30]. To illustrate the superhydrophobic properties of the nanofur, the video in Supporting Information File 1 shows water drops on a polypropylene sheet rolling around as the sheet is tilted. The high contact angle can be seen even with the naked eye.

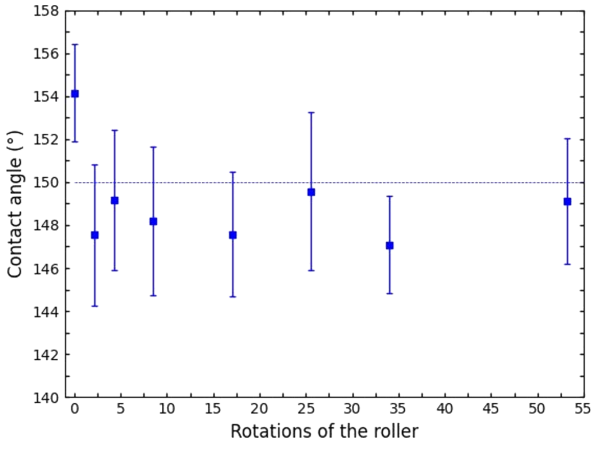


Figure 5: Contact angles measured along a 25 m long foil of nanofur produced in the described roll-to-roll process. A reduction by about 4° is measured when the newly sandblasted roller is first covered in fresh residues. As long as the production process is not interrupted, no further decrease in contact angle occurs.

Since oil absorption is one of the advantageous features of nanofur, we measured its oil absorption capacity. For that, we submerged pieces of the R2R-fabricated nanofur PP film for 20 s in motor oil, let excess oil drip off, and determined the absorbed oil mass by weighing [23]. We used two oils with different viscosity for this analysis. The hydraulic oil TOTAL Azolla ZS 32 had a viscosity and a density of 32 mm^2/s and 875 kg/m^3, respectively, and the gear oil TOTAL Carter EP 320 of 320 mm^2/s and 910 kg/m^3, respectively. As expected from a previous study [23] the absorption capacity increases with viscosity as the absorbed film thickness increases with this parameter. The PP nanofur absorbed 185 g/m^2 of Azolla 32 and 561 g/m^2 of Carter EP320. We conclude that the overall water repellency and oil absorption capacity of the R2R-fabricated nanofur film is in the same range as for nanofur fabricated with the traditional hot-pulling process in a hot-embossing machine [31]. (The videos in Supporting Information File 3 and Supporting Information File 4 show the capability of oil–water separation of nanofur.) Once contaminated with oil, the contact angle with water decreases to below 90°. This makes sense since the contact angle is now essentially measured between the oil film and water. The amount of material that can be fabricated in a R2R process, however, is considerably larger. Furthermore, it is much faster as it is a continuous process. Even with our lab machinery, which is not optimized for speed, relatively large quantities of nanofur can be processed in a matter of minutes (extrusion speed: 1.3 m/min, structuring speed = 2.3 m/min). This, together with the use of machines that are industry standard and the renunciation of complex and therefore costly molds, leads us to believe that our process can fabricate nanofur in a very cost-effective manner, especially on a commercial scale.

While the nanofur produced in this process does not differ significantly in function, that is, contact angle and oil absorption capacity, from nanofur produced by classical hot embossing, the overall structural appearance of the microstructures is different (Figure 6). While the hot-embossed nanofur consists of tiny hairs standing out relatively straight from the surface, R2R nanofur tends to form larger ridges that culminate in hair like tips. Also, since the rollers rotate, these ridges tend to be slightly slanted against the direction in which the polymer traveled through the calender.

Fabrication of nanopads

It is a remarkable quality of nanofur that it is superhydrophobic and oleophilic at the same time. Nonpolar liquids are immediately absorbed by the fractal polymeric surface while polar liquids are repelled [16]. Consequently, mixtures of oil (nonpolar) and water (polar) are easily separated. A promising application of nanofur is therefore the cleaning of oil spills [23,31]. This behavior can be also utilized for the fabrication of membranes that filter oil out of water (or vice versa) [17]. For that, the nanofur is perforated with small holes, so that oil passes through the polymeric film while water, due to its high contact angle with the surface, cannot penetrate the holes. As shown in the following, we used this property for the development of an

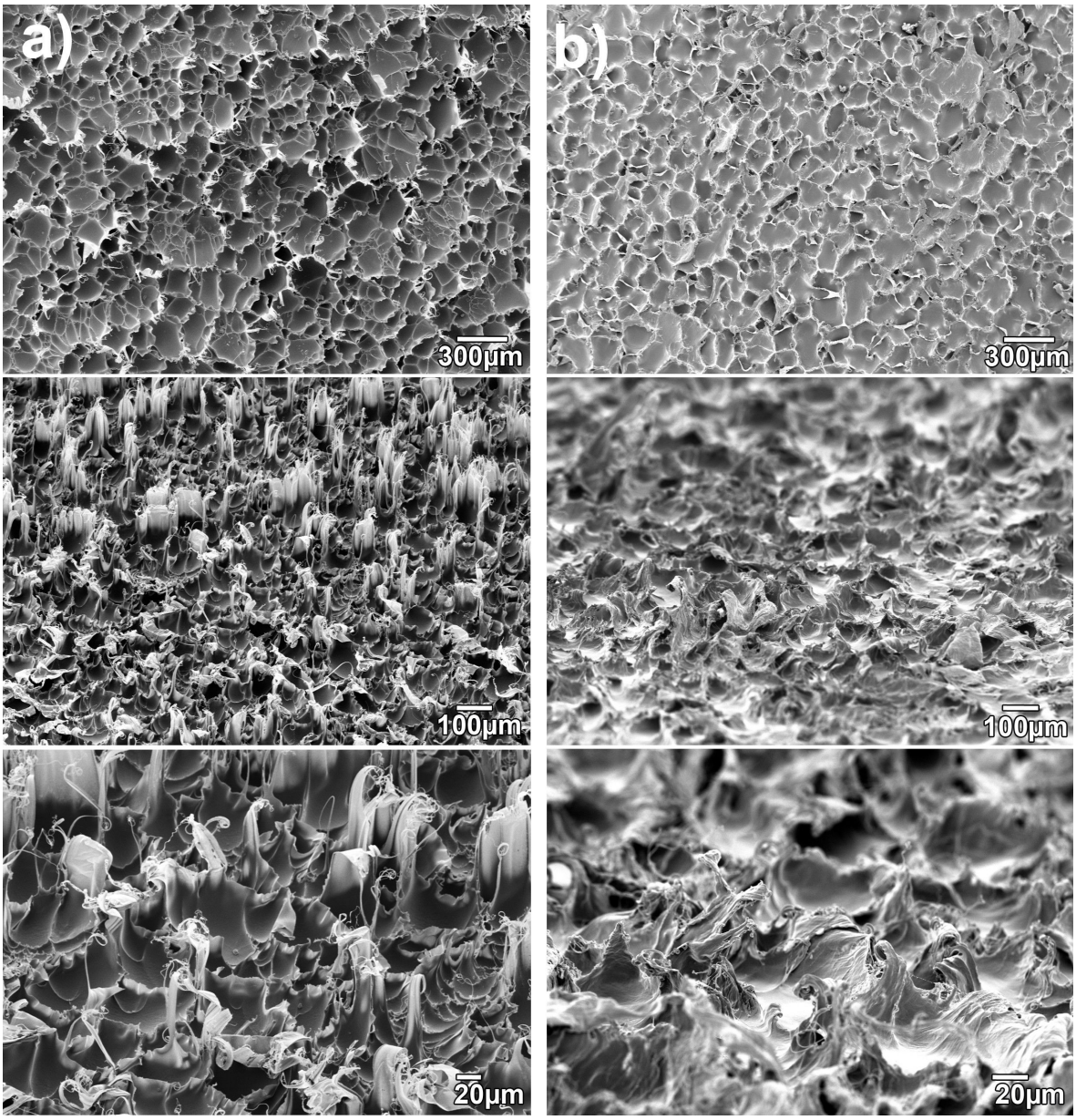


Figure 6: Comparison between nanofur produced by classical hot embossing and R2R nanofur. Even though morphological differences are obvious, the two samples do not differ in function, that is, contact angle. Column (a): Nanofur produced by classical hot embossing. The hairs stand out separately and are relatively straight with a high aspect ratio. Column (b): Nanofur produced by a roll-to-roll process. The topmost pictures are a top view, the others have been taken at a tilt angle of 60°. The structures consist of ridges that culminate in hair-like structures. These ridges can be slightly slanted against the direction in which the polymer traveled through the calender.

exemplary product made of nanofur for the clean-up of oil spills, so-called nanopads.

The standard practice for cleaning up oil spills is scooping the oil film together using barriers, skimming the oil slick, and using separators to clean the remaining water. This method is limited to suitable conditions and, even under optimal circumstances, only recovers about 35% of the spilled oil [32-34]. While somewhat effective for large-scale oil spills, this is unpractical for smaller spills, for example, after car accidents or small tank leaks. Burning the oil is a method often used as well, but requires a certain thickness of the oil film and a low water content in the oil. Furthermore secondary pollution is a problem with burning [34]. Chemical dispersion can be a last-ditch effort to protect sensitive areas from an oil spill but does not separate the oil from the water; many dispersants can also be

toxic to the environment [33]. Commonly used sorbents used in the emergency response to oil spills absorb not only oil but also large quantities of water [23,34].

The schematic design of the nanofur pads is shown in Figure 7a. The nanopads embed an oil-absorbing material, such as cotton, in a perforated polypropylene film covered in nanofur. The nanofur easily separates oil from water so that the absorbent material can trap the oil.

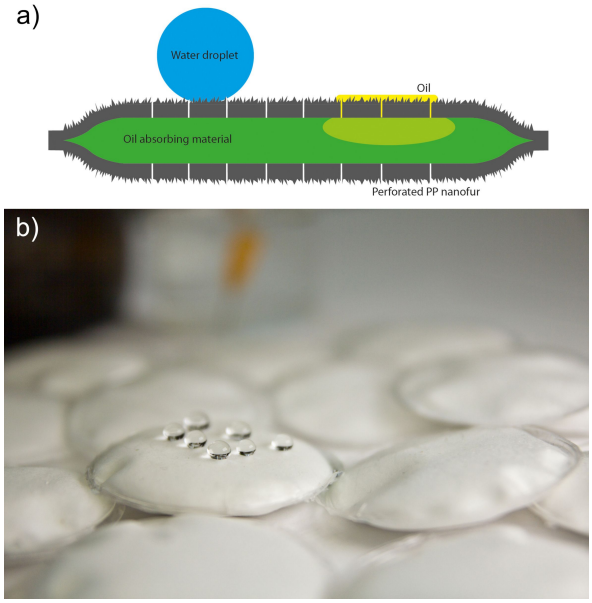


Figure 7: (a) Schematic side view of the nanopads indicating their functionality. Two perforated polypropylene foils, which are covered with nanofur on the outside, enclose an oil-absorbing material. The two foils are heat-sealed at the edge. If the nanopads are dipped in an oil spill, the oil is adsorbed by the nanofur, penetrates into the small holes, and is finally absorbed by the enclosed oil-absorbing material. The small holes are mechanically punched into the nanofur film and have diameters of about 100 µm. (b) Photo of several nanopads (diameter: 48 mm) produced as described in the text. Due to the nanofur cover, the pads are strongly water repellent as demonstrated by the water droplets positioned on the nanopad in the middle of the photo.

Figure 7b shows a photo of several manufactured nanopads. The fabrication steps are sketched in Figure 8. Figure 9 shows photos of intermediate fabrication steps. The nanopad fabrication starts with the cutting of circles with a diameter of 60 mm out of the structured PP film (Figure 8a). This is done with a round punch. Afterwards, the film is perforated. This can be done with various types of needles [17]. However, in order to speed up this process step, we used a Derma pen (DRS Dermaroller System) with 42 needles with a diameter of 100 µm each (Figure 8b, Figure 9a). After punching fifteen times, every circular nanofur film had about 600 holes. Afterwards two films are loosely connected with adhesive tape. This step simplifies filling the pad with a predetermined amount of oil-absorbing material (see Figure 9b). For the nanopads analyzed in the following, we used 1.1 g of cosmetic cotton (Rossmann AG). The filled pad is then placed between two polyimide films (DuPont Kapton, 50 µm) just covering the edge to prevent cutting through the material during heat sealing. The welding is carried out in a custom-made tool, consisting of two hollow brass cylinders with a diameter of 48 mm and a wall thickness of 2 mm. The cylinders were heated to 230 °C and pressed on the pad from both sides for about 15 s, welding the two PP films together (see Figure 8c and Figure 9c). The nanofur is destroyed in welded area. Afterwards, the uneven edges are cut off using another circular punch with a diameter of 48 mm (Figure 9d). The resulting pads have a surface area of $2\cdot(2\pi r^2) = 30.4\ \mathrm{cm}^2$ covered with nanofur. Due to the hot welding, a 2 mm margin is not covered. The height of the pads is about 10 mm. Extrapolating the shape of the pads as a spheroid, their volume can be calculated as $\frac{4}{3}\pi r^2 \frac{h}{2} = 10.13\ \mathrm{cm}^3$.

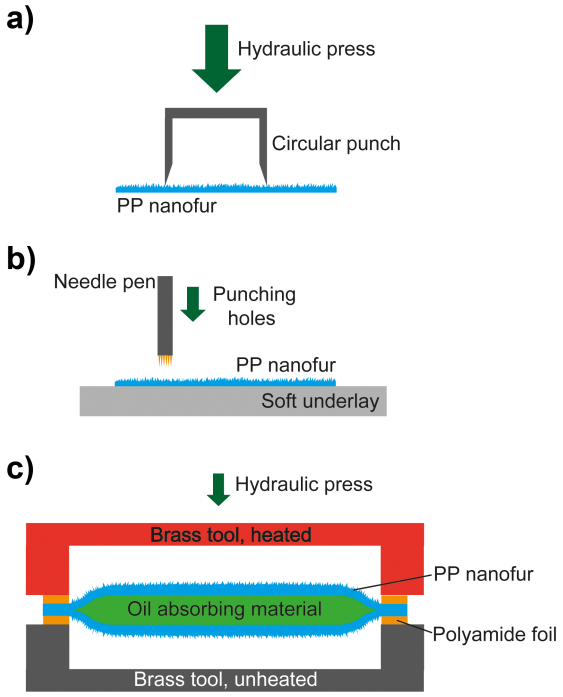


Figure 8: Schematic of the nanopad fabrication steps. (a) First, circular cut-outs are produced using a circular punch. (b) These pieces are perforated by punching holes with a needle pen. A soft underlay guarantees that the needles penetrate the film completely. (c) Two cut-outs are filled with oil-absorbing material, placed between polyimide masks, and heat-welded using a heated brass tool. Finally, the uneven edge is cut off with a circular punch giving the nanopad a round shape.

To measure the quantity of oil the pads can absorb, they were fully submerged in hydraulic oil, transmission fluid, and petrol. The viscosities (at 40 °C) and densities, respectively, of these exemplary oil products are: TOTAL Azolla ZS 32: 32 mm^2/s

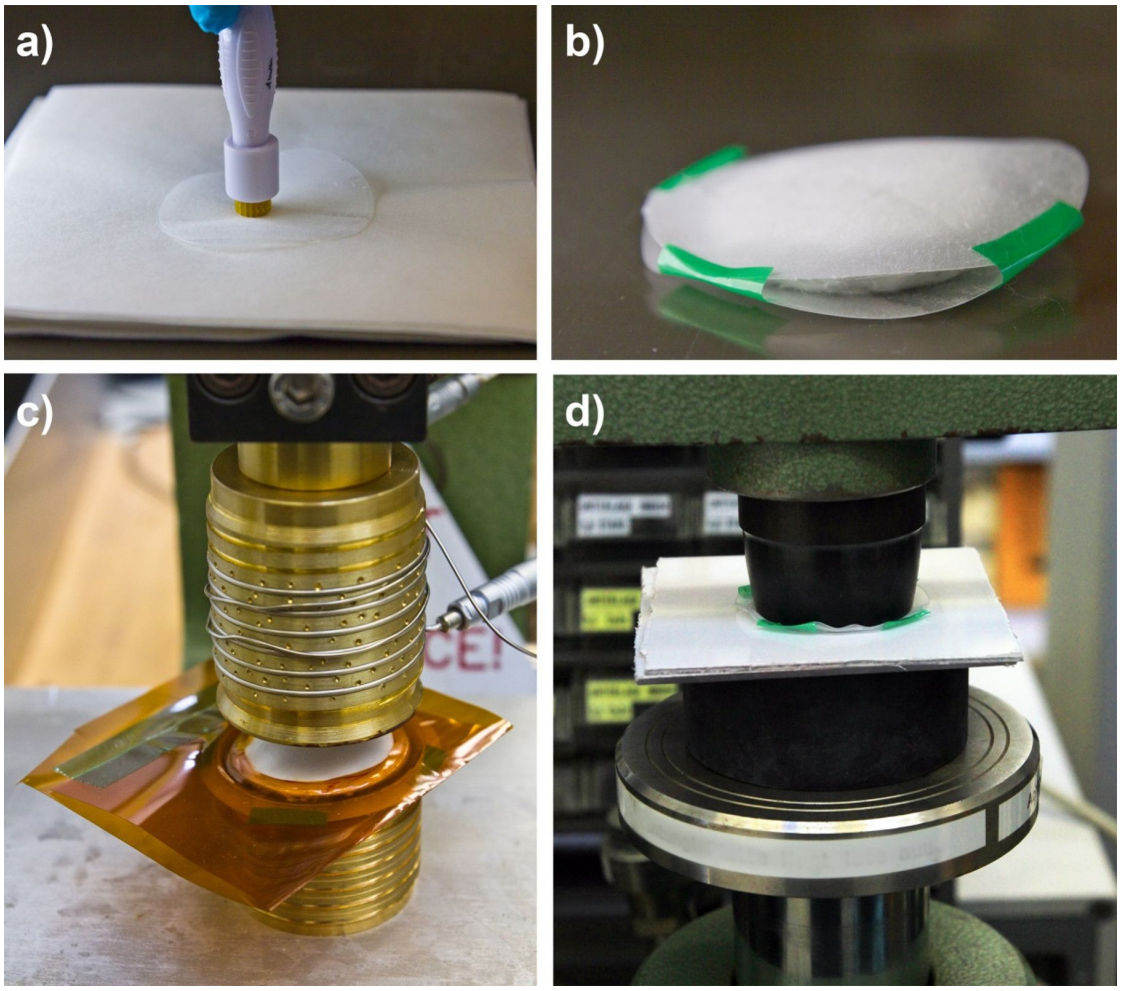


Figure 9: Fabrication of nanopads from polypropylene nanofur film. (a) In the first step, circular pieces are cut from nanofur film with a circular punch. Subsequently, tiny holes are pierced in the nanofur film using a needle pen. The needles have a diameter of about 100 µm. (b) To simplify filling the pads with oil absorbent material, the two halves are held together by scotch tape. (c) Such a preprocessed pad is placed between two polyimide films to avoid cutting through the material while welding. The upper hollow cylinder is heated and then pressed onto the pad for 15 s welding the two halves together. (d) Finally, a circular punch is applied to cut off the excess edge, leading to an evenly round pad.

and 875 kg/m^3; TOTAL Carter EP 320: 320 mm^2/s and 320 kg/m^3; and Super 95: 0.85 mm^2/s and 740 kg/m^3 at 40 °C. These values span a typical range of viscosities for various engine oils and transmission fluids used in everyday tasks and machines [35]. Therefore, such oils are typical products that are likely to cause oil spills, which are supposed to be cleaned up by the nanopads.

After different periods of time, the pads were taken out of the oil and excess oil was allowed to drip off for two minutes. Figure 10 shows the quantity of oil absorbed by the pads after different exposure times. The pads absorb immediately about 0.6 to 0.8 g of oil. This amount is consistent with the quantity of oil that the nanofur surface absorbs. After that, the oil absorption per time decreases because the oil has to penetrate into the nanopads through the punched holes. Therefore, it takes some hours before the pads start to saturate. Finally, additional oil is absorbed very slowly. The last measurement was taken after 48 h to ensure that the pads are saturated completely. The absorbed quantity of oil is similar for all three tested oils, the absorption speed, however, is not. As it can be expected, the viscosity of the oil determines how fast the oil penetrates the nanopads. A lower viscosity leads to faster absorption. As soon as the nanofur is in contact with the oil, an oil film builds up on its surface decreasing the water contact angle to below 90°. Since water and oil cannot mix and the holes are still covered by the oil film, the pads do not absorb any water.

To illustrate the capabilities of the nanopads for oil–water separation and their use in the cleanup of oil spills, the video in Sup-

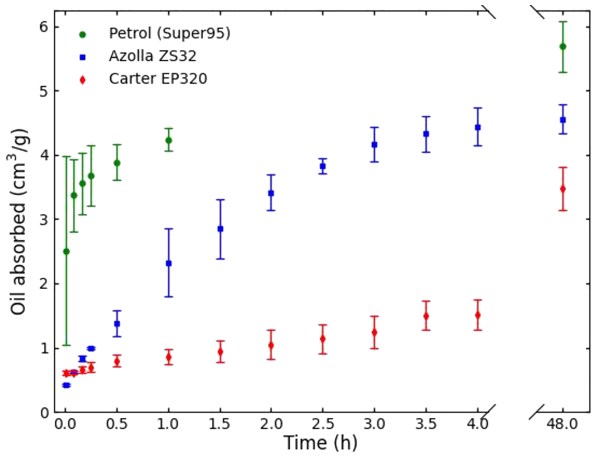


Figure 10: Oil absorption as a function of the time for pads filled with cotton and different oils. The higher the viscosity of the oil, the slower it is absorbed.

porting Information File 3 shows a droplet of water–oil emulsion being separated by nanofur. The video in Supporting Information File 4 shows a small drop of colored oil in a jar of water being absorbed completely by a single nanopad.

Conclusion

We introduced and evaluated a roll-to-roll process to fabricate a large thin polymeric film covered with superhydrophobic and oleophobic nanofur. This process has the potential to be upscaled to industrial standards by utilizing wider rollers in dedicated calenders and, to some extent, by increasing conveying speed and temperature of the roller. The most important parameters for the successful large-scale fabrication of thin nanofur, that is, gap size and roller temperature, have been identified and optimized. The structuring mold is an easy to produce sandblasted steel roller making mold fabrication, reconditioning, or testing of new parameters a straightforward process. Thus, the cost per unit area produced has been significantly reduced; furthermore, it is now possible to obtain large, continuous films covered in polymeric nanofur.

In a further optimization step, it is concievable that the polymer film used as a sacrificial layer, COC in our case, could be reused or recycled. This could be realized either directly, if the surface of the film is not damaged/contaminated or by shredding and extruding a new support film. This sacrificial layer is essential to produce a thin film. It is necessary to find a material that sticks to the polymer the nanofur is to be made of, but can also easily be separated after the structuring step. For films thicker than 1 mm, the mechanical stability of nanofur during hot pulling is sufficient, and the sacrificial layer is not needed. Future research might show how other polymers, especially biodegradable ones, can be hot-pulled in a R2R process. Furthermore, it might be possible to produce thin nanofur without sacrificial layer directly in the extruder from the polymer melt.

The produced thin PP nanofur served as base material to fabricate nanopads. These pads are designed for the clean-up of small oil spills on small waters. Their design might be further optimized for real-life applications. This might include size and shape, as well as the number and diameter of the punched holes. Furthermore, it might be possible to increase absorption speed and amount via the filling or the holes of the nanopads. The filling material itself or its amount might be improved.

Many other applications of thin nanofur, such as new kinds of food packaging and bottles, anti-fouling [36] and antibacterial [37] surfaces, or drag reduction [38] are imaginable. With the low-cost production of large areas of nanofur they seem also financially feasible.

Supporting Information

Supporting Information File 1

Single droplets of water on a thick sheet of nanofur produced with our roll-to-roll process. The droplets roll off easily at even the slightest tilt of the sample.
[https://www.beilstein-journals.org/bjnano/content/supplementary/2190-4286-13-102-S1.mp4]

Supporting Information File 2

Drops of water on slanted sheets of nanofur. The left sample has longer hairs, the hairs on the right sample are shorter. The video shows that longer hairs tend to pin the drops and, also, that, once the drops roll, they do so much slower than on the samples with short hairs.
[https://www.beilstein-journals.org/bjnano/content/supplementary/2190-4286-13-102-S2.mp4]

Supporting Information File 3

Droplets of oil water emulsion on a piece of nanofur showing oil–water separation.
[https://www.beilstein-journals.org/bjnano/content/supplementary/2190-4286-13-102-S3.mp4]

Supporting Information File 4

A drop of colored oil (TOTAL Carter EP 320 mixed with a small amount of oil paint) is dispensed in a jar of water and then completely absorbed by a single nanopad.
[https://www.beilstein-journals.org/bjnano/content/supplementary/2190-4286-13-102-S4.mp4]

Acknowledgements

It is a pleasure to thank our colleagues from IMT for continuous support and help in the lab.

Funding

This work was supported in part by the Karlsruhe Nano Micro Facility (KNMF) and the MWK through the research program "Ideenwettbewerb Biotechnologie – Von der Natur lernen".

ORCID® iDs

Patrick Weiser - https://orcid.org/0000-0001-9578-8504
Robin Kietz - https://orcid.org/0000-0002-5802-6997
Hendrik Hölscher - https://orcid.org/0000-0002-1033-1669

References

1. Barthlott, W.; Neinhuis, C. *Planta* **1997,** *202,* 1–8. doi:10.1007/s004250050096
2. Velten, T.; Bauerfeld, F.; Schuck, H.; Scherbaum, S.; Landesberger, C.; Bock, K. *Microsyst. Technol.* **2011,** *17,* 619–627. doi:10.1007/s00542-010-1158-x
3. Truworth-Homes, NeverWet Superhydrophobic Coatings – It Does Exactly What Its Name Implies. https://truworthhomes.com/collections/super-hydrophobic-coatings-spray-buy (accessed March 14, 2022).
4. Heinisch, M.; Miricescu, D. *MATEC Web Conf.* **2017,** *121,* 03009. doi:10.1051/matecconf/201712103009
5. Nosonovsky, M.; Bhushan, B. *Multiscale Dissipative Mechanisms and Hierarchical Surfaces;* Springer: Berlin, Heidelberg, 2008. doi:10.1007/978-3-540-78425-8
6. Montazer, M.; Harifi, T. *Nanofinishes for self-cleaning textiles;* Nanofinishing of Textile Materials; Elsevier: Amsterdam, Netherlands, 2018; pp 127–143. doi:10.1016/b978-0-08-101214-7.00009-1
7. Barthlott, W.; Mail, M.; Neinhuis, C. *Philos. Trans. R. Soc., A* **2016,** *374,* 20160191. doi:10.1098/rsta.2016.0191
8. Feng, J.; Tuominen, M. T.; Rothstein, J. P. *Adv. Funct. Mater.* **2011,** *21,* 3715–3722. doi:10.1002/adfm.201100665
9. Yan, Y. Y.; Gao, N.; Barthlott, W. *Adv. Colloid Interface Sci.* **2011,** *169,* 80–105. doi:10.1016/j.cis.2011.08.005
10. Jeong, H. E.; Kwak, M. K.; Park, C. I.; Suh, K. Y. *J. Colloid Interface Sci.* **2009,** *339,* 202–207. doi:10.1016/j.jcis.2009.07.020
11. Liu, X.; Coxon, P. R.; Peters, M.; Hoex, B.; Cole, J. M.; Fray, D. J. *Energy Environ. Sci.* **2014,** *7,* 3223–3263. doi:10.1039/c4ee01152j
12. Gharghi, M.; Sivoththamann, S. *J. Vac. Sci. Technol., A* **2006,** *24,* 723. doi:10.1116/1.2167974
13. Her, T.-H.; Finlay, R. J.; Wu, C.; Deliwala, S.; Mazur, E. *Appl. Phys. Lett.* **1998,** *73,* 1673–1675. doi:10.1063/1.122241
14. Carey, J. E.; Crouch, C. H.; Younkin, R. Fabrication of micrometer-sized conical field emitters using femtosecond laser-assisted etching of silicon. In *Proceedings of the IEEE International Vacuum Microelectronics Conference,* 2001; pp 75–76. doi:10.1109/ivmc.2001.939660
15. Shang, H. M.; Wang, Y.; Limmer, S. J.; Chou, T. P.; Takahashi, K.; Cao, G. Z. *Thin Solid Films* **2005,** *472,* 37–43. doi:10.1016/j.tsf.2004.06.087
16. Röhrig, M.; Mail, M.; Schneider, M.; Louvin, H.; Hopf, A.; Schimmel, T.; Worgull, M.; Hölscher, H. *Adv. Mater. Interfaces* **2014,** *1,* 1300083. doi:10.1002/admi.201300083
17. Kavalenka, M. N.; Vüllers, F.; Kumberg, J.; Zeiger, C.; Trouillet, V.; Stein, S.; Ava, T. T.; Li, C.; Worgull, M.; Hölscher, H. *Sci. Rep.* **2017,** *7,* 39970. doi:10.1038/srep39970
18. Worgull, M. *Hot embossing: theory and technology of microreplication;* Elsevier: Amsterdam, Netherlands, 2000.
19. Ahn, S. H.; Guo, L. J. *ACS Nano* **2009,** *3,* 2304–2310. doi:10.1021/nn9003633
20. Striegel, A.; Schneider, M.; Schneider, N.; Benkel, C.; Worgull, M. *Microelectron. Eng.* **2018,** *194,* 8–14. doi:10.1016/j.mee.2018.02.022
21. Liang, H.-L.; Bay, M. M.; Vadrucci, R.; Barty-King, C. H.; Peng, J.; Baumberg, J. J.; De Volder, M. F. L.; Vignolini, S. *Nat. Commun.* **2018,** *9,* 4632. doi:10.1038/s41467-018-07048-6
22. Deshmukh, S. S.; Goswami, A. *Microsyst. Technol.* **2022,** *28,* 1077–1114. doi:10.1007/s00542-022-05265-0
23. Zeiger, C.; Rodrigues da Silva, I. C.; Mail, M.; Kavalenka, M. N.; Barthlott, W.; Hölscher, H. *Bioinspiration Biomimetics* **2016,** *11,* 056003. doi:10.1088/1748-3190/11/5/056003
24. Vüllers, F.; Gomard, G.; Preinfalk, J. B.; Klampaftis, E.; Worgull, M.; Richards, B.; Hölscher, H.; Kavalenka, M. N. *Small* **2016,** *12,* 6144–6152. doi:10.1002/smll.201601443
25. Terpilowski, K.; Rymuszka, D.; Holysz, L.; Chibowski, E. Changes in wettability of polycarbonate and polypropylene pretreated with oxygen and argon plasma. In *Proceedings of the 8th International Conference MMT-20142,* July 28–Aug 1, 2014; Ariel, Israel, 2014; pp 155–165.
26. Brown, P. S.; Bhushan, B. *Philos. Trans. R. Soc., A* **2016,** *374,* 20160193. doi:10.1098/rsta.2016.0193
27. Fuentes, C. A.; Zhang, Y.; Guo, H.; Woigk, W.; Masania, K.; Dransfeld, C.; De Coninck, J.; Dupont-Gillain, C.; Seveno, D.; Van Vuure, A. W. *Colloids Surf., A* **2018,** *558,* 280–290. doi:10.1016/j.colsurfa.2018.08.052
28. Weiser, P, *Entwicklung eines kontinuierlichen Verfahrens zur Herstellung von superhydrophobem Nanopelz.* M.Sc. Thesis, Karlsruher Institut für Technologie, Karlsruhe, Germany, 2020.
29. Kolew, A. *Heißprägen von Verbundfolien für mikrofluidische Anwendungen*. Ph.D. Thesis, Karlsruher Institut für Technologie, Karlsruhe, Germany, 2012.
30. Vuckovac, M.; Latikka, M.; Liu, K.; Huhtamäki, T.; Ras, R. H. A. *Soft Matter* **2019,** *15,* 7089–7096. doi:10.1039/c9sm01221d
31. Zeiger, C. *Biomimetics for Efficient Oil Water Separation: From Natural Oil Sorbents to Bioinspired Micro- and Nanostructured Polymeric Sorbents and Membranes*. Ph.D. Thesis, Karlsruher Institut für Technologie, Karlsruhe, Germany, 2018.
32. The Federal Interagency Solutions Group; Oil Budget Calculator Science and Engineering Team. Oil Budget Calculator. 2010; https://purl.fdlp.gov/GPO/gpo1684.
33. Vorsorgeplan Schadstoffunfallbekämpfung der deutschen Küstenländer und des Bundes, Bekämpfunshandbuch, VPS.system. 2019; https://www.vpsserver2.de/vpsweb/vps_buch/vps_bekaempfungshandbuch_web/index.html.
34. Xue, Z.; Cao, Y.; Liu, N.; Feng, L.; Jiang, L. *J. Mater. Chem. A* **2014,** *2,* 2445–2460. doi:10.1039/c3ta13397d
35. Castrol. https://www.castrol.com/de_de/germany/home/car-engine-oil-and-fluids/engine-oils/engine-oil-viscosity-grades.html (accessed Nov 15, 2021).
36. Genzer, J.; Efimenko, K. *Biofouling* **2006,** *22,* 339–360. doi:10.1080/08927010600980223

37. Zhang, X.; Wang, L.; Levänen, E. *RSC Adv.* **2013,** *3,* 12003–12020. doi:10.1039/c3ra40497h
38. Choi, C.-H.; Kim, C.-J. *Phys. Rev. Lett.* **2006,** *96,* 066001. doi:10.1103/physrevlett.96.066001

License and Terms

This is an open access article licensed under the terms of the Beilstein-Institut Open Access License Agreement (https://www.beilstein-journals.org/bjnano/terms), which is identical to the Creative Commons Attribution 4.0 International License (https://creativecommons.org/licenses/by/4.0). The reuse of material under this license requires that the author(s), source and license are credited. Third-party material in this article could be subject to other licenses (typically indicated in the credit line), and in this case, users are required to obtain permission from the license holder to reuse the material.

The definitive version of this article is the electronic one which can be found at:
https://doi.org/10.3762/bjnano.13.102

BEILSTEIN JOURNAL OF NANOTECHNOLOGY

Laser-processed antiadhesive bionic combs for handling nanofibers inspired by nanostructures on the legs of cribellate spiders

Sebastian Lifka*[1], Kristóf Harsányi[1], Erich Baumgartner[1], Lukas Pichler[1], Dariya Baiko[1], Karsten Wasmuth[2], Johannes Heitz[3], Marco Meyer[4], Anna-Christin Joel[4], Jörn Bonse[2] and Werner Baumgartner[1]

Full Research Paper

Open Access

Address:
[1]Institute of Biomedical Mechatronics, Johannes Kepler University Linz, Altenberger Straße 69, 4040 Linz, Austria, [2]Bundesanstalt für Materialforschung und -prüfung (BAM), Unter den Eichen 87, 12205 Berlin, Germany, [3]Institute of Applied Physics, Johannes Kepler University Linz, Altenberger Straße 69, 4040 Linz, Austria and [4]Institute of Biology II (Zoology), RWTH Aachen University, Worringerweg 3, 52074 Aachen, Germany

Email:
Sebastian Lifka* - sebastian.lifka@jku.at

* Corresponding author

Keywords:
biomimetics; electrospinning; laser-induced periodic surface structures (LIPSS); nanofibers; nanostructures

Beilstein J. Nanotechnol. **2022,** *13,* 1268–1283.
https://doi.org/10.3762/bjnano.13.105

Received: 05 April 2022
Accepted: 25 October 2022
Published: 07 November 2022

This article is part of the thematic issue "Biomimetics on the micro- and nanoscale – The 25th anniversary of the lotus effect".

Guest Editor: M. Mail

© 2022 Lifka et al.; licensee Beilstein-Institut.
License and terms: see end of document.

Abstract

Nanofibers are drawing the attention of engineers and scientists because their large surface-to-volume ratio is favorable for applications in medicine, filter technology, textile industry, lithium-air batteries, and optical sensors. However, when transferring nanofibers to a technical product in the form of a random network of fibers, referred to as nonwoven fabric, the stickiness of the freshly produced and thus fragile nanofiber nonwoven remains a problem. This is mainly because nanofibers strongly adhere to any surface because of van der Waals forces. In nature, there are animals that are actually able to efficiently produce, process, and handle nanofibers, namely cribellate spiders. For that, the spiders use the calamistrum, a comb-like structure of modified setae on the metatarsus of the hindmost (fourth) legs, to which the 10–30 nm thick silk nanofibers do not stick due to a special fingerprint-like surface nanostructure. In this work, we present a theoretical model of the interaction of linear nanofibers with a sinusoidally corrugated surface. This model allows for a prediction of the adhesive interaction and, thus, the design of a suitable surface structure to prevent sticking of an artificially nonwoven of nanofibers. According to the theoretical prediction, a technical analogon of the nanoripples was produced by ultrashort pulse laser processing on different technically relevant metal surfaces in the form of so-called laser-induced periodic surface structures (LIPSS). Subsequently, by means of a newly established peel-off test, the adhesion of an electrospun polyamide fiber-based nonwoven was quantified on such LIPSS-covered aluminium alloy, steel, and titanium alloy samples, as well as on polished (flat) control samples as reference and, additionally, on samples with randomly rough

surfaces. The latter revealed that the adhesion of electrospun nanofiber nonwoven is significantly lowered on the nanostructured surfaces compared with the polished surfaces.

Introduction

Nanofibers have a diameter of approximately 10 to 800 nm, whereas their length is much greater than their diameter, which is why the term fiber or thread is used. These fibers are constantly drawing the attention of engineers because their surface-to-volume ratio is favorable for applications in medicine, filter technology, textile industry, lithium-air batteries, and optical sensors [1-7].

The inherently small scale makes production as well as further processing of nanofibers challenging [8]. For the technical production of artificial nanofibers, different methods such as electrospinning [1,2,6-8] or microfluidic spinning [4] have been established. Despite a lot of effort to facilitate the production and handling of nanofibers [3-7], the stickiness of freshly produced and, thus, fragile nanofiber nonwoven mats remains a problem. This is mainly because nanofibers strongly adhere to any surface due to van der Waals forces [9]. For a cylindrical fiber with radius R interacting with the plane surface of a semi-infinite body, the energy per unit length due to van der Waals interaction is given as [9]:

$$\mu = -\sqrt{2R}\cdot\frac{A_\mathrm{H}}{24d^{3/2}}, \tag{1}$$

with the Hamaker constant A_H, which is according to [9]:

$$A_\mathrm{H} = \pi^2\cdot\rho_1\cdot\rho_2\cdot c. \tag{2}$$

Here, the mass densities (ρ_1 and ρ_2) of the interacting bodies and the London coefficient c, which describes the particle–particle interaction, are multiplied.

The van der Waals energy U_vdW of the fiber obtained due to the interaction is the integral of the above interaction function μ over the entire fiber length l, which can depend on the position along the fiber:

$$U_\mathrm{vdW} = \int_l \mu(l)\,\mathrm{d}l. \tag{3}$$

This formulation could be interpreted in such a way that if the radius of the fiber decreases, the van der Waals force also decreases and can, therefore, be neglected if R is sufficiently small. However, this is not always the case for these reasons: (1) Due to the smaller radius, the fiber also becomes softer. In consequence, the easier deflection can increase the contact area, resulting in larger forces. The van der Waals force is proportional to the root of the radius, $\mu \sim \sqrt{R}$, and the materials stiffness, expressed by the area moment of inertia J, is proportional to the fourth power of the radius, $J \sim R^4$. Hence, the fiber gains more contact area much faster than the force decreases. (2) With a smaller radius, more fibers can attach simultaneously to the surface, which leads to a further increase in the total interacting surface area.

Though technical nanofiber handling and processing is limited today, in nature, there are animals that are actually able to efficiently produce, process, and handle nanofibers, namely cribellate spiders [10,11]. Their capture thread consists of one or two axial fibers as "construction elements" surrounded by a wool of nanofibers. This wool is used to capture prey, deploying van der Waals forces and additionally embedding the fibers into the viscous waxy layer of the insects' cuticle [12,13]. One thread typically consists of 5000 to 30000 single fibers with a thickness of 10–30 nm. In the spinning process, the spiders extract this silk from the cribellum (spinning plate) and process it by "combing" the fibers to form a puffy structure surrounding the axial fibers [10]. To process the fibers, the spiders use the calamistrum, a comb-like structure of modified setae on the metatarsus of the hindmost (fourth) legs [10] (Figure 1). The 10–30 nm thick silk nanofibers do not stick to the calamistrum due to a special fingerprint-like nanostructure. This was characterized recently [14] for the calamistrum of *Uloborus plumipes* (commonly named feather-legged lace weaver or the garden center spider). Its fingerprint-like outmost surface structure has an approximately sinusoidal cross section with a periodicity of 200–300 nm and a height (amplitude) of approx. 200 nm. During the combing process, the nanofibers are pulled orthogonally over these nanoripples. It was shown that the nanostructure on the calamistrum in fact reduces adhesion of native spider silk and that this reduced adhesion can be mimicked by artificially structured polymer foils [14]. In order to technically integrate these antiadhesive structures, the structures have to be adapted as typical technical nanofibers differ quite significantly from spider silk fibers regarding diameter and material properties (e.g., Young's modulus).

In this work, we present a theoretical model of the interaction of nanofibers with a sinusoidal surface based on an energy approach. This model allows for a prediction of the adhesive interaction and, thus, the design of a suitable surface structure to

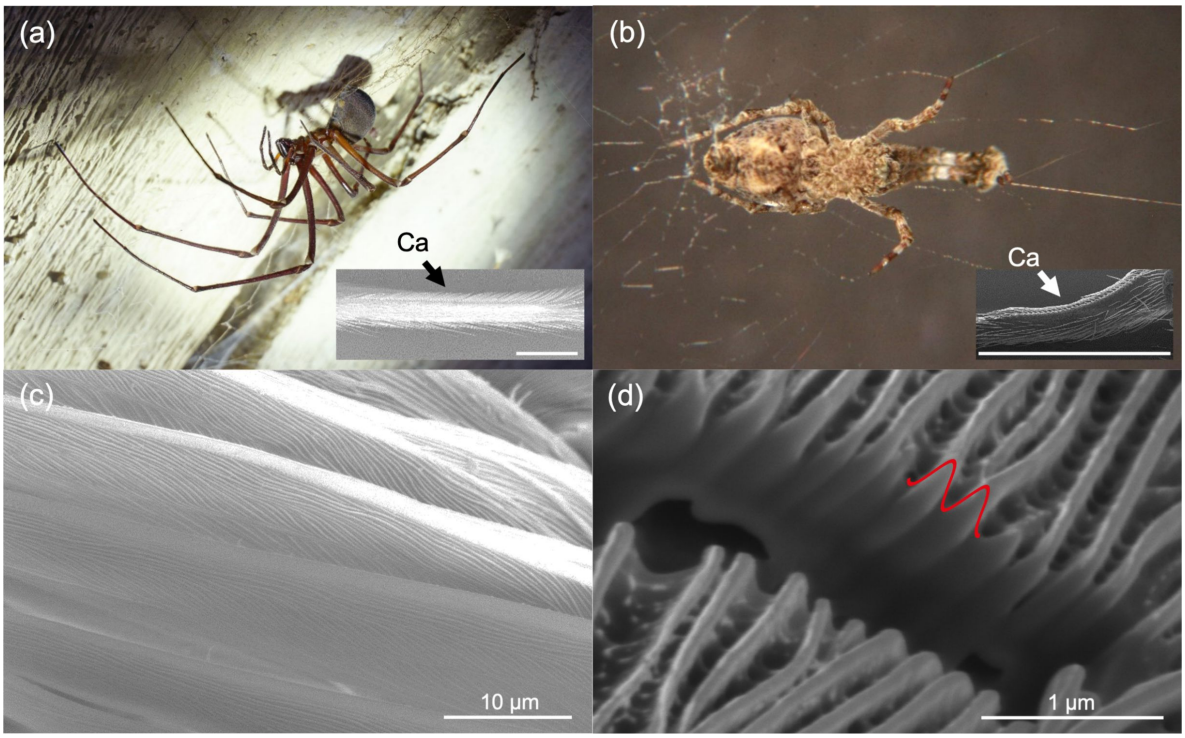


Figure 1: Images of four distantly related and differently sized cribellate spiders with same-sized nanoripples covering their calamistrum (antiadhesive comb to handle nanofibers). (a) Photography of the endemic and last species of an old Gondwanan lineage, the Tasmanian cave spider *Hickmania troglodytes* (body size of up to 2 cm [15] and a leg span up to 18 cm [16]). (b) Photography of the cosmopolitan feather-legged lace weaver *Uloborus plumipes* (body size up to 0.6 cm [17]). (c) Scanning electron micrograph of the calamistrum of *Jamberoo johnnoblei* (body size up to 0.8 cm [18]). (d) FIB-cut high resolution SEM image through the nanoripples on the calamistrum of the lace-webbed spider *Amaurobius similis* (body size up to 1.2 cm [19]), highlighting in red the abstracted sinusoidal surface corrugation as cross-sectional profile of the nanoripples. The insets in (a) and (b) provide SEM micrographs of the calamistra (Ca) of the respective spiders, with scale bars of 0.8 mm length. Data is presented in Table S1 of Supporting Information File 1.

prevent sticking of an artificially nonwoven of nanofibers. Similar to the description of the Lotus effect [20-23], where the wettability of the hierarchical surface structure of the lotus leaf can be described with an energy approach related to the surface free energy of the fluid, we use an energy approach related to the bending energy of the nanofibers to describe the fiber adhesion on structured surfaces. An important point is that the theory presented here deals with cylindrical fibers that come into contact with the surface structure, in contrast to earlier published works where solids with plane surfaces were assumed [24-28]. This is an important difference, which has to be considered when modelling the interaction of nanofibers with, in this case, a sinusoidal surface.

Laser-induced periodic surface structures (LIPSS) [29] represent a technical analogon of the nanoripples found on the calamistrum of the spider. They were produced by ultrashort pulse laser processing on different technically relevant metal surfaces (aluminium alloy, steel, and titanium alloy) according to theoretical predictions. Subsequently, the adhesion of electrospun polyamide fibers was quantified on these structures as well as on polished (flat) control samples as reference. In addition, different randomly rough surfaces were investigated and compared to the LIPSS. This bioinspired laser-based surface functionalization paves a new way for technologically improving the production of tools for handling of artificial nanofibers. This can facilitate and optimize the production of, for example, filter materials and nanofabrics.

Results and Discussion

Theoretical modelling

The general model is depicted in Figure 2. The course of the fiber is divided into two areas along the length coordinate x. These areas are (1) the contact area, that is, the area between the contact points (marked by red full circles in Figure 2), where the fiber adheres to the surface, and (2) the sagging area, where the fiber has no contact to the surface. The point of detachment of the fiber from the surface is defined as the detachment point x_0. This point can parametrize the curve and is initially assumed to be known. The fiber is assumed to have a certain bending stiffness and, thus, it can be modelled according to the linear elastic (Hookean) beam theory (Euler–Bernoulli beam theory).

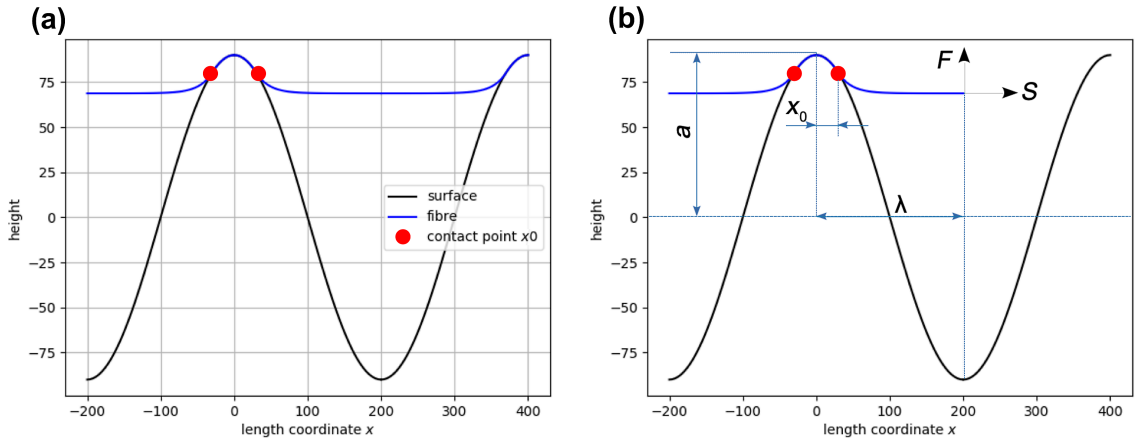


Figure 2: Principle geometry of the interaction of a nanofiber with a periodic sinusoidal surface topography (a) and as single length unit when cut free (b). The periodic surface structure is drawn in black, the fiber is drawn in blue. Surface and fiber are mathematically modelled by two functions, $f(x)$ and $w(x)$, respectively. The cross section of the surface is sinusoidal with a period of 2λ and an amplitude of a. A fiber on top of the surface is deflected partially due to van der Waals interactions. The point of detachment x_0 is used as a parameter to characterize the system. A longitudinal force S can stretch the fiber. For theoretical modelling, a single unit is cut free (b) and the action of the fiber at $x > \lambda$ is replaced by the yet unknown vertical force F. This is the force required to reach a value of zero for the slope of the fiber at $x = \lambda$.

Thus, we have to solve the ordinary differential equation (ODE) [30]

$$w''(x) = -\frac{M}{EJ}, \tag{4}$$

with w describing the deflection from the neutral position, M denoting the bending moment, E describing the Young's elastic modulus, and J denoting the second moment of area (moment of inertia of plane area).

In order to solve the above ODE, we need to know the bending moment and adequate boundary conditions. According to the model depicted in Figure 2 we assume to precisely know the position of the point of detachment x_0. At this location the two boundary conditions are

$$\begin{aligned} w(x_0) &= f(x_0) \quad \text{and} \\ w'(x_0) &= f'(x_0), \end{aligned} \tag{5}$$

that is, the mathematical curve describing the fiber $w(x)$ touches the curve describing the surface profile $f(x)$. To obtain the bending moment, we cut the fiber virtually at position λ, that is, in the middle of one period of the periodic surface structure. We know that a longitudinal force S is applied to the fiber in natural as well as in technical nanofiber production, and we assume a force F acting vertical at the position of the cut, λ, to bring the system back into equilibrium. This force is used to make the slope $w'(\lambda)$ assume a value of zero, that is, there is a horizontal tangent and, thus, $w'(x)$ is continuous and continuously differentiable at position λ. Hence, the ODE in Equation 4 can be solved by generally assuming a force F and calculate F according to the requirement that $w'(\lambda) = 0$.

The general solution of Equation 4 can be written as

$$\begin{aligned} w(x) = \frac{F\cdot\lambda}{S} - \frac{F\cdot x}{S} + w(\lambda) + C_1\cdot\exp\left[\sqrt{\frac{S}{EJ}}\cdot(x-\lambda)\right] \\ + C_2\cdot\exp^{-1}\left[\sqrt{\frac{S}{EJ}}\cdot(x-\lambda)\right]. \end{aligned} \tag{6}$$

For the following, this can be simplified as, at position $x = \lambda$, Equation 6 becomes

$$w(\lambda) = C_1 + C_2 + w(\lambda). \tag{7}$$

Thus, we obtain directly

$$C_1 = -C_2 \overset{\text{def}}{=} C. \tag{8}$$

After substituting Equation 8 into Equation 6 and performing a derivation with respect to x, we obtain $w'(x)$ as

$$\begin{aligned} w'(x) = -\frac{F}{S} + C\cdot\sqrt{\frac{S}{EJ}} \\ \cdot\left\{\exp\left[\sqrt{\frac{S}{EJ}}\cdot(x-\lambda)\right] + \exp^{-1}\left[\sqrt{\frac{S}{EJ}}\cdot(x-\lambda)\right]\right\}. \end{aligned} \tag{9}$$

In order to obtain $w'(\lambda) = 0$, we can insert $x = \lambda$ in Equation 9, yielding

$$w'(\lambda) = -\frac{F}{S} + C \cdot \sqrt{\frac{S}{EJ}} \cdot 2 = 0 \Rightarrow F = 2S \cdot C \cdot \sqrt{\frac{S}{EJ}}. \quad (10)$$

After inserting Equation 10 into Equation 6 and using the definition of the hyperbolic sine, we obtain

$$w(x) = 2C \cdot \left[\sinh\left(\sqrt{\frac{S}{EJ}} \cdot (x - \lambda) \right) \cdot (x - \lambda) \right] + w(\lambda). \quad (11)$$

Now, to fulfil the condition in the second part of Equation 5, we have to differentiate Equation 11 and solve the equation so that $w'(x = x_0) = f'(x = x_0)$.

$$w'(x_0) = 2C \cdot \left[\sqrt{\frac{S}{EJ}} \cdot \cosh\left(\sqrt{\frac{S}{EJ}} \cdot (x_0 - \lambda) \right) \right] - \sqrt{\frac{S}{EJ}} \quad (12)$$
$$\stackrel{\text{def}}{=} f'(x_0).$$

This directly yields

$$C = \frac{f'(x_0)}{2 \cdot \sqrt{\frac{S}{EJ}} \cdot \cosh\left(\sqrt{\frac{S}{EJ}} (x_0 - \lambda) \right)}. \quad (13)$$

Finally, in order to fulfil the boundary conditions $w(x = x_0) = f(x = x_0)$, one has to calculate $w(\lambda)$, which can be obtained from

$$w(\lambda) = f(x_0) - C \cdot \left[\sinh\left(\sqrt{\frac{S}{EJ}} \cdot (x_0 - \lambda) \right) - \sqrt{\frac{S}{EJ}} \cdot (x_0 - \lambda) \right]. \quad (14)$$

Taken together, if the topography function of the surface structure $f(x)$ is given, the bending line, which only depends on the position of the contact point x_0, is given to be

$$w(x) = 2C \cdot \left[\sinh\left(\sqrt{\frac{S}{EJ}} \cdot (x - \lambda) \right) \cdot (x - \lambda) \right] + w(\lambda)$$
$$\text{with } C = \frac{f'(x_0)}{2\sqrt{\frac{S}{EJ}} \cdot \cosh\left(\sqrt{\frac{S}{EJ}} (x_0 - \lambda) \right)} \quad (15)$$
$$\text{and } w(\lambda) = f(x_0) - C \cdot \left[\sinh\left(\sqrt{\frac{S}{EJ}} \cdot (x_0 - \lambda) \right) - \sqrt{\frac{S}{EJ}} \cdot (x_0 - \lambda) \right].$$

A special case should be considered separately, namely $S = 0$, that is, if no longitudinal force is applied and the fiber can freely form contact with the surface. Instead of reformulating the above result using L'Hôpital's rule, we could simply solve the initial differential Equation 4 with $S = 0$, which directly leads to

$$w(x) = f(x_0) + \frac{F}{EJ} \cdot \left(\frac{x_0^3}{3} - \frac{x \cdot x_0^2}{2} - \frac{\lambda \cdot x_0^2}{2} + \frac{\lambda \cdot x \cdot x_0}{1} - \frac{\lambda \cdot x^2}{2} + \frac{x^3}{6} \right) \quad (16)$$
$$+ f'(x_0) \cdot (x - x_0).$$

When, now, F is adjusted so that $w'(\lambda) = 0$, we obtain for this special case without longitudinal force

$$w(x) = f(x_0) - f'(x_0) \cdot \frac{x_0^2 + (3\lambda - x) \cdot x_0 + 2x^2 - 3\lambda \cdot x}{3(x_0 + x + 2\lambda)}. \quad (17)$$

Now, in any case, the position x_0 of the contact point remains to be determined. For this, we need to find the energy minimum of the system with respect to x_0, which would correspond to the position where, in equilibrium, the fiber detaches from the surface structure. There are three energetic contributions to the energy of the whole system that depend on x_0:

(i) The bending energy of a fiber in contact with the surface, that is, the elastic energy stored in the fiber in the region of contact from $x = 0 \ldots x_0$, which can be calculated for a linear elastic beam as

$$E_1(x_0) = \frac{EJ}{2} \cdot \int_0^{x_0} w''(x)^2 \, \mathrm{d}x = \frac{EJ}{2} \int_0^{x_0} f''(x)^2 \, \mathrm{d}x. \quad (18)$$

(ii) The bending energy of the free fiber, that is, in the region of no contact from $x = x_0 \ldots \lambda$, which follows to be

$$E_2(x_0) = \frac{EJ}{2} \cdot \int_{x_0}^{\lambda} w''(x)^2 \, \mathrm{d}x. \quad (19)$$

(iii) Finally, the van der Waals energy which, according to Equation 3, follows to be

$$E_3(x_0) = -\int_0^{x_0} \mu(x) \cdot \sqrt{1 + w'(x)^2} \, \mathrm{d}x. \quad (20)$$

It must be emphasized that, in principle, the above term can also account for other (additional) attractive energies such as electro-

static interactions. All these can be summarized in the term $\mu(x)$ and can, therefore, depend on the position and, thereby, on the distance of fiber and surface ($w(x) - f(x)$).

However, only the van der Waals energy E_3 exhibits a negative sign and, thus, decreases the total energy stored in the system, leading to more deflection and, thus, to more contact of the fiber with the surface. In contrast, the elastic energies E_1 and E_2 increase the total energy,

$$E_{\text{tot}}\left(x_0\right) = E_1\left(x_0\right) + E_2\left(x_0\right) + E_3\left(x_0\right). \tag{21}$$

In order to find the fiber detachment point x_0 in equilibrium, one needs to solve the optimization problem

$$\frac{\partial E_{\text{tot}}}{\partial x_0} = 0. \tag{22}$$

A general analytical solution to this optimization problem for any surface, that is, for any $f(x)$, cannot be found. However, numerical solutions are easily possible and, for some cases, even approximate analytical solutions are available. Let us assume the surface to be described by a cosine function (that is obviously identical with a laterally shifted sine function), that is,

$$f\left(x\right) = a \cdot \cos\left(\frac{\pi \cdot x}{\lambda}\right). \tag{23}$$

It has to be emphasized that, if the periodic modulation on the surface has a sinusoidal cross section but the fiber is not orthogonally oriented to these ridges, the cross section under an angle is still represented by a cosine function with same amplitude a but with a different characteristic length λ. Thus, the formal description derived here is still valid.

Due to the high exponent of the dependence of van der Waals energy and distance we can approximate the system and assume that we have a constant $\mu = \mu_{\text{vdW}}$ from $x = 0 \ldots x_0$ and $\mu = 0$ from $x = x_0 \ldots \lambda$. For this, we obtain the energy contributions in the case of a finite longitudinal force S as given below in Equation 24.

The integral for E_3 can be solved using complex incomplete elliptic integrals of the second kind. These can be calculated numerically. The system tends to the state of minimal total energy, $E_1 + E_2 + E_3 \rightarrow \min$.

In principle, there are three possible states: In state A, it requires more energy to bend the fiber to adapt to the surface than can be gained due to van der Waals interaction. A straight fiber touches only the tips of the surface. In state B, it is energetically favorable to deflect the fiber in order to obtain the interaction energy, but not all to the bottom of the sinusoidal surface topography. Thus, a clear total energy minimum exists. Finally, in state C, bending requires less energy than can be gained by the van der Waals interaction. Thus, the fiber adapts completely to the shape of the surface.

The energies and the corresponding shape of the fiber adaption to the surface of these three possible states, with an assumed

$$\begin{aligned}
E_1\left(x_0\right) &= \frac{\pi^3 \cdot EJ \cdot a^2 \cdot \left(\lambda \cdot \sin\left(\frac{2\pi \cdot x_0}{\lambda}\right) + 2\pi \cdot x_0\right)}{8\lambda^4}, \\
E_2\left(x_0\right) &= \int_{x_0}^{\lambda} \left(\frac{\left(\pi \cdot S \cdot a \cdot \sinh\left(\sqrt{(S/EJ)} \cdot (x-\lambda)\right) \cdot \sin\left((\pi \cdot x_0)/\lambda\right)\right)}{EJ \cdot \sqrt{(S/EJ)} \cdot \lambda \cdot \left(\cosh\left(\sqrt{(S/EJ)} \cdot (x_0 - \lambda)\right) - 1\right)} \right)^2 \mathrm{d}x \\
&\quad \cdot \left[\frac{\pi \cdot a}{\lambda} \cdot \sin\left(\frac{\pi \cdot x_0}{\lambda}\right)\right]^2 \cdot \frac{S}{16} \cdot \left[\cosh\left(\sqrt{\frac{S}{EJ}} \cdot (x_0 - \lambda)\right)\right]^{-1} \\
&\quad \cdot \left[\sqrt{\frac{EJ}{S}} \cdot e^{\left[-2 \cdot \sqrt{(S/EJ)} \cdot (x_0 + \lambda)\right]} \cdot \left(e^{\left(4\sqrt{\frac{S}{EJ}} x_0\right)} - e^{\left(4\sqrt{\frac{S}{EJ}} \lambda\right)} - 4\pi^2 \sqrt{\frac{S}{EJ}} \cdot e^{\left[2\sqrt{\frac{S}{EJ}} (x_0 + \lambda)\right]} \right) - 4\lambda \right], \\
E_3\left(x_0\right) &= -\mu_{\text{vdW}} \cdot \int_0^{x_0} \sqrt{1 + \frac{\pi^2 \cdot a^2}{\lambda^2} \cdot \sin\left(\frac{\pi \cdot x}{\lambda}\right)^2}\, \mathrm{d}x.
\end{aligned} \tag{24}$$

elastic modulus E = 80 MPa (a typical value for spider silk [31]) and S = 0 N, are shown in Figure 3. Figure 3a,b shows state A, Figure 3c,d shows state B, and Figure 3e,f shows state C.

State B only exists in a very narrow parameter window and, thus, can be neglected. We were able to find a solution for the transition from state C, in the following also called the adhesive state, into an anti-adhesive state A, in dependence on only a few parameters and some constants such as the Hamaker constant and the elastic modulus of the fiber. These free parameters are the amplitude a and the spatial period $\Lambda = 2\lambda$ of the sinusoidal surface, as well

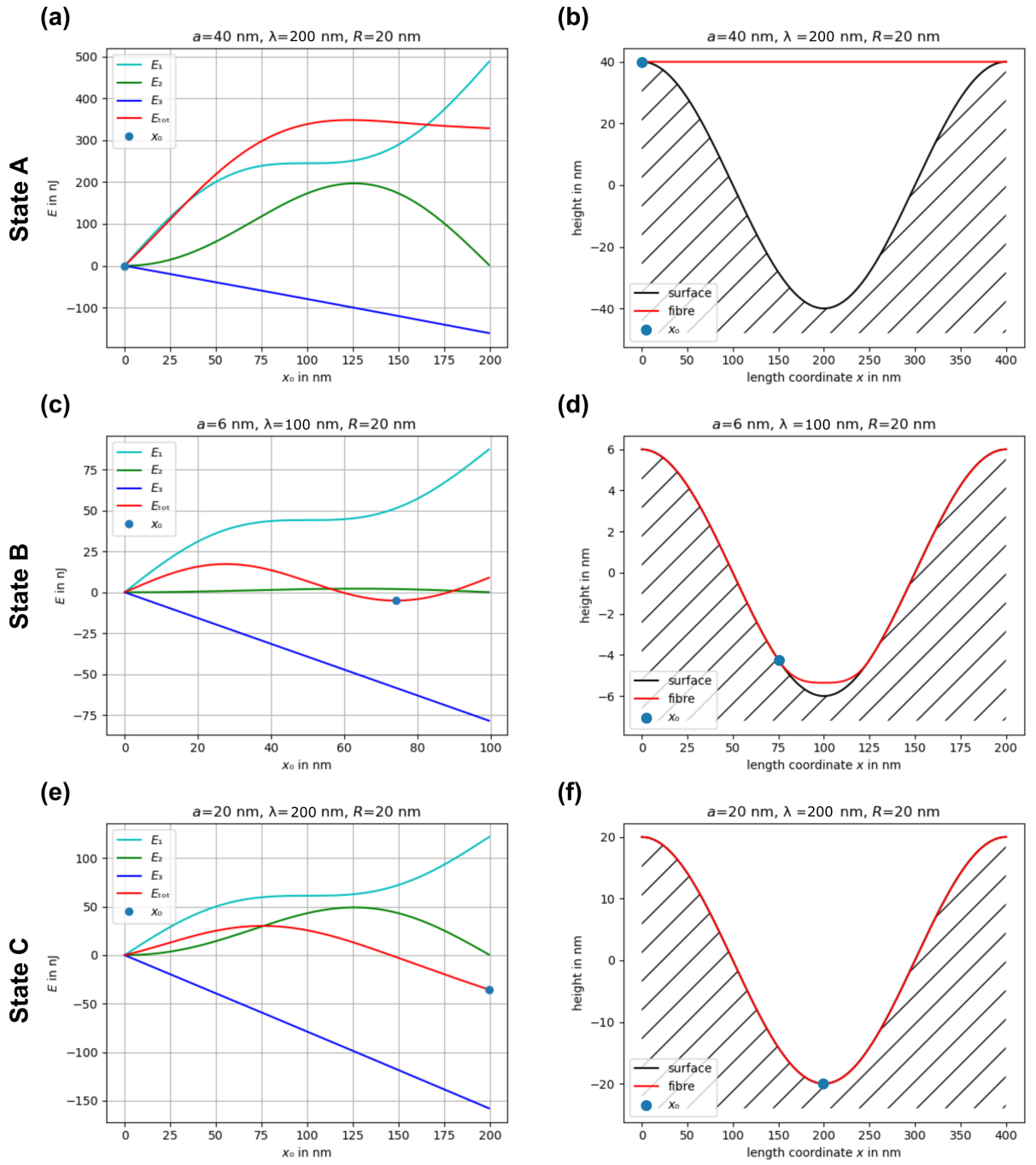


Figure 3: The three possible states: A (a, b), B (c, d), and C (e, f). (a, c, e) show the total energies E_{tot} as function of the parameter x_0. (b, d, f) show the corresponding energetically most favorable shape of the fiber adaption to the surface. The blue full circles mark x_0, at which E_{tot} is minimal and, thus, the point where the fiber detaches from the surface. The elastic modulus is assumed to be E = 80 MPa and S = 0 N. a denotes the amplitude, λ denotes the half of the period of the sinusoidal surface cross section and R is the fiber radius.

as the bending stiffness and the radius of the fiber in the case of $S = 0$.

While finding the minimum of the total energy is cumbersome when trying to find an analytical solution, the slope of the total energy can be calculated as

$$\left.\frac{\partial\left(E_1+E_2+E_3\right)}{\partial x_0}\right|_{x_0=0} = \frac{\pi^4 \cdot EJ \cdot a^2}{2\lambda^4} - \mu. \tag{25}$$

Thus, if

$$a \leq \sqrt{\frac{2\lambda^4 \cdot \mu}{\pi^4 \cdot EJ}}, \tag{26}$$

the fiber will adhere well as the energy directly decreases from $x_0 = 0$. The results are shown in Figure 4 for $E = 80$ MPa, a Hamaker constant $A_H = 7.5 \cdot 10^{-2}$, and for different fiber radii R (in nm).

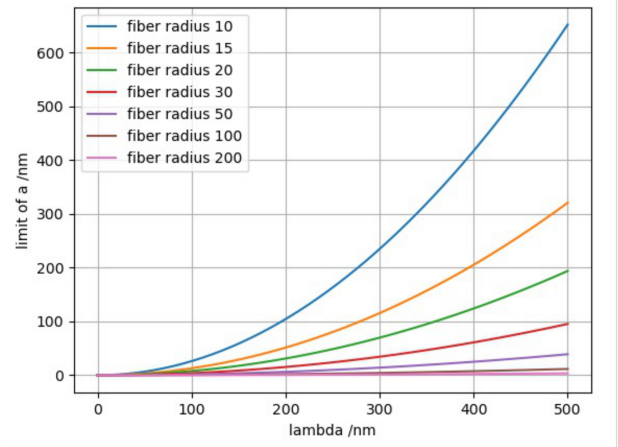


Figure 4: Transition from adhesive to anti-adhesive state for varying fiber radii ranging between 10 and 200 nm. The individual curves represent a lower limit of the surface modulation amplitude a, that is, the surface is adhesive for nanofibers through van der Waals forces only for values below the corresponding curves.

Another interesting phenomenon that can be described with this theory is that the total energy E_{tot} initially decreases with increasing amplitude a with regard to a flat surface. With increasing λ the effect becomes stronger. This means, that if the aspect ratio between amplitude a and λ is too low, the surface becomes even more adhesive for nanofibers than flat surfaces. Figure 5 shows the above-described effect for a fiber radius $R = 15$ nm and different characteristic lengths λ.

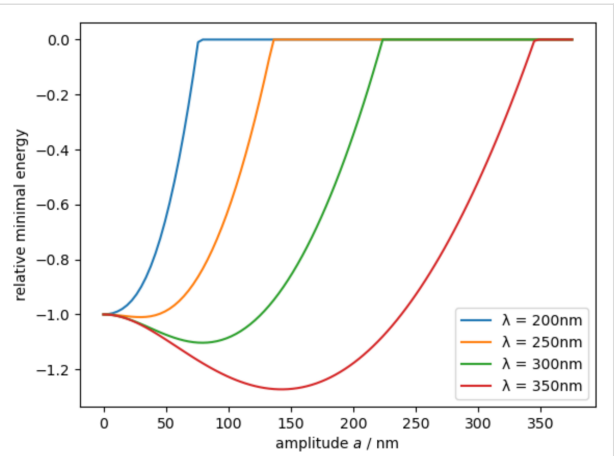


Figure 5: Relative total energy for different characteristic lengths λ for a fiber radius of $R = 15$ nm (the ordinate is normalized to a flat surface). One can see that the total energy initially decreases with increasing amplitude a with regard to a flat surface and, therefore, the adhesion increases if the amplitude a is too low.

Design and test of LIPSS-covered metal surfaces that are anti-adhesive for electrospun PA-6 fibers

In order to test the theory derived above, electrospinning of polyamide 6 (PA-6) in a laboratory setup onto structured metal samples (aluminum alloy, steel, and titanium alloy) was performed and the peel-off forces were determined using a custom-made peel-test device. PA-6 has an elastic modulus E of 0.6 up to 2.5 GPa, dependent on the treatment and the environmental conditions [32]. With our custom-made electrospinning setup, the typical diameters of the fibers are above 140 nm. Thus, from Equation 26, we can follow that adhesion is impaired if the modulation depth (double the amplitude) is approximately $2a > 250$ nm when assuming $E = 1$ GPa, $R = 70$ nm, and an average in-surface-plane inclination angle of the fiber of 45° with respect to the ripple ridge direction. The angle is used to take statistically into account that the fibers will orient randomly on the surface, that is, the fibers form a kind of mesh on the surface ripples, as can be seen in Figure 6. Thus, not all fibers will orient perpendicular to the surface ripples. During electrospinning, the first contact with the surface takes place in form of a single, thin nanofiber. Therefore, the theory presented above, where a single, thin fiber is assumed is still valid in this case. The modulation depth that typically can be achieved for LIPSS (LSFL type [33]) on metals is up to 400 nm. Thus, an antiadhesive effect can be assumed.

The peel-off force, that is, the force per unit length of the peeling edge necessary to separate the nonwoven from the surface, was measured for the LIPSS-covered samples, for polished surfaces, that is, flat samples as control, and for randomly rough surfaces produced by means of facing and

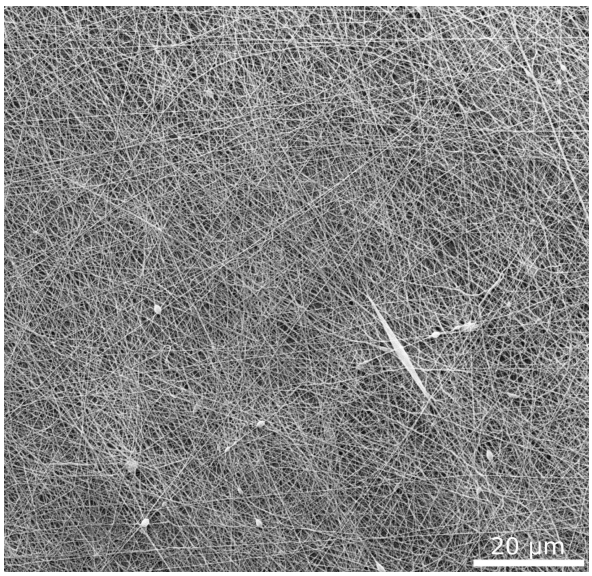


Figure 6: Scanning electron micrograph of electrospun nanofibers. One can see the random orientation of the individual fibers forming a kind of mesh.

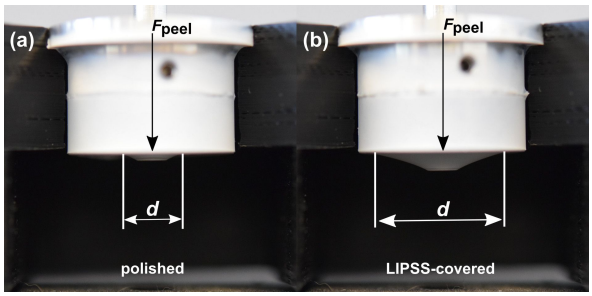


Figure 7: Peel-off force measurement of polished (a) and LIPSS-covered (b) steel samples. The applied weights and hence the normal forces are equal in panels (a) and (b). One can see that the cone diameter *d*, at equal applied forces, is larger on the LIPSS-covered sample than on the polished sample, which indicates that the peel-off force per unit length is smaller for the laser-structured samples.

grinding (sandpaper with grit size 80 and P240). Scanning electron micrographs of all samples can be found in Figure S1 in Supporting Information File 1. In Figure 7, the peel-off force measurement is exemplified for the polished (Figure 7a) and LIPSS-covered (Figure 7b) steel samples. The applied weights and, hence, the normal forces are equal in Figure 7a and Figure 7b. The cone diameter *d* of the nanofiber layer on the LIPSS-covered sample is larger than that on the polished sample, which indicates that the peel-off force for the laser-structured samples is lower than for the polished samples.

Nine different sample classes, that is, aluminium (Al) alloy polished, Al alloy LIPSS-covered, steel polished, steel LIPSS-covered, titanium (Ti) alloy polished, Ti alloy LIPSS-covered, Ti alloy faced, Ti alloy P240 (ground with P240 grit size sandpaper), and Ti alloy 80 (ground with 80 grit size sandpaper), were investigated as shown in Figure 7. For every sample class, $n = 5$ different measurements with different weights were performed and the mean values and the standard deviation were calculated for every sample class. Between the measurements, the samples were cleaned with 80% ethanol. The measured values of the peel-off forces per unit length needed for the LIPSS-covered and polished samples are listed in Table 1, the measured values of the randomly rough surfaces are listed in Table 2. All measurement results are also graphically shown as bar plots in Figure 8.

According to Table 1, the mean peel-off forces per unit length were 2.02 N/m for the LIPSS-covered Ti alloy and 2.79 N/m for the LIPSS-covered steel samples and, thus, significant lower than for the corresponding polished surfaces (7.69 N/m for Ti alloy and 8.87 N/m for steel). Thus, for both metals (Ti alloy and steel), the LIPSS reduce the adhesion forces by approximately 70–75% compared to the polished surfaces. For the aluminium alloy sample, the presence of LIPSS had no significant influence on the peel-off force.

Table 1: Peel-off force per unit length measurement results for the polished and LIPSS-covered samples.

Meas. no.	Al alloy polished (N/m)	Al alloy LIPSS (N/m)	steel polished (N/m)	steel LIPSS-covered (N/m)	Ti alloy polished (N/m)	Ti alloy LIPSS (N/m)
1	5.57	6.40	7.32	2.67	5.87	2.06
2	6.12	6.61	8.63	2.54	6.43	2.03
3	6.03	6.56	9.15	2.64	6.26	2.06
4	7.46	6.80	9.70	2.74	9.40	1.93
5	7.71	6.77	9.56	3.34	10.48	2.04
mean value	6.58	6.63	8.87	2.79	7.69	2.02
standard deviation	0.85	0.15	0.86	0.28	1.88	0.05

Table 2: Peel-off force per unit length measurement results for randomly rough samples.

Meas. no.	Ti alloy faced (N/m)	Ti alloy P240 (N/m)	Ti alloy 80 (N/m)
1	5.31	3.99	2.92
2	5.36	4.04	2.63
3	6.02	4.06	2.82
4	7.39	4.65	2.79
5	7.68	5.70	2.76
mean value	6.35	4.49	2.78
standard deviation	1.00	0.65	0.09

Furthermore, according to Table 2, the faced Ti alloy sample shows no significant difference in peel-off force compared to the polished control sample. The Ti samples ground with sandpaper showed a peel-off force reduced by approximately 40% (P240 grit size) and 65% (80 grit size), respectively. The investigated randomly rough surfaces did not reach the low peel-off forces for the LIPSS-covered samples. To prove the statistical significance of the measurement results, a statistical analysis was performed using Microsoft Excel. Details are presented in Table S2 in Supporting Information File 1.

To investigate the effects of the surface texture on the measured peel-off force in more detail, the surfaces of the Al alloy and the Ti alloy samples were investigated by means of atomic force microscopy (AFM). The arithmetic average roughness (*Ra*), the quadratic average roughness (*Rq*) and the maximum height (*Ry*) were measured; the results are shown in Table 3.

Table 3: Arithmetic average roughness (Ra), quadratic average roughness (Rq) and maximum height (Ry) of the samples measured by means of AFM.

Sample	*Ra* (nm)	*Rq* (nm)	*Ry* (nm)
Al alloy LIPSS-covered	19.7	25.0	170.0
Ti alloy LIPSS-covered	26.0	31.0	370.0
Ti alloy polished	3.3	4.6	19.7
Ti alloy faced	105.6	134.5	873.7
Ti alloy P240	86.0	108.0	909.0
Ti alloy 80	115.3	166.7	1450.0

The results of the AFM measurements revealed that the LIPSS covering the Al alloy surface are rather flat. *Ry*, which represents basically double the amplitude a of the LIPSS, is only 170 nm and, therefore, too low to reach the antiadhesive state according to the above theory ($2a > 250$ nm). This explains why the peel-off force measurement did not show a significant

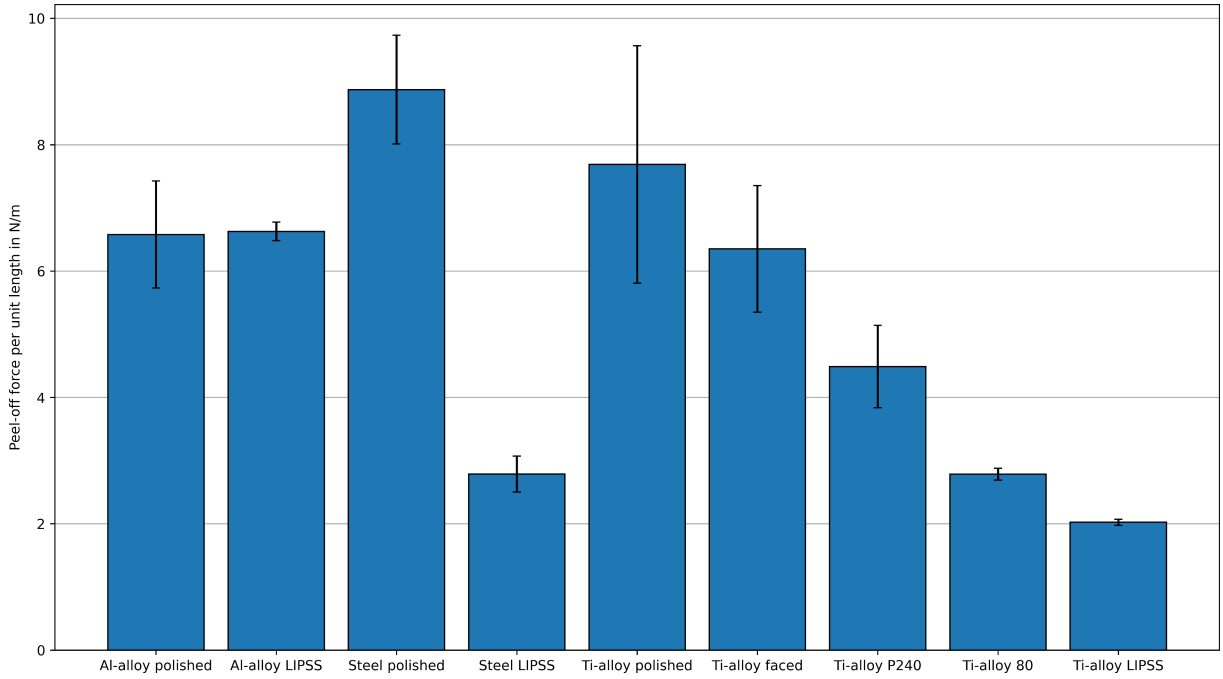


Figure 8: Peel-off force per unit length measurement results from Table 1 and Table 2 (mean values) visualized as bar plot. The error bars denote the standard deviations. Except for the Al alloy samples, the peel-off force for the LIPSS-covered samples is significantly lower than for the polished control samples and for the samples with randomly rough surface.

difference for the polished control and the LIPSS-covered Al alloy sample. Instead, the mean value is slightly higher for the LIPSS-covered sample than for polished control sample, which correlates with the behavior described in Figure 5. However, this effect could not be significantly proven.

Furthermore, Table 3 shows that an increasing surface roughness does not necessarily entail a decreasing peel-off force in the case of nanofibers. For example, the *Ra* value for all randomly rough surfaces is much higher than that for the LIPSS-covered Ti alloy sample, but the measured peel-off force is much lower for the LIPSS-covered Ti alloy sample. In addition, despite the high roughness of the faced sample, the peel-off force is not significantly lower than that of the polished control sample. However, a trend that the peel-off force decreases with coarser grit size can be observed for the samples ground with sandpaper. Therefore, in case of nanofibers a simple very rough surface is not enough to significantly lower the peel-off force.

Additionally, due to the lower peel-off force on the laser-structured samples, no fibers can be found after testing on the laser-structured surfaces, whereas on the polished surfaces a layer of fibers remains (OM and SEM). This is shown exemplary for the titanium alloy samples in Figure 9. Thus, the force measured for peel-off from the polished surface is not the force needed to detach the fibers from the surface, but to tear a superficial fiber layer from the rest of the nonwoven.

Conclusion

Mimicking the principle of nanostructures on the calamistrum of cribellate spiders, we were able to define an upscaled surface nanostructure with reduced adhesion force towards technical electrospun fibers. The biomimetic surface can be produced on metals by means of ultrashort pulse laser processing of self-organized laser-induced periodic surface structures, so-called LIPSS. For the technically relevant materials Ti alloy and steel, the presence of LIPSS reduced the peel-off forces by approximately 70–75% in both cases. Even more importantly, in contrast to the polished reference surface, no nanofibers remained at the LIPSS-covered surfaces. For the aluminium alloy samples, the presence of LIPSS had no significant influence on the peel-off force. This is due to the fact that the LIPSS on the aluminium alloy samples are rather flat and, therefore, do not have the required amplitude to reach the antiadhesive state. Furthermore, the measurements showed that a very rough surface does not necessarily entail a reduced peel-off force in case of cylindrical, thin nanofibers. Thus, one can conclude that the adhesion of electrospun nanofibers cannot be readily attributed to a simple roughness parameter, such as *Ra*. Rather, the correct aspect ratio of the sinusoidal surface structure as described in the above theory is important. Furthermore, as the experiments show, the sinusoidal structure based on the natural model allows us to adopt the structural dimensions to different fiber parameters, which is not possible with a random roughness of the surface.

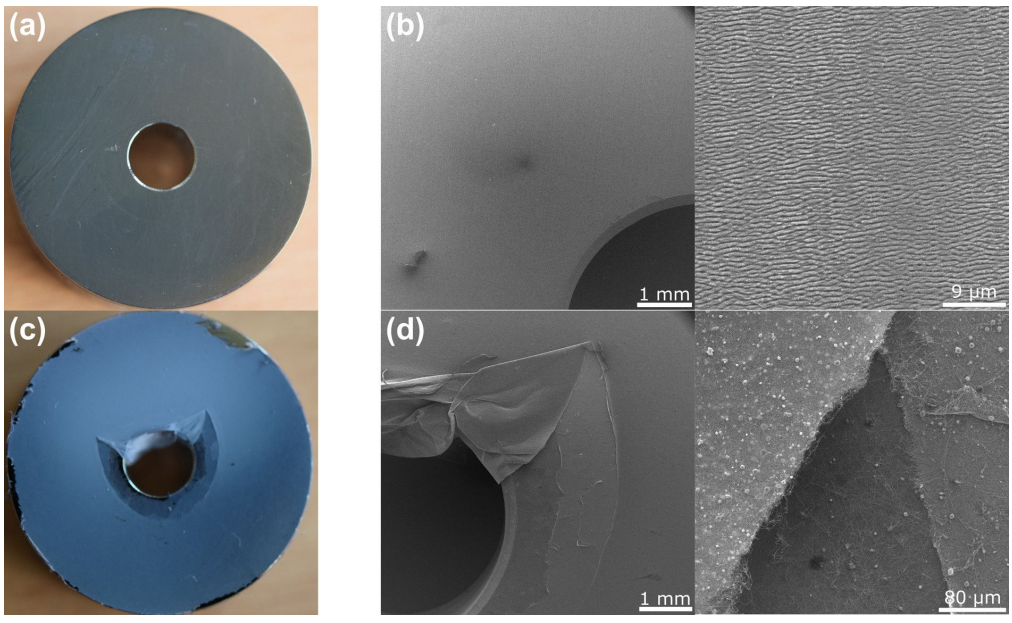


Figure 9: LIPSS-covered and polished titanium alloy surfaces after peel-off of an electrospun nonwoven. While the nanofibers could be removed entirely from the LIPSS (a, b), a film of nanofibers remains on the polished surface (c, d). This can be seen macroscopically (left) as well as in the SEM micrographs (right).

It must be mentioned that the dimensions of the LIPSS are much larger than the dimensions of the fingerprint-like structure found on *Uloborus plumipes*. This is because the diameter of the fibers produced by *Uloborus plumipes* is much smaller than the mean diameter of the electrospun fibers. Therefore, the periodicity and the amplitude of the surface structure must be adjusted accordingly.

In this work, only one fiber type was investigated. However, in principle, these surface structures can be adapted to the requirements for different fiber types, that is, different diameters and elastic moduli, and, thus, different bending stiffness values within technical limits. Such non-adhesiveness is beneficial for tools or parts of tools used in the production of nanofibers. A reduced adhesion of nonwovens would not only help prevent residues of nonwoven on tools used in the production, but will also reduce the chance of tearing or generally damaging the nonwoven at separation from a target or a tool. As one can imagine, even small damages of the nonwoven during production could lead to severe problems in the application. Refinement and consequent application of the theoretical model described here might help to further optimize the surface structure and/or to find even better surface topographies to make nanofiber nonwovens easier to handle for a broader field of applications.

Experimental

Sample materials

Different metal alloys (grade-5 titanium alloy: Ti6Al4V, aluminium alloy: AlMg3) were purchased from Schumacher Titan GmbH (Solingen, Germany) and Gemmel Metalle (Berlin, Germany) as rods of 25 mm diameter. The rods were reduced to 24 mm diameter and cut into ca. 8 mm thick slabs. Circular slabs of hardened 100Cr6 steel (24 mm diameter, 8 mm thickness) were purchased from Optimol Instruments Prüftechnik GmbH (Munich, Germany). The top surfaces of the samples were mechanically polished resulting in a mirror-like surface finish with an average roughness $R_a < 15$ nm.

Laser processing

The laser processing was performed using an ultrashort pulse laser (TruMicro 5050 femto edition, TRUMPF, Ditzingen, Germany) with a pulse duration of approx. 925 fs and a wavelength of 1030 nm, operated at 100 kHz pulse repetition rate. A galvanometer laser scanner (hurrySCAN II 14, SCANLAB GmbH, Puchheim, Germany), equipped with a f-theta lens of 160 mm focal length allowed us to scan the focused laser beam across the sample surface. The angle of incidence of the laser beam onto the sample surface was approx. 0°. The relative position of the sample to the scanner optics was adjusted to place the sample surface in the focal plane of the f-theta lens. At the sample surface, the focal diameter ($1/e^2$) of the Gaussian laser beam was determined by the D^2-method [34] as $2w_0 = 35.5$ µm. The samples were processed at optimized incident peak fluences of $\phi_0 = 0.35$ J/cm^2 for Ti6Al4V, and 0.54 J/cm^2 for 100Cr6 and AlMg3, while employing a meandering line-wise processing at a constant scan velocity of $v_x = 700$ mm/s and an inter-line separation of $\Delta = 5$ µm. The linear laser beam polarization was kept parallel to the scan direction. Immediately after laser processing, the samples were cleaned for 5 min in acetone in an ultrasonic bath and stored in a desiccator.

Figure 10 indicates the presence of the LIPSS at the entire top surface of the laser-processed Ti6Al4V sample through structural color effects, that is, optical diffraction of the ambient light at the sub-micrometric grating-like LIPSS. High-resolution

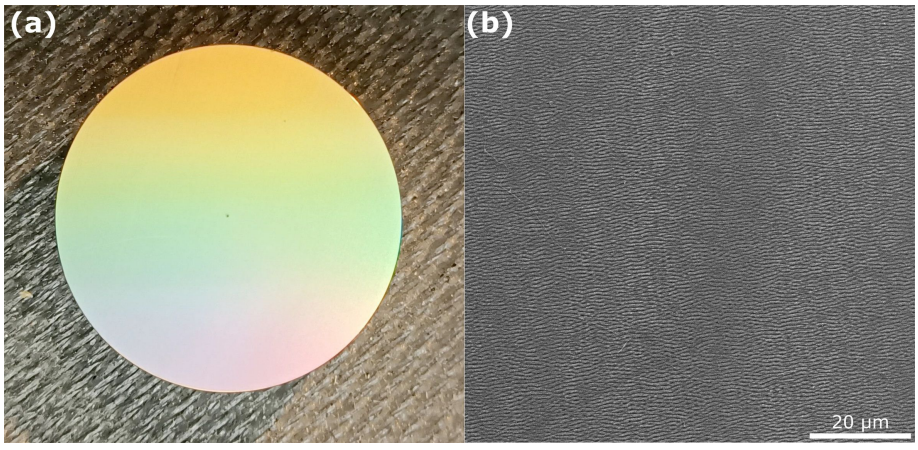


Figure 10: (a) Photography of a laser-structured titanium alloy sample after ultrafast laser processing. The colorful appearance arises from optical diffraction of the ambient natural light at the grating-like LIPSS-covered surface topography (structural colors). (b) Scanning electron micrograph of the LIPSS-covered titanium alloy surface.

optical microscopy (OM) confirmed the presence of LSFL-LIPSS with average spatial periods Λ between 700 and 800 nm (data not shown here). A 5 mm borehole was mechanically drilled through the laser-processed disks prior to the adhesion measurements.

Production of the randomly rough samples and measurement of the surface roughness

The Ti alloy samples with randomly rough surface were produced by means of facing and grinding with sandpaper. First, all Ti alloy samples were faced on a turning lathe. After facing, one sample was ground with sandpaper with grit size P240 and one sample was ground with sandpaper with grit size 80.

The surfaces of the polished, the LIPSS-covered, and the randomly rough Ti alloy samples, as well as the LIPSS-covered Al alloy sample were investigated by means of AFM on a Nanosurf Mobile S device (Nanosurf AG, Liestal, Switzerland). The investigated area had a size of 30 µm × 30 µm. The measurements were performed in contact mode with a Contr10 (Nanoworld, Neuchatel, Switzerland) pointprobe.

Electrospinning

Electrospinning was performed using a custom-made setup (Figure 11). The liquid PA-6 solution consisting of 6 g PA-6 polymer, 15 g formic acid, and 29 g acetic acid was mixed at 80 °C for about 90 min. The dope solution was delivered to the blunt needle tip (Sterican Standard Gr. 1 G20 x 1 ½'', B. Braun SE, Melsungen, Germany) using a custom-made syringe pump at a flow rate between 0.2 to 0.3 mL/h (Figure 11a) equipped with a 1 mL plastic syringe (Omnifix-F, B. Braun SE, Melsungen, Germany). The sample fixed on an aluminium sample carrier was placed horizontally opposite to the needle at a distance of about 10 cm. The positive electrode of a high-voltage generator (HCP 35 – 35 000, FuG Elektronik GmbH, Schechen, Germany) was clamped onto the needle and the ground electrode was clamped onto the aluminium sample carrier. The corresponding voltage was set to 20 kV. The spinning process was performed until a uniform layer of nonwoven was achieved on the sample surface. Figure 11b shows a spun sample after the electrospinning process. The surface is fully covered with a thin mesh layer of nanofibers, that is, the nonwoven.

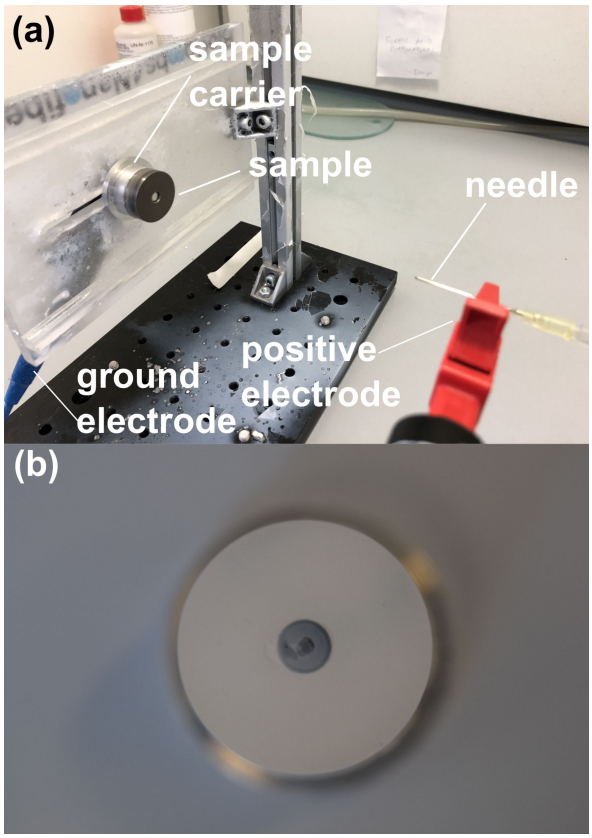


Figure 11: (a) Photography of the setup for the electrospinning process. (b) Top view of the spun sample after electrospinning, the surface is fully covered with a thin mesh layer of nanofibers (nonwoven).

Adhesion measurements

In order to quantify the adhesion of electrospun nonwoven, a new peel-off test had to be established. Existing peel-off tests are typically used for rather large samples; thus, the edge effects can be neglected. These effects become dominant when the width of the peeled homogeneous surface becomes small. In order to only peel the nonwoven from the interacting homogeneous surface and not from the sample edges (where unpredictable physical effects may take place) the adhesion test setup shown in Figure 12 was built.

The principle depicted in Figure 12 works as follows: The sample with a surface under investigation is mounted onto a sample carrier. Through this sample and the sample carrier a hole (diameter of 5 mm) is drilled. The hole is then filled with an aluminium piston that is fixed by a screw to form a straight surface. Then the nonwoven is spun onto the sample by means of electrospinning. After polymerization of the deposited nonwoven, the sample carrier is mounted into a holder and the fixation of the screw is removed. Then defined forces are applied onto the piston by placing weights on it. The nonwoven has only negligible bending stiffness macroscopically and, thus, the piston-induced force can only act longitudinal in the nonwoven. This force is split vectorial at the point of contact in a vertical peel off force and a local horizontal shear force. Due to the rotational symmetry the total horizontal forces cancel out. When exceeding a critical threshold value, the peel-off forces

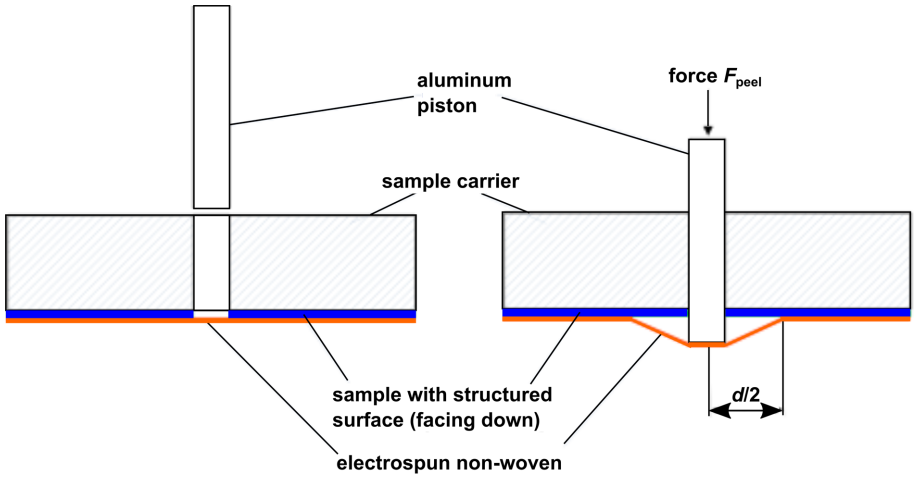


Figure 12: Measurement principle of the newly established peel-off test avoiding edge effects. Blue: sample with laser-structured surface; orange: electrospun nonwoven. Left: An aluminium piston is put into a 5 mm hole drilled into the sample carrier and the sample. Right: Defined forces F_{peel} are applied onto the aluminium piston by adding defined weights. When exceeding a critical threshold value, the peel-off forces separate the nonwoven from the sample surface, leading to the formation of a cone-like envelope with diameter d.

separates the nonwoven from the sample surface, leading to the formation of a cone-like envelope. Thus, the diameter d of the cone increases initially until, eventually, a force equilibrium occurs. This is due to the fact that the total peel-off force depends on the length c of the peeling edge. In our case this is

$$F_{\text{peel}} = p \cdot c = p \cdot d \cdot \pi. \tag{27}$$

Here, p is the peel-off force per unit length, which is a measure for the adhesion of the nonwoven to the surface under investigation. Thus, by optically measuring the diameter d of the cone, the peel-off force per unit length can be determined from the known force F_{peel}. The method was tested using siliconized paper and other materials, which were also tested by a commercially available peel-off meter. Both measurements were found to be in good agreement.

The measurement of the peel-off force was performed as follows: The investigated sample was fixed on the sample holder by means of double-sided tape and placed upside down in a custom-made 3D-printed mount. The whole setup was placed on a precision scale (Kern PLS 4200-2F, KERN & SOHN GmbH, Balingen-Frommen, Germany) and initially tared to zero. Then, successively different weights were applied, the measured weight was read from the display of the precision scale and a picture of the resulting cone was taken with an SLR-camera (Nikon D5300, Nikon Corporation, Tokio, Japan) equipped with a macro lens (AF-S Micro-NIKKOR 60 mm 1:2,8 ED, Nikon Corporation, Tokio, Japan). The resulting cone diameters d were then determined from the pictures using the free software Inkscape (V. 1.2.1, Inkscape Community). The peel-off was then calculated according to Equation 27 using Microsoft Excel for Mac (V 16.62, Microsoft, Washington, USA). The setup is depicted in Figure 13.



Figure 13: Setup used for the peel-off force measurements.

Measurement of the calamistral nanoripples

The species used in the experiments is not an endangered or protected species. Special permits were not required. All applicable international, national, and institutional guidelines for the care and use of animals were followed.

Amaurobius similis (Blackwall, 1861) and *Uloborus plumipes* (Lucas, 1846) were captured in Aachen, Germany, and kept in the laboratory before being frozen at −20 °C. *Jamberoo johnnoblei* (Gray & Smith, 2008) was captured in the wild at Mt. Wilson (Australia) and kept in the laboratory before preserving the species in 70% ethanol. Specimen of *Hickmania troglodytes* (Higgins & Petterd, 1883) preserved in 70% ethanol were kindly provided by the Australian Museum (Sydney, Australia). The fourth leg, bearing the calamistrum, was removed from the ethanol-preserved specimens, dried in an ascending ethanol

series, which was finally substituted by hexamethyldisilazane. After evaporation, the specimens were gold-sputtered (Hummer Technics Inc., Alexandria, USA; 7–10 mA, 5 min) and studied with the SEM (525 M, Philips AG, Amsterdam, Netherlands). Legs of *U. plumipes* were air-dried and otherwise prepared the same way for SEM analysis. Measurements were performed with ImageJ's FIJI software [35].

Legs of *A. similis* were air-dried and gold-sputtered (S150B, Edwards). The metatarsi were examined using a focused ion beam scanning electron microscope (FIB-SEM) tomography (Strata 400 STEM, FEI Company, Oregon, USA) at the Central Facility for Electron Microscopy at the RWTH Aachen University. Measurements were performed using the accompanying software (xT Microscope Control).

For all spiders, we measured the peak-to-peak amplitude of the nanoripples covering the calamistrum at the region of interest. In addition, FIB tomography was used to measure the depth of structure in *A. similis*.

Supporting Information

Supporting Information File 1

Additional experimental data.
[https://www.beilstein-journals.org/bjnano/content/supplementary/2190-4286-13-105-S1.pdf]

Acknowledgements

The authors would like to thank K. Zieger and C. Opitz (BAM division 9.5) for polishing the metal samples as well as K. Kistermann (GFE Aachen) for his active support at the FIB-SEM.

Funding

This work was supported by the European Union's Horizon 2020 research and innovation program within the project "BioCombs4Nanofibers" (Grant Agreement No. 862016, http://biocombs4nanofibers.eu). ACJ was funded by the Deutsche Forschungsgemeinschaft (JO1464/1-1).

ORCID® iDs

Sebastian Lifka - https://orcid.org/0000-0002-7032-8373
Kristóf Harsányi - https://orcid.org/0000-0002-2015-2875
Dariya Baiko - https://orcid.org/0000-0001-7216-6665
Johannes Heitz - https://orcid.org/0000-0002-5608-5133
Marco Meyer - https://orcid.org/0000-0002-7527-7165
Anna-Christin Joel - https://orcid.org/0000-0002-7122-3047
Jörn Bonse - https://orcid.org/0000-0003-4984-3896
Werner Baumgartner - https://orcid.org/0000-0002-3160-2050

Preprint

A non-peer-reviewed version of this article has been previously published as a preprint: https://doi.org/10.3762/bxiv.2022.23.v1

References

1. Wu, Y.; Wang, L.; Guo, B.; Ma, P. X. *ACS Nano* **2017,** *11,* 5646–5659. doi:10.1021/acsnano.7b01062
2. Ramakrishna, S.; Fujihara, K.; Teo, W.-E.; Yong, T.; Ma, Z.; Ramaseshan, R. *Mater. Today* **2006,** *9,* 40–50. doi:10.1016/s1369-7021(06)71389-x
3. Akampumuza, O.; Gao, H.; Zhang, H.; Wu, D.; Qin, X.-H. *Macromol. Mater. Eng.* **2018,** *303,* 1700269. doi:10.1002/mame.201700269
4. Costa-Almeida, R.; Gasperini, L.; Borges, J.; Babo, P. S.; Rodrigues, M. T.; Mano, J. F.; Reis, R. L.; Gomes, M. E. *ACS Biomater. Sci. Eng.* **2017,** *3,* 1322–1331. doi:10.1021/acsbiomaterials.6b00331
5. Vasita, R.; Katti, D. S. *Int. J. Nanomed.* **2006,** *1,* 15–30. doi:10.2147/nano.2006.1.1.15
6. Zhang, B.; Kang, F.; Tarascon, J.-M.; Kim, J.-K. *Prog. Mater. Sci.* **2016,** *76,* 319–380. doi:10.1016/j.pmatsci.2015.08.002
7. Wang, X.; Drew, C.; Lee, S.-H.; Senecal, K. J.; Kumar, J.; Samuelson, L. A. *Nano Lett.* **2002,** *2,* 1273–1275. doi:10.1021/nl020216u
8. SalehHudin, H. S.; Mohamad, E. N.; Mahadi, W. N. L.; Muhammad Afifi, A. *Mater. Manuf. Processes* **2018,** *33,* 479–498. doi:10.1080/10426914.2017.1388523
9. Parsegian, V. A. *van der Waals forces: A handbook for biologists, chemists, engineers, and physicists;* Cambridge University Press: New York, NY, USA, 2005. doi:10.1017/cbo9780511614606
10. Joel, A.-C.; Kappel, P.; Adamova, H.; Baumgartner, W.; Scholz, I. *Arthropod Struct. Dev.* **2015,** *44,* 568–573. doi:10.1016/j.asd.2015.07.003
11. Michalik, P.; Piorkowski, D.; Blackledge, T. A.; Ramírez, M. J. *Sci. Rep.* **2019,** *9,* 9092. doi:10.1038/s41598-019-45552-x
12. Bott, R. A.; Baumgartner, W.; Bräunig, P.; Menzel, F.; Joel, A.-C. *Proc. R. Soc. B* **2017,** *284,* 20170363. doi:10.1098/rspb.2017.0363
13. Hawthorn, A. C.; Opell, B. D. *J. Exp. Biol.* **2003,** *206,* 3905–3911. doi:10.1242/jeb.00618
14. Joel, A.-C.; Meyer, M.; Heitz, J.; Heiss, A.; Park, D.; Adamova, H.; Baumgartner, W. *ACS Appl. Nano Mater.* **2020,** *3,* 3395–3401. doi:10.1021/acsanm.0c00130
15. Piorkowski, D.; Blamires, S. J.; Doran, N. E.; Liao, C.-P.; Wu, C.-L.; Tso, I.-M. *J. Zool.* **2018,** *304,* 81–89. doi:10.1111/jzo.12507
16. Doran, N. E.; Kiernan, K.; Swain, R.; Richardson, A. M. M. *J. Insect Conserv.* **1999,** *3,* 257–262. doi:10.1023/a:1009677531343
17. Joel, A.-C.; Habedank, A.; Hausen, J.; Mey, J. *Zoology (Munich, Ger.)* **2017,** *121,* 10–17. doi:10.1016/j.zool.2016.12.002
18. Gray, M. R.; Smith, H. M. *Rec. Aust. Mus.* **2008,** *60,* 13–44. doi:10.3853/j.0067-1975.60.2008.1493
19. World Spider Catalog, 2022. World Spider Catalog. Version 23.0. Natural History Museum Bern. https://wsc.nmbe.ch/ (accessed Jan 21, 2022).
20. Barthlott, W.; Neinbuis, C. *Biol. Unserer Zeit* **1998,** *28,* 314–321. doi:10.1002/biuz.960280507
21. Barthlott, W.; Neinhuis, C. *Planta* **1997,** *202,* 1–8. doi:10.1007/s004250050096
22. Koch, K.; Bohn, H. F.; Barthlott, W. *Langmuir* **2009,** *25,* 14116–14120. doi:10.1021/la9017322

23. Koch, K.; Bhushan, B.; Barthlott, W. Multifunctional Plant Surfaces and Smart Materials. In *Springer Handbook of Nanotechnology,* 3rd ed.; Bhushan, B., Ed.; Springer: Berlin, Heidelberg, 2010; pp 1399–1436. doi:10.1007/978-3-642-02525-9_41
24. Fuller, K. N. G.; Tabor, D. *Proc. R. Soc. London, Ser. A* **1975,** *345,* 327–342. doi:10.1098/rspa.1975.0138
25. Briggs, G. A. D.; Briscoe, B. J. *J. Phys. D: Appl. Phys.* **1977,** *10,* 2453–2466. doi:10.1088/0022-3727/10/18/010
26. Persson, B. N. J.; Tosatti, E. *J. Chem. Phys.* **2001,** *115,* 5597–5610. doi:10.1063/1.1398300
27. Zilberman, S.; Persson, B. N. J. *J. Chem. Phys.* **2003,** *118,* 6473–6480. doi:10.1063/1.1558038
28. Persson, B. N. J.; Gorb, S. *J. Chem. Phys.* **2003,** *119,* 11437–11444. doi:10.1063/1.1621854
29. Bonse, J.; Krüger, J.; Höhm, S.; Rosenfeld, A. *J. Laser Appl.* **2012,** *24,* 042006. doi:10.2351/1.4712658
30. Gross, D.; Hauger, W.; Schröder, J.; Wall, W. A. Balkenbiegung. *Technische Mechanik 2;* Springer Vieweg: Berlin, Heidelberg, 2014; pp 87–173. doi:10.1007/978-3-642-40966-0_4
31. Opell, B. D.; Bond, J. E. *Evol. Ecol. Res.* **2001,** *3,* 507–519.
32. PA6 – Polyamide 6 PA6-I. https://akro-plastic.com/productfilter/details/2315/ (accessed March 25, 2022).
33. Bonse, J.; Kirner, S. V.; Krüger, J. Laser-Induced Periodic Surface Structures (LIPSS). In *Handbook of Laser Micro- and Nano-Engineering;* Sugioka, K., Ed.; Springer International Publishing: Cham, Switzerland, 2021; pp 879–936. doi:10.1007/978-3-030-63647-0_17
34. Liu, J. M. *Opt. Lett.* **1982,** *7,* 196–198. doi:10.1364/ol.7.000196
35. Schneider, C. A.; Rasband, W. S.; Eliceiri, K. W. *Nat. Methods* **2012,** *9,* 671–675. doi:10.1038/nmeth.2089

License and Terms

This is an open access article licensed under the terms of the Beilstein-Institut Open Access License Agreement (https://www.beilstein-journals.org/bjnano/terms), which is identical to the Creative Commons Attribution 4.0 International License (https://creativecommons.org/licenses/by/4.0). The reuse of material under this license requires that the author(s), source and license are credited. Third-party material in this article could be subject to other licenses (typically indicated in the credit line), and in this case, users are required to obtain permission from the license holder to reuse the material.

The definitive version of this article is the electronic one which can be found at: https://doi.org/10.3762/bjnano.13.105

BEILSTEIN JOURNAL OF NANOTECHNOLOGY

Growing up in a rough world: scaling of frictional adhesion and morphology of the Tokay gecko (*Gekko gecko*)

Anthony J. Cobos* and Timothy E. Higham

Full Research Paper

Open Access

Address:
Department of Evolution, Ecology, and Organismal Biology, University of California, Riverside, CA 92521, USA

Email:
Anthony J. Cobos* - acobo002@ucr.edu

* Corresponding author

Keywords:
allometry; biomechanics; ecology; habitat; ontogeny; substrate

Beilstein J. Nanotechnol. **2022,** *13,* 1292–1302.
https://doi.org/10.3762/bjnano.13.107

Received: 01 April 2022
Accepted: 18 October 2022
Published: 09 November 2022

This article is part of the thematic issue "Biomimetics on the micro- and nanoscale – The 25th anniversary of the lotus effect".

Guest Editor: M. Mail

© 2022 Cobos and Higham; licensee Beilstein-Institut.
License and terms: see end of document.

Abstract

Many geckos have the remarkable ability to reversibly adhere to surfaces using a hierarchical system that includes both internal and external elements. The vast majority of studies have examined the performance of the adhesive system using adults and engineered materials and substrates (e.g., acrylic glass). Almost nothing is known about how the system changes with body size, nor how these changes would influence the ability to adhere to surfaces in nature. Using Tokay geckos (*Gekko gecko*), we examined the post-hatching scaling of morphology and frictional adhesive performance in animals ranging from 5 to 125 grams in body mass. We quantified setal density, setal length, and toepad area using SEM. This was then used to estimate the theoretical maximum adhesive force. We tested performance with 14 live geckos on eight surfaces ranging from extremely smooth (acrylic glass) to relatively rough (100-grit sandpaper). Surfaces were attached to a force transducer, and multiple trials were conducted for each individual. We found that setal length scaled with negatively allometry, but toepad area scaled with isometry. Setal density remained constant across the wide range in body size. The relationship between body mass and adhesive performance was generally similar across all surfaces, but rough surfaces had much lower values than smooth surfaces. The safety factor went down with body mass and with surface roughness, suggesting that smaller animals may be more likely to occupy rough substrates in their natural habitat.

Introduction

Animals attach to surfaces in numerous ways, including claws, suction, and both wet and dry adhesion. In fact, some animals can utilize multiple attachment mechanisms [1,2], leading to multifunctionality across surfaces of varying roughness. Dry adhesion is found in many invertebrates and squamate reptiles, and has been a focus of both engineering and biological studies

[3]. Models are frequently used to describe adhesion, such as the Johnson–Kendall–Roberts (JKR) model [4]. In this case, the force required to pull an elastic sphere from a flat surface is determined using the radius of the sphere and the adhesion energy between a sphere and the surface. More recent studies use the JKR model to determine the role of setal density in adhesion from insects to geckos [5]. Despite many advancements in our understanding of adhesion across organisms, few studies have incorporated ecologically relevant variables.

The ability of geckos to adhere to smooth surfaces has fascinated scientists since Aristotle, and has been followed by countless studies focused on uncovering the mechanisms of gecko adhesion, from as early as the 1800's [6-10] to modern investigations (reviewed in [3]). Like the Lotus Effect [11], the Gecko Effect has seen a surge in attention over the past couple of decades [12]. There are over 1000 species of geckos with adhesive capabilities, with multiple origins of the system [13,14]. However, much of what is known about gecko adhesion and its associated structures is based on studies of a single species, the Tokay gecko (*Gekko gecko*) [15-19]. Additionally, the primary focus has been on adult geckos, likely given their larger size. Two key questions have received very little attention. First, how does adhesive performance vary across surfaces of different roughness? Second, how does adhesive performance and morphology vary with body size? Although the former has been the subject of a few studies, the latter has received almost no attention.

Surfaces in nature are rarely smooth and geckos are found on all types of surfaces from rough rocks to undulant tree bark [20-25] (Figure 1). Recent studies have begun to explore the role of surface roughness on frictional adhesion in geckos [1,21,25,26], and performance typically declines as roughness increases. For example, Vanhooydonck and colleagues examined the effects of substrate structure on speed and acceleration capacity in climbing geckos, and they found that acceleration was greatest on the smoothest surface (wood) where the most contact between the adhesive system and the surface could be made [27]. This illustrates that the main issue faced by geckos that are attaching via adhesive pads is the contact area between the setae and the surface. With increasingly rough surfaces, the area for contact decreases, leading to decreased adhesive performance. In a modeling framework, the force of adhesion can be related to surface energy of the substrate, the area of the adhering pad, and the compliance of the system [28]. However, most studies use widely varying surfaces [1] or uniform 3D printed surfaces [29] that do not capture the random fine-scale roughness that is likely apparent in natural habitats. For example, Huber et al. [26] measured the shear adhesive force of a single spatula on surfaces with asperities ranging from 100–300 nm, and Gillies et al. [29] manipulated the surface roughness of a macroscopic engineered rough surface in which they manipulated the wavelength and amplitude of peaks that were on the same length scale of the subdigital lamellae. Both studies found that shear adhesion was significantly reduced (up to 95% reduction of force produced on acrylic glass) on surfaces where the surface structure was close to matching the animal's adhesive structure, highlighting the importance of considering length-scale and the impact it has on gecko adhesion when testing the effects of roughness.

Surface roughness can be qualitatively characterized in different ways (rough vs smooth), but it is a complex parameter to quantify as real surfaces in nature vary over many length scales and can have significant effects on the efficacy of an adhesive system [30,31]. At this point in time, the ability to quantify the topography of surfaces of varying roughness [21], and to replicate them [32-36], rather than using vague categorizations, allows for the possibility to test fine-scale interactions of animal adhesion and traction with more accuracy [35-37]. A key factor that is relatively unexplored is that the morphology of the adhesive system likely changes with body size, which can then impact the amount of contact made between the adhesive system and the surface on which it is clinging or moving. For example, setal length and toepad area have been found to increase with body size in the southern African gecko *Chondrodactylus bibronii* [38]. Beyond intraspecific scaling, a recent study found extreme positive allometry in toepad area among animals that have adhesive pads, from mites to geckos [39]. Thus, it is likely that animals of different size will have varying clinging and locomotor performance on rough surfaces.

Allometry plays a significant role in natural systems by imparting physical constraints of supporting different body sizes, but also in the mechanical consequences in relation to locomotion [40-43]. Scaling becomes increasingly important when structures on the surface of the animal must support the body through adhesion on vertical or near-vertical surfaces [39,44]. In the case of dry adhesives, studies have focused on the scaling of toepad morphology because of the inherent signficance for adhesive locomotion (i.e., larger toepad area leads to greater area for surface contact). In a study of geckos, skinks, and anoles, Irschick et al. [45] found a strong correlation between shear adhesive force and toepad area. However, the slope of the relationship between toepad area and body mass was lower than that of clinging ability. This suggests that there are other underlying mechanisms that contribute to clinging ability apart from pad area. Adhesive pad area across climbing taxa spans seven orders of magnitude and scales with positive allometry [44] but, after accounting for size and phylogeny, toepad area scaled with isometry or sometimes negative allometry

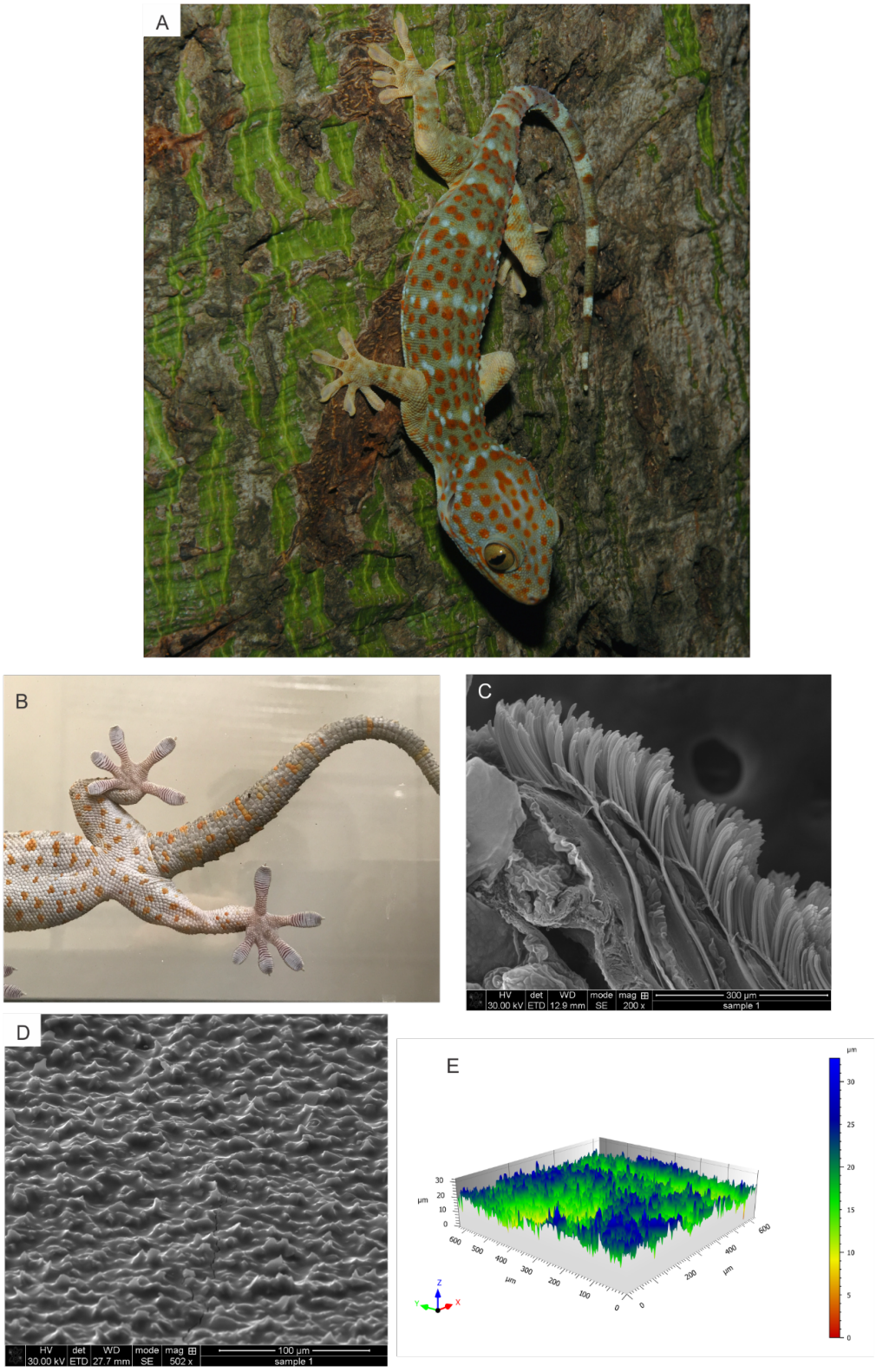


Figure 1: Images of a Tokay gecko in its natural habitat in Vietnam (photo courtesy of Lee Grismer. This content is not subject to CC BY 4.0.) (A), a Tokay gecko in the lab on a glass surface (photo by Timothy Higham, and has not been published previously) (B), an SEM image of the distal portion of the digit (C), an SEM image of the 2000 grit sandpaper surface (D), and a 3D image of the 2000 grit sandpaper surface using confocal laser scanning microscopy (E).

within certain clades. A key question is how larger organisms that use adhesion will support their body weight when climbing vertical surfaces.

The scaling of adhesive components has been addressed by Webster et al. [38] and, to a lesser extent, by Delannoy [46]. In a study of *Chondrodactylus bibronii*, setal density, setal basal diamter and setal spacing did not change significantly throughout ontogeny, but pad area and setal length increased with body size [38]. Despite these increases, estimated adhesive force capacity, relative to body size, decreased with ontogeny. However, there is a mismatch between morphological measurements and measurements of adhesive force in that morphology is often used to estimate force-generating capabilities on surfaces of varying roughness. What is missing is a study that examines both the scaling of adhesion on different surfaces and the changes in morphology throughout with body size. It is predicted that increasing roughness will decrease adhesive performance due to the limited area of contact islands [21,47].

The efficacy of adhesives that mimic a gecko's system depends upon knowing the natural interactions between the animal and the substrate. All else being equal, longer and softer setal shafts are predicted to result in better adhesion on rough surfaces due to a reduction in the effective elastic modulus [48]. However, it is currently unclear whether this translates into higher forces, relative to body mass, under whole-organism experimental studies. In order to fully understand how performance is influenced by roughness, incorporating variation in body size is important. Tokay geckos are ideal for investigating the role of body size variation given that they reach very large body sizes and they live in rainforests that likely exhibit variation in roughness (see Figure 1 for example).

Here we will measure Tokay gecko adhesive structures and compare theoretical force estimates to actual performance values to address several questions: 1) how does pad area scale with adhesive force over a significant range in body size, 2) do more compliant setae translate to higher adhesive force, and 3) do larger geckos exhibit greater adhesive force, relative to body mass? Additionally, to better understand how gecko adhesive structures interact with surface asperities on the setal level, we tested the impact of surface roughness on shear adhesion over a large size range of geckos, given that even the smallest change in setal length and compliance could impact the capacity to make local adjustments to rough surfaces [49]. To test how asperity size impacts adhesion, we generated 3D surface profiles of seven different sandpaper grits and carried out adhesion trials over a large size range of *G. gecko*. This research is significant given that most studies are limited to using 2D profiles, missing an entire axis of surface structure variation. Additionally, no study to date has quantified the effect of body size on adhesive performance.

Results

Scaling of morphology

Neither density nor basal setal diameter were significantly correlated with body size (Table 1). Relative to snout-vent length (SVL), toepad area scaled with isometry (Figure 2; slope = 2.03), whereas setal length scaled with negative allometry (slope = 0.24). Using these parameters, along with the force per seta [18], estimated frictional adhesive force scaled isometrically with body mass (slope = 0.61).

Surface roughness

The root mean square height of the sandpaper surfaces (Sq) ranged from 34.8 µm (100 grit) to 3.16 µm (3000 grit), high-

Table 1: Scaling relationships for the variables examined in this study. Scaling is relative to SVL for morphology (first three variables) and body mass for adhesion measurements, including estimated adhesion.

variable	*N*	R^2	*P* value	exp slope	obs slope	SE slope	lower CI	upper CI	scaling
toepad area	15	0.95	<0.001	2.00	2.03	0.13	1.76	2.30	isometric
setal length	15	0.74	<0.001	1	0.24	0.04	0.157	0.328	negative
setal diameter	15	0.00	0.85	1	0.02	0.09	–0.18	0.211	NA
est. adhesion	15	0.95	<0.001	0.66	0.61	0.08	0.53	0.69	isometric
adhesion (acrylic glass)	14	0.96	<0.001	0.66	0.54	0.03	0.473	0.614	negative
adhesion (100 g)	14	0.75	<0.001	0.66	0.55	0.09	0.348	0.750	isometric
adhesion (150 g)	14	0.58	0.002	0.66	0.64	0.16	0.294	0.985	isometric
adhesion (320 g)	14	0.56	0.002	0.66	0.71	0.18	0.313	1.103	isometric
adhesion (400 g)	14	0.87	<0.001	0.66	0.76	0.08	0.576	0.938	isometric
adhesion (1000 g)	14	0.85	<0.001	0.66	0.56	0.07	0.409	0.706	isometric
adhesion (2000 g)	14	0.95	<0.001	0.66	0.60	0.04	0.509	0.689	isometric
adhesion (3000 g)	14	0.82	<0.001	0.66	0.56	0.08	0.395	0.723	isometric

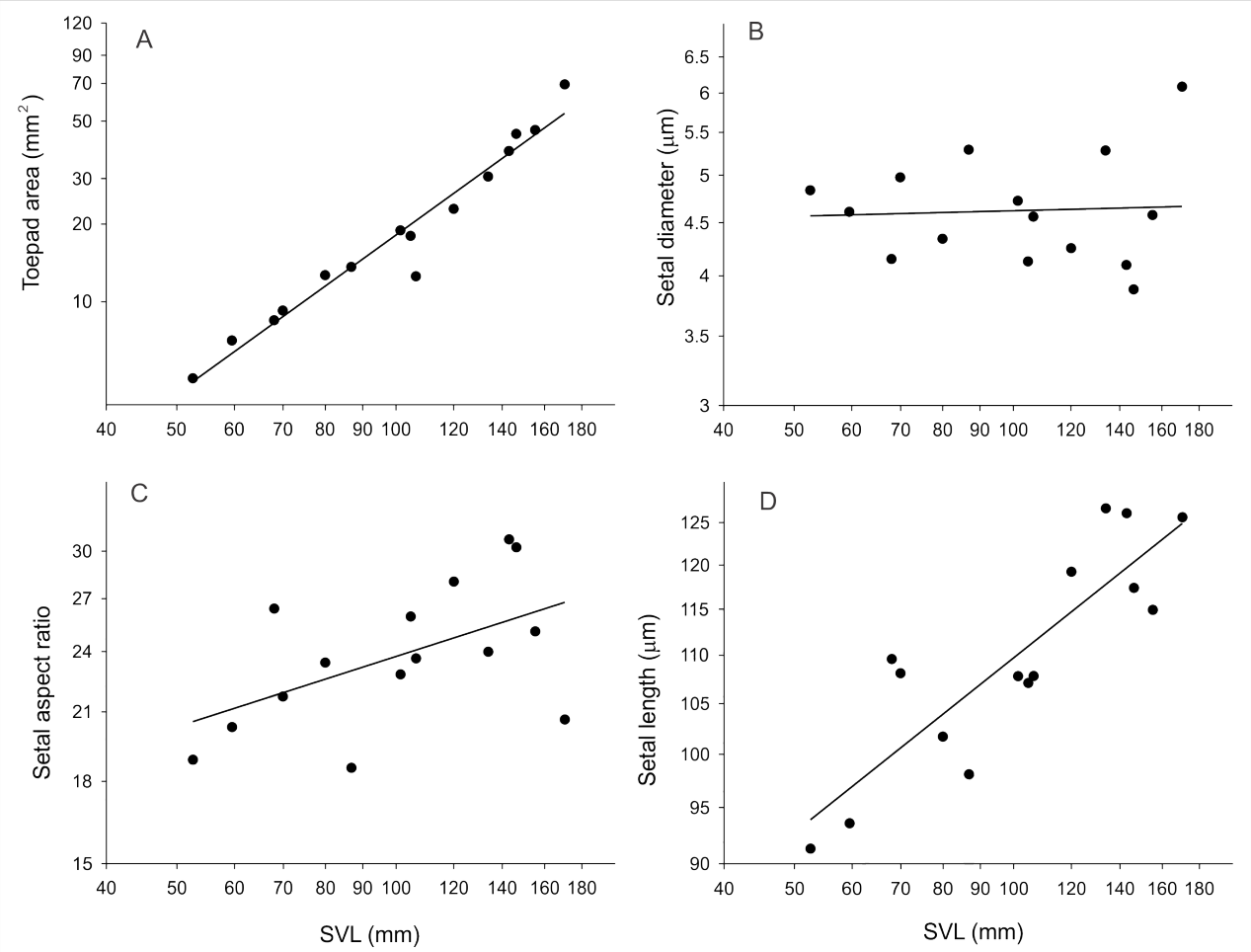


Figure 2: The relationship between morphological characters and SVL of 15 individuals. The relationship between toepad area (digit IV) and SVL ($y = 2.03x - 6.46$, $r^2 = 0.95$) (A). The relationship between setal diameter of scansor 2 and SVL ($y = 0.02x + 1.45$, $r^2 = 0.002$) (B). The relationship between setal aspect ratio and SVL ($y = 0.2251x + 2.13$, $r^2 = 0.28$) (C). The relationship between setal length of scansor 2 and SVL ($y = 0.24x + 3.58$, $r^2 = 0.74$) (D). Note that the axes are on a log scale and the equations of the lines are based on log–log plots for scaling purposes.

lighting the range of surface roughness values in our experiments (Table 2). This also encompasses much of the range of natural tree surfaces that might be found in the habitat of Tokay geckos.

Frictional adhesion and safety factor

Larger animals generated greater amounts of frictional adhesion compared to smaller individuals (Figure 3a). In general, frictional adhesive force decreased from the smooth surface

Table 2: Roughness parameters of the surfaces used in this study. Acrylic glass is not included as it is considered perfectly smooth.

roughness measure	100 grit	150 grit	320 grit	400 grit	1000 grit	2000 grit	3000 grit
Sq (µm)	34.7876	23.9627	11.7601	16.9816	9.24755	5.13478	3.15899
Ssk	0.59911	0.58176	0.937	0.35339	0.43645	–0.05521	–0.24058
Sku	2.76697	3.84052	4.68924	2.87272	4.42821	3.43064	3.64112
Sp (µm)	103.618	93.0858	72.6184	65.311	60.2142	28.2808	17.7521
Sv (µm)	52.7945	45.2815	31.4681	48.7146	38.91	23.8727	17.4907
Sz (µm)	156.41	138.37	104.09	114.03	99.12	52.15	35.24
Sa (µm)	28.2153	18.4699	9.09496	13.7147	7.15308	4.03302	2.50632

(acrylic glass) to the roughest surface (100 grit sandpaper) (Figure 3a). The strength of the correlation between body mass and adhesive force on each surface ranged from an R^2 of 0.56 (320 grit) to 0.96 (acrylic glass), with the strength of the correlation generally increasing with the smoothness of the surface.

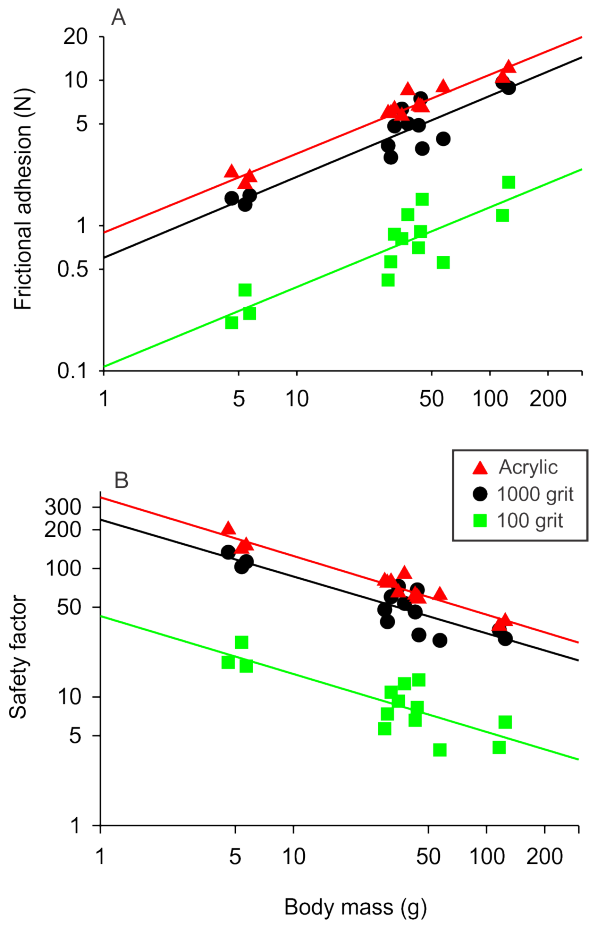


Figure 3: The relationships between frictional adhesion and body mass for acrylic glass ($y = 0.54x - 0.05$, $r^2 = 0.96$), 1000 grit sandpaper ($y = 0.56x - 0.22$, $r^2 = 0.85$), and 100 grit sandpaper ($y = 0.55x - 0.97$, $r^2 = 0.75$) (A). The relationships between safety factor and body mass for acrylic glass ($y = -0.46x + 2.55$, $r^2 = 0.94$), 1000 grit sandpaper mass ($y = -0.44x + 2.38$, $r^2 = 0.78$), and 100 grit sandpaper mass ($y = -0.45x + 1.63$, $r^2 = 0.67$) (B). Shown are values for acrylic glass (red triangles), 1000 grit sandpaper (black circles), and 100 grit sandpaper (green squares). Note that the axes are on a log scale and the equations of the lines are based on log–log plots for scaling purposes.

Safety factor decreased with body size and with increasing surface roughness (Figure 3b). The values ranged from 9.7 (large individual on rough surface) to 502.2 (small individual on smooth surface). Safety factor never fell below 1.0.

When compared to the predicted force based on morphology, the experimentally measured adhesive force was significantly lower (Figure 4). However, the slopes of the log-transformed regressions were comparable.

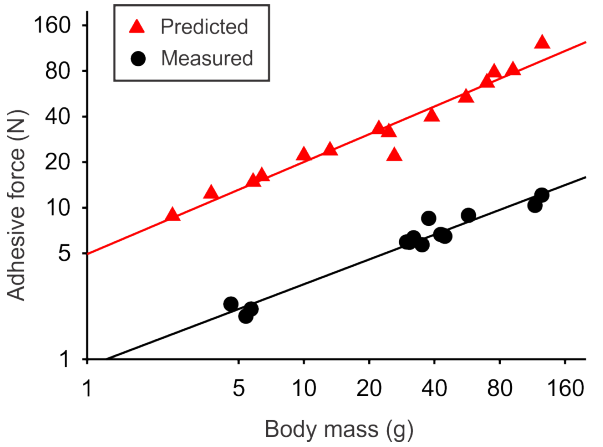


Figure 4: Frictional adhesive force predicted based on morphology (red triangles; $y = 0.61x + 0.69$, $r^2 = 0.95$) and force measured experimentally (black circles; $y = 0.54x - 0.05$, $r^2 = 0.96$). Note that the axes are on a log scale and the equations of the lines are based on log–log plots for scaling purposes.

Discussion

Our integrative approach, combining morphology, performance, and 3D surface topography, revealed key aspects of scaling that have significant impacts on our understanding of gecko adhesion. Setal diameter and density did not change with body size, whereas toepad area, and setal length, and therefore setal aspect ratio, increased with body size. Frictional adhesion, measured experimentally, increased with body size across all surfaces. However, adhesive safety factor was not only lower on rougher surfaces, but also lower for larger animals. This has implications for ecology, especially habitat use through ontogeny, but also biomimetics. If we are attempting to mimic the adhesive system, would it be beneficial to reconstruct the adhesive system of a small gecko or a large one? Can we create an adaptable system that could achieve a constant level of adhesive performance, relative to body mass, across surfaces of varying roughness?

Scaling of morphology and estimated frictional adhesion

Toepad area is important for gecko adhesion given than more points of contact will be made as area increases, assuming a constant density and a smooth surface. Indeed, density did not change with body mass in our study, but toepad area increased isometrically with body mass (slope of 2.03; Table 1). This is almost identical to that found for *Chondrodactylus bibronii* by Webster et al. [38]. Body mass increased relative to $SVL^{3.34}$, which is not different from isometry. This suggests that adhe-

sive force is greater, relative to body mass, for smaller individuals. Indeed, adhesive force estimates, based on toepad area and density, increased with body mass$^{0.61}$. This, again, is supported by the work of Webster et al. [38]. However, this differs from the interspecific study by Irschick et al. [45], in which a positively allometric relationship between pad area and body mass was observed. As noted by Webster and colleagues [38], this is like attributable to the fact that they included many types of subdigital pad design [50]. Two explanations for our observation are outlined by Webster et al. [38]. First, the lack of a positively allometric relationship may be the result of physical constraints. Having much larger toepads, relative to body size, in larger animals would potentially lead to overlapping pads and, ultimately, disruption of adhesion. Second, smaller animals may benefit from relatively larger toepads since few contact islands are likely to be encountered in any given footfall [38]. Ecological consequences are discussed below.

Scaling of frictional adhesion

In addition to the morphological analyses and the estimates of frictional adhesion, we experimentally measured the latter. Adhesive force increased with body size on the acrylic glass surface, with peak values approximating those in other studies. The scaling exponent was 0.54, and this was negatively allometric if we assume adhesive force is directly proportional to toepad area. This is in contrast to previous studies that examine multiple species of pad-bearing lizards that found a scaling exponent not significantly different from 1 [45,51]. One explanation for the difference between the current studies and the two former studies is that those included multiple types of toepads [50].

Predicted versus measured frictional adhesive force

In addition to the morphological analyses and the estimates of frictional adhesion, we experimentally measured the latter. This, to our knowledge, is the first study to directly compare estimates of adhesive force (from morphology) to experimental measurements. Although the slopes and the strength of the regression are comparable between the predicted and measured frictional adhesive forces (Figure 4), there are significant differences in the actual values. The predicted forces are much higher than the measured, with the experimental values averaging 50% of the predicted values. This may not be surprising. Theoretical estimates, based on density, pad area, and the average force per seta, are reliant upon the assumption that every single seta makes contact. Our results suggest that, even on incredibly smooth surfaces such as acrylic glass, quite a few setae are not in contact with the surface. However, there are other reasons for this mismatch. The manus and pes of the gecko, when pulled across a surface, do not have all of the toes aligned parallel to the direction of movement. In a study of Tokay geckos, Stewart and Higham [16] used an apparatus to pull individuals across an acrylic glass platform while obtaining high-speed video in ventral view. They found that the average digit angle started at approximately 30 degrees and decreased to approximately 10 degrees throughout a pulling trial. At the same time, overlap among toepads within a single foot also increased, reducing the area of contact from almost 100% to approximately 75% near the end of the pulling trial [16]. The angles of the toes, never becoming completely parallel, coupled with the decreased contact area of the toepads, likely decrease the force generating capacity of the setal fields. Beyond these macroscopic factors, it is unclear whether all of the setae, in a region of the pad that is seemingly in contact with the surface, are actually engaged with the surface. There could be interactions among setae that preclude their attachment. Damage to some setae may also decrease the efficacy of setal attachment. Future work that visualizes the actual contact across the entire setal field will reveal whether this is an important factor.

The influence of surface roughness

The roughness of the sandpaper surfaces in our study ranged from Sq = 34.8 μm (100 grit sandpaper) to Sq = 3.16 μm (3000 grit sandpaper). Acrylic glass is considered perfectly smooth. The roughness of the substrates had a large impact on the adhesive ability in Tokay geckos. Despite the similar slopes (with the exception of acrylic glass, which was negatively allometric), adhesive force on 100 grit sandpaper was, on average, only 13% of that on acrylic glass. The likely explanation for this result is that the available contact area was reduced with increasing roughness. This has been observed in other studies that model the contact between a gecko toe and surfaces that vary in asperity size [25,49,52,53]. Frictional adhesive force increased isometrically with body mass across all of the sandpaper surfaces, but this led to a decrease in safety factor (see below) since force is related to toepad area, and toepad increases at a slower rate compared to body mass.

Ecological consequences of reduced safety factor

Safety factor (SF), as measured experimentally, decreases with body size in Tokay geckos, and it also decreases with increasing roughness. The former result aligns with the previous work on *C. bibronii* by Webster et al. [38]. They found, using estimates of frictional adhesive force, that SF decreased with body mass$^{-0.47}$. We found that SF decreased with body mass$^{-0.46}$ on acrylic glass and with body mass$^{-0.45}$ on 100 grit sandpaper. Despite the similar slopes, SF on 100 grit sandpaper was, on average, only 13% of that on acrylic glass. Thus, large animals on rough surfaces will face the largest challenges due to lower safety factor. Indeed, the lowest SF was 9.7, which was a large

gecko on the 100 grit surface. The largest value was 502, which was the smallest gecko on the acrylic glass surface.

What does this mean for animals in nature? We predict that these drastic differences in SF will likely dictate, to some extent, habitat use. Wright et al., 2021 examined how clinging performance in geckos and anoles on natural surfaces might predict the surfaces used in nature [24]. They found that performance on natural substrates predicted which texture (rough vs smooth) was most often used by each species. Translating this interspecific study to our intraspecific experiments, we predict that larger animals should occupy lower regions of a tree to avoid the negative consequences of falling a large distance. This is assuming that they occupy the same type of substrate as a smaller gecko. If they do fall from a high position, the impact force is likely to exceed the adhesive force capacity of their feet [54]. In terms of surface texture, they might be expected to avoid very rough surfaces in order to preserve a modest SF. In contrast, smaller geckos will have larger values of SF, and will experience lower impact forces from a fall, suggesting that they might safely occupy higher regions of a tree. Future field observations that determine the potential for ontogenetic habitat shifts are needed. Additionally, an ecomechanical model [55], incorporating contact area information from surfaces in nature, would help to understand the mechanisms underlying any shifts.

Future directions and biomimetics

Our results detail the changes in both morphology and adhesive performance in relation to body size in a single species of gecko. These results generally align with other intraspecific studies, but not with interspecific studies. This mismatch is interesting, and requires further investigation. Specifically, there are different subdigital pad designs across geckos [50], but only one type has been investigated thus far. Do these patterns hold across geckos with different types of pads? If not, how and why?

Our results suggest important changes that occur throughout ontogeny. However, it is also clear that there are constraints in what changes are possible, such as setal width and density. These constraints may simply be due to spacing, which does not appear to change with body size. If spacing among setae does not change, it follows that the diameter of each seta is also likely to remain constant. If not, there might be negative interactions among the setal shafts (e.g., clumping). How can this be applied to biomimetics? Can we construct adaptable adhesive devices that accommodate different surfaces, or that can change depending on the need? Should robots be fitted with different systems depending on size? Although setal shaft diameter and density do not change in living animals, how does changing these conditions in artificial systems alter function? Not only might this assist with biomimetic initiatives, but it might also help us to understand why these do not occur in living animals. Regardless, we often use animals of a specific size when making connections to biomimetics, including the construction of artificial adhesives. Body size should be included given the large differences across individuals. This could be achieved by using an array of species that vary in size or, as in the case of our study, a series of individuals that span a wide range in body size. The benefits of the latter are that the general form of the toepad, and likely other aspects of the integrated adhesive system, are kept constant. However, the diversity among species will clearly offer other tantalizing insights into the possible solutions to adhesion.

Experimental

Morphology

We obtained 15 preserved individuals of *Gekko gecko* from local universities, encompassing the full range of body sizes for this species (mass = 4.6 g–124.9 g; snout-vent length (SVL = 52.6 mm–170.5 mm). For this part of the study, only SVL was measured given the potential issues during the preservation process. We used digital calipers (Mitutoyo Absolute) to the nearest 0.1 mm.

We used these individuals to measure the fine scale adhesive structures of *Gekko gecko*. The toe pad of the longest digit (digit IV) was first removed from the specimen and the ventral side was mounted on a glass slide using a clay putty on the dorsal side to secure the digit. A stereoscope with a mounted camera was then used to take images of each toe that were then used to measure toepad area using imageJ (version 1.53q; National Institutes of Health). Toe pad area was measured from the scansors bearing setae following previous methods [47].

Following toepad area measures, each toe was bisected sagittally and then stored in 100% ethanol for subsequent SEM imaging. The toes were removed from the ethanol and placed into a critical-point drying unit to dehydrate the tissue prior to imaging. They were then placed on a double stick conductive carbon tape affixed to a stub and sputter coated with a platinum/palladium coating. Toes were then viewed using a ThermoFisher Scientific Quanta™ 3D 200i SEM in the Central Facility for Advanced Microscopy and Microanalysis at UC Riverside (Figure 1). Each image was saved at multiple magnifications to facilitate more accurate measurements of setal length, setal diameter and setal density. Setal length was measured on the second (penultimate) scansor from the base of stalk to the tip along the midline of the shaft. Setal diameter was measured approximately 10 μm from the base of the stalk. Setal density was calculated following the methods described in [47],

where setae were counted along a 32 μm length on a scansor, squared, and then multiplied by 1000 to get an estimate of setal density per mm^2.

Surfaces

Our experiments were carried out using a series of artificial surfaces that varied in surface topography and asperity size. In considering both the appropriate length-scale of animal adhesive structures and relevant manufactured artificial surfaces, we chose 7 different sandpapers that encompassed a range of surface roughness based on an asperity size scale from smooth to rough (as per manufacturers specifications) as well as an acrylic glass sheet. Surface asperity size ranged from ≈3 μm to ≈200 μm, well within the range of gecko setal stalks lengths (91.3 μm–125.6 μm).

The topography of each surface was visualized using a confocal laser scanning microscope (CLSM; LEXT OLS4000, Olympus Corporation, Japan), as in [32]. Mountains Map Premium version 7.4 (Digital Surf SARL, Besançon, France) was used to analyze the images obtained from the CLSM (Figure 1). Three-dimensional surface area roughness parameters were calculated from the 3D images (see Figure 1) and are presented in Table 2. Unlike 2D metrics of roughness, derived from a single transect through the sample of interest, our area roughness values stemmed from numerous surface transects. We followed the methods outlined by Higham et al. and Kumar et al. [21,32]. Although we report other values of roughness associated with 3D methods (Table 2), we focus on room mean square roughness (Sq) in this study.

Adhesive force measurements

The specific experiments conducted in this study were approved by the University of California, Riverside (IACUC AUP 20200035). We assessed the clinging ability of 14 individuals (varying in size from hatchling to adult) on the aforementioned surfaces. These individuals were not the same as those in the morphological portion of this study, but covered a similar range in body size. The mass of each individual was obtained immediately before any performance measures were carried out to ensure that the scaling relationships were captured most accurately. We recorded mass using a standard high precision lab scale (Ohaus Scout Pro 400g). The surfaces were affixed to a portable force a gauge (Mark-10 series 5) and the animals were steadily pulled along the surface until slippage occurred or there was no more room to pull. The right manus of each individual was placed on the surface and allowed to adhere, followed by a series of 5 pulls in succession, of which the maximum force was recorded. We first determined the maximum shear adhesive force of each individual on an acrylic glass sheet to establish a control or peak performance. The remainder of the seven surfaces were then randomized for the remaining performance measures. If setae were detached from the toepads due to high forces or surface roughness issues, geckos were no longer used, and trials were resumed after the next shedding cycle or when toepads were healed. Additionally, to further attempt to achieve maximum force measurements, we tested individuals during their active periods as they are nocturnal.

Safety factor (SF) is defined as the measured performance (in Newton) divided by the force needed to support the body on a vertical surface. The latter was calculated as body mass multiplied by acceleration due to gravity. Our measurements on single appendages were multiplied by 4 and then divided by the force required to support the body. Values of 1 indicate that the adhesive force is equal to the force required to support the body. Values less than 1 indicate that the animal can no longer hold its body on a surface.

Statistics

We used linear models (LM) using the package ‘stats’ in Rstudio (version 4.1.2; Rstudio, Inc., USA) to determine how morphological traits scaled with SVL, and how adhesion scaled with body mass. We then used the package ‘ggplot2’ and generated regression plots of each model. Scaling was assessed by first log10-transforming each variable in order to linearize the data. We then obtained the slope of the regression and compared that to the expected values of isometry. For example, for linear measurements, a slope of 1 (relative to SVL) or 0.33 (relative to body mass) indicates isometry. The 95% confidence intervals around the slope were used to determine the allometric relationships.

Supporting Information

Supporting Information File 1

Adhesion data.
[https://www.beilstein-journals.org/bjnano/content/supplementary/2190-4286-13-107-S1.xlsx]

Supporting Information File 2

Morphology data.
[https://www.beilstein-journals.org/bjnano/content/supplementary/2190-4286-13-107-S2.csv]

Acknowledgements

We thank E. R. Naylor for help with experimental design and data collection, and the Higham Lab members for help with animal care. We thank R. E. Espinoza and L. L. Grismer for

their help obtaining live and preserved specimens used in this study. We thank the Central Facility for Advanced Microscopy and Microanalysis at UCR for use of their facilities.

Funding

We thank the EEOB department award (Irwin M. Newell Graduate Research Fund) for funds to purchase animals.

Author Contributions

A.C. and T.E.H. designed the study. A.C. collected the data. T.E.H. assembled all figures. Both A.C. and T.E.H. analyzed the data and wrote the manuscript.

ORCID® iDs

Timothy E. Higham - https://orcid.org/0000-0003-3538-6671

References

1. Naylor, E. R.; Higham, T. E. *Integr. Comp. Biol.* **2019,** *59,* 168–181. doi:10.1093/icb/icz027
2. Bullock, J. M. R.; Federle, W. *Insect Sci.* **2011,** *18,* 298–304. doi:10.1111/j.1744-7917.2010.01369.x
3. Russell, A. P.; Stark, A. Y.; Higham, T. E. *Integr. Comp. Biol.* **2019,** *59,* 101–116. doi:10.1093/icb/icz032
4. Johnson, K. L.; Kendall, K.; Roberts, A. D. *Proc. R. Soc. London, Ser. A* **1971,** *324,* 301–313. doi:10.1098/rspa.1971.0141
5. Arzt, E.; Gorb, S.; Spolenak, R. *Proc. Natl. Acad. Sci. U. S. A.* **2003,** *100,* 10603–10606. doi:10.1073/pnas.1534701100
6. Home, E. *Philos. Trans. R. Soc. London* **1816,** *106,* 149–155. doi:10.1098/rstl.1816.0010 plates VII, VIII.
7. Cartier, O. *Verh. Würzburger Phys.-Med. Ges.* **1872,** *1,* 83–96.
8. Simmermacher, V. G. *Zool. Garten* **1884,** *25,* 289–301.
9. Schmidt, H. *Jena. Z. Naturwiss.* **1905,** *39,* 551–580. + plate 551.
10. Dellit, W. D. *Jena. Z. Naturwiss.* **1934,** *68,* 613–656.
11. Barthlott, W.; Neinhuis, C. *Planta* **1997,** *202,* 1–8. doi:10.1007/s004250050096
12. Kamperman, M.; Kroner, E.; del Campo, A.; McMeeking, R. M.; Arzt, E. *Adv. Eng. Mater.* **2010,** *12,* 335–348. doi:10.1002/adem.201000104
13. Han, D.; Zhou, K.; Bauer, A. M. *Biol. J. Linn. Soc.* **2004,** *83,* 353–368. doi:10.1111/j.1095-8312.2004.00393.x
14. Gamble, T.; Greenbaum, E.; Jackman, T. R.; Russell, A. P.; Bauer, A. M. *PLoS One* **2012,** *7,* e39429. doi:10.1371/journal.pone.0039429
15. Russell, A. P. *J. Zool. (1965-1984)* **1975,** *176,* 437–476. doi:10.1111/j.1469-7998.1975.tb03215.x
16. Stewart, W. J.; Higham, T. E. *Biol. Lett.* **2014,** *10,* 20140701. doi:10.1098/rsbl.2014.0701
17. Russell, A. P. *Can. J. Zool.* **1986,** *64,* 948–955. doi:10.1139/z86-144
18. Autumn, K.; Liang, Y. A.; Hsieh, S. T.; Zesch, W.; Chan, W. P.; Kenny, T. W.; Fearing, R.; Full, R. J. *Nature* **2000,** *405,* 681–685. doi:10.1038/35015073
19. Autumn, K.; Niewiarowski, P. H.; Puthoff, J. B. *Annu. Rev. Ecol. Evol. Syst.* **2014,** *45,* 445–470. doi:10.1146/annurev-ecolsys-120213-091839
20. Higham, T. E. Lizard Locomotion: Relationships between Behavior, Performance, and Function. In *Behavior of Lizards;* Bels, V.; Russell, A. P., Eds.; CRC Press: Boca Raton, FL, USA, 2019; pp 47–86. doi:10.1201/9781498782739-3
21. Higham, T. E.; Russell, A. P.; Niewiarowski, P. H.; Wright, A.; Speck, T. *Integr. Comp. Biol.* **2019,** *59,* 148–167. doi:10.1093/icb/icz013
22. Collins, C. E.; Russell, A. P.; Higham, T. E. *Funct. Ecol.* **2015,** *29,* 66–77. doi:10.1111/1365-2435.12312
23. Naylor, E. R.; Higham, T. E. *Funct. Ecol.* **2022,** *36,* 471–484. doi:10.1111/1365-2435.13969
24. Wright, A. N.; Kennedy-Gold, S. R.; Naylor, E. R.; Screen, R. M.; Piantoni, C.; Higham, T. E. *Funct. Ecol.* **2021,** *35,* 2472–2482. doi:10.1111/1365-2435.13919
25. Johnson, M. K.; Russell, A. P.; Delannoy, S. Surface characteristics of locomotor substrata and their relationship to gekkonid adhesion: a case study of Rhoptropus cf biporosus. In *Functional Surfaces in Biology: Adhesion Related Phenomena;* Gorb, S. N., Ed.; Springer: Dordrecht, Netherlands, 2009; Vol. 2, pp 123–154. doi:10.1007/978-1-4020-6695-5_6
26. Huber, G.; Gorb, S. N.; Hosoda, N.; Spolenak, R.; Arzt, E. *Acta Biomater.* **2007,** *3,* 607–610. doi:10.1016/j.actbio.2007.01.007
27. Vanhooydonck, B.; Andronescu, A.; Herrel, A.; Irschick, D. J. *Biol. J. Linn. Soc.* **2005,** *85,* 385–393. doi:10.1111/j.1095-8312.2005.00495.x
28. Bartlett, M. D.; Croll, A. B.; King, D. R.; Paret, B. M.; Irschick, D. J.; Crosby, A. J. *Adv. Mater. (Weinheim, Ger.)* **2012,** *24,* 1078–1083. doi:10.1002/adma.201104191
29. Gillies, A. G.; Henry, A.; Lin, H.; Ren, A.; Shiuan, K.; Fearing, R. S.; Full, R. J. *J. Exp. Biol.* **2014,** *217,* 283–289.
30. Persson, B. N. J.; Gorb, S. *J. Chem. Phys.* **2003,** *119,* 11437–11444. doi:10.1063/1.1621854
31. Niewiarowski, P. H.; Stark, A. Y.; Dhinojwala, A. *J. Exp. Biol.* **2016,** *219,* 912–919. doi:10.1242/jeb.080085
32. Kumar, C.; Palacios, A.; Surapaneni, V. A.; Bold, G.; Thielen, M.; Licht, E.; Higham, T. E.; Speck, T.; Le Houérou, V. *Philos. Trans. R. Soc., A* **2019,** *377,* 20180265. doi:10.1098/rsta.2018.0265
33. Prüm, B.; Bohn, H. F.; Seidel, R.; Rubach, S.; Speck, T. *Acta Biomater.* **2013,** *9,* 6360–6368. doi:10.1016/j.actbio.2013.01.030
34. Kumar, C.; Le Houérou, V.; Speck, T.; Bohn, H. F. *R. Soc. Open Sci.* **2018,** *5,* 172132. doi:10.1098/rsos.172132
35. Surapaneni, V. A.; Aust, T.; Speck, T.; Thielen, M. *Beilstein J. Nanotechnol.* **2021,** *12,* 1326–1338. doi:10.3762/bjnano.12.98
36. Surapaneni, V. A.; Bold, G.; Speck, T.; Thielen, M. *R. Soc. Open Sci.* **2020,** *7,* 201319. doi:10.1098/rsos.201319
37. Prüm, B.; Seidel, R.; Bohn, H. F.; Speck, T. *J. R. Soc., Interface* **2012,** *9,* 127–135. doi:10.1098/rsif.2011.0202
38. Webster, N. B.; Johnson, M. K.; Russell, A. P. *Acta Zool. (Stockholm)* **2009,** *90,* 18–29. doi:10.1111/j.1463-6395.2008.00324.x
39. Labonte, D.; Clemente, C. J.; Dittrich, A.; Kuo, C.-Y.; Crosby, A. J.; Irschick, D. J.; Federle, W. *Proc. Natl. Acad. Sci. U. S. A.* **2016,** *113,* 1297–1302. doi:10.1073/pnas.1519459113
40. Biewener, A. A. *Science* **1989,** *245,* 45–48. doi:10.1126/science.2740914
41. Biewener, A. A. *J. Exp. Biol.* **2005,** *208,* 1665–1676. doi:10.1242/jeb.01520
42. McMahon, T. *Science* **1973,** *179,* 1201–1204.

43. Schmidt-Nielsen, K. *Scaling: why is animal size so important?;* Cambridge University Press: Cambridge, UK, 1984. doi:10.1017/cbo9781139167826
44. Labonte, D.; Federle, W. *Philos. Trans. R. Soc., B* **2015,** *370,* 20140027. doi:10.1098/rstb.2014.0027
45. Irschick, D. J.; Austin, C. C.; Petren, K.; Fisher, R. N.; Losos, J. B.; Ellers, O. *Biol. J. Linn. Soc.* **1996,** *59,* 21–35. doi:10.1111/j.1095-8312.1996.tb01451.x
46. Delannoy, S. M. Subdigital setae of the Tokay gecko (*Gekko gecko*): variation in form and implications for adhesion. Ph.D. Thesis, University of Calgary, Calgary, Canada, 2005. doi:10.11575/prism/422
47. Russell, A. P.; Johnson, M. K. *Can. J. Zool.* **2007,** *85,* 1228–1238. doi:10.1139/z07-103
48. Autumn, K.; Majidi, C.; Groff, R. E.; Dittmore, A.; Fearing, R. *J. Exp. Biol.* **2006,** *209,* 3558–3568. doi:10.1242/jeb.02469
49. Russell, A. P.; Johnson, M. K. *Acta Zool. (Stockholm)* **2014,** *95,* 299–318. doi:10.1111/azo.12028
50. Russell, A. P. Some comments concerning interrelationships amongst gekkonine geckos. In *orphology and Biology of Reptiles;* Bellairs, A. d. A.; Cox, C. B., Eds.; Linnean Society Symposium Series; Academic Press: London, UK, 1976; pp 217–244.
51. Higham, T. E.; Gamble, T.; Russell, A. P. *Biol. J. Linn. Soc.* **2017,** *120,* 503–517.
52. Johnson, M. K.; Russell, A. P. *J. Anat.* **2009,** *214,* 937–955. doi:10.1111/j.1469-7580.2009.01075.x
53. Johnson, M. K.; Russell, A. P.; Bauer, A. M. *Can. J. Zool.* **2005,** *83,* 1511–1524. doi:10.1139/z05-112
54. Higham, T. E.; Russell, A. P.; Niklas, K. J. *J. R. Soc., Interface* **2017,** *14,* 20170156. doi:10.1098/rsif.2017.0156
55. Higham, T. E.; Ferry, L. A.; Schmitz, L.; Irschick, D. J.; Starko, S.; Anderson, P. S. L.; Bergmann, P. J.; Jamniczky, H. A.; Monteiro, L. R.; Navon, D.; Messier, J.; Carrington, E.; Farina, S. C.; Feilich, K. L.; Hernandez, L. P.; Johnson, M. A.; Kawano, S. M.; Law, C. J.; Longo, S. J.; Martin, C. H.; Martone, P. T.; Rico-Guevara, A.; Santana, S. E.; Niklas, K. J. *Trends Ecol. Evol.* **2021,** *36,* 860–873. doi:10.1016/j.tree.2021.05.009

License and Terms

This is an open access article licensed under the terms of the Beilstein-Institut Open Access License Agreement (https://www.beilstein-journals.org/bjnano/terms), which is identical to the Creative Commons Attribution 4.0 International License (https://creativecommons.org/licenses/by/4.0). The reuse of material under this license requires that the author(s), source and license are credited. Third-party material in this article could be subject to other licenses (typically indicated in the credit line), and in this case, users are required to obtain permission from the license holder to reuse the material.

The definitive version of this article is the electronic one which can be found at: https://doi.org/10.3762/bjnano.13.107

BEILSTEIN JOURNAL OF NANOTECHNOLOGY

Straight roads into nowhere – obvious and not-so-obvious biological models for ferrophobic surfaces

Wilfried Konrad*[1,2], Christoph Neinhuis[1] and Anita Roth-Nebelsick[3]

Perspective

Open Access

Address:
[1]Institute of Botany, Technical University Dresden, Zellescher Weg 20b, D-01217 Dresden, Germany, [2]Department of Geosciences, University of Tübingen, Schnarrenbergstr. 94–96, D-72076 Tübingen, Germany and [3]State Museum of Natural History Stuttgart, Rosenstein 1, D-70191 Stuttgart, Germany

Email:
Wilfried Konrad* - wilfried.konrad@tu-dresden.de

* Corresponding author

Keywords:
air-retaining interfaces; bioinspiration; biomimetics; biomimicry; blast furnace; Collembola; gas/liquid interfaces; interfacial effects; persistant air layers; pits; *Salvinia molesta*; surfaces; tuyère failure; water transport in plants; xylem; Young–Laplace equation

Beilstein J. Nanotechnol. **2022,** *13,* 1345–1360.
https://doi.org/10.3762/bjnano.13.111

Received: 01 July 2022
Accepted: 18 October 2022
Published: 17 November 2022

This article is part of the thematic issue "Biomimetics on the micro- and nanoscale – The 25th anniversary of the lotus effect".

Guest Editor: M. Mail

© 2022 Konrad et al.; licensee Beilstein-Institut.
License and terms: see end of document.

Abstract

There are currently efforts to improve strategies for biomimetic approaches, to identify pitfalls and to provide recommendations for a successful biomimetic work flow. In this contribution, a case study of a concrete biomimetic project is described that started with a posed technical problem for which seemingly obvious biological models exist. The technical problem was to devise a ferrophobic surface that prevents the contact between the copper surface of a tuyère (a water cooled aeration pipe within a blast furnace) and liquid iron. Therefore, biological external surfaces that strongly repel liquids appeared to be suitable, particularly the hair cover of the water fern *Salvinia molesta* and the surface of Collembola (an arthropod group). It turned out, however, that it was not feasible to realise the functional structures of both biological models for the tuyère problem. Instead, a seemingly not obvious biological model was identified, namely micropores within the cell walls of water-transporting conduits of plants that connect the conduits to a three-dimensional flow network. These specially shaped pores are assumed to be able to create stable air bodies, which support the refilling of embolised conduits. By adopting the shape of these micropores, a successful prototype for a ferrophobic copper surface repelling liquid iron could be devised. This case study illustrates that straight road maps from technical problems to obvious biological models are no guarantee for success, and that it is difficult to arrive at a formalised biomimetic working scheme. Rather, a broad understanding of biological function and its complexity is beneficial.

Introduction and Motivation

The basic concept of biomimetics is the derivation of technical applications from biological models. The expectation to find technically useful functional systems in living nature is commonly explained with evolution, because selection would lead to “smart” and “efficient” structures [1]. A huge pool of high-performance structures, practically “ready to harvest” would,

therefore, be available. Engineers or other scientists from the applied sciences could benefit greatly from this natural resource by identifying biological "solutions to problems" and developing concepts of subsequent technical transfer.

Currently, two classes of biomimetic strategies are practiced. The first one, the "bottom-up" (or "biology push") approach, denotes the introduction of identified biological functional systems into applied sciences, by directly suggesting possible technical applications. The second one, the "top-down" (or "technology pull") approach, is initiated by a defined technical problem for which a suitable biological model is sought. The "Lotus effect" belongs to the first class. It was identified by Wilhelm Barthlott and suggested (later accompanied by one of the co-authors, C. Neinhuis) as relevant for surface technology. The highly water-repellent plant cuticles, which are equipped with hierarchically structured wax crystals, would represent "ready-made" models of superhydrophobic surfaces with versatile technical applications. The Lotus effect indeed proved to be attractive for applied sciences (as this special issue demonstrates), and its underlying physics was thoroughly studied.

Subsequently, more water-repellent biological structures were identified, with additional features and, therefore, higher and novel application potential [2,3]. For instance, various biological surfaces were described that are not only superhydrophobic but are additionally able to keep persistent air layers for an extended time after immersion in water. Principally, superhydrophobic surfaces are commonly surrounded by air when immersed. However, the air body is not persistent enough for most applications and dissolves after some time, in contrast to surfaces that can be described as "staying dry under water" for a much longer time [4,5]. Such surfaces usually feature functional structures that are larger than the wax crystals on the Lotus leaf (or other superhydrophobic leaf surfaces showing specially structured wax covers). Many of these surfaces possess hairs, such as those of the water spider or the floating fern *Salvinia molesta* (and other *Salvinia* species), and their surfaces have an appearance similar to that of terrycloth.

Both the Lotus effect and the surfaces with stay-dry-under-water potential became – after their introduction into biomimetics – popular items for the top-down strategy. They were included into various information resources on functional biological models, such as the popular and widely used "Ask nature" database (Biomimicry Institute, 2020. AskNature – Innovation Inspired by Nature. https://asknature.org/, [6]). In other words, once their functional potential is identified and described, biological systems migrate from the bottom-up realm to the top-down portfolio, together with their originally recognised application potential. Tapping this top-down portfolio is an attractive modus operandi because it appears to guarantee a straightforward and swift way to obtain the desired research results, apparently without any further need for biologists or biological expertise [7]. Another tool is TRIZ, a highly sophisticated approach that also focuses on a general biological design problem, namely trade-off conflicts [8-10].

The path from biological models to biomimetic prototypes or products can, however, be much less straightforward in practice. The complexity of the relationships between biology and technical applications leads to a high diversity of biomimetic projects with respect to procedures, strategies, project course and history [11,12]. Moreover, the biological model system and its functional aspects and contexts may not be fully understood and/or unraveled [1,7,13,14]. This hampers easy one-to-one translations of a (presumed) biological function to a technical solution or may even lead to potential conflicts with the originally intended technical application. Considering these difficulties, it appears to be desirable to obtain information on the state of the "biomimetic practice". This is generally recognised, with various attempts to gain insight into how "biomimetic procedures" are conducted. As an example, one approach is to hand out assessment sheets asking concrete questions to involved scientists [15].

To obtain insight on factors that enhance or reduce the prospect of success, it can also be instructive to analyze the history and developments of biomimetic projects as case studies. In this contribution, we reconstruct the winding path of a project originally initiated by a technical problem that appeared to be solved straightforwardly by focusing on water-repellent biological surfaces (i.e., adopting a bottom-up strategy). As it turned out, however, the way to a finally successful prototype was not to follow the straight bottum-up road map. The project finally did not progress along a straight strategic road map. Instead, it developed within a "structure–effect space" shaped by biological complexities, challenging technical demands, initial failures and – importantly – results and insights from various previous projects. The actual project, whose history will be reconstructed in this contribution and in which two co-authors participated (C. N. and W. K.), dealt with a technical problem encountered during steel production. The aim was to find a (biomimetic) way to prevent the adhesion of liquid iron at 1500 °C to a water-cooled copper surface, an application whose technical demands are extremely far away from the conditions of organismic functions.

The aim of this contribution is to provide a case study from the biomimetic practice, representing an in-depth history of a biomimetic project. This history is represented by a sequence of projects in which the co-authors of this paper were involved in

different combinations. The underlying biomimetic problems and physical as well as biological topics just provided the vehicle to describe the flow of concepts, inspirations and transfer problems.

Perspective

The problem: Failing blast furnace tuyères

In this section, the problem and its technical and economical relevance will be briefly outlined. Iron ore consists mostly of iron oxides, which have to be reduced in order to obtain metallic iron (or steel). This is primarily achieved via the blast furnace pathway: iron ore, coke and huge amounts of very hot air are supplied to a blast furnace (Figure 1a). Coke and air produce hot carbon monoxide, which reduces the iron ore to liquid metallic iron. The hot air is pressed into the lower part of the furnace via double-walled, water-cooled pipes called tuyères that extend a short distance into the blast furnace (Figure 1b,c).

Occasionally, liquid iron that runs down along the inner side of the outer wall of the furnace makes contact with the tuyère. If the heat input exceeds the capacity of the tuyère's water cooling system, the tuyère burns through, and, as a result, (liquid) water is injected into the oven. This requires the immediate deactivation and exchange of the tuyère because abruptly evaporating water may cause major destruction in and around the furnace.

Tuyère failure entails the shutdown of the blast furnace (in fact, it is the main reason for shutdowns [17-20]) and of the facilities for subsequent processing of iron and steel. This results in huge energy losses and economic cost due to additional heating and idle running of the periphery of the blast furnace. To find prospects to reduce such losses, the Betriebsforschungsinstitut at Düsseldorf (a research institute of the German steel industry) formed a collaboration with Hundt & Weber at Siegen (a manufacturer of tuyères) and the Institute of Botany of the Technical University of Dresden (C. N. and W. K.). The collaboration formulated the project proposal "Increase of energy efficiency of blast furnaces by using novel longlife-tuyères", which was approved by the German Federal Ministry of Economy and Energy and lasted from February 2015 to July 2018.

The concept was to equip the tuyère surface with a structure that mitigates heat input into the tuyère, in order to relieve the tuyère's water cooling system and to prevent heat damage to the tuyère. Since the heat conductivity of gas layers is about five orders of magnitude lower than that of copper, gas layers trapped in structured tuyère surfaces should substantially reduce the overall heat flow into the tuyère, and its outer walls should be much less prone to melting. The central idea was, therefore, to create a surface on the tuyère able to maintain an air layer that isolates the tuyère from the hot iron. For the persistence of the air layer, the following necessary conditions were identified:

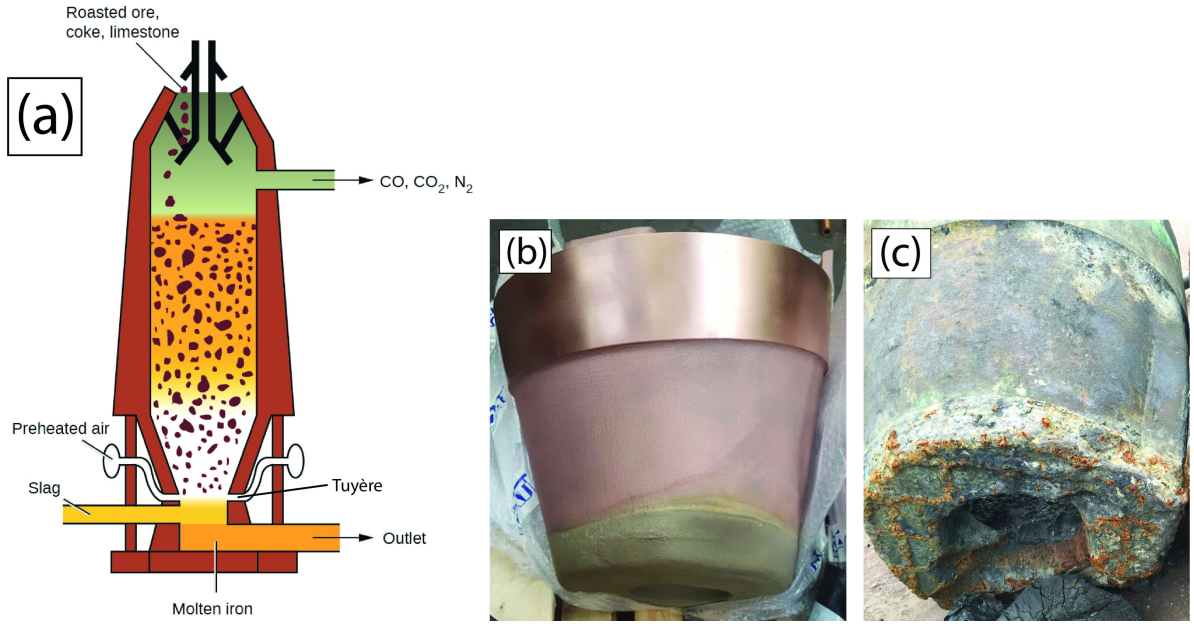


Figure 1: Left: Scheme of a typical blast furnace (picture from OpenStax, Blast Furnace Reactions, CC BY 4.0). Centre, right: a novel tuyère and a tuyère after a few weeks of usage; the lower parts extend into the blast furnace. (Figure 1a was reproduced from [16]. Accessible for free at https://openstax.org/books/chemistry-2e/pages/1-introduction (© 2019 P. Flowers et al., published by Openstax, distributed under the terms of the Creative Commons Attribution 4.0 International License, https://creativecommons.org/licenses/by/4.0). Figures Figure 1b,c: Photos by Siegfried Konietzko. This content is not subject to CC BY 4.0)

- The surface should create a gas/liquid interface and the forces acting on this interface should be in stable mechanical equilibrium, that is, the (extra) forces generated by a (small) displacement of the interface should be able to push the system back to its equilibrium position.
- In case of liquid iron flowing over the tuyère, persistence of the gas pockets within the structured surface should be energetically favourable over their displacement.
- The interfaces that separate the gas pockets from the liquid iron should form autonomously, that is, without the need for external manipulations.
- The typical dimensions of the structures creating the air layer should not exceed the capillary length, that is, surface forces should dominate forces trying to distort the gas/liquid interface (e.g., gravitational forces).

The straight top-down pathway: Identifying and following obvious biological models

As a first step, it appeared to be quite straightforward to search for suitable biological models of external surfaces that prevent the contact to a liquid and that are able to create stable air/liquid interfaces resilient to perturbation. The biological models we considered first were the structured surfaces of *Salvinia molesta* leaves (see Figure 2) and the skin structure of springtails (Collembola, see Figure 3) [3,21,22], both of which are known to accommodate gas layers.

Kariba weed (*Salvinia molesta*)

In the case of *Salvinia molesta*, stable water/air interfaces form at the tips of leaf hairs, which are topped by eggbeater-like structures (Figure 2). These are able to hold the resulting air layer for extended periods of time upon immersion. The interface is also resilient against perturbations. The "*Salvinia* effect" has considerable biomimetic potential, for instance, with respect to fuel reduction in maritime shipping [24,25] because an air layer between ship hull and water reduces the drag considerably.

The physical basis of the capability of the *Salvinia* hairs to hold persistent air layers was the topic of various studies [5,26], which also included their elastic properties [27,28]. Main factors for the persistence and resilience of the air/water interface are the peculiar combination of the superhydrophobic surface of the hairs with the hydrophilic tip of the "eggbeater" structure [5] and the circumstance that, upon perturbation, for example, upon pressure changes, they allow for an "air spring" effect within the trapped air [26]. The *Salvinia* hair type appears to represent the result of evolutionary adaptation to a high performance and is, therefore, considered as an attractive biologi-

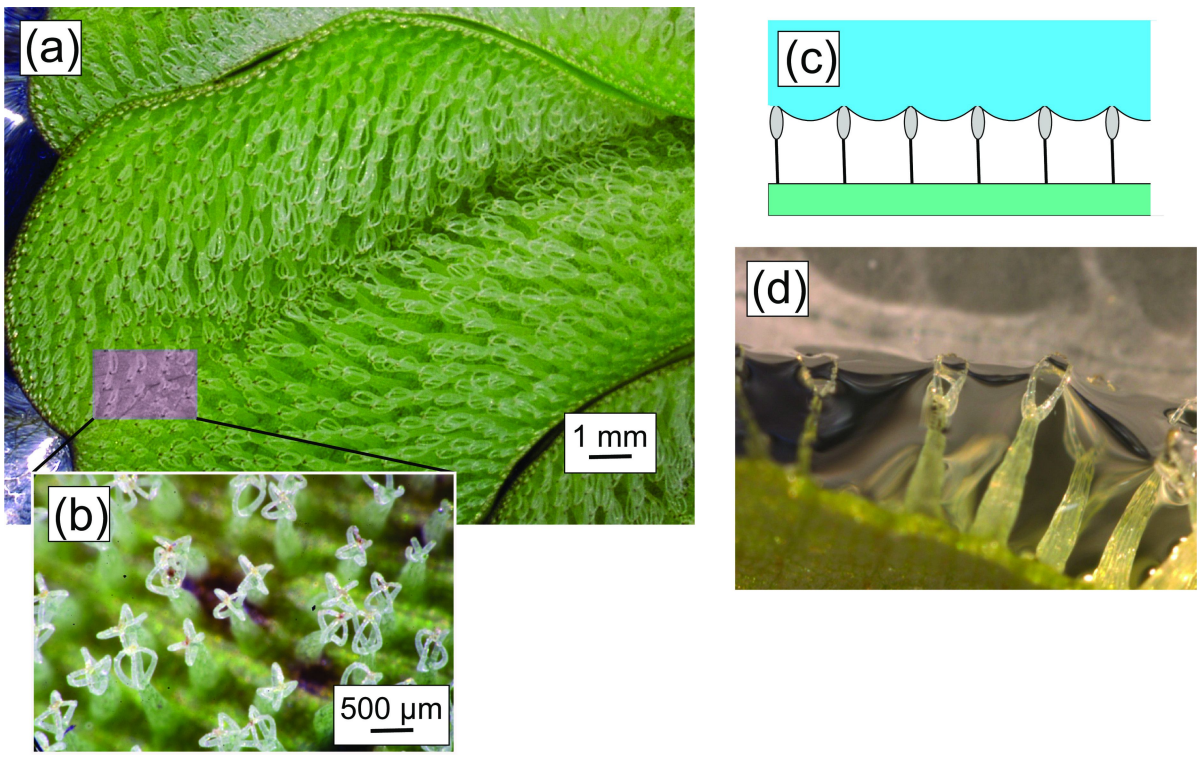


Figure 2: (a) A leaf of *Salvinia molesta* (Kariba weed) from above. The inset (b) shows the eggbeater-like structures. (c, d) Cross sections (schematic and photograph) through a leaf showing the pillar-like surface structures that seem to support the air/water interface covering the air layer.

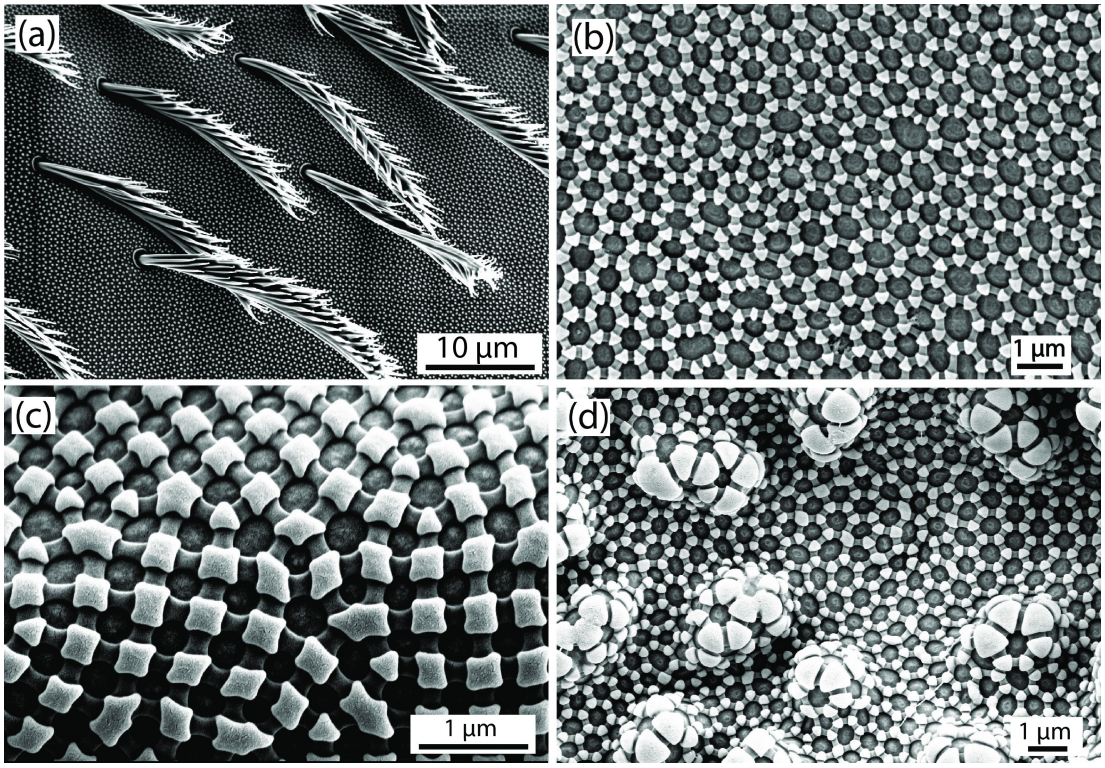


Figure 3: The skin structures of Collembola (springtails) show several levels of protection against wetting: (a) a hairy cover of bristles of *Sinella tenebricosa*, (b) nanoscopic hexagonal or rhombic comb structures formed by interconnected ridges in which gas bubbles can be trapped (*Ceratophysella scotica*) and (c) still smaller, very special structural elements with overhanging topographies ("undercuts") at each corner of the combs (*Ceratophysella scotica*). (d) Depending on the species, secondary granules may be present, which constitute an additional layer of structuring between the bristles and the combs (*Folsomia candida*). Pictures were taken from the same specimens as in [23].

cal model for applications requiring surfaces that remain dry upon immersion [5,29].

Springtails (Collembola)

Springtails (Collembola, Figure 3) are a group of small hexapods that occur worldwide in virtually all habitats. The number of described species approaches 10,000 [30] but is estimated to exceed 50,000 [31,32]. The name springtails originates from a tail-like appendage, the furca. It allows most of the species to jump in backflip style across distances of up to 10 cm. This is remarkable in view of their size, which rarely exceeds 1 mm, with a few exceptions of about 6 mm.

Most Collembola species are soil-dwelling organisms, which live in leaf litter, on the soil surface or in small spaces between soil particles. They feed on a variety of food sources and contribute substantially to the recycling of organic matter [32,33]. Collembola breathe through their body surface via skin breathing as well as with trachea [34]. Therefore, water films that may form as continuous layers on their body pose the risk of reducing respiration. As small hexapods, Collembola are furthermore at the risk of drowning during rain or when displaced into water bodies. To avoid suffocation and to secure oxygen supply under such conditions, Collembola form air layers on the body surface, so called plastrons, which are established above the skin via hierarchically organised hydrophobic surface structures when forced under water [3,21,22]. There are three levels of protection against wetting in Collembola: (i) a hairy cover consisting of bristles with water pinned to the tips (Figure 3a), (ii) nanoscopic hexagonal or rhombic comb structures formed by interconnected ridges in which gas bubbles can be trapped (Figure 3b) and (iii) still smaller, very special structural elements with overhanging topographies ("undercuts") called primary granules that are found at each corner of the combs (Figure 3c). Depending on the species, secondary granules may be present, which constitute an additional layer of structuring between the bristles and the combs (Figure 3d). Depending on systematic group and habitat, the surface structure is highly variable without changes of the basic pattern [21,23].

These specific surface structures are remarkable in so far as air layers are observed to form in liquids of diverse chemical compositions, including organic solvents and oils, which show a wide variety of surface tension values and contact angles with respect to the skin [3,21]. This "omniphobic" property allows

the Collembola to live in areas of soil or water bodies that contain a high concentration of organic liquids that are, for instance, the product of decay processes and may reduce considerably the surface tension of water. In addition, the plastron is able to withstand external pressure exceeding 0.4 MPa. The air, which is not able to escape from the pockets formed by the honeycombs, is compressed but expands again as soon as the pressure is released, reestablishing the plastron [21,22].

The straight pathway does not provide a solution

Transfer problems with the biological models. As fascinating as the air-holding hair cover of *Salvinia* and the surface structures of Collembola are, and despite the circumstance that these structures appear to fulfill all necessary conditions, the functional principles of these biological models are based on various properties that are not easily reproduced technically, at least not for the considered problem. With respect to the *Salvinia* hair, the combination of hydrophilic tip and superhydrophobic rest is difficult to realise, and particularly so for the current problem of protecting a metal body from hot iron. The working principle of *Salvinia* is based on a structural complexity that exceeds the technical feasibility (apart from the economic cost/benefit ratio, which is always a kind of elephant in the room for applied projects). Also, the surface elements of Collembola, particularly the undercut structure, are complex and difficult to realise for the pursued project.

Therefore, a simpler structure was sought, such as rigid pillars. In fact, various studies addressed the properties and application potential of this kind of technical surface structuring, for superhydrophobic surfaces as well as for surfaces with persistent air layers. Therefore, interfacial effects at surfaces covered with rigid columns have been well investigated phenomenologically [26,35-37]. There exists, also, a theoretical study from a former project, which will be shortly described in the following section.

Experience from previous studies. In a previous project, carried out by two co-authors of this study (W. K. and A. R.-N., "Drag-reducing air–water interfaces", see appendix A), it was attempted to tackle the problem of water/air interfaces at pillared surfaces theoretically. Principally, such an interface can be described by a differential equation. The main obstacle, however, is the complexity of this differential equation whose solutions describe – for given boundary conditions – the interface: It is non-linear and can only be solved if the interface (and its columnar supports) exhibit a high degree of symmetry (e.g., rotational symmetry, see below and appendix B, Equation 3 and Equation 4). Therefore, it is restricted to simple pillar shapes. Also, the arrangement of the pillars is essential. In a real *Salvinia* leaf, both quadratic or hexagonal patterns of hair arrangement may be recognised. This is unfortunately not sufficient to allow for a closed solution of the differential equation.

Konrad et al. [38] and Apeltauer [39] tried to circumvent this problem by establishing the existence of solutions and the stability and persistence of the related interface not from the solution but from properties of the differential equation itself. Their approach worked for hexagonally or quadratically arranged (Figure 2) circular columns of constant diameter and constant contact angle, but proved impracticable for more realistic protrusion models showing eggbeaters with hydrophilic tips (implying non-constant column diameter and contact angle, see the project "Drag-reducing air–water interfaces" in appendix A).

Approximating the eggbeater-like protrusions, however, by circular columns of constant diameter and constant contact angle, Konrad et al. [38] and Apeltauer [39] arrived at an interesting result: If the columns are hexagonally arranged, an interface trapping an air layer exists for arbitrary values of (i) the contact angle, (ii) the diameters of the columns and (iii) the distances between the columns. In case they are quadratically arranged, however, certain contact angle/size combinations have to be excluded because the related interfaces cannot exist. This result illustrates how seemingly simple properties are crucial for the persistence of the liquid/water interface and that the underlying physics is too complex for making straightforward assumptions and predictions about successful surface designs. Despite – or perhaps because of – the problems of the theoretical approach, more experimentally oriented research projects have been realised with the objective to fabricate drag-reducing surfaces for ship hulls [25].

Leaving the straight pathway. Therefore, no comprehensive "blueprint" from which such a simply surfaced structure could be devised exists so far, and, depending on conditions and application, the interfaces at a pillared surface may not be stable. As a consequence, there is no guarantee that an extensive empirical investigation of various test objects will be successful in identifying a suitable surface. To summarise, the interaction between *S. molesta* or Collembola and water does not constitute a good model for the interaction between liquid iron and blast furnace tuyères because of the following considerations:

- As described above, existing mathematical models are highly idealised and cover only partial aspects of the interaction between plant or animal, water and air layer. The identification of a suitable surface requires, therefore, empirical studies. The standard engineering approach to close such gaps of knowledge is to evaluate a

series of experiments in which the "system-defining parameters" are systematically varied. In a blast furnace, however, where temperatures between (roughly) 1000 and 2500 °C prevail, it is, at best, possible to continuously measure the temperature of a tuyère, but no further experimental studies are possible within such an extreme environment. This means that in the considered project, such kind of systematic investigation was not possible.

- Furthermore, putting such an "experimental approach" into practice would mean to repeatedly replace differently designed tuyères, requiring each time a partial shutdown of the furnace. Since even a partial shutdown of a blast furnace is (economically) very expensive, operators are extremely reluctant to make concessions to scientists who would like to perform experiments. (Ideally, blast furnaces produce without interruption. Only after 10 or 20 years major renovations are to be expected). This means that in the considered project such kind of systematic investigation would have been too costly.
- A blast furnace holds several thousand tons of iron ore and coke, which are supposed to subside continuously downwards, following gravity. But sometimes cavities do form that entail avalanches of the ore and coke conglomerate within the furnace. Since a tuyère protrudes a short distance into the furnace, its surface is exposed to abrading encounters with the processed material. It is expected that delicate protruding structures devised according to the biological model systems of *Salvinia* or Collembola (see Figure 2 and Figure 3) would suffer from erosion.

It should be emphasised that the problem lies, therefore, less in the transfer of a system consisting of biological tissues and water working at room temperature to an arrangement of a metallic device and hot liquid iron. Rather, (i) the structure of the original biological models is too complex for an economically realistic solution, (ii) the derived structures are too fragile for the application, (iii) when attempting to fall back on to a simpler solution, the interfacial physics is too complex to identify a functional construction and (iv) empirical experimental studies are not possible in the considered project, for practical and economic reasons.

Identification of a not-so-obvious biological model

An improbable biological model for ferrophobic surfaces: xylem structures of vascular plants

In a former biomimetic project (the research project "Hydrotex", see appendix A), in which one co-author (W. K.) participated, the project goal was to construct a drag-reducing surface for boat hulls with textile materials, including tests of a prototype. In this case, the biological model of *Salvinia*-like protrusions was also initially in the focus, following a top-down process. In the course of the project, after experiencing some difficulties with the development of stable air layers on the *Salvinia*-like textile structures, another strategy was pursued based not on protrusions, but on the opposite, namely indentations, which in fact provided promising results (see appendix A).

The origin of the idea to use recesses resembling cones as air-holding structures can be traced back to another research project already mentioned in an earlier section ("Drag-reducing air–water interfaces", see appendix A). The concept of a surface furnished with indentations instead of protrusions was also based on a biological model, although with a completely different functional background, which has, at first sight, nothing to do with water-repellent biological surfaces. It originated from research dealing with the xylem, the water transport system of plants, which had been pursued by two-co-authors for many years (A. R.-N. and W. K.). A technical exploitation of the transport principle was aimed at in the research project "Energy self-sufficient fibre based long-distance transport of liquids" (see appendix A).

The xylem is the plant tissue that transports water from the roots to the leaves. In trees and shrubs, the xylem is represented by the wood. It consists of conduits of dead cells forming capillaries in the lumina of which the water flows. To understand how this tissue can be the source for a biomimetic concept of a ferrophobic surface, some principles and problems of water transport in plants have to be briefly summarised.

The water transport system of vascular plants has to lift water against gravity from the roots to the leaves where it evaporates. The evaporation at the leaves (i.e., transpiration) represents the driving force for the flow, meaning that the water is not "pumped" upwards but rather "sucked". Plant water transport relies, therefore, on two basic principles [40]: (i) transpiration, occurring in the leaves, providing the driving force for the water flow to overcome gravity and (ii) the cohesion of water, provided by van der Waals forces between the water molecules.

The conduits consist of the cell walls of the dead xylem cells. The water molecules flowing inside them are connected to each other and to the conduit walls by cohesion generated by van der Waals forces. The conduits are interconnected by pores, termed "pits", which allow water to enter and leave the conduits on the way upwards (see Figure 4). In this way, a three-dimensional network flow of water molecules is formed whose upper end is fastened within the leaves where transpiration takes place at the

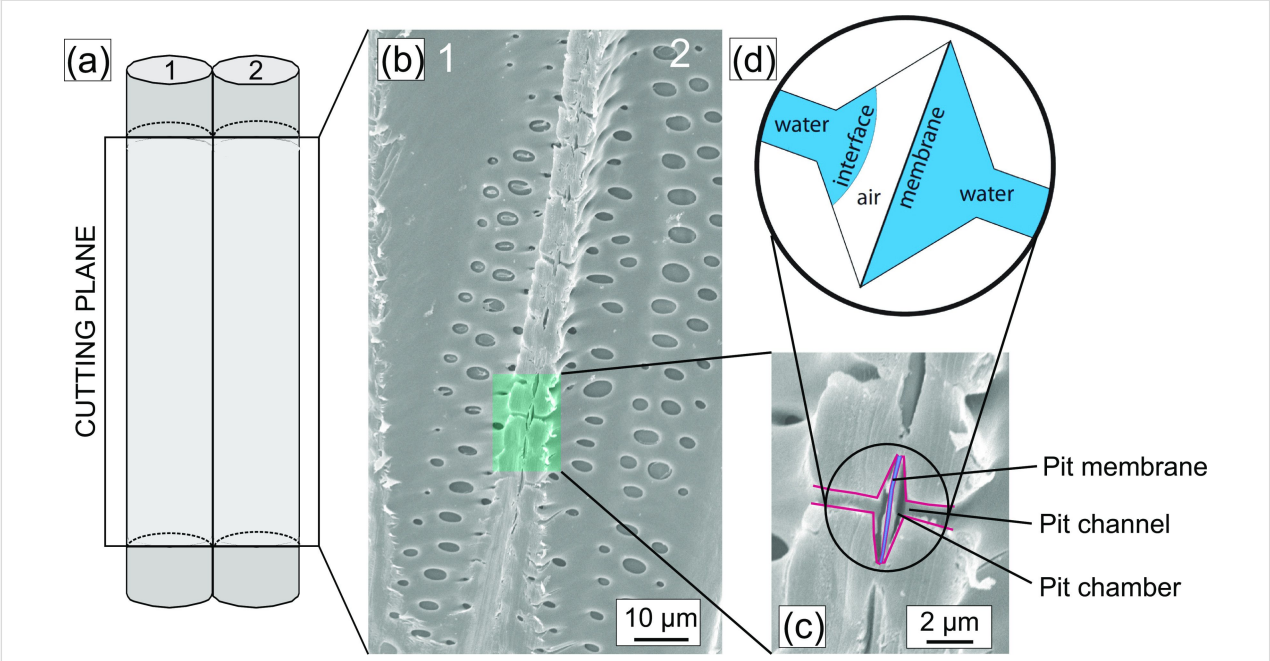


Figure 4: Basic structure of the xylem, the water transport tissue of plants. The xylem consists of elongated conduits, which are arranged parallel to the long axis of the plant stem, and which are connected to each other by pores termed "pits". Panel (a) shows a sketch of two adjacent conduits cut open longitudinally. Panel (b) shows a scanning electron microscope image of two adjacent conduits (denoted "1" and "2"). The conduits are connected by pits (some are highlighted by the green area) containing the pit membrane, which is a special nanoporous membrane. (c) Detailed image showing a pit pore connecting the two conduits. The pore resembles two funnels (highlighted by a red outline) that are attached at their wide ends forming the pit chamber. The narrow ends form the pit channels. The pit membrane separating the two funnels is highlighted in blue. (d) During repair (after one of the conduits has become dysfunctional due to gas filling), the refilling conduit is separated from its still functional water-filled neighbour by an air pocket. This air space is stable due to the interfacial forces created by the shape of the pit chamber.

living leaf cells. From there it "hangs down" through twigs, trunks, stem and roots into the ground water.

The stability of this transport mechanism relies on the comparatively weak van der Waals forces, whose range is at most 100 nm [41]. It is, therefore, prone to become unstable upon perturbations, particularly upon the entry of small air bubbles (by, for instance, damage such as broken twigs). If large enough, these perturbations initiate a process termed "air seeding", which disrupts the water chain and causes conduit failure by the development of embolism, meaning gas (air) spaces interrupting parts of the transport pathway [42].

Because air seeding events are inevitable, trees developed safety measures to minimise the consequences. Of essential importance is the segmentation of the water conduit network into compartments. Each pit pore connects two conduits, and this joint pore space is separated by a special nanoporous membrane, the pit membrane (Figure 4). When a conduit becomes dysfunctional due to embolism, the nanopores within the pit membranes prevent the spreading of air into conduits that are connected to the dysfunctional conduit. Thus, the embolised conduit becomes hydraulically isolated from the functional ones (Figure 4).

Embolised conduits may be repaired, meaning that they become "refilled" again with xylem water. This is supposed to happen when transpiration ceases and the "suction force" within the conduits reduces. The reason is straightforward: An incompletely repaired conduit would not fill with water but would be sucked empty again and again because the pressure in the adjacent conduits is lower than in the still dysfunctional conduit. Therefore, a mechanism was suggested that would be able to isolate a refilling conduit during the repair process [43].

An essential element of this special isolation mechanism is the formation of a stable interface (denoted "interface" in Figure 4e), which separates water and air within the pit cavity, thereby isolating the pit membrane from water (see appendix C). Various research was dedicated to this putative mechanism. Studies contributed by Konrad and Roth-Nebelsick [44,45], who considered the interfacial physics of the proposed mechanism, provided evidence that such an interface may be possible within pits. Its stability would depend on the water pressure, shape of the pit and the contact angle between water and pit walls (see appendix C and [45]). Central to the formation of an interface is the shape of a pit. It resembles two funnels connected at their wide ends with the narrow ends (the pit channels, Figure 4) opening into the two adjacent conduits.

The working principle of the “ice cream cone” derived from xylem pits

At first sight, the funnel-like pit structures and the working principles governing the interface behaviour within the pit lumen appear to have nothing to do with persistent gas layers around immersed objects, such as ship hulls or blast furnace tuyères. However, the proposed working principle, which was originally suggested to explain the possible refilling of embolised conduits despite adverse pressure conditions, means nothing else than the persistence of air spaces between a solid and a liquid.

A closer look at the funnel structure (Figure 4) reveals that only a part of it is required for the creation of a stable interface. The narrow channel of a pit funnel, the pit channel, is just the connection to the conduit interior. Only the wider part of the funnel, the pit chamber (Figure 4), is functional with respect to interface formation. Principally, the upper funnel part can be closed at its bottom by elongation of the tilted funnel walls. The result is a simple cone with a special but highly symmetric shape. In applications, this structure would not protrude from a surface but would rather be embedded, forming robust recesses for creating stable interfaces to maintain persistent air spaces and prevent them from being pushed away by perturbations.

In contrast to covering surfaces with pillars or other protrusions, the pit-based principle is based on cavities, which are much more protected against abrasion and erosion than pillars or columnar structures. Furthermore, surface structures such as the pillars of *Salvinia* (Figure 2d) or the discontinuous hexagonal ridges of *Ceratophysella scotica* (Figure 3b) will probably generate a joint air layer that encloses all protrusions, whereas, in a cluster of cavities the emergence of unconnected air layers that are attached to a single cavity is to be expected. Clearly, in the second case, a localised disturbance will cause the breakdown of a few air layers close to the disturbance, while, in the case of a joint air layer, a much larger surface area will lose its air cover.

Biomimetic realisation of the “ice cream cone” for blast furnace tuyères

Theoretical considerations

The great advantage of rotationally symmetric recesses (Figure 5) and the resulting, necessarily spherical interfaces [46] is their simple geometric structure, which can easily be described in terms of analytic functions.

When a sheet of liquid iron flows over the tuyère surface, a complex interaction between the gas in the recesses and the liquid evolves. It is, of course, hopeless to try to describe the interaction dynamics in terms of analytic functions. But once a more or less stationary state has been reached, which is usually the case when the cooling system of the tuyères becomes overstrained, simpler considerations are sufficient.

To discover whether the overflowing liquid iron wets the recesses completely, implying a massive heat inflow into the tuyère, or whether air pockets within the recesses survive, providing an efficient insulation against heat input, it is appropriate to compare the formation energy of the two possible states. The one with the lower energy demand will be realised, at least in the majority of indentations.

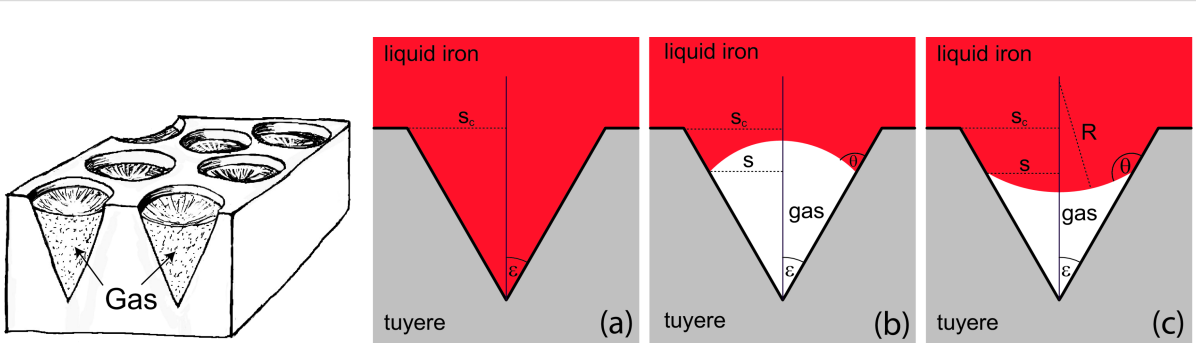


Figure 5: Left: Closely arranged “ice cream cones” on the surfaces of tuyères that contain gas pockets are able to mitigate heat inflow from an overflowing liquid iron sheet considerably (Drawing by Birgit Binder, Entringen. This content is not subject to CC BY 4.0). Right: The relation between the contact angle θ and the acute angle ε, which defines the cone geometry, is decisive for the existence and stability of the gas/liquid interfaces. Panels (a–c) show different possible states of the interface. (a) The cone is completely filled with liquid iron, and the system does not allow for the existence of a gas/liquid interface. (b) Contact angle and acute cone angle are related via $\theta < \varepsilon + 90°$. A gas/liquid interface can exist, but it is neither stable, nor does it emerge by itself. Eventually, the iron will displace the air pocket, leading to the situation in (a). (c) Contact angle and acute cone angle satisfy the condition $\theta > \varepsilon + 90°$, which guarantees existence and stability of the gas/liquid interface and of the air pocket it encloses. Figure 5 right (b) and (c) are from [47] and were reprinted by permission from Springer Nature from the journal Journal of Bionic Engineering (“When Lotus Leaves Prevent Metal from Melting – Biomimetic Surfaces for High Temperature Applications” by W. Konrad; J. Adam; S. Konietzko; C. Neinhuis), Copyright 2019 Springer Nature. This content is not subject to CC BY 4.0.

Calculation of the energy difference between the two situations (for details consult appendix D) results in a surprisingly simple relation: Leaving air pockets within the recesses is the energetically favourable option regarding the iron sheet if the contact angle θ and the acute angle ε of the cone satisfy the inequality

$$\theta > \varepsilon + 90°. \quad (1)$$

Refer to Figure 5 for the definitions of θ and ε. If θ is given, the relation in Equation 1 restricts the acute cone angle to the interval

$$0 < \varepsilon < \theta - 90°. \quad (2)$$

The next step is to clarify whether such air layers (or rather the interfaces that separate them from the liquid iron) do exist in the first place and whether they are stable against perturbations.

The existence problem (details are presented in appendix B) boils down to the question whether a cubic poynomial in s (s is the radius of the contact circle, see Equation 7 and Figure 5) has at least one real and positive solution. It can be shown that this is the case for all physically reasonable values of θ and ε. The mechanical stability of the interface is treated in appendix C. It turns out that the simple cone geometry (simple compared to the indentations shown in Figure 9) with a maximum radius $s_c \approx 5$ mm is a good choice. Interfaces that evolve within it are stable, regardless of the values of θ and ε and the pressure of the liquid iron.

Successful test of the concept

Due to its excellent heat conduction, tuyères are manufactured from copper. Unfortunately, copper is readily wetted by liquid iron, the contact angle between liquid iron and copper amounts to $\theta \approx 37°$. Equation 1, however, requires clearly $\theta > 90°$. The solution of this problem was to coat the copper surface with corundum (Al_2O_3), a material on which iron exhibits a contact angle of $\theta \approx 130°$. Equation 2 implies that the acute angle of the cone should then be in the interval $0 < \varepsilon < 40°$.

To test our concept, a copper plate was furnished with hexagonally arranged cones (cone radius at the surface of the plate $s_c = 2.5$ mm, cone depth = 4.5 mm and acute angle of the cones $\varepsilon \approx 30°$) and coated with corundum. Figure 6 shows the surface

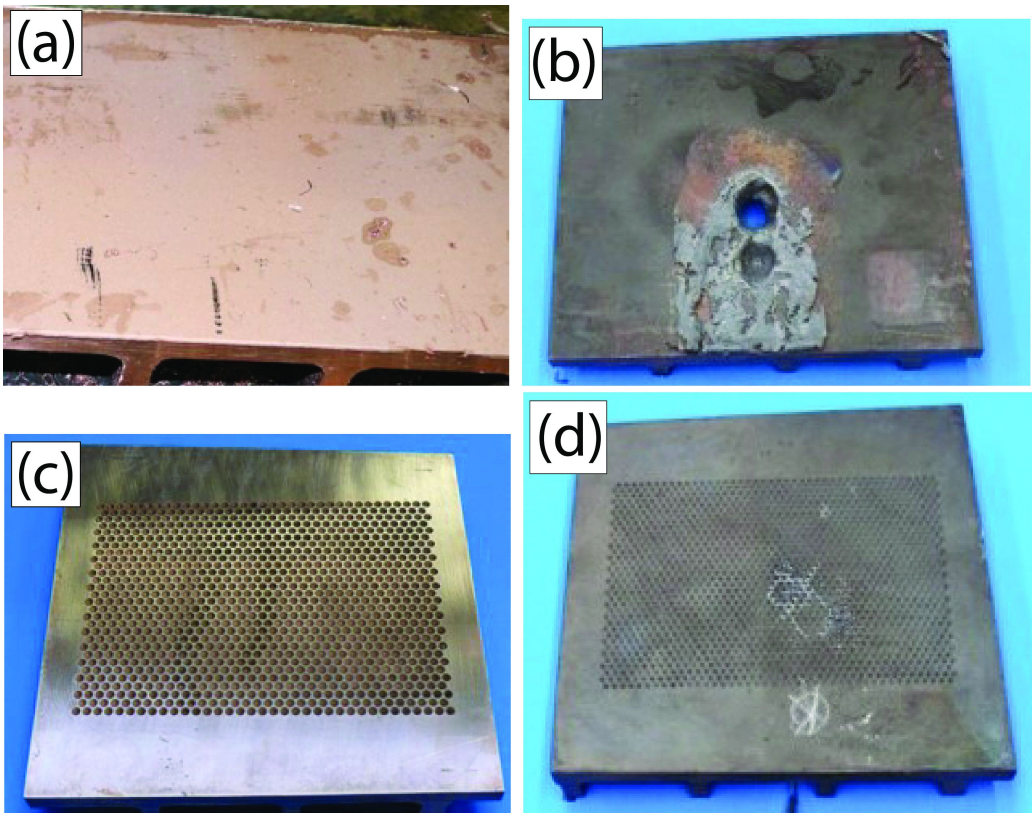


Figure 6: The two test objects before (a, c) and after (b, d) testing. (a, b) Unmodified copper plate, (c,d) copper plate equipped with cone-shaped cavities and a corundum coating. (Photos: Jörg Adam. Figure 6 is from [47] and was reprinted by permission from Springer Nature from the journal Journal of Bionic Engineering ("When Lotus Leaves Prevent Metal from Melting – Biomimetic Surfaces for High Temperature Applications" by W. Konrad; J. Adam; S. Konietzko; C. Neinhuis), Copyright 2019 Springer Nature. This content is not subject to CC BY 4.0.

of the plate before and after 14 kg of liquid iron were poured over it within one minute. For comparison, an unmodified plate of pure copper was treated in a similar way (but merely with 5 kg of liquid iron, for details see [47]). As is obvious from Figure 6, the prototype showing the structured surface remained unharmed by the liquid iron.

Conclusion: A broad understanding of biological function is beneficial for biomimetics

The project history presented in this contribution illustrates that seemingly straight paths in biomimetics can turn out to be dead ends whereas following more complex approaches that delve much deeper into the biological complexities can be successful (Figure 7). We would like to emphasise that we do not intend to draw general conclusions from a single case study, even if it encompasses experience accumulated over a time span of 15 years. However, we feel entitled to draw the following conclusions.

One underestimated problem in biomimetics is that the biological function of a biological structure is quite often neither really clear nor well-defined [12,14,28]. Clarity and correctness of a function are, however, considered to be essential for identifying suitable biological models for biomimetic projects [7,11,15]. In fact, the central role of an identified biological function is at the heart of the top-down strategy and also the basis of facilitating biomimetic research by devising formal schemes of biomimetic work [15,48].

As described in the Introduction, biomimetic tools such as TRIZ or other databases structured according to biological functions seem to make the participation of biologists superfluous. A large collection of biological systems connected to defined functions would make biomimetic work possible without biological expertise [6-8]. This is an attractive prospect, as it promises uncomplicated road maps that can be followed by, for instance, engineers without complex interdisciplinary discussions. Most bioinspired designs to date followed, however, a

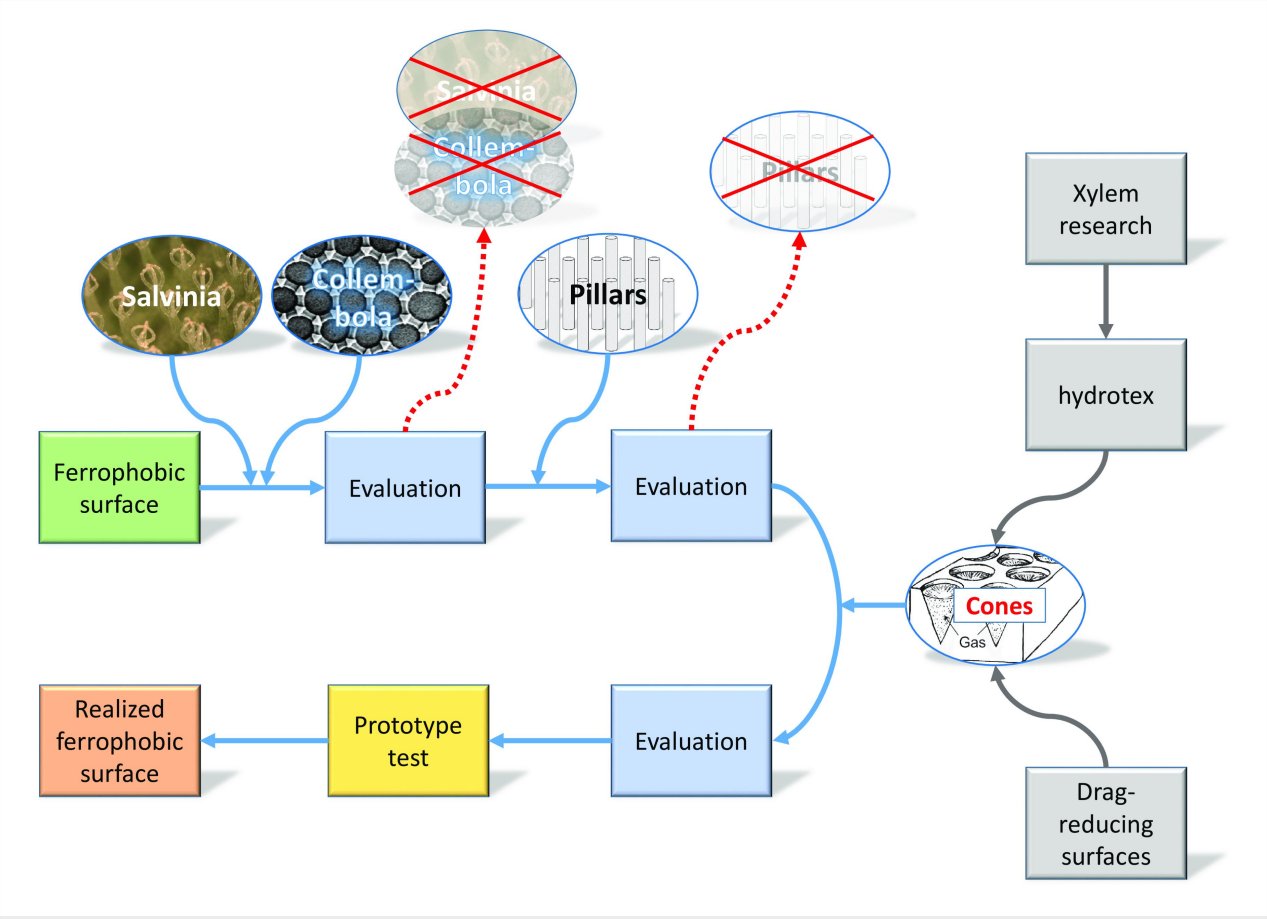


Figure 7: Sketch of the project progress. Initially, two biological models showing highly water-repellent surfaces, namely the arthropod group of Collembola and the water fern Salvinia molesta, were selected as biological models for the desired ferrophobic surface. These models, however, turned out to be not suitable; neither was a simplified design of rigid pillars (see text). In a next step, experiences from three former projects were considered, resulting in a surface decorated with cone-like indentations, which showed the desired liquid iron repellency. The projects are shortly described in appendix A.

bottom-up approach, meaning that they were initiated by a biological discovery and not by the top-down idea of tapping collections of models with biological functions [15].

The presented project example demonstrates the problem with the function in biomimetics quite nicely. The desired technical development was to devise an external surface of an object that repels a liquid, namely hot iron, reliably by allowing for the formation of an isolating stable air layer. It is then an obvious biomimetic routine to look for organisms showing external surfaces that repel water upon immersion with high efficacy.

Although the project was inspired by biological surfaces showing exactly this behaviour, *Salvinia molesta* and Collembola were not suitable for a technical transfer. The solution came from another biological structure with an apparently different and much more complex functional context, that is, the curved shape of micropores within walls of water-transporting conduits of plants. These structures might produce stable air layers to allow for refilling, which would mean a biological context of self-repair. It can be considered as quite impossible to make such complex functional contexts detectable by formal tools for users without a deeper understanding of biology.

By its core concept, biomimetics is an interdisciplinary endeavour, which attempts to bridge the gap between biology and engineering (or applied sciences in general). This gap is quite profound: Whereas biologists are interested in organisms, engineers are interested in designing successful technical constructions. Naturally, the aim of an applied science project (a biomimetic project is always an applied science project) is first and foremost the development of the desired technical item. This harbours the danger of considering the need to understand biology as a distraction rather than an asset (all the more so because real interdisciplinary cooperation can be strenuous due to differences in terminology, approaches and mentalities). In fact, there is increasing concern that an inadequate understanding of biology and insufficient evaluation of the richness of biological model systems and functional contexts will suppress the full potential of biomimetics [1,7,13,49]. The presented project example supports these claims.

Appendices

A. Related research projects into which one or more of the authors were involved

- "Drag-reducing air–water interfaces", 2007–2010. Participants: University of Tübingen, University of Bonn, funded by the German Science Foundation (DFG), https://gepris.dfg.de/gepris/projekt/39399990/ergebnisse
- "Energy self-sufficient fibre based long-distance transport of liquids", 2008–2011. Participants: University of Tübingen, Institut für Textil- und Verfahrenstechnik (Denkendorf), Helmholtz-Zentrum (Berlin), TWD Fibres GmbH (Deggendorf), funded by the German Federal Ministry of Education and Research (BMBF), http://edok01.tib.uni-hannover.de/edoks/e01fb13/742508609.pdf
- "Hydrotex", 2012–2014. Participants: University of Tübingen, Institut für Marine Ressourcen (IMARE, Bremerhaven), Institut für Textil- und Verfahrenstechnik (Denkendorf), Frottana (Großschönau), Rivers and Tides Boatbuilding (Elsenfeld), funded by the German Federal Ministry for Economic Affairs and Energy (BMWi). Masters thesis generated from the project: Michael Münster, 2014, "Bionik wasserabweisender Oberflächen (Biomimetics of superhydrophobic surfaces)", University of Tübingen, Department for Geosciences
- "Increase of energy efficiency of blast furnaces by using novel longlife-tuyères", 2015–2018. Participants: Betriebsforschungsinstitut (Düsseldorf) (a research institute of the german steel industry), Hundt & Weber at Siegen (a german subsidiary company of Lebronce Alloys, a manufacturer of tuyères), Institute of Botany of the Technical University of Dresden, funded by the German Federal Ministry for Economic Affairs and Energy (BMWi)

B. Existence of a gas/liquid interface and the Young–Laplace equation

General case

If the forces acting across an gas/liquid interface are in equilibrium, the Young–Laplace equation [50] states that the difference between liquid pressure p_l and gas pressure p_g is counterbalanced by the surface tension term $2\sigma H$, according to

$$p_g = p_l + 2\sigma H. \tag{3}$$

σ denotes the surface tension and H the mean curvature of the gas/liquid interface. If p_l and p_g are constant along the interface, H is constant, too, and the interface belongs to the class of constant-mean-curvature surfaces, which are defined and studied in the field of differential geometry. This correspondence allows one to exploit and to apply purely mathematical results to practical problems. If the values of p_l, p_g and H do not fulfill Equation 3 neither interface nor air layer form.

If Equation 3 is fulfilled by a given gas layer, the shape $z = u(x,y)$ of the gas/liquid interface (see Figure 8) can be calcu-

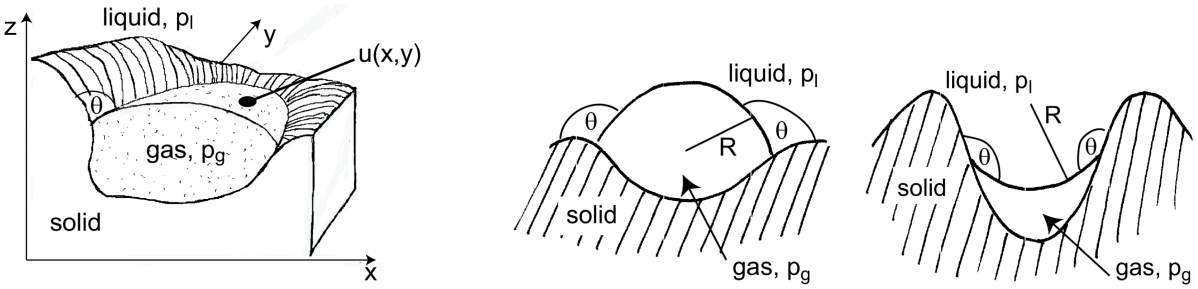


Figure 8: Illustration of the Young–Laplace equation. Left: The interface is given by the equation $z = u(x,y)$. Centre and right: If the contact line exhibits rotational symmetry, the surface $z = u(x,y)$ becomes a spherical section of radius R. The combination of the contact angle θ and the geometry of the solid dictate whether the gas/liquid interface is convex ($H = 1/R$) or concave ($H = -1/R$).

lated as the solution of a differential equation. Expressing H, the mean curvature of the gas/liquid interface, as

$$H = \frac{\left(1+u_x^2\right)u_{yy} - 2u_x u_y u_{xy} + \left(1+u_y^2\right)u_{xx}}{2\left(1+u_x^2+u_y^2\right)^{3/2}} \tag{4}$$

(subscripts denote partial derivatives), the Young–Laplace equation (Equation 3) becomes a non-linear differential equation for the surface $u(x,y)$. In order to obtain well-defined solutions suitable boundary values have to be prescribed, for example, the contact angle θ along the contact line where air, water and solid meet.

The case of rotational symmetry

Elementary geometry allows one to express the gas volume V shown in Figure 5 and the interface curvature H in terms of the cone geometry (s, θ and ε are defined in Figure 5) as

$$V = \frac{\pi s^3}{3}\left(\cot\varepsilon + \frac{\left[1-\sin\left(\theta-\varepsilon\right)\right]^2\left[2+\sin\left(\theta-\varepsilon\right)\right]}{\cos^3\left(\varepsilon-\theta\right)}\right) \tag{5}$$

and

$$H = \frac{\cos\left(\theta-\varepsilon\right)}{s}. \tag{6}$$

Insertion of Equation 3, Equation 5 and Equation 6 into the gas equation $p_g V = n\mathcal{R}T$ ($\mathcal{R}$: gas constant, n: number of gas particles, T: temperature) results in a cubic polynomial for the radius s of the contact line (see Figure 5):

$$0 = p_l s^3 + 2\sigma\cos\left(\theta-\varepsilon\right)s^2 - \frac{3\mathcal{R}Tn}{\pi}\left(\frac{\cos^3\left(\varepsilon-\theta\right)}{\cot\varepsilon\cos^3\left(\varepsilon-\theta\right)+\left[1-\sin\left(\theta-\varepsilon\right)\right]^2\left[2+\sin\left(\theta-\varepsilon\right)\right]}\right). \tag{7}$$

This polynomial has exactly one real and positive solution, provided $p_l > 0$, $T > 0$, $0 \le \varepsilon \le \pi/2$ and $0 \le \theta \le \pi$. This implies that in situations compatible with these specifications an interface forms that has the shape of a spherical surface [46].

C. Mechanical stability of a gas/liquid interface

An gas/liquid interface is mechanically stable if it reacts to a perturbation (such as a pressure fluctuation causing a small shift of the contact line) by returning back to its equilibrium position. (At the contact line, the gas/liquid interface touches the solid substrate.)

Upon Taylor expansion of the Young–Laplace equation and the gas equation $p_g V = n\mathcal{R}T$ around a point of mechanical equilibrium, it can be shown that the quantity

$$\Psi = \left[\frac{p_g}{V} + 2\sigma\frac{\mathrm{d}H}{\mathrm{d}V}\right]_0 \tag{8}$$

indicates whether a mechanical equilibrium is stable ($\Psi > 0$) or not ($\Psi < 0$). H denotes the curvature of the interface (see appendix B) and the subscript 0 indicates that all quantities should be evaluated at the point of equilibrium [38,39,51,52].

The term p_g/V in Ψ is always positive, the sign of Ψ depends, therefore, on the behaviour of $\mathrm{d}H/\mathrm{d}V$ when the gas volume is increased by the shift of the contact line: (i) If the interface curvature increases (left part of Figure 9), $\mathrm{d}H/\mathrm{d}V$ and Ψ are positive, indicating a stable interface. (ii) If the curvature decreases,

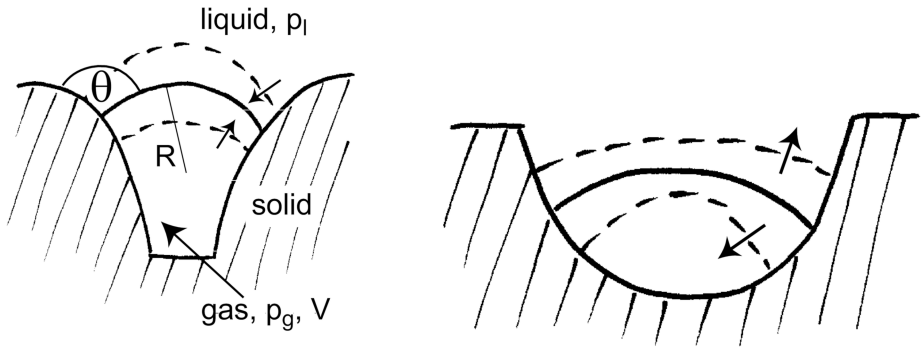


Figure 9: Mechanical stability of a gas/liquid interface. Left: After being deflected from its equilibrium position, the interface returns to the equilibrium position (Ψ > 0). Right: The interface reacts to a deflection by moving further away from the equilibrium position (Ψ < 0).

dH/dV is negative; if it exceeds p_g/V, Ψ becomes negative, and the interface is unstable (right part of Figure 9).

If the indentation resembles an ice cream cone, such as in Figure 5, application of Equation 8 leads to Ψ > 0, regardless of the sign of H [47].

The surface tension in the iron/gas interface should also be able to restrain other forces that try to deform the interface (such as the gravitational force). This is guaranteed as long as the typical dimensions of a gas-holding structure (such as the maximum radius s_c of the contact circle) do not exceed the capillary length,

$$l_c = \sqrt{\frac{\sigma}{\rho g}} \approx 4.8 \text{ mm}, \tag{9}$$

which results from the surface tension σ ≈ 1.6 N/m and the density ρ ≈ 7000 kg/m^3 of liquid iron and the gravitational acceleration g ≈ 9.81 m/s^2 [50].

D. Formation energy of a gas layer

When the gas pockets within cone-like structures on the tuyère surface are overflown by liquid iron they may stay fixed or they may become displaced. Both alternatives require the formation and/or destruction of surface and volume energy; it is reasonable to assume that the energetically favourable alternative will be realised. Comparison of Figure 5a with Figure 5b or Figure 5c allows one to calculate ΔE, the energy difference related to the alternatives:

$$\Delta E = \Delta E_V + \Delta E_{lg} + \Delta E_{sg} = \sigma\left[-2HV + A_{lg} + A_{sg}\cos\theta\right]. \tag{10}$$

ΔE_V, ΔE_{lg} and ΔE_{sg} are the energies necessary to remove liquid iron of volume V (and to replace it by gas), to form a liquid/gas interface of area A_{lg} and to separate liquid iron from the solid across an area A_{sg}, respectively (for details, see [47]).

Gas volume V and interface mean curvature H have already been calculated in Equation 5 and Equation 6 (see appendix B). Inserting them and the geometric relations $A_{lg} = 2\pi s^2/(1 + \sin(\theta - \varepsilon))$ and $A_{sg} = \pi s^2/\sin\varepsilon$ (see Figure 5) into Equation 10 results in

$$\Delta E = \pi\sigma s^2\left\{\frac{\cos\theta}{\sin\varepsilon} + \frac{2}{1+\sin(\theta-\varepsilon)} - \frac{2\cot\varepsilon\cos(\theta-\varepsilon)}{3} - \frac{2\left[1-\sin(\theta-\varepsilon)\right]^2\left[2+\sin(\theta-\varepsilon)\right]}{3\cos^2(\theta-\varepsilon)}\right\} \tag{11}$$

Obviously, the sign of ΔE depends only on the expression within the braces. Closer inspection shows that the energetically favourable case ΔE < 0 requires that the contact angle θ and the acute angle ε of the cone satisfy the inequality

$$\theta > \varepsilon + \pi/2 \tag{12}$$

(a situation as depicted in the left part of Figure 5), whereas θ < ε + π/2 leads to ΔE > 0 (cf. right part of Figure 5).

Acknowledgements

We would like to thank Siegfried Konietzko (CON-REA – Consulting & Realization, Steel & Iron Industry, Duisburg), Jörg Adam (BFI – Betriebsforschungsinstitut, Düsseldorf) and Birgit Binder (Entringen) for providing photographs and drawings.

We would also like to thank the Pyrenean sheepdog Barli for determining the order in which the authors appear on the title page by drawing lots (prepared as titbits).

ORCID® iDs

Wilfried Konrad - https://orcid.org/0000-0002-8686-7865
Christoph Neinhuis - https://orcid.org/0000-0001-9965-4394

References

1. Wolff, J. O.; Wells, D.; Reid, C. R.; Blamires, S. J. *Bioinspiration Biomimetics* **2017,** *12,* 051001. doi:10.1088/1748-3190/aa86ff
2. Barthlott, W.; Mail, M.; Neinhuis, C. *Philos. Trans. R. Soc., A* **2016,** *374,* 20160191. doi:10.1098/rsta.2016.0191
3. Hensel, R.; Neinhuis, C.; Werner, C. *Chem. Soc. Rev.* **2016,** *45,* 323–341. doi:10.1039/c5cs00438a
4. Balmert, A.; Bohn, H. F.; Ditsche-Kuru, P.; Barthlott, W. *J. Morphol.* **2011,** *272,* 442–451. doi:10.1002/jmor.10921
5. Barthlott, W.; Schimmel, T.; Wiersch, S.; Koch, K.; Brede, M.; Barczewski, M.; Walheim, S.; Weis, A.; Kaltenmaier, A.; Leder, A.; Bohn, H. F. *Adv. Mater. (Weinheim, Ger.)* **2010,** *22,* 2325–2328. doi:10.1002/adma.200904411
6. Graeff, E.; Maranzana, N.; Aoussat, A. *Proc. Int. Conf. Eng. Des.* **2019,** *1,* 319–328. doi:10.1017/dsi.2019.35
7. Graeff, E.; Maranzana, N.; Aoussat, A. *Biomimetics* **2020,** *5,* 62. doi:10.3390/biomimetics5040062
8. Vincent, J. F. V.; Bogatyreva, O.; Pahl, A.-K.; Bogatyrev, N.; Bowyer, A. *Creativity Innovation Manage.* **2005,** *14,* 66–72. doi:10.1111/j.1476-8691.2005.00326.x
9. Vincent, J. TRIZ as a Primary Tool for Biomimetics. In *Research and Practice on the Theory of Inventive Problem Solving (TRIZ);* Chechurin, L., Ed.; Springer International Publishing: Cham, Switzerland, 2016; pp 225–235. doi:10.1007/978-3-319-31782-3_13
10. Vincent, J. F. V. *Bioinspired, Biomimetic Nanobiomater.* **2017,** *6,* 67–76. doi:10.1680/jbibn.16.00005
11. Speck, O.; Speck, D.; Horn, R.; Gantner, J.; Sedlbauer, K. P. *Bioinspiration Biomimetics* **2017,** *12,* 011004. doi:10.1088/1748-3190/12/1/011004
12. Drack, M.; Limpinsel, M.; de Bruyn, G.; Nebelsick, J. H.; Betz, O. *Bioinspiration Biomimetics* **2017,** *13,* 016007. doi:10.1088/1748-3190/aa967c
13. Broeckhoven, C.; du Plessis, A. *Adv. Funct. Mater.* **2022,** *32,* 2110235. doi:10.1002/adfm.202110235
14. Roth-Nebelsick, A. *Theory Biosci.* **2022,** *141,* 233–247. doi:10.1007/s12064-022-00367-9
15. Fayemi, P. E.; Wanieck, K.; Zollfrank, C.; Maranzana, N.; Aoussat, A. *Bioinspiration Biomimetics* **2017,** *12,* 011002. doi:10.1088/1748-3190/12/1/011002
16. Flowers, P.; Theopold, K.; Langley, R.; Robinson, W. R. *Chemistry 2e;* OpenStax: Houston, TX, USA, 2019.
17. Adam, J.; Kordel, T.; Johnen, A.; Kannappel, M.; Thaler, C.; Kerschbaum, M.; Rittenschober, C.; Moger, R.; Titz, I. Investigations of measures for extension of BF tuyere life time (EXTUL). https://op.europa.eu/en/publication-detail/-/publication/2181367c-7677-11e5-86db-01aa75ed71a1.
18. Preiss, T. *Chemisch-physikalische Untersuchungen zum Schadensmechanismus an Hochofenblasformen;* Papierflieger: Clausthal-Zellerfeld, Germany, 2008.
19. Portnov, L. V.; Nikitin, L. D.; Bugaev, S. F.; Shchipitsyn, V. G. *Metallurgist (N. Y., NY, U. S.)* **2014,** *58,* 488–491. doi:10.1007/s11015-014-9938-7
20. Farkas, O.; Móger, R. *Steel Res. Int.* **2013,** *84,* 1171–1178. doi:10.1002/srin.201200328
21. Helbig, R.; Nickerl, J.; Neinhuis, C.; Werner, C. *PLoS One* **2011,** *6,* e25105. doi:10.1371/journal.pone.0025105
22. Hensel, R.; Helbig, R.; Aland, S.; Braun, H.-G.; Voigt, A.; Neinhuis, C.; Werner, C. *Langmuir* **2013,** *29,* 1100–1112. doi:10.1021/la304179b
23. Nickerl, J.; Helbig, R.; Schulz, H.-J.; Werner, C.; Neinhuis, C. *Zoomorphology* **2013,** *132,* 183–195. doi:10.1007/s00435-012-0181-0
24. Busch, J.; Barthlott, W.; Brede, M.; Terlau, W.; Mail, M. *Philos. Trans. R. Soc., A* **2019,** *377,* 20180263. doi:10.1098/rsta.2018.0263
25. Oeffner, J.; Hagemeister, N.; Bretschneider, H.; Schimmel, T.; Jahn, C. Reducing Friction with Passive Air Lubrication: Initial Experimental Results and the Numerical Validation Concept of AIRCOAT. In *12th Symposium on High-Performance Marine Vehicles,* Cortona, Italy; Bertram, V., Ed.; Technische Universität Hamburg, Schriftenreihe Schiffbau: Hamburg, Germany, 2020; pp 405–417.
26. Gandyra, D.; Walheim, S.; Gorb, S.; Ditsche, P.; Barthlott, W.; Schimmel, T. *Small* **2020,** *16,* 2003425. doi:10.1002/smll.202003425
27. Ditsche, P.; Gorb, E.; Mayser, M.; Gorb, S.; Schimmel, T.; Barthlott, W. *Appl. Phys. A: Mater. Sci. Process.* **2015,** *121,* 505–511. doi:10.1007/s00339-015-9439-y
28. Konrad, W.; Roth-Nebelsick, A.; Kessel, B.; Miranda, T.; Ebner, M.; Schott, R.; Nebelsick, J. H. *J. R. Soc., Interface* **2021,** *18,* 20210676. doi:10.1098/rsif.2021.0676
29. Mayser, M. J.; Bohn, H. F.; Reker, M.; Barthlott, W. *Beilstein J. Nanotechnol.* **2014,** *5,* 812–821. doi:10.3762/bjnano.5.93
30. Bellinger, P. F.; Christiansen, K. A.; Janssens, F. Checklist of the Collembola of the World. http://www.collembola.org.
31. Hopkin, S. P. *Collembola; the most abundant insects on Earth;* Antenna: London, UK, 1998.
32. Potapov, A.; Bellini, B.; Chown, S.; Deharveng, L.; Janssens, F.; Kováč, L.; Kuznetsova, N.; Ponge, J.-F.; Potapov, M.; Querner, P.; Russell, D.; Sun, X.; Zhang, F.; Berg, M. *Soil Org.* **2020,** *92,* 161–188. doi:10.25674/so92iss3pp161
33. Eisenbeis, G.; Wichard, W. *Atlas zur Biologie der Bodenarthropoden;* G. Fischer Verlag: Stuttgart, New York, 1985. doi:10.1007/978-3-642-39392-1
34. Noble-Nesbitt, J. *J. Exp. Biol.* **1963,** *40,* 681–700. doi:10.1242/jeb.40.4.681
35. Roach, P.; Shirtcliffe, N. J.; Newton, M. I. *Soft Matter* **2008,** *4,* 224–240. doi:10.1039/b712575p
36. Ensikat, H. J.; Ditsche-Kuru, P.; Neinhuis, C.; Barthlott, W. *Beilstein J. Nanotechnol.* **2011,** *2,* 152–161. doi:10.3762/bjnano.2.19
37. Bhushan, B.; Koch, K.; Jung, Y. C. *Soft Matter* **2008,** *4,* 1799. doi:10.1039/b808146h
38. Konrad, W.; Apeltauer, C.; Frauendiener, J.; Barthlott, W.; Roth-Nebelsick, A. *J. Bionic Eng.* **2009,** *6,* 350–356. doi:10.1016/s1672-6529(08)60133-x
39. Apeltauer, C. Eine praktische Anwendung von CMC-Flächen in der Bionik. Ph.D. Thesis, University of Tübingen, Tübingen, Germany, 2011. http://nbn-resolving.de/urn:nbn:de:bsz:21-opus-57492
40. Konrad, W.; Katul, G.; Roth-Nebelsick, A.; Jensen, K. H. *Tree Physiol. (Oxford, U. K.)* **2019,** *39,* 243–261. doi:10.1093/treephys/tpy097
41. Ambrosetti, A.; Ferri, N.; DiStasio, R. A., Jr.; Tkatchenko, A. *Science* **2016,** *351,* 1171–1176. doi:10.1126/science.aae0509
42. Shen, F.; Wang, Y.; Cheng, Y.; Zhang, L. *Tree Physiol. (Oxford, U. K.)* **2012,** *32,* 1413–1419. doi:10.1093/treephys/tps089
43. Holbrook, N. M.; Zwieniecki, M. A. *Plant Physiol.* **1999,** *120,* 7–10. doi:10.1104/pp.120.1.7

44. Konrad, W.; Roth-Nebelsick, A. *J. Theor. Biol.* **2003,** *224,* 43–61. doi:10.1016/s0022-5193(03)00138-3
45. Konrad, W.; Roth-Nebelsick, A. *J. Biol. Phys.* **2005,** *31,* 57–71. doi:10.1007/s10867-005-6094-0
46. López, R.; Pyo, J. *J. Geom. Phys.* **2014,** *76,* 256–262. doi:10.1016/j.geomphys.2013.10.021
47. Konrad, W.; Adam, J.; Konietzko, S.; Neinhuis, C. *J. Bionic Eng.* **2019,** *16,* 281–290. doi:10.1007/s42235-019-0023-6
48. Lenau, T. A.; Metze, A.-L.; Hesselberg, T. Paradigms for biologically inspired design. In *Proceedings of SPIE,* Bioinspiration, Biomimetics, and Bioreplication VIII, Denver, CO, March 4–8, 2018; SPIE: Bellingham, WA, USA, 2018; p 1059302.
49. Snell-Rood, E. *Nature* **2016,** *529,* 277–278. doi:10.1038/529277a
50. Adamson, A. W.; Gast, A. P. *Physical chemistry of surfaces;* Wiley-Interscience: Hoboken, NJ, USA, 1997.
51. Kreyszig, E. *Differential Geometry;* University of Toronto Press: Toronto, Canada, 1959.
Reprinted by Dover Publications, 1991.
52. Finn, R. *Equilibrium capillary surfaces;* Springer: New York, NY, USA, 1986.

License and Terms

This is an open access article licensed under the terms of the Beilstein-Institut Open Access License Agreement (https://www.beilstein-journals.org/bjnano/terms), which is identical to the Creative Commons Attribution 4.0 International License (https://creativecommons.org/licenses/by/4.0). The reuse of material under this license requires that the author(s), source and license are credited. Third-party material in this article could be subject to other licenses (typically indicated in the credit line), and in this case, users are required to obtain permission from the license holder to reuse the material.

The definitive version of this article is the electronic one which can be found at:
https://doi.org/10.3762/bjnano.13.111

BEILSTEIN JOURNAL OF NANOTECHNOLOGY

Dry under water: air retaining properties of large-scale elastomer foils covered with mushroom-shaped surface microstructures

Matthias Mail[*1,2], Stefan Walheim[2], Thomas Schimmel[2], Wilhelm Barthlott[1], Stanislav N. Gorb[3] and Lars Heepe[3,4]

Full Research Paper

Open Access

Address:
[1]Nees Institute for Biodiversity of Plants, University of Bonn, Venusbergweg 22, D-53115 Bonn, Germany, [2]Institute of Nanotechnology (INT) and Karlsruhe Nano Micro Facility (KNMF), Karlsruhe Institute of Technology (KIT), Hermann-von-Helmholtz-Platz 1, D-76344 Eggenstein-Leopoldshafen, Germany, [3]Department of Functional Morphology and Biomechanics, Institute of Zoology, Christian-Albrechts-University of Kiel, Am Botanischen Garten 1–9, D-24118 Kiel, Germany and [4]Gottlieb Binder GmbH & Co KG, Bahnhofstr. 19, D-71088 Holzgerlingen, Germany

Email:
Matthias Mail[*] - matthias.mail@kit.edu

* Corresponding author

Keywords:
adhesive tape; air layer; air retention; bionics; fouling; gecko tape; mushroom structures; passive air lubrication; Salvinia effect; superhydrophobicity

Beilstein J. Nanotechnol. **2022,** *13,* 1370–1379.
https://doi.org/10.3762/bjnano.13.113

Received: 01 August 2022
Accepted: 26 October 2022
Published: 21 November 2022

This article is part of the thematic issue "Biomimetics on the micro- and nanoscale – The 25th anniversary of the lotus effect".

Associate Editor: K. Koch

© 2022 Mail et al.; licensee Beilstein-Institut.
License and terms: see end of document.

Abstract

Superhydrophobic surfaces are well known for most different functions in plants, animals, and thus for biomimetic technical applications. Beside the Lotus Effect, one of their features with great technical, economic and ecologic potential is the Salvinia Effect, the capability to keep a stable air layer when submerged under water. Such air layers are of great importance, e.g., for drag reduction (passive air lubrication), antifouling, sensor applications or oil–water separation. Some biological models, e.g., the floating fern *Salvinia* or the backswimmer *Notonecta*, show long term stable air retention even under hydrodynamic conditions. Therefore, they are ideal models for the development of technical biomimetic air retaining surfaces. Up to now, several prototypes of such surfaces have been developed, but none provides both, stable air retention and cost effective large scale production. Meanwhile, a novel biomimetic surface is commercially available and produced on a large scale: an adhesive elastomeric film with mushroom-shaped surface microstructures that mimic the adhesion system of animals. In this study, we show that these films, which have been initially developed for a different purpose, due to their specific geometry at the microscale, are capable of stable air retention under water. We present first results concerning the capabilities of mushroom-shaped surface microstructures and show that this elastomer foil is able to stabilize a permanent air layer under water for more than two weeks. Further, the stability of the air layer under

pressure was investigated and these results are compared with the predicted theoretical values for air retention of microstructured surfaces. Here, we could show that they fit to the theoretical predictions and that the biomimetic elastomer foil is a promising base for the development of an economically and efficient biomimetic air retaining surface for a broad range of technical applications.

Introduction

Superhydrophobicity is one of the key innovations in the biological evolution of organisms for the conquest of land [1]. Recently it was shown that this fascinating surface property evolved already in the cyanobacterium *Hassallia* [2] and is known for more than thousand years [3], but after the Lotus effect publication [4], this research led to a paradigm shift in surface science [5] and was the starting point for novel technologies in surface science [5]. Today many products in forms of coatings, sprays and paints providing superhydrophobic surfaces and self-cleaning properties are available on the market [1,6,7]. A most interesting feature of certain superhydrophobic surfaces is their ability to maintain a persistent air layer submerged under water. This ability is called Salvinia effect [5,8-10]. Due to the hydrophobic chemistry of the hierarchically structured surfaces water cannot penetrate and air remains trapped in between the structures [1], which is indicated by a silvery shine of the submerged surface (See Figure 1a). For technical applications, the Salvinia effect bears an immense potential, as air layers kept between water and a solid surface might serve as friction reduction agents, fouling protectors, corrosion protectors or for other applications, such as sensors [11-14].

Biological examples for such air retaining surfaces with most stable and persistent air layers were found on the floating ferns of the genus *Salvinia* (Figure 1a,c) and in the backswimmers *Notonecta* [1,15,16] and other aquatic organisms. In terms of technical applications, the Salvinia effect gained increasing interest in the past few years [1,3,9,10,13,15,17-25]. The most promising function for biomimetic air retaining surfaces is drag reduction. If an air layer is mounted between a solid surface and water flowing over this surface, the air layer serves as slip agent [26-28]. Such a drag reducing coverage allows significant friction reduction (up to 30%) in applications, where liquids flow

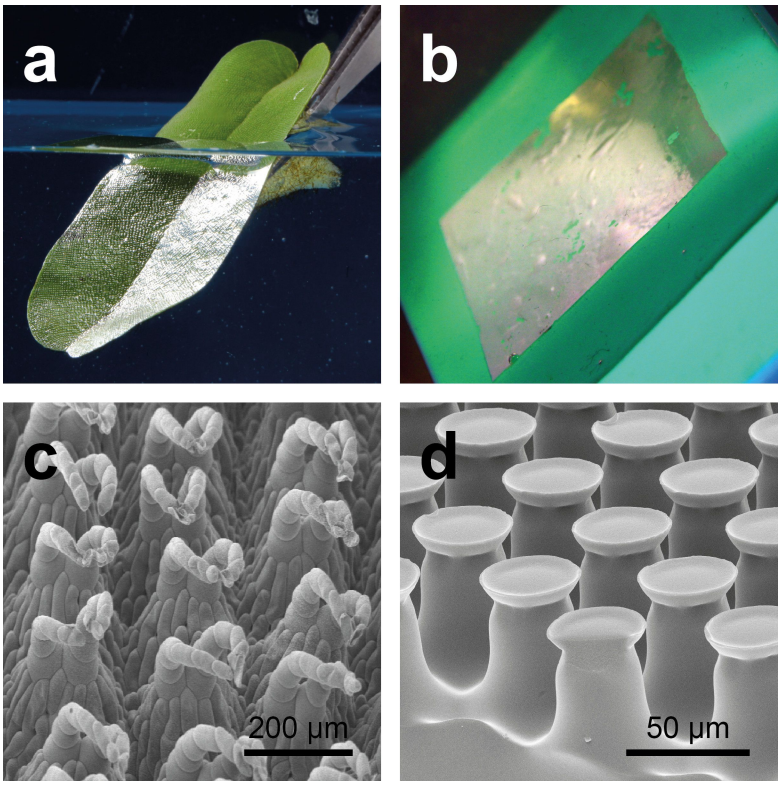


Figure 1: Biological role model and biomimetic air retaining surfaces. a) Leaf of the floating fern *Salvinia oblongifolia* submerged in water. The silvery shine indicates the kept air layer. b) Elastomer foil covered with mushroom-shaped surface microstructures (MSM) submerged in water. MSM-surfaces were glued to a green silicon surface to enhance contrast. Like on the biological role model, the silvery shine indicates the kept air. c) SEM image of the surface structure of the *Salvinia* leaf. d) SEM image of the MSM.

over solid surfaces [29,30]. The highest economic and ecological potential for this technology is the shipping industry [31]. The optimal parameters for stable air retention have been previously investigated [1,32] and theoretical calculations have been performed [33-35]. Four criteria for the development of biomimetic air retaining surfaces have been found [1].

Transferring these parameters into technical surfaces, different prototypes have been developed, showing air retention over several years and drag reduction values up to 30% [24,36]. Up to now, all these prototypes are only at the laboratory scale and for different reasons difficult to realize in large-scale industrial productions. Here, a new and promising surface type is elastomer foils covered with mushroom-shaped surface microstructures (MSM) is introduced. These surfaces originate from the development of biomimetic adhesion systems. They are inspired by the feet of beetles, flies, spiders and geckos and have been shown to strongly enhance adhesion [37-51]. But these surfaces were also shown to be the structure of choice to produce omniphobic surfaces, their wetting behavior has been also previously described [52,53]. As these surfaces showed very good air retention properties, some of their structural parameters are in good accordance with some biological air retaining surfaces, and as they can be produced rather cost effective and on large scale, they could also be a promising base for the further development of biomimetic air retaining surfaces (Figure 1b,d). Further, this is a very nice example for the multifunctionality of some biomimetic-structured surfaces, showing that in nature often almost similar structures have evolved for completely different tasks. Here, we investigate the air retention capabilities of MSM for the first time. We analyzed the long term stability of the kept air layers as well as the behavior of the air layers at different pressures.

Materials and Methods

1 Mushroom-shaped microstructured elastomer foil

Microstructured elastomer foils were made from poly(vinylsiloxane), a silicone elastomer. The surface has about 30,000 hexagonally distributed mushroom-shaped surface microstructures (MSM) per square centimeter (Figure 1d) [37-44]. Individual elements have a height of about h = 60 µm, an effective radius of about r = 15 µm, and a lattice constant a = 62 µm.

2 Persistence of air layers attached to microstructured surfaces immersed in water

Following the theory presented by Konrad et al. [33], h_{max} is the maximum persistence depth of an air layer attached to a microstructured surface immersed in water, i.e., for immersion depth below h_{max} the air layer is persistent and does not vanish, above it will disappear in time τ. All following calculations were performed for a temperature of 20 °C and an atmospheric pressure p_{atm} = 1 bar. The maximum persistence depth is given by

$$h_{max} = \frac{\sigma \cos\theta \left|\hat{\Sigma}\right|}{\rho_w g \left|\Omega\right|} \approx 2 \text{ cm}, \quad (1)$$

whereas σ = 72.75 mN/m is the surface tension of water, cos θ is the water contact angle of poly(vinylsiloxane) which was assumed to be 95°, $|\Omega| = \frac{\sqrt{3a^2 - 2\pi r^2}}{12}$ and $\left|\hat{\Sigma}\right| = \frac{\pi r}{3}$, ρ_w = 997 kg/m^3 the density of water, and g the gravitational acceleration.

The reduced bubble lifetime for $h > h_{max}$

$$\tau^* = \frac{\tau\varepsilon}{V_i} = \frac{k_H}{4\pi D_a RT}\left(1 + \frac{p_{atm}}{\rho_w g\left(h - h_{max}\right)}\right), \quad (2)$$

whereas V_i is the initial volume of the air layer, $\varepsilon = \sqrt{\frac{A_i}{4\pi}}$ with A_i the interface area of V_i, k_H is the Henry's law volatility constant of air in water. In order to calculate k_H we assume air is composed of approx. 78% nitrogen and approx. 20% oxygen. Following Sander [54], the Henry's law solubility constant for oxygen in water at 20 °C is approx. 1.42 × 10^{-5} mol/(m^3·Pa), for nitrogen it is approx. 6.90 × 10^{-6} mol/(m^3·Pa). Equating Henry's law volatility constant for air, one gets approx. 1.27 m^3·Pa/mol. D_a is the diffusion constant of air in water which is 2.5 × 10^{-5} cm^2/s [55], R is the gas constant and T the absolute temperature.

3 Underwater air retention and its persistence

To demonstrate the underwater air retention and to analyze the stability of air layers kept by MSM, different samples were submerged in five different immersion depths, here 0.5, 5, 10, 15 and 20 cm. As a measure of the stability in dependence on the immersion depth the lifetime of the air layers were determined. Deionized water was used throughout all experiments.

3.1 Air–water interface of a persistent air-layer

To investigate the shape of the air–water interface of the air layers kept by MSM and to proof the expected durability of the air layer in a water depth lower than 2 cm, a 2.0 × 2.0 cm^2 sample was placed in a Petri dish filled with deionized water. In this first experiment, the air layer of the sample immersed at 0.5 cm depth, i.e., smaller than h_{max}, was visualized with a confocal laser scanning microscope (CLSM, TCS SP II, Leica Microsystems, Wetzlar) using an objective lens (HCX APO L 63x/0.90 W U-V-I, Leica Microsystems, Wetzlar) with 63-fold

magnification directly after submergence and after two weeks. Using the total reflection of the laser light at the air–water interface this method allowed us to analyze the shape of the air–water interface at high resolution. The method as well as the results are shown in Figure 2. For the analysis of the shape of the air–water interface, cross sections trough the image stacks have been generated by using the software Leica TFS.

3.2 Static lifetime tests of air layer submerged deeper than h_{max}

In a second experiment, which was done in two different laboratories, the air layer of samples placed at 5, 10, and 15 cm immersion depth, respectively and at 5, 10, and 20 cm immersion depth, respectively, i.e., larger than h_{max} were analyzed.

In one case, in each depth (5, 10, and 15 cm) two samples with a size of 2 × 2 cm^2 have been placed. The semi-transparent MSM surfaces were glued to a green silicon surface to enhance contrast (air layer/wet surface). The samples were photographed using a digital camera (EOS-650D, Canon, Krefeld) every 3 min until the samples were completely wetted and no retaining air was visible. The area of the silvery shining air layer covering MSM was measured using Photoshop CS6 (Adobe Systems Software, Dublin, Ireland).

Also for the second set of samples (depth 5, 10, and 20 cm) a camera (PX-8085-919, Somicon®, Pearl GmbH, Buggingen, Germany) was used to take time series of images, which then where analyzed automatically using a self-written software tool based on the platform processing in Java.

In Figure 3b–d examples of the images taken of a sample at different times are shown. Figure 3a exemplarily shows the measured time curves of one of the setups (depth 5, 10, and 20 cm). This method allows no quantitative analysis, but as the sample images and the curves in Figure 3 indicate, the air layers

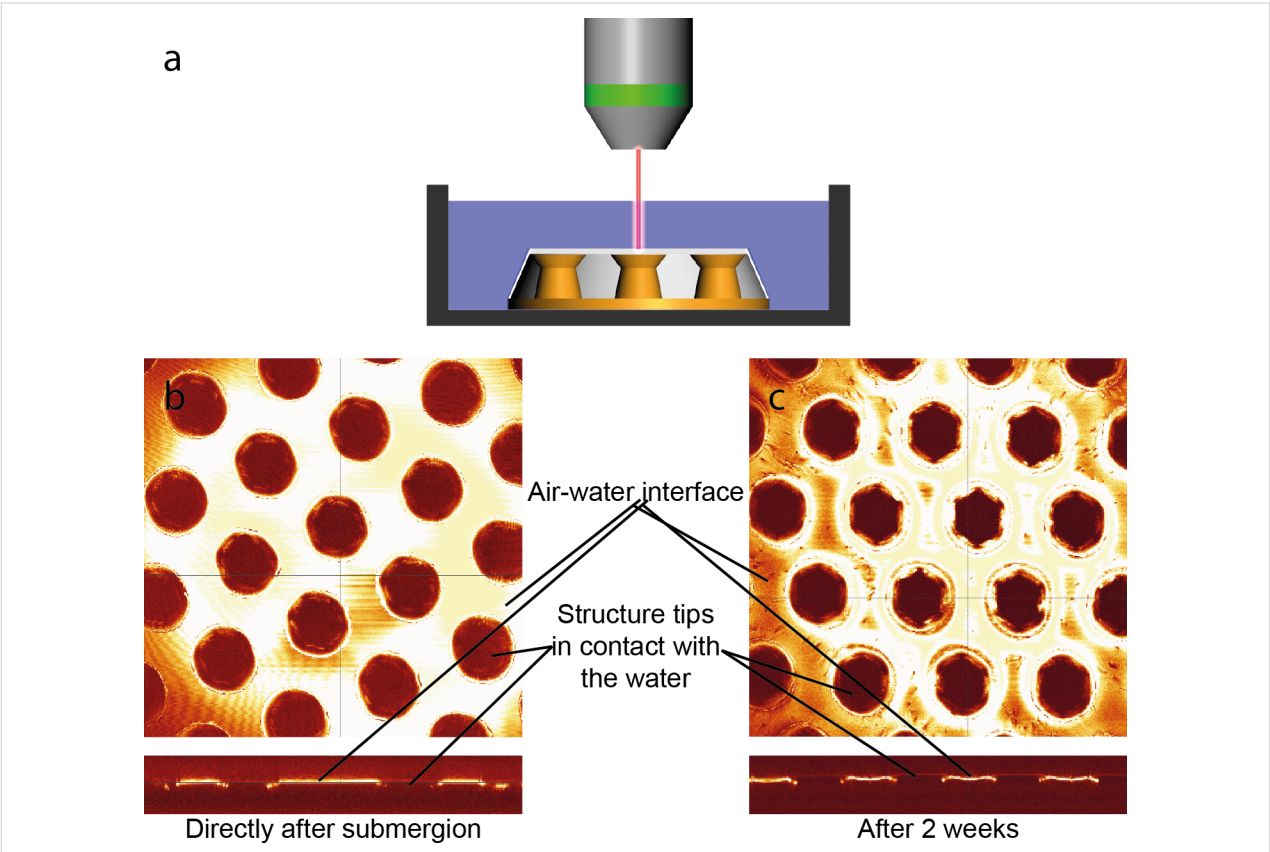


Figure 2: Confirmation of the persistence of the air layer in low water depth and analysis of the shape of the air–water interface by confocal laser scanning microscopy (CLSM) investigations. a) Schematic drawing of the principle of the measurement. The sample is submerged under water and keeps an air layer. The laser beam of the CLSM is reflected at the air–water interface. This enables the 3 dimensional analysis of the air layer. b) Result of the measurement directly after submerging the sample in 5 mm water depth. A top view image as well as a cross section of the air–water interface is shown. The dark parts in the top view image represent the MSM, the bright parts show the air–water interface in between. Also in the cross section the air–water interface is represented by the bright areas of the image while the MSM in between appear darker. It could be seen that the shape of the air layer is almost completely flat. c) Results of the measurement of the same sample after 2 weeks under water. Still the air–water interface is spanned between the tips of the MSM. The cross section shows almost no deformation of the air layer, indicating that almost no air is lost and the system is in an equilibrium state.

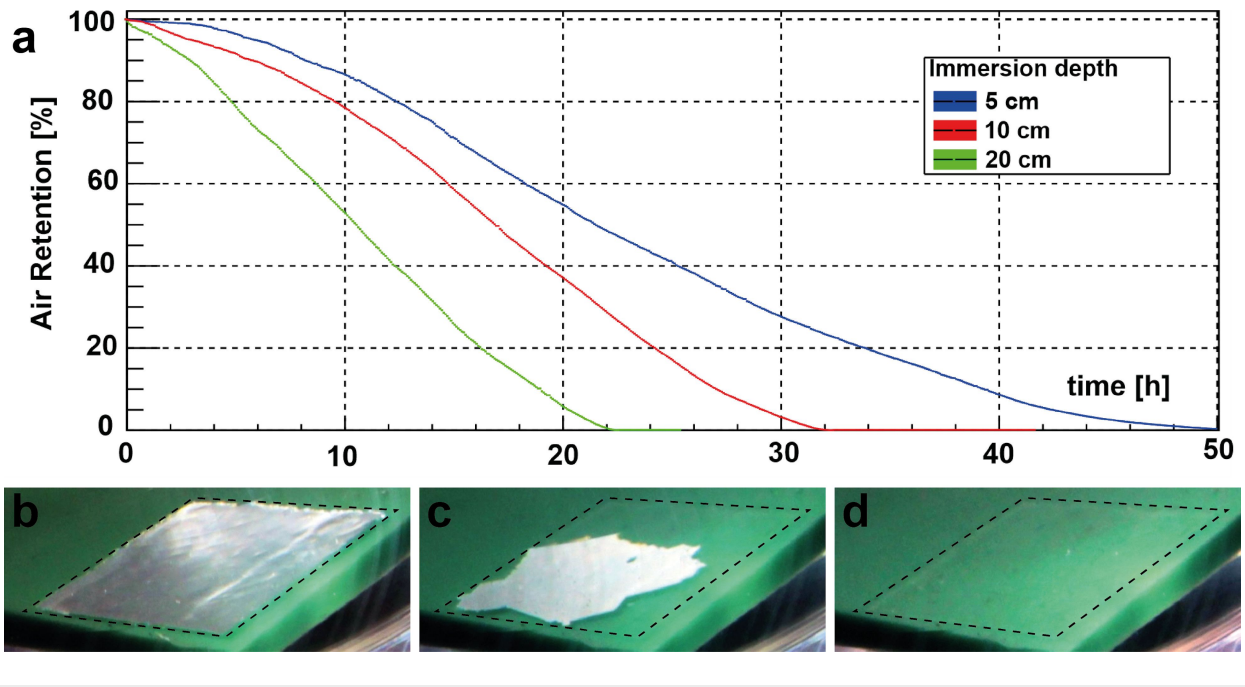


Figure 3: Results of the long term investigations of air layers on MSM in three different depths. a) The graphs show the sample area covered by an air layer in three different depths (5, 10 and 20 cm) over time. b–d) Examples of the images taken in the experiment. MSM surfaces were glued to a green silicon surface to enhance contrast, and imaged in defined time steps. b) At the beginning of the experiment, the sample (indicated by a dotted line) was completely covered by air. c) After several hours under water, part of the layer was lost. d) Finally, all the air was lost and the sample was completely wetted.

showed the expected behavior and disappeared faster in cases where the samples were placed deeper in the water as in those samples placed closer to the water surface.

3.3 Simulation of static durability for immersion depth much deeper than h_{max}

In order to simulate even greater immersion depth of the order of several meters the air layer kept by the microstructured elastomer foil was analyzed within a home-build pressure chamber. The setup is shown in Figure 4. The pressure chamber was connected to a compressor. To avoid pressure fluctuations, a compensator has been mounted between the pressure chamber and the compressor. Further a digital manometer has been connected to the pressure chamber to control the pressure in the sample chamber. With a valve the pressure in the chamber was regulated. Four circular samples with a diameter of 1.5 mm were placed simultaneously inside the pressure chamber. Then, the chamber was flooded with deionized water. The chamber was placed under a Zeiss LSM700 confocal laser scanning microscope system (Carl Zeiss Microscopy GmbH, Jena, Germany). The air–water interface of the samples was observed while the pressure was increased and kept at a certain level. Imaging was continued until all the air disappeared. First, a pressure of 500 mbar was applied corresponding to an immersion depth of about 5.1 m. Then the same procedure was performed with an applied pressure of 1000 mbar corresponding to an immersion depth of about 10.2 m. Analysis of the air covered areas was performed using Photoshop CS3 (Adobe Systems Software, Dublin, Ireland).

4 Calculation of the air layer volumes

From the measured areas of air layers covering the microstructured elastomer foils, the corresponding air volumes were estimated as follows:

$$V = Ah\left(1-\rho\pi r^2\right) \tag{3}$$

with A the measured areas of air layers, h the height of a surface microstructure, r the effective radius of a surface microstructure, and ρ the number of surface microstructures per unit area which was assumed to 30,000 per cm^2.

Upon hydrostatic pressure, either applied by immersion depth or by an applied pressure (see sections 3.2 and 3.3), an initial air layer with volume V_0 will reduce to the volume V_1 by

$$V_1 = \frac{p_0 V_0}{p_1 + p_0}. \tag{4}$$

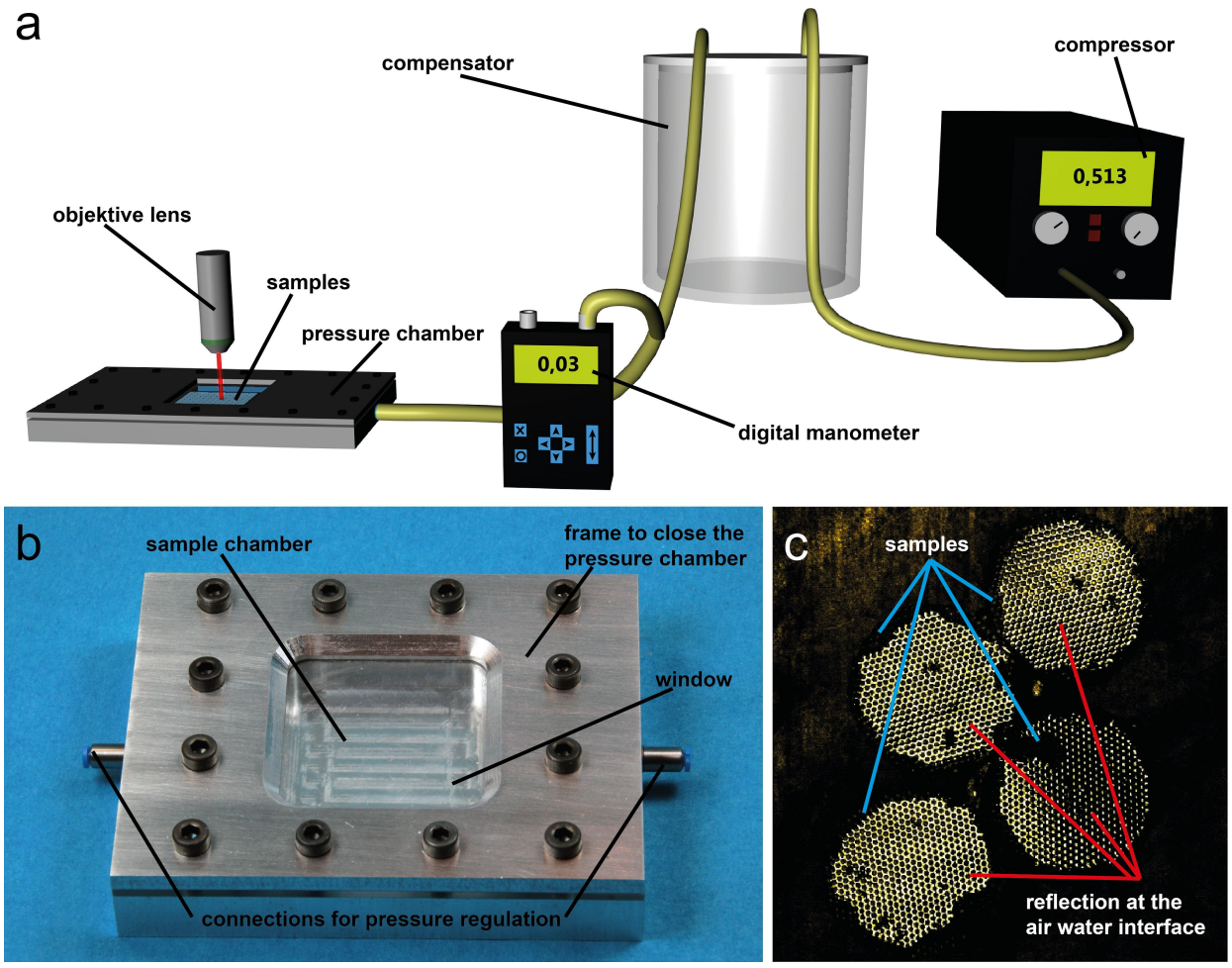


Figure 4: To determine pressure stability and diffusion behavior of the MSM, CLSM and a custom-made pressure chamber were used. a) Schematic drawing of the experimental setup, described in the experimental section. b) Photo of the custom-made pressure chamber. c) Examples of the images taken with the CLSM to investigate pressure and diffusion behavior. The bright areas on the four rounded samples in the image show the surface parts which keep an air layer and therefore show total reflection at the air–water interface. These areas have been measured and their size has been monitored over time, to analyze the changes at different pressure loads.

5 Long term storage

MSM samples were submerged in a jam jar filled with tap water to a height of about 1.5 cm, i.e., below h_{max} to allow for a persistent air layer. The jar was closed and stored on a rack in the office. After one month, the samples were taken out of the water and dried in air. The dried samples were mounted to aluminum stubs and fixated using silver paste. To enhance the conductivity, the samples were sputtered with a thin gold layer (thickness 20 nm, Sputter Coater 108 auto, Cressington, Dortmund). Afterwards the samples have been analyzed using SEM (15 kV, CAMBRIDGE Stereoscan 200 SEM, Zeiss AG, Oberkochen).

Results and Discussion

As a first step of the investigation of the air retaining capabilities of mushroom-shaped surface microstructures (MSM) the long-term stability of the air layers was analyzed. Calculations according to Konrad et al. [33] predicted a maximum immersion depth underwater h_{max} of about 2 cm for a persistent air layer kept by MSM with the given geometric dimensions and the given surface energy (see section 2). If they are submerged deeper than 2 cm, the air layer gets lost over time due to diffusion effects.

To confirm the predicted persistence of the air layer in a water depth below 2 cm samples have been submerged in a depth of about 5 mm for two weeks. The analysis of these samples by confocal laser scanning microscopy (CLSM) showed the expected persistence of the air layer (see Figure 2). The images taken directly after the submersion of the sample show an almost perfectly flat air–water interface. After two weeks under water the same sample still kept an air layer and was analyzed

again by CLSM. In Figure 2 it could be seen that the air–water interface showed only a slight indentation between the MSM. This is due to a little loss of air which happens before air layer and water were in an equilibrium state which from then on was stable over the entire time period. This result is in good agreement with the theoretical predictions of Konrad et al. [33] and shows the long term stable air retention capabilities of the MSM under this shallow water conditions.

Tests with samples immersed in depths larger than h_{max}, i.e., 5, 10, 15 and 20 cm showed the expected vanishing of the air layer over time. With higher immersion depth the faster the air got lost (see Figure 3). The time it took till the entire air was lost is in good accordance with the predicted time calculated with the methods of Konrad et al. [33].

To further investigate the stability of the air layers kept by MSM and to analyze their pressure and diffusion behavior, measurements under static pressure in a custom-made pressure chamber and again by using CLSM were carried out. The principle of these measurements is described in the experimental section and shown in Figure 4. By applying a constant pressure a deeper submersion of the samples was simulated. As expected, it turned out that the higher the pressure, the faster the decrease of the air layers. The first reduction of the air covered area on the surfaces was due to the compression of the air under pressure. This compression of the air led to a lateral decrease in the area covered by air, leaving an unchanged high layer of air between the MSM structures. This lateral "melting" of the air layer patch then continued by diffusion of the air into the water until finally no air was visible.

After elimination of the volume loss due to compression of the air layer, the loss of air due to diffusion can be quantified. The graphs of these measurements show the expected progress (see Figure 5).

For comparison and validation, the theoretical lifetime of the air layer at different pressures/depth and maximum depth for persistent air retention on MSM has been calculated, using the structural parameters of the MSM and the equations of Konrad et al. [33] (see sections 2 and 4). The result is shown in

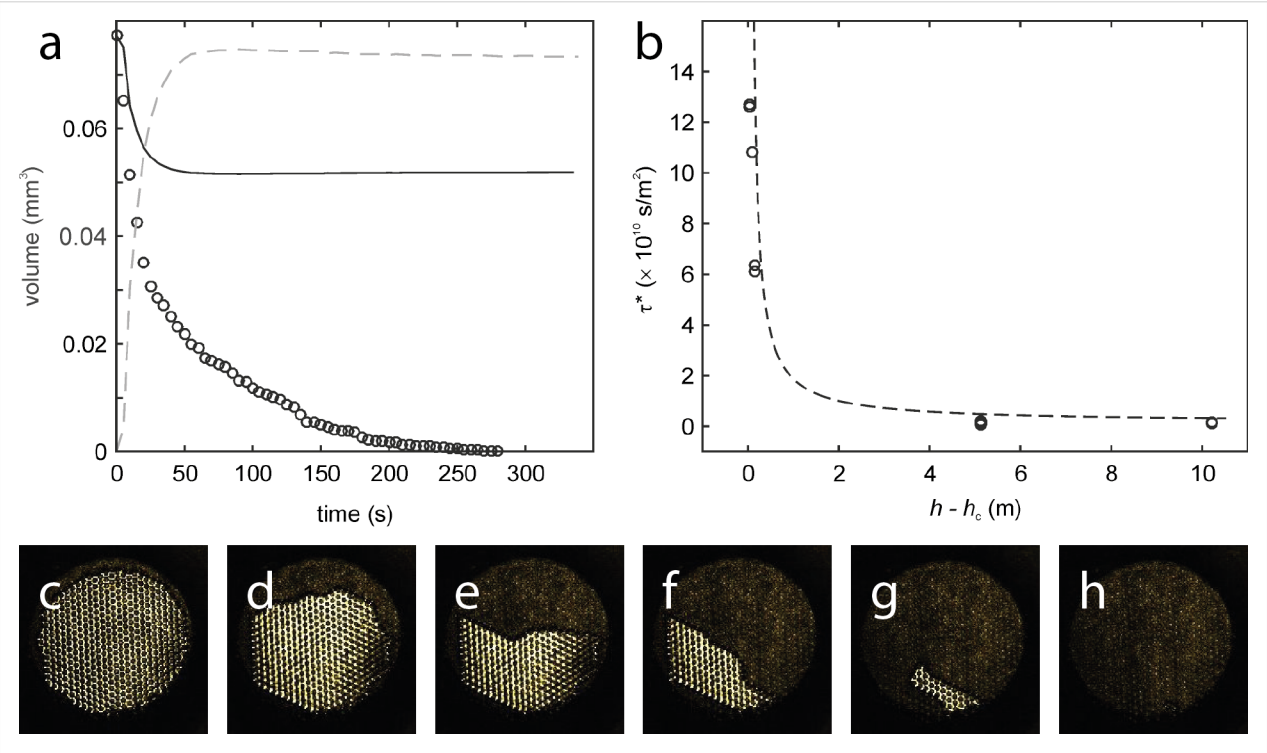


Figure 5: Results of the pressure stability and diffusion behavior experiments. a) With increasing pressure (dashed line), the air volume gets compressed. After calculation of the theoretical compression of the air volume (continuous line) and the decreasing of the air covered surface area due to this compression it was possible to calculate the loss of air due to diffusion over time (circles). The results are in good accordance with the predicted behavior after Konrad et al. [33]. b) Comparison of measured results with theoretical predictions. The dashed curve shows the theoretically predicted life time of the air layer on a submerged MSM surface depending on the immersion depth, calculated after Konrad et al. [33]. The various circles represent the results of the long term stability tests and the pressure stability and diffusion behavior experiments. The results are in good accordance with the predicted values. c–h) Examples of the images used for these calculations. The images show the decrease of an air layer on a sample in a time span of 6 min at pressure of 1 bar. c) Initial state directly after closing the pressure chamber. Almost the entire sample surface is covered by a reflecting air layer. d–g) With increasing pressure and due to diffusion the air gets lost. h) After 6 min the entire air was lost.

Figure 5. The maximum depth for permanent air retention was about 2 cm. Further, the results of the stability tests at different depth and the investigations of the diffusion behavior at different pressures are plotted in the graph. The results are in good agreement with the theoretically predicted values.

Further, our results indicate that both the size and shape of the contact area between water and air plays a crucial role for the stability of the air layer. The loss of air happened not only at the interface of water and air between the top side of the MSM, but also on the sides. This means the water-contact-area/volume ratio of the air layer is a crucial parameter for the long term stability of the kept air. Previous works have focused primarily on the behavior of the air–water interface at the tips of the surface structures. However, the sides also play a decisive role. Assuming a round surface section, the air volume resembles a cylinder. Thus, there is not only contact between air and water at the top surface structures, but also at the shell surface, through which additional diffusion takes place. Therefore, the surface should be compartmented to exclude the influence of these side surfaces. Furthermore, a subdivision of the air volume into small individual volumes ensures better stability, since individual defects only affect a partial volume and not the total volume. This once more indicates that compartmentation of air retaining surfaces is of great importance, as this would lead to much more stable air retention [56].

Beside the investigation of the air layers kept by submerged MSM in deionized water and the comparison with the theoretically predicted values, also the SEM investigation of the samples submerged for one month in tap water offered some important results for the practical application of air retaining MSM.

Mushroom-like microstructures are known for their antifouling properties against such hard-foulers as barnacles [53,57-59]. However, in air–water boundaries under non-sterile and static conditions an „interphase microbial community“ (neuston) usually becomes established in fresh- and saltwater – like acetobacter and yeast communities in the production of vinegar [60].

Since the air layers on some Salvinia-like biomimetic surfaces are permanent over years, like in many air–water interfaces a neustonic microbial biofilm (“Bacterioneuston”), usually associated with fungi, becomes established under non-sterile and non-turbulent conditions rather fast. On the MSM already after one month the air–water interface is contaminated by bacteria and the tips of the MSM are contaminated by bacteria and connected by straight filaments which probably represent fungal hyphae (see Figure 6, compare, e.g., illustrations in [61]). Under hydrodynamic conditions this microbial fouling effect can probably be neglected and thus does not hinder the application of MSM under turbulent conditions.

Conclusion

In this work the air retaining properties of large-scale elastomer foils covered with mushroom-shaped surface microstructures (MSM) have been analyzed for the first time. It has been shown that these surfaces are able to keep stable air layers under water for more than two weeks, but, due to the morphology of the surface a permanent stabilization of air is only possible to maximum depth of about 2 cm. The theoretical predictions of Konrad et al. [33] were confirmed. These results and the fact, that MSM are comparatively cheap and easy to produce on large scales, show, that MSM are a promising new alternative for the development of biomimetic under water air retaining surfaces. However, as other prototypes, they show stable air retention in low depth but lose their air layers in higher depth due to diffusion of the air into the water. For a use of their air retention capabilities in technical applications in higher water

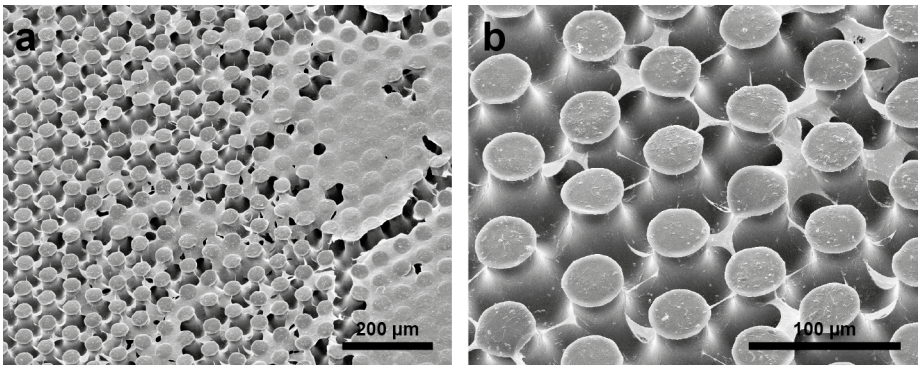


Figure 6: SEM images of the MSM after they have been submerged for one month in tap water. a) A microbial neustonic on the MSM. The biofilm covers large areas of the MSM surface. b) Already after one month the tips of some of the MSM are contaminated by bacteria and connected by straight filaments, which are most probably fungal hyphae.

depths and under real conditions, a method to refill the air layer after a loss of air occurred have to be found.

Acknowledgements

The authors thank Karlsruhe Nano Micro Facility (KNMF, http://www.kit.edu/knmf), a Helmholtz Research Infrastructure at Karlsruhe Institute of Technology (KIT) for providing technical facilities for our work. Further, the authors thank Sebastian Onasch, Peter Baumann, Thomas Pfeffer, Birte Böhnlein and Manuel Karl for their help in constructing the experimental setups and performing the experiments.

Funding

Funding of the work presented in this paper was provided by the Federal Ministry for Education (BMBF) in the joint research project ARES (Air REtaining Surfaces, grant 03V0752) in the VIP program. Furhter, funding was prvided by the Deutsche Forschungsgemeinschaft (DFG) within the Graduiertenkolleg 'Bionik - Interaktion über Grenzflächen zur Außenwelt' (GRK1572) and within the project 'Grundprinzipien der Gasretention an Oberflächen unter Wasser: Ein materialorientierter Ansatz auf Basis von Kohlenstoffnanoröhren Architekturen' (MA8804/2-1).

ORCID® iDs

Matthias Mail - https://orcid.org/0000-0002-9732-8453
Stanislav N. Gorb - https://orcid.org/0000-0001-9712-7953

References

1. Barthlott, W.; Mail, M.; Neinhuis, C. *Philos. Trans. R. Soc., A* **2016,** *374,* 20160191. doi:10.1098/rsta.2016.0191
2. Barthlott, W.; Büdel, B.; Mail, M.; Neumann, K. M.; Bartels, D.; Fischer, E. *Front. Plant Sci.* **2022,** *13,* 880439. doi:10.3389/fpls.2022.880439
3. Barthlott, W.; Rafiqpoor, M. D.; Erdelen, W. R. Bionics and Biodiversity – Bio-inspired Technical Innovation for a Sustainable Future. In *Biomimetic Research for Architecture and Building Construction. Biologically-Inspired Systems;* Knippers, J.; Nickel, K.; Speck, T., Eds.; Springer International Publishing: Cham, Switzerland, 2016; pp 11–55. doi:10.1007/978-3-319-46374-2_3
4. Barthlott, W.; Neinhuis, C. *Planta* **1997,** *202,* 1–8. doi:10.1007/s004250050096
5. Barthlott, W.; Mail, M.; Bhushan, B.; Koch, K. *Nano-Micro Lett.* **2017,** *9,* 23. doi:10.1007/s40820-016-0125-1
6. Antony, F.; Grießhammer, R.; Speck, T.; Speck, O. *Beilstein J. Nanotechnol.* **2016,** *7,* 2100–2115. doi:10.3762/bjnano.7.200
7. Drelich, J.; Marmur, A. *Surf. Innovations* **2014,** *2,* 211–227. doi:10.1680/si.13.00017
8. Koch, K.; Bohn, H. F.; Barthlott, W. *Langmuir* **2009,** *25,* 14116–14120. doi:10.1021/la9017322
9. Barthlott, W.; Mail, M.; Bhushan, B.; Koch, K. Plant Surfaces: Structures and Functions for Biomimetic Applications. In *Springer Handbook of Nanotechnology;* Bhushan, B., Ed.; Springer: Berlin, Heidelberg, 2017; pp 1265–1305. doi:10.1007/978-3-662-54357-3_36
10. Barthlott, W.; Schimmel, T.; Wiersch, S.; Koch, K.; Brede, M.; Barczewski, M.; Walheim, S.; Weis, A.; Kaltenmaier, A.; Leder, A.; Bohn, H. F. *Adv. Mater. (Weinheim, Ger.)* **2010,** *22,* 2325–2328. doi:10.1002/adma.200904411
11. Marmur, A. *Biofouling* **2006,** *22,* 107–115. doi:10.1080/08927010600562328
12. Mail, M.; Klein, A.; Bleckmann, H.; Schmitz, A.; Scherer, T.; Rühr, P. T.; Lovric, G.; Fröhlingsdorf, R.; Gorb, S. N.; Barthlott, W. *Beilstein J. Nanotechnol.* **2018,** *9,* 3039–3047. doi:10.3762/bjnano.9.282
13. McHale, G.; Flynn, M. R.; Newton, M. I. *Soft Matter* **2011,** *7,* 10100. doi:10.1039/c1sm06140b
14. Jeong, C.; Lee, J.; Sheppard, K.; Choi, C.-H. *Langmuir* **2015,** *31,* 11040–11050. doi:10.1021/acs.langmuir.5b02392
15. Balmert, A.; Bohn, H. F.; Ditsche-Kuru, P.; Barthlott, W. *J. Morphol.* **2011,** *272,* 442–451. doi:10.1002/jmor.10921
16. Ditsche-Kuru, P.; Schneider, E. S.; Melskotte, J.-E.; Brede, M.; Leder, A.; Barthlott, W. *Beilstein J. Nanotechnol.* **2011,** *2,* 137–144. doi:10.3762/bjnano.2.17
17. Tricinci, O.; Terencio, T.; Mazzolai, B.; Pugno, N. M.; Greco, F.; Mattoli, V. *ACS Appl. Mater. Interfaces* **2015,** *7,* 25560–25567. doi:10.1021/acsami.5b07722
18. Röhrig, M.; Mail, M.; Schneider, M.; Louvin, H.; Hopf, A.; Schimmel, T.; Worgull, M.; Hölscher, H. *Adv. Mater. Interfaces* **2014,** *1,* 1300083. doi:10.1002/admi.201300083
19. Zeiger, C.; Rodrigues da Silva, I. C.; Mail, M.; Kavalenka, M. N.; Barthlott, W.; Hölscher, H. *Bioinspiration Biomimetics* **2016,** *11,* 056003. doi:10.1088/1748-3190/11/5/056003
20. Kavalenka, M. N.; Vüllers, F.; Lischker, S.; Zeiger, C.; Hopf, A.; Röhrig, M.; Rapp, B. E.; Worgull, M.; Hölscher, H. *ACS Appl. Mater. Interfaces* **2015,** *7,* 10651–10655. doi:10.1021/acsami.5b01772
21. McHale, G.; Shirtcliffe, N. J.; Evans, C. R.; Newton, M. I. *Appl. Phys. Lett.* **2009,** *94,* 064104. doi:10.1063/1.3081420
22. Lee, C.; Choi, C.-H.; Kim, C.-J. *Exp. Fluids* **2016,** *57,* 176. doi:10.1007/s00348-016-2264-z
23. Barthlott, M.; Böhnlein, B.; Mail, M. Grid Structures for Stable Gas Retention Under Liquids. WO Pat. Appl. WO2017/108958A1, 2016.
24. Babu, D. J.; Mail, M.; Barthlott, W.; Schneider, J. J. *Adv. Mater. Interfaces* **2017,** *4,* 1700273. doi:10.1002/admi.201700273
25. Barthlott, W.; Moosmann, M.; Noll, I.; Akdere, M.; Wagner, J.; Roling, N.; Koepchen-Thomä, L.; Azad, M. A. K.; Klopp, K.; Gries, t.; Mail, M. *Philos. Trans. R. Soc., A* **2020,** *378,* 20190447. doi:10.1098/rsta.2019.0447
26. McHale, G.; Newton, M. I.; Shirtcliffe, N. J. *Soft Matter* **2010,** *6,* 714–719. doi:10.1039/b917861a
27. Gogte, S.; Vorobieff, P.; Truesdell, R.; Mammoli, A.; van Swol, F.; Shah, P.; Brinker, C. J. *Phys. Fluids* **2005,** *17,* 051701. doi:10.1063/1.1896405
28. Daeian, M. A.; Moosavi, A.; Nouri-Borujerdi, A.; Taghvaei, E. *J. Phys. D: Appl. Phys.* **2017,** *50,* 105301. doi:10.1088/1361-6463/aa59d5
29. Latorre, R. *Ocean Eng.* **1997,** *24,* 161–175. doi:10.1016/0029-8018(96)00005-4
30. Butterworth, J.; Atlar, M.; Shi, W. *Ocean Eng.* **2015,** *110,* 2–10. doi:10.1016/j.oceaneng.2015.10.022

31. Busch, J.; Barthlott, W.; Brede, M.; Terlau, W.; Mail, M. *Philos. Trans. R. Soc., A* **2019,** *377,* 20180263. doi:10.1098/rsta.2018.0263
32. Mail, M.; Mayser, M.; Böhnlein, B.; Barthlott, W. Air Retaining Surfaces: Backswimmers and Floating Ferns Inspire Ships to Save Fuel. In *Proceedings of the 38rd Annual Meeting of The Adhesion Society,* Savannah, GA, USA, Feb 20–25, 2015; The Adhesion Society, 2015.
33. Konrad, W.; Apeltauer, C.; Frauendiener, J.; Barthlott, W.; Roth-Nebelsick, A. *J. Bionic Eng.* **2009,** *6,* 350–356. doi:10.1016/s1672-6529(08)60133-x
34. Konrad, W.; Apeltauer, C.; Roth-Nebelsick, A. In *Bionik: Patente aus der Natur,* 5. Bremer Bionik-Kongress, Bremen, Germany; 2010.
35. Marmur, A. *Langmuir* **2006,** *22,* 1400–1402. doi:10.1021/la052802j
36. Melskotte, J.-E.; Brede, M.; Wolter, A.; Barthlott, W.; Leder, A. *Fachtagung "Lasermethoden in der Strömungsmesstechnik";* Dt. Ges. für Laser-Anemometrie GALA e.V.: Karlsruhe, Germany, 2013.
37. Gorb, S. N.; Sinha, M.; Peressadko, A.; Daltorio, K. A.; Quinn, R. D. *Bioinspiration Biomimetics* **2007,** *2,* S117–S125. doi:10.1088/1748-3182/2/4/s01
38. Gorb, S. N.; Varenberg, M. *J. Adhes. Sci. Technol.* **2007,** *21,* 1175–1183. doi:10.1163/156856107782328317
39. Varenberg, M.; Gorb, S. *J. R. Soc., Interface* **2007,** *4,* 721–725. doi:10.1098/rsif.2007.0222
40. Varenberg, M.; Gorb, S. *J. R. Soc., Interface* **2008,** *5,* 383–385. doi:10.1098/rsif.2007.1171
41. Varenberg, M.; Gorb, S. *J. R. Soc., Interface* **2008,** *5,* 785–789. doi:10.1098/rsif.2007.1201
42. Gorb, S.; Varenberg, M.; Peressadko, A.; Tuma, J. *J. R. Soc., Interface* **2007,** *4,* 271–275. doi:10.1098/rsif.2006.0164
43. Heepe, L.; Carbone, G.; Pierro, E.; Kovalev, A. E.; Gorb, S. N. *Appl. Phys. Lett.* **2014,** *104,* 011906. doi:10.1063/1.4860991
44. Heepe, L.; Gorb, S. N. *Annu. Rev. Mater. Res.* **2014,** *44,* 173–203. doi:10.1146/annurev-matsci-062910-100458
45. Heepe, L.; Kovalev, A. E.; Gorb, S. N. *Beilstein J. Nanotechnol.* **2014,** *5,* 903–909. doi:10.3762/bjnano.5.103
46. Heepe, L.; Kovalev, A. E.; Filippov, A. E.; Gorb, S. N. *Phys. Rev. Lett.* **2013,** *111,* 104301. doi:10.1103/physrevlett.111.104301
47. Heepe, L.; Kovalev, A. E.; Varenberg, M.; Tuma, J.; Gorb, S. N. *Theor. Appl. Mech. Lett.* **2012,** *2,* 014008. doi:10.1063/2.1201408
48. Hebets, E. A.; Chapman, R. F. *J. Insect Physiol.* **2000,** *46,* 13–19. doi:10.1016/s0022-1910(99)00096-7
49. Filippov, A. E.; Kovalev, A.; Gorb, S. N. *J. R. Soc., Interface* **2018,** *15,* 20180217. doi:10.1098/rsif.2018.0217
50. Durak, D.; Kalender, Y. *C. R. Biol.* **2009,** *332,* 34–42. doi:10.1016/j.crvi.2008.10.004
51. Hinton, H. E. *Annu. Rev. Entomol.* **1969,** *14,* 343–368. doi:10.1146/annurev.en.14.010169.002015
52. Hensel, R.; Helbig, R.; Aland, S.; Braun, H.-G.; Voigt, A.; Neinhuis, C.; Werner, C. *Langmuir* **2013,** *29,* 1100–1112. doi:10.1021/la304179b
53. Petersen, D. S.; Kleinteich, T.; Gorb, S. N.; Heepe, L. *J. R. Soc., Interface* **2018,** *15,* 20180396. doi:10.1098/rsif.2018.0396
54. Sander, R. *Atmos. Chem. Phys.* **2015,** *15,* 4399–4981. doi:10.5194/acp-15-4399-2015
55. Wise, D. L.; Houghton, G. *Chem. Eng. Sci.* **1966,** *21,* 999–1010. doi:10.1016/0009-2509(66)85096-0
56. Mail, M.; Moosmann, M.; Häger, P.; Barthlott, W. *Philos. Trans. R. Soc., A* **2019,** *377,* 20190126. doi:10.1098/rsta.2019.0126
57. Petersen, D. S.; Gorb, S. N.; Heepe, L. *Front. Mar. Sci.* **2020,** *7,* 664. doi:10.3389/fmars.2020.00664
58. Petersen, D. S.; Heepe, L.; Gorb, S. N. *Biointerphases* **2020,** *15,* 061013. doi:10.1116/6.0000608
59. Petersen, D. S.; Schultz, M.; Gorb, S. N.; Heepe, L. *Appl. Phys. A: Mater. Sci. Process.* **2020,** *126,* 712. doi:10.1007/s00339-020-03870-2
60. Wimpenny, J. *Symposia-Society for General Microbiology 2000;* Cambridge University Press: Cambridge, UK, 1999.
61. Zeisler-Diehl, V. V.; Barthlott, W.; Schreiber, L. Plant Cuticular Waxes: Composition, Function, and Interactions with Microorganisms. *Hydrocarbons, oils and lipids: diversity, origin, chemistry and fate;* Handbook of Hydrocarbon and Lipid Microbiology; Springer International Publishing: Cham, Switzerland, 2020; pp 123–138. doi:10.1007/978-3-319-90569-3_7

License and Terms

This is an open access article licensed under the terms of the Beilstein-Institut Open Access License Agreement (https://www.beilstein-journals.org/bjnano/terms), which is identical to the Creative Commons Attribution 4.0 International License (https://creativecommons.org/licenses/by/4.0). The reuse of material under this license requires that the author(s), source and license are credited. Third-party material in this article could be subject to other licenses (typically indicated in the credit line), and in this case, users are required to obtain permission from the license holder to reuse the material.

The definitive version of this article is the electronic one which can be found at:
https://doi.org/10.3762/bjnano.13.113

BEILSTEIN JOURNAL OF NANOTECHNOLOGY

Atmospheric water harvesting using functionalized carbon nanocones

Fernanda R. Leivas* and Marcia C. Barbosa

Full Research Paper

Open Access

Address:
Instituto de Física, Universidade Federal do Rio Grande do Sul, CP 15051, 91501-970, Porto Alegre, RS, Brazil

Email:
Fernanda R. Leivas* - fernanda.leivas@ufrgs.br

* Corresponding author

Keywords:
atmospheric water harvesting; hydrophilicity; hydrophobicity; nanocones; nanotechnology

Beilstein J. Nanotechnol. **2023,** *14,* 1–10.
https://doi.org/10.3762/bjnano.14.1

Received: 27 July 2022
Accepted: 14 December 2022
Published: 02 January 2023

This article is part of the thematic issue "Biomimetics on the micro- and nanoscale – The 25th anniversary of the lotus effect".

Guest Editor: M. Mail

© 2023 Leivas and Barbosa; licensee Beilstein-Institut.
License and terms: see end of document.

Abstract

In this work, we propose a method to harvest liquid water from water vapor using carbon nanocones. The condensation occurs due to the presence of hydrophilic sites at the nanocone entrance. The functionalization, together with the high mobility of water inside nanostructures, leads to a fast water flow through the nanostructure. We show using molecular dynamics simulations that this device is able to collect water if the surface functionalization is properly selected.

Introduction

Despite water being abundant on Earth, there are at least four billion people suffering from water scarcity [1]. The lack of potable water results from a number of factors such as monoculture, increasing deforestation, and a growing population [2-5]. In order to circumvent the problem of lack of fresh water, scientists are developing alternative processes such as filtration of contaminated water [6], desalinization [7], and the collection of water from the atmosphere [8]. Atmospheric water harvesting (AWH) is an interesting option to obtain fresh water, particularly in arid and semi-arid areas, where other sources of water are inaccessible, and populations have long been suffering from water scarcity [9]. There are different processes to develop AWH such as condensing and collecting moisture, cooling ambient air below its dew point [10,11], and using chemical and physical processes involving absorption and adsorption [9,12,13]. Many of these mechanisms are inspired by structures found in nature (biomimetic designs), which use hierarchical nano/microstructures to collect water. Some examples are the *Trifolium pratense* plant, the *Cotula fallax* cactus, and the *Uloborus walckenaerius* spider [14-16]. Usually, these biomimetic designs have an asymmetrical shape that energetically drives the directional transport of water. The cactus for example has spikes where droplets move from the tip to the base, or from the higher to the lower Laplace area.

One mechanism developed by nature to capture liquid water from water vapor is present in the Namibian desert beetle, which collects water from morning steam in the desert [17].

This beetle has hydrophilic spots on its back, which transform vapor into liquid water. For the collection to be efficient, below the hydrophilic spots, its wings are hydrophobic, and the captured water moves from hydrophilic to hydrophobic parts driven by gravity. The efficiency of this process led to the development of mimetic strategies [18-21], which require the combination of wetting and dewetting properties used by the beetle. The hydrophobic region, as is also the case for the cactus, is fundamental for the mobility of water.

Water presents other kinds of anomalous behavior in addition to the hydrophobicity described above. The phenomena of density increasing with temperature at constant pressure and diffusion coefficients increasing with density at constant temperature were observed in experiments and simulations in bulk water [22-24]. Water presents both super flow and slowing down when confined in biological structures with the presence of hydrophobic and hydrophilic sites [25]. Water confined in hydrophobic structures, such as carbon nanotubes with diameters below 2 nm, exhibits a fast flow that exceeds values provided by classical hydrodynamics [26]. This super flow is observed because water is pushed away from the hydrophobic surface, forming a single line of molecules that moves in a stressless manner. This behavior only appears because at the nanometric scale water cannot be described as a continuous medium, and classical hydrodynamic equations fail.

Water super flow in nanostructures has been explored in processes of separating water from salt or from other contaminants. This high mobility of water under nanoconfinement requires huge pressure and, consequently, a lot of energy [27,28]. In order to help water entrance and decrease the amount of required pressure, nanotubes have been functionalized with hydrophilic groups [29,30]. The addition of hydrophilic regions in small diameter environments, however, decreases the velocity of water molecules [31].

The high flow of water in nanostructures is also useful for capturing water from the atmosphere. Nanotubes with hydrophilic sites for water capture and hydrophobic regions for the movement of water to reservoirs [32,33] have been analyzed. Despite reasonable results on the capacity of capturing water, the small diameter of the nanotube entrance requires high pressures for the water to enter, which makes the process energetically costly.

A geometry that combines a large surface for capturing water and a small radius for making water molecules flow fast is the nanocone. Carbon nanocones (CNCs), also called nanohorns are conical structures that are predominantly made of carbon, typically 2–5 nm in diameter and 40–50 nm in length. They occur on the surface of natural graphite. Void CNCs can be produced, for example, by decomposing hydrocarbons with a plasma torch [34]. Other simple techniques of production [35] and reduction [36] have also been recently developed. CNCs are completely hydrophobic, but they can be functionalized to make some parts hydrophilic while keeping the other parts hydrophobic.

The study of the behavior of water inside nanocones is relevant because of the structural advantages of nanocones [37,38]. The flow of water in nanocones is higher than the mobility observed in nanotubes [39,40]. In the presence of ions, water flows through a charged nanocone under an electrical field [41,42], and this flow is higher than the one induced by pressure. Consequently, the desalination performance observed in carbon nanocones is better than that observed in nanotubes or nanometric monolayers of graphene and MoS_2 [43,44]. Another advantage of the cone format is the possibility of capturing more water at the larger diameter entrance, without losing the high flow at the reduced diameter in other parts of the cone. As the example of the Namibian desert beetle shows, the introduction of hydrophilic groups at the nanocone entrance favors the condensation of water while the hydrophobic sites at the smaller side of the cone generate a fast flow. This combination of nanotube shape and functionalization is key for making a device able to capture water.

In this work, we investigate through molecular dynamics simulations the process of capturing and collecting water in a functionalized carbon nanocone. The process is analyzed in a system in which the larger diameter of the cone is in contact with a vapor reservoir and the smaller diameter is in contact with an initially empty reservoir. The nanocone has hydrophilic and hydrophobic regions, the combination of which generates a fast flow without the need of imposing pressure to the system. Note that unlike the case of cactus spines, we present a model in which water is driven from the base (larger area) to the tip of the canonical structure by wettability variations combined with a nanometric design to improve water flow [39,40].

The paper is organized as follows: In the section “Model and Simulation Details”, the model is presented and the simulation method is explained. In the “Results and Discussion” section, the simulation results are shown and the water harvesting by the nanocone for different hydrophilic interactions is evaluated. Section “Conclusion” summarize the results.

Model and Simulation Details

The system is illustrated in Figure 1. It is composed of a conical carbon nanochannel between two slabs with a length of 50 Å. One slab represents hydrophilic atoms (green), and the other

slab represents hydrophobic carbon atoms (gray). Both slabs are coupled to a reservoir. The hydrophobic slab is connected to a water vapor reservoir while the hydrophilic slab is connected initially to a vacuum reservoir. All slabs are maintained rigid during the simulation.

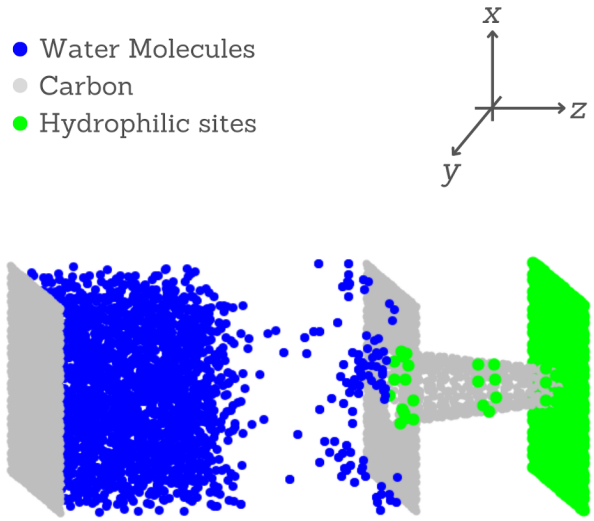


Figure 1: A snapshot of the simulation system. A liquid–vapor reservoir in contact with a carbon slab and with the nanocone hydrophilic base. The nanocone tip is in contact with the hydrophilic slab of a collecting reservoir.

The system shown in Figure 1 is made of a reservoir of size $50 \times 54 \times 50$ Å^3. This reservoir has two regions, namely a liquid water region on the left and a water vapor region on the right. The number of water molecules in this simulation is 1473. The density of the vapor system is 0.38 g/cm^3. As the simulation is conducted using an NVT ensemble, the pressure is variable.

The condensation is produced by a combination of thermostats, as illustrated in Figure 2, where the liquid region is illustrated in red while the vapor region is shown in blue. The red region does not have fixed thermostat, but the temperature varies from 800 to 300 K in a dynamic process every 10000 temporal steps. The blue region, thermostat 2, maintains a constant temperature of 300 K during the entire simulation. The variation of temperature in thermostat 1 is responsible for the condensation at reservoir 2. The idea of combining thermostats to produce vapor is not new. It has already been used to reproduce water evaporation and condensation [45,46].

In contact with the carbon slab on region 1, there is a carbon nanocone constructed by cutting the apex angle, as illustrated in Figure 3. This nanocone has a length of 26 Å. The smaller pore at the tip has a diameter of 8.2 Å, and the larger pore at the base has a diameter of 17Å. Along the CNC, there are three ring-shaped regions with hydrophilic sites at the base, at the middle, and at the tip. The hydrophilic rings are modeled as effective water-wall potentials ε_r. The CNC and the sheets were held fixed during the simulations, and water molecules inside the nanocone were treated with a thermostat at 300 K.

Carbon nanocones can be produced with five different apex angles [47]. Here we use the aperture of 19.2° since it is easier to produce at large scale [34]. Also, it is the nanocone that achieves the highest values of water flux compared with the other apex angles. It also presents a lower energy barrier when compared with carbon nanotubes [39].

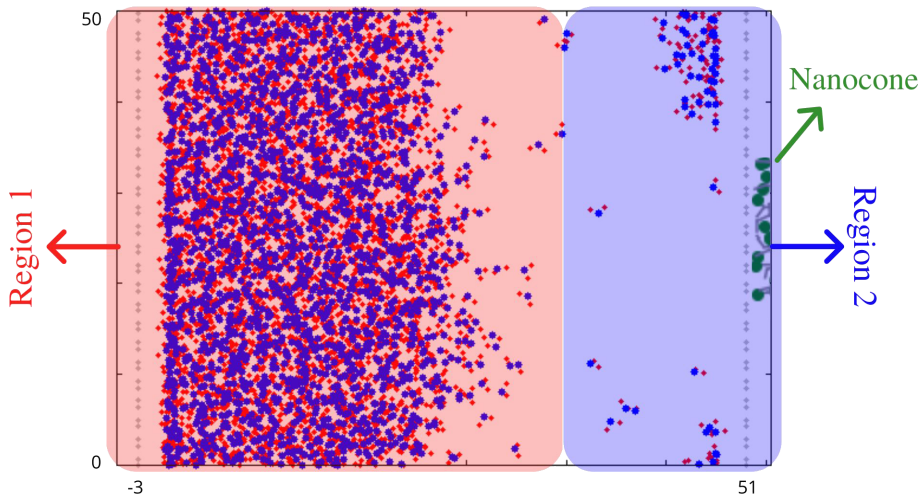


Figure 2: Part of the simulation box illustrating the two types of thermal control used in the simulation. The red area represents region 1 with a temperature dynamically changing between 800 and 300 K while the blue area is region 2 with a fixed temperature of 300 K.

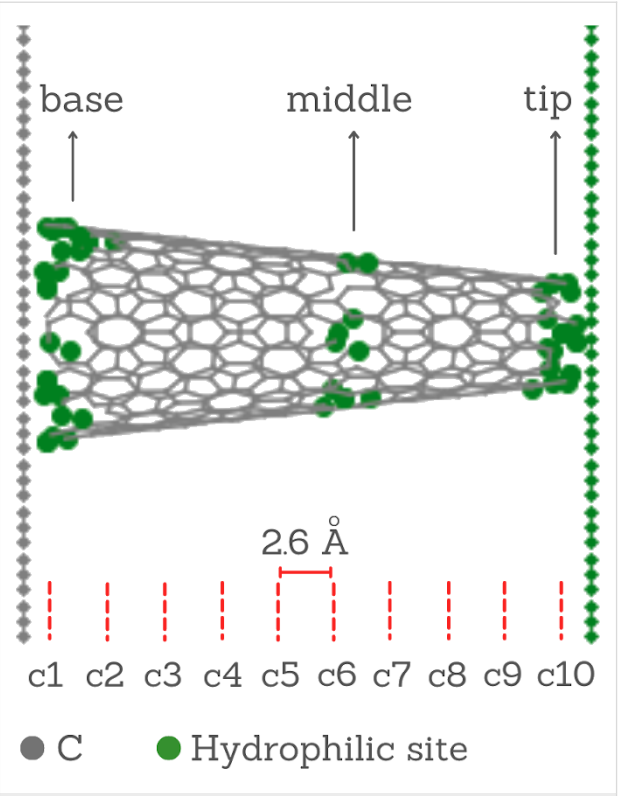


Figure 3: Carbon nanocone with 26 Å length, 8.2 Å tip diameter, and 17 Å of base diameter. Hydrophilic rings are present at the base, the tip, and the middle of the nanocone.

The smaller side of the nanocone ends in a hydrophilic surface, which has the same structure as the hydrophobic slab. This hydrophilic surface forms the collector reservoir, in which there is no water at the beginning of the simulation. The dimensions of this reservoir are 50 × 20 × 50 $Å^3$. The water molecules collected by this reservoir are maintained at 300 K in a thermostat as in region 2 (Figure 2).

Molecular dynamics simulations were performed using the LAMMPS [48] package using an NVT ensemble with a timestep of 0.1 fs. The TIP4P/2005 [49] water model was used since it provides a satisfactory description of self-diffusion coefficient [50], phase diagram, vapor–liquid equilibria [51,52], vapor pressure, and critical temperature, despite being a simple model [15,53].

The SHAKE algorithm was employed to keep the rigidity of water molecules. The oxygen–carbon Lennard-Jones (LJ) pairwise non-bonded interaction, ε_{O-C} = 0.126 kcal/mol and σ_{O-C} = 3.279 Å, was calculated using the Lorentz–Berthelot mixing rules [54]. For the interaction between hydrophilic sites and water, the same σ of oxygen–carbon interaction was fixed ($\sigma_{O-HS} = \sigma_{O-C}$), but the potential well $\varepsilon_{O-HS} = \varepsilon_i$ was varied. The LJ cutoff distance was 12 Å, and the long-range electrostatic interaction was treated by the particle–particle mesh method. Periodic boundary conditions were applied along the *x*- and *y*-directions, and non-periodic boundary conditions were applied along the *z*-direction (see Figure 1).

Results and Discussion

Figure 1 illustrates the analyzed system, composed of a water vapor reservoir in contact with the base of the nanocone. If the nanocone is fully hydrophobic, no water crosses the nanocone. Therefore, hydrophilic rings are necessary for the water to enter and flow through the nanocone. We employ the Lennard-Jones potential to calculate the interaction between the nanocone wall and water. Within this approach, the variable that determines the wettability of the surface is the potential well defined by ε_r. The higher the value of ε_r, the more hydrophilic the surface is. Here we employed $1.5 \geq \varepsilon_r \geq 0.8$.

The water harvesting has been modeled according to the following mechanism: First, the vapor generated in region 1 from Figure 2 condenses into the slab of region 2, forming droplets. These droplets are attracted to the hydrophilic sites of the nanocone, as shown in Figure 4. Eventually, the droplets are moved to the middle and, then, to the tip of the nanocone due to the combination of hydrophilic and hydrophobic sites. Without them, the droplet is stuck at the base of the nanochannel. After an initial period (see t = 0.15 ns in Figure 4), only a large droplet remains being absorbed by the nanocone. This drop is fed by the vapor, forming a continuous flow of molecules that reach from the base to the tip of the nanocone, crossing to the collecting reservoir. This process stops once the collecting slab is filled. The time it takes for this to happen, after the first molecule is captured, depends on the initial conditions and ranges from 0.3 to 0.5 ns.

The number of collected molecules and the histogram versus time for the vapor reservoir system are presented in Figure 5a and in Figure 5b, respectively. Both graphs were obtained for one sample. The water harvesting (time interval 0.1–0.4 ns) exhibits a linear growth, called here “linear regime”. This regime is achieved when a large droplet is formed at the base of the nanocone as described above, enters the nanocone, and undergoes cohesive dynamics.

In order to characterize and understand the impact of the hydrophilic rings along the nanocone, we also present in Figure 6 snapshots of the temporal evolution and the number of water molecules collected over time by a completely hydrophobic nanocone. In the presence of hydrophilic rings, the nanocone captured more than 350 molecules in 0.4 ns. During the same period of time, the hydrophobic nanocone captured 11 molecules (less than 10%). For this simulation, we did not change

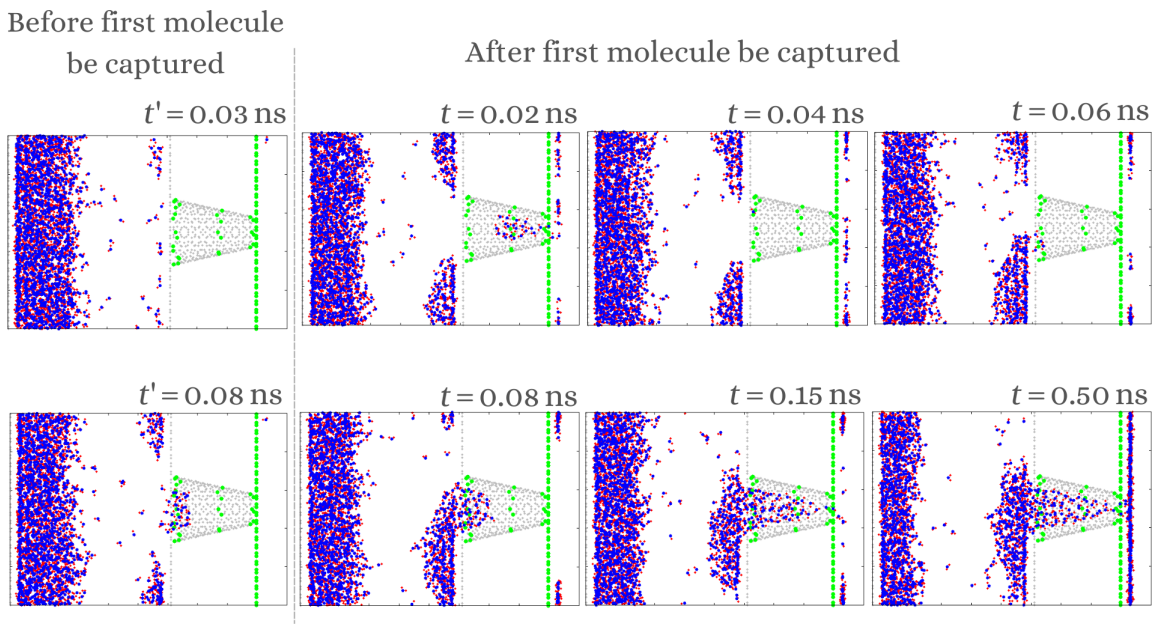


Figure 4: Snapshots of the temporal evolution of the vapor system using ε_i = 1.1.

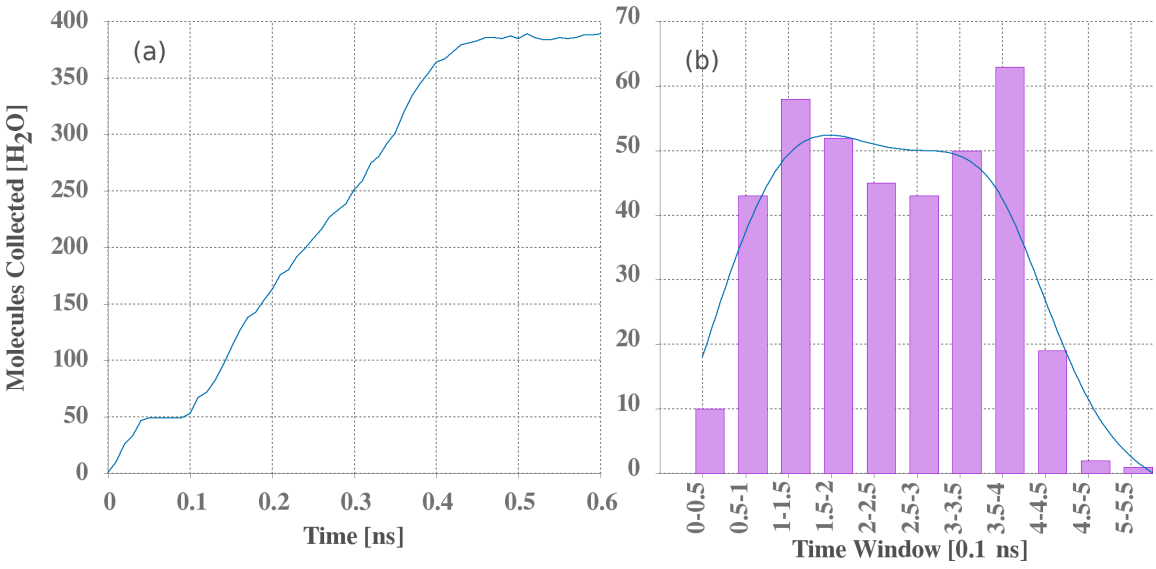


Figure 5: (a) Number and (b) histogram of collected water molecules as functions of (a) the time and (b) time intervals.

the wettability of the hydrophilic slab (ε_r = 1.1). Without that, no molecule would have been captured. In the case of the completely hydrophobic nanocone, no droplet is formed in the base of the nanocone. Only very few molecules randomly enter and are successfully harvested, but this number is negligible. In Figure 6 (bottom right), we also present a 3D snapshot for t = 0.37 ns to demonstrate that there are no molecules at the entrance of the nanocone.

For the case of the nanocone with hydrophilic rings, Figure 7 shows a snapshot of the water molecules on the hydrophilic slab of the collector reservoir, after the flow ceases and the number of water molecules in the reservoir becomes constant. Note that these molecules and their hydrogen bonds are placed in a crystal-like arrangement. Figure 8a shows the radial distribution function, which is characteristic of an ordered structure in two dimensions. Figure 8b illustrates the mean square displace-

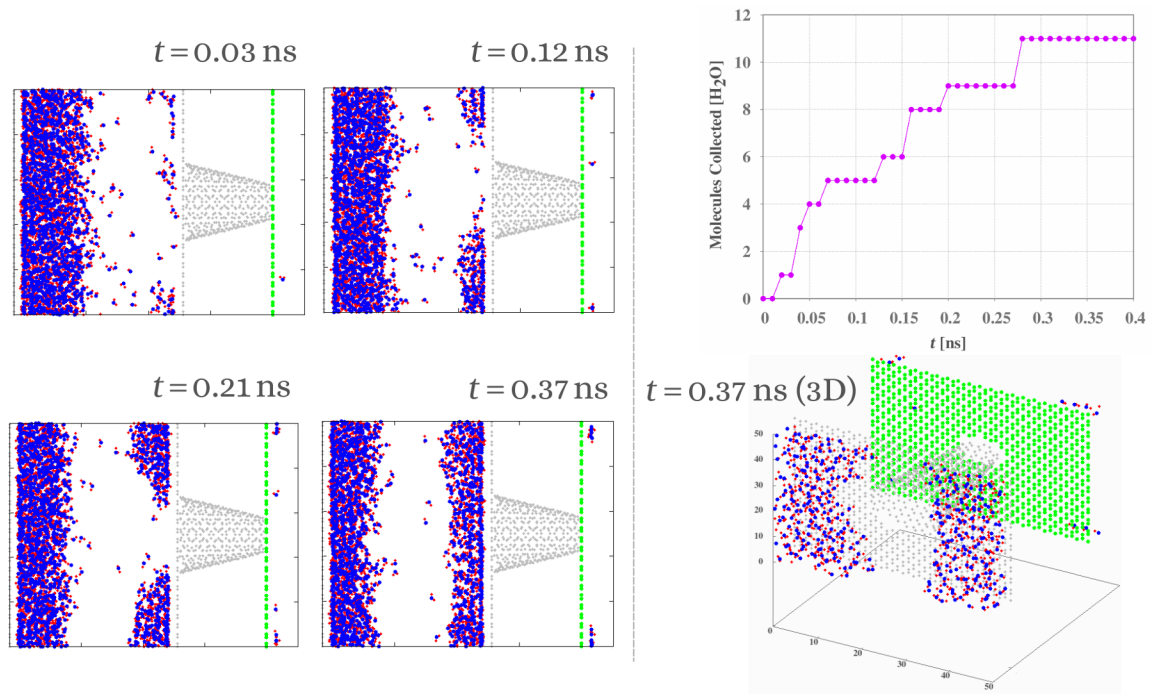


Figure 6: 2D snapshots of the temporal evolution for vapor for a hydrophobic nanocone (left), the number of collected water molecules as a function of the time (top right), and a 3D snapshot for t = 0.37 ns (bottom right).

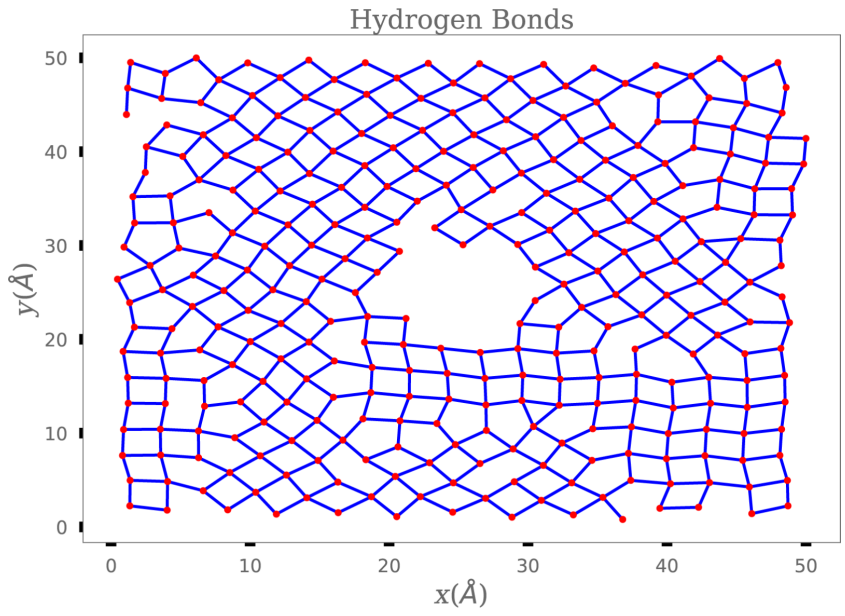


Figure 7: A snapshot of water molecules (red dots) on the attractive slab and hydrogen bonds (blue lines) at t = 0.5 ns. The central region is where the nanocone is placed; we did not plot the molecules for this region. The hydrogen bonds were calculated using the distances and angles between water molecules.

ment of the water molecules on the collecting slab, indicating a very small and constant mobility, thus confirming the ice-like behavior.

What happens to the system when hydrophilic interactions between water and surfaces are increased? In order to answer this question, Figure 9 illustrates the number of collected molecules

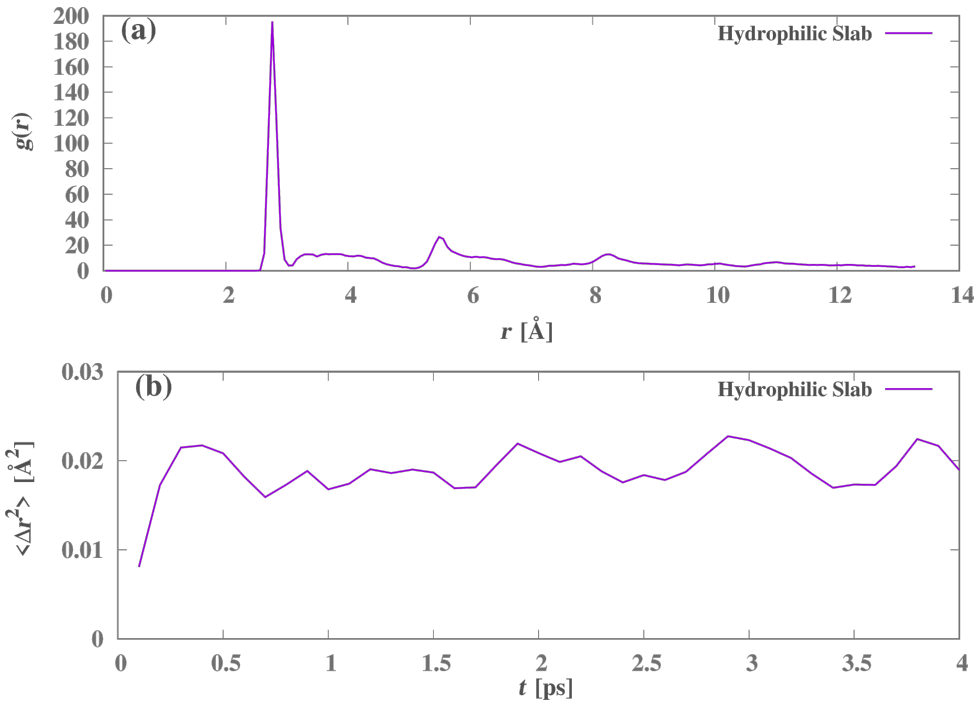


Figure 8: (a) Radial distribution function and (b) mean square displacement of the water molecules on the attractive slab at t = 0.5 ns and ε_r = 1.1.

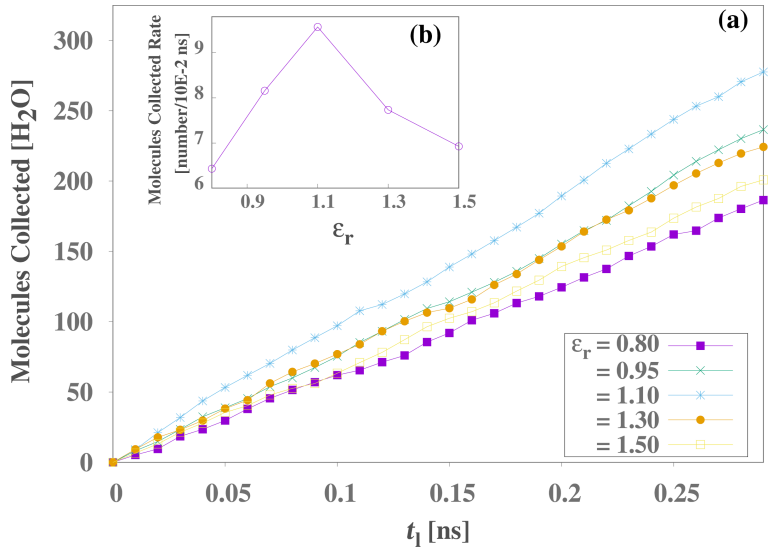


Figure 9: (a) Number of collected molecules as a function of the time (ns) for different ε_r. (b) Mean collected rate (MCR) as a function of ε_r.

as a function of time for different values of water–wall attraction, that is, ε_r = 0.80, 0.95, 1.1, 1.3, and 1.5. Each line is averaged over five samples. Note that the slopes of lines for fixed ε_r present a non-monotonic behavior with ε_r. In order to understand the impact of varying attraction, we calculated the mean collected rate of molecules (MCR) per unit of time (10^{-2} ns), using

$$\mathrm{MCR} = \sum_{i=0}^{i=t_{\mathrm{tot}}} \frac{\left(Nm_i - Nm_{i-1}\right)}{t_{\mathrm{tot}}}. \quad (1)$$

Figure 9b shows the MCR of molecules as a function of ε_r. For values of ε_r below a certain threshold, the MCR increases in proportion to ε_r. The movement of molecules in the nanocone

depends on the combination of attraction on hydrophilic sites and repulsion on hydrophobic sites. Enhancing hydrophilic attraction increases the number of water molecules attracted to the base of the nanocone. For ε_r values above a certain threshold, however, the MCR decreases. In this case, the hydrophilic interaction with the rings is too strong, and water molecules tend to be stuck at the rings. The maximum rate occurs for $\varepsilon_r \approx 1.1$. This result for the optimum interaction between the oxygen and the nanocone atoms might be helpful to select potential functional groups to be added to the carbon nanocone.

In order to understand how ε_r impacts the water movement, we computed the flow. As the diameter of a conical object varies with length, the axial flux of molecules also varies from point to point in the cone. Therefore, we selected ten regions equally spaced along the nanocone, as shown in Figure 1, and we calculated the flux at each segment using the expression

$$J_i = \frac{n_{\text{ltr}} - n_{\text{rtl}}}{A_i N_{\text{steps}} \delta t}, \tag{2}$$

where n_{ltr} is the number of molecules that cross a region of the nanotube from left to right, and n_{rtl} is the number of molecules that cross from right to left. $A_i = \pi a_{\text{i,eff}}^2$ is the area of region i with radius a_i, and $a_{\text{i,eff}} = a_i - \sigma/2$ is the effective radius available for water $\sigma = 3.1589$. $N_{\text{steps}} = 10^4$ is the total number of steps used to calculate the flux, and $\delta t = 0.1$ fs is the time step.

Figure 10 shows the flux J_i as a function of the region (length) c_i (Figure 3) of the nanocone for different values of attraction ε_r. Each value was averaged over five samples with 8×10^5 fs. This graph confirms the behavior observed in Figure 9. The increase of water mobility with the increase of ε_r up to $\varepsilon_r = 1.1$, and the decrease of J_i for $\varepsilon_r > 1.1$. In addition, Figure 10 shows the increase in J_i with the decrease in diameter for the lower values of hydrophobicity, $\varepsilon_r = 0.80$, 0.95, and 1.1.

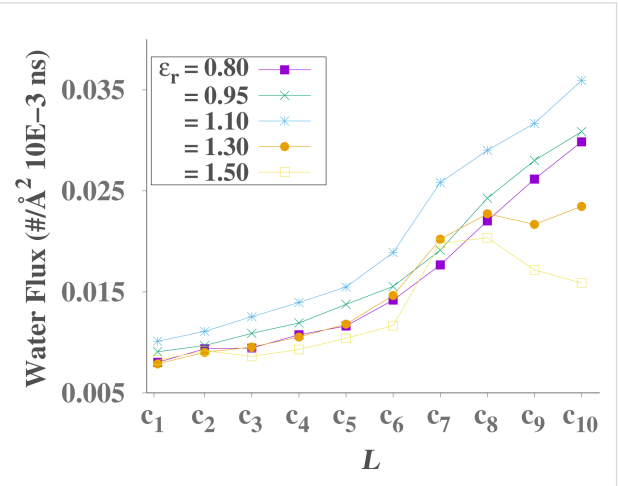


Figure 10: Graph of water flux in different regions of the nanocone (Figure 3), for different values of the potential well ε_r.

When $\varepsilon_r > 1.1$, a non-monotonic behavior is observed. The decrease in flux with the decrease in diameter for c_8, c_9, and c_{10} and $\varepsilon_r = 1.30$ and 1.50 is a consequence of the strong interaction between water molecules and the hydrophilic ring in the middle of the nanocone. The increase in flux as the radius decreases is a behavior also observed in carbon nanotubes [55]. The increase in flux, followed by a decrease, with increase in hydrophobicity was also observed regarding the transport properties of nanotubes with tunable hydrophilic sites [56,57].

Conclusion

Molecular dynamics simulations were performed to study water harvesting, using a combination of hydrophobic and hydrophilic sites in carbon nanocones in contact with a vapor water reservoir. The nanocone was constructed modeling three ring-shaped hydrophilic regions. Different from simulations and experiments with water flow in nanotubes, no external pressure was applied.

First, we observed that without the hydrophilic slab, no water molecule passes through the hydrophobic nanocone. In the presence of the hydrophilic slab at the end of a completely hydrophobic nanocone, isolated water molecules pass through, but no droplet is formed.

Then, hydrophilic rings were introduced in the nanocone, and different hydrophilic strengths of the rings were explored. Water dynamics in this case is governed by the formation of droplets outside the nanocone, and a combination of regimes forms. At the beginning, droplets condense on the slab surface. Then, these droplets are attracted by the hydrophilic base of the nanocone. They form a larger drop, which enters into the cone, thus generating a steady flux to the nanocone tip and reaching the collecting slab. This flow is generated by the combination of hydrophilic and hydrophobic sites.

The flow only stops when the collecting slab becomes filled. This slab is hydrophilic and attracts water molecules. These molecules form an ordered structure on the slab that freezes the water once the hydrophilic slab is completely filled. So, the flow is interrupted even when the collector is kept at a temperature of 300 K. A solution to keep the flow of water would be to continuously remove water molecules from the collecting slab.

The strength ε_r of the hydrophilic sites affects water collection and water mobility in two ways. Increasing ε_r pushes more

droplets to the nanocone. However, if ε_r is too large, water molecules become trapped at the hydrophilic regions, decreasing the water mobility.

Thus, the nanocone can be suggested as an alternative to collect water from vapor without the use of high pressure, provided that it combines hydrophobic and hydrophilic regions with an optimized value of ε_r.

Acknowledgements

The authors thank CENAPAD/SP and CESUP/UFRGS for providing computational infrastructure.

Funding

This work was supported by the Brazilian agencies CNPq (through INCT-Fcx) and CAPES (Coordenação de Aperfeiçoamento de Pessoal de Nível Superior).

ORCID® iDs

Marcia C. Barbosa - https://orcid.org/0000-0001-5663-6102

Preprint

A non-peer-reviewed version of this article has been previously published as a preprint: https://doi.org/10.3762/bxiv.2022.65.v1

References

1. Mekonnen, M. M.; Hoekstra, A. Y. *Sci. Adv.* **2016,** *2,* e1500323. doi:10.1126/sciadv.1500323
2. Mapulanga, A. M.; Naito, H. *Proc. Natl. Acad. Sci. U. S. A.* **2019,** *116,* 8249–8254. doi:10.1073/pnas.1814970116
3. Levia, D. F.; Creed, I. F.; Hannah, D. M.; Nanko, K.; Boyer, E. W.; Carlyle-Moses, D. E.; van de Giesen, N.; Grasso, D.; Guswa, A. J.; Hudson, J. E.; Hudson, S. A.; Iida, S.; Jackson, R. B.; Katul, G. G.; Kumagai, T.; Llorens, P.; Ribeiro, F. L.; Pataki, D. E.; Peters, C. A.; Carretero, D. S.; Selker, J. S.; Tetzlaff, D.; Zalewski, M.; Bruen, M. *Nat. Geosci.* **2020,** *13,* 656–658. doi:10.1038/s41561-020-0641-y
4. Ercin, A. E.; Hoekstra, A. Y. *Environ. Int.* **2014,** *64,* 71–82. doi:10.1016/j.envint.2013.11.019
5. Ju, J.; Bai, H.; Zheng, Y.; Zhao, T.; Fang, R.; Jiang, L. *Nat. Commun.* **2012,** *3,* 1247. doi:10.1038/ncomms2253
6. Köhler, M. H.; Bordin, J. R.; Barbosa, M. C. *J. Chem. Phys.* **2018,** *148,* 222804. doi:10.1063/1.5013926
7. Abal, J. P. K.; Dillenburg, R. F.; Köhler, M. H.; Barbosa, M. C. *ACS Appl. Nano Mater.* **2021,** *4,* 10467–10476. doi:10.1021/acsanm.1c01982
8. Zhou, X.; Lu, H.; Zhao, F.; Yu, G. *ACS Mater. Lett.* **2020,** *2,* 671–684. doi:10.1021/acsmaterialslett.0c00130
9. Zhong, L.; Zhu, L.; Li, J.; Pei, W.; Chen, H.; Wang, S.; Razaa, A.; Khan, A.; Hou, Y.; Zheng, Y. *Mol. Syst. Des. Eng.* **2021,** *6,* 986–996. doi:10.1039/d1me00019e
10. Wahlgren, R. V. *Water Res.* **2001,** *35,* 1–22. doi:10.1016/s0043-1354(00)00247-5
11. Wang, J. Y.; Liu, J. Y.; Wang, R. Z.; Wang, L. W. *Appl. Therm. Eng.* **2017,** *127,* 1608–1616. doi:10.1016/j.applthermaleng.2017.09.063
12. Ura, D. P.; Knapczyk-Korczak, J.; Szewczyk, P. K.; Sroczyk, E. A.; Busolo, T.; Marzec, M. M.; Bernasik, A.; Kar-Narayan, S.; Stachewicz, U. *ACS Nano* **2021,** *15,* 8848–8859. doi:10.1021/acsnano.1c01437
13. LaPotin, A.; Kim, H.; Rao, S. R.; Wang, E. N. *Acc. Chem. Res.* **2019,** *52,* 1588–1597. doi:10.1021/acs.accounts.9b00062
14. Mohd, G.; Majid, K.; Lone, S. *ACS Appl. Mater. Interfaces* **2022,** *14,* 4690–4698. doi:10.1021/acsami.1c20463
15. Vega, C.; Abascal, J. L. F. *Phys. Chem. Chem. Phys.* **2011,** *13,* 19663–19688. doi:10.1039/c1cp22168j
16. Zheng, Y.; Bai, H.; Huang, Z.; Tian, X.; Nie, F.-Q.; Zhao, Y.; Zhai, J.; Jiang, L. *Nature* **2010,** *463,* 640–643. doi:10.1038/nature08729
17. Parker, A. R.; Lawrence, C. R. *Nature* **2001,** *414,* 33–34. doi:10.1038/35102108
18. Bai, H.; Zhang, C.; Long, Z.; Geng, H.; Ba, T.; Fan, Y.; Yu, C.; Li, K.; Cao, M.; Jiang, L. *J. Mater. Chem. A* **2018,** *6,* 20966–20972. doi:10.1039/c8ta08267g
19. Dai, X.; Sun, N.; Nielsen, S. O.; Stogin, B. B.; Wang, J.; Yang, S.; Wong, T.-S. *Sci. Adv.* **2018,** *4,* eaaq0919. doi:10.1126/sciadv.aaq0919
20. Wang, X.; Zeng, J.; Yu, X.; Liang, C.; Zhang, Y. *Appl. Surf. Sci.* **2019,** *465,* 986–994. doi:10.1016/j.apsusc.2018.09.210
21. Cao, M.; Xiao, J.; Yu, C.; Li, K.; Jiang, L. *Small* **2015,** *11,* 4379–4384. doi:10.1002/smll.201500647
22. Kell, G. S. *J. Chem. Eng. Data* **1967,** *12,* 66–69. doi:10.1021/je60032a018
23. Angell, C. A.; Finch, E. D.; Bach, P. *J. Chem. Phys.* **1976,** *65,* 3063–3066. doi:10.1063/1.433518
24. Netz, P. A.; Starr, F. W.; Stanley, H. E.; Barbosa, M. C. *J. Chem. Phys.* **2001,** *115,* 344–348. doi:10.1063/1.1376424
25. Corti, H. R.; Appignanesi, G. A.; Barbosa, M. C.; Bordin, J. R.; Calero, C.; Camisasca, G.; Elola, M. D.; Franzese, G.; Gallo, P.; Hassanali, A.; Huang, K.; Laria, D.; Menéndez, C. A.; Montes de Oca, J. M.; Longinotti, M. P.; Rodriguez, J.; Rovere, M.; Scherlis, D.; Szleifer, I. *Eur. Phys. J. E: Soft Matter Biol. Phys.* **2021,** *44,* 136. doi:10.1140/epje/s10189-021-00136-4
26. Holt, J. K.; Park, H. G.; Wang, Y.; Stadermann, M.; Artyukhin, A. B.; Grigoropoulos, C. P.; Noy, A.; Bakajin, O. *Science* **2006,** *312,* 1034–1037. doi:10.1126/science.1126298
27. Köhler, M. H.; Bordin, J. R.; de Matos, C. F.; Barbosa, M. C. *Chem. Eng. Sci.* **2019,** *203,* 54–67. doi:10.1016/j.ces.2019.03.062
28. Barati Farimani, A.; Aluru, N. R. *J. Phys. Chem. B* **2011,** *115,* 12145–12149. doi:10.1021/jp205877b
29. Köhler, M. H.; Bordin, J. R.; da Silva, L. B.; Barbosa, M. C. *Phys. A (Amsterdam, Neth.)* **2018,** *490,* 331–337. doi:10.1016/j.physa.2017.08.030
30. Bordin, J. R.; Barbosa, M. C. *Phys. A (Amsterdam, Neth.)* **2017,** *467,* 137–147. doi:10.1016/j.physa.2016.10.007
31. Hong, Y.; Zhang, J.; Zhu, C.; Zeng, X. C.; Francisco, J. S. *J. Mater. Chem. A* **2019,** *7,* 3583–3591. doi:10.1039/c8ta10941a
32. Zhou, Z.; Gao, T.; McCarthy, S.; Kozbial, A.; Tan, S.; Pekker, D.; Li, L.; Leu, P. W. *Carbon* **2019,** *152,* 474–481. doi:10.1016/j.carbon.2019.06.012
33. Ozden, S.; Ge, L.; Narayanan, T. N.; Hart, A. H. C.; Yang, H.; Sridhar, S.; Vajtai, R.; Ajayan, P. M. *ACS Appl. Mater. Interfaces* **2014,** *6,* 10608–10613. doi:10.1021/am5022717
34. Karousis, N.; Suarez-Martinez, I.; Ewels, C. P.; Tagmatarchis, N. *Chem. Rev.* **2016,** *116,* 4850–4883. doi:10.1021/acs.chemrev.5b00611
35. Schaub, T. A. *Angew. Chem., Int. Ed.* **2020,** *59,* 4620–4622. doi:10.1002/anie.201914830

36. Voiry, D.; Pagona, G.; Canto, E. D.; Ortolani, L.; Morandi, V.; Noé, L.; Monthioux, M.; Tagmatarchis, N.; Penicaud, A. *Chem. Commun.* **2015,** *51,* 5017–5019. doi:10.1039/c4cc10389k
37. Hassan, J.; Diamantopoulos, G.; Homouz, D.; Papavassiliou, G. *Nanotechnol. Rev.* **2016,** *5,* 341–354. doi:10.1515/ntrev-2015-0048
38. Curcio, M.; Cirillo, G.; Saletta, F.; Michniewicz, F.; Nicoletta, F. P.; Vittorio, O.; Hampel, S.; Iemma, F. *C* **2021,** *7,* 3. doi:10.3390/c7010003
39. Li, W.; Wang, W.; Zheng, X.; Dong, Z.; Yan, Y.; Zhang, J. *Comput. Mater. Sci.* **2017,** *136,* 60–66. doi:10.1016/j.commatsci.2017.04.024
40. Sarapat, P.; Thamwattana, N.; Cox, B. J.; Baowan, D. *J. Math. Chem.* **2020,** *58,* 1650–1662. doi:10.1007/s10910-020-01153-y
41. Li, W.; Yan, Y.; Wang, M.; Král, P.; Dai, C.; Zhang, J. *J. Phys. Chem. Lett.* **2017,** *8,* 435–439. doi:10.1021/acs.jpclett.6b02640
42. Li, W.; Wang, W.; Hou, Q.; Yan, Y.; Dai, C.; Zhang, J. *Phys. Chem. Chem. Phys.* **2018,** *20,* 27910–27916. doi:10.1039/c8cp05285a
43. Li, W.; Wang, W.; Zhang, Y.; Yan, Y.; Král, P.; Zhang, J. *Carbon* **2018,** *129,* 374–379. doi:10.1016/j.carbon.2017.12.039
44. Razmkhah, M.; Ahmadpour, A.; Mosavian, M. T. H.; Moosavi, F. *Desalination* **2017,** *407,* 103–115. doi:10.1016/j.desal.2016.12.019
45. Chandra, A.; Keblinski, P. *J. Chem. Phys.* **2020,** *153,* 124505. doi:10.1063/5.0018726
46. Rokoni, A.; Sun, Y. *J. Chem. Phys.* **2020,** *153,* 144706. doi:10.1063/5.0024722
47. Krishnan, A.; Dujardin, E.; Treacy, M. M. J.; Hugdahl, J.; Lynum, S.; Ebbesen, T. W. *Nature* **1997,** *388,* 451–454. doi:10.1038/41284
48. Plimpton, S. *J. Comput. Phys.* **1995,** *117,* 1–19. doi:10.1006/jcph.1995.1039
49. Abascal, J. L. F.; Vega, C. *J. Chem. Phys.* **2005,** *123,* 234505. doi:10.1063/1.2121687
50. Tsimpanogiannis, I. N.; Moultos, O. A.; Franco, L. F. M.; Spera, M. B. d. M.; Erdős, M.; Economou, I. G. *Mol. Simul.* **2019,** *45,* 425–453. doi:10.1080/08927022.2018.1511903
51. Vega, C.; de Miguel, E. *J. Chem. Phys.* **2007,** *126,* 154707. doi:10.1063/1.2715577
52. Alejandre, J.; Chapela, G. A. *J. Chem. Phys.* **2010,** *132,* 014701. doi:10.1063/1.3279128
53. Vinš, V.; Celný, D.; Planková, B.; Němec, T.; Duška, M.; Hrubý, J. *EPJ Web Conf.* **2016,** *114,* 02136. doi:10.1051/epjconf/201611402136
54. Losey, J.; Kannam, S. K.; Todd, B. D.; Sadus, R. J. *J. Chem. Phys.* **2019,** *150,* 194501. doi:10.1063/1.5086054
55. Qin, X.; Yuan, Q.; Zhao, Y.; Xie, S.; Liu, Z. *Nano Lett.* **2011,** *11,* 2173–2177. doi:10.1021/nl200843g
56. Moskowitz, I.; Snyder, M. A.; Mittal, J. *J. Chem. Phys.* **2014,** *141,* 18C532. doi:10.1063/1.4897974
57. Melillo, M.; Zhu, F.; Snyder, M. A.; Mittal, J. *J. Phys. Chem. Lett.* **2011,** *2,* 2978–2983. doi:10.1021/jz2012319

License and Terms

This is an open access article licensed under the terms of the Beilstein-Institut Open Access License Agreement (https://www.beilstein-journals.org/bjnano/terms), which is identical to the Creative Commons Attribution 4.0 International License (https://creativecommons.org/licenses/by/4.0). The reuse of material under this license requires that the author(s), source and license are credited. Third-party material in this article could be subject to other licenses (typically indicated in the credit line), and in this case, users are required to obtain permission from the license holder to reuse the material.

The definitive version of this article is the electronic one which can be found at:
https://doi.org/10.3762/bjnano.14.1

BEILSTEIN JOURNAL OF NANOTECHNOLOGY

The origin of black and white coloration of the Asian tiger mosquito *Aedes albopictus* (Diptera: Culicidae)

Manuela Rebora[1], Gianandrea Salerno[*2], Silvana Piersanti[1], Alexander Kovalev[3] and Stanislav N. Gorb[3]

Full Research Paper

Open Access

Address:
[1]Dipartimento di Chimica, Biologia e Biotecnologie, University of Perugia, Via Elce di Sotto 8, 06121 Perugia, Italy, [2]Dipartimento di Scienze Agrarie, Alimentari e Ambientali, University of Perugia, Borgo XX Giugno, 06121 Perugia, Italy and [3]Department of Functional Morphology and Biomechanics, Zoological Institute, Kiel University, Am Botanischen Garten 9, 24098 Kiel, Germany

Email:
Gianandrea Salerno[*] - gianandrea.salerno@unipg.it

* Corresponding author

Keywords:
biological optics; insects; nanostructure; scales; structural white

Beilstein J. Nanotechnol. **2023,** *14,* 496–508.
https://doi.org/10.3762/bjnano.14.41

Received: 16 January 2023
Accepted: 30 March 2023
Published: 17 April 2023

This article is part of the thematic issue "Biomimetics on the micro- and nanoscale – The 25th anniversary of the lotus effect".

Associate Editor: S. Giordani

© 2023 Rebora et al.; licensee Beilstein-Institut.
License and terms: see end of document.

Abstract

Micro- and nanostructures of the white and black scales on the tarsi of the mosquito *Aedes albopictus* are analysed using scanning electron microscopy, transmission electron microscopy, and fluorescence microscopy. Reflectance spectra of the white areas are measured. No clear difference is present in the morphology of micro- and nanostructures of black and white scales in SEM and TEM, but black scales contain a dark pigment. The white colour of the scales has a structural origin. The structural white produced by the micro- and nanostructures of the scales on the tarsi of *Ae. albopictus* appears bright and is angle-dependent, since the reflected light changes according to the angle detection and according to the tarsus orientation. The optical appearance of the scale system of *Ae. albopictus* has a complex nature and can be explained by the combination of several effects. Among them, multiple refraction and reflection on the micro- and nanostructures of the scales are mainly responsible for the white appearance. The results suggest that mosquito scales, in addition to their superhydrophobic function, produce structural white. The biological role of white and black patches in mate recognition and defensive behaviour in the mosquitoes of the genus *Aedes* is hypothesized.

Introduction

Body color (coloration) and light signals (bioluminescence) have a fundamental role in insect inter- and intra-specific visual communication allowing for species recognition, mating, prey capture, and predator avoidance [1]. Insect colours may be due to pigments (e.g., melanins, carotenoids, ommochromes, and pteridins situated in the cuticle or under a transparent cuticle) [2] able to absorb visible electromagnetic radiation in a selective way, or due to various physical phenomena, such as reflec-

tion, refraction, interference, diffraction and scattering, that cause the selective reflection of light [3]. Quite often, structural colors are present together with pigment colors, to increase or to reduce the brightness and to produce particular effects [4]. Insect exoskeletons with their multilayered internal organisation and the cuticular micro- and nanostructures present on the surface offer remarkable examples of structural colours in the animal kingdom. The relationship between shining (sometimes iridescent) colors and surface microstructures located on scales has been extensively studied in butterflies, especially in the *Morpho* genus [4-7].

Among Diptera, representatives from the family Culicidae bear scales typically covering their body [8,9]. Their shape and structure vary among different taxa and have been previously used as a taxonomic character [10]. The function of the body scales in mosquitoes is probably related to the superhydrophobicity of their body surface, as an adaptation of an aquatic insect to the subaerial life at the adult stage. Indeed, leg scales with their nanostructures are able to entrap air [11-13] and play an important role in contact with water during egg laying, giving the mosquito high water buoyancy and floating ability, and during emergence from the aquatic pupa, preventing adults from wetting and allowing them to fly away from the water surface without being trapped by capillary forces.

The scales on the mosquito body can also produce a colouration pattern, which is often used in the species determination [14,15]. Notwithstanding such scales are rather similar to those of butterfly wings [16], the mosquito scale nanostructures have not been deeply investigated so far regarding the structural colours they generate. Structural colours are common in insects [4] and have been described mainly in Lepidoptera and Coleoptera [16,17]. As far as Diptera are concerned, investigations on structural colours are scanty.

The aim of the present investigation is to describe in detail the nanostructures and microstructures of the scales in the Asian tiger mosquito *Aedes albopictus* Skuse (Diptera: Culicidae). The species belonging to this genus (among which *Ae. aegypti* L. is present) are visually distinctive, because they have noticeable black and white markings on their bodies and their legs, whose different distributions in different species allows for species identification. The ultrastructure of the white and black scales on the hindlegs of *Ae. albopictus* is analysed using scanning electron microscopy, transmission electron microscopy, and fluorescence microscopy. Moreover, reflectance spectra of the white areas are measured. The scales are present also on other body parts, but we mainly focused our attention on the hindlegs, because of their bright white stripes.

Ae. albopictus or Asian tiger mosquito is an invasive species native to tropical and subtropical areas of Southeast Asia, nowadays established in all Mediterranean countries. It is recognised as one of the 100 most invasive species in the world being an aggressive day-biting species. It is of high medical importance as a vector of chikungunya virus, dengue virus, and dirofilariasis [18]. Detailed studies regarding the optical properties of the body surface of insects, such as *Ae. albopictus* can be relevant to both species recognition and surveillance. Moreover, these studies increase our knowledge on inter- and intraspecific communication of these dangerous species, thus helping to develop new control methods.

Results

The body of the adult (male and female) of *Ae. albopictus* is typically characterised by the presence of white and black areas (Figure 1). White patches are present on abdominal segments, thorax, head, and legs of both sexes. They are particularly evident on the hindlegs (Figure 1c–f). Males and females differ in size and in shape of antenna and mouthpart, but their hindlegs are similar in colour and shape. Their tarsi are characterised by five segments, whose length decreases from the first to the last tarsal segment. Each segment is white in its proximal portion and black in its distal portion, except for the last segment, which is totally white (Figure 1f).

Observations with SEM reveal that the body of *Ae. albopictus* is covered with scales and microtrichia (Figure 2). Scales of different shape are present on different body parts. Spatulate scales are the most common kind of scales. They are found on the thorax (Figure 2a,b), wings (Figure 2c), halters (Figure 2d), head (Figure 2e), abdomen (Figure 2f), and legs (Figure 2g), while falcate scales belong to the dorsal side of the thorax (Figure 2h).

To analyse the micro- and nanostructures located on the scales of *Ae. albopictus* in detail, we focused on the tarsi of the hindlegs, which show particularly evident white patches. In particular, we examined the scales at the articulation between different tarsal segments of the hindlegs, where black scales are situated very close to white scales (Figure 3a and inset). Scales are spatulate, convex and show a rounded apex. Their size is variable, and some small scales are visible under wider scales (Figure 3a). The lower surface of a scale is flat, without specialized micro- and nanostructures (Figure 3b). The upper surface is covered by longitudinal ridges (Figure 3c–e). The distance between the ridges is 1.189 ± 0.03 μm (average ± SE) in the black scales and 1.283 ± 0.03 μm in the white scales. The cuticle between longitudinal ridges is decorated with anisotropically situated nanostructures with a herringbone pattern (Figure 3e). The ridges show overlapping lamellae from which fine folds

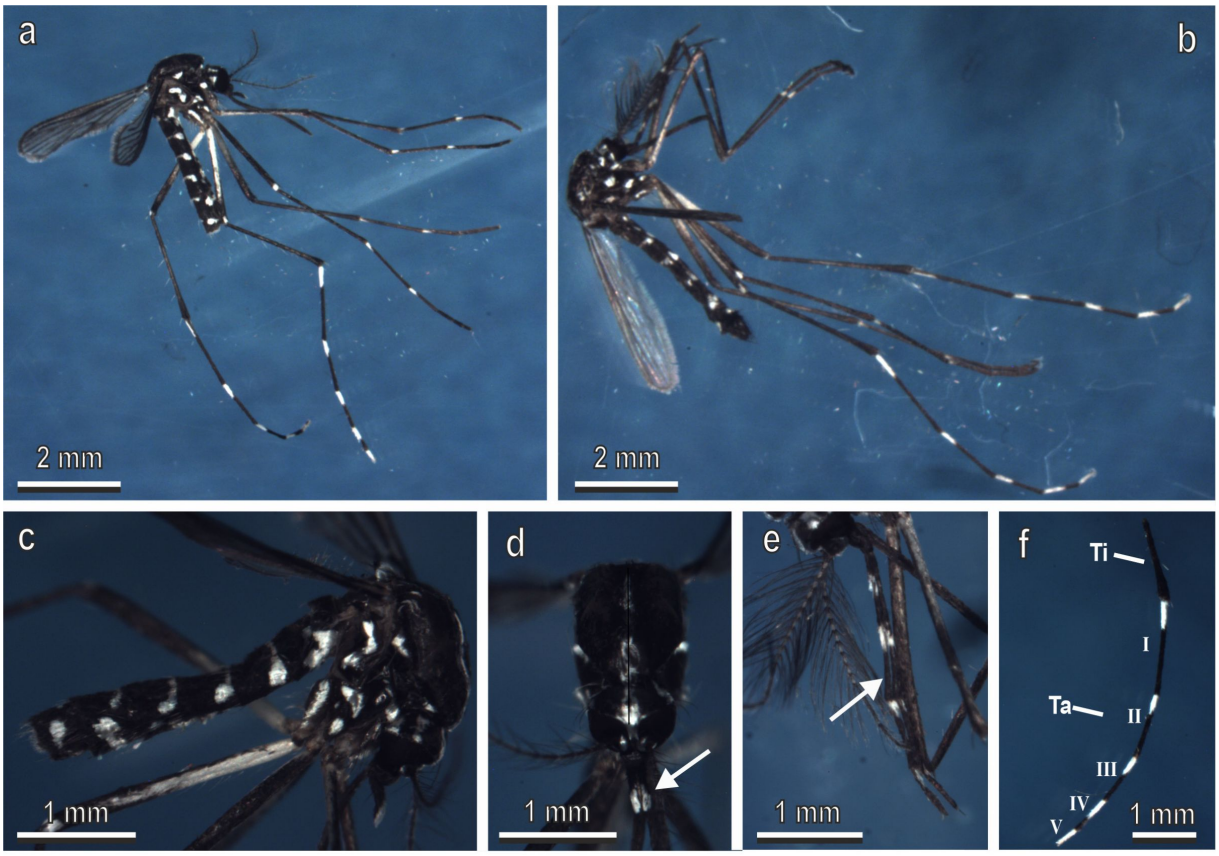


Figure 1: Adults of *Aedes albopictus* under a stereomicroscope. Female (a) and male (b) typically characterised by the presence of white and black areas on their body. (c) Detail of the abdomen and thorax of the female. (d) Detail of the head and maxillary palps (arrow) of a female. (e) Detail of the maxillary palp (arrow) of a male. (f) Detail of the tarsi (Ta) of the hindlegs of the female. Note that each segment is white in its proximal portion and black in its distal portion except the last segment which is totally white. Ti, tibia.

or microribs run down the sides, along the sides of the ridges (Figure 3d). The longitudinal ridges extend beyond the apical portion of the scale, thus forming an apical fringe (Figure 3c).

Some details of the nanostructures, characterising the tarsal scales of *Ae. albopictus,* have been clarified with the aid of TEM (Figure 4). Cross sections of the tarsi in their white (Figure 4a–d) or black (Figure 4e–h) portions reveal that series of four to five convex scales overlap each other (Figure 4a,b,e,f). The scales are very thin (about 0.2 µm thick). Their lower and the upper surfaces are closely juxtaposed, even if some empty spaces (nanovoids) are occasionally visible between them (Figure 4b–d,h). Such nanovoids originate from the rests of epidermal cells and appear in TEM as white or light grey areas inside the scales, together with electron-dense debris (Figure 4h). Their occurrence is higher at the bases of microribs, because the cuticle thickness is higher there (Figure 4h). Along the upper surface of the scale, the longitudinal ridges run orthogonal with respect to the herringbone pattern floor (Figure 4b,c,f,g). The cuticular microribs along the ridges appear in the cross section as small lateral globular bulges (Figure 4c,d,f,g). We did not observe any clear difference in the morphology of black and white scales in SEM and TEM, except for the small difference in the distance between the longitudinal ridges.

The scales appear black and white only under reflected light at low magnification. In our observation of the tarsal scales of *Ae. aegypti* in a light microscope under transmitted and reflected light we could observe that in dry specimens under transmitted light white scales appear transparent and black scales appear dark (Figure 5a,b). Under reflected light, at high magnification, both white and black scales demonstrate a faint iridescent spotted pattern (Figure 5a,b). The colour of the pattern depends on the illumination direction in black scales, while in the white scales only the spot saturation changes at different illumination directions. Scales loose the whitish coloration when observed immersed in oil (with a refractive index closer to that of the cuticle material as to that of air) under

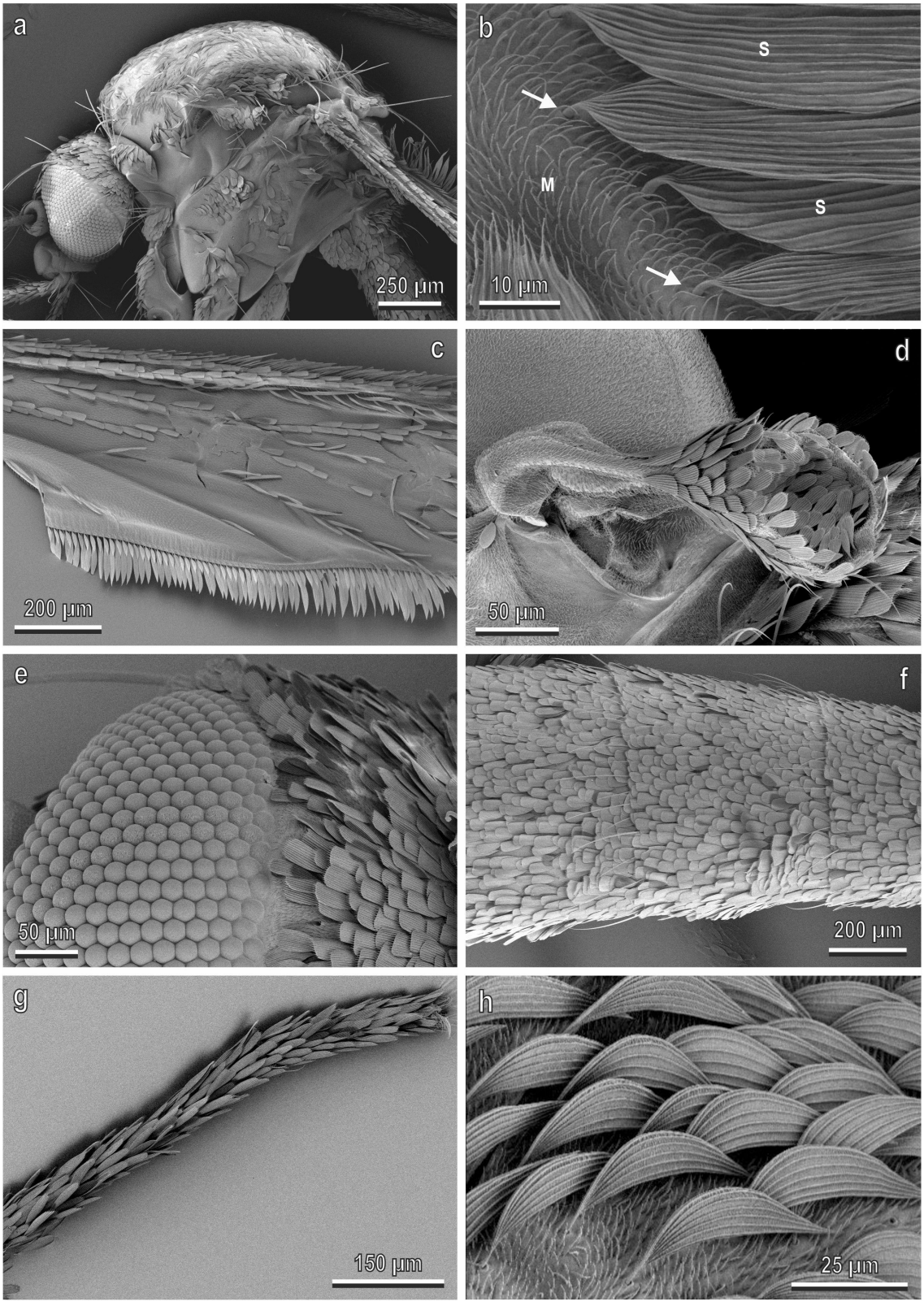


Figure 2: *Aedes albopictus* (female) in a cryo-SEM. (a) Lateral view of the thorax of *Ae. albopictus* covered with scales and microtrichia. (b) Detail of (a) showing microtrichia (M) and scales (S) with their articulated insertion (arrow) in the cuticle. (c–g) Scales with different shape located on the different body parts such as wings (c), halters (d), head (e), abdomen (f) and legs (g). (h) Detail of dorsal side of the thorax with falcate scales.

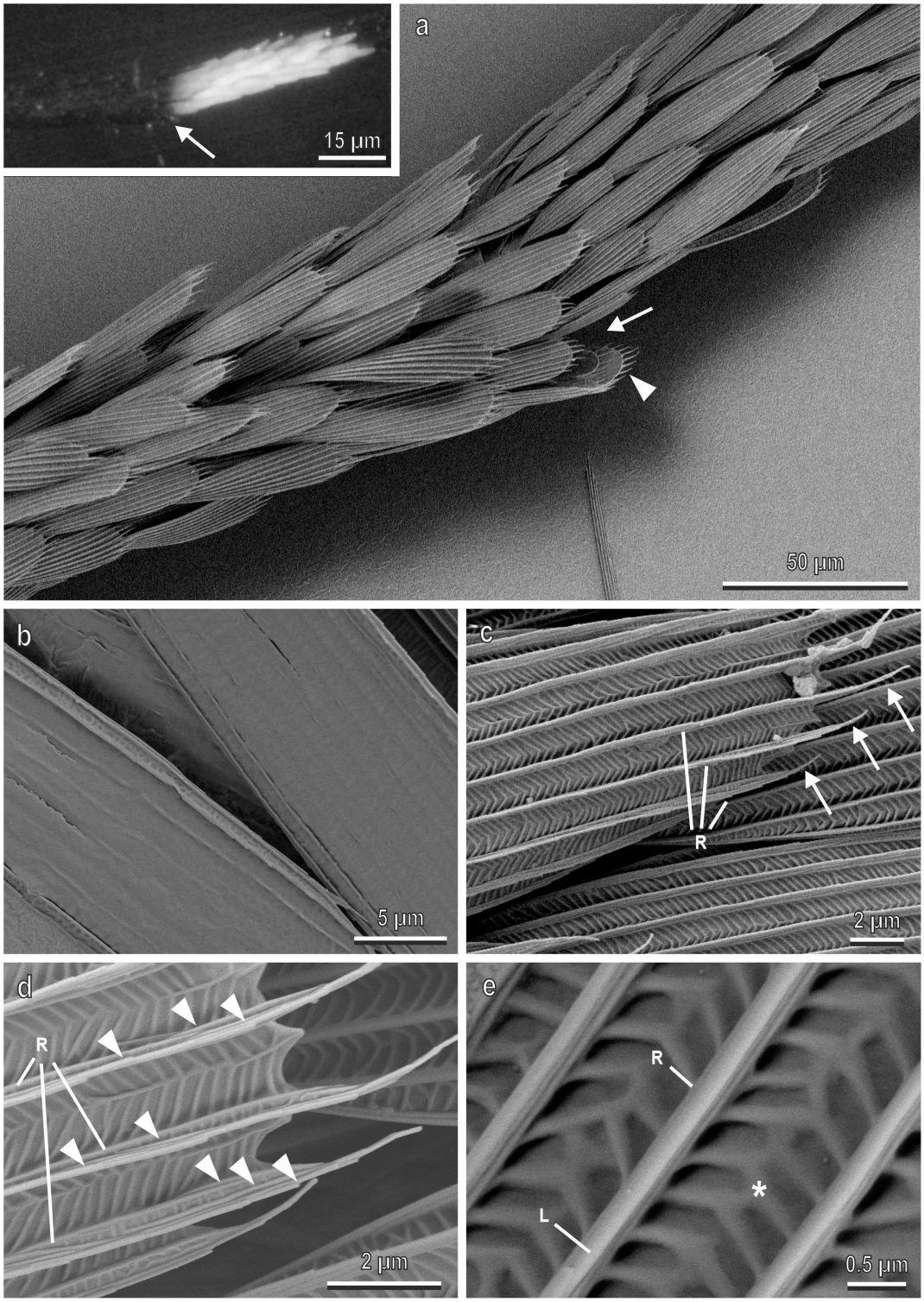


Figure 3: Tarsal black and white scales of *Aedes albopictus* (female) in a cryo-SEM. (a) Scales at the articulation (arrow) between the tarsal segments of the hindlegs, where the black scales are close to the white scales (in the inset the same image under stereomicroscope is shown). Note that both scales are spatulate, convex and show a rounded apex. Their size is variable, and some small scales are visible under wider scales (arrow head). (b) The lower surface of two scales without special micro- or nanostructures. (c) Upper surface of the scale with numerous longitudinal ridges (R) extending beyond the apical portion of the scale thus forming an apical fringe (arrows). (d) Detail of the longitudinal ridges (R) constituted of overlapping cuticular folds generating microribs (arrow heads) along the sides of the ridges. (e) Cuticle between longitudinal ridges (R) decorated with anisotropically situated nanostructures with a herringborne pattern (asterisk). L, lamella.

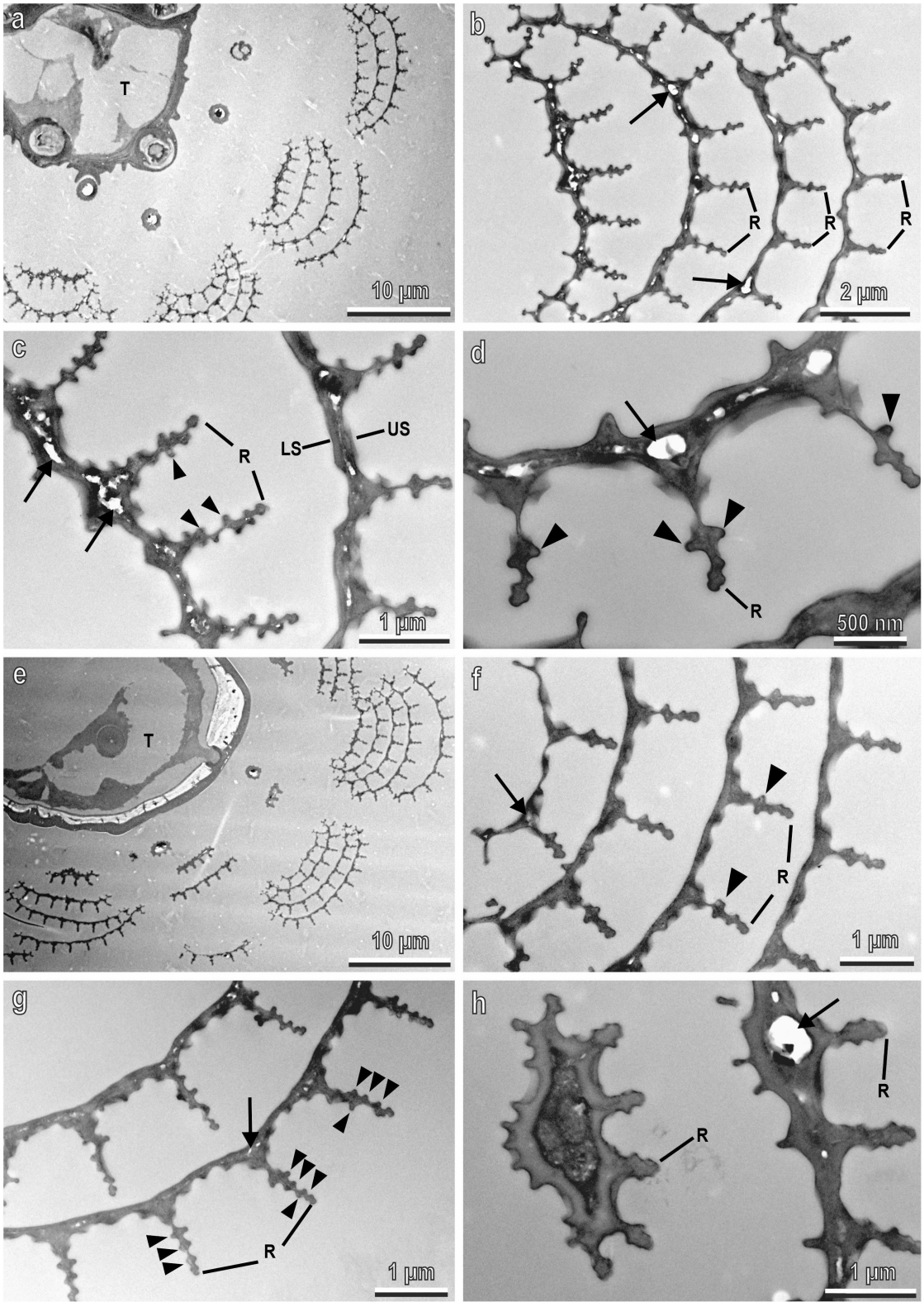


Figure 4: Tarsal black and white scales of *Aedes albopictus* female in a TEM. Cross sections of the tarsi in their white (a–d) and black (e–h) portions. In (a) and (e) note the series of overlapping four to five convex scales around the tarsus (T). The lower (LS) and the upper (US) surfaces are closely juxtaposed even if some empty spaces representing nanovoids, originating from the rest of epidermal cells, are occasionally visible between them (arrows). The cuticular microribs (arrow heads) along the ridges (R) appear in the cross section as small lateral globular bulges.

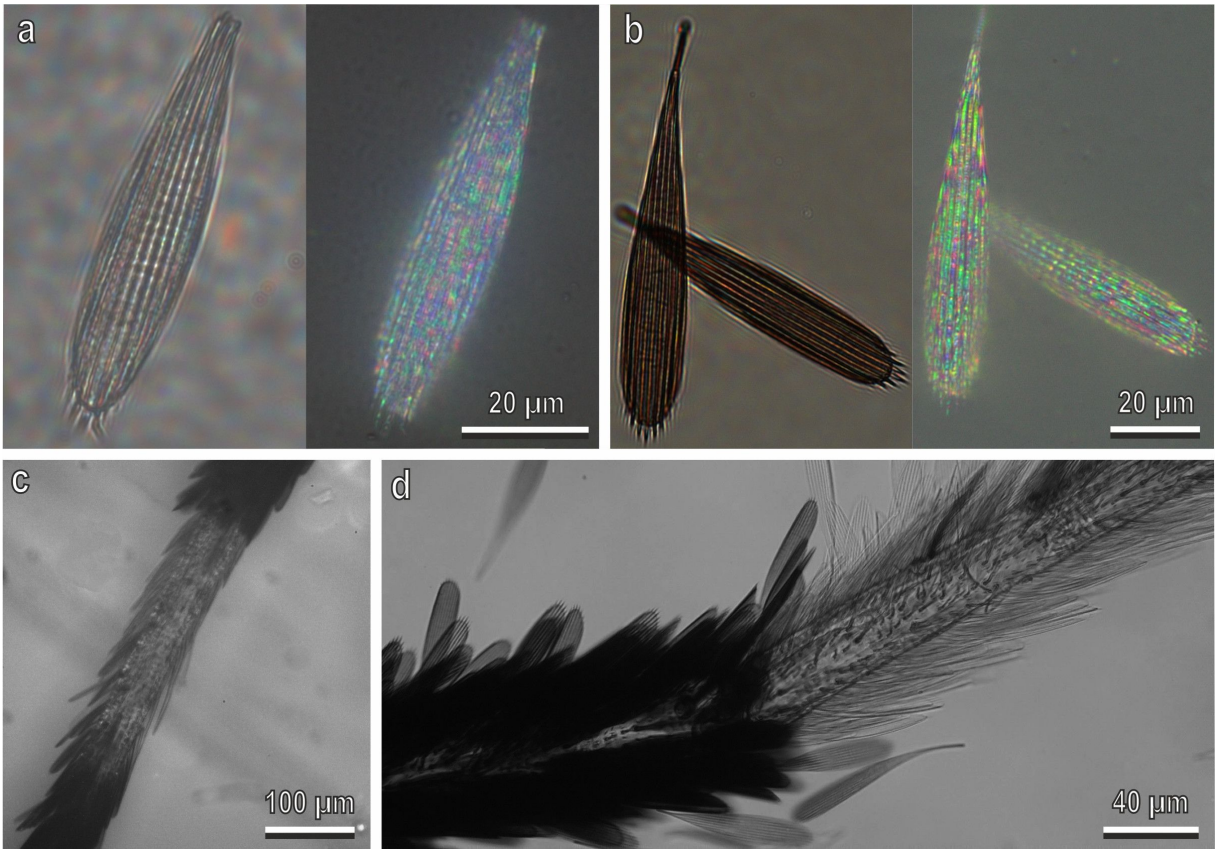


Figure 5: Tarsal black and white scales of *Aedes albopictus* female in a light microscope. (a) Dry white scales under transmitted (left) and reflected (right) light; (b) Dry black scales under transmitted (left) and reflected (right) light. (c) White and black scales immersed in oil under reflected light. Note that the white scales do not appear white, but rather transparent, while the black scales appear dark due to the presence of a certain amount of dark pigment in the cuticle. (d) White and black scales immersed in oil under transmitted light.

reflected (Figure 5c) and transmitted (Figure 5d) light. White scales look transparent under these conditions, white black scales remain dark because of melanization. All reflection spectra are homogenous without evident peaks (Figure 6). The reflection intensity in the near-infrared spectral range (>900 nm) is about 2.5 times stronger than the WS1 reflection (!) and up to five times stronger (at 45° detection) than in the UV spectral range (<300 nm) (Figure 6). Pronounced specular reflection (at 45° detection) could be seen at proximal and distal illumination (Figure 6). Enhanced reflection at 30° detection and distal illumination (compared with proximal illumination) (Figure 6a,b) should be related to the tilt angle of the individual scales (Figure 3a). There is also relative strong light scattering on the thin scale surface structure (Figure 3c–e; Figure 4), which amounts for even backwards reflection (proximal illumination, −20° detection) of about 1/3 of the WS1 standard reflection (at 45° illumination/detection). From geometrical considerations, it is clear that backwards reflection (−20° detection) is the strongest and reflection at 30° is the weakest at perpendicular illumination. In UV spectral range, the light scattering has no specific trends (corresponding to, e.g., Rayleigh scattering), though absorption by molecules with aromatic groups might modulate the reflection. There are no pigments in the white scales (Figure 5d), so interference on the single scales structure is responsible for the reduced visible and UV (compared to near-IR) reflection.

Sputter coating with Au/Pd (10 nm thickness) of the tarsal scales of *Ae. albopictus* (Figure 7) almost eliminates the visual difference between white and black scales. Since the scale surface is optically smooth, the metal-coated scales demonstrated specular reflection. A thin Au/Pd film on the scale surface effectively screens the pigment presented inside the scales and traps the light so that the white as well as the black appearance of the scales disappears.

Observations of the legs of dry adults using a fluorescence microscope revealed that the white areas on the tarsi show UV-induced fluorescence (Figure 8). The excitation occurs at 365 nm (UV light) and the emission from 397 nm (blue light).

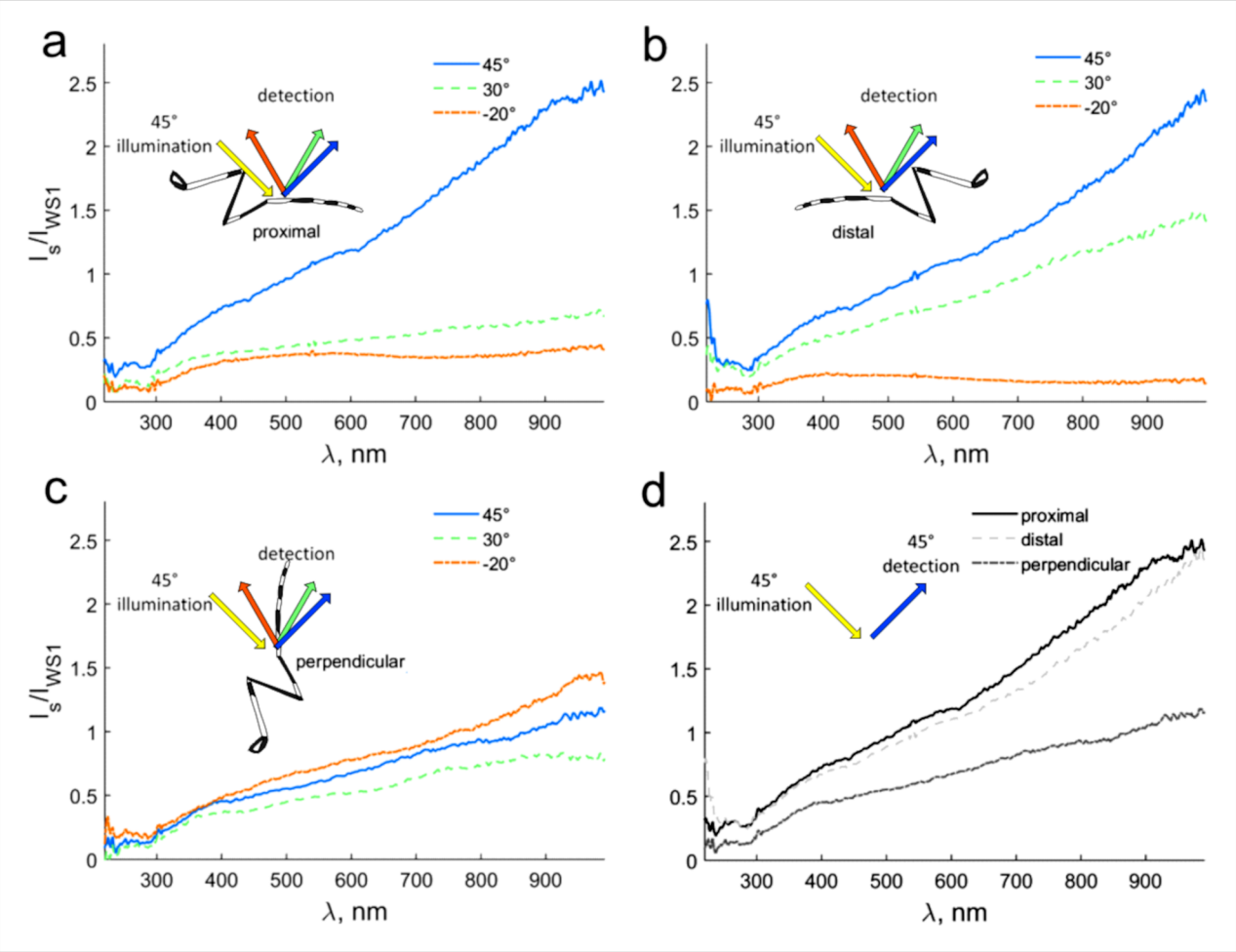


Figure 6: The light scattering spectra from a white area of the hindleg tarsus of *Aedes albopictus* male at different leg orientations. The white spot was illuminated at 45°. The light scattering was detected at 45°, 30°, and –20° (relative to the normal to the surface). Illumination was performed at different leg orientation relative to the illumination source: illumination was from the proximal direction (a), from the distal direction (b), and perpendicular to the tarsus main axis (c). Reflection at 45° for different leg orientations is summarized in (d).

Discussion

Multifunctional role of the scales

The present investigation reveals that the white bright scales on the body of *Ae. albopictus* are constituted of transparent cuticle, and their micro- and nanostructures can generate structural white. These results suggest a multifunctional role of the mosquito scales which, in addition to a superhydrophobic function [11-13], produce structural colours similar to those of butterfly scales. The involvement of these structures in the origin of structural white is clearly demonstrated by our optical microscopy observations. Indeed, when we observed the tarsal scales under transmitted and reflected light, we could observe white bright scales only in dry specimens under reflected light, while the white scales observed under transmitted light appear transparent. Moreover, the white scales immersed in oil with a refractive index close that of chitin do not appear white, but rather transparent, while the black scales appear dark due to the presence of a certain amount of a dark pigment melanin in the cuticle. This means that neither pigments nor inclusions with strongly different refractive index (e.g., voids) are responsible for white appearance of the scales.

Structural whiteness requires scattering processes for all visible wavelengths [19]. Two kinds of structural whiteness can be recognised, namely diffuse whiteness, which is angle-independent and metallic silver, which is angle-dependent. Diffuse whiteness produces matt white and is due to the multiple scattering of light within a randomly structured medium, such as the three-dimensional photonic solid in the scales of *Cyphochilus* spp. beetles [20]. An example of structural white in Diptera has been recently described in the white patches located on the thorax of *Bactrocera oleae* (Rossi) (Diptera: Tephritidae) [21]. In this fly, the structural white is due to modified air sacs under transparent cuticle and is independent on the diffuse angle. This structure shows internal arborisations with beads in an empty space, constituting a three-

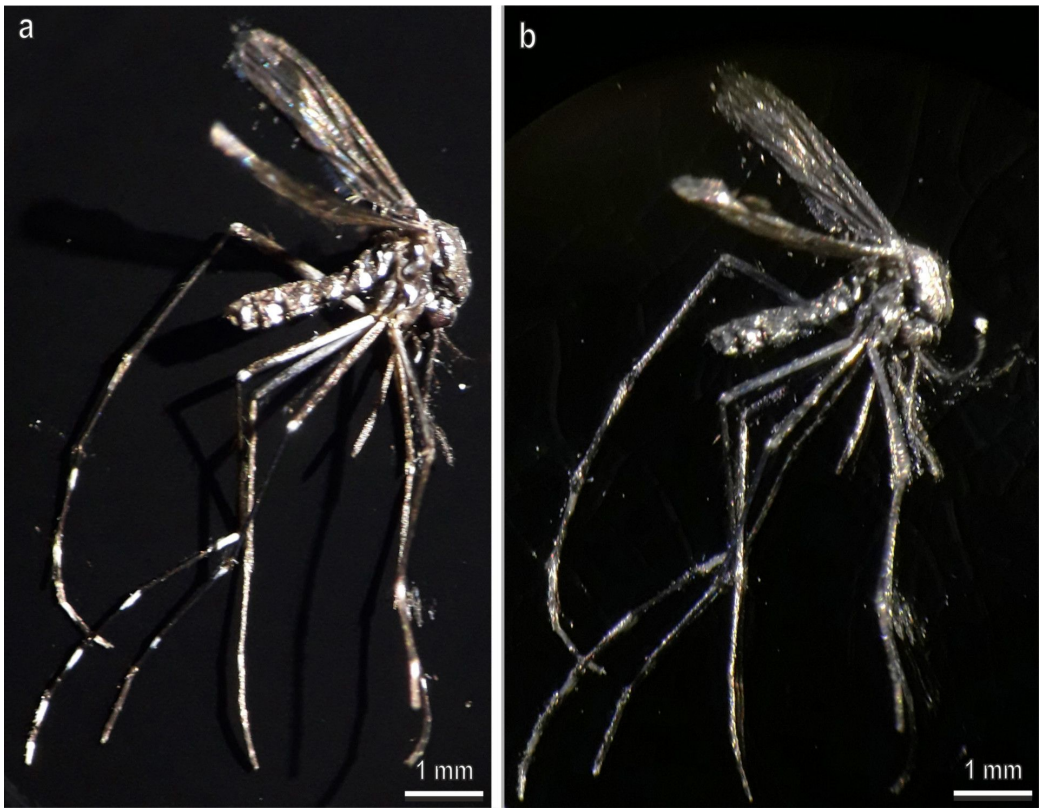


Figure 7: *Aedes albopictus* before (a) and after (b) Au/Pd sputter coating (10 nm film thickness). Note that in (b) the thin Au/Pd film screens the pigment inside the scales and eliminates the visual difference between white and black scales originally visible in the intact animal (a).

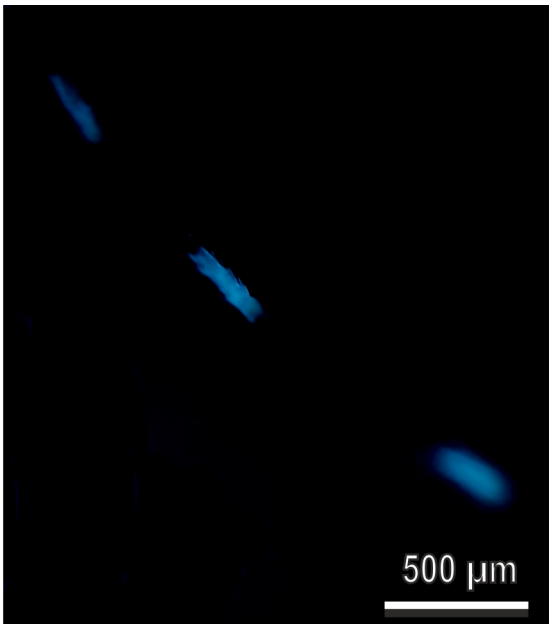


Figure 8: Tarsal black and white scales of *Aedes albopictus* (female) in a fluorescence microscope. Tarsi observed with an excitation filter 365 nm, chromatic beam splitter FT 395 nm, emission 397 nm. Note the blue autofluorescence of the white areas of the tarsi.

dimensional photonic solid responsible for light scattering. Metallic silver produces a bright, shining white caused by a variation of the reflected light intensity under different incident or viewing angles, such as in the scales on the ventral side of the wings of the butterfly *Curetis acuta* Moore (Lepidoptera: Lycaenidae) [22] or in the *Ae. albopictus* scales described here. Indeed, the structural white produced by the micro- and nanostructures of the scales on the tarsi of *Ae. albopictus* appears bright and is angle-dependent since the reflected light changes according to the angle detection and according to the tarsus orientation (from the proximal direction, from the distal direction, and perpendicular to the tarsus main axis).

Optical effects on the mosquito leg scale system

The optical appearance of the scale system of *Ae. albopictus* has a complex nature and can be explained by the combination of several effects, which contribute to different extent: (1) the cylindrical shape of the leg, which may alter scattering depending on the illumination/observation configuration; (2) light scattering, which might be subdivided in (a) Rayleigh scattering on nanostructures, (b) scattering on partially regular micro- and nanostructures, and (c) thin film interference scales;

(3) selective absorption by various molecules present in the cuticle; and (4) collective effects of the overlapping scales. The whole structural hierarchy determines the reflection properties of the white scales, but different micro- and nanostructures are presumably involved in the light scattering at different illumination/detection conditions. Below, we provide a detailed discussion of these effects and their contribution to the measured spectra.

Cylindrical shape of the leg

The cylindrical shape of the leg in combination with the structural white makes the white scales well visible, independent on the observation direction in the plane perpendicular to the legs (Figure 6c). The reason for this is that in the plane crossing the cylinder perpendicular to the cylinder axis, a point on the cylinder surface exists where the incident and reflected angles (from the light source and to the detector, respectively) are equal.

Rayleigh scattering

The contribution of the Rayleigh scattering to the white appearance is almost negligible. The scales look slightly bluish under a light microscope, but there is no evidence for a λ^{-4}-dependence (typical for Rayleigh scattering) in the reflection spectra that increases with increasing wavelength (Figure 6). Besides, the scales are transparent when they are immersed into oil. This means, that there are no or just a few intracuticular nanostructures whose refractive index differs from that of the cuticle itself. In the TEM images, only a small number of nanovoids could be found (Figure 4).

Scattering on micro- and nanostructures

Multiple refraction and reflection on the ridges and microribs, as well as reflection from the upper surface of the scales between ridges (and the corresponding herringbone surface pattern) are mainly responsible for the white appearance of the scales. Coating of scales with a thin Au/Pd layer eliminates the white (and also the black) appearance and demonstrates the importance of multiple reflections for the appearance of the white scales (Figure 6c).

Thin film interference

In the microscopic areas on the scales with relatively constant cuticle thickness, the effect of interference in thin films can be observed, which modulates the reflection spectra. Its contribution is about 11% (considering the refractive index of chitin of 1.56 and an illumination angle of 45°), and it is visible as faint colours on the white background in microscopic observations (Figure 5a). A similar but weaker interference is present in the black scales (Figure 5b) because of the partial light absorption by melanin.

Light absorption

Some substances absorbing UV light are present even in the white scales. They attenuate the reflection in the UV–visible, but not in the red–IR, spectral range. Multiple refractions and reflections enhance this effect.

Collective effects of the overlapping scales

Finally, the fact that the scales overlap each other (Figure 5d) may lead to an increase of both reflection and scattering. Thus, the specular reflection from four overlapping chitin scales at 45° should be three times stronger than the reflection from a single scale. The variation in the scale orientation at the level of one scale and between neighbouring scales is responsible for the strong small-angle scattering and for the absence of the prominent specular reflection. The scales are tilted with respect to the surface and directed distally (Figure 5d). Highly diffuse scattering might be the only reason for the strong reflection at 30° and distal illumination compared to proximal illumination (Figure 6a,b).

Therefore, the main contribution to the white coloration is provided by non-coherent light scattering (diffuse scattering) on hierarchical randomized multiscale 3D structures (Figure 4a–d, Figure 3d). The coherent contribution (interference), which was estimated to be around 10%, appears due to structure regularity.

Functional significance of the mosquito leg scale system

Structural colors producing matte white and bright silver brilliancy can be readily distinguished and can be involved in inter- and intraspecific visual communication including recognition and mating [23,24]. Our data on *Ae. albopictus* scales and the above discussion show that the main contribution to the white appearance of the scale system comes from the multiple refraction and reflection on the ridges and microribs. Interestingly the white scales of *Ae. albopictus* show UV-induced blue autofluorescence as it has been demonstrated by [24] and confirmed here, exactly as it happens in the white patches of the olive fruit fly *B. oleae* [21]. The biological role of white patches is not known, neither in the olive fruit fly *B. oleae* nor in the mosquitoes of the genus *Aedes*. However, we can hypothesize a role in mate recognition in *Ae. albopictus*. The use of visual cues in mate recognition has been described in other Diptera, such as the two predatory fly species *Lispe consanguinea* Loew (Diptera: Muscidae) and *L. tentaculata* DeGeer (Diptera: Muscidae), which use visual cues from reflective concave silvery scales on the head face during mating [25]. It is well known that in mating swarms, mosquitoes mainly use acoustic signals created by conspecific wingbeats to locate and respond to one another through harmonic convergence [26]. Yet, visual trap components can be important, especially in diurnally active

mosquitoes, such as the yellow fever mosquito *Ae. aegypti* (and the tiger mosquito *Ae. albopictus*). Indeed, it has been previously demonstrated that the use of visual cues can improve the attractiveness of sound-baited traps [27,28]. The mechanisms underlying swarm formation and long-range detection of females by males remain largely unexplored in mosquitoes of the genus *Aedes,* but an investigation [29] demonstrated that swarm formation and mate recognition in *Ae. aegypti* are mediated, in part, by visual cues represented by wingbeat light flashes. Such flashes had no signal function for crepuscular house mosquitoes, such as *Culex pipiens* L. (Diptera: Culicidae) [29].

Another possible role of the black and white coloration of the *Aedes* genus could be related to defensive behaviour. The influence of prey coloration of animals living in groups on the "confusion effect" towards predators is a field still largely unexplored. However, there is some evidence in "human predators" that motion dazzle camouflage could enhance the confusion effect [30-32]. In this context, fast moving black-and-white mosquitoes reflecting light that changes owing to the angle-dependent structural white produced by the scales could create a visual effect causing confusion in predators and disrupting perception. Further studies are necessary to test this hypothesis.

In conclusion, the present research analysed in detail the ultrastructure of the scales producing bright white areas alternating with dark areas on the tarsi of the mosquito *Ae. albopictus.* We could identify micro- and nanostructures responsible for the production of an angle-dependent structural white, confirmed by reflection spectra measurements of the white areas. We believe that to deepen the knowledge on the nanostructures producing structural colours in mosquitoes of the genus *Aedes,* is important not only to widen our knowledge on the origin, variability, and function of structural colours in insects, but also to better understand the nature of the cues potentially driving the behaviour of these medically and economically significant insects. This knowledge will allow for the development of more effective traps to collect, monitor, and control these dangerous insect species.

Experimental

Insects

Single alive females of *Ae. albopictus* were collected in Perugia, Italy in vials using human beings as attractants. Insects were placed in a net cage (300 mm × 300 mm × 300 mm) and transferred to the laboratory. In the laboratory, some specimens were immediately fixed for TEM investigations, while some specimens were frozen at −20 °C for further use. For the terminology regarding the morphological description of mosquito scales we used as reference [16].

Light microscopy

Tarsal black and white scales of *Ae. albopictus* were observed using light microscopy with transmitted and reflected light in an inverted bright-field microscope ZEISS Axio Observer (Carl Zeiss Microscopy GmbH). Dry specimens and specimens immersed in oil (immersion oil 518, Carl Zeiss, Oberkochen, Germany) were observed. Sputter-coated samples (see SEM procedure) were observed using a stereomicroscope under reflected light.

Fluorescence microscopy

Observations of the legs of dry adults were performed using a fluorescence microscope Zeiss Axiophot (Zeiss, Jena, Germany) with an excitation filter 365 nm, chromatic beam splitter FT 395 nm, emission 397 nm, with an excitation filter 450–490 nm, chromatic beam splitter FT 510 nm, emission 520 nm, and with an excitation filter 546 nm, chromatic beam splitter FT 580 nm, emission 590 nm. Insect legs were removed from the insects and placed on a microscope slide for observations.

Scanning electron microscopy and cryo-SEM

Dry insects were observed in a scanning electron microscope Hitachi S-4800 (Hitachi High-Technologies Corp., Tokyo, Japan) at 3 kV acceleration voltage. Specimens were sputter-coated with gold/palladium (10 nm layer thickness).

In a similar manner to a procedure from [33], for cryo-SEM, insect samples were either glued with Tissue-Tek® O.C.T.TM Compound (Sakura® Finetek Europe B.V., Zoeterwoude, Netherlands) to metal holders or mechanically gripped in a small vice on holders and then frozen in a cryo-stage preparation chamber at −140 °C (Gatan ALTO2500 cryo-preparation system, Gatan Inc., Abingdon, UK). Frozen samples, either whole or fractured with a cold metal fracture knife in the cryo-stage preparation chamber, were sputter-coated with gold/palladium (6 nm thickness) and examined under freeze conditions (−120 °C) in the SEM Hitachi S-4800 at 3 kV acceleration voltage. Sputter-coated samples were also used to demonstrate the modulation of the light reflection properties of both black and white scales after introduction of a metal layer on top of the scales.

Transmission electron microscopy

In a similar manner to a procedure from [21], the tarsi and tibiae of *Ae. albopictus* were dissected from anaesthetized insects and fixed for 3 h in 2.5% glutaraldehyde in cacodylate buffer (Electron Microscopy Sciences, Hatfield, England), pH 7.2. The fixed legs were repeatedly rinsed in sodium cacodylate buffer and post-fixed for 1 h at 4 °C in 1% osmium tetroxide in sodium cacodylate buffer (Electron Microscopy Sciences). The

samples were then repeatedly washed in the same buffer, dehydrated in ascending ethanol concentrations, and finally embedded in an Epon-Araldite resin mixture (Sigma-Aldrich). Afterwards, ultrathin sections were cut using a Leica EM UC6 ultramicrotome (Leica Microsystem GmbH, Wetzlar, Germany), collected on formvar-coated copper grids, and examined using a TEM Philips EM 208 (Philips, Eindhoven, Netherlands).

Reflectance spectra measurements

The light scattering spectra from the white areas on the proximal parts of the hind leg tarsus of *Ae. albopictus* male were measured at different orientations of the light source relative to the leg and at different detection angles. For this purpose, the observation area was illuminated at 45° with a light source (DH-2000-BAL, Ocean Optics Inc, Dunedin, Florida, USA) through an optical fiber (200 µm diameter) equipped with a one-lens condenser, which was placed 22 mm away from the sample. The illumination spot was one millimetre in diameter. The illuminated area was calculated based on the microscopy image of the leg (similar to Figure 1f). The mosquito hind leg was fixed using double-sided adhesive tape (Tesa®, Hamburg, Germany) so that the tarsus was parallel to the horizontal plane with the dorsal side up. Measurements were performed for three different orientations of the tarsus relative to the light source, namely illumination along the tarsus main axis proximally and distally, and perpendicular to the tarsus main axis.

The light scattering was relatively homogeneous. Therefore, just three different angles were selected to characterize the reflection properties of the white areas. Reflection spectra at angle of incidence (45°, from the normal to the surface), small-angle scattering (30°), and the backscattering (−20°) were measured. The scattered light was collected by another condenser, which was placed 46 mm away from the sample and was mounted on an optical fiber (200 µm diameter), similarly to [18]. The optical fiber was connected to a spectrometer (Ocean Optics Inc, Dunedin, Florida, USA). The spectra were recorded with the software Spectral Suite (Ocean Optics Inc, Dunedin, Florida, USA). Further spectral processing was performed in Matlab 7.10 (The MathWorks, Natick, NA, USA) and includes dark noise subtraction and smoothing with a Savitzky–Golay filter of fourth order with 12 nm window. All spectra were normalized to the WS1 standard (Ocean Insight, Ostfildern, Germany) reflection spectrum (illumination and observation at 45°). No correction on the observation angle was performed.

Funding

We are very grateful to DAAD (German Academic Exchange Service) for supporting the Research Stays of Manuela Rebora at the Department of Functional Morphology and Biomechanics (Kiel University) (Funding programme/-ID: Research Stays for University Academics and Scientists, 2022 (57588362) Personal ref. no.: 91725732).

Author Contributions

The study was designed by all the authors. S.G. performed the cryo-scanning electron microscopy investigations. M.R. and S.P. performed the transmission electron microscopy investigations. G.S. performed the light microscopy and the fluorescence microscopy investigations. A.K. performed the reflectance spectra observations. The manuscript was written by M.R., A.K. and S.G. All authors discussed the analysis and interpretation of the results and participated in the final editing of the manuscript.

Conflicts of Interest/Competing Interests

All the authors declare that they have no conflict of interest.

ORCID® iDs

Manuela Rebora - https://orcid.org/0000-0002-4271-6336
Gianandrea Salerno - https://orcid.org/0000-0002-8357-7598
Silvana Piersanti - https://orcid.org/0000-0001-7956-9416
Alexander Kovalev - https://orcid.org/0000-0002-9441-5316
Stanislav N. Gorb - https://orcid.org/0000-0001-9712-7953

References

1. Cuthill, I. C.; Allen, W. L.; Arbuckle, K.; Caspers, B.; Chaplin, G.; Hauber, M. E.; Hill, G. E.; Jablonski, N. G.; Jiggins, C. D.; Kelber, A.; Mappes, J.; Marshall, J.; Merrill, R.; Osorio, D.; Prum, R.; Roberts, N. W.; Roulin, A.; Rowland, H. M.; Sherratt, T. N.; Skelhorn, J.; Speed, M. P.; Stevens, M.; Stoddard, M. C.; Stuart-Fox, D.; Talas, L.; Tibbetts, E.; Caro, T. *Science* **2017,** *357,* eaan0221. doi:10.1126/science.aan0221
2. Shamim, G.; Ranjan, S. K.; Pandey, D. M.; Ramani, R. *Eur. J. Entomol.* **2014,** *111,* 149–164. doi:10.14411/eje.2014.021
3. Burg, S. L.; Parnell, A. J. *J. Phys.: Condens. Matter* **2018,** *30,* 413001. doi:10.1088/1361-648x/aadc95
4. Kinoshita, S.; Yoshioka, S.; Miyazaki, J. *Rep. Prog. Phys.* **2008,** *71,* 076401. doi:10.1088/0034-4885/71/7/076401
5. Ghiradella, H. *J. Morphol.* **1989,** *202,* 69–88. doi:10.1002/jmor.1052020106
6. Vukusic, P.; Sambles, J. R.; Lawrence, C. R.; Wootton, R. J. *Proc. R. Soc. London, Ser. B* **1999,** *266,* 1403–1411. doi:10.1098/rspb.1999.0794
7. Berthier, S.; Charron, E.; Da Silva, A. *Opt. Commun.* **2003,** *228,* 349–356. doi:10.1016/j.optcom.2003.10.032
8. Theobald, F. V. *J. Trop. Med.* **1901,** *4,* 229–235.
9. Theobald, F. V. Diptera. Fam. Culicidae. *Genera Insectorum;* V. Verteneuil & L. Desmet: Brussels, Belgium, 1905; Vol. 26, pp 1–50.
10. Khalaf, K. T.; Khalaf, R. K. *Fla. Entomol.* **1984,** *67,* 300–309. doi:10.2307/3493952
11. Wu, C. W.; Kong, X. Q.; Wu, D. *Phys. Rev. E* **2007,** *76,* 017301. doi:10.1103/physreve.76.017301
12. Kong, X. Q.; Liu, J. L.; Zhang, W. J.; Qu, Y. D. *AIP Adv.* **2015,** *5,* 037101. doi:10.1063/1.4908027

13. Iikura, H.; Takizawa, H.; Ozawa, S.; Nakagawa, T.; Matsui, Y.; Nambu, H. *Sci. Rep.* **2020,** *10,* 14480. doi:10.1038/s41598-020-71406-y
14. Wilkerson, R. C.; Peyton, E. L. *J. Med. Entomol.* **1990,** *27,* 207–224. doi:10.1093/jmedent/27.2.207
15. Westphal-Ferreira, B.; Navarro-Silva, M. A. *Rev. Bras. Entomol.* **2017,** *61,* 91–98. doi:10.1016/j.rbe.2016.11.001
16. Ghirardella, H. *Adv. Insect Physiol.* **2010,** *38,* 135–180. doi:10.1016/s0065-2806(10)38006-4
17. Seago, A. E.; Brady, P.; Vigneron, J.-P.; Schultz, T. D. *J. R. Soc., Interface* **2009,** *6* (Suppl. 2), S165–S184. doi:10.1098/rsif.2008.0354.focus
18. Hawley, W. *J. Am. Mosq. Control Assoc.* **1988,** *4,* 1–39.
19. Stavenga, D. G. *Mater. Today: Proc.* **2014,** *1,* 109–121. doi:10.1016/j.matpr.2014.09.007
20. Vukusic, P.; Hallam, B.; Noyes, J. *Science* **2007,** *315,* 348. doi:10.1126/science.1134666
21. Rebora, M.; Salerno, G.; Piersanti, S.; Kovalev, A.; Gorb, S. *Commun. Biol.* **2021,** *4,* 881. doi:10.1038/s42003-021-02396-4
22. Liu, X.; Wang, D.; Yang, Z.; Zhou, H.; Zhao, Q.; Fan, T. *Adv. Opt. Mater.* **2019,** *7,* 1900687. doi:10.1002/adom.201900687
23. Ge, D.; Wu, G.; Yang, L.; Kim, H.-N.; Hallwachs, W.; Burns, J. M.; Janzen, D. H.; Yang, S. *Proc. Natl. Acad. Sci. U. S. A.* **2017,** *114,* 7379–7384. doi:10.1073/pnas.1701017114
24. Croce, A. C.; Scolari, F. *Molecules* **2022,** *27,* 713. doi:10.3390/molecules27030713
25. Frantsevich, L.; Gorb, S. *Arch. Insect Biochem. Physiol.* **2006,** *62,* 26–42. doi:10.1002/arch.20118
26. Steele, C. H.; McDermott, E. G. *Ann. Entomol. Soc. Am.* **2022,** *115,* 113–126. doi:10.1093/aesa/saab045
27. Balestrino, F.; Iyaloo, D. P.; Elahee, K. B.; Bheecarry, A.; Campedelli, F.; Carrieri, M.; Bellini, R. *Acta Trop.* **2016,** *164,* 448–454. doi:10.1016/j.actatropica.2016.09.002
28. Jakhete, S. S.; Allan, S. A.; Mankin, R. W. *J. Med. Entomol.* **2017,** *54,* 1415–1419. doi:10.1093/jme/tjx074
29. Ko, E.; Blake, A. J.; Lier, C.; Takács, S.; Gries, G. *bioRxiv* **2021,** 04.27.441577. doi:10.1101/2021.04.27.441577
30. Hogan, B. G.; Cuthill, I. C.; Scott-Samuel, N. E. *Behav. Ecol.* **2016,** *27,* 1547–1551. doi:10.1093/beheco/arw081
31. Hogan, B. G.; Cuthill, I. C.; Scott-Samuel, N. E. *Anim. Behav.* **2017,** *123,* 349–353. doi:10.1016/j.anbehav.2016.11.022
32. Hogan, B. G.; Scott-Samuel, N. E.; Cuthill, I. C. *R. Soc. Open Sci.* **2016,** *3,* 160180. doi:10.1098/rsos.160180
33. Gorb, E. V.; Kozeretska, I. A.; Gorb, S. N. *Beilstein J. Nanotechnol.* **2022,** *13,* 807–816. doi:10.3762/bjnano.13.71

License and Terms

This is an open access article licensed under the terms of the Beilstein-Institut Open Access License Agreement (https://www.beilstein-journals.org/bjnano/terms), which is identical to the Creative Commons Attribution 4.0 International License (https://creativecommons.org/licenses/by/4.0). The reuse of material under this license requires that the author(s), source and license are credited. Third-party material in this article could be subject to other licenses (typically indicated in the credit line), and in this case, users are required to obtain permission from the license holder to reuse the material.

The definitive version of this article is the electronic one which can be found at:
https://doi.org/10.3762/bjnano.14.41

BEILSTEIN JOURNAL OF NANOTECHNOLOGY

Suspension feeding in Copepoda (Crustacea) – a numerical model of setae acting in concert

Alexander E. Filippov[1,2], Wencke Krings[*1,3,4,5] and Stanislav N. Gorb[1]

Full Research Paper

Open Access

Address:
[1]Department of Functional Morphology and Biomechanics, Zoological Institute, Christian-Albrechts-Universität zu Kiel, Am Botanischen Garten 1–9, 24118 Kiel, Germany, [2]Donetsk Institute for Physics and Engineering, National Academy of Sciences of Ukraine, 83114 Donetsk, Ukraine, [3]Department of Behavioral Biology, Institute of Cell and Systems Biology of Animals, Universität Hamburg, Martin-Luther-King-Platz 3, 20146 Hamburg, Germany, [4]Department of Mammalogy and Paleoanthropology, Leibniz Institute for the Analysis of Biodiversity Change, Martin-Luther-King-Platz 3, 20146 Hamburg, Germany and [5]Department of Cariology, Endodontology and Periodontology, Universität Leipzig, Liebigstraße 12, 04103 Leipzig, Germany

Email:
Wencke Krings[*] - wencke.krings@uni-hamburg.de

* Corresponding author

Keywords:
adhesion; confocal laser scanning microscopy (CLSM); feeding efficiency; feeding structures; mechanical properties

Beilstein J. Nanotechnol. **2023,** *14,* 603–615.
https://doi.org/10.3762/bjnano.14.50

Received: 02 March 2023
Accepted: 26 April 2023
Published: 17 May 2023

This article is part of the thematic issue "Biomimetics on the micro- and nanoscale – The 25th anniversary of the lotus effect".

Associate Editor: K. Koch

© 2023 Filippov et al.; licensee Beilstein-Institut.
License and terms: see end of document.

Abstract

Suspension feeding via setae collecting particles is common within Crustacea. Even though the mechanisms behind it and the structures themselves have been studied for decades, the interplay between the different setae types and the parameters contributing to their particle collecting capacities remain partly enigmatic. Here, we provide a numerical modeling approach to understand the relationship among the mechanical property gradients, the mechanical behavior and the adhesion of setae, and the feeding efficiency of the system. In this context, we set-up a simple dynamic numerical model that takes all of these parameters into account and describes the interaction with food particles and their delivery into the mouth opening. By altering the parameters, it was unraveled that the system performs best when the long and short setae have different mechanical properties and different degrees of adhesion since the long setae generate the feeding current and the short ones establish the contact with the particle. This protocol can be applied to any system in the future as the parameters (i.e., properties and arrangement of particles and setae) can be easily altered. This will shed light on the biomechanical adaptations of these structures to suspension feeding and provide inspiration for biomimetics in the field of filtration technologies.

Introduction

Particle capture mechanisms are common in a huge variety of aquatic animals, such as polychaetes, bryozoans, bivalves, sponges, echinoderms, cnidarians, or crustaceans [1-7]. Even though living conditions and bauplans differ between suspension feeders, there are two main mechanisms for particle collection from the water body (for in-depth reviews on suspension feeding, see [8-11]). The first one can be described as filtering or sieving with, for example, setae, cilia, or mucous nets, and is present in form of passive or active suspension feeding. Passive feeders rely on external water currents that bring food particles to the filtering structures and active feeders create a feeding flow by pumping systems. The second mechanism involves structures manipulating the water flow (e.g., setae and tentacles) that redirect the food particles and lead them to specialized structures that contact and capture them. A good example for the latter mechanism are the filtering setae of crustaceans (for in-depth reviews, see [12,13]). Even though most crustaceans are primarily raptorial, suspension feeding plays an important role. In general, multiple pairs of appendages generate the feeding current, and the particles are captured by plumate "filter setae", which cover the trunk and head appendages. These setae have to establish contact with the particles by inertial impaction and capture and transport them to the mouth opening [14-18].

These interactions (i.e., making contact with and handling of or manipulating particles) were previously documented in detail through observation under a binocular microscope [19-28]. In this context, setae morphology and mesh size of the filtering structure and the surface chemistry and forces (e.g., van der Waals forces) of feeding structures and particles are of high importance, especially when the particles are of smaller diameter than the meshes of the sieve [14,29-36]. Additionally, the mechanical property gradients of the setae, with soft bases or soft tips, seem to play a role [25,37,38].

All of the abovementioned parameters influence the capability of the setae to capture and transport the particles, but to which extent is unknown since these parameters cannot be manipulated in living organisms. To test how the feeding efficiency depends on the mechanical property gradients and the adhesion forces of the setae, we here present a numerical model that simulates the interplay between setae during suspension feeding. In the past, numerical simulations were used to study the detection of prey, mates, or predators and the feeding current generation by limb motion [28,39-41]. However, mechanical property gradients and adhesion of setae were previously not addressed. As model organism we chose the copepod *Centropages hamatus* (Lilljeborg, 1853). This species belongs to the Calanoida, where filter feeding is the derived condition [19,20,29,42-54]. For this species (Figure 1), previous confocal laser scanning microscopy (CLSM) studies on the cuticle's mechanical properties revealed that the setae on maxillae 1 (long setae) and 2 (short setae) possess very soft bases full of the elastic protein resilin [55-57]. Additionally, the tips of the short setae on maxilla 2 exhibited a blue autofluorescence signal, which strongly indicated that these tips are also rather soft and flexible, similar to attachment hairs in insects showing high adhesion at the tips [58]; for in-depth reviews, see [59-61]. In contrast, the tips of the long setae did not emit blue signals.

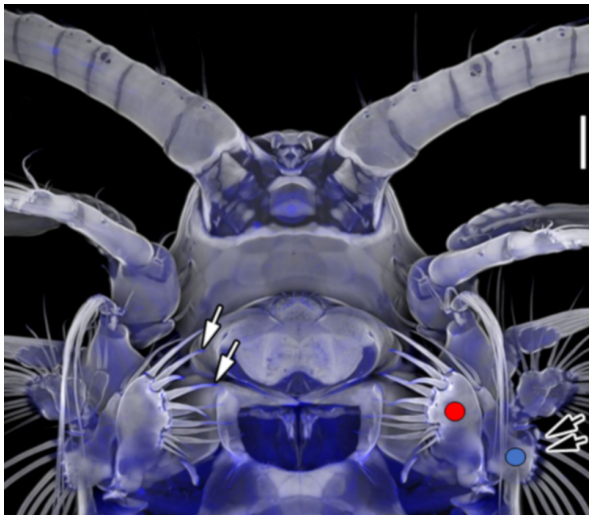


Figure 1: Confocal laser scanning micrograph (maximum intensity projection) showing the exoskeleton of a female copepod crustacean *Centropages hamatus* in ventral view. The black arrows highlight the outer long setae with resilin occurring at their bases. The white arrows indicate the setae with resilin occurring at their tips. The red circle highlights maxilla 1 and the blue one maxilla 2. Scale bar on the right side = 50 µm. Figure 1 was adapted (by adding arrows and circles) from [57], J. Michels, "Confocal laser scanning microscopy – detailed three-dimensional morphological imaging of marine organisms", Imaging Marine Life, with permission from John Wiley and Sons. Copyright © 2014 Wiley-VCH Verlag GmbH & Co. KGaA. This content is not subject to CC BY 4.0.

The simulation presented here takes into account the actual physical processes of the water body (including the interplay between particles). Two types of setae (long and short ones) were arranged on crests, similar to the real situation in copepods, and their parameters (adhesion and mechanical property gradients) were altered. The model produces data on the effectivity of particle collection, the particle motion patterns, and the transfer of particles to the mouth opening. It clearly depicts that short and long setae are more effective when they work in concert and have different mechanical properties and different adhesion forces. This study is rather a protocol for carrying out more extensive numerical modeling in the future as the model can be easily computed with MatLab, and the parameters of the

model (e.g., the size of the food particles and the quantity and mechanical properties of setae) can be adjusted to specific systems or problems. This model shall serve as a basis to unravel the interplay between the feeding structures of suspension feeders, the preferred food, and the gathering performance.

Additionally, it could open new avenues in the development of new filtration technologies (e.g., mucus-like filter media or bioinspired membranes) that use adhesive forces to retain particles. In contrast to organisms, which collect particles at the nano- to millimeter scale, most industrial cross-flow filtration systems can capture material only in more limited size ranges, highlighting the necessity to investigate particle retention in biological systems.

Results and Discussion

Numerical simulations

In this study, we restricted ourselves to a few biologically important questions:

1. Is there a difference in feeding performance between a system possessing only short setae near the mouth opening and a system with both types of setae, long and short ones?
2. Which mechanical properties (flexible or stiff) of the setae segments facilitate the feeding of particles?
3. How does the feeding efficiency change when the setae tips have a high adhesion?
4. How does the feeding efficiency change when the basic segments of each setae are more flexible and allow for a higher bending amplitude?

To elucidate this, we performed a set of numerical simulations with different configurations of the setae, the segments' elasticity, and the adhesion of the segments. The relationship between different variants of elasticity for a system composed of only short setae, as well as for a system containing short and long setae, and the number of eaten particles is summarized below in Figures 2–5.

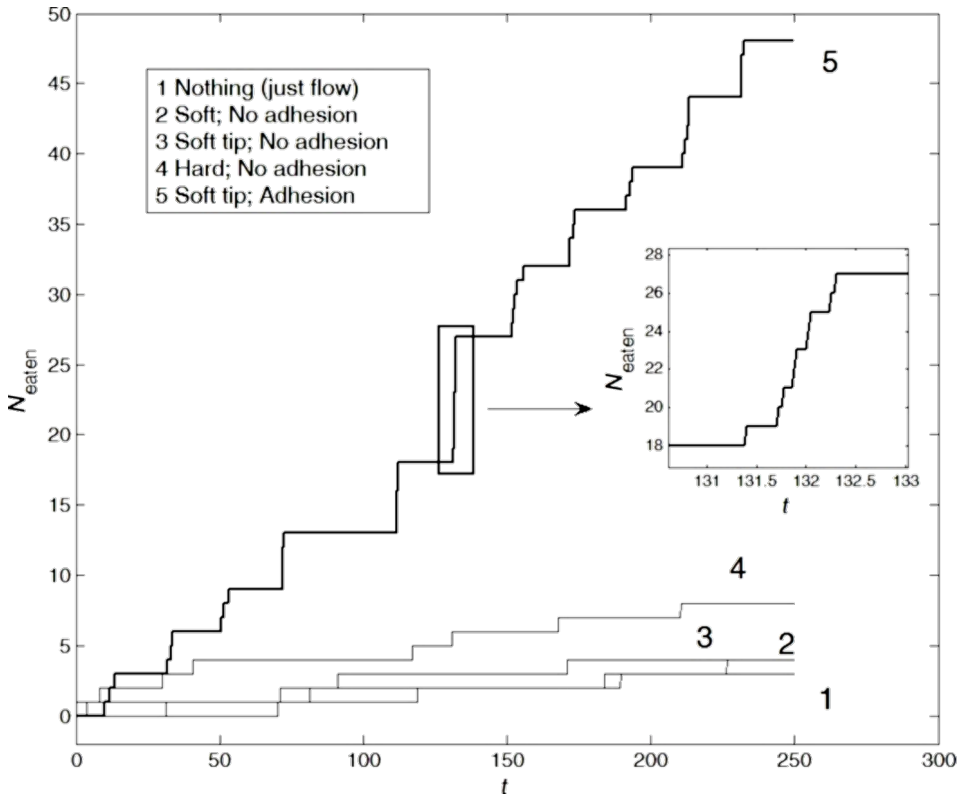


Figure 2: Number of eaten particles as a function of the time for systems containing only short setae (lines 2–5). Line 2 corresponds to a system with soft setae without high adhesion at the tips, line 3 to hard setae with soft tips and without high adhesion at the tips, line 4 to hard setae without high adhesion at the tips, and line 5 to hard setae with soft tips and high adhesion at the tips. Line 1 corresponds to the reference system, which does not contain setae at all (food particles are transported into the mouth by water motion). The insert depicts the fine structure of one typical big step corresponding to an avalanche of eaten particles during a relatively short time interval. The characteristic time intervals between the avalanches correlate with the periodic oscillations (rotations) of the system. The bold curve highlights the optimal configuration (hard setae with soft tips and high adhesion at the tips).

Figure 2 represents the time dependencies of $N_{eaten}(t)$ for four different variants of short setae. Line 2 represents soft setae without high adhesion at the tips, line 3 represents hard setae with soft tips and without high adhesion at the tips, line 4 represents hard setae without high adhesion at the tips, and line 5 represents hard setae with soft tips and high adhesion at the tips. The latter configuration led to the consumption of the highest number of particles.

These variants were numbered correspondingly in Figure 2. For comparison, we also included a curve (line 1 in Figure 2) that depicts the number of eaten particles $N_{eaten}(t)$ in a system without setae. Here, only the flow of water randomly transports particles to the mouth opening and causes a slow accumulation of $N_{eaten}(t)$.

It is important to note that the large steps in the curves are not caused by the accuracy of the calculations, but appear only as an "optical illusion" due to the presentation of the figure in limited size. In fact, each step is one of the consumption avalanches that appear quasi-periodically during the simulation. At appropriate magnification, every large step of the curve has a fine structure with plenty of small steps. Due to the small accumulation window (coinciding with the elementary time interval of the actual calculation), every such step can be resolved down to the independent consumption of sole particles. This fine structure is illustrated for one of the typical avalanches in Figure 2. Most particles are eaten when the short setae are hard and contain soft tips with high adhesion at the tips. Such properties of short setae were previously determined by using CLSM with real specimens [55-57] and are here shown to increase the feeding efficiency.

Analogous dependencies $N_{eaten}(t)$ are plotted in Figure 3 for the system with both short and long setae. For this scenario, we chose the optimal case from the previous scenarios (hard short setae with soft tips and high adhesion at the tips, highlighted with a bold line in Figure 2) as a reference curve (number 1) in

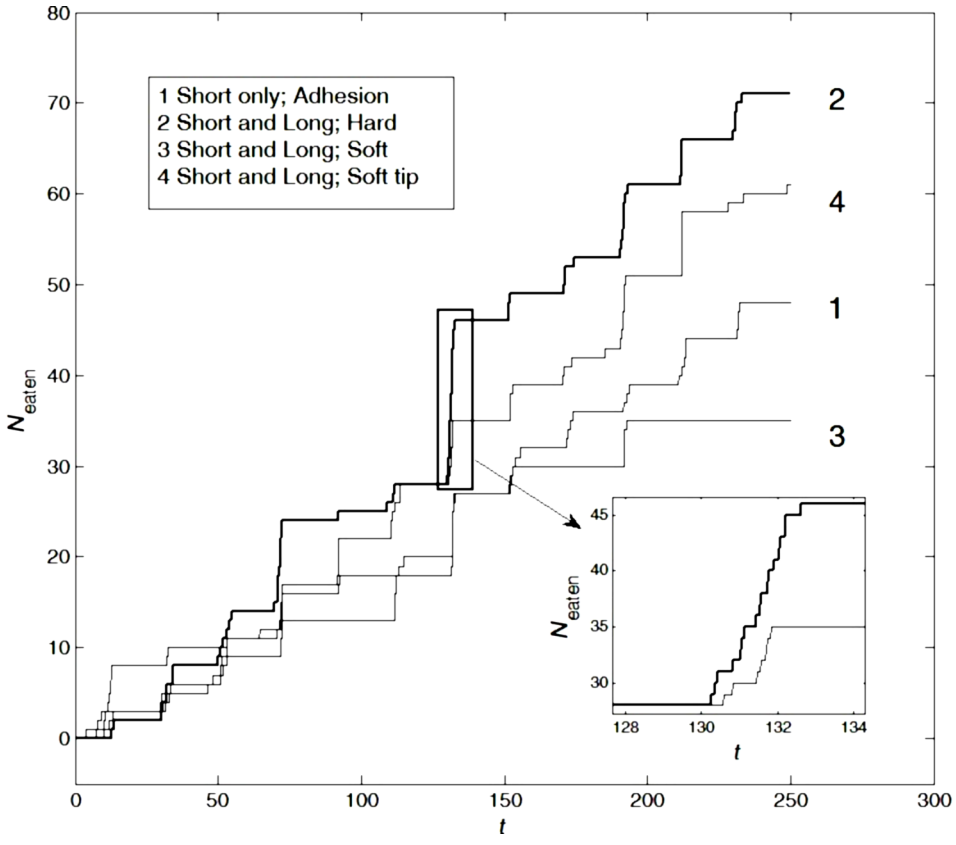


Figure 3: The same as Figure 2, but for systems containing both long and short setae. Line 1 corresponds to the optimal configuration of short setae, taken from the Figure 2 (hard short setae with soft tips and high adhesion at the tips; line 5). For the long setae, no adhesion was chosen. Lines 2–4 correspond to configurations in which the short setae had the same optimal properties and the properties of the long setae were varied: Line 2 depicts the quantity of ingested particles by hard long setae without adhesion at their tips, line 3 represents soft long setae with high adhesion at their tips, and line 4 represents hard setae with soft tips without adhesion at their tips. The insert shows a minor time interval with visually resolved avalanches. Different time intervals between larger steps with different heights correspond to random mutual correlations in motion of the short and long setae. The bold line 2 highlights the optimal configuration with hard long setae without adhesion at their tips.

Figure 3. For the long setae we have chosen a setup without adhesion at their tips. We simulated the following scenarios for long setae: Line 2 represents hard setae (this configuration led to the consumption of most particles), line 3 represents soft setae, and line 4 represents hard setae with soft tips. It is obvious that line 2 corresponds to the maximal value of $N_{\text{eaten}}(t)$. As above, a bold line highlights the optimal case, and some typical avalanches are magnified in Figure 3.

The above CLSM image reveals that the long setae do not exhibit blue autofluorescence, and that there is most likely no adhesion on the tips [55-57]. However, to test if adhesion on these setae would influence the feeding capacity, we varied the degree of adhesion. Figure 4 shows the time dependencies of $N_{\text{eaten}}(t)$ for three different variants of the long setae, namely (1) without adhesion at the tips, (2) with strong adhesion at the tips, and (3) with intermediate adhesion at the tips. This configuration leads to the consumption of more particles, because, due to adhesion, food particles follow the setae and come in the vicinity of the mouth, where short setae collect them and transport them into the goal. However, when the adhesion is too strong, the food particles continue to follow the setae, even after their appearance in the vicinity of the short setae, and almost never enter the mouth.

We additionally altered the degree of adhesion in more detail and performed multiple experiments (Figure 4 and Figure 5). From these experiments, it becomes obvious that there is an optimal degree of adhesion for the long setae, which supports the system. Whether adhesion is present in real structures should be investigated in the future by using either high-resolution CLSM imaging or atomic force microscopy.

As it was visualized by CLSM [55-57], the basal parts of some short and long setae appear to be relatively soft and seem to contain resilin or other proteins. This should influence the mobility of the rotating setae. To account for this in the numerical simulations, one can integrate an angle to which every seta can rotate toward the mouth, ϕ_{min}.

For the first simulations with ϕ_{min}, we excluded the long setae and only simulated the system with short setae (with the optimal configuration, i.e., with soft adhesive tips). The results of this simulation are summarized in Figure 6.

As seen directly from the plots, the well-pronounced threshold angle is $\phi_{\text{min}} = -0.375\pi$. Below this threshold, there is practically zero food consumption. Paradoxically, the quantity of ingested particles is even smaller than in the reference system without setae, that is, with only water flow. Visual observation of the behavior in the simulations showed that when the absolute value of ϕ_{min} was smaller than the critical value, the short setae caught surrounding particles and permanently moved them back and forth (“screening”). As result, they prac-

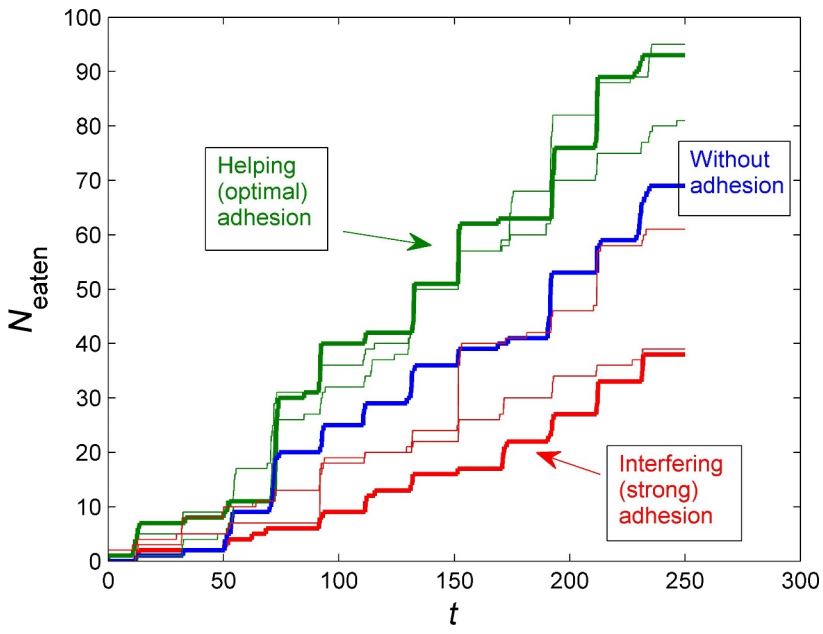


Figure 4: Number of eaten particles as a function of the time for the systems containing both short and long setae, where nonzero adhesion of the long setae also exists. All other parameters are the same as those optimized for the system without adhesion of the long setae. The blue line corresponds to a system with setae without adhesion at their tips, the red line to setae with strong adhesion at their tips, and the green line to setae with intermediate adhesion at the tips. The green curve represents the optimal configuration.

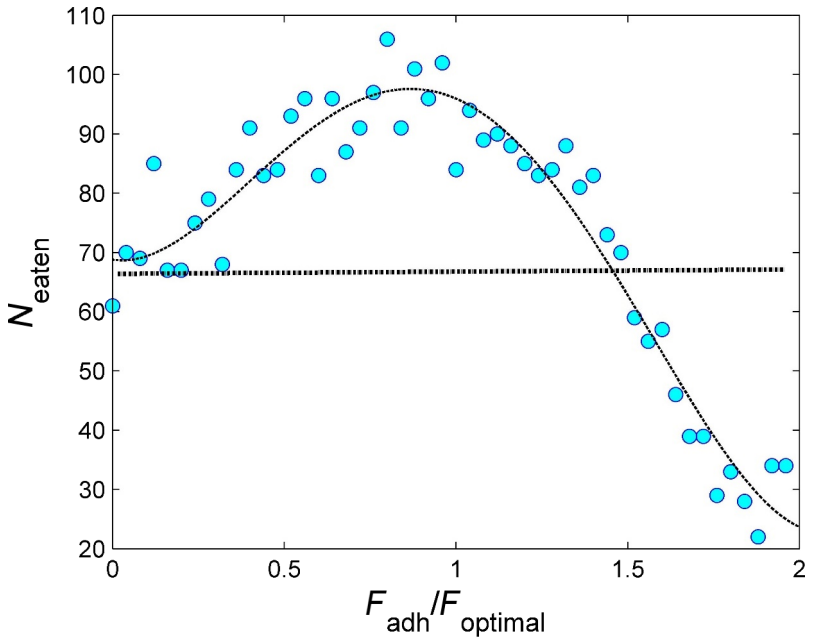


Figure 5: Number of eaten particles for different degrees of adhesion of the long setae tips. Multiple experiments were performed. Each blue circle here corresponds to the final number $N_{eaten}(t)$ obtained at the end t = 250 of a long-time simulation run, analogous to the results in the previous figure at random initial configuration of the food particles and varied step-by-step adhesion force. It is obvious that the highest number of particles is eaten at intermediate adhesion. When the adhesion is too strong, the food particles cannot be transported into the mouth opening. If, and to which extent, long setae have adhesion on their tips in real copepods awaits further investigations.

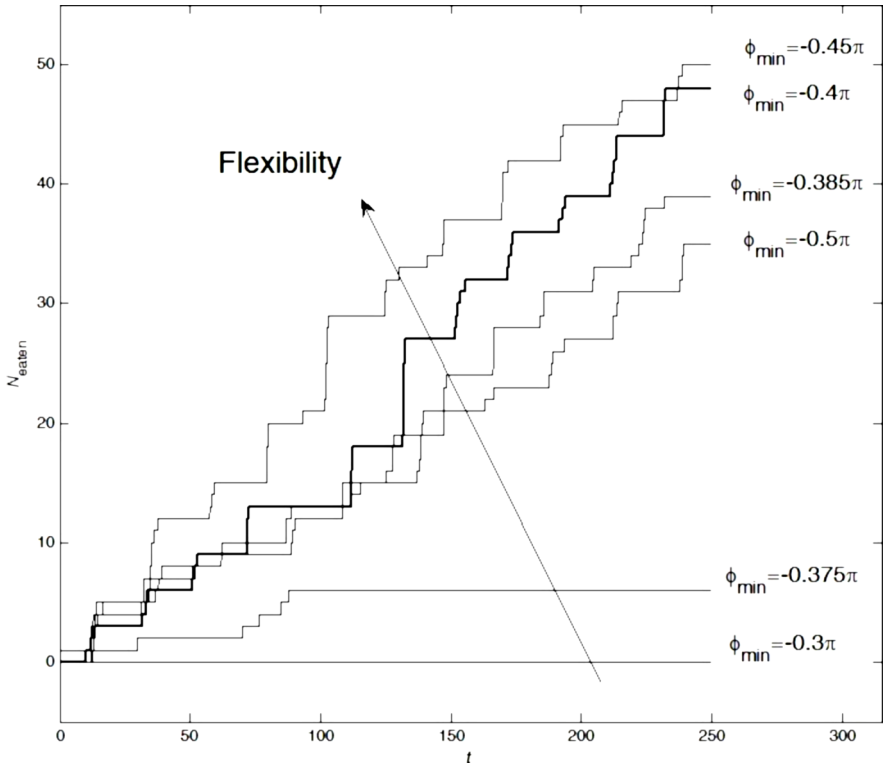


Figure 6: Time dependencies of N_{eaten} at different angles of rotation for the basic segments of the short setae. The threshold angle, ϕ_{min} = −0.375π, at which the system stopped delivering particles into the mouth opening is easily identified. The optimum ϕ_{min} = −0.4π is highlighted with the bold line and was used for all previous simulations.

tically blocked the mouth entrance. It was also found, that the particular angle $\phi_{min} = -0.4\pi$ is very close to the optimum. This value was actually used for all the simulations presented in the previous Figures 2–5 and to record the movie in the Supporting Information File 1.

The same calculations were done for a system containing short and long setae. The results are presented in Figure 7. It is important to note that the angle $\phi_{min} = -0.5\pi$ (here the basic segments run parallel to the surface $z = 0$) yields worse results than the optimal angle $\phi_{min} = -0.4\pi$.

The dynamic behavior of the systems with different parameters can be presented in a static form by density distributions projected on the (y,z) plane and histograms of the distributions along the y axis accumulated during long-time simulation runs. Figure 8 and Figure 9 present the results of such an accumulation for four cases with extremely different kinds of behavior. Darker colors in the grayscale maps correspond to a higher food particle density. Thin curves represent instant snapshots of the particles' location, and the bold curves represent the number of particles averaged over time, respectively.

The panels in Figure 8 illustrate the particle distributions for short setae with (Figure 8a,c) and without (Figure 8b,d) adhesion. The first pair of the panels (Figure 8a,c) clearly demonstrates what happens during the "screening" described above, which appears when the rotation angle is smaller than the critical angle and the setae do not allow particles to enter the mouth opening. One can see very dark regions in the map where particles spent most of the time, following the periodic rotation of the setae without entering the mouth opening. The corresponding histogram integrated over time and the vertical direction confirmed the particle localization in a small region. It even reproduced well-pronounced maximums near so-called "stopping points", where the rotation changes direction. In these places, particles, due to inertia, left for a short time the close proximity of the setae tips, but were very soon attracted to the setae again. The second pair of the panels (Figure 8b,d) shows that particles are much more widely dispersed when the system lacks adhesion. In this case, particles enter the mouth from time to time, but many of the trajectories still lead into the "wrong direction". As a result, the particles periodically repeat many "parasitic" oscillations before they finally enter the mouth.

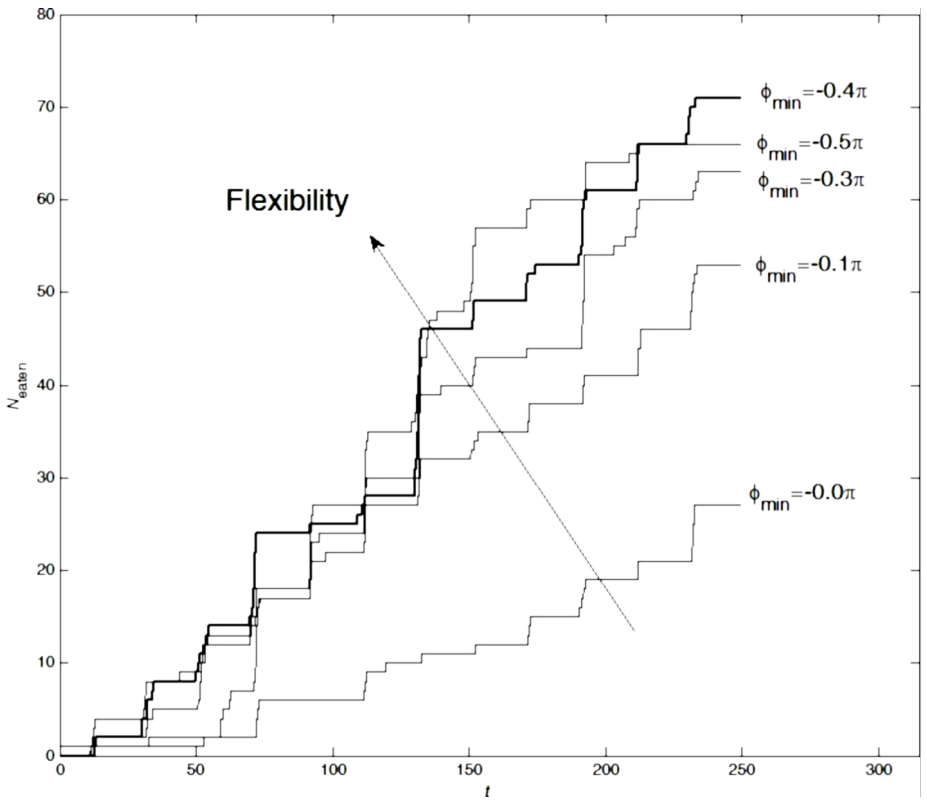


Figure 7: The same as in Figure 6 for the system containing both long and short setae. The short setae had the optimal fixed angle of rotation $\phi_{min} = -0.4\pi$; the angle of rotation for the long setae was varied. The bold line highlights the curve corresponding to the optimal angle.

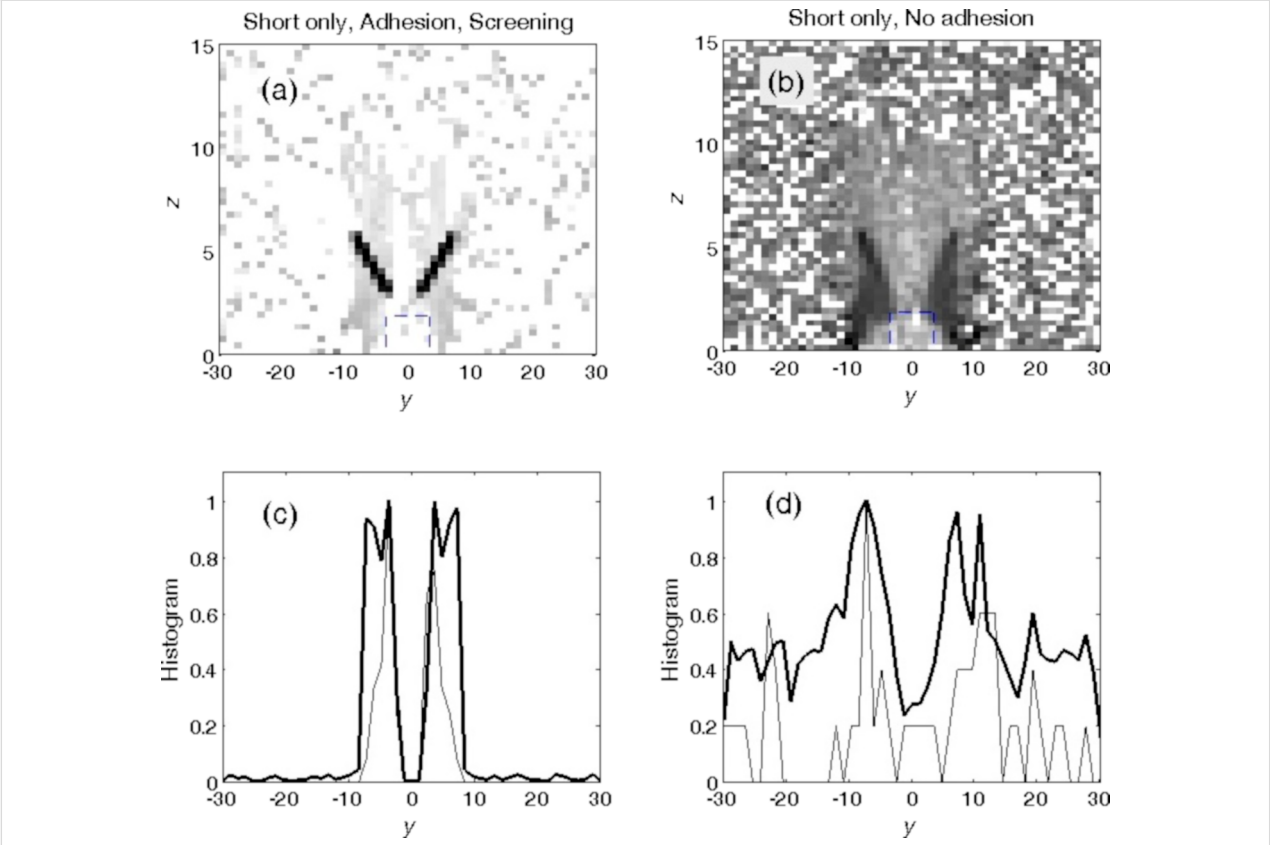


Figure 8: Density distributions obtained from long-time simulation runs in the (*y*,*z*) plane shown by grayscale maps, which were normalized to the density maximums, and the corresponding histograms integrated additionally over the *z* axis. Darker colors correspond to a higher density of particles. The thin curves represent instant histograms, and the bold curves the number of particles averaged over time. Panels (a, c) and (b, d) illustrate the particle distributions for short setae with and without adhesion, respectively. "Screening" in (a, c) means that the rotation angle was smaller than the critical angle. This means that the setae practically did not allow particles to enter the mouth.

The plots in Figure 9 reproduce the results of two almost optimal configurations found above for a system containing only short setae (with adhesion at their tips) and for the system containing long and short setae (short setae with adhesion at their tips and hard long setae without adhesion on their tips; rotation angle $\phi_{min} = -0.4\pi$). They are depicted in Figure 9a,c and Figure 9b,d, respectively. The smooth gray areas correspond to the regions with good statistics, where plenty of food particles are accumulated efficiently by the rotation of the setae and quickly move into the mouth. The black spots on the left and right sides of the mouth show places where particles accumulate with time, but cannot enter the mouth and quasi-periodically oscillate over a long period of time. The difference in accumulation for these two cases is obvious and highlights that a system containing both setae types (Figure 9b,d) is optimal for gathering particles from the surrounding water.

The long setae rather generate water currents that bring food particles to the short setae, which contact and capture them [14-18]. The interaction between setae and particles, which depends on setae morphology, mesh size of the filtering structure, and the surface chemistry and forces of feeding structures and particles [14,29-36], has been observed previously under binocular microscopes [19-28]. It has also been determined previously that mechanical property gradients of the setae, with soft bases or soft tips, are important [25,37,38]. Our model clearly depicts that the mechanical properties of the setae, including the adhesiveness of the tip, determine the feeding efficiency. Additionally, it shows that short and long setae are more effective when they work in concert and have different mechanical properties and different adhesiveness.

This present study is rather a protocol for carrying out more extensive numerical modeling in the future as the model can be easily computed with MatLab and the parameters of the model (e.g., the size of the food particles and the quantity and mechanical properties of setae) can be adjusted to a specific system or animal.

Conclusion

We present here the first numerical model of the feeding setae of crustaceans taking into account the actual physical processes

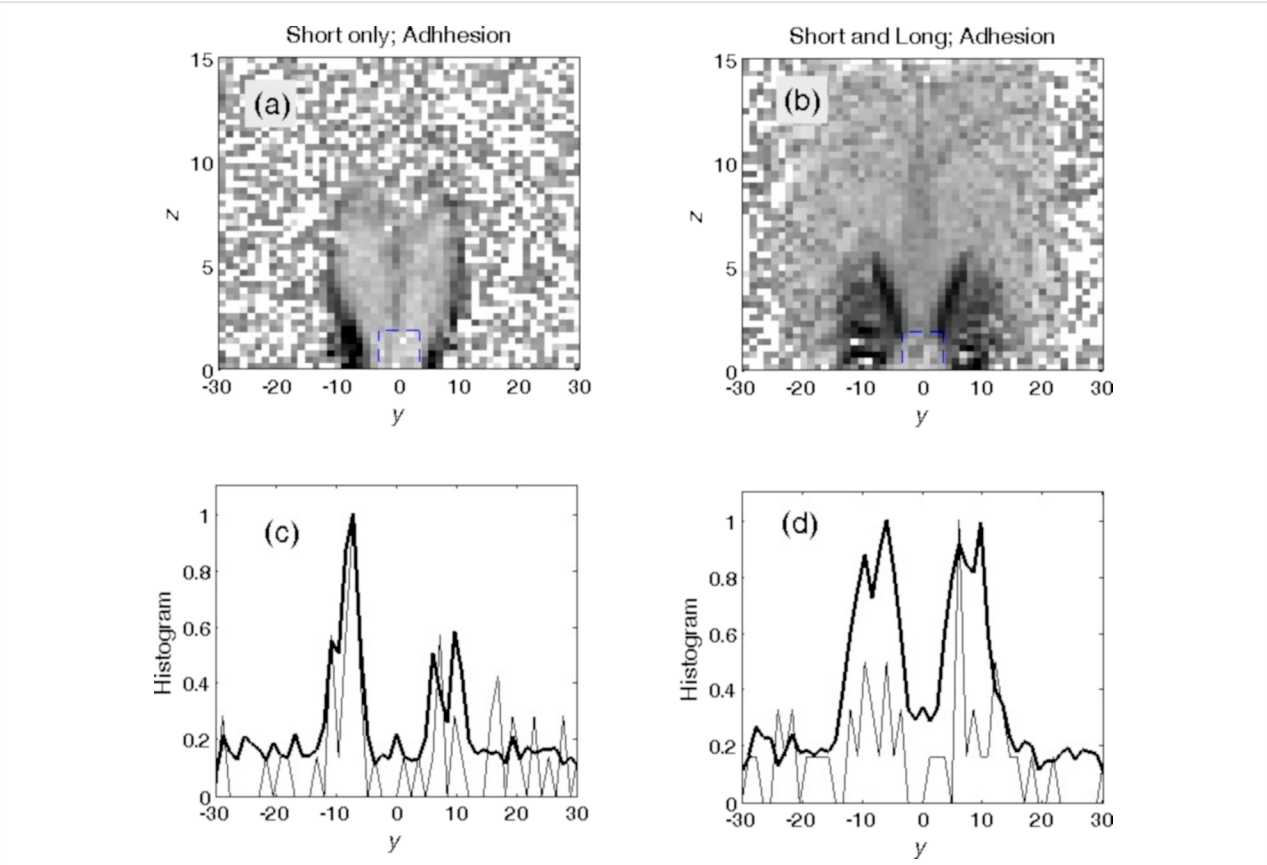


Figure 9: The same as in Figure 8 for two optimal configurations. (a, c) Only short setae (hard setae with soft tips and high adhesion at the tips) and (b, d) long setae (hard with no adhesion at their tips) and short setae (hard with soft tips and high adhesion at the tips). Smooth gray areas correspond to regions with good statistics, where plenty of the particles were accumulated and quickly moved into the mouth. Black spots on the left and right sides of the mouth show the places where particles accumulate over time but cannot enter the mouth. The difference in accumulation for these two cases can be directly seen. The results in (b, d) can be identified as the optimal configuration to collect particles from the surrounding water.

of the environment. The model estimates the particle collecting efficiency depending on mechanical property gradients and adhesion of the different setae. Following this protocol, the model can be easily extended through adjustment of the parameters to fit a specific suspension feeding system or different food items. It also could serve as an inspiration to develop new filtering techniques with adhesive elements retaining particles on the micro- to millimeter scale.

Experimental

Specimens studied

As a model organism, we chose *Centropages hamatus* (Crustacea, Copepoda, Calanoida). The mechanical properties of the setae were previously documented by CLSM [55-57]. The short setae on maxilla 2 possess soft tips and soft bases, and the long setae on maxilla 1 possess only soft bases (Figure 1).

Mathematical model

For the simulations, we employed MatLab R2022a (The MathWorks, Inc., Natick, Massachusetts, USA). Our discrete numerical model describes the dynamics of two pairs of initially parallel aligned elastic crests, resembling the maxillae 1 and 2. The conceptual structure of the model is depicted in Figure 10. The dynamic behavior of the model can be found in the movie in Supporting Information File 1.

Each seta is constructed of a number of elastic segments (long setae: $N_x = 14$, $N_z = 15$; short setae: $N_{x2} = 14$, $N_{z2} = 7$) each having the same length dR. The model does not reproduce exactly realistic numbers of the setae segments or particles. It only provides more or less natural dynamics of the process, which allows us to make some conclusions about the efficiency of the feeding process at different properties of the setae.

The segments were provided with longitudinal ($K^{\parallel}$) and transverse ($K^{\perp}$) stiffness, $K^{\parallel} = K^{\perp}$. The transverse stiffness tends to hold the angle between the neighboring segments close to 180°. According to the goals of this study, we varied the stiffness from segment to segment depending on the hypothetical particular structure.

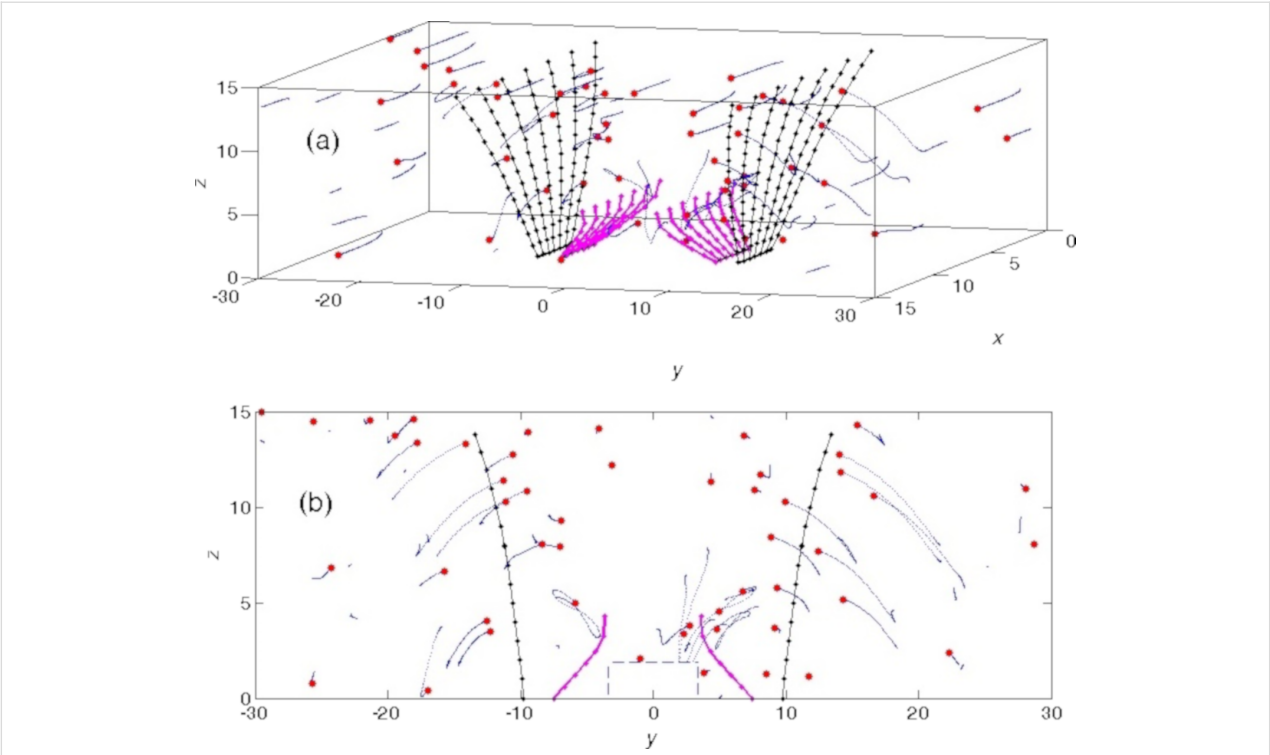


Figure 10: Concept of the numerical model. Setae, arranged as two pairs of seta rows (internal short setae and external long setae), were simulated by lines with small circles. Each small circle separated two elastically connected seta segments. The big red circles represent the instant position of the movable particles ("food"). The dotted comet tails behind each particle visualize small fragments of particle trajectories. (a) shows a three-dimensional view on the system and (b) its projection on the (*y*,*z*) plane. The mouth opening was simulated as the dashed-lined box.

A deformation of the setae produced elastic forces proportional to the seta stiffness. The forces were described by the following equations (see [62] for the formula):

$$\vec{F}_{jk}^{\parallel} = K^{\parallel}\left(\vec{R}_j - \vec{R}_k\right)\left[1-\left(\frac{\vec{R}_j-\vec{R}_k}{\mathrm{d}R}\right)^2\right], \text{ and}$$
$$\vec{F}_j^{\perp} = K^{\perp}\left(2\vec{R}_j - \vec{R}_{j+1} - \vec{R}_{j-1}\right), \quad (1)$$

where $\vec{R}_j$ is a position vector of the middle of the segment (the node) j; $k = j \pm 1$. The longitudinal force, $\vec{F}_{jk}^{\parallel}$, is described here by a double-well potential, which tends to keep the distance between the nodes $\vec{R}_j$ and $\vec{R}_{j\pm1}$ close to the equilibrium length of each segment dR.

This particular form of the longitudinal force equation was chosen, because it is linear at small displacement and increases non-linearly at large displacement. The transverse force, $\vec{F}_j^{\perp}$, is directly proportional to the lateral deflection and tends to keep the position $\vec{R}_j$ close to the mean value between its nearest neighbors, $\left(\vec{R}_{j+1}+\vec{R}_{j-1}\right)/2$. Additionally, it keeps the direction of every segment as close to parallel with the adjacent ones as possible, at current balance of all forces. The transverse force in the present form is easy to realize numerically, but it is not purely the bending force since this may include a longitudinal component.

In the model, each long seta is constructed from 15 segments and each short one from seven segments. Each seta is rotated around a base segment from minimal to maximal angles, $\phi_{\min}$ and $\phi_{\max}$, respectively. We varied these angles in a wide interval to simulate the different rotational mobility of the individual long and short setae. The angular velocity (frequency of the rotation in both directions) was also widely varied for each seta.

The food was represented by an array of $N_p = 50$ particles moving in three-dimensional space with periodic boundary conditions. The particles were created following established protocols [63-68]. For all results presented below, the number $N_p = 50$ was fixed as a compromise between a statistically representative value and the computational cost of the calculations.

It was supposed that every particle interacts viscously with a "water flow" caused by both external flow and motion of the setae. Instead of solving time-consuming Stokes equations

(which in such a case should involve also a motion of the food particles and movable segments of the setae, making a general solution of the problem extremely complex), we simulate a presence of the liquid by a "mutual friction" between the particles and setae, which aims to reduce the difference between the particle and setae velocity at relatively short distances according to simple factors in the dynamic equations of motion. The particles move in an "empty space", but interact with the flows caused by the eternal flux and the motion of the setae via an "imaginary liquid", which influences their motion.

Initially, the particles were placed randomly in a box $[0,L_x; -L_y,L_y; 0,L_z]$ and their velocity was equal to the velocity of external "water flow", v_{ext}. The x component of the external velocity is $v_{ext} = 1.2$, and the two other components are zero. We chose, for simplicity, a constant flow along one of the coordinates with a relatively low velocity compared to the local instant velocities caused by the motion of the setae. This flow transported the food particles to the region where all further handling of the particles took place. This allowed for the permanent generation of particles outside the system to substitute the eaten particles.

If any particle leaves the box, it is randomly injected back to the system with the same velocity. The same is also done in the case of the particle being "eaten". A particle is treated as "eaten" when it appears inside the region "mouth", which is represented by a small box in the center of the ground plane with rectangular (parallelepipedal) borders: $[0,L_{mouth,x}; -L_{mouth,y},L_{mouth,y}; 0,L_{mouth,z}]$.

Being separated by water, the particles move practically independently of one another. Thus, particles do not interact directly with each other in our model. However, each particle interacts with the setae via the liquid. Due to strong damping, each particle tends to equilibrate its speed with the local velocity of the liquid. This velocity, in turn, is determined by a combination of the external flow v_{ext} and perturbations caused by the motion of the setae.

For simplicity and to increase calculation efficiency, instead of solving the huge complete set of dynamic and hydrodynamic equations for particles of complex form with rough surfaces, we separated the potential (exponentially depending on the distance) interaction (interaction caused by a mutual friction, which tends to reduce a difference between velocities).

The appropriate force from the setae acting on every particle is represented as a combination of the following velocity- and distance-dependent factors (see [62] for the formula):

$$f_{kj} = \Theta\left(\vec{r}_k - \vec{r}_j\right)\Phi\left(\vec{v}_k - \vec{v}_j\right). \tag{2}$$

Here, the first factor describes the tendency to equilibrate the velocities of every particle and each segment of the seta. The second one determines how this interaction decays with the distance between the particle and segment. As a first approximation, one can accept that these factors linearly depend on the difference between the velocities and exponentially decrease with the distance in phase (velocity, coordinate) space $\{v,r\}$ between the chosen particle and each segment:

$$\begin{aligned}&\Theta\left(\vec{r}_k - \vec{r}_j\right) \sim \exp\left(-\left|\vec{r}_k - \vec{r}_j\right|/r_0\right);\\ &\Phi\left(\vec{v}_k - \vec{v}_j\right) \sim \left(\vec{v}_k - \vec{v}_j\right)\exp\left(-\left|\vec{v}_k - \vec{v}_j\right|/v_0\right)\Theta\left(\vec{r}_k - \vec{r}_j\right).\end{aligned} \tag{3}$$

As it was mentioned, the particles are involved in the water motion. Thus, the same velocity-dependent interaction exists between the particles and the external flow of water. It can be written in the form

$$\Phi\left(\vec{v}_k - \vec{v}_{ext}\right) \sim \left(\vec{v}_k - \vec{v}_{ext}\right)\exp\left(-\left|\vec{v}_k - \vec{v}_{ext}\right|/v_0\right)\Theta\left(\vec{r}_k - \vec{r}_j\right). \tag{4}$$

Besides the equilibration of the velocities, there is a direct mechanical (or chemical) interaction between the setae and the particles. This interaction becomes important especially for the thin elastic ends of the short setae near the mouth opening. In particular, the adhesion by van der Waals attraction becomes possible at such scales. This part of the interaction must also be included in the model, namely in a form of potential interaction between the setae (or their tips) and the food particles. The corresponding force can be written in the following gradient form:

$$f_{\mathrm{vdW}}\left(\vec{r}_k - \vec{r}_j\right) = -\frac{\partial U_{\mathrm{vdW}}(r)}{\partial r}\left(\vec{r}_k - \vec{r}_j\right)\Big/\left|\vec{r}_k - \vec{r}_j\right|, \tag{5}$$

where $\left|\vec{r}_k - \vec{r}_j\right|$ is the modulus of the difference, and $\vec{r}_j$ is the position of the particle. For definiteness and minimization of the numerical calculations $U_{\mathrm{vdW}}(r)$ can be represented by a relatively simple Morse potential $U_{\mathrm{vdW}}(r) = U_0(1 - \exp(-a(r - r_{\mathrm{vdW}})))^2$, where r_{vdW} is the position of the minimum of the van der Waals potential.

The combined influence of all forces mentioned above leads to a typical dynamic scenario, which has been recorded in the movie in Supporting Information File 1. It reproduces quite realistically the behavior of particles moving around a real animal [69].

It is important to note that due to the randomness of the initial conditions and the injection of "eaten" particles back into the system, particular feeding sequences never exactly repeat. However, after a short transient period, a well-defined quasi-periodic ("strange attractor") motion self-organized in the system, which could be easily analyzed statistically. Besides, one can vary the parameters of the model equation and obtain similar kinds of behavior.

Supporting Information

Supporting Information File 1

Dynamic behavior of the model.
[https://www.beilstein-journals.org/bjnano/content/supplementary/2190-4286-14-50-S1.avi]

Acknowledgements

We would like to thank the reviewers for their supportive comments.

Funding

This research was financed by the DFG grant 470833544 to WK and Alexander von Humboldt Alumni Fellowship UKR 1118826 GFPR to AEF.

Author Contributions

AF created the numerical model. AF and WK wrote the first draft of the manuscript. SG initiated and designed the study.

ORCID® iDs

Wencke Krings - https://orcid.org/0000-0003-2158-9806
Stanislav N. Gorb - https://orcid.org/0000-0001-9712-7953

Preprint

A non-peer-reviewed version of this article has been previously published as a preprint: https://doi.org/10.3762/bxiv.2023.7.v1

References

1. Jørgensen, C. B. *Biology of suspension feeding;* Pergamon Press: Oxford, UK, 1966.
2. Jørgensen, C. B. *Annu. Rev. Physiol.* **1975,** *37,* 57–79. doi:10.1146/annurev.ph.37.030175.000421
3. Strathmann, R. R. Larval feeding. In *Reproduction of marine invertebrates. Vol. IX. General aspects: seeking unity in diversity;* Giese, A. C.; Pearse, J. S.; Pearse, V. B., Eds.; Blackwell Scientific Publications: Palo Alto, CA, USA, 1987; pp 465–550.
4. Wotton, R. S. Methods for capturing particles in benthic animals. In *The biology of particles in aquatic systems;* Wotton, R. S., Ed.; CRC Press: Boca Raton, FL, USA, 1994; pp 183–204. doi:10.1201/9781003070146-8
5. Riisgård, H. U.; Larsen, P. S. *Biol. Rev. Cambridge Philos. Soc.* **1995,** *70,* 67–106. doi:10.1111/j.1469-185x.1995.tb01440.x
6. Riisgård, H. U.; Larsen, P. S. *Limnol. Oceanogr.* **2000,** *45,* 1192–1195. doi:10.4319/lo.2000.45.5.1192
7. Riisgård, H. U.; Larsen, P. S. *Limnol. Oceanogr.* **2001,** *46,* 882–891. doi:10.4319/lo.2001.46.4.0882
8. Hentschel, B. T.; Shimeta, J. Suspension feeders. In *Encyclopedia of Ecology;* Jørgensen, S. E.; Fath, B. D., Eds.; Academic Press: Oxford, UK, 2008; pp 3437–3442. doi:10.1016/b978-008045405-4.00548-6
9. Riisgård, H. U.; Larsen, P. S. *Mar. Ecol.: Prog. Ser.* **2010,** *418,* 255–293. doi:10.3354/meps08755
10. Kiørboe, T. *Biol. Rev.* **2011,** *86,* 311–339. doi:10.1111/j.1469-185x.2010.00148.x
11. Hamann, L.; Blanke, A. *J. R. Soc., Interface* **2022,** *19,* 20210741. doi:10.1098/rsif.2021.0741
12. Garm, A.; Watling, L. The crustacean integument: setae, setules, and other ornamentation. In *The Natural History of the Crustacea;* Thiel, M.; Watling, L., Eds.; Oxford University Press: Oxford, UK, 2013; Vol. 1, pp 167–198. doi:10.1093/acprof:osobl/9780195398038.003.0006
13. Riisgård, H. U. Filter-feeding mechanisms in crustaceans. Lifestyles and feeding biology. In *The Natural History of the Crustacea;* Thiel, M.; Watling, L., Eds.; Oxford University Press: Oxford, UK, 2015; Vol. 2, pp 418–463.
14. Rubenstein, D. I.; Koehl, M. A. R. *Am. Nat.* **1977,** *111,* 981–994. doi:10.1086/283227
15. LaBarbera, M. *Am. Zool.* **1984,** *24,* 71–84. doi:10.1093/icb/24.1.71
16. Jumars, P. A. *Concepts in biological oceanography. An interdisciplinary primer;;* Oxford University Press: Oxford, UK, 1993.
17. Vogel, S. *Life in moving fluids. The physical biology of flow;* Princeton University Press: Princeton, NJ, USA, 1994.
18. Shimeta, J.; Koehl, M. A. R. *J. Exp. Mar. Biol. Ecol.* **1997,** *209,* 47–73. doi:10.1016/s0022-0981(96)02684-6
19. Rosenberg, G. G. *Limnol. Oceanogr.* **1980,** *25,* 738–742. doi:10.4319/lo.1980.25.4.0738
20. Paffenhöfer, G.-A.; Strickler, J. R.; Alcaraz, M. *Mar. Biol. (Heidelberg, Ger.)* **1982,** *67,* 193–199. doi:10.1007/bf00401285
21. Wägele, J. W. *Philos. Trans. R. Soc., B* **1987,** *316,* 429–458. doi:10.1098/rstb.1987.0031
22. Gerritsen, J.; Porter, K. G.; Strickler, J. R. *Bull. Mar. Sci.* **1988,** *43,* 366–376.
23. Hamner, W. M.; Hamner, P. P. *Can. J. Fish. Aquat. Sci.* **2000,** *57* (Suppl. 3), 192–202. doi:10.1139/f00-195
24. Garm, A.; Høeg, J. T. *Biol. Bull. (Chicago, IL, U. S.)* **2001,** *200,* 281–297. doi:10.2307/1543510
25. Garm, A.; Hallberg, E.; Høeg, J. T. *Biol. Bull. (Chicago, IL, U. S.)* **2003,** *204,* 126–137. doi:10.2307/1543548
26. Garm, A. *J. Morphol.* **2004,** *260,* 85–100. doi:10.1002/jmor.10213
27. Gonçalves, R. J.; van Someren Gréve, H.; Couespel, D.; Kiørboe, T. *Mar. Ecol.: Prog. Ser.* **2014,** *517,* 61–74. doi:10.3354/meps11039
28. Giuffre, C.; Hinow, P.; Jiang, H.; Strickler, J. R. *Sci. Rep.* **2019,** *9,* 17742. doi:10.1038/s41598-019-54264-1
29. Koehl, M. A. R.; Strickier, J. R. *Limnol. Oceanogr.* **1981,** *26,* 1062–1073. doi:10.4319/lo.1981.26.6.1062
30. Gerritsen, J.; Porter, K. G. *Science* **1982,** *216,* 1225–1227. doi:10.1126/science.216.4551.1225
31. Gophen, M.; Geller, W. *Oecologia* **1984,** *64,* 408–412. doi:10.1007/bf00379140
32. Ganf, G. G.; Shiel, R. J. *Aust. J. Mar. Freshwater Res.* **1985,** *36,* 371–381. doi:10.1071/mf9850371

33. Monger, B. C.; Landry, M. R. *Mar. Ecol.: Prog. Ser.* **1990,** *65,* 123–140. doi:10.3354/meps065123
34. Garm, A.; Høeg, J. T. *Mar. Biol. (Heidelberg, Ger.)* **2000,** *137,* 123–138. doi:10.1007/s002270000318
35. Koehl, M. A. R. *J. Biomech.* **2004,** *37,* 789–795. doi:10.1016/j.jbiomech.2003.06.001
36. Geierman, C.; Emlet, R. *J. Exp. Mar. Biol. Ecol.* **2009,** *379,* 68–76. doi:10.1016/j.jembe.2009.08.003
37. Garm, A. *Mar. Biol. (Heidelberg, Ger.)* **2005,** *147,* 1179–1190. doi:10.1007/s00227-005-0020-7
38. Vittori, M.; Srot, V.; Bussmann, B.; Predel, F.; van Aken, P. A.; Štrus, J. *Micron* **2018,** *112,* 26–34. doi:10.1016/j.micron.2018.06.009
39. Visser, A. W. *Mar. Ecol.: Prog. Ser.* **2001,** *222,* 1–24. doi:10.3354/meps222001
40. Yen, J.; Okubo, A. *Hydrobiologia* **2002,** *480,* 165–173. doi:10.1023/a:1021249521259
41. Shen, X.; Yao, X.; Marcos; Fu, H. C. *Limnol. Oceanogr.* **2021,** *66,* 4096–4111. doi:10.1002/lno.11945
42. Cannon, H. G. *Br. J. Exp. Biol.* **1928,** *6,* 131–144. doi:10.1242/jeb.6.2.131
43. Marshall, S. M.; Orr, A. P. *J. Mar. Biol. Assoc. U. K.* **1966,** *46,* 513–530. doi:10.1017/s0025315400033312
44. Boyd, C. M. *Limnol. Oceanogr.* **1976,** *21,* 175–180. doi:10.4319/lo.1976.21.1.0175
45. Nival, P.; Nival, S. *Limnol. Oceanogr.* **1976,** *21,* 24–38. doi:10.4319/lo.1976.21.1.0024
46. Nival, P.; Nival, S. *Limnol. Oceanogr.* **1979,** *24,* 995–998. doi:10.4319/lo.1979.24.5.0995
47. Price, H. J.; Paffenhöfer, G.-A. *Limnol. Oceanogr.* **1986,** *31,* 189–194. doi:10.4319/lo.1986.31.1.0189
48. Hansen, B.; Tiselius, P. *J. Plankton Res.* **1992,** *14,* 821–834. doi:10.1093/plankt/14.6.821
49. Kiørboe, T.; Saiz, E. *Mar. Ecol.: Prog. Ser.* **1995,** *122,* 135–145. doi:10.3354/meps122135
50. Kiørboe, T. *Sci. Mar.* **1997,** *61,* 141–158.
51. Kiørboe, T. *A mechanistic approach to plankton ecology;* Princeton University Press: Princeton, NJ, USA, 2008. doi:10.1515/9780691190310
52. Jansen, S. Feeding behaviour of calanoid copepods and analyses of their faecal pellets. Ph.D. Thesis, Universität Bremen, Bremen, Germany, 2006.
53. Tiselius, P.; Saiz, E.; Kiørboe, T. *Limnol. Oceanogr.* **2013,** *58,* 1657–1666. doi:10.4319/lo.2013.58.5.1657
54. Kadiene, E. U.; Ouddane, B.; Hwang, J.-S.; Souissi, S. *Sci. Rep.* **2019,** *9,* 9492. doi:10.1038/s41598-019-45987-2
55. Michels, J.; Gorb, S. N. *J. Microsc. (Oxford, U. K.)* **2012,** *245,* 1–16. doi:10.1111/j.1365-2818.2011.03523.x
56. Michels, J.; Gorb, S. N. *Beilstein J. Nanotechnol.* **2015,** *6,* 674–685. doi:10.3762/bjnano.6.68
57. Michels, J. Confocal laser scanning microscopy – detailed three-dimensional morphological imaging of marine organisms. In *Imaging marine life: macrophotography and microscopy approaches for marine biology;* Reynaud, E. G., Ed.; Wiley-VCH: Weinheim, Germany, 2013; pp 69–91. doi:10.1002/9783527675418.ch4
58. Peisker, H.; Michels, J.; Gorb, S. N. *Nat. Commun.* **2013,** *4,* 1661. doi:10.1038/ncomms2576
59. Gorb, S. N. *Am. Entomol.* **2005,** *51,* 31–35. doi:10.1093/ae/51.1.31
60. Gorb, S. N. *Philos. Trans. R. Soc., A* **2008,** *366,* 1557–1574. doi:10.1098/rsta.2007.2172
61. Büscher, T. H.; Gorb, S. N. *Beilstein J. Nanotechnol.* **2021,** *12,* 725–743. doi:10.3762/bjnano.12.57
62. Filippov, A. E.; Gorb, S. N. *Combined Discrete and Continual Approaches in Biological Modelling;* Springer: Cham, Switzerland, 2020. doi:10.1007/978-3-030-41528-0
63. Monaghan, J. J. *Comput. Phys. Commun.* **1988,** *48,* 89–96. doi:10.1016/0010-4655(88)90026-4
64. Pöschel, T.; Schwager, T. *Computational granular dynamics: Models and algorithms;* Springer: Berlin, Germany, 2005.
65. Hoover, W. G. *Smooth particle applied mechanics. The state of the art;* Advanced Series in Nonlinear Dynamics, Vol. 25; World Scientific Publishing: Singapore, 2006. doi:10.1142/6218
66. Radjai, F.; Dubois, F. *Discrete-element modeling of granular materials;* Wiley-ISTE: London, UK, 2011.
67. Dmitriev, A. I.; Nikonov, A. Y.; Filippov, A. E.; Psakhie, S. G. *Phys. Mesomech.* **2019,** *22,* 375–381. doi:10.1134/s1029959919050047
68. Filippov, A. E.; Popov, V. L. *Facta Univ., Ser.: Mech. Eng.* **2023,** in press. doi:10.22190/fume220327020f
69. Youtube, Strickler Lab. http://www.youtube.com/watch?v=5RZwLbRd3b4 (accessed April 11, 2023).

License and Terms

This is an open access article licensed under the terms of the Beilstein-Institut Open Access License Agreement (https://www.beilstein-journals.org/bjnano/terms), which is identical to the Creative Commons Attribution 4.0 International License (https://creativecommons.org/licenses/by/4.0). The reuse of material under this license requires that the author(s), source and license are credited. Third-party material in this article could be subject to other licenses (typically indicated in the credit line), and in this case, users are required to obtain permission from the license holder to reuse the material.

The definitive version of this article is the electronic one which can be found at:
https://doi.org/10.3762/bjnano.14.50